

STATUS OF THESIS

Title of thesis

A Novel Approach to The Fabrication of Aluminium Foam Through Pressure Assisted High-Frequency Induction Heated Sintering Dissolution Process (PASDP)

I, **MAZLI BIN MUSTAPHA**, hereby allow my thesis to be placed at the Information Resource Centre (IRC) of Universiti Teknologi PETRONAS (UTP) with the following conditions:

1. The thesis becomes the property of UTP.
2. The IRC of UTP may make copies of the thesis for academic purposes only.
3. The thesis is classified as:

☐

Confidential

☒

Non-confidential

If this thesis is confidential, please state the reason:

The contents of the thesis will remain confidential for _____ years.

Remarks on disclosure:

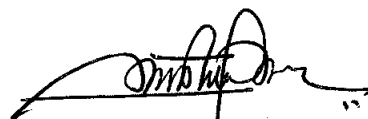
Endorsed by



Signature of Author

Permanent Address: AMREC, SIRIM Berhad
Lot 34, Jalan Hi-Tech 2/3, Kulim Hi-Tech Park
09000 Kulim, Kedah

Date: 18/06/2010



Signature of Supervisor
AP. Dr. Othman Mamat

Date: 18/06/2010

UNIVERSITI TEKNOLOGI PETRONAS

A NOVEL APPROACH TO THE FABRICATION OF ALUMINIUM FOAM
THROUGH PRESSURE ASSISTED HIGH-FREQUENCY INDUCTION
HEATED SINTERING DISSOLUTION PROCESS (PASDP)

by

MAZLI BIN MUSTAPHA

The undersigned certify that they have read, and recommend to the Postgraduate Studies Programme for acceptance this thesis for the fulfilment of the requirements for the degree stated.


Signature:



Main Supervisor:

Assoc. Prof. Dr. Othman Mamat


Signature:



Co-Supervisor:

Assoc. Prof. Dr. Patthi Hussain

Signature:



Head of Department:

Dr. Ahmad Majdi Abdul Rani

Date:

15.6.2010

Dr Ahmad Majdi Abdul Rani
Head of Department/Senior Lecturer
Mechanical Engineering Department
Universiti Teknologi PETRONAS
Bandar Seri Iskandar 31750 Tronoh
Perak Darul Ridzuan, Malaysia

A NOVEL APPROACH TO THE FABRICATION OF ALUMINIUM FOAM
THROUGH PRESSURE ASSISTED HIGH-FREQUENCY INDUCTION
HEATED SINTERING DISSOLUTION PROCESS (PASDP)

By

MAZLI BIN MUSTAPHA

A Thesis

Submitted to the Postgraduate Studies Programme
as a Requirement for the Degree of

DOCTOR OF PHILOSOPHY
MECHANICAL ENGINEERING
UNIVERSITI TEKNOLOGI PETRONAS
BANDAR SERI ISKANDAR,
PERAK

JUNE 2010

DECLARATION OF THESIS

Title of thesis

A Novel Approach to The Fabrication of Aluminium Foam Through Pressure Assisted High-Frequency Induction Heated Sintering Dissolution Process (PASDP)

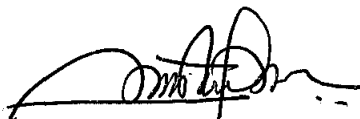
I, MAZLI BIN MUSTAPHA, hereby declare that the thesis is based on my original work except for quotations and citations which have been duly acknowledged. I also declare that it has not been previously or concurrently submitted for any other degree at UTP or other institutions.



Signature of Author
Permanent Address: AMREC, SIRIM Berhad
Lot 34, Jalan Hi-Tech 2/3, Kulim Hi-Tech Park
09000 Kulim, Kedah

Date: 18/06/2010

Witnessed by



Signature of Supervisor
AP. Dr. Othman Mamat

Date: 18/06/2010

ACKNOWLEDGEMENTS

In the name of ALLAH, most Gracious, the most Merciful

All the praises and thanks to ALLAH

Frankly speaking, the space given here is indeed not enough for me to express my deepest gratitude to the people that have contributed the most in completing my phd work and at the end to make this thesis possible. I will try my best to convey many thanks to these good people and may ALLAH bless you all.

First in place, I would like to thank to my very friendly supervisor, Assoc. Prof. Dr. Othman Mamat for his great wisdom and expertise, guidance and enthusiasm throughout the duration of my knowledge acquisition study in Universiti Teknologi PETRONAS. I also thank to Assoc. Prof. Dr. Patthi Hussain for his endless support, useful suggestions, constructive remarks and excellent supervision in making my way to complete my research work. Your professional and supervising skills will always be remembered by me and I have really enjoyed being under the supervision of these two outstanding people.

I am greatly indebted to the technical advisory guys lead by Mr Zuber Me and Mr Shahidan Kasim for their kind assistance and unstoppable technical advice in completing my experimental works. I would also like to extend my thanks to all members of Structural Materials Programme and to all my AMREC friends.

To my Mum and Dad, for their constant prayers, continous love and support since the day I was born, thanks for raising and teaching me so well and may ALLAH bless you two. This credit also goes to the rest of my family, my sisters Zaleha, Zapina and my only brother, Faizal.

Finally I would like to acknowledge the support provided by Malaysian Government (MOSTI) for awarding a research grant to conduct this research and the support of the AMREC, SIRIM Berhad is greatly appreciated.

ABSTRACT

It was known that it is difficult to form a metallurgical bonding in a packed aluminium (Al) powder during solid state sintering due to the encapsulation of Al by a thermo chemically stable Al_2O_3 film which hinders the mass transport mechanism by the diffusion process. The disruption of this oxide film is indeed crucial for achieving strong metallurgical bonding during solid state sintering of Al powder. This is largely due to the ability of this oxide film to serve as a hard shell which prevents the Al particle from establishing a direct contact with adjacent Al particles. This work discusses the improvement made by pressure assisted high-frequency induction heated sintering dissolution process (PASDP) as opposed to the solid state sintering dissolution process (SSSDP) which was used in producing a much improved open celled Al foam. In the preparation of PASDP Al foam specimens, the Al powder and the sodium chloride (NaCl) acting as filler material were dry-mixed together in order to prepare homogenously mixture. The blended mixture was then subjected to pressure assisted sintering in which a pressure beyond atmospheric level is externally applied to the specimen during high-frequency induction heated sintering. The embedded filler material was then dissolved in order to leave behind an open-celled Al with the same chemical composition as that of the original Al powder. The final material is highly porous and has an interconnected porosity network. The structure of the resulting material has three levels of porosity (i.e. main cells, windows and microporosity). The cell morphology and the size of Al foam closely match those of the filler materials used. The X-ray diffraction analysis shows that as the content of NaCl is increased to the volume fraction of 60%, no compound of NaCl presents in the foam. The improvement of this PASDP technique leads to an aluminium foam possessing a high dense of cell wall which can be attained in a much shorter time and possesses superior mechanical properties. The influence of processing parameters on the physical and mechanical of the fabricated foams were studied. The compressibility behaviour of sodium chloride / aluminium (NaCl/Al) specimen with different amount of filler material content was investigated. The Heckel equation was used to assume pressure effect at elevated temperature on the density of the specimen. Due to lower plastic deformation capacity, the specimen with higher content of filler material

exhibited lower compressibility. The relationship was established between the compaction pressure and the density of specimens. Williamson-Hall plot method was also applied to determine the crystallite size and lattice strain of the consolidated samples at various pressures. As can be observed, the crystallite size tends to decrease with increasing NaCl content. Results indicate that the compressive properties (i.e. compressive strength, modulus, and stress at densification) increase with compaction pressure at elevated temperature, sintering temperature and sintering time. Considering all contributing factors in forming Al foam using PASDP method, statistical evaluation utilising the Taguchi's Design of Experiments were carried out extensively to predict the optimum processing parameters in this work. The processing parameters were analysed based on the Taguchi's signal to noise ratio (S/N) and analysis of variance (ANOVA) which is a major improvement from the conventional Full Factorial Design of Experiment statistical method. Results show that the most notable factor influencing the fabrication of Al foam was the compaction at elevated temperature, followed by temperature, time and heating rate of the process. The viability of electrical conductivity as a tool for evaluating variations in morphology of PASDP Al foam and the influence of processing parameters: volume fraction of leaching agent, compaction pressure at elevated temperature, sintering temperature, sintering time and heating rate on the electrical conductivity of the final foams were investigated. It was found that all the chosen factors have significant effects on the physical and mechanical properties of the foam and Al volume fraction is the most important parameter affecting the relative electrical conductivity and relative density of the resultant foam. The findings also suggests that the relationship between relative electrical conductivity and density of the specimen does not follow the mathematical description given by Skorohod and Solonin, instead the power law seems to be a good characterization of the relationship between experimental data of electrical conductivity and density of the resultant foams. It was observed that the addition of silicon carbide, which was synthesised at lower reaction temperature using structured alteration local silica sand from the carbothermal nitridation process, improved the physical and mechanical properties of the foam.

ABSTRAK

Telah diketahui bahawa ianya amat sukar untuk pembentukan ikatan metalurgi di dalam padatan serbuk aluminium (Al) semasa proses persinteran keadaan pepejal disebabkan oleh penyalutan lapisan terma Al_2O_3 yang stabil yang menghalang mekanisme pemindahan jisim oleh proses pembauran. Penggangguan ke atas lapisan oksida ini amat kritikal untuk pencapaian ikatan metalurgi yang kuat semasa proses persinteran keadaan pepejal. Ini adalah disebabkan oleh kemampuan lapisan oksida ini bertindak sebagai cangkerang yang menghalang partikel Al daripada penubuhan sentuhan langsung dengan partikel Al yang bersebelahan. Kerja ini membincangkan penambahbaikan oleh proses persinteran bantuan tekanan kaedah rangsangan aliran elektrik frekuensi tinggi dan pembubaran (PASDP) yang boleh menghasilkan peningkatan dalam sifat aluminium berbusa jenis sel terbuka jika dibandingkan dengan proses persinteran keadaan pepejal dan pembubaran. Di dalam penyediaan spesimen berbusa tersebut, serbuk aluminium (Al) dan natrium klorida (NaCl) yang bertindak sebagai agen peresapan, telah diadunkan bersama secara kering untuk menghasilkan adunan yang sehati. Campuran tersebut kemudiannya didedahkan kepada tekanan yang melebihi paras atmosfera ketika proses persinteran yang menggunakan kaedah frekuensi tinggi. Bahan peluntur kemudiannya dilarutkan untuk meninggalkan aluminium yang mempunyai sel terbuka dan mengandungi komposisi kimia yang sama dengan serbuk aluminium yang asal. Spesimen yang dihasilkan adalah berliang sapat dan mengandungi jaringan keadaan lubang yang bersambung. Struktur bahan yang dihasilkan mengandungi lubang yang mempunyai tiga paras. (iaitu sel utama, tingkap dan lubang mikro). Keadaan permukaan sel dan saiz Al berbusa hampir menyamai partikel agen peresapan yang digunakan. Analisis pengimbas X-ray menunjukkan apabila kandungan NaCl ditingkatkan kepada 60% pecahan isipadu, tiada lagi tinggalan NaCl wujud di dalam liang bersapat. Kelebihan teknik PASDP ini membawa kepada penghasilan Al berbusa yang mempunyai dinding sel yang tumpat yang boleh dicapai di dalam jangka masa yang pendek dan ia juga memiliki sifat mekanik yang jitu. Pengaruh proses parameter keatas sifat fizikal dan mekanikal berbusa yang dibina telah dikaji. Tabiat kemampuan gabungan NaCl/Al dengan pelbagai kandungan agen pengisi juga dikaji. Persamaan Heckel

digunakan untuk mengandaikan kesan tekanan pada suhu tinggi ke atas ketumpatan spesimen tersebut. Oleh kerana kekurangan kemampuan pencacatan plastik, spesimen dengan kandungan agen pengisi yang tinggi mempamerkan sifat kemampatan yang lebih tinggi. Perhubungan di antara tekanan pemadatan dan ketumpatan specimen telah ditubuhkan. Cara Williamson-Hall telah dikaitkan untuk menentukan saiz hablur dan kekisi terikan cantuman sample pada pelbagai tekanan. Keputusan menunjukkan sifat mampatan (iaitu kekuatan mampatan, modulus dan tegasan pada kepadatan) bertambah dengan pertambahan tekanan pemadatan pada suhu tinggi, suhu dan masa persinteran. Dengan mengambil kira kesemua sumbangan faktor di dalam pembentukan Al berbusa dengan menggunakan kaedah PASDP, taksiran statistik menggunakan kaedah Taguchi telah dijalankan dengan giatnya untuk meramalkan proses parameter yang optima di dalam kerja ini. Data-data yang diperolehi telah dianalisis berdasarkan nisbah isyarat kepada bisingan Taguchi dan analisis varians (ANOVA) yang mempunyai peningkatan utama daripada kaedah faktor Penuh. Keputusan menunjukkan bahawa faktor tekanan pemadatan pada suhu tinggi paling mempengaruhi pembuatan Al berbusa diikuti dengan faktor suhu, masa dan kadar pemanasan. Kesesuaian pengaliran elektrik sebagai alat untuk penilaian variasi dalam morfologi Al berbusa PASDP dan kesan ke atas proses parameter: pecahan isipadu agen peluntur, tekanan pemadatan pada suhu tinggi, suhu persinteran, masa persinteran dan kadar pemanasan ke atas sifat pengaliran elektrik specimen berbusa juga diselidiki. Didapati bahawa semua faktor yang terpilih mempunyai kesan penting ke atas sifat fizikal dan mekanikal specimen berbusa dan didapati juga bahawa pecahan isipadu Al merupakan parameter yang terpenting yang mempengaruhi relative pengaliran elektrik dan relative ketumpatan specimen berbusa. Keputusan perolehan juga mencadangkan bahawa perhubungan di antara relatif pengaliran elektrik dan relative ketumpatan specimen tidak mengikuti huraian matematik yang dinyatakan oleh Skorohod dan Solonin, sebaliknya hukum ganda merupakan penilaian yang baik untuk mengaitkan perhubungan di antara data eksperimen yang diperolehi untuk pengaliran elektrik dan ketumpatan specimen berbusa tersebut. Telah diperhatikan bahawa penambahan silikon karbida, yang telah disintesis pada suhu tindak balas yang lebih rendah menggunakan tanah silica tempatan yang telah diubahsuaikan daripada proses karbonterma, meningkatkan sifat fizikal dan mekanikal aluminium berbusa.

COPYRIGHT PAGE

In compliance with the terms of the Copyright Act 1987 and the IP Policy of the university, the copyright of this thesis has been reassigned by the author to the legal entity of the university,

Institute of Technology PETRONAS Sdn Bhd.

Due acknowledgement shall always be made of the use of any material contained in, or derived from, this thesis.

© Mazli Bin Mustapha, 2010

Institute of Technology PETRONAS Sdn Bhd

All rights reserved.

TABLE OF CONTENTS

DECLARATION OF THESIS.....	iv
DEDICATION.....	v
ACKNOWLEDGEMENTS.....	vi
ABSTRACT.....	vii
ABSTRAK.....	ix
COPYRIGHT PAGE.....	xi
TABLE OF CONTENTS.....	xii
LIST OF TABLES.....	xvi
LIST OF FIGURES.....	xix
PREFACE.....	xlvi

Chapter

1 INTRODUCTION.....	1
1.1 Background.....	1
1.2 Problem Statement.....	1
1.3 Research Objectives.....	3
1.4 Scope of Research.....	4
1.5 Thesis Outline.....	6
2 REVIEW OF LITERATURE.....	7
2.1 Chapter overview.....	7
2.2 Introduction to metallic foam.....	7
2.3 The fabrication method of metallic foam.....	10
2.3.1 Powder Metallurgy Technique.....	10
2.3.1.1 Sintering of metal powders and fibres.....	11
2.2.1.2 Sintering of hollow metal spheres.....	12
2.2.1.3 Powder Metallurgical Space Holder Method.....	14
2.3.2 Liquid Metallurgy.....	15
2.3.2.1 Casting.....	15
2.3.2.2 Infiltration / Investment casting using water soluble preform	14
2.3.2.3 Two stage investment casting using plaster mould.....	15
2.3.3 Foaming.....	17
2.3.3.1 Direct injection of gases to metal with enhanced viscosity	18
2.3.3.2 Dissociating blowing agent.....	19
2.3.3.3 Foamable precursor produced by melt-route processing	20
2.3.3.4 Foamable precursor produced by powder metallurgy techniques	22
2.4 Review on the fabrication technique of aluminium foam at AMREC and UTP	22
2.4.1 Powder Compacting Foaming Technique.....	25
2.4.1.1 Foam synthesis.....	25
2.3.1.2 The influence of temperature on foaming process.....	26

2.4.1.3	The influence of time on foaming process.....	29
2.4.2	Sintering Dissolution Process (SDP).....	32
2.5	Compaction at elevated temperature.....	34
2.5.1	Hysteresis of the radial pressure.....	34
2.6	Taguchi's philosophy.....	39
2.6.1	Selection of an orthogonal array (OA).....	40
2.6.2	Analysis procedure for the selected orthogonal array.....	41
2.6.3	Raw data analysis.....	42
2.7	Solid state sintering.....	45
2.8	Powder fabrication – Atomization.....	48
2.9	The range of application of structural foams based on cellular metals	50
2.10	Prototype by powder compact foaming.....	53
2.11	The synthesis of ceramic reinforcement materials for Al foam from the carbothermal nitridation process using structured alteration silica sand	62
2.11.1	Exploitation of local silica sand for use in advanced material application	63
2.11.2	Exploitation of silica sand – Malaysia perspective	65
2.11.3	Processing of industrial minerals for advanced applications of silica-saturated water	67
2.11.3.1	Silicon nitride from geothermal silica	67
2.11.3.2	Silicon carbide from geothermal silica	69
2.12	Structural defects in silica during high intensity grinding process	71
2.12.1	Milling intensity in the formation of structured alteration silica sand	72
2.12.1.1	Ball to powder ratio.....	73
2.12.1.2	Milling speed.....	73
2.13	Chapter summary.....	74
3	EXPERIMENTAL PROCEDURE.....	76
3.1	Chapter overview.....	76
3.2	Raw Materials.....	77
3.3	Powder Mixing.....	79
3.4	Calculation for shrink-fitted die.....	79
3.5	Pressure assisted sintering process.....	86
3.6	Dissolution Process.....	87
3.7	Lattice strain and crystallite measurement using X-ray Diffraction	89
3.8	Electrical conductivity measurement.....	91
3.9	Morphology evaluation of foam specimen.....	92
3.10	Compressive mechanical properties determination.....	93
3.11	Statistical optimization of processing parameters for the fabrication of aluminium foam	94
3.12	Carbothermal nitridation process of mechanical milled silica sand for producing ceramic reinforcement materials	97
3.12.1	Raw material characterization.....	99
3.12.1.1	Silica sand.....	99
3.12.1.2	Carbon.....	100
3.13	Fabrication of reinforced Al foam.....	101
3.14	Chapter summary.....	101

4: RESULTS AND DISCUSSION.....	103
4.1 Chapter overview.....	103
4.2 Preliminary development of the fabrication of Al foam through pressure assisted high-frequency induction heated sintering / dissolution process (PASDP)	104
4.2.1 Morphology evolution and physical properties of SDP and PASDP Al foam	104
4.2.2 Dissolution characteristic of NaCl/Al compacts, physical behaviour and morphology evolution of PASDP Al foam	108
4.2.3 Monotonic compression test.....	112
4.3 The influence of processing parameters on the physical and mechanical properties of Al foam fabricated through pressure assisted sintering / dissolution process	114
4.3.1 The physical and compressibility behaviour of NaCl/Al compact at elevated temperature	114
4.3.2 The influence of sintering temperature on surface morphology and physical measurement on the fabricated Al foam	127
4.3.3 The influence of sintering time on surface morphology and physical measurement on the fabricated Al foam	135
4.3.4 The influence of heating rate on the physical properties of fabricated Al foam	140
4.4 The monotonic compression properties of Al foam produced by pressure assisted sintering process	143
4.4.1 The influence of compaction pressure on the compressive properties of Al foam	144
4.4.2 The influence of sintering temperature on the compressive properties of Al foam	149
4.4.3 The influence of sintering time on the compressive properties of Al foam	155
4.4.4 The influence of heating rate on the compressive properties of Al foam	160
4.4.5 The modulus and compressive strength of Al foam.....	165
4.4.6 The energy absorbing capabilities.....	176
4.5 Determination of the optimum processing parameters for the fabrication aluminium foam using Taguchi method	180
4.6 The electrical conductivity behaviour of aluminium foam.....	186
4.7 The influence of pore shape and its width of size distribution on the empirical relationship between physical and mechanical properties of Al foam	198
4.7.1 The dissolution characteristic of the NaCl in the NaCl/Al compact during leaching process	198
4.8 The effect of pore size on the electrical conductivity of aluminium foam	214
4.9 The compressive properties of Al foam of different pore size and the width of pore size distribution	218
4.7.1 Energy absorption capacity.....	234
4.10 The synthesis of ceramic reinforcement materials for Al foam from the carbothermal nitridation process using structured alteration silica sand	243

4.10.1	The effect of mechanical milling treatment on silica sand	244
4.10.2	Carbothermal nitridation process of structured silica sand	246
4.10.3	Statistical optimization for the carbothermal nitridation process of structured alteration silica sand using Taguchi's method	254
4.11	The influence of silicon carbide addition on the physical and mechanical properties of fabricated Al foam	258
4.11.1	Surface morphology of the reinforcement Al foam.....	258
4.11.2	Mechanical properties.....	261
4.12	Summary of findings.....	268
5.0	CONCLUSION AND SUGGESTION FOR FUTURE WORK.....	272
5.1	SUGGESTION FOR FUTURE WORK.....	273
	REFERENCES	276
	APPENDIX A: Record of Publications	288

LIST OF TABLES

2.1	The influence of temperature on foaming process.....	28
2.2	The properties of the fabricated closed-cell foam at different time	30
2.3	The L ₉ (3 ⁴) OA (parameters assigned) with response.....	41
2.4	A comparison of typical gas and water atomization process...	49
2.5	Comparison of various mould materials.....	62
2.6	Sources, exploitation and estimated reserves of silica sand in Malaysia	65
2.7	Composition of silica sand.....	66
2.8	Properties of Al foam from various fabrication technique.....	75
3.1	Physical parameters of different size of filler material and Al matrix	78
3.2	Estimated values of material properties at 20 °C and 650 °C..	80
3.3	Summary of calculated values for shrink-fitted die.....	85
3.4	Thermodynamics of aluminium –water reaction.....	88
3.5	Process parameters and their value at different level.....	96
3.6	The L ₉ (3 ⁴) (parameters assigned) with response.....	96
3.7	Processing parameters and their levels for orthogonal experiment	98
3.8	The L ₉ (3 ⁴) OA (parameters assigned) with response.....	99
4.1	The physical parameter of the sintered and pressure assisted sintered compacts of Al foam of volume fraction initially at 60 %	108
4.2	Variation of the fraction of the dissolved NaCl in the Al foam, 1-φ, with the NaCl/Al fraction	109
4.3	Fitting constants of the Heckel compaction equation.....	120
4.4	Variation of fraction of the dissolved NaCl in the Al foam (1-φ) at different compaction pressure	121

4.5	Crystallite size and lattice strain for PASDP Al foam obtained from Williamson-Hall method [128]	127
4.6	Variation of fraction of the dissolved NaCl in the Al foam (1- ϕ) at different sintering temperature	131
4.7	The activation energy for the formation of Al foams	135
4.8	Variation of fraction of the dissolved NaCl in the Al foam (1- ϕ) at different sintering time	136
4.9	Variation of fraction of the dissolved NaCl in the Al foam (1- ϕ) at different heating rate	141
4.10	Correlation coefficients of equations (4.4) and (4.5) for the Al foams at different processing parameters	167
4.11	Experimental results and their S/N ratios.....	181
4.12	The average effects on compressive strength of factors at each level	182
4.13	ANOVA table.....	183
4.14	Pooled ANOVA table.....	184
4.15	Estimate of the optimum condition of design.....	185
4.16	The obtained fitting parameters for the dependence of relative electrical conductivity on the relative density for different pore shape and size	217
4.17	Intensity value and d_{50} at various milling time.....	246
4.18	The influence of temperature on the reaction yield and the product composition	252
4.19	Experimental results and their S/N ratios.....	254
4.20	The average effects of factors for each level.....	255
4.21	ANOVA table.....	255
4.22	Pooled ANOVA table.....	256
4.23	Estimate of the optimum condition of design.....	256
4.24	Chemical composition of the cell wall of aluminium foam....	259
4.25	Chemical composition of the cell wall of reinforced	260

aluminium foam at point A

- 4.26 Correlation coefficients equations (4.4) & (4.5) for the Al 265
and Al-1% wt. SiC

LIST OF FIGURES

2.1	Fabrication of metallic foam by direct sintering of metal powder [41].	11
2.2	The main step involved in the fabrication of hollow spheres from a slurry containing metal powder [41].	13
2.3	A more cost effective process for the fabrication of foams made of hollow sphere [29].	13
2.4	Production of an open-cell foam by infiltration/investment casting using a water-soluble perform [41].	16
2.5	Replication of a polymer foam structure by the production and infiltration of a plaster mould [29].	17
2.6	Continuous production of metal foam sheet by direct addition of gas to a melt with enhanced viscosity [29].	19
2.7	The first step of the FORMGRIP process: melt-route production of a foamable precursor [41].	21
2.8	Processing techniques for cellular metals classified according to the state of the metal, the formation of the cellular architecture and the pore-forming ingredients [31].	24
2.9 (a)	Foaming Die: Side view.....	26
2.9 (b)	Foaming Die: Plan View.....	26
2.10 (a)	Melted metal at the base of the die.....	27
2.10 (b)	The solid samples.....	27
2.11 (a)	Cross-section of foam sample.....	27
2.11 (b)	The solid samples.....	27
2.12 (a)	Morphology of foam formed at different temperature of 750 °C	28
2.12 (b)	Morphology of foam formed at different temperature of 800 °C	28
2.12 (c)	Morphology of foam formed at different temperature of 850 °C	28
2.12 (d)	Morphology of foam formed at different temperature of 900 °C	28

2.13 (a)	Mechanism of collapsing process of foam specimen: Drainage	29
2.13 (b)	Mechanism of collapsing process of foam specimen: Coalescence	29
2.14 (a)	The morphology of the foam structure formed after 0.5 minute of foaming process	30
2.14 (b)	The morphology of the foam structure formed after 1 minutes of foaming process	30
2.14 (c)	The morphology of the foam structure formed after 2 minutes of foaming process	30
2.14 (d)	The morphology of the foam structure formed after 3 minutes of foaming process	30
2.15 (a)	The morphology of the foam structure formed after 4 mins	31
2.15 (b)	Streomicrograph of the selected area of Figure 3.2.3.2 (a) at higher magnification	31
2.15 (c)	The morphology of the foam structure formed after 6 mins	31
2.15 (d)	Streomicrograph of the selected area of Figure 3.2.3.2 (c) at higher magnification	31
2.15 (e)	The morphology of the foam structure formed after 8 mins	31
2.15 (f)	Streomicrograph of the selected area of Figure 3.2.3.2 (e) at higher magnification	31
2.16 (a)	The streomicrograph of the foam body at different sintering temperature of 600 °C	32
2.16 (b)	The streomicrograph of the foam body at different sintering temperatures of 660 °C	32
2.16 (c)	The streomicrograph of the foam body at different sintering temperature of 670 °C	32
2.16 (d)	The streomicrograph of the foam body at different sintering temperature of 680 °C	32
2.17 (a)	Images (SEM) of SDP Al foam showing the existence of individual Al particles at X500	33
2.17 (b)	Images (SEM) of SDP Al foam showing the existence of individual Al particles at X1000	33

2.18	Relationship between radial and axial pressure occurring in a cylindrical metal plug inside a rigid die during a cycle of loading and releasing the axial pressure	36
2.19	Possible diffusion path for mass transfer during sintering process [24]	45
2.20	The two classes of sintering mechanism as applied to the sphere sintering particles model (E-C = evaporation-condensation, SD = surface diffusion, VD = volume diffusion, PF = plastic flow, GB = grain boundary) [25]	46
2.21	Schematic diagram of the pore structure changes and grain boundary development during sintering [24]	47
2.22	Atomiser facility at pilot plant in AMREC.....	49
2.23	Applications of cellular metals grouped according to the degree of open porosity needed and whether the application is functional or structural	50
2.24	Components of metal foam developed by Fraunhofer IFAM [74]	51
2.25	Typical loading of car body structure (Audi A8): strategy for structural foam reinforcements [76]	52
2.26 (a)	The melting furnace.....	54
2.26 (b)	Simple foam parts [74].....	54
2.27 (a)	Batch type furnace [74].....	56
2.27 (b)	Continuous furnace [74].....	56
2.28	A laboratory beaker which is to be filled to a certain level during a given time period [30]	58
2.29	Losses in the system [30].....	58
2.30	Retaining heat at equilibrium (steady state), inflow must match outflow	59
2.31	Thermal losses for the mould [30].....	60
2.32	Deposit of silica sand at Johore Silica processing plant at Bandar Penawar	64
2.33 (a)	Johore Silica processing plant : Separator for use in	66

	reducing iron and other heavy mineral content in the silica sand	
2.33 (b)	Johore Silica processing plant : Vibrator for sieving silica sand into various mesh sizes	66
2.34	Thermodynamic analysis of $\text{SiO}_2 + 2\text{C}$ in Nitrogen.....	68
2.35	Thermodynamic analysis of $\text{SiO}_2 + 3\text{C}$ in Nitrogen.....	69
2.36	TGA/MS analysis of $\text{SiO}_2 + 3\text{C}$ in Argon showing DTG and evolved Carbon Monoxide data. Heating rate 2°Cmin^{-1}	70
2.37	Thermodynamic analysis of rate of CO evolution for $\text{SiO}_2 + 3\text{C}$ in Argon	71
2.38	Schematic view of motion of powder mixture and grinding balls	72
3.1	Process flow for the fabrication of Aluminium foam using PASDP process	76
3.2 (a)	Morphology of Al powders.....	77
3.2 (b)	Particle size distribution of Al powders.....	77
3.3 (a)	Different size of filler material of TS-NaCl.....	78
3.3 (b)	Different size of filler material of AC-NaCl.....	78
3.3 (c)	Different size of filler material of HI-NaCl.....	78
3.3 (d)	Different size of filler material of SA-NaCl.....	78
3.4	Three dimensional mixer.....	79
3.5	Dimension of carbide/steel tool.....	81
3.6	High-frequency induction heated system.....	86
3.7	Valhalla resistivity meter.....	91
3.8	LEO Scanning electron microscope arrangement.....	92
3.9	Typical compression curves obtained on metallic foams which present a complete three-stage showing the “elastic/plastic” loading (1), the progressive plastic deformation (2) and the densification (3)	93

3.10	Enlarge portion of the beginning of the curve illustrating the methods used for evaluating the yield strength and the elastic modulus using the specimen loading	94
3.11	Ishikawa cause effect diagram for Pressure assisted sintering – dissolution process for Al foam	95
3.12	Process flow for the carbothermal nitridation process using structured alteration silica sand	98
3.13 (a)	SEM micrograph of Un-MM silica sand.....	100
3.13 (b)	SEM micrograph of MM silica sand.....	100
3.14 (a)	XRD spectrum of Un-MM silica sand.....	100
3.14 (b)	XRD spectrum of MM silica sand.....	100
3.15 (a)	SEM micrograph of ball milled carbon.....	101
3.15 (b)	XRD spectrum of ball milled carbon.....	101
4.1(a)	Images (SEM) of the cell wall of Al matrix for SDP foam	104
4.1(b)	Images (SEM) of the cell wall of Al matrix for PASDP foam	104
4.2 (a)	Images (SEM) of sintered aluminium foam of which the sample was interrupted after undergone 2 hours leaching process in order to avoid the collapse of the structure showing the existence of individual aluminium particle indicating that no diffusion process occurred during solid state sintering at	106
4.2 (b)	Images (SEM) of sintered aluminium foam of which the sample was interrupted after undergone 2 hours leaching process in order to avoid the collapse of the structure showing the existence of individual aluminium particle indicating that no diffusion process occurred during solid state sintering at x250)	106
4.2 (c)	Images (SEM) of sintered aluminium foam of which the sample was interrupted after undergone 2 hours leaching process in order to avoid the collapse of the structure showing voids between the original Al particles at x1000	106
4.2 (d)	Images (SEM) of sintered aluminium foam of which the sample was interrupted after undergone 2 hours leaching process in order to avoid the collapse of the structure showing voids between the original Al particles at x2000	106

4.3 (a)	Photograph of PASDP Al foam of plan view.....	107
4.3 (b)	Photograph of PASDP Al foam of cross section view.....	107
4.3 (c)	SEM images of PASDP Al foam of selected area at x150 showing the cell and window	107
4.3 (d)	SEM images of PASDP Al foam of selected area at x1000 showing the quality of cell wall	107
4.4	Variation of density and porosity of PASDP compact with NaCl volume fraction	108
4.5	XRD spectrum of NaCl/Al composite at different volume fraction after dissolution process	110
4.6	Variation of density and porosity of pressure assisted sintered compact with NaCl/Al volume fraction after dissolution process	111
4.7 (a)	SEM micrographs of 30%vol NaCl/Al foam with different relative density made by pressure assisted sintering technique	112
4.7 (b)	SEM micrographs of 40%vol NaCl/Al foam with different relative density made by pressure assisted sintering technique	112
4.7 (c)	SEM micrographs of 50%vol NaCl/Al foam with different relative density made by pressure assisted sintering technique	112
4.7 (d)	SEM micrographs of 60%vol NaCl/Al foam with different relative density made by pressure assisted sintering technique	112
4.8	Compressive stress-strain curve of the Al foam with different NaCl/Al volume fraction	113
4.9 (a)	Photographs of pressure assisted sintered NaCl/Al compact at different compaction pressure of 10 MPa	115
4.9 (b)	Photographs of pressure assisted sintered NaCl/Al compact at different compaction pressure of 15 MPa	115
4.9 (c)	Photographs of pressure assisted sintered NaCl/Al compact at different compaction pressure of 130 MPa (plan view)	115
4.9 (d)	Photographs of pressure assisted sintered NaCl/Al compact	115

	at different compaction pressure of 130 MPa (side view)	
4.9 (e)	Photographs of pressure assisted sintered NaCl/Al compact at different compaction pressure of 20 MPa (plan view)	115
4.9 (f)	Photographs of pressure assisted sintered NaCl/Al compact at different compaction pressure of 20 MPa (side view)	115
4.10	Variation of porosity and density of PASDP composites with compaction pressure of different NaCl particle size and its widths of size distribution	116
4.11	Variation of porosity and density of PASDP composites with NaCl/Al volume ratio of different NaCl particle size and its widths of size distribution	116
4.12	Variation of density of NaCl/Al specimen with NaCl/Al volume fraction at different compaction pressure	117
4.13	Variation of porosity of pressure assisted sintered NaCl/Al specimen with NaCl/Al volume fraction at different compaction pressure	119
4.14	Relative density vs compaction pressure fitted to Heckel equation for NaCl/Al blended powders with different volume fraction	120
4.15 (a)	Stereomacrograph of Al foam with relative density 0.2.....	122
4.15 (b)	SEM image of PASDP Al foam of selected area at magnification of 100X	122
4.16 (a)	Photographs of PASDP Al foam (after dissolution process) using different size and its width of size distribution of filler material for TS-NaCl/Al	123
4.16 (b)	Photographs of PASDP Al foam (after dissolution process) using different size and its width of size distribution of filler material for AC-NaCl/Al	123
4.16 (c)	Photographs of PASDP Al foam (after dissolution process) using different size and its width of size distribution of filler material for HI-NaCl/Al (d) SA-NaCl/Al	123
4.16 (d)	Photographs of PASDP Al foam (after dissolution process) using different size and its width of size distribution of filler material for SA-NaCl/Al	123
4.17 (a)	SEM images of cell wall of PASDP Al foam with a porosity of 80% at x250.	124

4.17 (b)	SEM images of cell wall of PASDP Al foam with a porosity of 80% at x1000.	124
4.18 (a)	Images (SEM) of the Al matrix (compacted at 15 MPa) showing voids between the original Al particles at x500	124
4.18 (b)	Images (SEM) of the SDP Al matrix showing voids between the original Al particles at x1000.	124
4.19	Variation of density and porosity of NaCl/Al specimens sintered at 620 °C for 30 min with NaCl/Al volume ratio at different compaction pressure after dissolution process	125
4.20	Williamson-Hall plot for Al foam with different NaCl/Al volume ratio	126
4.21 (a)	Partially melting of the foam which was pressed and sintered at 630 °C at 500X	128
4.21 (b)	Partially melting of the foam which was pressed and sintered at 630 °C at 1000X	128
4.21 (c)	Partially melting of the foam which was pressed and sintered at 630 °C at 2000X	128
4.21 (d)	Partially melting of the foam which was pressed and sintered at 630 °C at 3000X	128
4.22	XRD spectrum of NaCl/Al composites at different volume fraction, fabricated at sintering temperature of 620°C for 30 min, after dissolution process	132
4.23	Variation of density and porosity of specimens with NaCl/Al volume fraction at various sintering temperature after dissolution process	132
4.24 (a)	Images (SEM) of the formation of the interconnected metallic framework of the Al cell wall, which becomes denser as sintering temperature is increased, at 570 °C	133
4.24 (b)	Images (SEM) of the formation of the interconnected metallic framework of the Al cell wall, which becomes denser as sintering temperature is increased, at 580 °C	133
4.24 (c)	Images (SEM) of the formation of the interconnected metallic framework of the Al cell wall, which becomes denser as sintering temperature is increased, at 590 °C	133

4.24 (d)	Images (SEM) of the formation of the interconnected metallic framework of the Al cell wall, which becomes denser as sintering temperature is increased, at 600 °C	133
4.24 (e)	Images (SEM) of the formation of the interconnected metallic framework of the Al cell wall, which becomes denser as sintering temperature is increased, at 610 °C	133
4.24 (f)	Images (SEM) of the formation of the interconnected metallic framework of the Al cell wall, which becomes denser as sintering temperature is increased, at 620 °C	133
4.25	The influence of sintering temperature on the grain size of Al foams at various volume fraction compacted at 120 MPa	134
4.26	Arrhenius plot of log grain size against reciprocal of sintering temperature for Al foams at various volume fraction	134
4.27	XRD spectrum of 60% vol. NaCl/Al composites at different sintering time after the dissolution process	137
4.28	Variation of density and porosity of specimens with NaCl/Al volume fraction at various sintering time after dissolution process	137
4.29	The influence of sintering time on the crystallite size of Al foams at various relative densities compacted at 120 MPa	138
4.30 (a)	Images (SEM) of the formation of the interconnected metallic framework of the Al cell wall, which becomes denser as sintering time is increased, for 5 minutes	139
4.30 (b)	Images (SEM) of the formation of the interconnected metallic framework of the Al cell wall, which becomes denser as sintering time is increased, for 10 minutes	139
4.30 (c)	Images (SEM) of the formation of the interconnected metallic framework of the Al cell wall, which becomes denser as sintering time is increased, 15 minutes	139
4.30 (d)	Images (SEM) of the formation of the interconnected metallic framework of the Al cell wall, which becomes denser as sintering time is increased, for 20 minutes	139
4.30 (e)	Images (SEM) of the formation of the interconnected metallic framework of the Al cell wall, which becomes denser as sintering time is increased, for 25 minutes	139

4.30 (f)	Images (SEM) of the formation of the interconnected metallic framework of the Al cell wall, which becomes denser as sintering time is increased, 30 minutes	139
4.31	XRD spectrum of 60% vol NaCl/Al composites at different heating rate after the dissolution process	142
4.32	Variation of density and porosity of specimens with NaCl/Al volume fraction at various sintering time after dissolution process	142
4.33	Compressive stress-strain curve of the Al foam with different NaCl/Al volume fraction	143
4.34	Compressive stress-strain curves at different compaction pressure sintered at 620 °C for 30 minutes	144
4.35	Enlarge portion of the beginning of the compressive stress-strain curves at different compaction pressure sintered at 620 °C for 30 minutes	145
4.36	Variation of compressive strength of NaCl/Al with compaction pressure at different NaCl/Al volume ratio	147
4.37	Variation of compressive modulus of NaCl/Al with compaction pressure at different NaCl/Al volume ratio	147
4.38	Variation of strength at densification of NaCl/Al with compaction pressure at different NaCl/Al volume ratio	148
4.39	Variation of deformation at densification of NaCl/Al with compaction pressure at different NaCl/Al volume ratio	148
4.40	Compressive stress-strain curves of Al foam at different sintering temperature	150
4.41	Enlarge portion of the beginning of the compressive stress-strain curves at different sintering temperature compacted at 120 MPa for 1 hour	150
4.42	Variation of compressive strength of Al foam with sintering temperature at different NaCl/Al volume fraction	153
4.43	Variation of compressive modulus of Al foam with sintering temperature at different NaCl/Al volume fraction	153
4.44	Variation of strength at densification of Al foam with sintering temperature at different NaCl/Al volume fraction	154
4.45	Variation of deformation at densification of Al foam with	154

	sintering temperature at different NaCl/Al volume fraction	
4.46 (a)	Compressive stress-strain curves of Al foam at different sintering time	156
4.46 (b)	Enlarge portion of the beginning of the compressive stress-strain curves of Al foam at different sintering time	156
4.47	Variation of compressive strength of NaCl/Al with sintering time at different NaCl/Al volume ratio	158
4.48	Variation of compressive modulus of NaCl/Al with sintering time at different NaCl/Al volume ratio	158
4.49	Variation of strength at densification of NaCl/Al with sintering time at different NaCl/Al volume ratio	159
4.50	Variation of deformation at densification of NaCl/Al with sintering time at different NaCl/Al volume ratio	154
4.51	Compressive stress-strain curves at different heating rate	160
4.52	Enlarge portion of the beginning of the compressive stress-strain curves at different heating rate	1161
4.53	Variation of compressive strength of NaCl/Al with heating rate at different NaCl/Al volume fractions	163
4.54	Variation of compressive modulus of NaCl/Al with heating rate at different NaCl/Al volume fractions	163
4.55	Variation of strength at densification of NaCl/Al with heating rate at different NaCl/Al volume fractions	164
4.56	Variation of deformation at densification of NaCl/Al with heating rate at different NaCl/Al volume fractions	164
4.57 (a)	Relative Young's modulus of Al foam as function of relative density at compaction pressure of 20 MPa	168
4.57 (b)	Relative Young's modulus of Al foam as function of relative density at compaction pressure of 40 MPa	168
4.57 (c)	Relative Young's modulus of Al foam as function of relative density at compaction pressure of 60 MPa	168
4.57 (d)	Relative Young's modulus of Al foam as function of relative density at compaction pressure of 80 MPa	168
4.57 (e)	Relative Young's modulus of Al foam as function of	168

	relative density at compaction pressure of 100 MPa	
4.57 (f)	Relative Young's modulus of Al foam as function of relative density at compaction pressure of 120 MPa	168
4.58 (a)	Relative Young's modulus of Al foam as function of relative density at sintering temperature of 570 °C	169
4.58 (b)	Relative Young's modulus of Al foam as function of relative density at sintering temperature of 580 °C	169
4.58 (c)	Relative Young's modulus of Al foam as function of relative density at sintering temperature of 590 °C	169
4.58 (d)	Relative Young's modulus of Al foam as function of relative density at sintering temperature of 600 °C	169
4.58 (e)	Relative Young's modulus of Al foam as function of relative density at sintering temperature of 610 °C	169
4.58 (f)	Relative Young's modulus of Al foam as function of relative density at sintering temperature of 620 °C	169
4.59 (a)	Relative Young's modulus of Al foam as function of relative density at sintering time of 5 minutes	170
4.59 (b)	Relative Young's modulus of Al foam as function of relative density at sintering time of 10 minutes	170
4.59 (c)	Relative Young's modulus of Al foam as function of relative density at sintering time of 15 minutes	170
4.59 (d)	Relative Young's modulus of Al foam as function of relative density at sintering time of 20 minutes	170
4.59 (e)	Relative Young's modulus of Al foam as function of relative density at sintering time of 25 minutes	170
4.59 (f)	Relative Young's modulus of Al foam as function of relative density at sintering time of 30 minutes	170
4.60 (a)	Relative Young's modulus of Al foam as function of relative density at heating rate of 5 °C/min	171
4.60 (b)	Relative Young's modulus of Al foam as function of relative density at heating rate of 10 °C/min	171
4.60 (c)	Relative Young's modulus of Al foam as function of relative density at heating rate of 15 °C/min	171

4.60 (d)	Relative Young's modulus of Al foam as function of relative density at heating rate of 20 °C/min	171
4.60 (e)	Relative Young's modulus of Al foam as function of relative density at heating rate of 25 °C/min	171
4.60 (f)	Relative Young's modulus of Al foam as function of relative density at heating rate of 30 °C/min	171
4.61 (a)	Relative compressive strength of Al foam as function of relative density at compaction pressure of 20 MPa	172
4.61 (b)	Relative compressive strength of Al foam as function of relative density at compaction pressure of 40 MPa	172
4.61 (c)	Relative compressive strength of Al foam as function of relative density at compaction pressure of 60 MPa	172
4.61 (d)	Relative compressive strength of Al foam as function of relative density at compaction pressure of 80 MPa	172
4.61 (e)	Relative compressive strength of Al foam as function of relative density at compaction pressure of 100 MPa	172
4.61 (f)	Relative compressive strength of Al foam as function of relative density at compaction pressure of 120 MPa	172
4.62 (a)	Relative compressive strength of Al foam as function of relative density at sintering temperature of 570 °C	173
4.62 (b)	Relative compressive strength of Al foam as function of relative density at sintering temperature of 580 °C	173
4.62 (c)	Relative compressive strength of Al foam as function of relative density at sintering temperature of 590 °C	173
4.62 (d)	Relative compressive strength of Al foam as function of relative density at sintering temperature of 600 °C	173
4.62 (e)	Relative compressive strength of Al foam as function of relative density at sintering temperature of 610 °C	173
4.62 (f)	Relative compressive strength of Al foam as function of relative density at sintering temperature of 620 °C	173
4.63 (a)	Relative compressive strength of Al foam as function of relative density at sintering time of 5 minutes	174

4.63 (b)	Relative compressive strength of Al foam as function of relative density at sintering time of 10 minutes	174
4.63 (c)	Relative compressive strength of Al foam as function of relative density at sintering time of 15 minutes	174
4.63 (d)	Relative compressive strength of Al foam as function of relative density at sintering time of 20 minutes	174
4.63 (e)	Relative compressive strength of Al foam as function of relative density at sintering time of 25 minutes	174
4.63 (f)	Relative compressive strength of Al foam as function of relative density at sintering time of 30 minutes	174
4.64 (a)	Relative compressive strength of Al foam as function of relative density at heating rate of 5 °C/min	175
4.64 (b)	Relative compressive strength of Al foam as function of relative density at heating rate of 10 °C/min	175
4.64 (c)	Relative compressive strength of Al foam as function of relative density at heating rate of 15 °C/min	175
4.64 (d)	Relative compressive strength of Al foam as function of relative density at heating rate of 20 °C/min	175
4.64 (e)	Relative compressive strength of Al foam as function of relative density at heating rate of 25 °C/min	175
4.64 (f)	Relative compressive strength of Al foam as function of relative density at heating rate of 30 °C/min	175
4.65	The energy absorbing efficiency, η , is the ratio between absorbed energy of the material and absorbed energy of an ideal plastic material in a certain strain range	177
4.66	Variation of energy absorbed with compressive strength of different NaCl/Al volume fraction at different compaction pressure	178
4.67	Variation of energy absorbed with compressive strength of different NaCl/Al volume fraction at different sintering temperature	178
4.68	Variation of energy absorbed with compressive strength of different NaCl/Al volume fraction at different sintering time	179
4.69	Variation of energy absorbed with compressive strength of	179

different NaCl/Al volume fraction at different heating

4.70	Variation of relative electrical conductivity of NaCl/Al pressure assisted sintering foams (at 620 °C for 30 min) with compaction pressure at different NaCl/Al volume fraction	187
4.71	Variation of relative electrical conductivity of NaCl/Al pressure assisted sintering foams (at compaction pressure of 120 MPa for 30 min) with sintering temperature at different NaCl/Al volume fraction	188
4.72	Variation of relative electrical conductivity of NaCl/Al pressure assisted sintering foams (at compaction pressure of 120 MPa and at 620 °C) with sintering time at different NaCl/Al volume ratio	189
4.73	Variation of relative electrical conductivity of NaCl/Al pressure assisted sintering foams (at compaction pressure of 120 MPa and at 620 °C) with heating rate at different NaCl/Al volume fraction	190
4.74	Relative electrical conductivity of foam specimens as a function of total porosity at different compaction pressure	192
4.75	Relative electrical conductivity of foam specimens as a function of total porosity at different sintering temperature	192
4.76	Relative electrical conductivity of foam specimens as a function of total porosity at different sintering time	193
4.77	Relative electrical conductivity of foam specimens as a function of total porosity at different heating rate	193
4.78	Relative electrical conductivity of foam specimens as a function of density at different compacting pressure	194
4.79	Relative electrical conductivity of foam specimens as a function of density at different sintering temperature	194
4.80	Relative electrical conductivity of foam specimens as a function of density at different sintering time	195
4.81	Relative electrical conductivity of foam specimens as a function of density at different heating rate	195
4.82	Relative electrical conductivity of foam specimens as a function of density at different compaction pressure	196
4.83	Relative electrical conductivity of foam specimens as a	196

	function of density at different sintering temperature	
4.84	Relative electrical conductivity of foam specimens as a function of density at different sintering time	197
4.85	Relative electrical conductivity of foam specimens as a function of density at different heating rate	197
4.86	Relationship between fraction of dissolved NaCl, relative foam density and NaCl/Al volume fraction for TS-NaCl/Al	199
4.87	Relationship between fraction of dissolved NaCl, relative foam density and NaCl/Al volume fraction for AC-NaCl/Al	199
4.88	Relationship between fraction of dissolved NaCl, relative foam density and NaCl/Al volume fraction for HI-NaCl/Al.	200
4.89	Relationship between fraction of dissolved NaCl, relative foam density and NaCl/Al volume fraction for SA-NaCl/Al	200
4.90 (a)	SEM images of PASDP Al foam with volume fraction initially at 80% volume fraction using different size and its width of size distribution of filler material for TS-NaCl	201
4.90 (b)	SEM images of PASDP Al foam with volume fraction initially at 80% volume fraction using different size and its width of size distribution of filler material for AC-NaCl	201
4.90 (c)	SEM images of PASDP Al foam with volume fraction initially at 80% volume fraction using different size and its width of size distribution of filler material for HI-NaCl	201
4.90 (d)	SEM images of PASDP Al foam with volume fraction initially at 80% volume fraction using different size and its width of size distribution of filler material for SA-NaCl	201
4.91 (a)	XRD spectrum of different size and its width of size distribution of filler material at different volume fraction for TS-NaCl	202
4.91 (b)	XRD spectrum of different size and its width of size distribution of filler material at different volume fraction for AC-NaCl	202
4.91 (c)	XRD spectrum of different size and its width of size distribution of filler material at different volume fraction for HI-NaCl	202
4.91 (d)	XRD spectrum of different size and its width of size	202

	distribution of filler material at different volume for SA-NaCl	
4.92 (a)	Streomicrographs of Al foam with volume fraction of 20% for TS-NaCl	203
4.92 (b)	SEM micrographs of selected area of 5.5.1.7 (a) at magnification of 100X for TS-NaCl \Al	203
4.92 (c)	Streomicrographs of Al foam with volume fraction of 20% for AC-NaCl	203
4.92 (d)	SEM micrographs of selected area of 5.5.1.7 (c) at magnification of 100X for AC-NaCl	203
4.92 (e)	Streomicrographs of Al foam with volume fraction of 20% for HI-NaCl	203
4.92 (f)	SEM micrographs of selected area of 5.5.1.7 (e) at magnification of 100X for TS-NaCl AC-NaCl HI-NaCl SA-NaCl	203
4.92 (g)	Streomicrographs of Al foam with volume fraction of 20% for SA-NaCl.	203
4.92 (h)	SEM micrographs of selected area of 5.5.1.7 (g) at magnification of 100X for SA-NaCl	203
4.93 (a)	Variation of foam density and porosity of pressure assisted sintering compact with NaCl/Al volume fraction for TS-NaCl	204
4.93 (b)	Variation of foam density and porosity of pressure assisted sintering compact with NaCl/Al volume fraction for AC-NaCl.	204
4.93 (c)	Variation of foam density and porosity of pressure assisted sintering compact with NaCl/Al volume fraction for HI-NaCl	204
4.93 (d)	Variation of foam density and porosity of pressure assisted sintering compact with NaCl/Al volume fraction for SA-NaCl	204
4.94 (a)	SEM micrographs of 60% TS-NaCl/Al foams with different relative density made by PASDP	206
4.94 (b)	SEM micrographs of 64% TS-NaCl/Al foams with different relative density made by PASDP	206

4.94 (c)	SEM micrographs of 66% TS-NaCl/Al foams with different relative density made by PASDP	206
4.94 (d)	SEM micrographs of 70% TS-NaCl/Al foams with different relative density made by PASDP	206
4.94 (e)	SEM micrographs of 72% TS-NaCl/Al foams with different relative density made by PASDP	206
4.94 (f)	SEM micrographs of 75% TS-NaCl/Al foams with different relative density made by PASDP	206
4.94 (g)	SEM micrographs of 78% TS-NaCl/Al foams with different relative density made by PASDP	206
4.94 (h)	SEM micrographs of 80% TS-NaCl/Al foams with different relative density made by PASDP	206
4.95 (a)	SEM micrographs of 60% AC-NaCl/Al foams with different relative density made by PASDP	207
4.95 (b)	SEM micrographs of 64% AC-NaCl/Al foams with different relative density made by PASDP	207
4.95 (c)	SEM micrographs of 66% AC-NaCl/Al foams with different relative density made by PASDP	207
4.95 (d)	SEM micrographs of 70% AC-NaCl/Al foams with different relative density made by PASDP	207
4.95 (e)	SEM micrographs of 72% AC-NaCl/Al foams with different relative density made by PASDP	207
4.95 (f)	SEM micrographs of 75% AC-NaCl/Al foams with different relative density made by PASDP	207
4.95 (g)	SEM micrographs of 78 % AC-NaCl/Al foams with different relative density made by PASDP	207
4.95 (h)	SEM micrographs of 80 % AC-NaCl/Al foams with different relative density made by PASDP	207
4.96 (a)	SEM micrographs of 60% HI-NaCl/Al foams with different relative density made by PASDP	208
4.96 (b)	SEM micrographs of 64% HI-NaCl/Al foams with different relative density made by PASDP	208
4.96 (c)	SEM micrographs of 66% HI-NaCl/Al foams with different relative density made by PASDP	208

4.96 (d)	SEM micrographs of 70% HI-NaCl/Al foams with different relative density made by PASDP	208
4.96 (e)	SEM micrographs of 72% HI-NaCl/Al foams with different relative density made by PASDP	208
4.96 (f)	SEM micrographs of 75% HI-NaCl/Al foams with different relative density made by PASDP	208
4.96 (g)	SEM micrographs of 78% HI-NaCl/Al foams with different relative density made by PASDP	208
4.96 (h)	SEM micrographs of 80% HI-NaCl/Al foams with different relative density made by PASDP	208
4.97 (a)	SEM micrographs of 60% SA-NaCl/Al foams with different relative density made by PASDP	209
4.97 (b)	SEM micrographs of 64% SA-NaCl/Al foams with different relative density made by PASDP	209
4.97 (c)	SEM micrographs of 66% SA-NaCl/Al foams with different relative density made by PASDP	209
4.97 (d)	SEM micrographs of 70% SA-NaCl/Al foams with different relative density made by PASDP	209
4.97 (e)	SEM micrographs of 72% SA-NaCl/Al foams with different relative density made by PASDP	209
4.97 (f)	SEM micrographs of 75% SA-NaCl/Al foams with different relative density made by PASDP	209
4.97 (g)	SEM micrographs of 78% SA-NaCl/Al foams with different relative density made by PASDP	209
4.97 (h)	SEM micrographs of 80% SA-NaCl/Al foams with different relative density made by PASDP	209
4.98 (a)	SEM micrographs of pressure assisted sintering aluminium foam of 80% TS-NaCl/Al at 15X.	210
4.98 (b)	SEM micrographs of pressure assisted sintering aluminium foam of 80% TS-NaCl/Al at 50X showing the cells and windows	210
4.98 (c)	SEM micrographs of pressure assisted sintering aluminium foam of 80% TS-NaCl/Al at 500X showing the quality of particle sintering.	210

4.98 (d)	SEM micrographs of pressure assisted sintering aluminium foam of 80% TS-NaCl/Al at 3000 X showing the quality of particle sintering.	210
4.99 (a)	SEM micrographs of pressure assisted sintering aluminium foam of 80% AC-NaCl/Al at 20X.	211
4.99 (b)	SEM micrographs of pressure assisted sintering aluminium foam of 80% AC-NaCl/Al at 50X showing the cells and windows	211
4.99 (c)	SEM micrographs of pressure assisted sintering aluminium foam of 80% AC-NaCl/Al at 500X showing the quality of particle sintering	211
4.99 (d)	SEM micrographs of pressure assisted sintering aluminium foam of 80% AC-NaCl/Al at 3000 X showing the quality of particle sintering	211
4.100 (a)	SEM micrographs of pressure assisted sintering aluminium foam of 80% HI-NaCl/Al at 20X	212
4.100 (b)	SEM micrographs of pressure assisted sintering aluminium foam of 80% HI-NaCl/Al at 50X showing the cells and windows	212
4.100 (c)	SEM micrographs of pressure assisted sintering aluminium foam of 80% HI-NaCl/Al at 500X showing the quality of particle sintering	212
4.100 (d)	SEM micrographs of pressure assisted sintering aluminium foam of 80% HI-NaCl/Al at 3000 X showing the quality of particle sintering	212
4.101 (a)	SEM micrographs of pressure assisted sintering aluminium foam of 80% SA-NaCl/Al at 20X	213
4.101 (b)	SEM micrographs of pressure assisted sintering aluminium foam of 80% SA-NaCl/Al at 50X showing the cells and windows	213
4.101 (c)	SEM micrographs of pressure assisted sintering aluminium foam of 80% SA-NaCl/Al at 500X showing the quality of particle sintering	213
4.101 (d)	SEM micrographs of pressure assisted sintering aluminium foam of 80% SA-NaCl/Al at 3000 X showing the quality of particle sintering	213

4.102	Relative electrical conductivity of foam specimens as a function of total porosity at different pore size and the width of pore size distribution	215
4.103	Relative electrical conductivity of foam specimens as a function of density at different pore size and the width of pore size distribution	216
4.104	Relative electrical conductivity of foam specimens as a function of relative density at pore size and the width of its size distribution	217
4.105	Compressive stress-strain curves of the TS-NaCl/Al for highly porous specimens	219
4.106	Compressive stress-strain curves of the AC-NaCl/Al for highly porous specimens	219
4.107	Compressive stress-strain curves of the HI-NaCl/Al for highly porous specimens	220
4.108	Compressive stress-strain curves of the SA-NaCl/Al for highly porous specimens	220
4.109	Compressive stress-strain curves of the Al foam with different volume fraction for TS-NaCl	222
4.110	Compressive stress-strain curves of the Al foam with different volume fraction for AC-NaCl	222
4.111	Compressive stress-strain curves of the Al foam with different volume fraction for HI-NaCl	223
4.112	Compressive stress-strain curves of the Al foam with different volume fraction for SA-NaCl	223
4.113	The influence of pore size and the width of pore size distribution on compressive stress-strain behaviour of 72% volume fraction.	225
4.114	The influence of pore size and the width of pore size distribution on compressive stress-strain behaviour of 75% volume fraction	225
4.115	The influence of pore size and the width of pore size distribution on compressive stress-strain behaviour of 78% volume fraction	226
4.116	The influence of pore size and the width of pore size distribution on compressive stress-strain behaviour of 80%	226

	volume fraction	
4.117	Compressive strength of TS-NaCl/Al foam as a function of density	228
4.118	Relative compressive strength of TS-NaCl/Al foam as a function of relative density	228
4.119	Compressive strength of AC-NaCl/Al foam as a function of density	229
4.120	Relative compressive strength of AC-NaCl/Al foam as a function of relative density	229
4.121	Compressive strength of HI-NaCl/Al foam as a function of density	230
4.122	Relative compressive strength of HI-NaCl/Al foam as a function of relative density	230
4.123	Compressive strength of SA-NaCl/Al foam as a function of density	231
4.124	Relative compressive strength of SA-NaCl/Al foam as a function of relative density	231
4.125	Compressive modulus of TS-NaCl/Al foam as a function of density	234
4.126	Relative compressive modulus of TS-NaCl/Al foam as a function of relative density	234
4.127	Compressive modulus of AC-NaCl/Al foam as a function of density	235
4.128	Relative compressive modulus of AC-NaCl/Al foam as a function of relative density	235
4.129	Compressive modulus of HI-NaCl/Al foam as a function of density	236
4.130	Relative compressive modulus of HI-NaCl/Al foam as a function of relative density	236
4.131	Compressive modulus of SA-NaCl/Al foam as a function of density	237
4.132	Relative compressive modulus of AC-NaCl/Al foam as a function of relative density	238

4.133	Variation of energy absorbed with compressive strength at different volume fraction for different pore size of foam	238
4.134	Variation of compressive strength of different pore shape and size of different pore size of TS, AC, HI and SA-NaCl/Al specimens at different NaCl/Al volume ratio	239
4.135	Variation of compressive modulus of different pore size of TS, AC, HI and SA-NaCl/Al specimens at different NaCl/Al volume ratio	239
4.136	Variation of strength at densification of different pore size of TS, AC, HI and SA-NaCl/Al specimens at different NaCl/Al volume ratio	240
4.137	Energy absorbed by TS-NaCl/Al foams after compression strains of 20, 30, 40 and 50%.	241
4.138	Energy absorbed by AC-NaCl/Al foams after compression strains of 20, 30, 40 and 50%	241
4.139	Energy absorbed by HI-NaCl/Al foams after compression strains of 20, 30, 40 and 50%.	242
4.140	Energy absorbed by HI-NaCl/Al foams after compression strains of 20, 30, 40 and 50%	242
4.141 (a)	The surface morphology of as-received SiO ₂ sand.....	244
4.141 (b)	The surface morphology of SiO ₂ sand after undergoing mechanical treatment at grinding times: of 20 hrs	244
4.141 (c)	The surface morphology of SiO ₂ sand after undergoing mechanical treatment at grinding times: of 40 hrs	244
4.141 (d)	The surface morphology of SiO ₂ sand after undergoing mechanical treatment at grinding times: of 60 hrs	244
4.141 (e)	The surface morphology of SiO ₂ sand after undergoing mechanical treatment at grinding times: of 80 hrs	244
4.141 (f)	The surface morphology of SiO ₂ sand after undergoing mechanical treatment at grinding times: of 100 hrs	244
4.142	X-ray diffractograms of milled silica at different milling time	245
4.143 (a)	SEM micrograph of Un-MM mixture at 1350 °C.....	246
4.143 (b)	XRD spectrum of Un-MM mixture at 1350 °C.....	246

4.144 (a)	SEM micrograph of MM mixture at 1350 °C.....	247
4.144 (b)	XRD spectrum of MM mixture at 1350 °C.....	247
4.145 (a)	SEM micrograph of Un-MM mixture at 1450 °C.....	248
4.145 (b)	XRD spectrum of Un-MM mixture at 1450 °C.....	248
4.146 (a)	SEM micrograph of MM mixture at 1450 °C.....	249
4.146 (b)	XRD spectrum of MM mixture at 1450 °C.....	249
4.147 (a)	SEM micrograph of Un-MM mixture at 1550 °C.....	250
4.147 (b)	XRD spectrum of Un-MM mixture at 1550 °C.....	250
4.148 (a)	SEM micrograph of MM mixture at 1550 °C.....	250
4.148 (b)	XRD spectrum of MM mixture at 1550 °C.....	250
4.149 (a)	SEM micrograph of Un-MM mixture at 1650 °C.....	251
4.149 (b)	XRD spectrum of Un-MM mixture at 1650 °C.....	251
4.150 (a)	SEM micrograph of MM mixture at 1650 °C.....	252
4.150 (b)	XRD spectrum of MM mixture at 1650 °C.....	252
4.151	X-ray diffractograms of mechanical carbon mixture after carbothermal nitridation process at various temperatures	253
4.152 (a)	Electron micrographs of the cell walls of pure aluminium foam at magnification of 2kX	259
4.152 (b)	Electron micrographs of the cell walls of pure aluminium foam at magnification of 3kX	259
4.152 (c)	Electron micrographs of the cell walls of pure aluminium foam at magnification of 5kX	259
4.152 (d)	EDX of the cell wall aluminium.....	259
4.153 (a)	Electron micrographs of the cell walls of reinforced aluminium foam	260
4.153 (b)	EDS analysis result taken from point A.....	260
4.153 (c)	EDS analysis result taken from point B.....	260

4.153 (d)	EDX of the cell wall of reinforced aluminium foam.....	260
4.154	Compression curves of pure Al and Al-1%SiC foams.....	261
4.155	Enlarge portion of the beginning of the curve of point A of the compression graphs pure Al and Al-1%SiC foams	262
4.156	Compressive strength of pure Al and Al-1%SiC foams as a function of density	263
4.157	Relative compressive strength of pure Al and Al-1%SiC foams as a function of relative density	263
4.158	Compressive modulus of pure Al and Al-1%SiC foams as a function of density	264
4.159	Relative compressive modulus of pure Al and Al-1%SiC foams as a function of relative density	264
4.160	Strength at densification of pure Al and Al-1%SiC foams as a function of density	266
4.161	Deformation at densification of pure Al and Al-1%SiC foams as a function of density	266
4.162	Energy absorbed at densification of pure Al and Al-1%SiC foams as a function of density	267
4.163	Energy absorbed at densification of pure Al and Al-1%SiC foams as a function of compressive strength	267

PREFACE

A process based on powder metallurgy approach was developed to produce open-celled aluminium foam. In the preparation of foam specimens, the aluminium (Al) powder and the sodium chloride (NaCl) acting as leaching agent were dry-mixed together in order to prepare homogenously mixture. The blended mixture was then subjected to pressure assisted sintering in which a pressure beyond atmospheric level is externally applied to the specimen during high-frequency induction heated sintering. The embedded leaching agent was then dissolved in order to leave behind an open-celled Al with the same chemical composition as that of the original Al powder. The final material is highly porous and has an interconnected porosity network. The structure of the resulting material has three levels of porosity (i.e. main cells, windows and microporosity). The cell morphology and the size of Al foam closely match those of the leaching particles used. The X-ray diffraction analysis shows that as the content of NaCl is increased to the volume fraction of 60%, no traces of NaCl presents in the foam. In comparison to the sintering dissolution process (SDP), the most outstanding technical advantage of pressure assisted sintering dissolution (PASDP) process is that the Al foam can be fabricated in much shorter time to attain high dense of cell wall and it possesses superior mechanical properties. The principals of Taguchi's method were also employed in characterizing and optimizing the processing factors for the pressure assisted sintering-dissolution process of Al foams. The Taguchi orthogonal array L_9 was used for the experimental design with three levels of consideration for each factor. The response was analysed based on the Taguchi's signal to noise ratio (S/N) and analysis of variance (ANOVA). The results show that the most notable factor influencing the fabrication of Al foam was the compaction at elevated temperature, followed by temperature, time and heating rate of the process. The optimum processing parameters for the PASDP process was then predicted based on these results. The compressibility behaviour of sodium chloride / aluminium (NaCl/Al) composite with different amount of leaching agent content was studied. The Heckel equation was used to assume pressure effect at elevated temperature on the density of the specimen. Due to lower plastic deformation capacity, the specimen with higher content of leaching agent exhibited higher

compressibility. The relationship was established between the compaction pressure and the density of specimens. Williamson-Hall method was also applied to determine the crystallite size and lattice strain of the consolidated samples at various pressures. The influence of pressure on the compressive mechanical properties of the resultant foams were investigated. The results show that the compressive properties (i.e. compressive strength, modulus, and stress at densification) increase with density. The viability of electrical conductivity as a tool for evaluating variations in morphology of PASDP Al foam and the influence of processing parameters: volume fraction of leaching agent, compaction pressure at elevated temperature, sintering temperature, sintering time and heating rate on the electrical conductivity of the final foams were investigated. It was found that all the chosen factors have significant effects on the physical and mechanical properties of the foam and Al volume fraction is the most important parameter affecting the relative electrical conductivity and relative density of the resultant foam. The findings also suggest that the relationship between relative electrical conductivity and density of the specimen does not follow the mathematical description given by Skorohod and Solonin, instead the power law seems to be a good characterization of the relationship between experimental data of electrical conductivity and density of the resultant foams.

This work was also carried out to understand the influence of processing parameters in synthesizing the silicon carbide in the form of whisker which is best suited for use as reinforcement in aluminium foam materials. The results show that the most notable factor influencing the formation of SiC_w was the duration of mechanical milling of silica sand, followed by temperature, time and heating rate of the process. The optimum processing parameters for the carbothermal nitridation process was then predicted based on these results. This research also presents the work that has been carried out to study the influence of silicon carbide addition on the physical and mechanical properties of the fabricated Al foam. The study reveals that addition of SiC could improve the mechanical properties of the foam.

The major contribution of this research work leads to the innovative process in the fabrication of aluminium foam through pressure assisted sintering dissolution process (PASDP). In the process of completing the thesis write up, research articles were accepted in the Powder Metallurgy and Journal of Materials Processing Technology.

In addition, another topic was already published in American Institute of Physics (AIP) in May 2008 which was cited in SCOPUS. The details of these articles are as attached in APPENDIX A.

This work has bagged few awards which include:

- i. Gold medal in Postgraduate Studies in the 24th edition of Universiti Teknologi PETRONAS Engineering Design Exhibition
- ii. 2nd runner up in Most Innovative Award in the 24th edition of Universiti Teknologi PETRONAS Engineering Design Exhibition.

CHAPTER 1

INTRODUCTION

1.1 Background

Owing to increased availability of practical technologies and improved understanding of their physical, chemical and mechanical properties of cellular metallic materials, they have attracted more and more attention in the last few decades [1]-[2]. Banhart *et al.* [3] described that there is a great diversity of cellular metallic materials that show various structures and properties and according to the connectivity of cells, cellular metals can be categorised as either closed- or open-celled. According to Gibson and Ashby [1], cellular metals are also dominantly used for light-weight constructional or functional purposes. It was also mentioned [1]-[3] that in most cases, the functions such as filtration, separation, heat or mass exchange, and sound or energy absorption required open-celled structures. They predicted that cellular metallic materials with open-celled structures have wider application in structural and functional purposes. [2]-[3].

1.2 Problem Statement

Most of the techniques used in producing aluminium foam have limitation in addressing the need of various type of porosity and other important parameters which should be versatile, tailoring to different types of application. Precursor filler materials were thought to contribute largely to the structures obtainable by liquid infiltration technology such as cell size, cell shape and porosity [3]. Few examples were demonstrated [4]-[6] that the porosity is usually lower than 70% and cell size larger than 0.5 mm in preform infiltration [4]-[6], while investment casting technique produced Al foam with higher porosities (>80%) and larger sizes (0.8 mm) [7]-[9].

This confinement in structures limits the range of properties and application of the fabricated foam.

Zhao *et al.* [8] described that the porosity of the as-manufactured foam is determined by the density of the pre-prepared compact of the sodium chloride (NaCl) powder in the liquid infiltration process. It was reported [7], [9], [10]-[14] that no changes in porosity of the resultant foam as the density of the compacts falls within a relatively narrow range between the apparent density and the tap density of the powder. They also postulated that it is also difficult to reduce the cell sizes of the foam to below 0.5 mm, although in theory smaller cell sizes can be obtained by using a NaCl powder with the particles finer than 0.5 mm. This observation is attributed to the fact that the greatly reduced interstices in a compact of very fine NaCl particles inhibit the full infiltration by the Al melt due to the fact that liquid Al does not wet NaCl [15], [16]-[21].

Fabrication of porous Al metals from Al powder is however more difficult due to the encapsulation of Al particles by a thermo chemically stable alumina (Al_2O_3) as reported by Zhao *et al.* [8]. They also described that in order to achieve strong metallurgical bonding during solid-state sintering of Al powder, the oxide film at the surface of the Al particles must be disrupted. This is largely due to the ability of the oxide film to serve as a hard shell which prevents the Al particle from establishing a direct contact with adjacent Al particles. Previously the open celled al foams had been developed by Zhao and Sun [22] through the powder metallurgy (P/M) technique which is known as the sintering and dissolution process (SDP). This approach consists of three stages. The first stage involved die-pressing of Al and NaCl powders into a green compact under appropriate pressure. This is then followed by sintering the compact at temperature either above or below the melting point of Al to form a well-bonded and net-shaped structure. Finally, the NaCl particles of the sintered compacts are removed by leaching process in hot water. However, the Al foams made by SDP may have inferior mechanical properties due to the existence of Al particles in its individual form indicating that the compacted metal particles did not bond together by atomic motion during sintering process. The process of sintering in this fabrication technique also varies from 3 to 5 hours and the temperature of the process is above the melting point of Al.

Using similar technique, Mazli and Othman [23] found that a completely intact Al foam specimens could not be produced in all solid sintering temperature process in which all the compacts collapsed in the subsequent leaching process. Some of the Al globules diffuse out of the compact's surface at sintering temperature above 660 °C [24]-[26]. The size of the Al globules increased with increase temperature and the loss of Al resulted in non-homogenous cell wall structure and cell size distribution. Similar observations were also reported in the work of Zhao *et al.* [8].

It was known that the mechanical properties of Al foam decrease with increasing porosity, leading to unsatisfactory performance in light weigh structures and impact mitigation devices [8]. Addition of ceramic material such as silicon carbide materials will improve the mechanical properties of the fabricated foam [8]. However, the synthesis of silicon carbide whisker from the silica sand using Acheson process is not successful [27]. It was reported that the produced silica carbide also possesses large grains and was produced at high temperature of 2400°C [27].

1.3 Research Objectives

By considering the limitation as mentioned in previous section, the objectives of the present study are:

- To develop an improved method for fabricating open-celled Al foams with superior morphological, physical and mechanical properties through conventional powder metallurgy (P/M) route.
- To study the influence of four processing parameters of compaction pressure at elevated temperature, sintering temperature, sintering time, and heating rate on the properties of the fabricated Al foam.
- To study the effect of adjusting the NaCl-to-Al volume fraction in the compact according to the rule of mixture on density and hence porosity of the fabricated foam.
- To determine the lattice strain and crystallite size of the consolidated samples at various volume fraction using Williamson-Hall plot method.

- To discuss the empirical relationship between the physical, electrical and mechanical properties of the foam.
- To perform the experiment based on the principals of Taguchi's Design of Experiments method and analysis of variance (ANOVA) technique in order to establish the relative significant of these factors.
- To investigate the influence of pore size on the mechanical properties of the fabricated Al foam.
- To develop an improved process for producing silicon carbide material which can be synthesised using simple set up that can be worked without high conversion engineering cost and using distorted structure silica sand as cheap precursor materials.
- To investigate the addition of silicon carbide on the physical and mechanical properties of fabricated al foam.

1.4 Scope of Research

The scope of this work was to develop an improved method for producing open celled aluminium foam through powder metallurgy approach known as pressure assisted sintering dissolution process (PASDP). In the preliminary development of the fabrication of foam specimens, the aluminium powder and sodium chloride of different volume fraction ranging from 30 to 60% which act as filler materials were dry mixed together in order to prepare a homogenous mixture. The blended mixture was then subjected to pressure assisted sintering in which a pressure beyond atmospheric level is externally applied to the specimen during high frequency induction heated sintering. The embedded filler material was then dissolved in order to leave behind an open celled Al with the same chemical composition as that of original aluminium powder. For comparison purpose, aluminium foam produced by sintering dissolution process (SDP) was also prepared. The minimum volume fraction of NaCl/Al mixture which show the characteristic of typical metallic foam when subjected to compression mode and having only a small amount of NaCl residue in the resultant foam was to be determined.

Such volume fraction of NaCl in the specimen will be used as the minimum volume fraction in the next study to investigate the influence of processing parameters on the physical and mechanical properties of the Al foam fabricated through pressure assisted sintering technique. The effect of processing parameters pertaining to the compaction pressure, temperature-time profile and heating rate have to be characterized and optimized in order to achieve the optimum physical and mechanical and electrical properties of the foam. The empirical relationship between the physical, electrical and mechanical properties of the foam will also be studied.

In this work, Taguchi's Design of Experiments technique, which is a major improvement from the conventional Full Factorial Design of Experiment statistical method, were also employed in order to optimize the processing factors for the fabrication of Al foam. The optimal processing parameters for the PASDP process was then to be predicted based on these results.

In order to control the intended pore size of the final foam, the filler material of different size and its width of size distribution were prepared. The influence of relative density and pore size and its width of distribution on the properties of aluminium foam fabricated using optimal processing parameters of PASDP method were to be identified. The empirical relationship between physical, mechanical and electrical properties of foam with different pore size and its widths of size distribution will also to be determined.

The addition of ceramic material such as silicon carbide in the fabrication of Al foam in order to improve its mechanical properties which degrade with the increase of porosity will also be investigated. An improved process of synthesizing silicon carbide whisker compound from carbothermal nitridation process using distorted structure silica sand as a precursor will be developed. A distinctive aspect of the present study resides in employing mechanical milling method which is based on impact and friction among particle to alter the regularity of the crystalline network in the silica sand used. The principals of Taguchi's method will be applied to determine the optimal processing parameters for the synthesis of silicon carbide material.

1.5 Thesis Outline

The thesis is organized into 5 chapters. In Chapter 2, the subject is treated from the general underlying principals and a review of relevant literature is given associated with the basic understanding of process of cellular materials. This chapter also contains a detailed review of the previous work on the open and closed cell-Al foam produced using different technique. The details on method of investigation used during this work are covered in Chapter 3. In Chapter 4, the analysis of data and discussion of results are presented. This chapter mainly discusses on the optimum processing parameters for the fabrication of Al foam. Chapter 5 deals with the conclusion that can be derived from this work and specific suggestions for further work.

CHAPTER 2

REVIEW OF LITERATURE

2.1 Chapter overview

This chapter discusses previous development on the fabrication of metallic foam using various manufacturing techniques and their disadvantages. The review will cover the summary of the properties and drawbacks of the Al foam developed by various methods which lead to the rationale of the present study. Previous studies on the two different methods of fabricating aluminium foam at AMREC and UTP will be reviewed. A model to understand the higher densities distribution which can be achieved with compaction at elevated temperature will also be discussed. The effectiveness application of Taguchi's principal rather than advanced statistical techniques will be covered. The synthesis of ceramic reinforcement materials for Al foam from the carbothermal nitridation process using structured alteration local silica sand will also be described.

2.2 Introduction to metallic foam

The real issue confronting Malaysia is not so much lack of appropriate mineral resources nor the source of energy to manufacture the materials. It is the lack of technological knows how which is the brain of metal industry. In the metal industries the need to move from labour intensive activities like assembling and manufacturing to a higher level technology based activities like Research and Development (R & D) and design works is necessary. As there are many players in the world today who are already at the forefront with their R & D and design and capabilities, Malaysian researcher should search and capitalize on certain nichie technology that could serve a specific nichie market. They may not have the time to do research on all the

technology available in this world especially in trying to learn what others have done. Instead they have to conduct research in niche technology for certain niche market that can provide them a fair share of the market size [28].

When the veil on the Ninth Malaysia Plan was lifted, the country's economic blueprint for the next five years on 31st March 2006, the application of high technology and production of higher value products will be given emphasized in the manufacturing sector in order to migrate the economy up the value chain (stated in THRUST 1 of the RMK-9 (2006 – 2010) [29]. In tandem with this aspiration, the fabrication technique for producing metallic foams will be focused in the study. This material which is considered a relatively new class of structural materials in Malaysia offers a variety of applications in field such as lightweight construction or crash energy management. Recent improvements as well as the development of production methods for metallic foams have given rise to renewed interest in these materials. Currently, Al foams are on the verge of being used in industry application [29]-[30].

It is well known that porous structures are good for insulation, packaging, or filtering, but it is believed that they can also be very effective in structural applications. Thousands of scientific publications deal with the minimization of porosity in load-bearing parts. Engineers work hard to eliminate pores from casting, powder metallurgy parts, weld joints or coatings, thinking that a defect-free part is a pore-free one. With this attitude it is difficult to accept that a load bearing material can include pores, even quite large ones. However, large natural structures of porous material have existed for thousands of years, demonstrating how evolution has generated cellular structures that optimize mechanical properties and structural function for minimum weight [31].

Mankind tries to learn from nature. Understanding the benefits of natural structures gives us information to help us produce man-made cellular structural materials. The cell wall material has to be chosen carefully if the structure is expected to carry loads. Polymers appear to be insufficiently rigid and ceramics are too brittle. Perhaps metal could be the right choice. Several of the engineering properties of metallic foams are superior to those of polymeric ones: they are stiffer by an order of magnitude, they are stable at elevated temperatures, they possess superior fire resistance, and they do not produce toxic fumes in a fire. Moreover, these materials

are fully recyclable without any pollution or waste problems. The latter fact can do no longer be ignored, because the production, disposal, and use of stronger and stiffer materials in new products often have negative environmental impacts over the product cycle [30].

Owing to their pores, cellular metal possesses a set of unusual properties compared with bulk structures; they are crushable, they exhibit a plateau stress if compressed, and they exhibit a change in Poisson ratio on deformation. The excellent combination of good mechanical properties (mostly strength and stiffness) and low weight is the prime advantage. In addition, cellular metals absorb high impact energies regardless of the impact direction, and are very efficient in sound absorption, electromagnetic shielding, and vibration damping [30]-[31].

Most of the mechanical properties of foam materials can be achieved with other materials, sometimes more effectively, but foams can offer a unique combination of several (apparently contradictory) properties that cannot be obtained in one conventional material at the same time (e.g., ultra-low density, high stiffness, the capability to absorb crash energy, low thermal conductivity, low magnetic permeability, and good vibration damping). Cellular metals are thus promising in applications where several of these functions can be combined [12], [32]-[34].

These properties depend significantly on the porosity, so that a desired portfolio of properties can be tailored by changing the foam density. This is one of the most attractive features of this remarkable material. Cellular materials properties also depend on the pore structure. This influence, imperfectly understood at present, is a topic of intense study. Various constitutive laws have been suggested for the characterization and modeling of this relationship. These laws, originally developed for polymeric foams, are usually based on the relative density of the foam, and therefore suppose uniform cellular structure, at least at a macroscopic level. However, metallic foams are dramatically different from polymeric foams: polymeric foams generally have a regular microstructure, whereas metallic foam may be highly distorted with a wide dispersion of cell size and shape. Moreover, many imperfections exist in a cell structure, such as cracks or holes in the cell walls, corrugated cells etc. These effects are inevitable due to manufacturing at significantly higher temperatures than in the case of polymers. If these features are not taken into account and the

properties of the foam are characterized only in relation to apparent density, a high scatter of properties is to be expected. This is why it is still widely believed that the acceptable reproducibility of the properties of metallic foams is questionable [10], [17], [20], [35]-[38].

The structure of metallic foam is often non-uniform especially in the case of complex 3D parts. It should be noted that a uniform structure is not necessary for obtaining acceptable and reproducible properties. Anisotropic or gradient pore structure allow the distribution of load bearing material according to load conditions (simulating the optimum bone-like structure), without a need to increase the overall weight or volume of the component. Therefore, the challenge for manufacturing is not to produce a uniform structure, but to achieve reproducible properties with a controlled non-uniform structure [37], [39]-[40].

2.3 The fabrication method of metallic foam

Cellular metals can be prepared by various processing methods. They may all be called “metallic foams”, but they are very different materials, depending on the manufacturing technique. The production method affects the distribution of the cell-wall material in such a way that the properties of differently manufactured materials are not comparable [35], [37]-[41]. Generally, the methods of fabricating foamed metal can be divided into four broad categories [41]:

2.3.1. Powder Metallurgy Technique

In this part, solid state methods for the manufacturing of cellular metals are reviewed with regard to their most important processing features. The term “solid-state method” means that directly before the formation of the cellular structure, the metal is in the solid state. All solid-state methods require a sintering step before the final cellular metallic structure is obtained. Naturally, powder metallurgical methods play a dominant role in this area. Porosity in cellular structures made from powders often exhibits two different size scales: macroporosity of the order of the targeted cell size, and a microporosity in the order of the primary particle or, in case of reactive

The porosity can be increased by incorporating a filler material which will evaporate or disintegrate during the sintering process. By partially or completely substituting metal fibres for the metal powders, a still higher range of porosity can be obtained - up to 96-98% - meaning they can be used as high permeability filters. Foams produced from fibres have significantly higher strength and ductility than those made from powders. This produces open-cell foam-like materials, though the porosities obtainable using powders are relatively low. Meanwhile fibres can produce foams with higher porosities, but are expensive to produce and handle. The strength of the material is limited by the thinnest points of contact between powder grains or fibres, with a lot of mass wasted in the bulk of the particles. This means that the specific strength of these foams is poor. Generally, the foams made by these methods tend to be of fairly poor quality [41].

2.3.1.2 Sintering of hollow metal spheres

Foams can also be made by sintering hollow spheres of metal, rather than powders. As the foams produced do not contain a large proportion of solid metal, far lower densities can be obtained than for foams made by simply sintering solid spheres. There are two main processes, which differ only in the technique used to produce the spheres.

One method involves a coaxial double-nozzle set-up [41], [42]-[44], as shown schematically in Figure 2.2 (a). A gas is fed through the inner nozzle, and a slurry, made up of dispersed solid particles (which can be metal, ceramic, or a mixture), a binder, a film stabilising agent, a dispersing agent, and a continuous volatile liquid phase, is fed through the outer nozzle. The gas jet is pulsating, and a transverse jet periodically sprays liquid at the exit of the coaxial nozzle, to aid the formation (b) and detachment (c) of closed bubbles. The volatile liquid phase evaporates to some extent, and the solid particles coalesce to form a relatively stable sphere (d). The spheres are then held at high temperature (e) to remove the remaining liquid and other phases, leaving metal spheres with reasonably uniform diameter and skin thickness (f).

sintering, the grain size. For all metallurgical process, the cost of the powders is a major concern. Some of the methods, especially those using slurries of metal powder dispersed in a dissolved binder, are capable of using cheap oxides and thus have the potential for a significant cost reduction [29], [41].

2.3.1.1 Sintering of metal powders and fibres

This type of foams are really just combinations of materials which happen to give a lot of open space - for example metal powders or fibres which have been compressed together [29], [32], [41]. By partially sintering packed metal powders, foam-like materials with relatively low porosities (typically between 30 to 50%) can be fabricated (Figure 2.1).

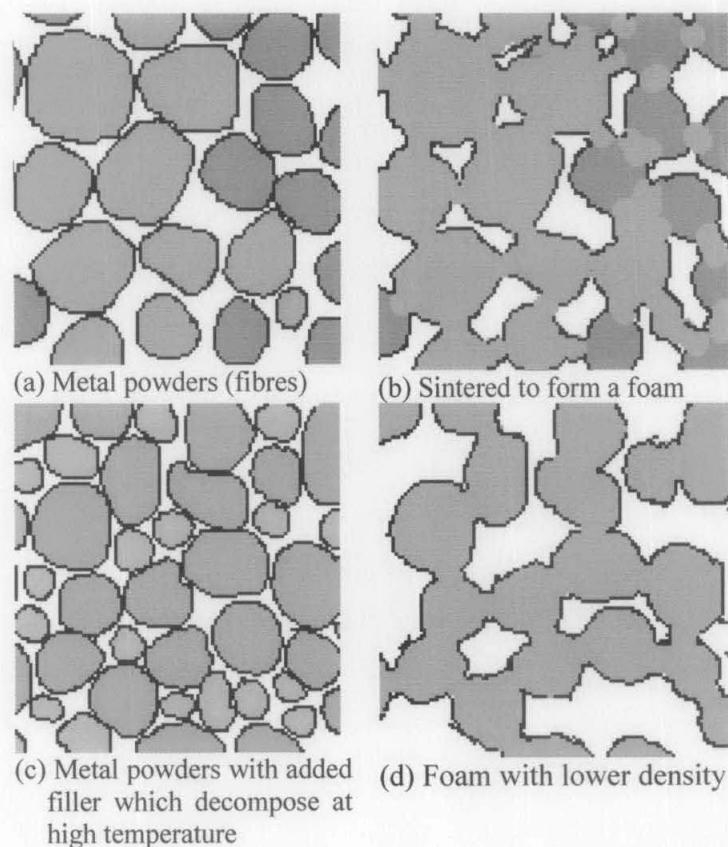


Figure 2.1: Fabrication of metallic foam by direct sintering of metal powder [41]

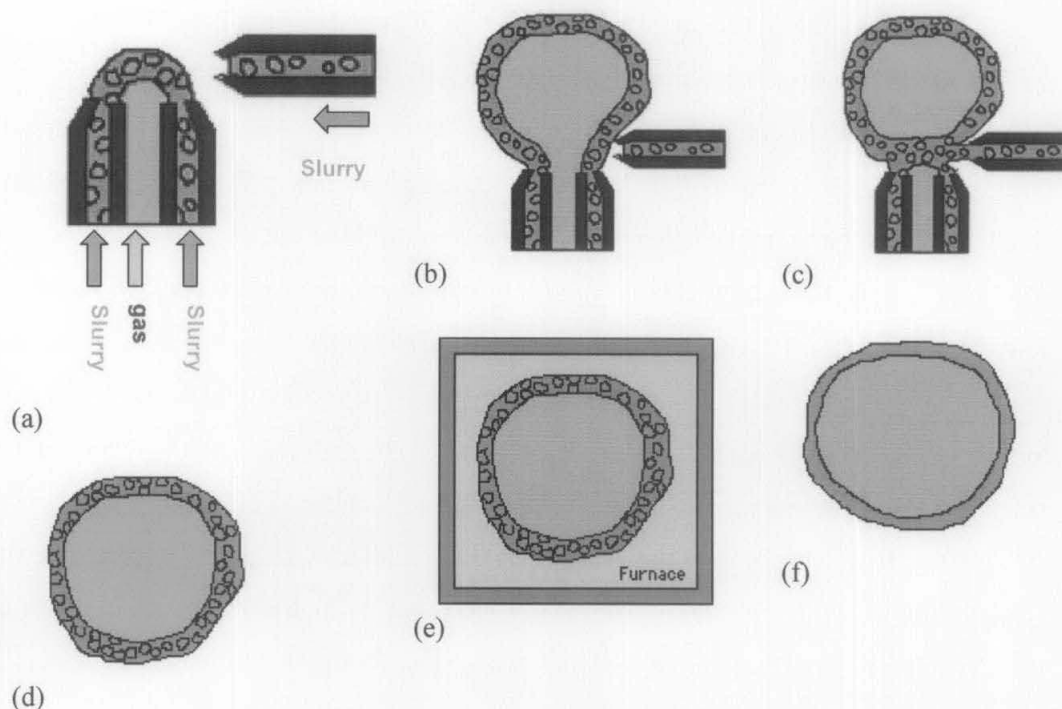


Figure 2.2: The main step involved in the fabrication of hollow spheres from a slurry containing metal powder [41]

Spheres can be produced with diameters ranging between 500 and 6000 μm , with wall thicknesses between 5 and 400 μm . As the diameter of these spheres is reasonably uniform, they can easily be packed in regular arrangements. Another slurry, of similar composition to the one used to make the spheres, can be used to bond the spheres together. Alternatively, the oxide on the metal surface can be directly reduced during sintering of the spheres, so that they fuse together at their points of contact. Steel foams have been produced with relative densities between 80 and 87%. Carburizing these foams further improved the mechanical properties [41].

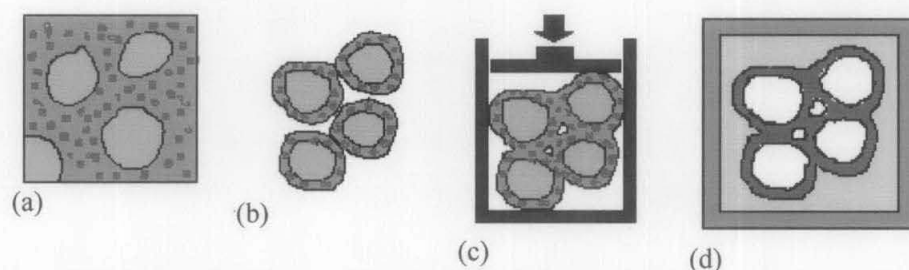


Figure 2.3: A more cost effective process for the fabrication of foams made of hollow sphere [29]

The other method, shown schematically in Figure 2.3, involves coating solid spheres made of a disposable material (typically polystyrene) with a similar slurry (a), which is similarly heated to produce 'green' hollow spheres (b). This way of producing spheres is less complex, and hence cheaper. The polystyrene inside the slurry-coated spheres makes them less vulnerable to fracture, so that they can be compressed together before sintering (c) - leading to improved contact between spheres in the foam. By combining the sintering of the spheres and the joining of the spheres to produce foams in a single step (d), the process complexity and cost are further reduced. By mixing appropriate proportions of different metal powders into the slurries used, a wide range of alloys can be used. Because of the close control over the sphere size, the packing of the spheres can be remarkably regular. The structure of these foams is not determined by statistical laws, and is highly homogenous, with a correspondingly small scatter in material properties. Unlike the situation with many melt-based foams, the pore size, cell arrangement and relative density are completely independent of each other. The main disadvantage of this type of process is cost: it is a batch process which is relatively difficult to scale up, the production and handling of metal powders to produce the slurry is expensive, and there are a large number of process steps. A development which may be significant stems from the observation that hollow metal spheres are produced as an unwanted by-product during gas atomisation of metal powders. These hollow spheres can be separated from the solid powder spheres in a series of simple steps. It is possible to select spheres of one size only - including sizes significantly smaller than those obtainable by the methods previously described. These spheres have been successfully used to produce Ti and Ni foams made of spheres 500µm wide [38]-[41].

2.3.1.3 Powder Metallurgical Space Holder Method

The use of space holders in powder metallurgy is a well-known technique to create different pore size and achieve relative densities lower than 0.4. The space holder is mixed with the metal powder and, depending on the final shape of product, several methods are used for forming of the powder mixture: die compaction, extrusion, and rolling. A general difficulty of these methods is the need to remove large quantities of organic or inorganic space holder material from the parts. Good results can be

achieved with carbamide (urea), which can be thermally removed below temperature of 200 °C. Pore sizes are typically in the range of few hundreds microns up to a few millimeters, and relative density of 0.4-0.2 are reported [13], [22]. The size of the pores is closely controlled by choosing filler material with appropriate grain sizes. There are no particular restrictions on the metal alloys used. Provided the shapes are sufficiently simple to be pressed, this process can be used to produce net-shape foams. This process produces high-quality open-cell foams, with highly reproducible material properties, but is relatively expensive due to the cost of handling of fine powders. The dissolution of the filler material is a significant rate-limiting step: in large samples, the tortuosity of the foam structure means that it takes a long time to dissolve all the salt [8], [41].

2.3.2 Liquid Metallurgy

In this method, generally it can be grouped into casting and foaming process. In the casting process the substrate act as space holder and is removed for creating the open pores. Meanwhile in the foaming process the gas is evolved to create the closed pores characteristic of the structure [31], [33], [41].

2.3.2.1 Casting

The process of replicating a structure has been known to the metallurgist for centuries. For example, casting can be thought of as a replication procedure in which a metal is used to reproduce the negative form of mould. In the study of porous materials, however, replication refers to a process used to replicate the open-pore architecture of a porous material. By making a preform of the cell shapes, which is subsequently used as a disposable mould during an infiltration stage, cell structures can be 'designed' [41].

2.3.2.2 Infiltration / Investment casting using water soluble preform

In this process, preforms are made of a water-soluble material which is capable of withstanding the temperature of the molten metal. A mould is filled with the mould material - typically rock salt due to its low cost - which is vibrated and tapped until a stable density is achieved ((a) in Figure 2.4). It is then sintered in air (b) and cooled. By fusing the salt grains together at the points of contact this produces a rigid block of salt in the shape of the mould, with open channels in the spaces between the original grains (c). In the simplest process, molten aluminium is simply poured onto the block to infiltrate the channels. The entire structure is then removed from the mould, cooled, and placed in water to dissolve the salt (f). This produces a foam with open-celled grains whose size and layout closely matches that of the original salt grains, and a minimum cell size of approximately 1 mm [41], [44]-[47].

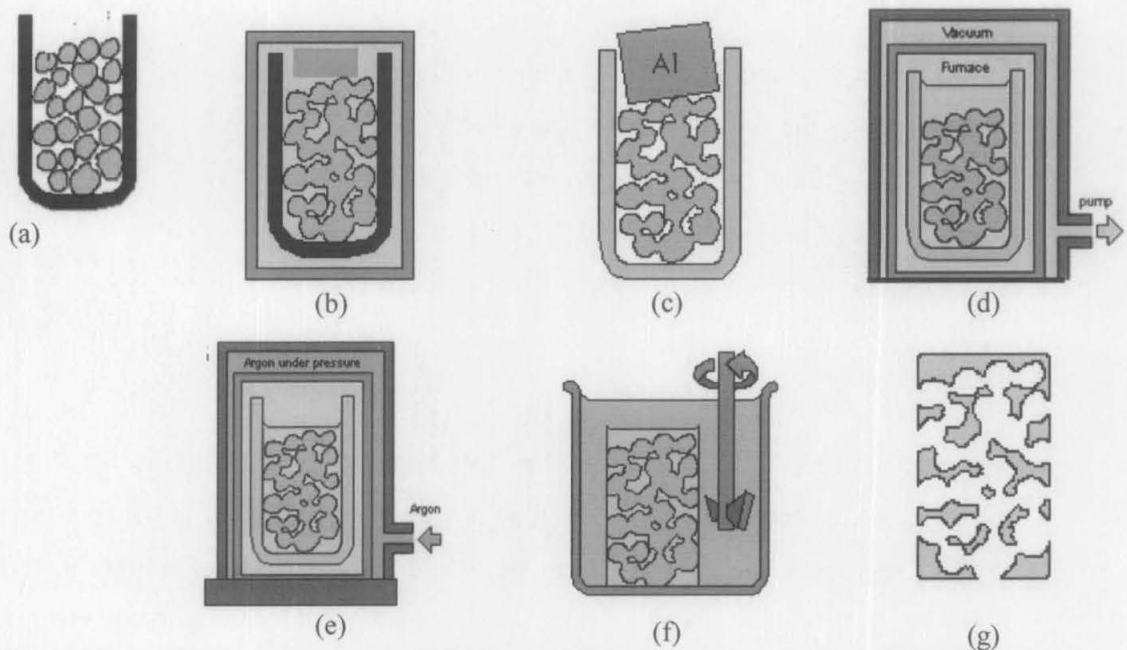


Figure 2.4: Production of an open-cell foam by infiltration/investment casting using a water-soluble preform [41]

A more advanced version of this process uses a hot-wall pressure infiltration process, where the salt preform is held under vacuum while a block of aluminium on the preform is melted (d), and high pressure of an inert gas is applied during a subsequent infiltration step (e). The salt is then dissolved (f) to give an open-cell foam (g). This use of pressure during the infiltration step enables foams with cells as small

as 50 μ m to be produced [41]. The disadvantages are that the process is slow, difficult to scale up, and involves many steps and is correspondingly costly. Besides that the foam produced has more or less fixed density [41].

2.3.2.3 Two stage investment casting using plaster mould

Two-stage investment casting processes can be used to make open-cell metal foams which replicate the shape of polymeric foams. The processing steps to produce polymeric foams are straightforward, with good control over the cellular nature of the foams and the process step is as shown in Figure 2.5.

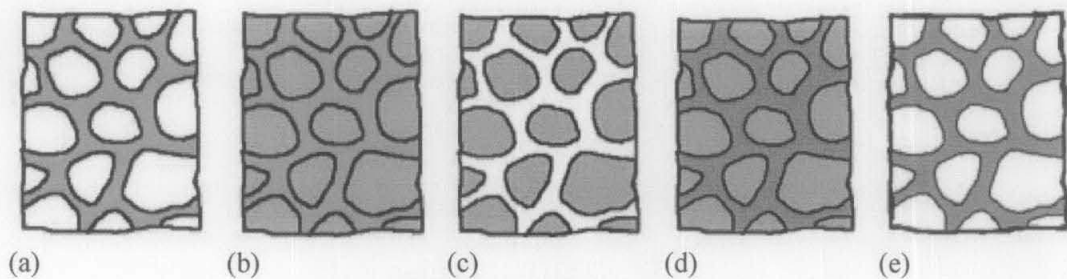


Figure 2.5: Replication of a polymer foam structure by the production and infiltration of a plaster mould [29]

A polyurethane foam is first infiltrated with plaster. The assembly is then heated to 700°C, to fire the plaster and remove the polyurethane foam. Molten metal is then poured onto the mould. The combinations of vacuum and high pressure can be used to ensure full infiltration. The plaster is then dissolved, to give a net-shape metal foam with an identical structure to the original polymer foam [41].

2.3.3 Foaming

The melt route for processing closed-cell metal foams is very attractive since this approach allows economic handling of large quantities of material. Melt-route processes are also well suited to the use of scrap as feedstock. In order to foam the melt properly, gas must be introduced. This can be done by gas injection or by in-situ gas generation by a chemical decomposition of a foaming agent [41].

2.3.3.1 Direct injection of gases to metal with enhanced viscosity

A rapid, low-cost method of producing metal foams involves direct injection of gas in to molten metal. It is necessary to increase the viscosity of the metal: if gas was directly added to molten aluminium, it would simply bubble through the melt and escape. One approach to this problem, developed by Alcan International and CYMAT Corporation [38], is to add a dispersion of fine particles of a refractory material to the molten metal. Addition of 5-15% by volume of particles smaller than 20 μ m makes the molten metal sufficiently viscous for molten foams to be stable against collapse. It appears that this is partly due to enhanced viscosity of the melt, and partly due to the particles acting as surfactants on the metal/gas interface [36]-[41].

The choice of material is restricted - many non-metallic reinforcements will react with molten metals. Alumina, boron carbide, silicon nitride and boron nitride are all suggested as possible materials, but silicon carbide is the only material used in practice. Although silicon carbide will react with molten aluminium to form aluminium carbide and silicon, it has been established that the rate of reaction can be reduced to an acceptable level by holding the melt at a relatively low temperature during mixing, coating the particles, and inhibiting the reaction by raising the Si content of the aluminium. A rotating dispersing impeller is used to shear the melt and the particles past each other, ensuring wetting between the particles and the metal without creating a vortex (which would draw gas into the melt). The production process is shown in Figure 2.6 In a preliminary stage, the ceramic particles are dispersed within the melt. Gas is then added under the surface of the melt using a rotating impeller designed to produce small bubbles. The foam which forms on the surface is drawn off, rolled slightly to form flat sheets, and cooled [38], [41].

The main disadvantage of this process is the poor quality of the foams produced is poor. The cell size is large and often irregular, and the foams tend to have a marked density gradient. Although various methods have been developed to improve the drawing off of the foam, including vertical solidification to avoid settling of the foam towards the base, the shape of the foam and the size distribution of the pores is still difficult to control. The cell structure is influenced by the gas flow rate, the viscosity and temperature of the melt, the mechanism used to draw off the foam, the compression required to form the semi-liquid foam into a useful shape, and the

design and rotation speed of the impeller. According to Banhart [41] an attempts have been made to use alloys which do not require the addition of solid particles. In one case, a 91% Mg-9% Al alloy was stirred rapidly at a temperature between the solidus and liquidus temperatures, producing a viscous dendritic melt, to which argon gas was added. In general, such attempts have been unsuccessful, only producing metals with up to 20% porosity. The main difficulty lies in maintaining a uniform temperature within a very narrow range. If the temperature is too low the melt is too viscous to process, and if the temperature is too high the dendrites in the melt do not grow sufficiently quickly, and the melt is not sufficiently viscous to trap the gas. It can also be difficult to produce dendrites which are sufficiently fine to generate a slurry on the scale of the cell wall thickness [32], [41]-[46].

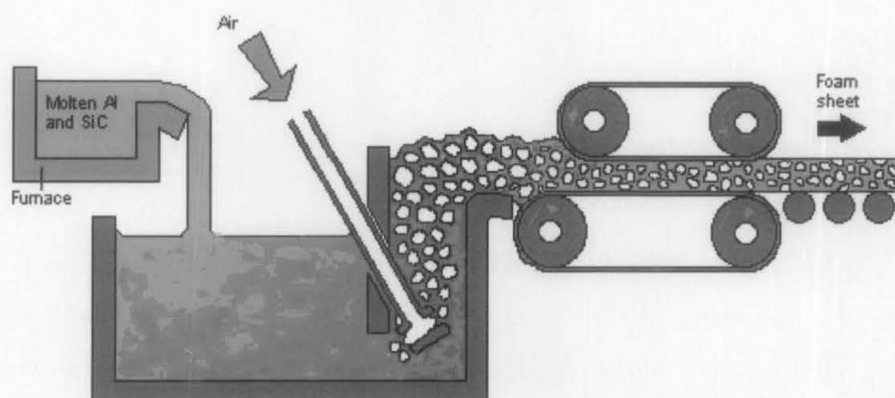


Figure 2.6: Continuous production of metal foam sheet by direct addition of gas to a melt with enhanced viscosity [29]

2.3.3.2 Dissociating blowing agent

The use of chemical foaming agents gives more control of cell structure of the foam than the direct injection of a gas into the melt. However, it is still relatively difficult to control the dispersion of the foaming agent within the melt, meaning that foam components cannot easily be made with homogenous cell structures. Because access to the full melt volume is necessary in order to fully disperse the powder within the melt, the foam produced has to have a relatively simple shape. The time available for foaming, and the temperature at which it takes place, are restricted by the need to accommodate the stirring of the powder into the melt [41], [47].

A number of processes have been developed which seek to improve on the process by separating the dispersion of the foaming agent within the melt from the decomposition of the agent to form a foam. This provides a number of advantages over the single-step process. As foaming is not taking place during the mixing, more time is available to mix the powdered foaming agent with the melt, meaning that finer powders can be used, and they can be more uniformly dispersed. Another significant advantage is that a foamable precursor is produced which can be stored indefinitely, and cut sections of it can be heated within complex-shaped moulds without the need for access by a propeller. Net-shape foam products can thus be produced with a solid outer skin matching the shape of the desired end product. With a two-step process it is possible to control the temperature during the foaming stage more closely than in the direct gas or powder injection methods, which in turn gives better control over the porosity and cell structure [41], [48].

2.3.3.3 Foamable precursor produced by melt-route processing

The FORMGRIP process uses melt processing to produce a foamable precursor material [42]. By subjecting titanium hydride to heat treatment, as shown in Figure 2.7 (a) and (b), it is possible to produce a layer of titanium oxide on the surface, which has only limited permeability to hydrogen. The hydride is then mixed into an aluminium melt (c) which has added silicon carbide particles to increase the viscosity, with the oxide layer on the hydride particles acting as a barrier to delay the decomposition. The oxide delays the foaming for a sufficiently long time to enable the titanium hydride to be thoroughly dispersed within the melt. This produces a slightly porous precursor made of metal, foaming agent, and silicon carbide (d).

In a second step, the precursor is baked inside a mould, typically at 630°C, to melt the alloy and cause the decomposition of titanium hydride to give off hydrogen gas. By adjusting the time of baking, foams with porosities between 50% and 95% can be obtained, with cell sizes between 1 and 10 mm. The main disadvantage of this process is the requirement to add viscosity enhancing SiC particles to the melt, which adds to the cost of the process and makes the resulting foams more brittle [41].

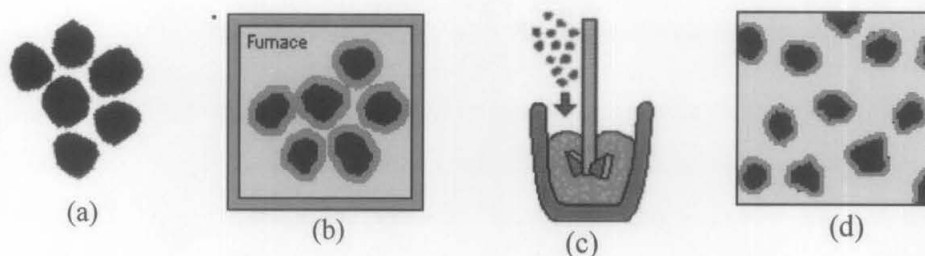


Figure 2.7: The first step of the FORMGRIP process: melt-route production of a foamable precursor [41]

Rather than directly adding gas to molten metal, it is possible to add a powdered material or compound which is stable at room temperature, but which will decompose at a higher temperature to give off a gas. By using a solid foaming agent it is possible to disperse gas more uniformly throughout the melt. Titanium hydride, TiH_2 , is well suited to this process as it is stable at room temperature, but readily decomposes at temperatures similar to the melting point of aluminium to give off large volumes of hydrogen gas [39], [41]-[43].

In order to prevent the bubbles of gas from coalescing, floating or escaping from the melt, it is necessary to increase the melt viscosity. This can be achieved by mixing powders or fibres into the melt. In an alternative approach, developed by the Shinko Wire Company, approximately 1.5wt.% of Ca or Mg is stirred into an aluminium melt at 680°C , and air is bubbled through the melt. By promoting oxidation of the melt, this forms a dispersion of fine oxide particles throughout the molten metal, raising its viscosity [44].

In the Shinko Wire Company process, 1.6% wt.% of TiH_2 is added to this melt and stirred thoroughly, followed by a 15 minute curing time where the foam is held at 680°C and the hydride decomposes according to the reaction. This forms pores within the viscous melt, producing foams with porosities between 84 and 95%, and cell sizes of approximately 5mm. The foams have a significantly more homogenous microstructure than those produced by direct addition of gas, and do not require the addition of silicon carbide particles. The process is easily scaled up, but remains expensive and relatively hazardous, due to the use of calcium and the need to handle escaped hydrogen gas [41], [44].

2.3.3.4 Foamable precursor produced by powder metallurgy techniques

There are many different ways to manufacture cellular materials [29]. One of the available processes to manufacture cellular materials which has become increasingly popular in the past few years and is at the stage of industrial implementation now is called powder-compact foaming technique (PCF). Fabrication of Al foams through PCF technique consists of mixing aluminium or aluminium alloy powders with appropriate foaming agents, which get entrapped by compacting this mix to a dense product called “foamable precursor material”. The powder mix can be compacted directly by hot-pressing, conform extrusion, or powder rolling. Alternatively the powder may be cold compacted for better handling in conventional extrusion or rolling. The following step is heating the precursor above its solidus temperature, which results in the nucleation of pores, due to gas release from the decomposing of foaming agent, followed by rapid expansion to a maximum and then collapse of the foam structure [29], [41]-[45].

The appropriate selection of the raw powders with respect to purity, particle size and distribution, alloying elements, and other powder properties is essential for successful foaming. Commercial air-atomised aluminium powders were shown to be of sufficiently quality. However, powders from different manufacturers led to notable differences in foaming behaviour and empirical criteria have been derived to facilitate the selection of powders. The cost of powders and the ability of a manufacturer to provide sufficient quantity with a constant quality are also crucial [38], [44].

The mixing procedure should yield a homogenous distribution of metal powder and foaming agent to ensure that high quality foams with uniform pore-size distribution are obtained [33], [38].

Powder consolidation can be carried out by various techniques. It has to be ensured that the foaming agent is completely embedded in the metal matrix and no residual open porosity remains. One way to obtain foamable precursor material with nearly 100% theoretical density is the combined use of cold isostatic pressing (CIP) and ram extrusion. CIP is first applied to consolidate the powder mix to billet with a relative density of 70-80% and a mass of typically 50 kg. These billets are used in the subsequent extrusion step. Although CIPing is not absolutely necessary (powders have been filled into thin-walled aluminium cartouches and inserted into the extrusion

machine without prior consolidation) it has additional advantages such as the prevention of powder contamination and powder de-mixing. The CIP billets themselves are not foamable because of their large content of residual porosity, which causes massive hydrogen losses when the material is heated [44].

Heat treatment at temperatures above the solidus temperature of the foamable matrix is necessary to produce the foam structure. The gas released by decomposition foaming agent may form pores in the solid state but only above the solidus are bubbles formed and the matrix expands up to a maximum volume, that is to a minimum density. The density and density distribution of the growing foam can be controlled by several parameters. The foaming agent content in the precursor material is obviously important, but furnace temperatures and heating rates also have an influence. The mold material, the mold shape, and the type of furnace naturally influence the heating rate and have therefore also to be considered. A careful control of the heating conditions during foaming is essential for obtaining high-quality foams. The difficulty is that the liquid foam foam is thermodynamically unstable and conditions changes constantly during foaming. There are various intermediate stages: at first only the mold is heated directly, whereas the foamable material receives heat only indirectly via heat conduction through mold. Initially there are merely some points contact between the piece of foamable material in the mold and the mold walls. However, as the temperature increases, the precursor softens and assumes the contour of the mold thus increasing the transfer of heat. Moreover, heat transfer via radiations gains importance with rising temperatures. The reflectivity of the mold and precursor surfaces may change during the process and add a further variable. Finally, after foaming has started, the thermal conductivity of the precursor rapidly decreases thus reducing heat flow. As soon as the mould has been filled with foam it has to be cooled down below its solidus temperature to stabilize the foam structure. The phenomena during cooling are also quite complex and difficult to describe for reason similar to those mentioned for the heating phases [29], [43]-[46].

2.4 Review on the fabrication technique of aluminium foam at AMREC and UTP

This section reviews and discusses two different methods of fabricating aluminium foam at AMREC and UTP. The first method deals with the technique known as

powder compact foaming (PCF) process which can be effectively used as net-shape components, stiffing cores in castings, or in complicated hollow profiles [44]-[45], [48]. In the second method, called sintering and dissolution process (SDP) which was developed by Zhao *et al.* [22]. As described in the previous section, the architecture of the cellular structure is the result of the processing technique, which can be classified according to Figure 2.8 [31].

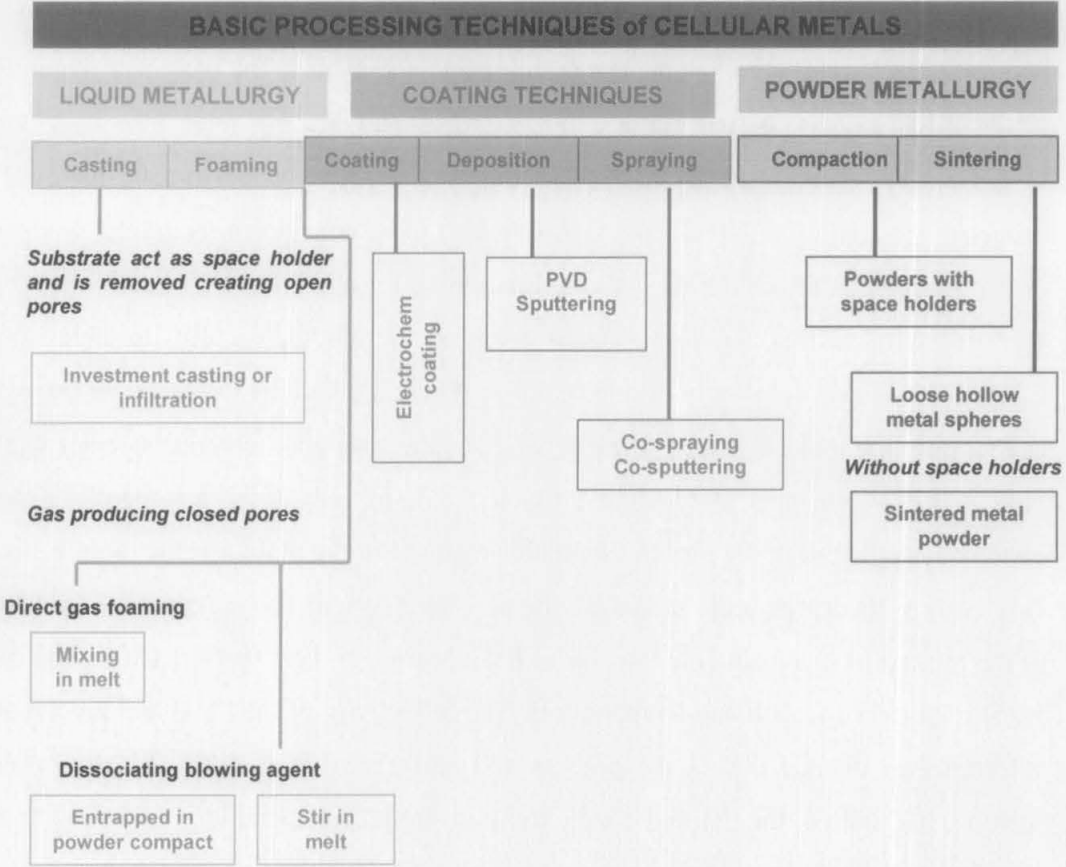


Figure 2.8: Processing techniques for cellular metals classified according to the state of the metal, the formation of the cellular architecture and the pore-forming ingredients [31]

2.4.1 Powder Compacting Foaming Technique

One of the earliest methods developed to produce a foamable precursor was to mix powdered metal with a foaming agent and any reinforcement required to increase the melt viscosity. The key to producing a suitable precursor is to compress the mixed powders into a relatively solid block, so that when foaming takes place the gas evolved does not simply escape from the material [38], [41].

2.4.1.1 Foam synthesis

The first task of the effort to synthesize aluminium foam using this technique was to select a suitable foaming agent [47], [49]-[51]. The foaming agent must undergo thermal decomposition near melting temperature of matrix (T_m) and generate gas pressure in the Al matrix sufficient to overcome atmospheric pressure and cause foaming. The decomposition temperature (T_D) must lie between the solidus and liquidus temperatures for the aluminium alloys (generally between 580 and 900°C) [52]-[54]. The foaming agent selected for the work is TiH_2 , and it undergoes decomposition via:



Ideally, T_D for the foaming agent should be closely matched to the melting temperature of the aluminium alloy. If T_D is higher than the melting temperature, the foaming agent may dissolve in the melt or float to the melt surface, while if T_D is lower than the melting temperature of the aluminium, the sample may develop internal pressure and crack prematurely. If these general conditions are met, and the heating and cooling are carefully controlled, aluminium foam with acceptable porosity can be synthesized [54].

The composition of the powder blend, including the amount of foaming agent strongly affected ultimate density and quality of the foam. To establish an understanding of the amount of foaming agent needed, foams were synthesized with

selected amount of TiH_2 from 0.2 up to 1.5 wt.%. The best results were obtained with 1 wt. %, although foams synthesized with 0.8-1.2 wt.% showed similar structures. Increasing the amount of foaming agent beyond 1.2wt.% led to poor compaction behaviour in the semi-finished material, and much of the gas that was evolved by decomposition and escaped prior to expansion [54]-[60]. Similar results were reported by Asavavisithchai et al. [20].

2.4.1.2 The Influence of temperature on foaming process

The PCF technique was used to fabricate closed-cell Al foam in which the foamable precursor were made by mixing Al powder, with an average particle size $45\ \mu\text{m}$ (purity 99.7%) with 1% TiH_2 powder, with an average particle size of $20\ \mu\text{m}$, followed by cold compaction, in a lubricated 30 mm diameter die to a pressure of 400 MPa.

Ex-situ foaming was performed by placing precursors in a steel tube (see Figure 2.9 (a) & (b)) and foaming in a pre-heated resistance furnace at varying temperature from 700 to 900 °C.

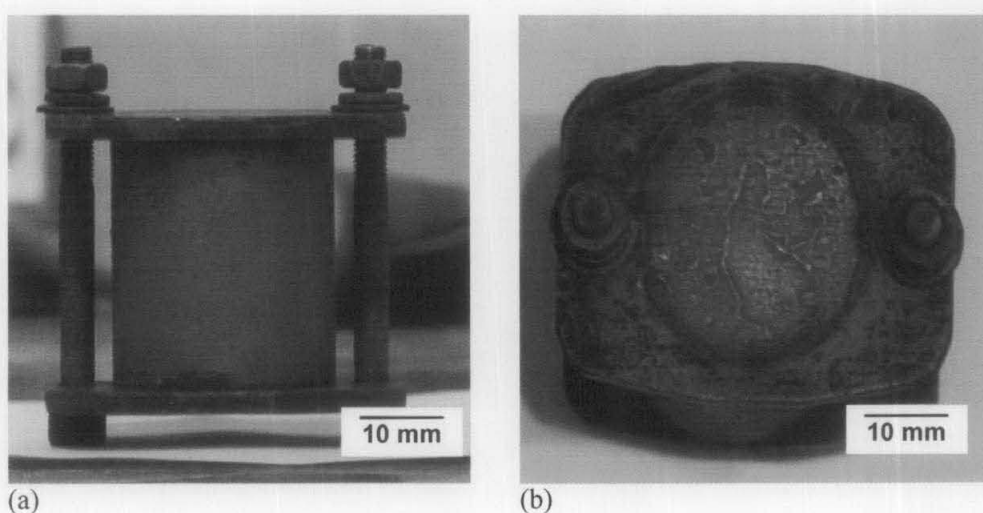


Figure 2.9: Foaming Die (a)Side view (b)Plan View

From Figure 2.10 (a), a thick layer of melted metal was observed at the base of the foaming die. This accumulation of liquid metal indicates that extensive, gravity-driven drainage of liquid metal occurs through the cell structure. This shows that only the

bottom part of the precursors was melted and the blowing process occurs during the semi solid state of the metal. The product of the foaming process at 700 °C under air atmosphere exhibited solid sample without the cellular networking within the structure (Figure 2.10 (b)).

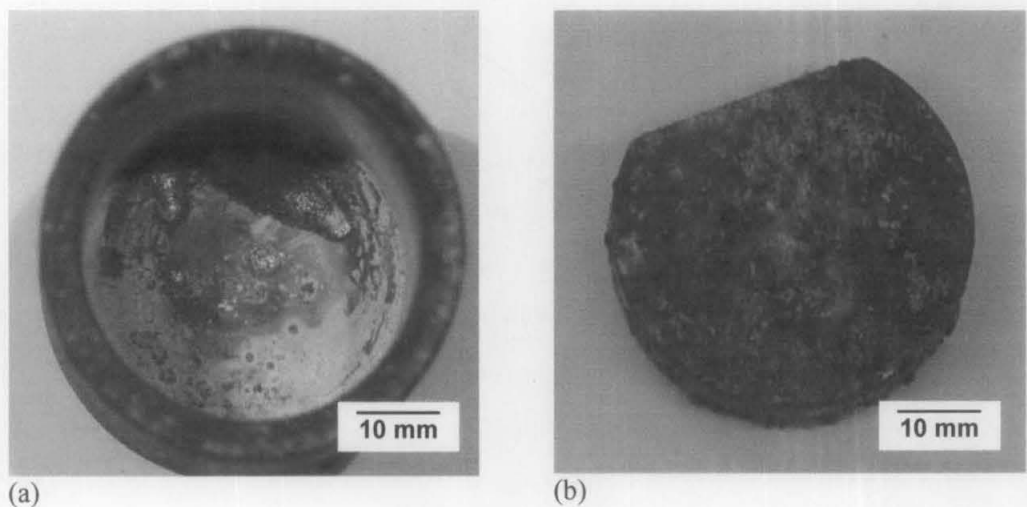


Figure 2.10: (a) Melted metal at the base of the die (b) The solid samples

Figure 2.11 (a) shows the cross-section of the specimen that had been subjected to foaming process at 700 °C under air atmosphere. The pore nucleated at the centre of the specimen which is due to the fact that the gas release from the decomposition of TiH_2 . However, only small part of the specimen experienced this decomposition process which leads to poor distribution of the expansion of the sample as the degree of fluidity is still low [62].

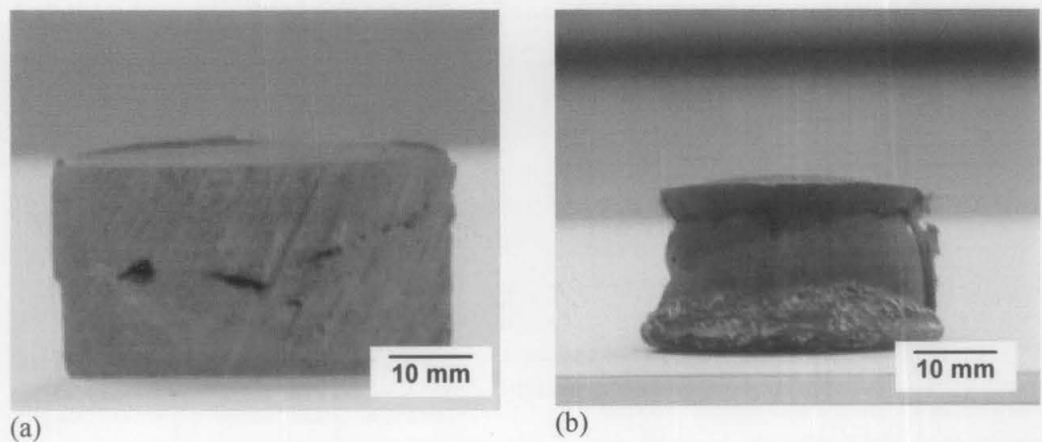


Figure 2.11: (a) Cross-section of foam sample (b) The solid sample

The following observation was noted when the temperature of foaming was varied from 750 and 900 °C:

Table 2.1: The influence of temperature on foaming process

Temperature / °C	Environment	Observation	Volume expansion / %
750	Air	solid state expansion	25
800	Air	cellular network exist	125
850	Air	cellular network exist	325
900	Air	cellular network exist	400

Figures 2.12 (a)-(d) show the influence of temperature on the foaming behaviour of the sample. It is evident that the foaming process is sensitive to the forming temperature chosen. If the final sample temperature is below the solidus temperature of the metal, there is not very much more of an effect than a slight solid state expansion. If the final temperature lies in the solidus/liquidus interval, the foam formation can be observed, but it is limited to quite low expansion. The viscosity of the semi-molten material is still quite high at this temperature and surface oxidation leads to an additional resistance towards bubble inflation, counteracting the internal gas pressure built up by the decomposing blowing agent [64], [65].

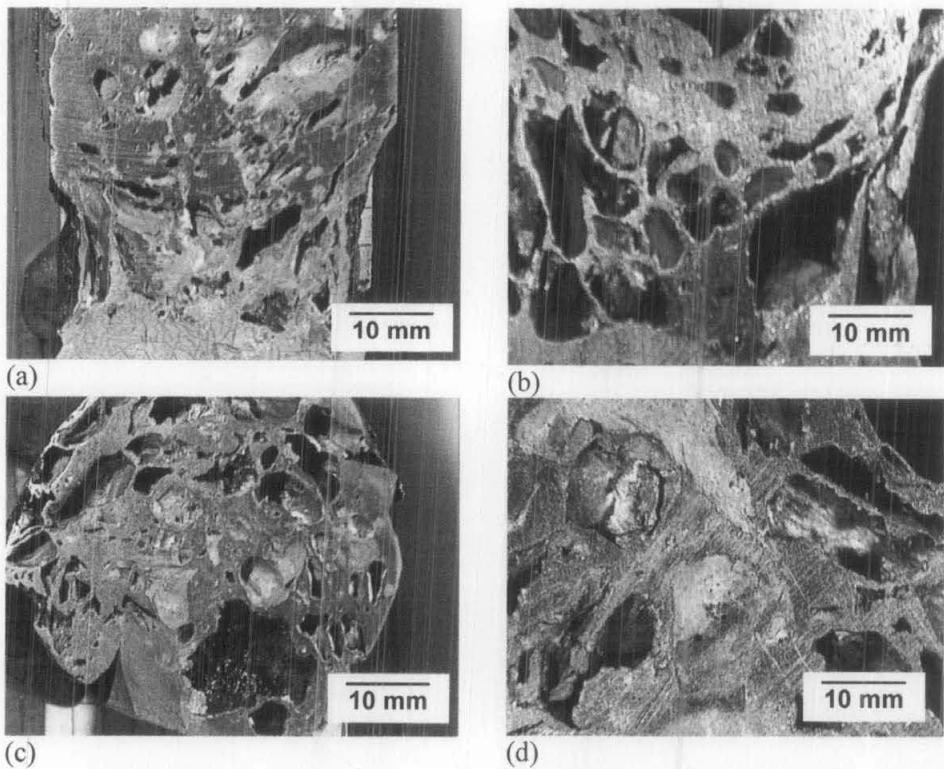


Figure 2.12: Morphology of foam formed at different temperature (a) 750°C (b) 800°C (c) 850 °C (d) 900°C

Increasingly higher temperatures reduce viscosity and promote gas production so that higher and higher volume expansion can be observed. Besides reducing viscosity, high furnace temperatures naturally also lead to high heating rates. This can be advantageous for obtaining high volume expansion. The maximum of foam expansion for the Al is at 900 °C, as can be seen from Table 2.1 which relates the maximum expansion as a function of foaming temperature [54], [64].

The foam owes their collapse to two mechanism, drainage and coalescence as shown in Figures 2.13 (a) and (b). Drainage is the flow of molten metal from the cell walls into the cell edges downward driven by gravity. A thick layer of metal at the bottom of the samples is the result of this process. Coalescence occurs whenever two cells merge to form one large cell. It is thought that cell rupture is the reason for such processes but no definite investigations have been carried out yet [54], [55]-[60].

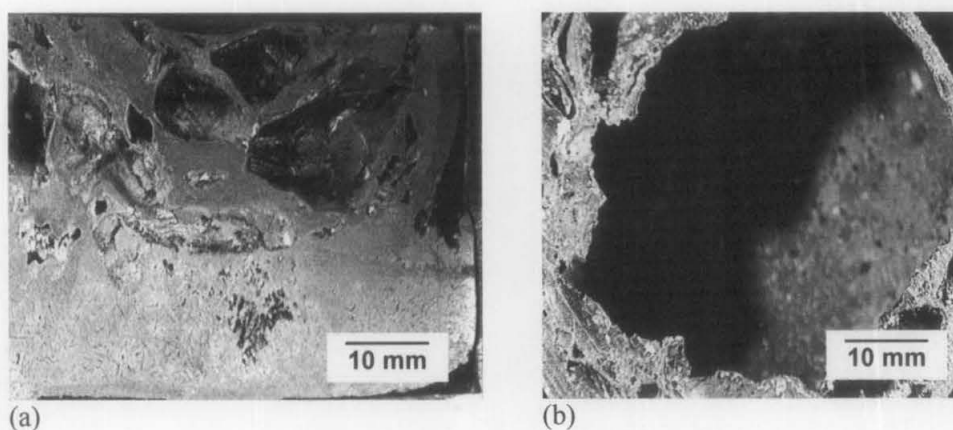


Figure 2.13: Mechanism of collapsing process of foam specimen: (a) Drainage (b) Coalescence

2.4.1.3 The influence of time on foaming process

Ex situ foaming was also performed by placing precursors in a mild steel tube and foaming in a pre-heated resistance furnace and the time of foaming was varied from 4 to 10 minutes. The foaming temperature was maintained at 800 °C in all experiments performed. The volume of expansion was measured by calculating the volume of foam filled in the die and the following physical parameters was recorded [61]-[63].

Time / min	Volume expansion / %	Density / gcm^{-3}
4	30	2.602
6	100	2.404
8	400	1.302
10	300	1.302

It is evident that the foaming process is also dependent on the foaming time chosen. If the time is not sufficient for the melting process of Al, there is not very much more of an effect than a slight solid state expansion (see Figures 2.14 (a)-(d)).

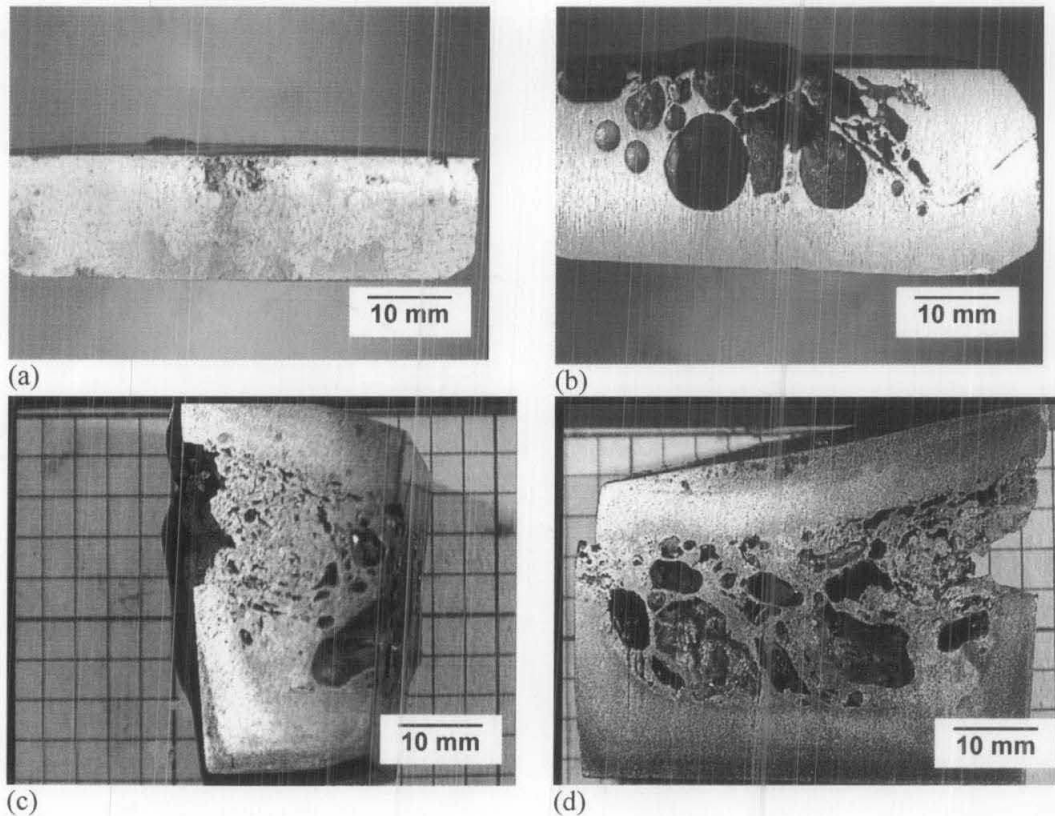


Figure 2.14: The morphology of the foam structure formed after (a) 0.5 minutes (b) 1 minute (c) 2 minutes (d) 3 minutes of foaming process

As can be seen from Figure 2.14 (a), the aluminium shows the foaming stages, namely: the initiation and evolution of porosity stage in which pores elongated perpendicular to the compaction direction (which was from top to bottom) are formed. Figures 2.14 (b)-(d) present the pore growth stage where the pores are inflated by the evolving hydrogen and increasing rounded off as the foam expands [63]-[65].

If the time is in the verge of melting process of Al, the foam formation can be observed, but it is limited to quite low expansion. The viscosity of the semi-molten

material is still quite high at this temperature and surface oxidation leads to an additional resistance towards bubble inflation, counteracting the internal gas pressure built up by the decomposing blowing agent.

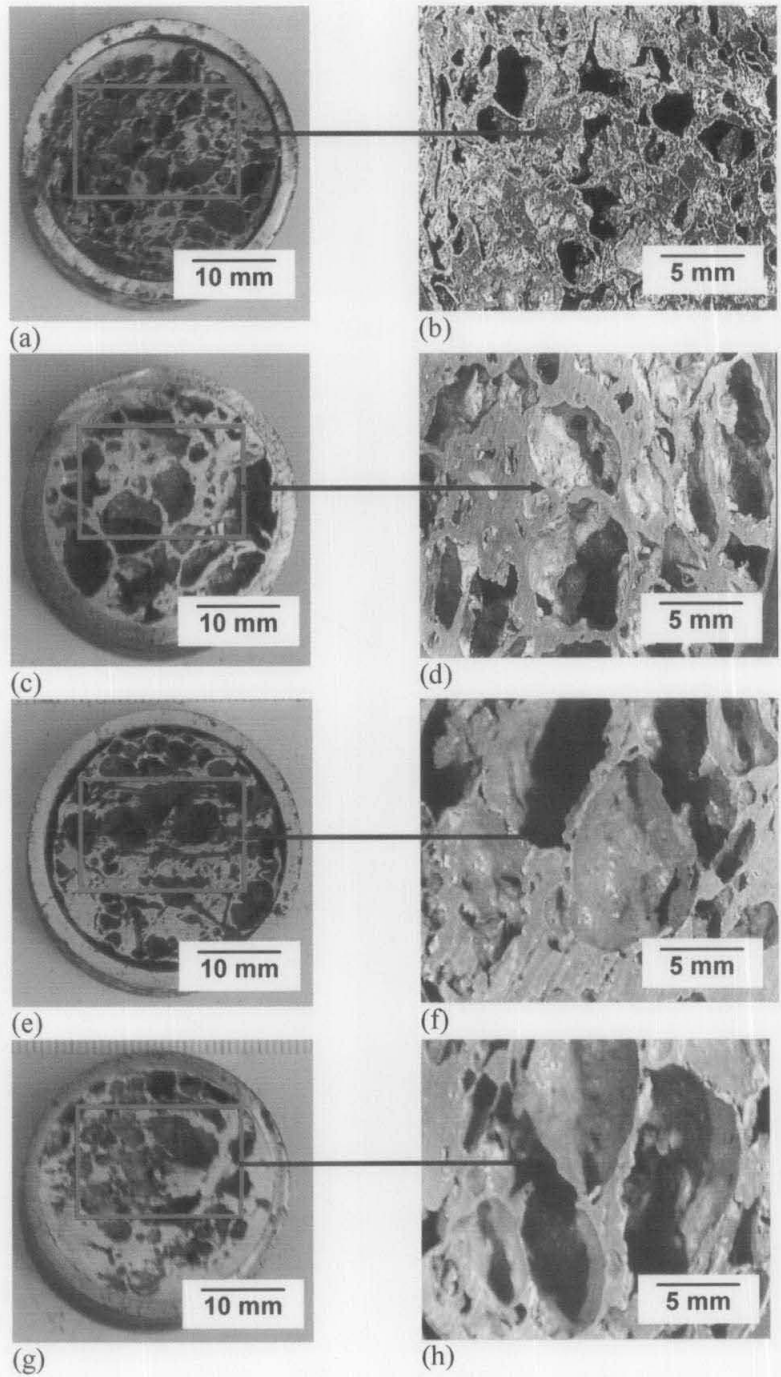


Figure 2.15: The morphology of the foam structure formed after (a) 4 mins (b) 6 mins (c) 8 mins (d) 10 mins (e)-(f): stereomicrograph of the respective selected area at higher magnification

Increasingly time of foaming reduces viscosity and promotes gas production so that higher and higher volume expansion can be observed as shown in Figure 2.15 (a). Besides reducing viscosity, longer time naturally also lead to high heating rates. These can be advantageous for obtaining high volume expansion. Figures 2.15 (c), (e) and (g) present the collapse stage where after maximum expansion had occurred and no more hydrogen gas is released and foams begins to decay. This decay leads to foams with large and irregular pores, collapsed and oxidized pores especially at the top of sample and a solid metal layer at the bottom [54], [60], [63].

2.4.2 Sintering Dissolution Process (SDP)

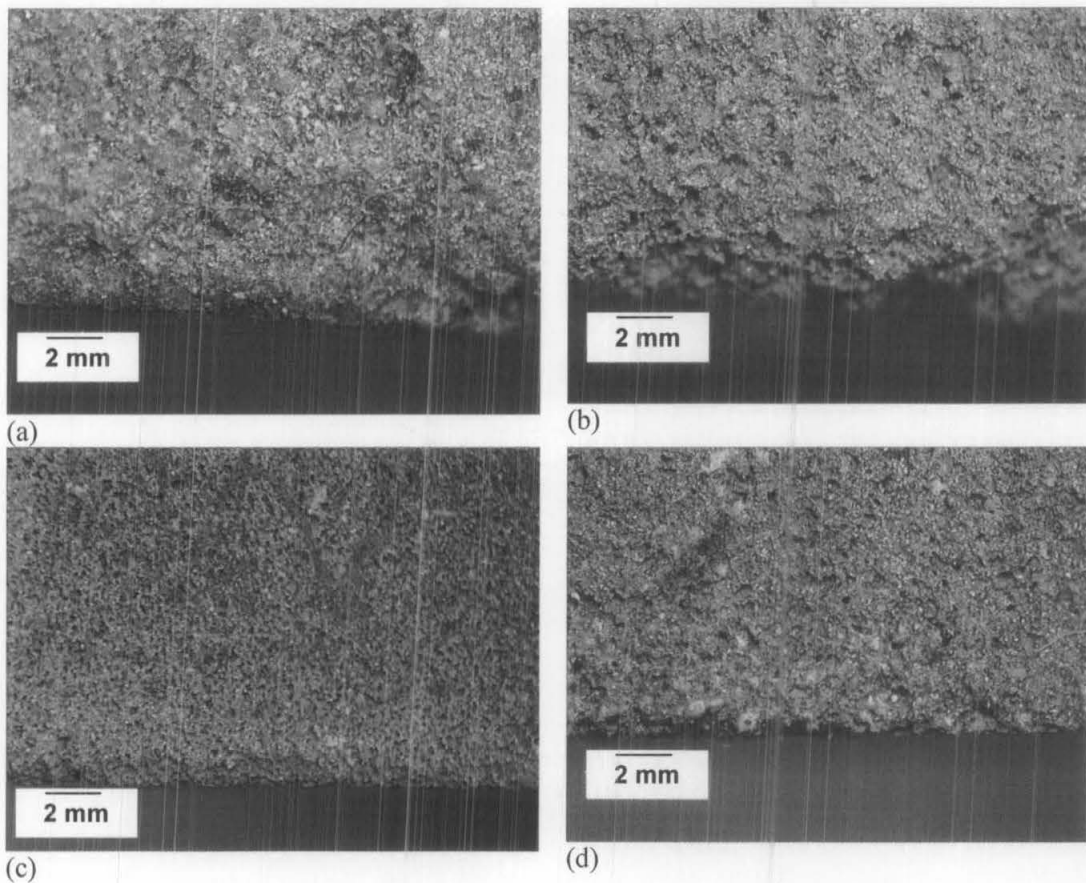


Figure 2.16: The stereomicrographs of the foam body at different sintering temperatures (a) 600°C (b) 660°C (c) 670°C (d) 680°C

Zhao *et al.* [22] have developed a method for fabricating open-celled Al foams through conventional powder metallurgy (P/M) route known as the sintering and dissolution

process (SDP). This approach consists of three stages. Firstly, a mixture of Al and NaCl powders is die-pressed into a green compact under appropriate pressure. Secondly, the compact is sintered at a temperature either above or below the melting point of Al to form a well-bonded and net-shaped structure. Finally, the NaCl particles are removed by leaching the sintered compact in hot water leaving behind an open-celled Al foam. But the Al foams made by SDP may have inferior mechanical properties [7], [13], [22], [66]-[71].

Mazli and Othman [23] had also employed this method to fabricate the Al foam. The streomicrograph of the 60% vol NaCl/Al samples fabricated using this SDP technique at different sintering temperature were shown in the respective Figure 2.17 (a)-(d). In all cases, a completely intact Al foam specimens could not be produced in all sintering temperature process. All the compacts collapsed in the subsequent leaching process. Some Al moved out of the surface of the compacts in the form of globules when the sintering temperature was above 660 °C. The size of the Al globules increased with increase temperature. The loss of Al from the compact led to inhomogenous cell wall structure and cell size distribution. It was observed that the Al foams fabricated under the medium compaction pressure between 200 and 250 MPa are not fully dense but contain Al particles which have almost certainly existed in the green compacts and retain after sintering process [8], [10]-[15].

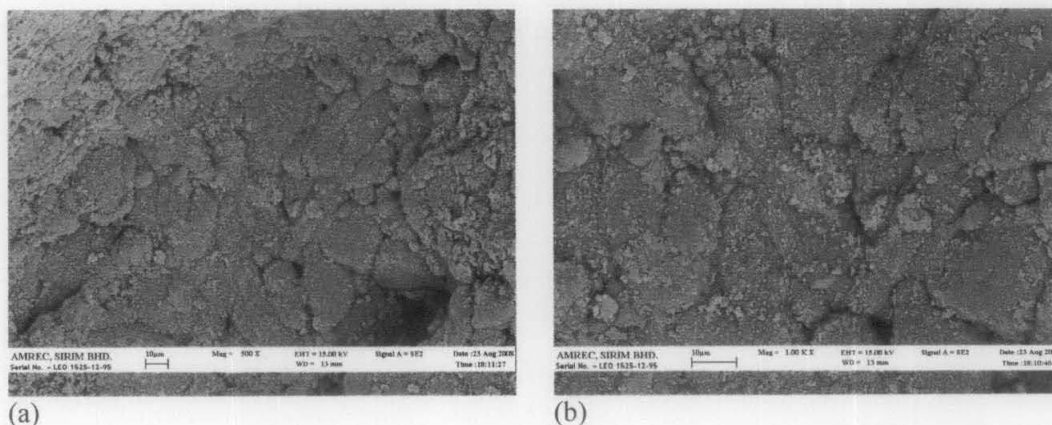


Figure 2.17: Images (SEM) of SDP Al foam showing the existence of individual Al particles at (a) X500 (b) X1000

2.5 Compaction at elevated temperature

This section presents a model to understand the higher densities, and more even density distribution, achieved with hot compaction compared to conventional “cold” compaction. The model focuses on the effect of yielding in the radial and axial stresses during uniaxial pressing [72]-[74].

When the piston of hydraulic cylinder exerts pressure upon the liquid inside the cylinder, the pressure applied in axial direction is transformed 1:1 to radial pressure upon the cylinder wall. When the powder is being compacted in a rigid cylindrical die, the axial pressure, exerted upon the powder by the compacting punch, is only partially transformed to radial pressure upon the die wall. The radial pressure can be quite substantial, but it cannot reach the level of the axial pressure because a powder is not liquid and has no hydraulic properties [73], [74].

2.5.1 Hysteresis of the radial pressure

The way in which the empirical relationship between the radial and axial pressure is governed by general laws of physics and mechanics can be understood, in principle at least, from simple model, suggested by W.M. Long [72] and presented in detail below. First a free-standing cylindrical plug of metal having a modulus of elasticity E and a poisson factor ν . A compressive axial stress σ_a , applied to the end-faces of plug, provoked by laws of elasticity, a radial stress σ_r , and the radius of plug is expanded by the factor:

$$\varepsilon_r = (\sigma_r - \nu\sigma_r - \nu\sigma_a) / E \quad (2.2)$$

By considering, the same plug being put into a tightly fitting cylindrical die and the die is assumed to have a modulus of elasticity much larger than that of metal plug [72]. Also, it is assumed that the die is extremely well lubricated, such that any friction between the plug and the die-wall is negligible. Exerting, via two counteracting punches, axial pressure upon the plug, its radial expansion ε_r is

relatively small because the die expands extremely little due to its large modulus of elasticity [72]. Thus $\varepsilon_r = 0$ is a sufficiently close approximation of reality, and from (2.2), it follows:

$$\sigma_r - \nu\sigma_r - \nu\sigma_a = 0 \quad (2.3)$$

Hence, the relationship between radial and axial stress in the plug is:

$$\sigma_r = \sigma_a \nu / (1 - \nu), \text{ elastic loading} \quad (2.4)$$

The maximum shearing-stress in the plug (derived from Mohr's circle) is always:

$$\tau_{\max} = (\sigma_a - \sigma_r) / 2 \quad (2.5)$$

With increasing axial stress in the plug, τ_{\max} increases too, until it exceeds the shearing yield-stress $\tau_0 = \sigma_0/2$, i.e. until $\tau_{\max} \geq \sigma_0$. Then, from (2.4), the following condition of flow emerges:

$$(\sigma_a - \sigma_r) \geq \sigma_0, (\sigma_0 = \text{yield point of metal plug}) \quad (2.6)$$

Now, plastic flow occurs in the plug, and the relationship between radial and axial stress in the plug is:

$$\sigma_r = \sigma_a - \sigma_0, \text{ plastic loading} \quad (2.7)$$

At axial pressure release, τ_{\max} immediately falls below the level of the shearing yield-stress ($\tau_{\max} < \sigma_0/2$), and the stresses in the metal plug are being released according to:

$$\sigma_r = \sigma_a \nu / (1 - \nu) + k, \text{ elastic releasing (k = constant)} \quad (2.8)$$

In the course of continued release, the axial stress in the plug decreases and eventually becomes even smaller than the radial stress. From this point on, the following condition of flow rules:

$$(\sigma_r - \sigma_a) \geq \sigma_0 \quad (2.9)$$

and the relationship between radial and axial stress is:

$$\sigma_r = \sigma_a + \sigma_0, \text{ plastic releasing} \quad (2.10)$$

From the above description, it is evident that the entire loading-releasing cycle, which the metal plug undergoes in the compacting die, forms a hysteresis (see Figure 2.18).

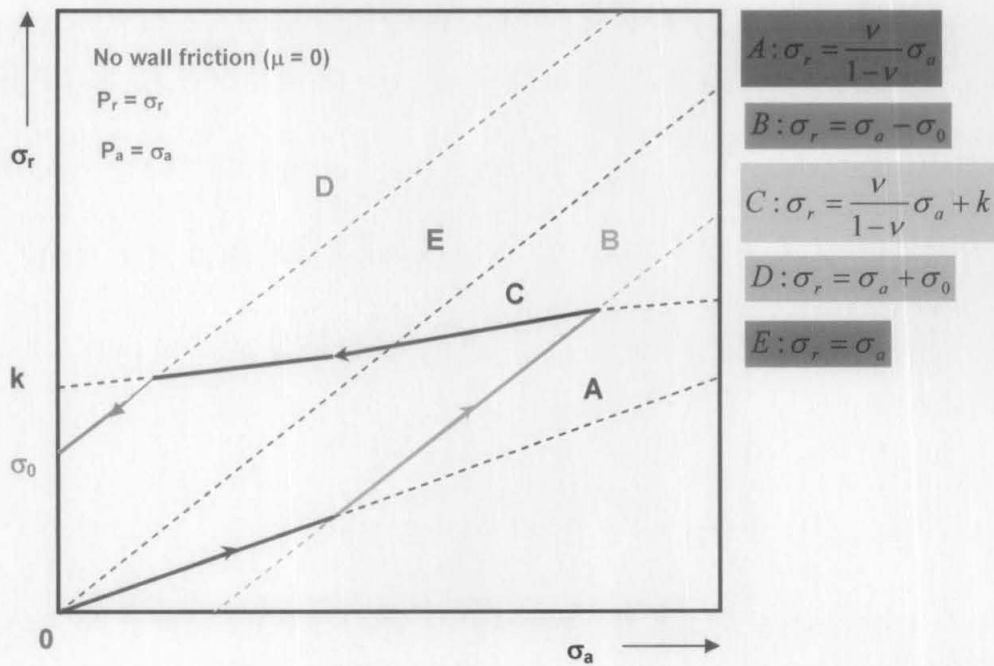


Figure 2.18: Relationship between radial and axial pressure occurring in a cylindrical metal plug inside a rigid die during a cycle of loading and releasing the axial pressure [72]

On a fundamental level, densification occurs simply by the motion of particles centres toward each other in several stages. The first stage of the compaction process is sliding and restacking of powder particles at low pressures, which lead to

relatively small because the die expands extremely little due to its large modulus of elasticity [72]. Thus $\varepsilon_r = 0$ is a sufficiently close approximation of reality, and from (2.2), it follows:

$$\sigma_r - \nu\sigma_r - \nu\sigma_a = 0 \quad (2.3)$$

Hence, the relationship between radial and axial stress in the plug is:

$$\sigma_r = \sigma_a \nu / (1 - \nu), \text{ elastic loading} \quad (2.4)$$

The maximum shearing-stress in the plug (derived from Mohr's circle) is always:

$$\tau_{\max} = (\sigma_a - \sigma_r) / 2 \quad (2.5)$$

With increasing axial stress in the plug, τ_{\max} increases too, until it exceeds the shearing yield-stress $\tau_0 = \sigma_0/2$, i.e. until $\tau_{\max} \geq \sigma_0$. Then, from (2.4), the following condition of flow emerges:

$$(\sigma_a - \sigma_r) \geq \sigma_0, (\sigma_0 = \text{yield point of metal plug}) \quad (2.6)$$

Now, plastic flow occurs in the plug, and the relationship between radial and axial stress in the plug is:

$$\sigma_r = \sigma_a - \sigma_0, \text{ plastic loading} \quad (2.7)$$

At axial pressure release, τ_{\max} immediately falls below the level of the shearing yield-stress ($\tau_{\max} < \sigma_0/2$), and the stresses in the metal plug are being released according to:

$$\sigma_r = \sigma_a \nu / (1 - \nu) + k, \text{ elastic releasing } (k = \text{constant}) \quad (2.8)$$

Among the proposed equations for powder compaction, the Heckel equation [87] has been used frequently which proposed that increasing in relative density obeys a first order type of reaction with applied pressure:

$$-\frac{dD}{dP} = K(1 - D) \quad (2.11)$$

or

$$\ln\left(\frac{1}{1 - D}\right) = KP + B \quad (2.12)$$

where D is the relative density, P the applied pressure, and B and K are constants. Heckel [87] found an empirical relationship between K and the yield strength, σ_0 , for a range of metal powders:

$$K = \frac{1}{3\sigma_0} \quad (2.13)$$

In above equation K is related to plastic deformation capacity of the material and $3\sigma_0$ is often called the yield pressure. This yields the following integrated form of equation which correlates relative density to applied pressure:

$$\ln\left(\frac{1}{1 - D}\right) = \ln\left(\frac{1}{1 - D_0}\right) + \frac{P}{3\sigma_0} \quad (2.14)$$

where D_0 is relative density at P equals zero.

However, in conventional Heckel equation, the effect of applied pressure on yield strength was neglected and this could make error in fittings. In order to show the dependence of yield strength with pressure, the linear relationship was introduced:

$$\sigma = \sigma_0 + K_1 P \quad (2.15)$$

where σ is the yield strength of consolidated materials. This relationship could explain increasing constraint caused by neighboring particles as the compaction reduces the volume fraction of porosity. So equation (2.13) could be written according to equation (2.15):

$$\ln\left(\frac{1}{1-D}\right) = \ln\left(\frac{1}{1-D_0}\right) + \frac{1}{3k_1} \ln\left(1 + \frac{k_1 P}{\sigma_0}\right) \quad (2.16)$$

Denny [86] proposed that in order to reach yield strength of the material, the applied stress must be increased by:

$$k_1 = \frac{2\nu^2}{1-2\nu} \quad (2.17)$$

where ν is the Poisson's ratio.

The required conditions for this relation are applying axial and radial pressures within the die, and assuming a perfectly rigid die.

Recently, another compaction equation has been proposed by Panelli and Ambrosio Filho [91]:

$$\ln\left(\frac{1}{1-D}\right) = KP^{1/2} + B \quad (2.18)$$

This equation is also exhibits good accuracy in predicting compaction behaviour of loose powders. Some researchers have tried to correlate compressibility parameters with mathematical equations. For instance, Fogagnolo *et al.* [90] reported the effect of mechanical milling on morphology of powders. They related compaction behaviour of powders to the microstructural evolution occurred during milling and applied Paneelli-Ambrosio Filho equation [91]. In this study, Heckle equation will be used to assume the pressure effect on the consolidated samples at elevated temperature.

2.6 Taguchi's philosophy

Dr. Taguchi's comprehensive system of quality engineering is one of the greatest engineering achievements of the 20th century [92]-[97]. This method focus on the effective application of engineering strategies rather than advanced statistical techniques. It includes both upstream and shop-floor quality engineering. Upstream methods efficiently use small-scale experiments to reduce variability and cost-

effective, robust designs for large-scale production and market place. Shop-floor techniques provide cost-based, real time methods for monitoring and maintaining quality in production. The further upstream a method is applied, the greater leverages it produces on the improvement, and the more it reduces the cost and time. Taguchi's philosophy is founded on the following three very simple and fundamental concepts [92]:

- Quality should be designed into the product and not inspect into it.
- Quality is best achieved by minimizing the deviations from the target. The product or process should be designed that it is immune to controllable environmental variables.
- The cost of quality should be measured as function of deviation from the standard and the losses should be measured system-wide.

Taguchi proposes an “off-line” strategy for quality improvement in place of an attempt to inspect quality into a product on the production line. He observes that poor quality cannot be improved by the process of inspection, screening and salvaging. No amount of inspection can put quality back into the product [93]. Taguchi recommends a three-stage process: system design, parameter design and tolerance design [95]. In present work, Taguchi's parameter design approach is used to study the influence of processing parameters on the physical and mechanical properties of Al foam fabricated through PASDP technique.

2.6.1 Selection of an orthogonal array (OA)

Before selecting a particular OA to be used for conducting the experiments, the following two points must be considered [92].

- The number of parameters and interaction of interest
- The number of levels for the parameters of interest

The non-linear behaviour, if exist, among the process parameter can only be studied if more than two levels of the parameters are used. Therefore, each parameter was analysed at three levels [93]. The number of process parameters and their level

values are already decided. To limit the study, it was decided not to study the second order of interaction among the parameters. Each three level parameters has 2 degrees of freedom (DOF) (number of level – 1), the total DOF required for four parameters, each at three levels is 8 [=4 X (3-1)]. As per Taguchi's method the total DOF of selected OA must be greater than or equal to the total DOF required for the experiment. So an L_9 OA (a standard three-level OA) having 8 (=9-1) degrees of freedom was selected for the present analysis. This OA has four columns and nine experiments-runs. The four parameters at three levels can be assigned to these four columns [93]-[95].

2.6.2 Analysis procedure for the selected orthogonal array

The analysis procedure of the selected L_9 OA is presented using the parameter A assigned to column 1 of the L_9 OA (Table 2.3). The same step by step procedure is applicable to all parameters assigned to the various column of the OA. Since experiments for each trial condition of the selected OA's have been repeated three times, three responses have been recorded [95]-[97].

Let the three responses against each trial condition of the L_9 OA be y_{ij} , $i = 1, 2, \dots, 9$, $j=1, 2, 3$ (Table 2.3). Three responses (y_{ij}) are shown under R_1 , R_2 and R_3 of the response column. R stands for repetition.

Table 2.3: The L_9 (3^4) OA (parameters assigned) with response

Serial number	Run order	Parameter trial conditions				Responses (raw data)			Signal-to-noise ratio (dB)
		A(1)	B(2)	C(3)	D(4)	R_1	R_2	R_3	
1	3	1	1	1	1	Y_{11}	Y_{12}	Y_{13}	S/N(1)
2	7	1	2	2	2	Y_{21}	Y_{22}	Y_{23}	S/N(2)
3	5	1	3	3	3	Y_{31}	Y_{32}	Y_{33}	S/N(3)
4	1	2	1	2	3	Y_{41}	Y_{42}	Y_{43}	S/N(4)
5	4	2	2	3	1	Y_{51}	Y_{52}	Y_{53}	S/N(5)
6	6	2	3	1	2	Y_{61}	Y_{62}	Y_{63}	S/N(6)
7	9	3	1	3	2	Y_{71}	Y_{72}	Y_{73}	S/N(7)
8	2	3	2	1	3	Y_{81}	Y_{82}	Y_{83}	S/N(8)
9	8	3	3	2	1	Y_{91}	Y_{92}	Y_{93}	S/N(9)
Total						Σ	Σ	Σ	

R_1, R_2, R_3 represent responses values for three repetition of each trial. The 1's, 2's and 3's represent levels 1, 2 and 3 of the parameters, which appear at the top of column. Y_{ij} are measured values of the quality characteristic (response).

2.5.3 Raw data analysis

(a) Level totals and their averages

The average values of the response at each parameter level are obtained by adding the results of all trials conditions at the level considered, and then dividing by the number of data points added. Those for parameter A, the levels totals of the response at A1, A2 and A3 are calculated as:

$$A(1) = (y_{11} + y_{12} + y_{13}) + (y_{21} + y_{22} + y_{23}) + (y_{31} + y_{32} + y_{33})$$

$$A(2) = (y_{41} + y_{42} + y_{43}) + (y_{51} + y_{52} + y_{53}) + (y_{61} + y_{62} + y_{63})$$

$$A(3) = (y_{71} + y_{72} + y_{73}) + (y_{81} + y_{82} + y_{83}) + (y_{91} + y_{92} + y_{93})$$

The average values of responses at A1, A2 and A3 are:

$$\bar{A}(1) = \frac{A(1)}{9}, \quad \bar{A}(2) = \frac{A(2)}{9}, \quad \bar{A}(3) = \frac{A(3)}{9}$$

(b) Main effects due of parameter

The main effect of parameter A when level changes from L_1 to $L_2 = A(2) - A(1)$. The main effect of parameter A when level changes from L_2 to $L_3 = A(3) - A(2)$ where L_1 , L_2 and L_3 are the levels of parameters.

(c) Analysis of variance (ANOVA)

(i) Total of all results (T):

$$T = \sum_{i=1}^n \sum_{j=1}^R y_{ij}$$

where n is the total number of trials = 9 and R is the total number of repetitions = 3.

- (ii) Correction factor (C.F.):

$$C.F. = \frac{T^2}{N}$$

where N is the total number of experiments = 9 X 3 = 27

- (iii) Total sum of squares (SS_T):

$$SS_T = \sum_{i=1}^n \sum_{j=1}^R y_{ij}^2 - C.F.$$

- (iv) Sum of squares due to a parameter (SS):

$$SS_A = \left[\frac{A(1)^2}{N_{A_1}} + \frac{A(2)^2}{N_{A_2}} + \frac{A(3)^2}{N_{A_3}} \right]$$

where N_{A1} , N_{A2} and N_{A3} are the number of trials with parameter A at level 1, 2 and 3 respectively. The sum of squares SS_B , SS_C and SS_D are calculated in similar way.

- (v) Error of sum of squares:

$$SS_e = SS_T - (SS_A + SS_B + SS_C + SS_D)$$

The symbol 'e' stands for error term.

- (vi) Total and parameter degrees of freedom (DOF):

$$f_T = \text{Total DOF} = (\text{total number of trials} - 1) = (R \times n - 1)$$

$$f_A = \text{DOF of parameter A} = (\text{number of levels of parameter A} - 1)$$

The DOF f_B , f_C , f_D and f_e are calculated in similar way.

(vii) Mean square of variance (V):

Variance due to parameter A:

$$V_A = \frac{SS_A}{f_A}$$

(viii) F-ratios:

$$F_A = \frac{V_A}{V_e}$$

F_B , F_C , F_D and F_e are calculated in similar way.

(ix) Pooling

If the calculated F-ratio for a parameter is less than F-ratio at a stated confidence level (95% confidence level), the effect of the parameter is insignificant and the parameter is pooled. If the parameter is pooled, the sum of squares due to the parameter is added to the error sum of squares and other ANOVA terms are modified. If the parameter A is pooled.

(x) S/N data analysis

The raw data are converted to S/N ratios (dB). This transformation consolidates the repeated response (raw data) in each trial condition into a single number. Thus, 9 S/N ratios are calculated which in turn also reduces the total DOF of the experiments. The quality characteristic for compressive strength is of higher-the-better type. So, the signal-to-noise (S/N ratio) for the “higher-the-better” type was used and is given below:

$$\left(\frac{S}{N}\right)_{HB} = -10 \log \left[\frac{1}{n} \sum_{j=1}^R \left(\frac{1}{Y_j^2} \right) \right]$$

2.7 Solid state sintering

At sintering temperatures of approximately half of the absolute melting temperature, the compacted metal particles bond together by atomic motion that eliminate the high surface energy associated with powder particles. Predominantly in metal powder, the mechanisms are usually by thermally activated diffusion along either over the surface, along the grain boundary, or lattice paths [24]-[25], as shown in Figure 2.19.

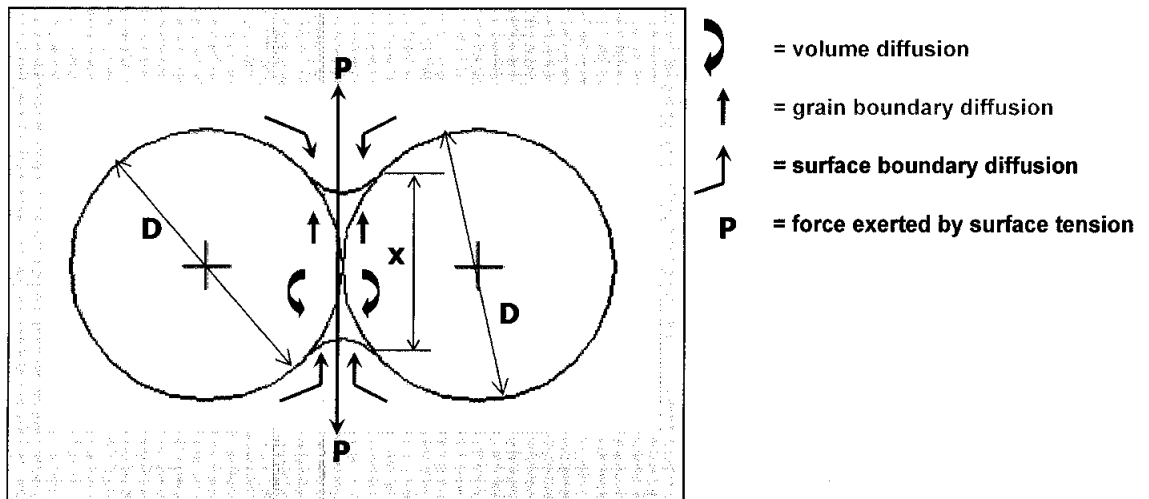


Figure 2.19: Possible diffusion path for mass transfer during sintering process [24]

Transport mechanism developed will determine how mass flow in respond to the driving force. These transport events can either be surface or bulk mechanisms dependent on material, particle size, sintering time and temperature. They are composed of the actual atomic mechanisms contributing to mass flow, as sketched on the two sphere geometries in Figure 2.20.

Surface transport involves neck growth without a change in inter particle spacing due to mass flow activities from the particle surface sources. During the surface transport controlled sintering, surface diffusion and evaporation-condensation are the major contributors to mass flow from the particle surface [25].

Bulk transport mechanisms involve a net change in the dimensions (shrinkage) of the compact, as mass is transported from the particle interior to the neck region. Such mechanism includes volume diffusion, grain boundary diffusion, plastic flow and viscous flow. At higher temperatures bulk transport processes tend to be dominant in latter stages of the sintering process contributing significantly to compact densification (or shrinkage) [24]-[25].

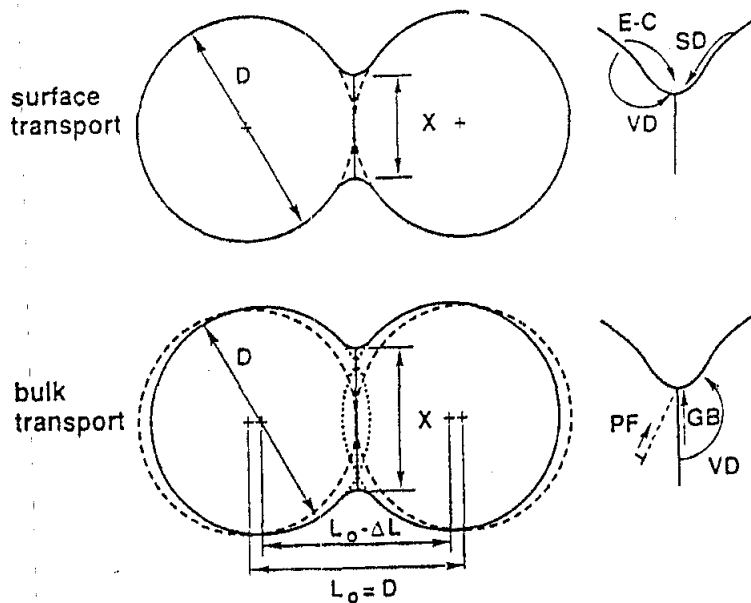


Figure 2.20: The two classes of sintering mechanism as applied to the sphere sintering particles model (E-C = evaporation-condensation, SD = surface diffusion, VD = volume diffusion, PF = plastic flow, GB = grain boundary) [25]

Neck growth between the particles, at the original sites of point contacts, causes changes in the important sintering properties, such as densification, shrinkage, surface area loss, increasing strength, conductivity and hardness. Several stages in the sintering process have been identified based on pore spheroidisation and grain boundaries development (see Figure 2.21).

The initial stage of sintering is characterized by rapid growth of the interparticle neck. During this stage, a large amount of energy is available which facilitates the movement of particle within the matrix. In the intermediate stage, the pore become smoother and has an interconnected, cylindrical nature as the compact properties are developed. As the grain growth boundaries begin to form, the pore volume between the particles decreases so that the grain growth can occur, controlled by volume and grain boundary diffusion. During this stage, the pore geometry is complicated and the pores are located at grain boundary intersections. Surface transport events may allow pore migration to the grain boundaries [24].

The pores developed in the previous stages become unstable and collapse into spherical pores. Interaction between pores and grain boundaries can take three forms: the pore can retard grain growth, the pores can be dragged by the moving grain boundaries during grain growth, or the grain boundaries can break away from the pores, leaving them isolated in the grain interior. Pore isolation occurs as the grain boundaries continue to develop. Bulk diffusion is now dominant mechanism since the exposed surface area is negligible [25].

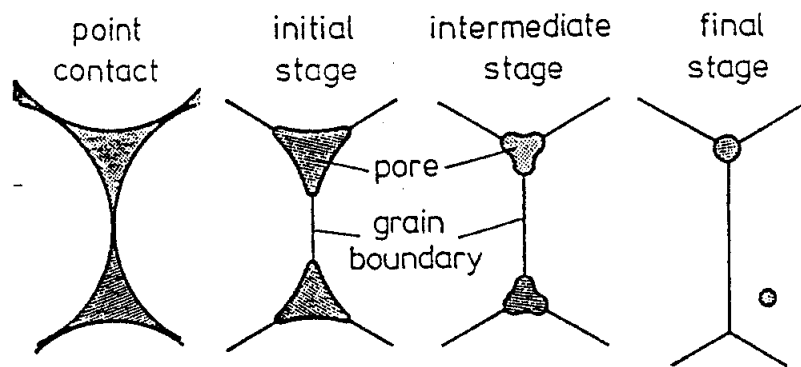


Figure 2.21: Schematic diagram of the pore structure changes and grain boundary development during sintering [24]

The sintering kinetics is diffusion controlled and therefore is affected by the sintering temperature and the amount of available free surface energy, known as the “driving force”. The driving force varies according to the amount of surface curvature present in compact. As the grain boundaries grow, the surface energy is converted to grain boundary energy and the amount of available free energy decrease, slowing down the transport mechanism. Consequently the net driving force is low and sintering progresses slowly. However, it should be noted that the initial surface energy per unit volume varies inversely with particle diameter, so that finer particles increase the driving force [24]-[25].

During sintering of a particular material several sintering mechanisms could operate together, involving several modes of mass flow. Since surface energy is

generally a small driving force, only a few materials sinter to full density by solid state sintering. In order to design mechanical properties comparable with wrought or cast materials, densification can be aided by simultaneously applying compaction pressure during sintering process.

2.8 Powder fabrication - Atomization

Basically all materials can be made into powder form. The particular fabrication method selected depends on the properties of the material and process economic. There is always a correlation between the powder fabrication mode and size, shape, microstructure and chemistry of the product. Generally metal powders are produced commercially by one of four approaches: chemical, electrolytic, mechanical and atomization. The diversity in size, shape and surface morphology of powders reflects the underlying conditions that control the formation of the metal and alloy in a finely divided form. Irrespective of the method of fabrication, the major event in the production metal or alloy in a finely divided form is the generation of new surfaces. Historically, the mechanical, chemical and electrolytic methods of fabrication were dominant. Examples include the granulation of copper powder; the grinding of reduced oxide iron powder, the reduction of precipitated copper carbonate, and the reduction of tungsten oxide [24]-[26].

Atomization (see Figure 2.22) involves the formation of powder from molten or liquid metal using a spray of droplets. Most of the elemental and prealloyed powders are formed by this process. This process is attractive due to the applicability to many alloys and its easy process control. Basically, atomization consists of disintegration of a molten metal stream by gas (air, nitrogen, helium or argon), water or oil jets, at high pressure. The pressure range applied depends on the final particle size required. Normally for the gas atomization, the pressure is typically below 5 MPa, but on a few occasions range up to 18 MPa. Meanwhile in water atomization, the most common technique for producing elemental and alloy powders, pressure is the main control process parameter. Higher water pressure result in higher water velocities hence smaller particle size produced. Because of rapid cooling, the powder shape produce is irregular and rough with some oxidation [24].

Gas atomization used inert gas, which rapidly expands from a nozzle placed at the bottom of the tundish. The metal now forms spherical droplet which are allowed to cool through the chamber length. Due to the spherical shape of the particle, gas atomized powders are not easily compressible and give low green density, therefore they have to be consolidated by canning and hot isostatic pressing into bars or billets or hot working, e.g. extrusion. Air / water atomized powders can be die compacted into compacts with high enough green density and which are strong enough to be handled because of the irregular morphology of the particles. The properties of the atomized powder are quite different in both cases – Table 2.7.1 provides a contrast between water and gas atomization [25].

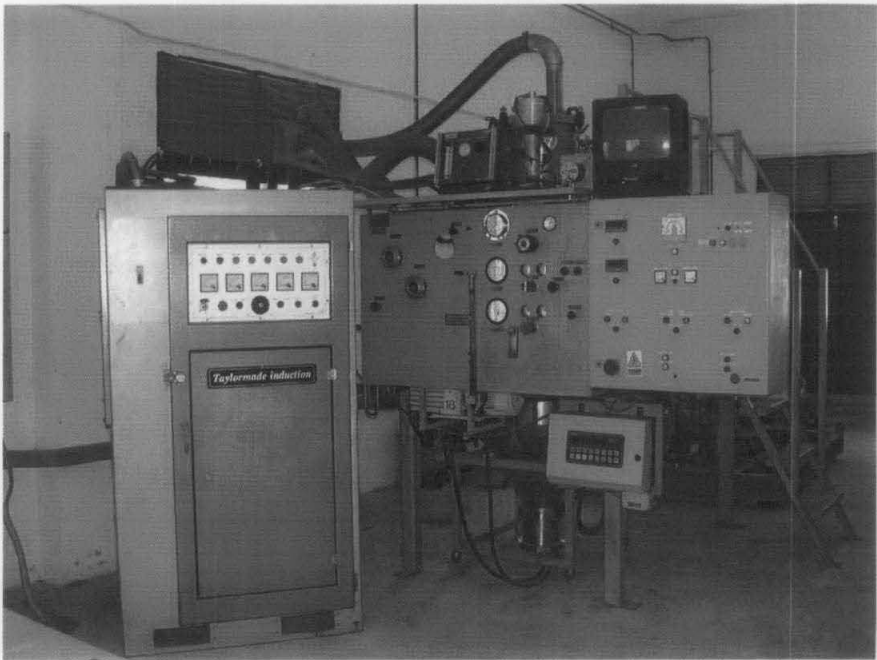


Figure 2.22: Atomiser facility at pilot plant in AMREC

Table 2.4: A comparison of typical gas and water atomization process

Attribute	Gas atomization	Water atomization
Particle size, μm	100	150
Particle shape	Spherical	Nodular, irregular
Agglomeration	Some	Little
Apparent density, %	55	35
Cooling rate, $^{\circ}\text{C}/\text{min}$	10^4	10^5
Segregation	Slight	Negligible
Oxide content, ppm	120	3000
Fluid pressure, MPa	3	14
Fluid velocity, m/s	100	100

2.9 The range of application of structural foams based on cellular metals

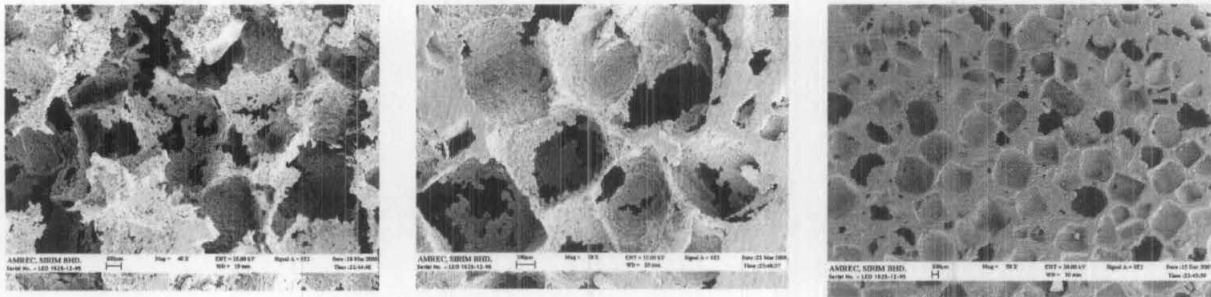
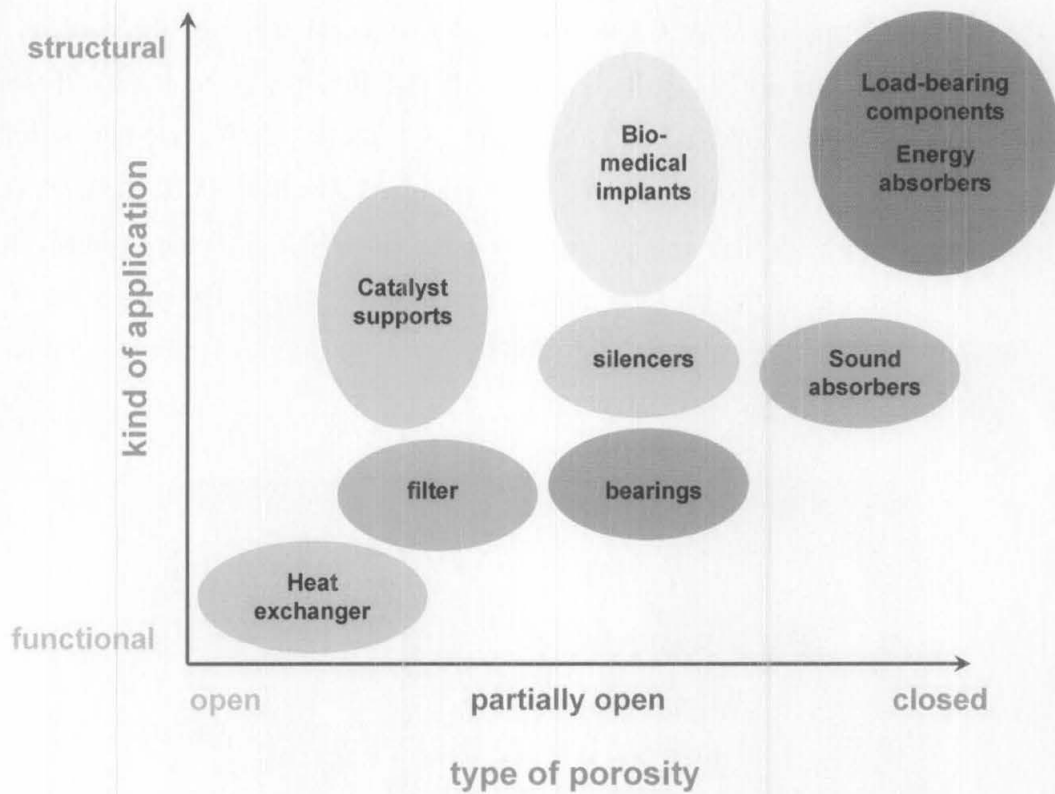


Figure 2.23: Applications of cellular metals grouped according to the degree of open porosity needed and whether the application is functional or structural

The type of porosity needed (open versus closed), amount of porosity needed and size of porosity desired is, in particular, crucial for any evaluation of applications for cellular metallic materials. Many applications require that a medium, either liquid or gaseous, be able to pass through the cellular material. There may be a need for various degrees of “openness” ranging from “very open” for high rate fluid flow to “completely closed” for load-bearing structural application, and appropriate materials satisfying these conditions have to be found. Figure 2.23 shows which types of porosity the various application fields require. Normally, a difference is made

between whether an application is ‘functional’ or ‘structural’, but there is considerable overlap between these two notions [1]-[3], [26].

The question of from which metals or alloys a given type of cellular structure can be manufactured is also important. Structural load-bearing parts (Figure 2.24) have to be light because otherwise they would be made from conventional massive metals or alloys. Therefore, aluminium, magnesium, or titanium cellular or porous metals are preferred for such applications. For medical application, titanium may be preferred because of its compatibility with tissue. Stainless steel or titanium is required for applications in which aggressive media are involved or high temperatures occur [3], [30].

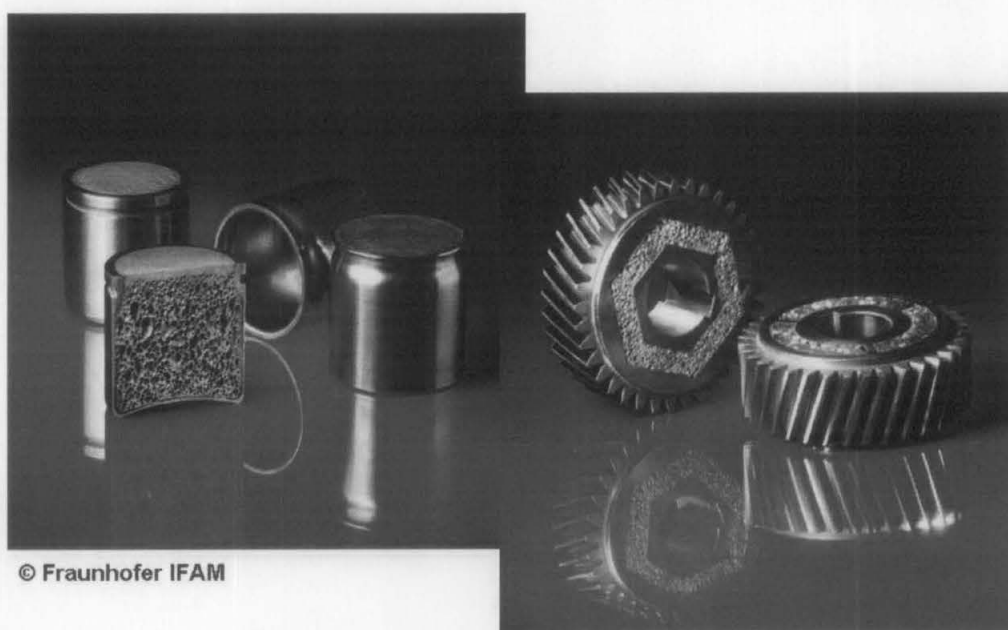


Figure 2.24: Components of metal foam developed by Fraunhofer IFAM [98]

Finally, processing and cost issues have to be considered. The technology must be available to bring the selected cellular metal into the required shape and to incorporate it into the machine or vehicle where it has its function. A technology for making cellular metal will be futile if the required component cannot be manufactured at a reasonable price. Traditionally powder metallurgy (PM) has created porous sintered metals for a wide range of applications [26], [98].

Light weight construction is gaining importance in automobile. Alongside improvements in wind resistance and tribology, weight reduction measures are of

primary importance. This is necessary because for each particular automobile there are increasing customers demand for safety, comfort, performance, and available internal space. Using conventional methods of construction to provide these customer-oriented features leads to a considerable increase in weight, giving rise to strong pressure to reverse the weight gain. It is therefore regarded as an imperative development objective to achieve a reduction in weight relative to axle loads [98]-[100].

Apart from using single materials in light weight construction, increasing use is made of mixed construction methods and various forms of composite materials to achieve weight reduction. However, since these materials frequently incur higher cost, it is of primary importance to ensure that they play a multifunctional role [30], [76].

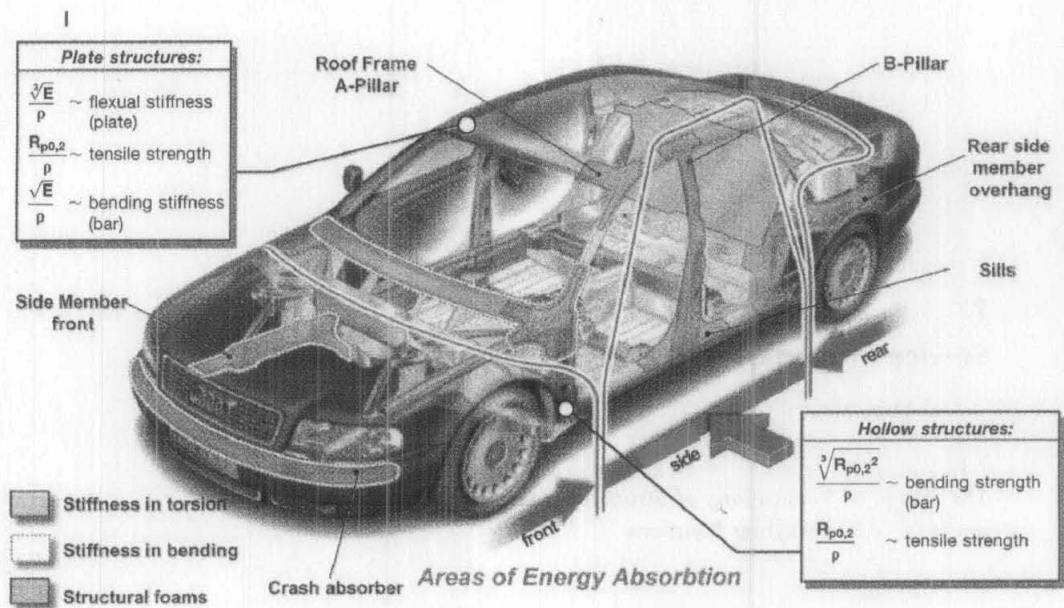


Figure 2.25: Typical loading of car body structure (Audi A8): strategy for structural foam reinforcements [100]

This also applies to structural foams in the form of cellular metals based on aluminium or alternative systems based on expanding plastics, such as epoxy or polyurethane resins foams. These are required to take over functions such energy absorption, stiffness, thrust-field reinforcement, and sound absorption in different methods of construction [100].

The area where these kinds of material are of potential use can be derived at an early stage in design using finite element (FE) analysis of typical stresses in a car body. The result makes it possible to evaluate which structural components in the body structure can play a multifunctional role and what measures can be adopted to achieve the desired result cost-effectively, taking into account space availability and the factors inherent in lightweight construction. As illustrated in the car body of the Audi A8 (Figure 2.25), there are many areas in the bodywork where structural foams can be used. They are particularly suitable for hollow structures where space is too restricted for other more cost-effective measures. Particular areas where the multifunctional application profile can be exploited to beneficial effect are the side-members, the boundaries of the floor of the passenger compartment, and in the region of the sills and pillars [98]-[100].

2.10 Prototype by powder compact foaming

When metallic foams were revived by new manufacturing technologies such as powder metallurgy, investment casting, and other process in the early nineties, the new material was introduced to the industry and to potential customers in a very enthusiastic manner and with great advertising expense [99]-[101]. Information was widely spread by companies and institutes who worked on the development of metallic foams. Metallic foams became highlights at industrial fairs and at many conferences researchers, designers and material engineers discussed the structures and the properties of cellular metals that are relevant to industrial application. The foam developers missed no chance to present their work and to introduce their new product, although the first material samples were only demonstrator: they were small, had irregular pore size and pore distributions and high degree of scattering in their properties. They were all “hand made” and their producers were very proud of their creations from porous metals [98]-[101].

But very soon the discussion came round to real parts or components and then the foam manufacturers had to think about manufacturing net-shape parts, considering particular problems of geometry or function. Since real net-shape parts are not flats, cubes or cylinders, new manufacturing methods using mould and furnace technologies had to be introduced [1], [98]. The manufacturing of the powder

metallurgical (PM) precursor material as well as the foaming technique for the compacted powder are called the powder compact foaming technique (PCF), which is practised by IFAM, Germany [101]. Step-by-step prototype manufacturing methods were developed, starting with the foaming of parts in crucible melting furnace (Figure 2.26 (a)) and the use of steel mould. The geometry of the first aluminium-foam parts was rather simple, as shown in Figure 2.26 (b).

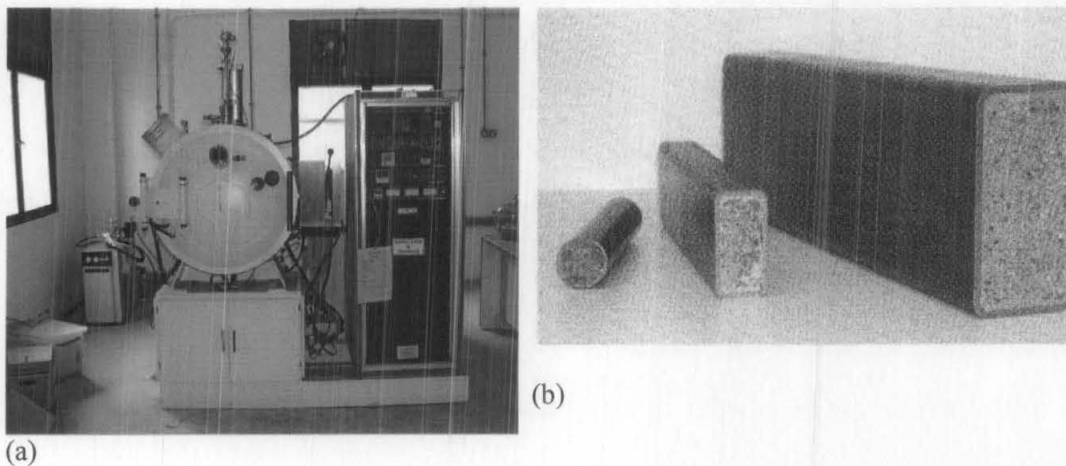


Figure 2.26: (a) The melting furnace (b) Simple foam parts [74].

From the very beginning the application of the PCF route for making net-shape parts was the goal. This method, using compacted aluminium powder and titanium hydride as a foaming agent is described by several authors [29], [41], [98].

The first step in the PM process is to make foamable precursor material from aluminium powder. Small amounts of aluminium powder were mixed by mechanical stirring, then poured into aluminium liners, then closed and extruded by a conventional aluminium extrusion machine. However, the bulky liner material in some cases caused insufficient foaming [41].

An alternative route for producing precursor material for PCF is the Conform process [102] and this route could be a suitable manufacturing method for strip like dimensions of precursor material. Generally, the small batches of manufactured aluminium-foam prototype parts made in this stage of development led to a large scatter in the foam properties. The reproducibility of the whole process and the properties of the components were relatively poor. This was due to the handwork involved in producing the parts, which typically resulted in varying process

parameters. With growing demand for precursor material and with an increasing volume of foamed prototypes the process flow and the quality of the prototypes could be improved by an approach to series production conditions.

The process steps as it is currently performed in PCF are:

- Manufacturing of Al powder (alloyed or unalloyed) and grain size classification
- Mixing Al powder with foaming agent (TiH_2)
- Cold isostatic pressing of the mixture to form foamable extrusion billets
- Heating and extrusion of the billets to form precursor material
- Filling the precursor in steel or cast-iron moulds
- Foaming in a suitable foaming furnace (heating rate, temperature above solidus)
- Cooling and removal of the foamed parts from the mould

For successful manufacturing of aluminium-foam parts in the PCF, it is necessary to observe furnace temperature, heating rate, temperature distribution within the mould, foaming time and cooling conditions that have to be kept in certain ranges to achieve aluminium-foam components of high quality. These parameters are not the same for all types of component; they depend on their geometry and dimensions (wall thickness), on the alloy and also on the properties and design of the mould [98]-[102].

In prototype manufacturing it is not possible to modify the whole equipment or to change the layout of machines whenever a new component with a new geometry has to be foamed [99]. Compromises concerning the furnace used and the process parameters must be made to enable the best possible technical and economic manufacturing conditions to be achieved. Nevertheless, it is possible to make parts in a wide range of different geometries with the use of adequate equipment. From the beginning of aluminium foam development, prototype manufacturing was the main goal. The development of the foaming process, applied to a particular component, was carried out along with component testing to verify material properties [99]-[102].

In series production it would be necessary to adapt the furnace and the mould to the product to achieve the optimized foaming parameters as well as the most economic production conditions for the particular product. The number of parts that

has to be produced is also an important process parameter to be considered in the design of an aluminium foam production machine and the necessary additional equipment [101].

One of the most important pieces of equipment in the aluminium foam manufacturing route is the foaming furnace (Figure 2.27 (a) & (b)). The foaming parameters have to be kept in their optimized range, the precursor material in the mould has to be heated to the foaming temperature in the foreseen time and the temperature distribution within the mould must be kept within small tolerances to avoid irregular foaming within the mould [98], [102].

The heat transfer from the furnace to the mould with the precursor material can occur by three different mechanisms: conduction, convection and radiation. For the development of prototype manufacturing methods various furnaces working with these three physical principals were tested. Basic calculation concerning heat capacity and heat transfer were carried out before testing the different furnace system. The heating rate in the foamable precursor material is the key parameter, influenced by the foam part dimensions and foaming mould properties. In order to have enough power to heat the mould one must first consider in what time the furnace has to be heated up from room temperature and secondly, the heat that has to be put into the mould during operation at the proper temperature (steady state). Thus two separate calculations have to be made in order to know which phase is dimensioning the power need of the furnace [99]-[102].

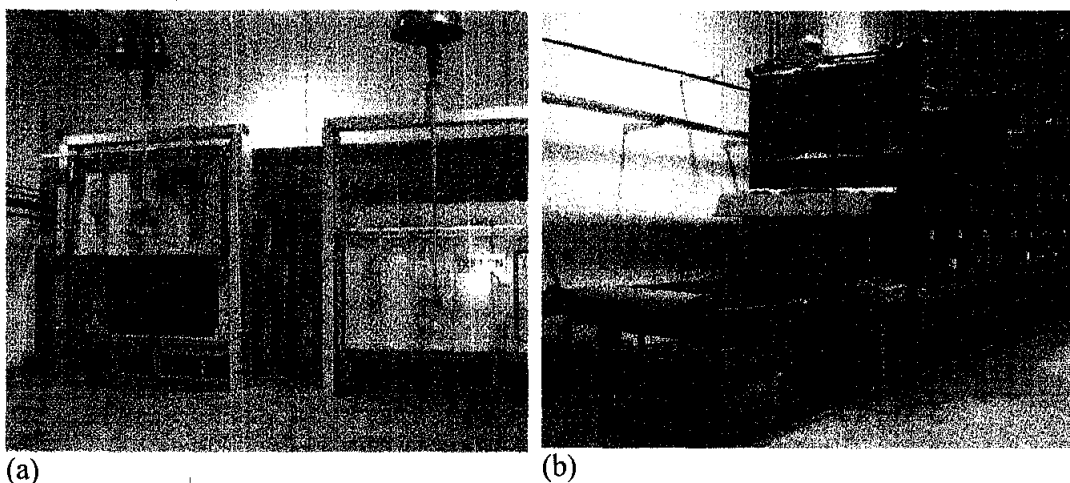


Figure 2.27: (a) Batch type furnace (b) Continuous furnace [74]

A widely used approximate calculation method, when predicting the power need for heating the mould from room temperature to operation temperature is based on the heat capacity, heating time and the mass of the mould and its precursor material, assuming that the heat losses are zero [1], [98], [101]. This basically wrong assumption is corrected by assumptions about the heat losses or the use of safety factors (SF). Different safety factors are used by different authors in the literature. In this case a conservative figure has been chosen, $SF = 2$ as shown in equation (2.19).

$$P = \frac{m.C_p.\Delta T}{t}.SF \quad (2.19)$$

where;

m = heated mass in kg

C_p = average heat capacity over the temperature range in Jkg^{-1}K

ΔT = temperature range in K

t = heating time in seconds

P = power need in W (Js^{-1})

SF = safety factor

Heating can be compared to a lab beaker which is to be filled to a certain level during a given time period [30], [102]. The flow to the beaker (or system, as it is called in the study of thermodynamics) is the controlling parameter. Flow F = volume per unit time, can be equated with the energy/time unit required to heat the tool, volume is the amount of thermal energy supplied to the system ($mC_p\Delta T$) and time is the targeted heating interval. The figure below describes a closed system with no losses (Figure 2.28).

In reality, however, heat losses do occur, and they are proportional to the temperature level to be attained in the material heated. Losses increase with increasing temperature, presupposing that room temperatures remain constant. Losses during heating are likely to be smaller than at equilibrium. The beaker, thereby includes ‘holes’ whose size increase with increasing temperature (see Figure 2.29).

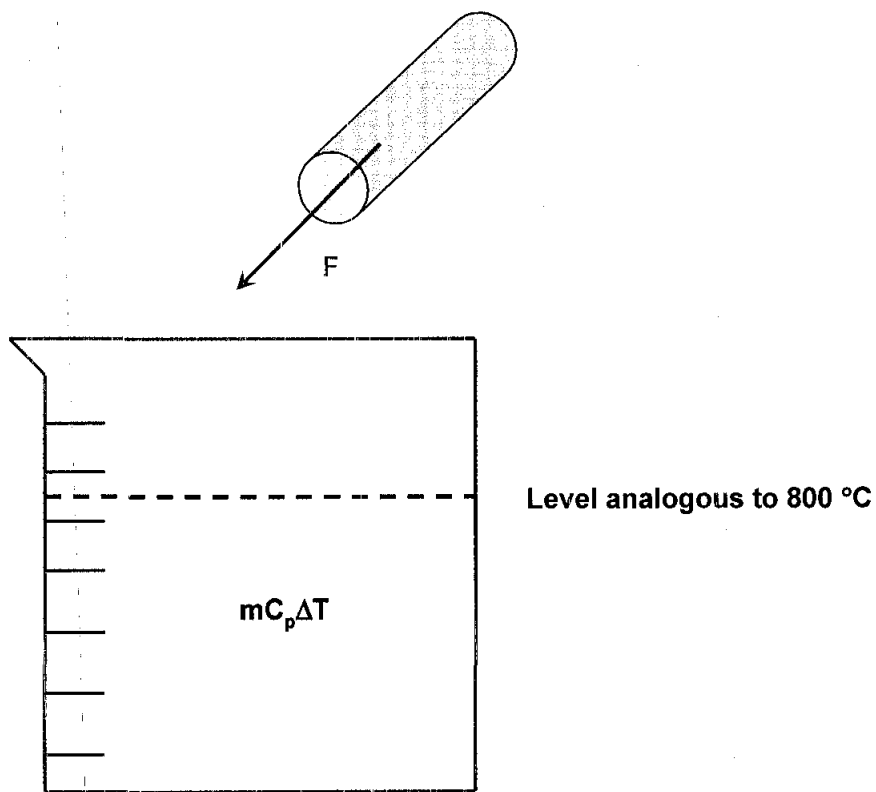


Figure 2.28: A lab beaker which is to be filled to a certain level during a given time period [31]

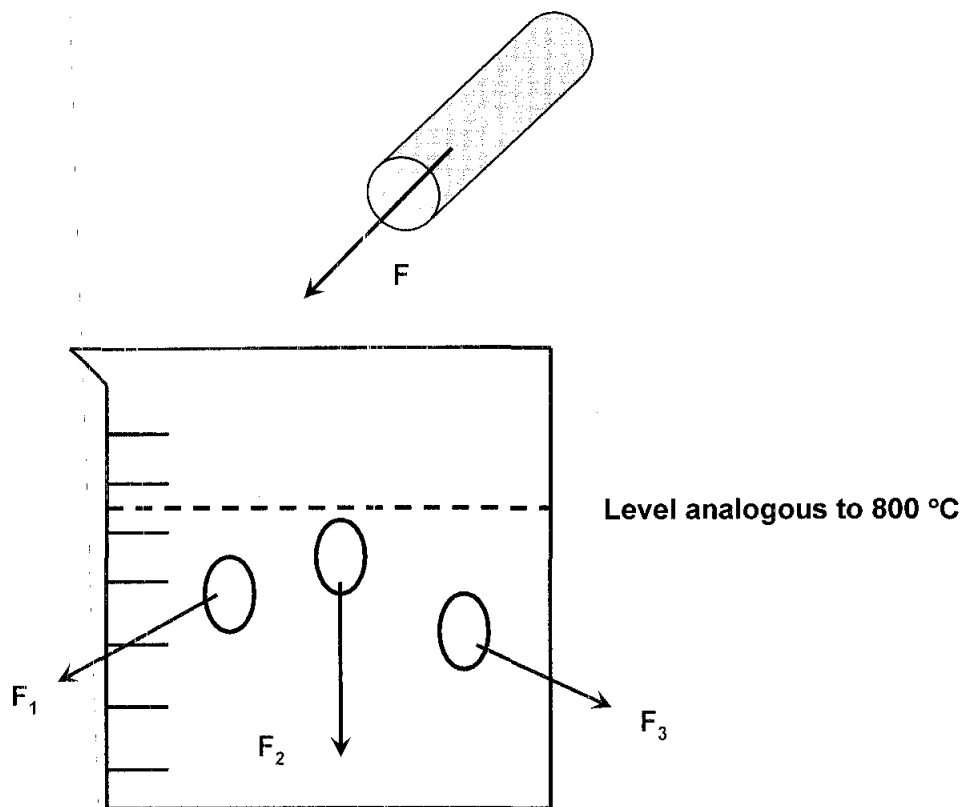


Figure 2.29: Losses in the system [31]

During heating (as opposed to equilibrium), the thermal inflow is greater than the sum of heat losses, as a given level must accumulate in the tool. At equilibrium, the 'beaker' is 'full' but, to remain so, a continuous heat flow must be supplied which fulfils the following criteria:

$$F = F_1 + F_2 + F_3 \quad (2.20)$$

The thermal equilibrium that has to be maintained in the mould is constituted by different heat sources and heat consumers or losses. In order to have a thermal equilibrium, at the proper temperature, a certain amount of heat energy has to be stored or maintained, within the furnace (see Figure 2.30). The three 'holes' in the beaker symbolize the three heat loss sources:

- Radiation
- Conduction
- Convection

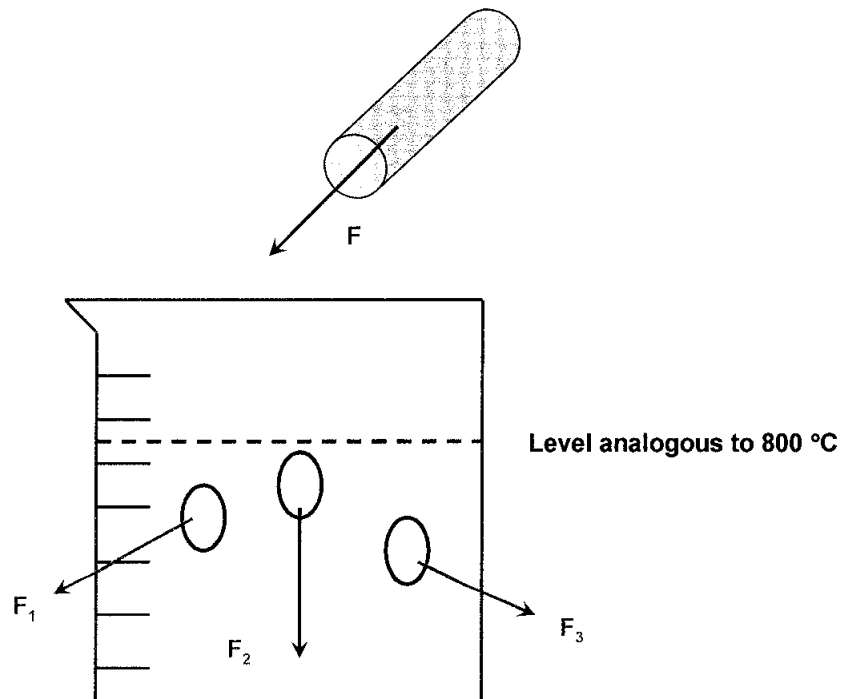


Figure 2.30: Retaining heat at equilibrium (steady state), inflow must match outflow [31]

The heat loss in the mould and its precursor material is schematically shown in Figure 2.31. As can be seen three different types of heat losses via heat transports

exist. These different losses can be expressed according to equations (2.21) – (2.23) in the case of stationary conditions:

Conduction:

$$P_{Condu} = A \cdot \frac{k}{\Delta x} \cdot \Delta T \quad (2.21)$$

Radiation:

$$P_{Rad} = A \cdot \varepsilon \cdot \sigma \cdot (T_1^4 - T_2^4) \quad (2.22)$$

Convection:

$$P_{Conv} = A \cdot h \cdot (T_1 - T_2) \quad (2.23)$$

where:

P = energy loss per time unit in W

A = exposed area in m^2

k = thermal conductivity of material in $Wm^{-1}K^{-1}$

T = temperature in K

x = heat transport distance in the solid media

ε = thermal emissivity of the radiating surface

σ = Stefan-Boltzmann constant

h = heat transfer coefficient between gas bulk and material surface

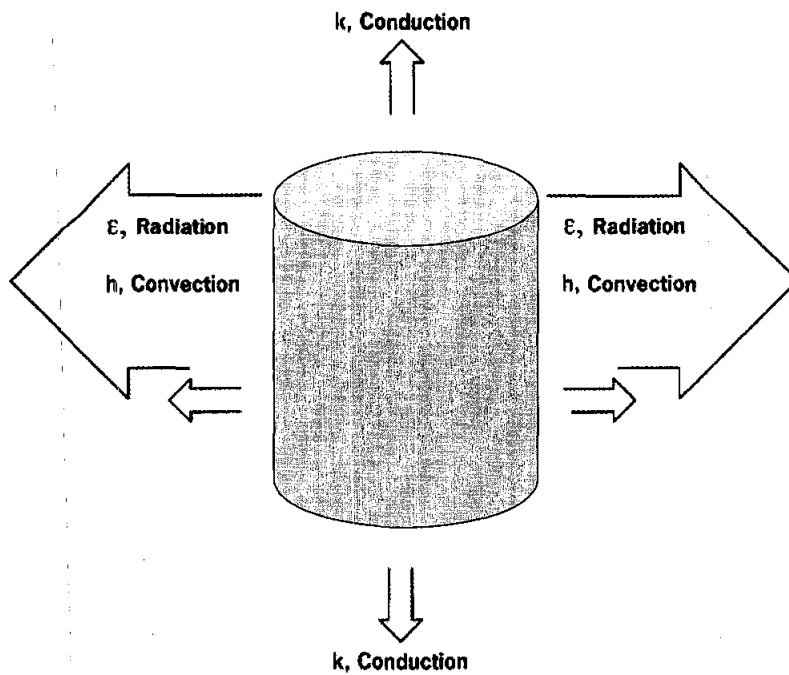


Figure 2.31: Thermal losses for the mould [31]

Considering the described intentions, the very first trials to make simple foam parts were performed by immersion of the mould into an aluminium melt. According to Kertz [101] in order to achieve a high heating rate by intensive heat transfer by conduction, the moulds containing the precursor material were submerged into liquid aluminium that was kept in a conventional holding furnace. The conductive heat transfer was very high and a uniform temperature distribution could be achieved. This method worked quite well and the aluminium foam samples yielded good properties but chemical attack of the moulds by the Al melt causes short lifetimes of the moulds and the mould attachments. Furthermore, the handling of the moulds in liquid aluminium is dangerous and problematic [98]-[101].

High-convection furnaces (air-circulating furnaces) are used in industry for rapid heating processes. A ventilator in the furnace effects very high heat transfer from the heat source to the mould. The rapid heat transfer, caused by high flow velocity, causes high heating rates, but the gas flow is influenced by the geometry of the mould and that leads to uneven temperature distribution within the mould. This effect can be avoided by the installation of baffle plates, which must be adapted for every new mould that is used in the furnace. Therefore air-circulating furnaces can be employed in series production, where high numbers of aluminium parts have to be made with the same mould geometry, but they are not suitable for prototype manufacturing, where flexible and universal furnace systems are required [99].

In the PCF process the mould giving the aluminium foam part its shape contains the foamable precursor material during the heating cycle [102]. The thermal energy that is necessary to start the foaming of the precursor material has to be transmitted through the mould. Consequently the thermal conductivity of the mould should be as high as possible and thermal capacity of the mould as low as possible. On the other hand the moulds must be stable enough to keep the required dimensional tolerances of the net-shape foam part. The first moulds for the PCF process were made from common steel sheets. The very first aluminium foam parts were very simple, regular shaped pieces such as small plates, cubes or cylinders and the development was focused mainly on the foaming behaviour of the precursor material and the production of test samples. But when 3D net-shape prototype is required the mould becomes an important part of the prototype development [98]-[102]. The experience of foundry

die makers was combined with the experience in foaming precursor material. Conventional casting dies are very heavy and bulky. A lot of energy is wasted on heating the whole die during the foaming process. The precursor material would not be heated fast enough to achieve sound foams components. An economic is to use cast iron, which allows casting of thin walled foaming dies using wood or plastic patterns as well as the lost foam casting process. Depending on the mould sand used, the surface in the die may require machining. This method was used for foaming car structural parts, the largest prototypes so far manufactured in net shape [102].

Besides structural steel and cast iron, high temperature tool steel, copper and ceramic were also used as mould materials in a large number of prototype development projects. Table 2.5 shows an overview of different mould materials and their properties [101].

Table 2.5: Comparison of various mould materials

Mould material	Advantages	Disadvantages
Steel 5 10 mm thick	<ul style="list-style-type: none"> • easy machining • low material costs • heat conductivity 	<ul style="list-style-type: none"> - mould life time - distortion
Cast iron	<ul style="list-style-type: none"> • heat conductivity • free-form shapes 	<ul style="list-style-type: none"> - high material costs - high production costs - mould lifetime
High-temperature tool steel	<ul style="list-style-type: none"> • mould life time • low distortion 	<ul style="list-style-type: none"> - high material costs

2.11 The synthesis of ceramic reinforcement materials for Al foam from the carbothermal nitridation process using structured alteration silica sand

Optimum utilization of natural mineral resources such as silica sand is directly proportional to the level of knowledge about the materials. The same silica sand can be used for simple, bulky products, but after small modification it may well be used for advance products. Silica sand has a potential to be exploited further and with some investment, it can be turned into more high value added materials such as silicon carbide.

Silicon carbide is ceramic material that exhibit very good behaviour at high temperature because of their chemical stability and their good mechanical and thermal properties. It has attractive properties such as high strength, stiffness, good wear and

corrosion resistance and semiconductivity, which are mainly characteristic of covalent bonded ceramic materials [103]-[107]. It was known that [108] although these materials are generally produced and used in powdered form, the form of whisker has gained an increasing importance. This is due to the fact that the latter's characteristics are best suited for use as reinforcements in composite materials of different matrix compositions (metallic, ceramic and polymeric) [108]. Silicon carbide is an industrial manufactured synthetic product made by the high temperature reaction of high quality silica sand (99.5% SiO₂) and low sulphur petroleum coke. The reaction takes place in an electric resistance (Acheson) furnace and requires large quantities of electricity (23.7 J/kg), where voltage passing through the core producing a temperature of 2400°C [106], [109]-[114].

The produced silicon carbide possesses large grains and batches which demand grinding and purification processes for further usage. The manufacture of silicon carbide whisker by milling of Acheson silicon carbide products are not successful. Submicron SiC particles can be obtained by several advanced technologies such as chemical vapour deposition process, sol-gel process and laser gas phase pyrolysis or laser evaporation process. Since the most easily scalable process is the carbothermal reduction of silica, a large effort has been made in improving the control of Silicon carbide particle size by the appropriate control of the size of carbon and silica particles in the reaction mixture [109], [112], [115].

The apparent existing problem of the mentioned technique is the high temperature requirement of about 2400 °C for the reaction to be feasible when using silica sand as its starting precursor [111].

2.11.1 Exploitation of local silica sand for use in advanced material application

Optimum utilization of natural mineral resources such as silica sand is directly proportional to the level of knowledge about the materials. The same silica sand can be used for simple, bulky products, but after small modification it may well be used for advanced products. Silica sand has a potential to be exploited further and with some investment, silica sand can be turned into useful reinforcement to support advanced material industry. With the advancement of advanced materials industries in

Malaysia, it appears that the demand for high grade silica sand would be increasing and Malaysia needs to further exploit the various sources of silica sand. This section briefly describes the exploitation of local silica sand and a review on the advanced materials which utilized silica as the main raw materials is also presented.

Malaysia is endowed with a variety of industrial mineral resources, which when processed, can be of potential use for advanced materials application. Among the more important are widely distributed deposits of primary and secondary clays, silica sand and other industrial minerals. However, these material resources are not fully utilized for the production of higher value added products.



Figure 2.32: Deposit of silica sand at Johore Silica processing plant at Bandar Penawar

This is partly because of the lack of investigation for better utilization of local mineral resources. Research into mineral resources in developed countries has advanced principally by industrial innovations and has contributed to the creation of new products. The study and evaluation of the indigenous mineral resources in Malaysia will contribute to the development and growth of advanced materials. However, due to the lack of technical knowledge and technology, many good resources are used for low grade products and large quantities of useful mineral resources are wasted. In many instances, insufficient information is available about

the potentialities of alternative mineral resources. Current problems in commercial production and formulation of materials concern the benefit of indigenous mineral resources. Improvement in the technology of processing and optimization will lead to a wider variety of applications of certain minerals resources.

2.11.2 Exploitation of silica sand – Malaysia perspective

In terms of availability, sand must be the most abundant industrial mineral. However, only a relatively small percentage of this is of commercial significance since each consuming industry requires a particular set of specifications both chemical and physical. At its least refined, it finds numerous applications in the construction and related industries. At the opposite end of the quality spectrum is the special glass sands used for premium grade optical glass.

Occurrences of silica sand are, as might be expected, common throughout Malaysia. Known deposits containing sufficiently high silica content are, however limited. Table 2.6 shows the various sources, current exploitation and estimated reserves of silica sand in Malaysia.

Table 2.6: Sources, exploitation and estimated reserves of silica sand in Malaysia

Sources	Current exploitation	Estimated reserves
Natural silica sand	Sarawak	9.3 million tones
	Johore	1.1 million tones
	Pahang	Not available
	Kelantan	Not available
	Perak	Not available
Processing of ex-mine tailing sand	Selangor, Perak	Not available
Quarrying and crushing of massive quartz rock	Selangor	Not available

In Malaysia currently, the low to medium grade silica sand is produced, mainly for the domestic consumption in the glass, ceramic and cement industries and some high grade silica for export. In general, the local silica processing plants consists of screening/washing and gravity circuits with some kind of floatation step process (Figure 2.33 (a) and (b)). In contrast to the lower to medium grade exports, Malaysia imports the premium grade silica sand.

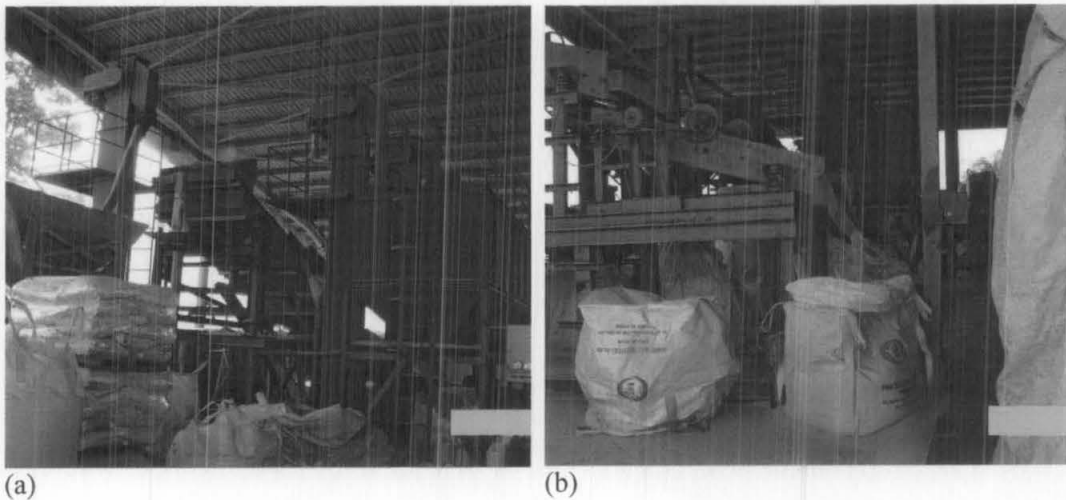


Figure 2.33: Johore Silica processing plant (a) Separator for use in reducing iron and other heavy mineral content in the silica sand (b) Vibrator for sieving silica sand into various mesh sizes

Laboratory test work which includes deposit evaluation and beneficiation routes has been conducted to investigate the potentials of upgrading the silica content of tailing sand from ex-mining land and natural silica sand to grades suitable for use as feed stock to various industries particularly in advanced materials application. As sand is a natural material, the variability in mineralogical, physical and chemical characteristic must be clearly defined before the beneficiation process which will be used to meet the chemical and physical specification of the end-product can be considered, at which point the economic viability of the process can be assessed to determine the realistic values which can be produced. Typical analysis of sand deposits in Malaysia is shown in Table 2.7.

Table 2.7: Composition of silica sand

Compound	Methods	Results
Silica (SiO_2)	Gravimetric	99.7 %
Alumina (Al_2O_3)	AAS	0.18 %
Iron oxide Fe_2O_3	AAS	0.07 %

2.11.3 Processing of industrial minerals for advanced applications of silica-saturated water

The application of carbothermal reduction technology to the synthesis of advanced ceramic powders has been demonstrated for a number of minerals indigenous to New Zealand are well known [104], [116]-[120]. In its most simplified form the process may be summarized as follow:



or



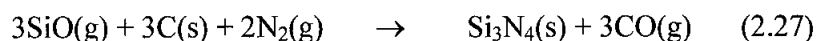
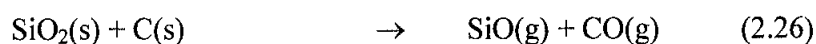
(where M = metal, eg. Si, Ti, Al etc.)

Many of the processes dealt with in this section involve complex, multi-step reactions often involving gaseous intermediates.

2.11.3.1 *Silicon Nitride from geothermal silica*

The geothermal power stations of the central North Island of New Zealand discharge vast tonnages of silica-saturated water, the silica having been dissolved in the geothermal water at high temperature and pressure. Procedures have been developed [105] which allow the controlled precipitation of very fine, high purity silica. Perera [106], [107] has demonstrated the use of this silica as the starting material for the carbothermal preparation of high purity silicon nitride powder. Specifically, it was shown that micron-submicron silicon nitride could be produced with a ratio α - $\text{Si}_3\text{N}_4/\beta$ - Si_3N_4 of up to 95/5.

The reaction was carried out at a temperature of 1400 °C, using an excess of carbon in an atmosphere of flowing oxygen-free nitrogen. The reaction chemistry is believed to follow a two step process involving gaseous silicon monoxide:





It is valuable to use thermodynamic modeling to review the process chemistry and to relate this to physical observations made by a number of researchers, namely the wide range of “successful” reaction temperatures quoted in the literature and the observation of β -SiC formation at higher temperatures. Thermodynamic calculations were performed using Thermodata programme developed by Turnabull and Wadsley [116]. Figure 2.34 shows the thermodynamically stable phase formed from the major reactants involved in equation (2.24) as a function of temperature for two levels of Nitrogen addition: 10 moles N_2 : 1 mole SiO_2 and 100 N_2 : 1 SiO_2 . Figure 2.35 shows the result of using excess carbon in the reaction in the reaction ($1\text{SiO}_2:3\text{C}$).

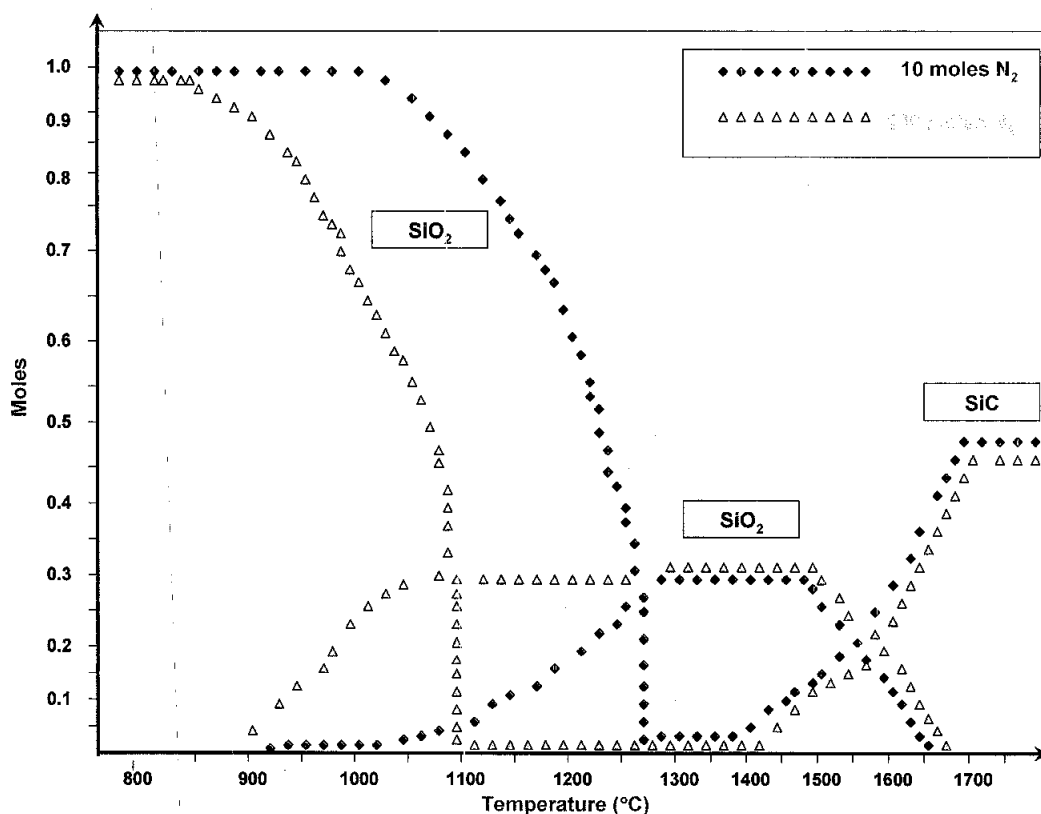


Figure 2.34: Thermodynamic analysis of $\text{SiO}_2 + 2\text{C}$ in Nitrogen [106]

Two features on these graphs are important. First, the N_2 level has a dramatic effect on the extent of the $\text{SiO}_2 \rightarrow \text{Si}_3\text{N}_4$ reaction; the completion temperature using 100 moles N_2 is 200 lower than for 10 moles N_2 . The example can be extended to a calculation using 1000 moles N_2 (not graphed here) in which the completion

temperature is further reduced to $\sim 950\text{ }^{\circ}\text{C}$. The thermodynamic analysis also reveals that the main function of increasing the moles of N_2 available is to reduce the partial pressure of carbon monoxide in the system. The molar ratio of CO/N_2 upon formation of Si_3N_4 is 0.17 for 10 moles N_2 , whereas it drops to 0.02 for 100 moles N_2 . A second feature is that, with a carbon excess, $\beta\text{-SiC}$ becomes thermodynamically stable with respect to Si_3N_4 above $\sim 1350\text{ }^{\circ}\text{C}$ (Figure 2.35).

Overall, the thermodynamic data show that Si_3N_4 formation is most favoured when the N_2 gas flow is high, that is, the partial pressure of carbon monoxide is low. Use of high temperatures and excess carbon, encourages the formation of $\beta\text{-SiC}$.

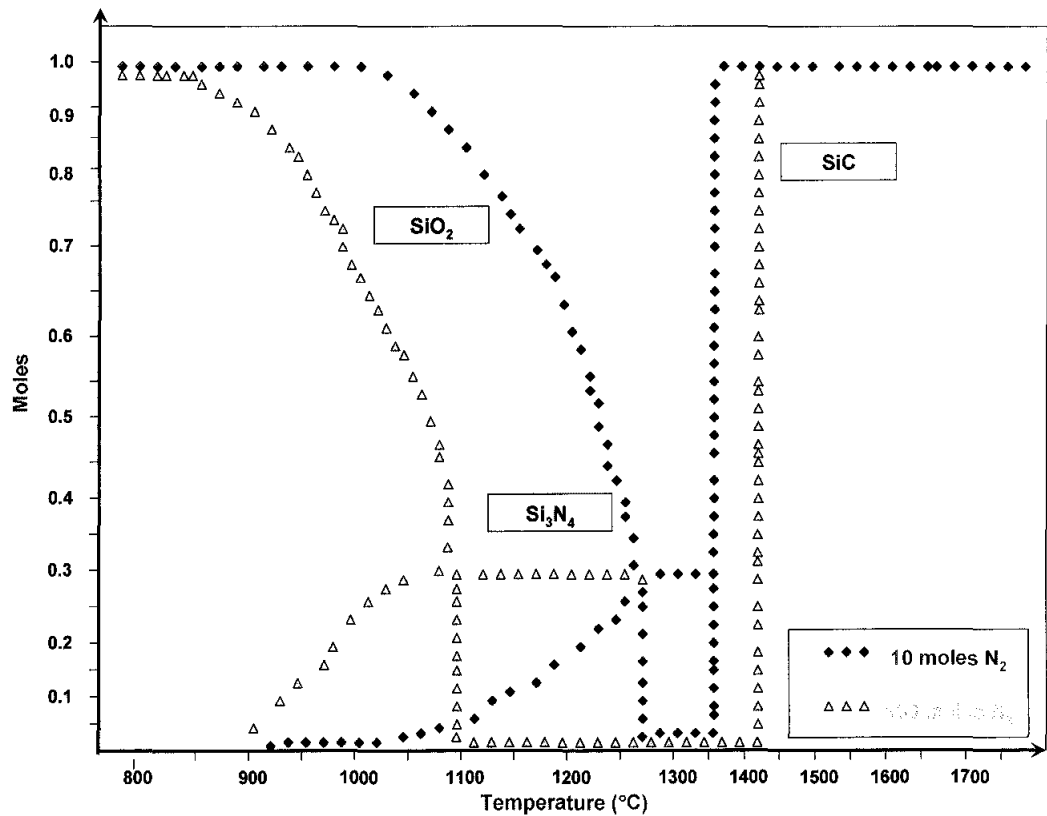


Figure 2.35: Thermodynamic analysis of $\text{SiO}_2 + 3\text{C}$ in Nitrogen [106]

2.11.3.2 Silicon Carbide from geothermal silica

The same features which promote the use of geothermal silica for the manufacture of silicon nitride (fine particle size, high purity) have promoted a complementary study of the formation of silicon carbide [104], [117]-[124]. High purity $\beta\text{-SiC}$ has been

prepared by carbothermal reduction of geothermal silica in flowing argon in the temperature range 1250-1450 °C [121]. The generally accepted reaction mechanism involves the formation of SiO as an intermediate:

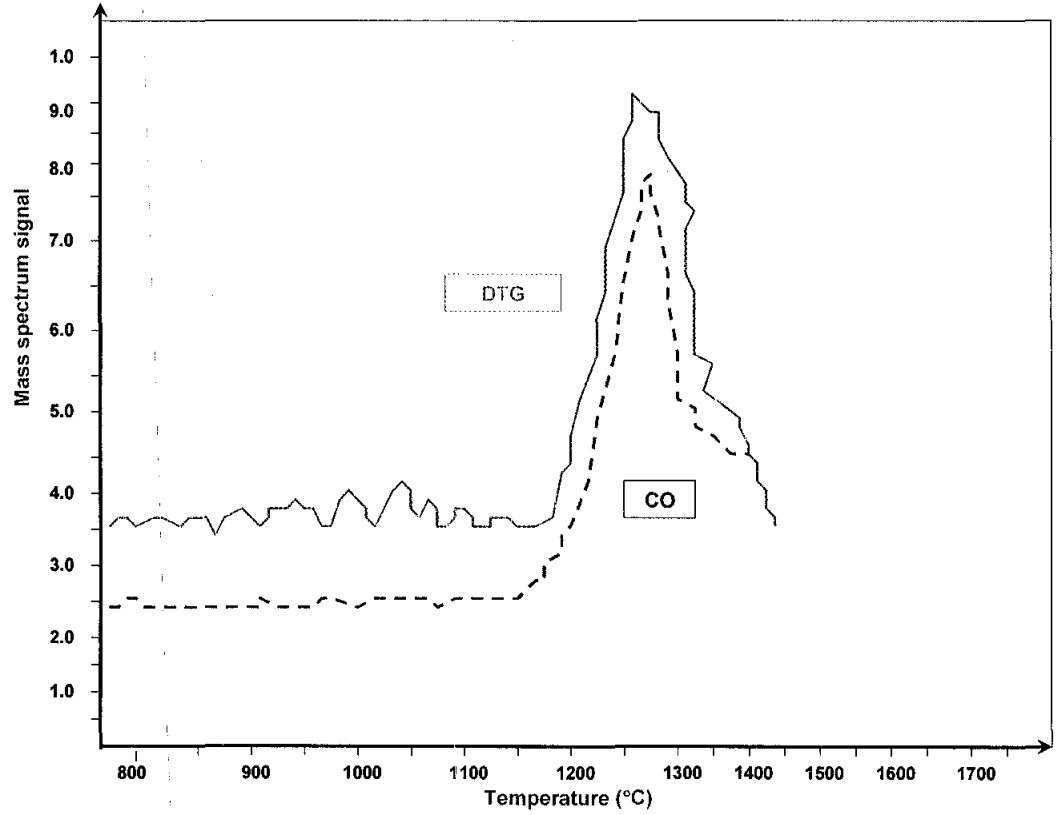
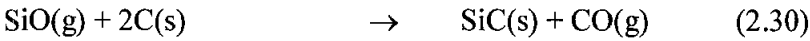
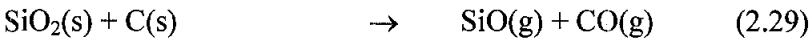


Figure 2.36: TGA/MS analysis of $\text{SiO}_2 + 3\text{C}$ in Argon showing DTG and evolved carbon monoxide data. Heating rate 2 °C/min [106]

Figure 2.36 reports thermoanalytical data for $\text{SiO}_2 + 3\text{C}$ in argon, measured at a low heating rate 2 °C/min and showing a maximum in both the DTG peak (Differential Thermogravimetric Analysis) and Mass 28 signal (carbon monoxide) at ~ 1380 °C. Figure 2.10.3.2.1 presents CO data generated by thermodynamic analysis of reaction (2.28) differentiated to provide a theoretical rate of CO evolution which can be compared with the experimental TGA/MS data in Figure 2.37.

It would appear that an effective argon level of greater than 1 mole but less than 10 moles would describe the present experimental observations, implying a relatively

static atmospheric environment in the immediate reaction zone surrounding the sample.

Thermodynamic analysis of the above reaction sequence suggests that although SiO is present as an equilibrium phase at all temperatures of interest, it is not sufficiently thermodynamically stable with respect to SiO₂ and SiC to act as a discrete intermediate phase.

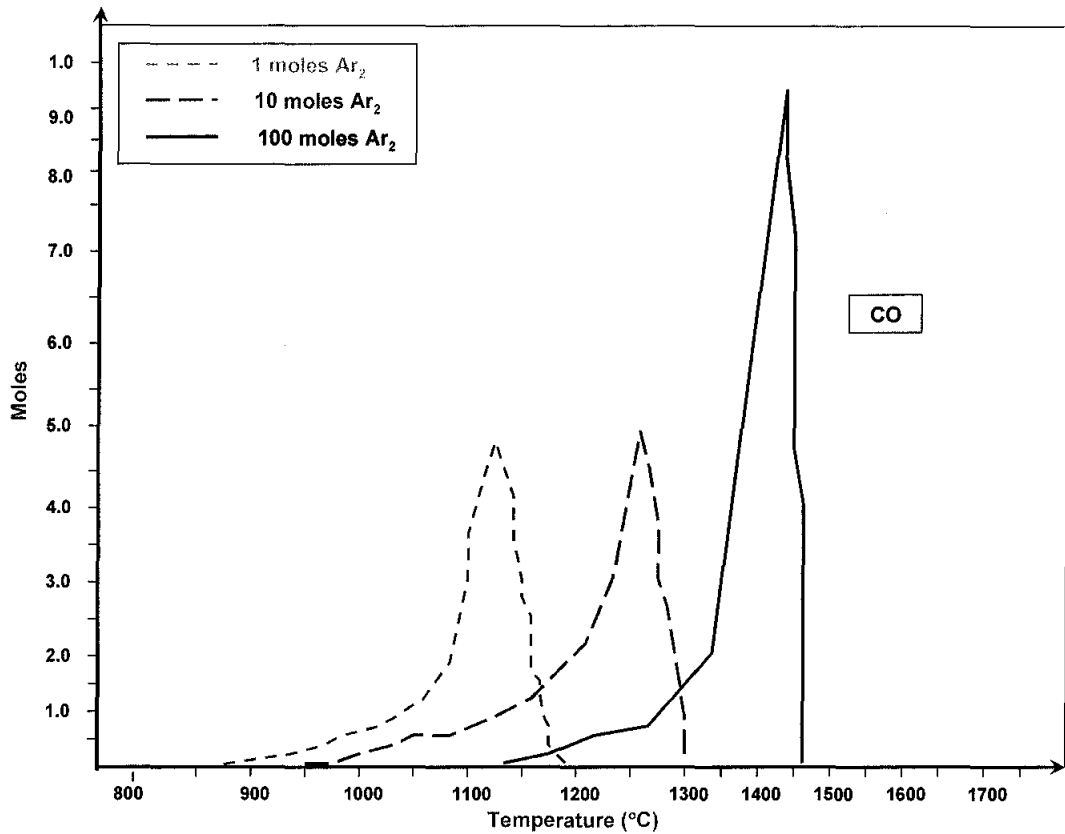


Figure 2.37: Thermodynamic analysis of rate of CO evolution for SiO₂ + 3C in Argon [106]

2.12 Structural defects in silica during high intensity grinding process

Mechanical milling in which the process without material transfer plays an important role in various disciplines in terms of size reduction of the rocks from the mountains, in mining to the preparation of ultra fine particles (below 5 µm) for the down stream process for the advance material application. The scope of mechanical milling caters the size reduction and also the nature of the ground product that involves the structural changes during the high intensity grinding process [125], [126].

Planetary ball mill is a popular machine for mechanical milling research. Two well-known manufacturers of planetary ball mill Fritsch GmbH and Retsch from Germany. The ball mill consists of a rotating support disc and vials. The vials are arranged on the rotating support disc and a special drive mechanism causes the vial to rotate around their own axis. The centrifugal forces are created by the rotation of the disc. Since the vials and rotating support disc rotate in opposite direction, the centrifugal forces alternately act in like and opposite direction.

The centrifugal forces acting on the wall of the vial initially carry the grinding balls in the direction in which the vial is rotating (Figure 2.38). Thus friction resulted from the grinding balls and the powder mixture being ground alternately rolling on the inner wall of the vials, while impact results when they are lifted and thrown across the bowl to strike at the opposite wall. The impact is intensified when the balls strike one another. Thus, the combination of the friction and impact forces planetary ball mill causes the high degree of particle size reduction.

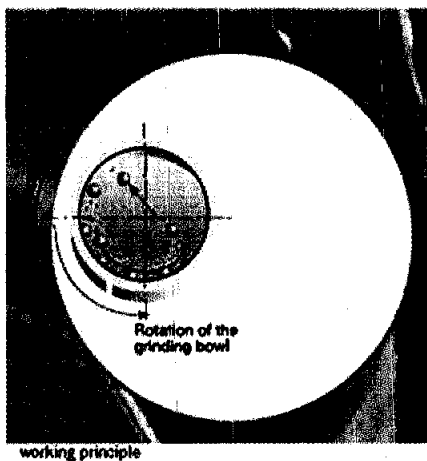


Figure 2.38: Schematic view of motion of powder mixture and grinding balls [105]

2.12.1 Milling intensity in the formation of structured alteration silica sand

Milling intensity is a measure of the milling energy which is directly proportional to the power generated during milling process and factors that can change the milling intensity are ball to powder ratio (BPR) and milling speed.

2.12.1.1 *Ball to powder ratio*

Generally, the ball to powder weight ratio (BPR) employed is in the range between 10:1 and 20:1 for small capacity of ball mill such as SPEX mill [127]. However, when mechanical alloying is carried out in attritor (large capacity ball mill), the BPR of 50:1 or even 100:1 is possible [128]. In general, the higher the BPR, the shorter is the time required to achieve a particular phase in the powder being milled. The rate of refinement of grain size with milling time increases with higher BPR. At high BPR, the number of collision per unit time increases, as there is an increase in the weight proportion of the grinding balls. Consequently, there is more energy transferred to the powder particles. Thus alloying process takes place in a faster rate. However, more heat will be generated if energy is higher. Consequently, this could alter the constitution of the powders. At constant BPR, the sequence of phase formation can be determined as a function of milling time [129].

2.12.1.2 *Milling speed*

Similar to the effect of BPR, it is obvious that when milling speed is increased, ball energy increased and thus more energy will be transferred to powder particles during impact and more energy will be dissipated in heat and temperature of vials may increase. In some cases, this is an advantage since diffusion occurred and the mechanical alloyed powders are homogenized and the alloying process is successful. However, the increased temperature may cause decomposition of supersaturated solid solution or other metastable phases formed during milling [127].

It has been reported that milling intensity affects the formation of amorphous material [130], [131]. With high milling intensity, the amorphous phase will form, but if too much energy transferred to powders and the temperature increase substantially, which exceeds the critical temperature of crystallization, the amorphous phase may even crystallize. On the other hand, if the milling intensity is too low, the time needed for alloying and amorphization become very long. This is because introduction of defects under plastic deformation will increase the free energy of powders, which is dependent upon the milling intensity. Therefore, it may not be sufficient to promote the pure amorphous phase formation if milling intensity is too low. Thus, the original

crystalline phase are still remained. The influence of milling intensity on mechanical alloying was also studied by Gonzalez *et. al.* [132] and the X-ray diffraction pattern obtained showed the complete FeAl solid solution formation is obtained for high milling speed after 1 hour, however, for low milling speed, the alloy has not completely formed even after 5 hours.

Even though the BPR and milling speed are the major factors affecting the milling intensity, however when, when the numbers of milling balls was taken into account, the effective impact frequency is found to increase when smaller balls are used but the impact energy is lower compared to those using bigger balls [127]. By considering equal amount of impact energy but varying the ball size in mechanical alloying of Ti-58Al, it was shown that super saturated solid solution has formed if smaller balls with 15 mm diameter are employed, while the XRD diffraction peaks of Ti and Al are still visible if larger ball size (20 or 25 mm diameter) is used [129]. However, there are still other factors that might be considered in the energy transferred from impact of the balls to powder particles, such as the angular velocity of rotating disc in the case of planetary ball mill, the motion and the impact event of milling balls and vials [127], [130], [132].

2.13 Chapter summary

Most of the techniques used in producing aluminium foam lacking in suiting the need of various type of porosity and other important parameters which should be versatile, tailoring to different types of application. This confinement in structures limits the range of properties and application of the fabricated foam. Table 2.8 shows the properties of Al foam fabricated from various processes and their drawbacks. By considering the drawback of the mentioned process, the improvement of the foaming process is aiming at raising the quality of the foam. This is mainly in developing technique which is more stable in term of high dense cell wall and produce foam density which can be varied in a much wider range than the current methods.

As the produced silicon carbide for the reinforcement of Al foam possess large grains and batches which demand grinding and purification processes for further usage and also the manufacture of silicon carbide whisker by milling of Acheson

silicon carbide products are not successful, an improved process for producing silicon carbide whisker should be developed.

Table 2.8: Properties of Al foam from various fabrication techniques

Process	Property of Al foam	Limitation
Sintering metal powders [41]	<ul style="list-style-type: none"> ➤ Fixed relative density ➤ Compressive strength = 0.04-0.6 (MPa) ➤ Densification stress = 2.0-6.0 (MPa) 	<ul style="list-style-type: none"> ➤ Low porosity ➤ Fairly poor quality ➤ Limited strength
Sintering of hollow metal spheres [41]	<ul style="list-style-type: none"> ➤ Fixed relative density 	<ul style="list-style-type: none"> ➤ Suitable for Ti and Ni
Powder metallurgy space holder [8], [22], [41]	<ul style="list-style-type: none"> ➤ Can vary the relative density ➤ Compressive strength = 0.06-0.30 (MPa) ➤ Densification stress = 2.4-5.5 (MPa) 	<ul style="list-style-type: none"> ➤ Above the melting temperature of pure Al powder ➤ Longer sintering time ➤ Inferior mechanical properties due to the presence of individual Al powder
Infiltration / Investment casting [41]	<ul style="list-style-type: none"> ➤ Fixed relative density ➤ Compressive strength = 0.04-0.35 (MPa) ➤ Densification stress = 3.5-7.5 (MPa) 	<ul style="list-style-type: none"> ➤ slow, difficult to scale up, and involves many steps and is correspondingly costly
Foamable precursor produced by melt-route processing [41]	<ul style="list-style-type: none"> ➤ cell sizes between 1 and 10 mm 	<ul style="list-style-type: none"> ➤ the requirement to add viscosity enhancing SiC particles to the melt, which adds to the cost of the process and makes the resulting foams more brittle

The challenge of current research is to produce an improved method of producing open celled Al foam which possesses superior morphological, physical and mechanical properties. An improved method of producing reinforcement material of Al foam that used simple setup which can be worked without high conversion engineering cost will also be developed. Local silica sand will be used as cheap precursor for the synthesis of silicon carbide whisker from the carbothermal nitridation process.

CHAPTER 3

EXPERIMENTAL PROCEDURE

3.1 Chapter overview

To overcome the solid state sintering of Al powder, an improved process technique which leads to Al foam possessing a high dense of cell wall which can be attained in a much shorter time and possesses superior mechanical properties was developed based on powder metallurgy approach. This technique known as pressure assisted high frequency induction heated sintering dissolution process (PASDP) consists of mixing, pressure assisted sintering and dissolution stages is shown in Figure 3.1.

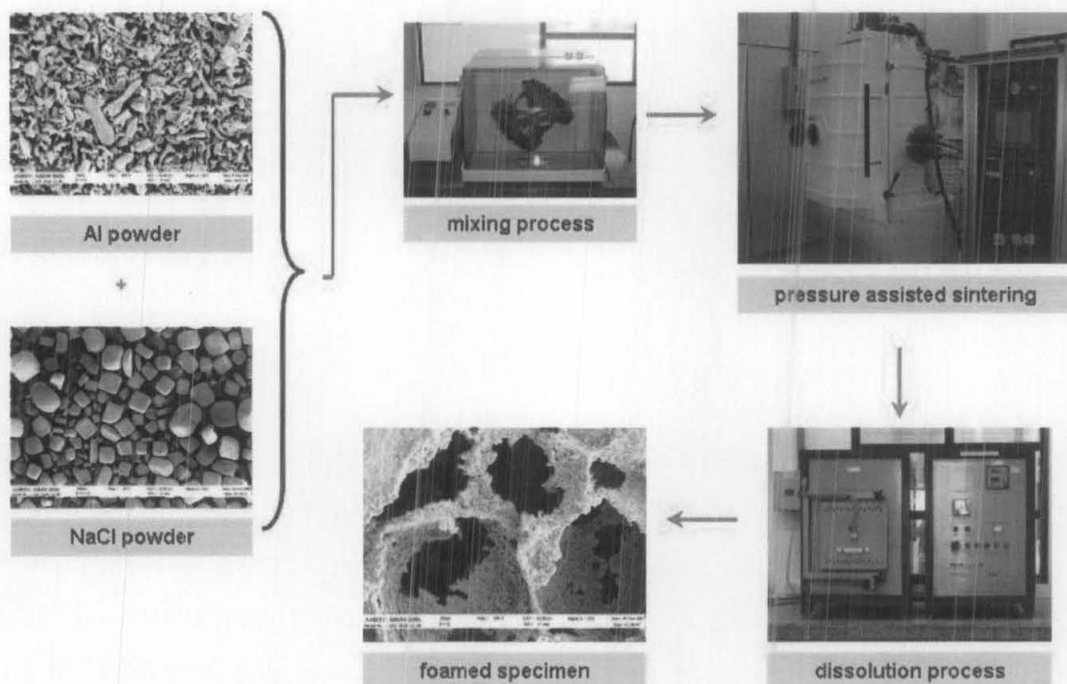


Figure 3.1: Process flow for the fabrication of Al foam using PASDP process

3.2 Raw Materials

The pure Al powder (99.97%) used in this study is of 37 μm mean particle size as supplied by ADV System Technology. The particle shapes of the powder was determined by scanning electron microscopy (Leo 1510). The Al powder which exhibits an irregular shape which is a typical of air atomised powder and the particle size distribution of the powder are as shown in Figure 3.2 (a) and (b) respectively.

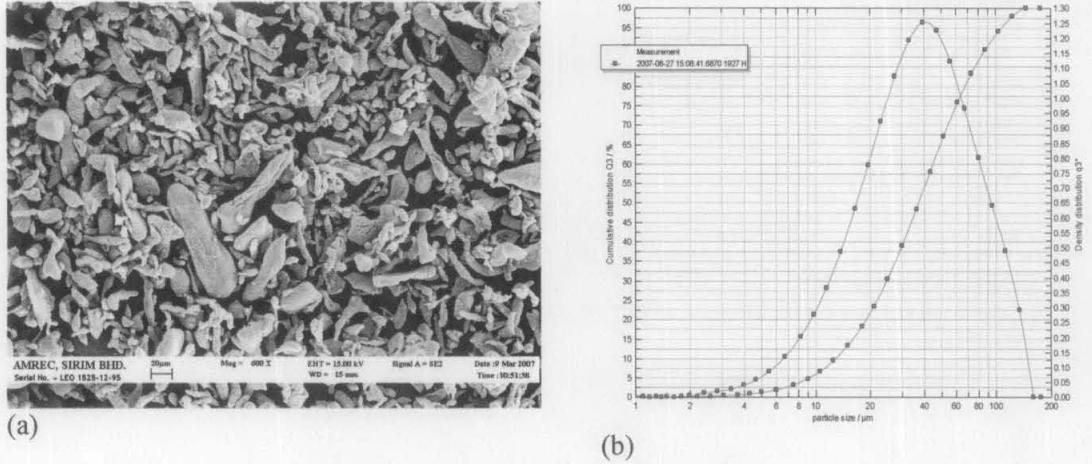


Figure 3.2: (a) Morphology of powders of Al powders (b) Particle size distribution of Al powders

In order to control the intended pore size of the final foam, the NaCl particles of different sizes and its widths of distribution were prepared and denoted as TS, AC, HI and SA respectively as shown in Figure 3.3 (a)-(d). The NaCl particles are roughly cubic with rounded edges. Along with median sizes, measures of widths of the size distribution, S_w , were obtained from 10% and 90% 'finer than' size values, denoted as D_{10} and D_{90} using the following equation:

$$S_w = 2.56 / \log \left(\frac{D_{90}}{D_{10}} \right) \quad (3.1)$$

where the numerator represents the fact that 10 and 90% are 2.56 standard deviation apart on a Gaussian distribution; however, powders usually follow a log-normal distribution and the logarithmic size is appropriate for obtaining Gaussian behaviour. The median particle size, D_{50} , and the distribution slope, S_w , provide important

parameters of powder. The parameter S_w is the slope of the log-normal cumulative distribution and is similar to a coefficient of variation on standard deviation. Large values of the distribution slope S_w correspond to narrow particle size distribution and small value corresponds to broad distribution. Table 3.1 summarizes the physical parameters for NaCl and al matrix used in the experiments. The width of the particle distribution affects the compressibility, with increasing width aiding compressibility.

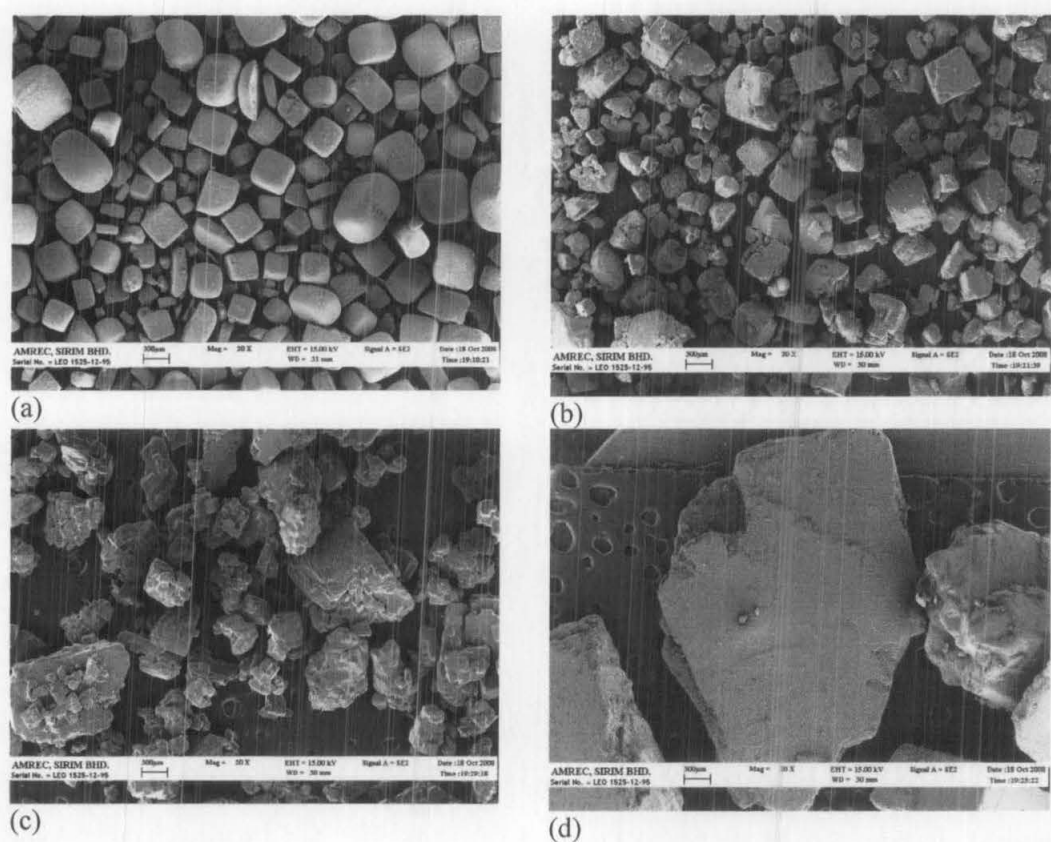


Figure 3.3: Different size of filler material (a) TS-NaCl (b) AC-NaCl (c) HI-NaCl (d) SA-NaCl

Table 3.1: Physical parameters of different size of filler material and Al matrix						
Filler material	Mean size (μm)	D ₁₀	D ₉₀	S_w	Density (gcm ⁻³)	Melting point (°C)
TS-NaCl	200	150	395	6.08	2.17	800
AC-NaCl	200	100	500	3.66	2.17	800
HI-NaCl	350	170	850	3.66	2.17	800
SA-NaCl	2000	950	2500	6.09	2.17	800
Al	37	12	89	2.94	2.70	660

3.3 Powder Mixing

A 100g blend containing 60 to 80% volume fraction of NaCl powder in Al is loaded in a 200 ml polypropylene container. The blended powders are mixed at a mixing rate of 50 rev min⁻¹ for 30 min to homogenously blend the constituents using three-dimensional mixer (Figure 3.4).

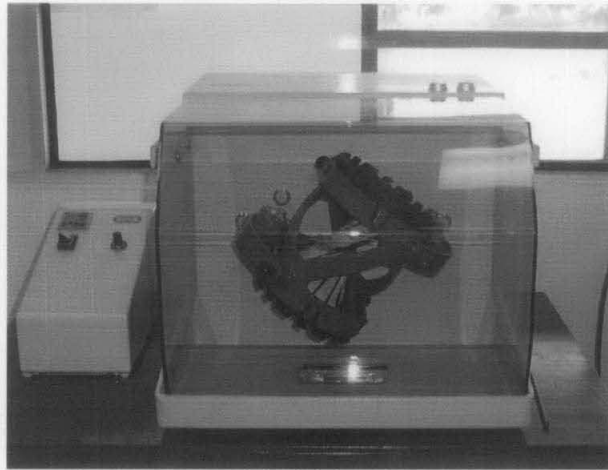


Figure 3.4: Three-dimensional mixer

3.4 Calculation for shrink-fitted die

The clearance between punches and die insert and shrink fit of die inserts in the die should be adjusted at the operation temperature, giving the same level of clearance and shrink fit as in conventional tool for cold compaction. As a matter of fact, all moving parts with close tolerances, exposed to higher temperatures should be fitted in the hot condition. This is of great importance especially if materials with different thermal expansions are used together in the tool, for instance tungsten carbide and steel. Most steels have a coefficient of thermal expansion approximately of $11.5 \times 10^{-6}/\text{K}$ and tungsten carbide $\sim 5.5 \times 10^{-6}/\text{K}$.

This means that tungsten carbide has approximately half the expansion compared to steel. In this respect a steel tool might be easier to start with, but a more rigid die is always preferred in respect to spring back and residual forces on the component

during ejection. The calculations presented here are based on equations and theory from reference [113]. The examples describe the situation for a carbide or a high speed steel insert comparing the “cold” and the “hot state”.

Let (d_n) and (D_n) be respectively the inside and the outside, nominal diameter, diameter of the insert and (d_a) and (D_a) the inside and outside, nominal, diameter of the ring. Assuming that the inner radial pressure (P_i) at compaction end is 200 MPa, it is possible to calculate the diameter relationship I/Φ (I =Interference, Φ =common diameter) according to equation (3.2):

$$\frac{I}{\phi} = \frac{P_i}{E_n} \left\{ \frac{1+\alpha^2}{2} \cdot S_1 \cdot \left[\frac{1+\alpha^2}{1-\alpha^2} - \nu_n + \frac{E_n}{E_a} \cdot \left(\frac{1+\beta^2}{1-\beta^2} + \nu_a \right) \right] - \frac{2\alpha^2}{1-\alpha^2} \right\} \quad (3.2)$$

where

I is the interference calculated on the diameter, mm.

Φ is the common diameter, mm.

P_i is the inner radial pressure at compaction end, Nmm^{-2} (assuming 200 Nmm^{-2}).

α is the ratio between the inside and the outside diameter of the insert ($\alpha=d_n/D_n$).

E_n is the Young modulus of the material used for the die insert, Nmm^{-2} .

ν_n is the Poisson ratio of the material used for the die insert.

β is the ratio between the inside and the outside diameter of the ring ($\beta=d_a/D_a$).

E_a is the Young modulus of the material used for the shrink-fitting ring, Nmm^{-2} .

ν_a is the Poisson ratio of the material used for the shrink-fitting ring.

S_1 is a safety factor.

Table 3.2. lists all the material properties that are needed for the fabrication of shrink-fitted die.

Table 3.2: Estimated values of material properties at 20 °C and 650 °C			
Property	Temperature (°C)	Low alloyed steel	Tungsten carbide (10%Co)
Yong modulus (MPa)	20	20.6×10^4	58.0×10^4
	650	19.6×10^4	55.5×10^4
Poisson ratio	20	0.296	0.220
	650	0.299	0.220
Thermal expansion coefficient (°C)	20	12.0×10^{-6}	5.5×10^{-6}
	650	12.5×10^{-6}	5.5×10^{-6}

Compaction at room temperature (20 °C)

For the insert, let:

$$D_n = 30 \text{ mm}$$

$$D_n = 50 \text{ mm}$$

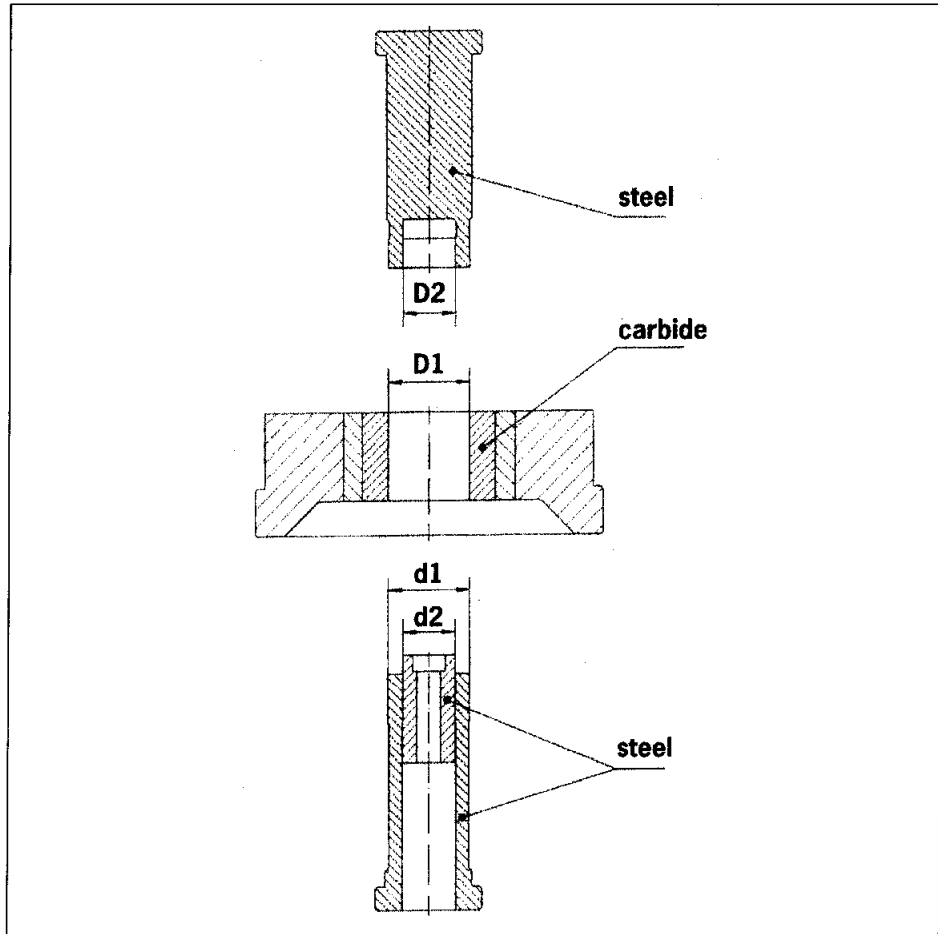


Figure 3.5: Dimension of carbide/steel tool

and for the ring,

$$d_a = 50 \text{ mm}$$

$$D_a = 125 \text{ mm}$$

this means that the ratio α and β are:

$$\alpha = 30/50 = 0.6$$

$$\beta = 50/125 = 0.4$$

For simplicity it is convenient to calculate the ratios in equation (3.2):

$$\frac{1+\alpha^2}{1-\alpha^2} = \frac{1+(0.6)^2}{1-(0.6)^2} = 2.125$$

$$\frac{2\alpha^2}{1-\alpha^2} = \frac{2x(0.6)^2}{1-(0.6)^2} = 1.125$$

$$\frac{1+\beta^2}{1-\beta^2} = \frac{1+(0.4)^2}{1-(0.4)^2} = 1.381$$

Carbide insert

In the case of a carbide insert (hard metal) and a shrink ring of low alloyed steel, values according to Table 3.2 can be inserted in equation (3.2.) resulting a calculated interference.

$$\Phi = 50 \text{ mm}$$

$$E_n = 58.0 \times 10^4 \text{ Nmm}^{-2}, \nu_n = 0.220$$

$$E_a = 20.6 \times 10^4 \text{ Nmm}^{-2}, \nu_a = 0.296$$

If imposing a safety factor of 2 (i.e. $S_1 = 2$), using equation. (3.2), the following value will be obtained:

$$\frac{I}{50} = \frac{200}{58 \times 10^4} \left\{ \frac{1+(0.6)^2}{2} \cdot 2 \left[2.125 - 0.22 + \frac{58.0 \times 10^4}{20.6 \times 10^4} \cdot (1.381 + 0.296) \right] - 1.125 \right\} = 0.00272$$

This means that $I = 0.136 \text{ mm}$, which in turn means that the difference in diameter between the inner diameter of the ring and the outer diameter of the insert has to be 0.136 mm , i.e. $D_n - d_a = 0.136 \text{ mm}$. If one choose $D_n = 50.045 \text{ mm}$ corresponding $d_a = 49.909$ since $50.045 - 49.909 = 0.136$. Normally it is simpler to use all the interference on the shrink ring, i.e. $d_a = 49.864$

In order to check if the strength of the shrink ring is sufficient the highest mutual pressure between the insert and the shrink ring is calculated according to equation (3.3):

$$P_m = E_n \cdot \frac{\left(\frac{I}{\phi} + \frac{2 \cdot \alpha^2}{1 - \alpha} \cdot \frac{P_i}{E_n} \right)}{\left[\frac{1 + \alpha^2}{1 - \alpha^2} - \nu_n + \frac{E_n}{E_a} \cdot \left(\frac{1 + \beta^2}{1 - \beta^2} + \nu_a \right) \right]} \quad (3.3)$$

All the data needed in equation (3.3) is known from previous calculations. Inserted in equation (3.3), the following value will be obtained:

$$P_m = 58.0 \times 10^4 \cdot \frac{\left(0.00272 + 1.125 \cdot \frac{200}{58.0 \times 10^4} \right)}{\left[2.125 - 0.22 + \frac{58.0 \times 10^4}{20.6 \times 10^4} \cdot (1.381 + 0.296) \right]} = 272 \text{ Nmm}^{-2}$$

If no load is exerted upon the die, $P_i = 0$ and the maximum stress is calculated according to equation (3.3) is at 238 Nmm^{-2} . Once P_m (max) is calculated (in this case equated to 272 Nmm^{-2}) it is possible to find the highest normal and transverse stress and determine the maximum, ideal stress according to von Misses (equation (3.4)).

$$\sigma_r = -P_i \quad (3.4)$$

$$\sigma_r = -272 \text{ Nmm}^{-2}$$

$$\sigma_t = \frac{1 + \beta^2}{1 - \beta^2} \cdot P_i \quad (3.5)$$

$$\sigma_t = (1.381) \times (272) = 376 \text{ Nmm}^{-2}$$

$$\sigma_{vM} = \sqrt{\sigma_t^2 + \sigma_r^2 - \sigma_r \cdot \sigma_t} \quad (3.6)$$

$$\sigma_{vM} = \sqrt{(376)^2 + (-272)^2 - (272) \times 376} = 564 \text{ Nmm}^{-2}$$

This stress level is well below the working limit of tool steels such as Uddeholms Orvar® (corresponding to SS 2242 (Swedish standard), DIN 2344), where the yield strength is in the range of 1500-1600 Nmm⁻².

Compaction at 650 °C

Calculations on a tool with the same nominal dimensions as before will be made for compaction at elevated temperature.

Carbide insert

At 650 °C values from Table 3.2 give:

$$E_n = 55.5 \times 10^4 \text{ Nmm}^{-2}, \nu_n = 0.220 \text{ and } E_a = 19.6 \times 10^4 \text{ Nmm}^{-2}, \nu_a = 0.299$$

$$E_n / E_a = 55.5 \times 10^4 / 19.6 \times 10^4 = 2.832$$

$$S_1 = 2$$

$$P_i = 200$$

The interference at 650 °C is calculated according to equation (3.2):

$$\frac{I}{50} = \frac{200}{55.5 \times 10^4} \left\{ \frac{1 + (0.6)^2}{2} \cdot 2 \cdot \left[2.125 - 0.22 + \frac{55.5 \times 10^4}{19.6 \times 10^4} \cdot (1.381 + 0.299) \right] - 1.125 \right\} = 0.00286$$

The calculated value represents the condition at 650 °C. In order to know the conditions at room temperature Bocchini *et al.* [133] have proposed a method to calculate the ratio I/Φ .

$$\left(\frac{I}{\Phi} \right)_{HC} = \left(\frac{I}{\Phi} \right)_{TC} + ([\lambda_a - \lambda_n][T_C - T_{RT}]) \quad (3.7)$$

where *HC* stands for hot compaction and *TC*, compaction temperature, λ the thermal expansion coefficient at compaction temperature for the insert (n) and the ring (a), T_C the compaction temperature and T_{RT} the room temperature. In this case, using the thermal expansion data from Table 3.2, it would result in:

$$\left(\frac{I}{\Phi}\right)_{HC} = 0.00286 + \left[(12.5 \times 10^{-6} - 5.5 \times 10^{-6})[650 - 20]\right] = 0.00727$$

$$\Rightarrow I = 50 \times 0.00727 = 0.363 \text{ mm}$$

The needed interference, I , at room temperature is thus 0.363 mm. The value has to be corrected because of temperature according to equation (3.7) and $P_i = 0$ is substituted into equation (3.3):

$$P_m = 58.0 \times 10^4 \left[\frac{0.00727}{2.125 - 0.22 + \frac{58.0 \times 10^4}{20.6 \times 10^4} (1.381 + 0.296)} \right] = 636 \text{ Nmm}^{-2}$$

According to Eqns. (4.4)-(4.6), the highest ideal stress is calculated:

$$\sigma_r = -636 \text{ Nmm}^{-2}$$

$$\sigma_i = (1.381) \times (636) = 879 \text{ Nmm}^{-2}$$

$$\sigma_{\text{max}} = \sqrt{(879)^2 + (-636)^2} - (636) \times 879 = 1317 \text{ Nmm}^{-2}$$

Summary of calculations

The calculation in previous section show that there are differences when shrink-fitting is inserted in a ring at different temperatures and the calculated data is summarized in Table 3.3. below.

Table 3.3: Summary of calculated values for shrink-fitted die

	Hard metal insert	
	20	650
Temperature (°C)	20	650
Interference (mm)	0.136	0.363
Maximum ideal stress (Nmm ⁻²)	564	1317

3.5 Pressure assisted sintering process

The pressure assisted sintering process was performed by means of induction heated Korea-Vac hot press machine. The homogenously blended powders were placed in shrink-fitted die of 30 mm diameter and introduced into the high-frequency induction heated sintering system (an induced current of frequency 15 kHz) as shown in Figure 3.6.

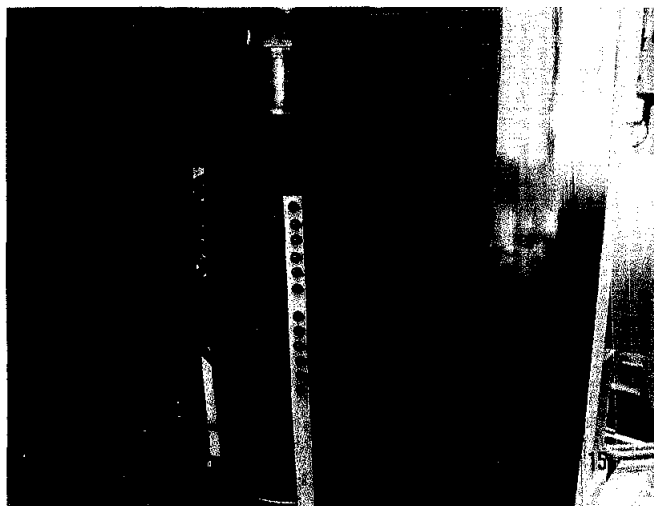


Figure 3.6: High-frequency induction heated system

The compressibility behaviour of the NaCl/Al composite was evaluated by subjected the homogenously blended powder at different pressures. To meet this purpose the pressure was varied between 20-120 MPa. The system was firstly evacuated to 5×10^{-5} torr and the sintering temperature was varied between 570 and 620°C and the holding time was also varied over a range of 5-30 min. The heating rate of was also varied from 5 to 30°C min⁻¹. The temperature was measured using a K type thermocouple inserted in the die (horizontal direction) and external thermocouple was inserted into the die in the vertical direction in order to monitor the accuracy of the sintering temperature. When the temperature reached the sintering temperature, the pressure was applied to consolidate the blended powders. The specimens were then allowed to cool to room temperature and were removed from moulds.

The densities of pressure assisted sintered specimens were weighed to the nearest 0.001g and dimensions were measured to the nearest 0.01 mm using a micrometer. Density was simply calculated by dividing the weight of sample by its volume.

The porosity of the hot pressed Al/NaCl compact P_c , can be estimated by the simple equation:

$$P_c = 1 - \frac{\rho_{hc}}{\rho_s} \quad (3.8)$$

where ρ_c is the density of the hot pressed compact and ρ_s is the theoretical density of a fully dense NaCl/Al mixture with the same NaCl/Al ratio as compact. The density of the compact, ρ_{hc} , was determined by measuring its dimensions and mass whereas the theoretical density of the dense mixture, ρ_s , was calculated by rule of mixture:

$$\rho_s = \rho_{Al}V_{Al} + \rho_{NaCl}(1 - V_{Al}) \quad (3.9)$$

where ρ_s and ρ_{NaCl} are the densities of Al and NaCl, respectively, and V_{Al} is the volume fraction of Al in the NaCl/Al mixture.

3.6 Dissolution Process

The embedded NaCl particles in the NaCl/Al compacts were leached out by placing samples in hot water at approximately 95 °C for four hours, leaving behind a highly porous metallic framework [8]. The following are possible reactions of aluminium with water [134]:



The (3.10) reaction forms the aluminium hydroxide bayerite ($\text{Al}(\text{OH})_3$) and hydrogen, the (3.11) reaction forms the aluminium hydroxide ($\text{AlO}(\text{OH})$) and hydrogen and the reaction (3.12) forms aluminium oxide and hydrogen. All these reaction are thermodynamically favourable from room temperature past the melting point of aluminium (660°C). All are also highly exothermic. From room temperature to 280°C , $\text{Al}(\text{OH})_3$ is the most stable product, while from 280 - 480°C , $\text{AlO}(\text{OH})$ is most stable. Above 480°C , Al_2O_3 is the most stable product. The reaction thermodynamic is shown in Table 3.4. The reaction thermodynamic reveals that aluminium should spontaneously react with water. However, in practice a piece of aluminium dropped into water will not react under room temperature conditions, or even with boiling water. This is because the aluminium has a thin coherent, adhering layer of aluminium oxide, Al_2O_3 , on its surface and this alumina layer prevents the reaction [134].

Table 3.4: Thermodynamics of aluminium –water reaction

$2/3\text{Al} + 2\text{H}_2\text{O} \rightarrow 2/3\text{Al}(\text{OH})_3 + \text{H}_2$			
T ($^\circ\text{C}$)	ΔH ($\text{kJmol}^{-1} \text{H}_2$)	ΔS (JK^{-1})	ΔG ($\text{kJmol}^{-1} \text{H}_2$)
0	-277	26.2	-284
100	-284	3.29	-285
200	-291	-12.1	-285

The density of specimen after dissolution process was measured by water displacement method. A surface impregnation technique with a water stop spray was employed to prevent penetration of water into the specimen's surface. Similarly, the porosity of as manufactured Al foam, P_f , can be estimated by:

$$P_f = 1 - \frac{\rho_f}{\rho_{\text{Al}}} \quad (3.13)$$

where ρ_f is the measured density of foam.

The fraction of the dissolved NaCl in the Al foam with respect to the total NaCl in the initial NaCl/Al preform, $1-\phi$, was determined by: [8], [11]

$$1 - \varphi = \frac{W_p - W_f}{W_p \left(1 - \frac{f_{Al}}{f_{Al} + f_{NaCl}}\right)} \quad (3.14)$$

where W_f and W_p are the weights of the Al foam and the corresponding pre-dissolution NaCl/Al preform respectively and f_{Al} is the Al weight fraction in the initial NaCl/Al powder mixture. In order to give a direct indication of the porosity of the Al foam, the foam was characterised by relative density, which is the ratio of the density of the foam to that of the bulk Al. Theoretically, the relative density is equivalent to the volume fraction of Al in the initial NaCl/Al preform, if the preform is 100% dense and all the NaCl particles in the preform are completely dissolved away in the dissolution stage. The theoretical relative density of the resultant foam, ρ , was therefore calculated from the Al weight fraction in the preform by [8], [11]:

$$\rho = \frac{f_{Al} \rho_{NaCl}}{f_{Al} \rho_{NaCl} + (1 - f_{Al}) \rho_{Al}} \quad (3.15)$$

where $\rho_{Al} = 2.70 \text{ gcm}^{-3}$ and $\rho_{NaCl} = 2.17 \text{ gcm}^{-3}$ are the Al and NaCl densities respectively.

3.7 Lattice strain and crystallite measurement using X-ray Diffraction

The lattice strain and crystallite size of the composite NaCl/Al and the Al foam were determined by Bruker model D8 Advanced X-ray Diffractometer (Cu K_α radiation, $\lambda = 0.15406 \text{ nm}$) from Bragg's angle (2θ) of 10 to 90 ° with steps of 0.040 °. Phase identification of the powders were carried out using EVA software. Phase identification using x-ray diffraction relies mainly on the positions of the peaks in a diffraction profile and to some extent on the relative intensities of the peak in a diffraction profile and to some extent on the relative intensities of these peaks. The shapes of the peaks contain additional and often valuable information. The shape, particularly the width, of the peak is a measure of amplitude of thermal oscillations of the atoms at their regular lattice sites. It can also be a measure of vacancy and impurity element concentrations and even plastic deformation, any factor which results in a distribution of d-spacings.

Crystallite size can cause peak broadening. The well known Scherrer equation explains peak broadening in terms of incident beam divergence which makes it possible to satisfy the Bragg condition for non-adjacent diffraction planes [128]. Once instrument effects have been excluded, the crystallite size is easily calculated as a function of peak width (specified as the full width at half maximum peak intensity (FWHM)), peak position and wavelength.

The Williamson Hall plot method's is based on a Fourier deconvolution of the measured peaks and the instrument broadening to obtain the true diffraction profile [128]-[130]. This method is capable of yielding both the crystallite size distribution and lattice microstrain. For those specimens after experiencing large plastic deformation, the residual strain will lead to a parallel shift in the x-ray diffraction peaks, while the non uniform residual strain will cause the x-ray diffraction peaks to broaden. Since the broadening parameter of the x-ray peaks is due to strain effect as well as size effect, therefore, then it could be written as:

$$B_s = \frac{0.9\lambda}{d \cos \theta} + \eta \tan \theta \quad (3.13)$$

By multiplying $\cos \theta$ to equation (3.13), the formula becomes:

$$B_s \cos \theta = \frac{k\lambda}{d} + \eta \sin \theta \quad (3.14)$$

where B_s refers to full width at half maximum (FWHM), θ the Bragg angle, d is the crystallite size, η the lattice strain, λ the x-ray wavelength, k is Scherrer constant ($=0.9$). The instrumental broadening (B_i) should be corrected by the following equation:

$$B_s^2 = B_e^2 - B_i^2 \quad (3.15)$$

where B_e is the FWHM of the measured XRD peak.

Thus, when $B \cos \theta$ is plotted against $\sin \theta$, a straight line will be obtained with the slope as η (lattice strain) and the intercept being $k\lambda/d$ where crystallite size, d , can be determined by using this method.

For the measurement of activation energy for grain growth was determined from the crystallite size measurement by constructing an Arrhenius plot for a constant sintering time [129]. The slope of the equation was used to determine the activation energy.

3.8 Electrical conductivity measurement

Measuring the electrical conductivity as a tool for describing the porosity of the foam could be a very interesting method because of the following technical and scientific reasons. This property is an essential characteristics of certain products, such as electric contacts, semiconductors, soft magnets, and non-ohmic resistors [135]-[137]. It can be used for assessment of mechanical properties without the requirement of destructive test and related consumption of time and money [136]. Study of the presence of porosity of the foam especially after dissolution process, could be carried out by this measurement. The measurement might afford a sensitive appreciation of the influence of the sintering parameters [138]-[144]. The result of the measurement can be used for rapid inspection of fabricated foam using PASDP technique.

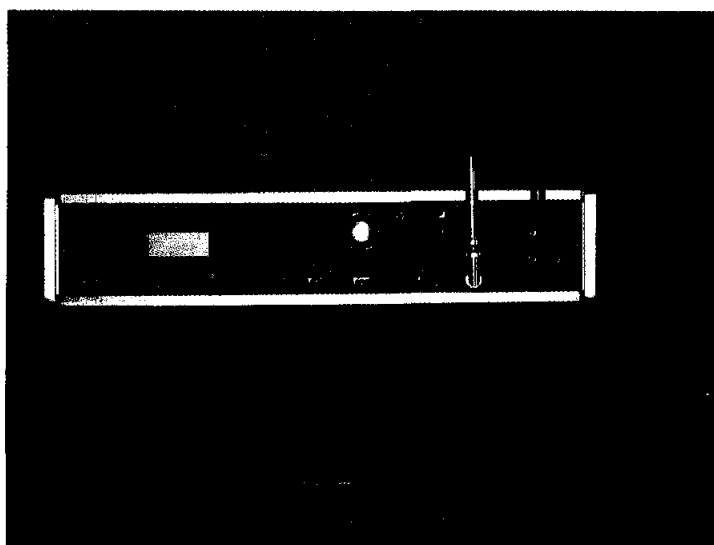


Figure 3.7: Valhalla resistivity meter

The electrical resistivity of the specimen was examined by Vallhala resistivity meter (Figure 3.7) and determined by the following equation:

$$\rho = R \frac{A}{l} \quad (3.16)$$

where R is the resistance, A and l are the area and length of the specimen respectively.

3.9 Morphology evaluation of foam specimen



Figure 3.8: LEO Scanning electron microscope arrangement

Scanning electron microscope was a valuable means of observing the morphology of the fabricated specimen. When a high energy electron beam emitted from a LaB_6 cathode interacts with the specimen, several types of radiations are produced from which the following are detected by a scanning electron microscope: secondary electrons, back scattered electrons and X-ray emission. These radiations are used either to form images (secondary and back scattered electrons) or chemically analyse the microstructural elements (X-rays).

The morphology of the foam specimen was analysed by LEO Scanning Electron Microscope (FE-SEM, model LEO 1525) as shown in Figure 3.8. In this SEM image analysis, aperture size is important. Small apertures gave a lower current of the e-

beam, which was good for high-precision work. Larger apertures gave more current in the e-beam, thus it was possible to use shorter dwell times and/or larger step size during exposure. In addition, aperture alignment, stigmatism and working distance in SEM system need to be adjusted several times to obtain sharp and good quality images.

3.10 Compressive mechanical properties determination

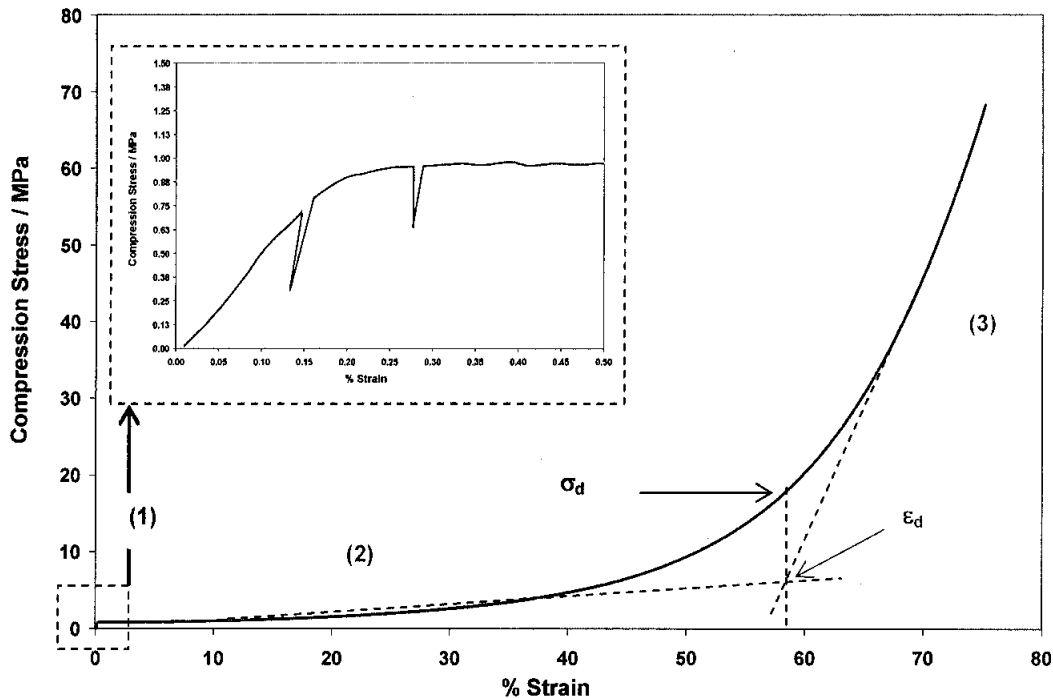


Figure 3.9: Typical compression curves obtained on metallic foams which present a complete three-stage showing the “elastic/plastic” loading (1), the progressive plastic deformation (2) and the densification (3)

The compression tests were performed on a Instron 50 kN testing machine using a crosshead speed of 1 mm/min. The compression strength was determined on the compression curves as the intersection of the loading and plastic deformation plateau, as shown in Figure 3.8. The modulus was measured as the slope of the first unloading during the compression test (i.e. vertical lines on the compression curves in Figure 3.8). Unloading was used to isolate elastic deformation from plastic deformation and obtain the true elastic response of the material [145]. The deformation at densification (ϵ_d) was taken as the intersection of the plastic deformation plateau and the densification loading, as presented in Figure 3.9 and Figure 3.10 respectively. The

strength at densification (σ_d) was evaluated as the strength corresponding to the deformation at densification on the compression curves while the energy at densification (W_d) was evaluated as the area under the curve up to densification (ϵ_d) [146].

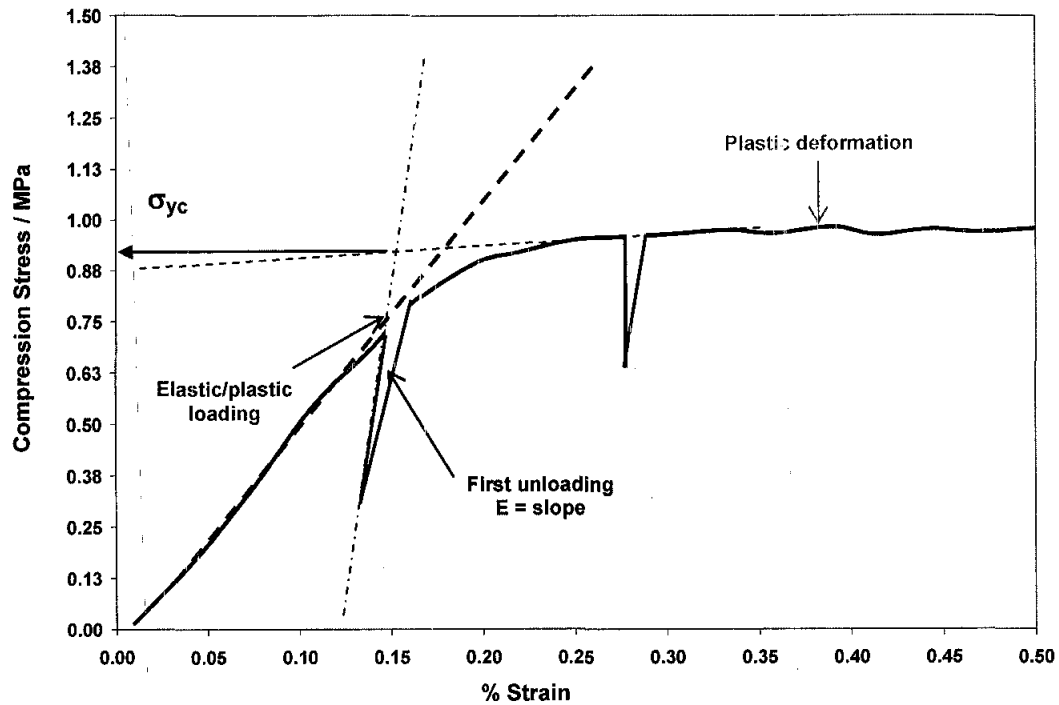


Figure 3.10: Enlarge portion of the beginning of the curve illustrating the methods used for evaluating the yield strength and the elastic modulus using the specimen loading

3.11 Statistical optimization of processing parameters for the fabrication of aluminium foam

The processing parameters of the fabrication of aluminium foam need to further be investigated in order to study the dependence of the final structure on the processing condition. The effects of four processing factors: sintering temperature, sintering time, heating rate and compaction pressure at elevated temperature on the physical and mechanical properties of final foam fabricated from PASDP technique will be investigated. The experiments have been performed according to the principals of Taguchi's design of experiment and the analysis of variance (ANOVA) technique was

used to establish the relative significant of these factors and in determining the optimum set of factors that would maximize the properties.

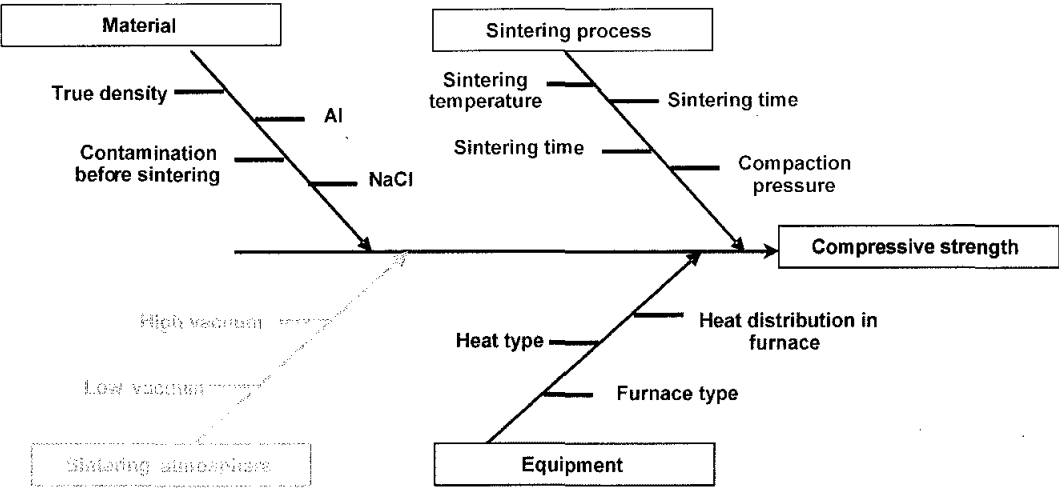


Figure 3.11: Ishikawa cause effect diagram for Pressure assisted sintering dissolution process for Al foam

In order to identify the process parameter that affects the physical and mechanical properties of foams, an Ishikawa cause-effect diagram was constructed, as shown in Figure 3.11. Four processing factors were selected in order to visualize the effect of processing parameters on the physical and mechanical properties of PASDP fabricated foam: sintering time (A, 5-30 min), sintering temperature (B, 570-620°C), compaction pressure (C, 20-120 MPa) and heating rate (D, 30-50 °C/min).

The factor involved and their levels are shown in Table 3.5. The influence of these factors on the compressive strength and density of the PASDP Al foam was studied through experiments designed using the L_9 orthogonal array, with each factor having 3 levels. As three level parameters has 2 degrees of freedom (DOF) obtained from the number of levels – 1, the total DOF for four parameters, each at three levels is 8 [=4 x (3-1)]. As described by Ibrahim *et al.* [92] on Taguchi’s Design of Experiments, the total DOF of a selected Orthogonal Array (OA) must be greater than or equal to the total DOF required for the experiment. Therefore by using the L_9 orthogonal array, the number of trial runs was reduced to 9 simple and effective experiments. Obviously, this saves experimental cost and time. The use of Taguchi orthogonal arrays helps determine the minimum number of experiments needed in order to produce relevant information for a given set of factors. As described by Ibrahim *et al.*

[92], Kishore *et al.* [93], Mahapatra *et al.* [94] and Ozbay *et al.* [95], if full factorial experimental design were used, it would require 81 trial runs for all possible permutations of these factors

Table 3.5: Process parameters and their value at different levels

Process parameter	Process parameter	Level 1	Level 2	Level 3
A (min)	Sintering time	5	15	30
B (°C)	Sintering temperature	570	600	620
C (°C/min)	Heating rate	5	10	30
D (MPa)	Pressure applied at sintering temperature and holding at sintering time	40	80	120

Table 3.6 illustrates the L₉ orthogonal array as described by Kishore *et al.* [93] and, since there were four three levels factors, these factors were assigned to all four columns in the array. In this work, interaction effects between factors were considered insignificant and hence, not examined. Nine trial runs with certain factor level combinations determined from the array were carried out in triplicate (R_1 , R_2 and R_3 refer to the 1st, 2nd and 3rd readings respectively).

Table 3.6: The L₉ (3⁴) (parameters assigned) with response

Serial No	Factor				Process parameter			
	A	B	C	D	Time (min)	Temperature (°C)	Heating rate (°C/min)	Compaction Pressure (MPa)
1	1	1	1	1	5	570	5	40
2	1	2	2	2	15	570	10	80
3	1	3	3	3	30	570	30	120
4	2	1	2	3	5	600	10	120
5	2	2	3	1	15	600	30	40
6	2	3	1	2	30	600	5	80
7	3	1	3	2	5	620	30	80
8	3	2	1	3	15	620	5	120
9	3	3	2	1	30	620	10	40

3.12 Carbothermal nitridation process of mechanical milled silica sand for producing ceramic reinforcement materials

Silica sand of purity 99.5 %, obtained from Johore Silica was screened to less than 32 μm . The carbon powder, which had undergone ball milling treatment for five hours, was obtained from Petronas refinery. The C/SiO₂ mixtures in a molar ratio of 6/1 were prepared by mixing in a rotary mixer for 30 minutes. Two batches of mixture were prepared, i.e. one batch was subjected to mechanical milling (MM) and the other was in 'as received' state (Un-MM). The mechanical treatment of the silica sand was performed in a planetary ball mill of four stations using a stainless steel jar with a ball to powder ratio (BPR) 20:1 by weight and milling speed of 200 rev min⁻¹. The synthesis process was carried out in tube furnaces of 250 cm³ working volume with mixed gas flow above the layer of mixture. The 1-2 mm thick layer of mixture was placed in boats made of alumina and then put into a heating zone of a furnace. The furnace was purged with mixed gas for about 15 minutes before the process. The furnace was heated up to the desired temperature at a chosen rate, then the temperature was kept constant over the desired time. The process was carried out at temperatures ranging from 1350 to 1650°C, then the samples were furnace cooled. The samples were removed from the furnace, ground in mortar and then analysed according to the prescribed procedure. The particle shape and chemical composition of the product syntheses at various temperatures were determined by scanning electron microscopy (Leo 1510) and X-ray diffraction methods. An elemental analyser, Leco, model TC-600, was used to determine the elemental analysis of C and N [5]. The flow diagram of the carbothermal nitridation process is shown in Figure 3.12.

The influence of four factors; temperature, time, heating rate of the process and duration of mechanical milling of silica sand; on the yield of formation of SiC_w was studied by using the L₉ orthogonal array, with each factor having 3 levels. The factors involved and their levels are shown in Table 3.7. Table 3.8 illustrates the L₉ orthogonal array [93]. Since there were four three-level factors, these factors were assigned to all four columns of the L₉ array. In this work, interaction effects between factors were considered insignificant and hence, not examined.

Nine trial runs with certain factor level combinations determined from the array were carried out and duplicated (R_1 refer to the 1st reading and R_2 refer to the 2nd reading). The composition of the products was determined from elemental analysis by weight% of C and N in the samples, based on the work of Silva and Figueiredo [113] which used the following assumptions:

- Species considered in the samples: SiC and Si₃N₄, (the free carbon was previously burned off).
- All carbon was present as SiC and all nitrogen as Si₃N₄. The unreacted silica was dissolved by the reaction with hydrofluoric acid.

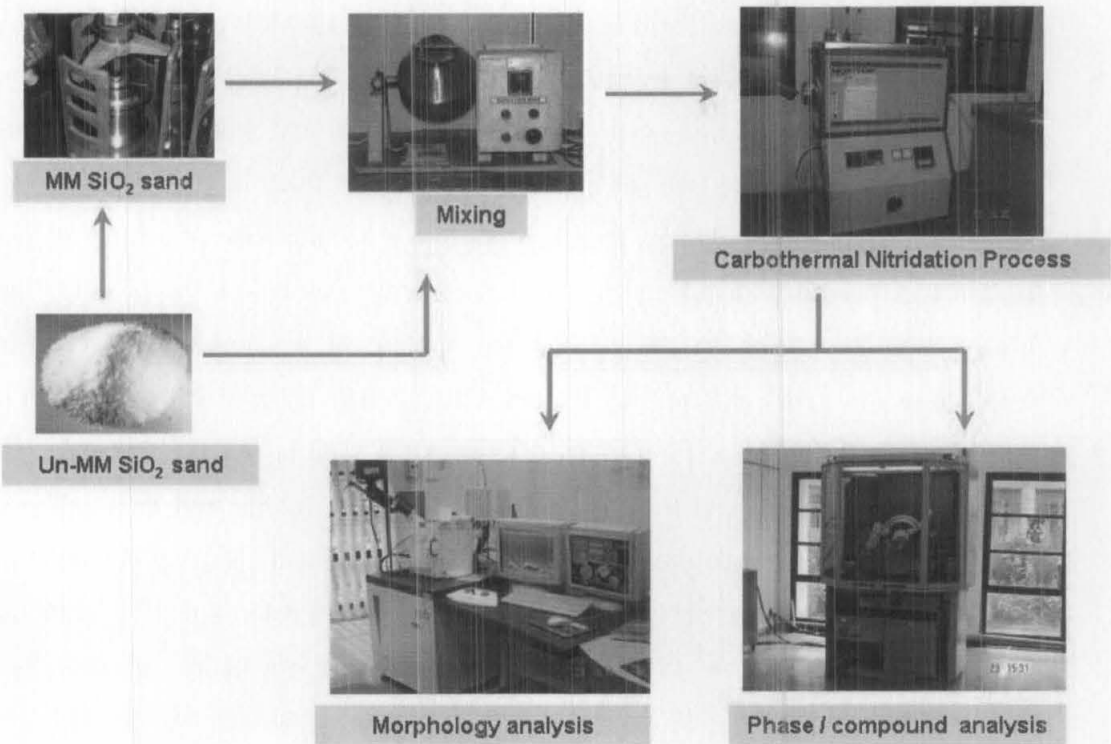


Figure 3.12: Process flow for the carbothermal nitridation process using structured alteration silica sand

Table 3.7: Processing parameters and their levels for orthogonal experiment

Column	Process parameter	Level 1	Level 2	Level 3
A (°C)	Temperature	1450	1550	1650
B (min)	Time	60	120	180
C (°C/min)	Heating rate	5	10	20
D (hour)	Duration of mechanical milling process of silica sand	20	60	100

Table 3.8: The L₉ (3⁴) OA (parameters assigned) with response

Serial number	Run order	Parameter trial conditions				Responses (raw data)		Signal-to-noise ratio (dB)
		A(1)	B(2)	C(3)	D(4)	R ₁	R ₂	
1	3	1	1	1	1	Y ₁₁	Y ₁₂	S/N(1)
2	7	1	2	2	2	Y ₂₁	Y ₂₂	S/N(2)
3	5	1	3	3	3	Y ₃₁	Y ₃₂	S/N(3)
4	1	2	1	2	3	Y ₄₁	Y ₄₂	S/N(4)
5	4	2	2	3	1	Y ₅₁	Y ₅₂	S/N(5)
6	6	2	3	1	2	Y ₆₁	Y ₆₂	S/N(6)
7	9	3	1	3	2	Y ₇₁	Y ₇₂	S/N(7)
8	2	3	2	1	3	Y ₈₁	Y ₈₂	S/N(8)
9	8	3	3	2	1	Y ₉₁	Y ₉₂	S/N(9)
Total						Σ	Σ	

*R*₁, and *R*₂, are responses values for two repetition of each trial. The 1's, 2's and 3's denote the levels 1, 2 and 3 of the parameters. *Y*_{*ij*} are measured values of the quality characteristic for the % yield of SiC_w formation (weight of SiC_w obtained)

The reaction yields were based on silicon and were computed as follows [113]:

$$Total_{yield} = \frac{nSiC + 3nSi_3N_4}{nSiO_2} \times 100 \quad (3.17)$$

$$SiC_{yield} = \frac{nSiC}{nSiO_2} \times 100 \quad (3.18)$$

where *nSiC* is the number of moles of silicon carbide present in the sample and *nSiO*₂ is the number of moles of silica initially present.

3.12.1 Raw material characterization

3.12.1.1 Silica sand

The surface morphology of the Un-MM and MM silica sand are shown in Figure 3.13 (a) and (b) respectively. The powder of Un-MM silica sand exhibits angular shape whereas the MM batch type has distorted structure after undergone mechanical milling process.

The XRD analysis of the Un-MM silica sand shows the crystallinity behaviour of the sample (see Figure 3.13 (a)). The mechanical milled silica, however exhibits crystal lattice distortion which has the pattern of a vast broadening effect at the base of the peaks and also reduction in intensity as shown in the spectrum of Figure 3.14 (b).

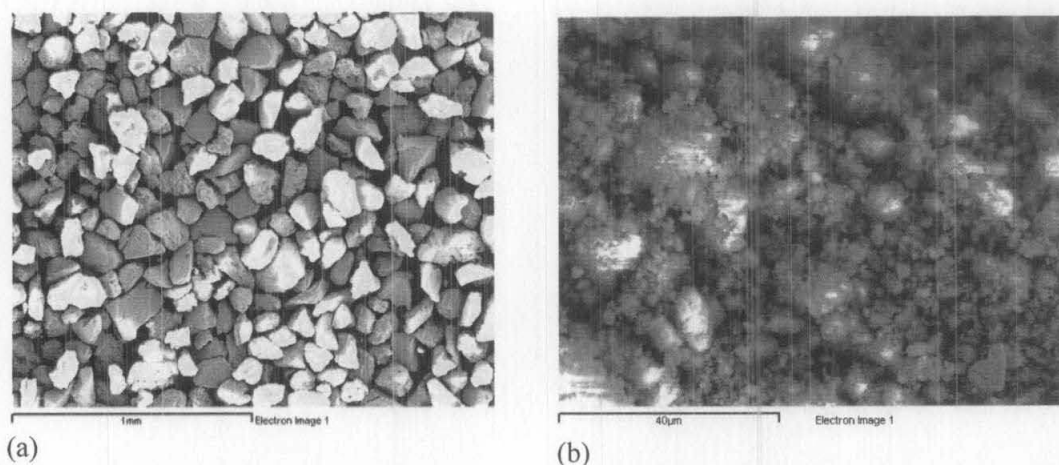


Figure 3.13: SEM micrograph of (a) Un-MM silica sand (b) MM silica sand

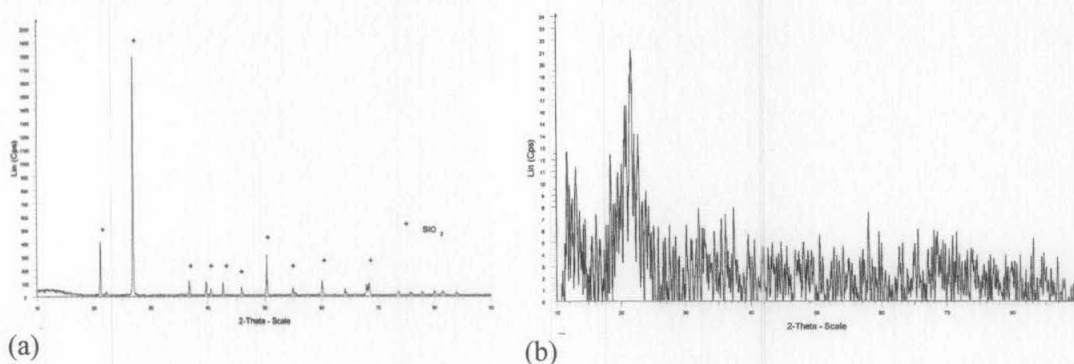


Figure 3.14: XRD spectrum of (a) Un-MM silica sand (b) MM silica sand

3.12.1.2 Carbon

The main problems of the carbothermal reduction process are the particle size of reactant and the need for an intimate contact among them [90]. In an attempt to avoid these problems, ball-milled carbon has been used as starting reactant. This carbon had undergone ball milling treatment for five hours. The carbon powder exhibits angular and cubic shape as shown in Figure 3.15 (a). This carbon powder has been studied by

means of X-ray diffractometry proving their amorphous structure as shown in Figure 3.15 (b).

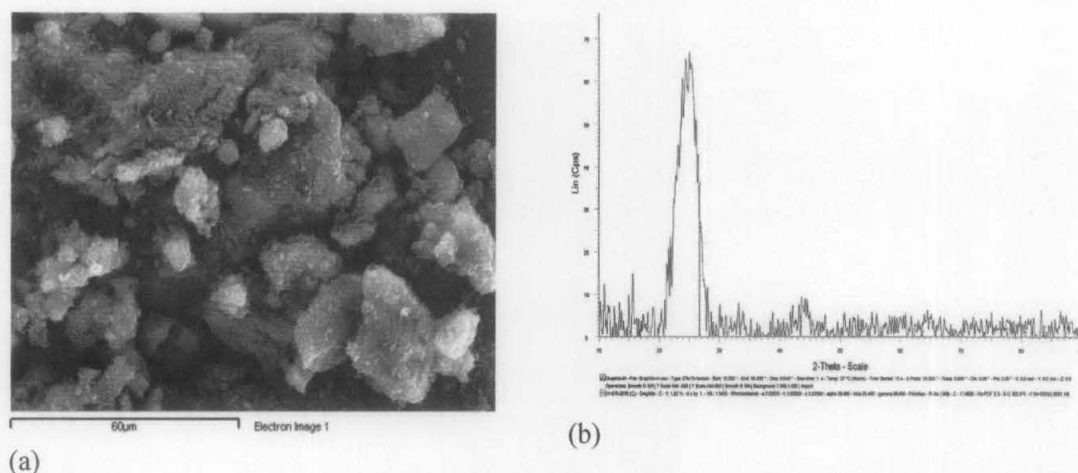


Figure 3.15: (a) SEM micrograph of ball milled carbon (b) XRD spectrum of ball milled carbon

3.13 Fabrication of reinforced Al foam

In the preparation of reinforced Al foam, the aluminium powder was first mixed thoroughly with the SiC particulate powder of 1 weight % in a propylene container using three dimensional mixer for 1 hour [14]. The NaCl particles were then added at different volume fraction of 60 to 80% in the mixer and were mixed at a mixing rate of 50 rpm for 30 min to homogenously blend the mixture. The blended mixture was consolidated into cylindrical specimen using pressure assisted sintering technique. The influence of the reinforcement addition on the compressive mechanical properties of the resultant foam was investigated.

3.14 Chapter summary

In summary, the following describes the division of work that needs to be performed in order to achieve the objectives of the study:

Identification of feasible experimental review and experimental development

- Literature search and identification of experimental development of foaming process
- To establish the experimental set up based on current technology i.e. sintering dissolution process (SDP)

Compaction at elevated temperature based on model suggested by W.M. Long

- Determination of shrink-fitted die

Pressure assisted high frequency induction heated sintering dissolution process

- Optimization of the processing parameters
- Statistical optimization using Taguchi's Design of Experiments and analysis of variance (ANOVA) technique will be employed in order to obtain the optimum combination of the process parameter settings.

Evaluation of foam specimens

- Physical properties: morphological, density and porosity
- Electrical properties: empirical equations such as Skorohod and Solinin, Langlois and Couret, Liu and Lang and percolation theory
- Mechanical properties: compression behaviour (stress-strain curve)

Synthesis of reinforcement material for Al foam from the carbothermal nitridation process

- Planetary ball mill method will be employed in order to alter the regularity of the crystalline network in silica sand used.
- Optimization of the processing parameters of the carbothermal nitridation process

Evaluation of reinforced Al foam

- Physical and mechanical properties determination

CHAPTER 4

RESULTS AND DISCUSSION

4.1 Chapter overview

This chapter discusses the improvement made by pressure assisted sintering dissolution process (PASDP) as opposed to the solid state sintering dissolution process (SSSDP) which was used in producing a much improved open celled aluminium foam. The improvements leads to an aluminium foam possessing a high dense of cell wall which is attainable in a much shorter time and possesses superior mechanical properties. By varying the local sodium chloride (NaCl) volume fractions in the sodium chloride/aluminium (NaCl/Al) compact, it is possible to fabricate aluminium foam with different relative densities. When subjected to monotonic compression mode, the fabricated aluminium foam exhibits typical stress-strain behaviour of metallic foam. The chapter also assimilates the results on understanding the influence of processing parameters on the physical and mechanical properties of Al foam fabricated through PASDP technique. Considering all contributing factors in fabricating the Al foam using PASDP method, statistical evaluation that utilizes the Taguchi's Design of Experiments was carried out extensively to predict the optimum processing parameters in this work. The processing parameters were analysed based on Taguchi's signal to noise ratio (S/N) and analysis of variance (ANOVA) which is a major improvement from the conventional Full Factorial Design of Experiment statistical method. The viability of electrical conductivity as a tool for evaluating variations in morphology of PASDP Al foam and the influence of processing parameters on the electrical conductivity of the final foam will be discussed.

4.2 Preliminary development of the fabrication of aluminium foam through pressure assisted high-frequency induction heated sintering/dissolution process (PASDP)

This section presents work carried out on developing a technique to produce open celled aluminium foam based on the pressure assisted sintering dissolution process (PASDP). In contrast to metallic foams made by the sintering dissolution process (SDP), aluminium foams made using this technique has high density cell walls which are attainable in a much shorter time and possess superior mechanical properties. This section also discusses the preliminary results on the morphology evolution and physical properties of Al foam fabricated using the two different modes of fabrication. It also describes the mechanical response behaviour of PASDP Al foam when subjected to compression mode testing.

4.2.1 Morphology evolution and physical properties of SDP and PASDP Al foam

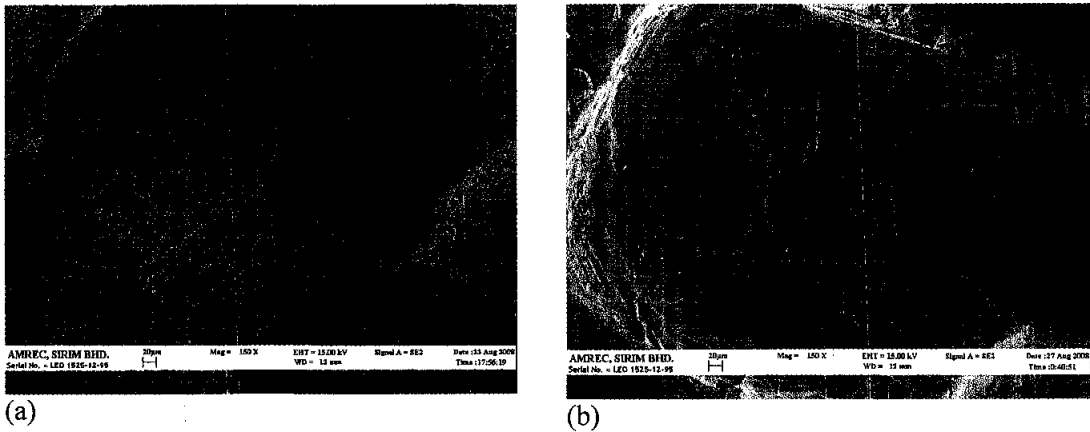


Figure 4.1: Images (SEM) of the cell wall of Al matrix for: (a) SDP foam (b) PASDP foam

The electron micrographs from the two different processing techniques (SSSDP and PASDP) are shown in the Figures 4.1 (a) and (b) respectively. It can be noticed that the formation of metallurgical bonds in packed Al powder during solid state sintering is a difficult process due to the encapsulation of Al by a thermo chemically stable Al_2O_3 film as reported by Zhao *et al.* [8]. They also postulated that mass transport by

diffusion is hindered as this dense and stable oxide layer exhibits extremely low-reactive diffusion rates.

As can be observed from Figure 4.2 (a)-(d), the Al particles exist in its individual form indicating that the compacted metal particles did not bond together by atomic motion during solid state sintering process. The cell walls of the Al foam compacts also consists of some voids (see arrows) which were thought to be also pre-exist in the green compact before the sintering process as revealed through higher magnification, shown in Figures 5 (c) and (d) respectively. Similar findings were also observed by Zhao *et al.* (2004). They assumed that this behaviour might be understood by considering the stress and strain distribution in the aluminium/sodium chloride (NaCl/Al) compact during compaction. According to them the NaCl and Al powders used in the study have different morphologies and sizes, in which the former is brittle and hard whereas the latter is ductile and soft. They also observed that the local Al particles may not undergo much deformation and the destruction of the oxide film may not occur at all.

Mechanical disruption of the surface oxide film by the application of simultaneous heat and compaction pressure to the NaCl/Al composite can lead to an effective solid state sintering of Al powder. When a considerable amount of the surface oxide film has been removed or disrupted, a strong metallurgical bonding could be formed. As reported by Zhao *et al.* [8], the disruption of the oxide film is indeed crucial as this film tends to encapsulate the Al particle or liquid, forming a hard shell that prevents the progress of necking growth process between the Al particles.

The fresh metal-metal contacts that formed during pressure assisted sintering process become effective bonding points between the Al particles. As a consequence of simultaneous action of heat and pressure during the fabrication process, an interconnected metallic framework was formed as evident in the micrograph of the matrix as shown in Figure 4.1 (b).

Zhao *et al.* [8] reported that the application of pressure will break the metal oxide layer which surrounded the metal particles and lowers the vacancy concentration at the grain boundaries (vacancy sinks) relative to the pores (vacancy sources) and, by

thus increasing the concentration gradient of vacancies moving out of the pores per unit time, the pore shrinkage rate, and hence the densification rate, increases. They postulated that when high pressure is applied, the contribution of plastic yielding to densification is enhanced such that lower temperatures and shorter times than in conventional process are conceivable for the overall compaction process. According to them the attainment of high density in a short time using induction heating may be attributed to a combination of electrical discharge, resistance heating and pressure application effects.

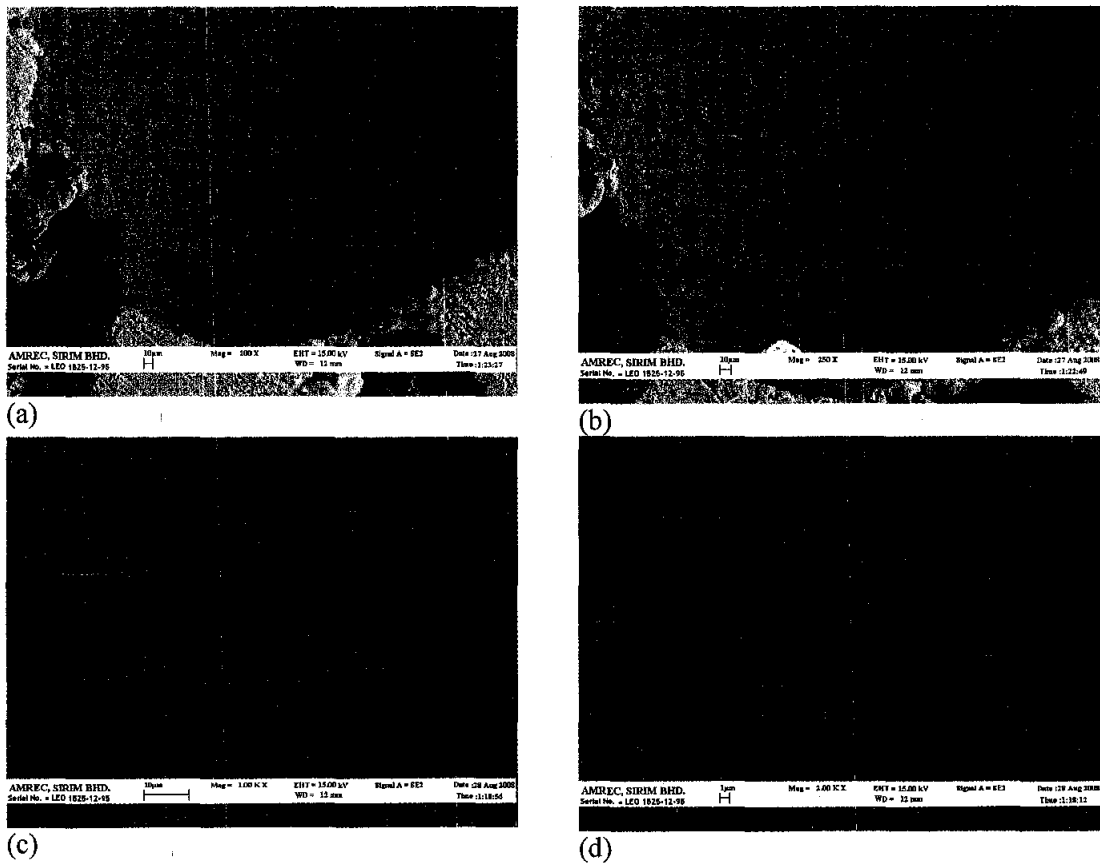


Figure 4.2: Images (SEM) of sintered aluminium foam of which the sample was interrupted after undergone 2 hours leaching process in order to avoid the collapse of the structure (a),(b) showing the existence of individual aluminium particle indicating that no diffusion process occurred during solid state sintering at (a x200 and b x250) (c),(d) showing voids between the original Al particles at (c x1000 and d x2000)

They also reported that when the induction current is applied, energy emission may be concentrated at particle contacts that attain high temperatures and these concentrated heat effects at particle surface may cause surface melting and oxide breakdown.

Figures 4.3 (a) and (b) show the photographs of PASDP Al foam and it can be observed that the foam has an open-pore structure featuring two level of porosity. The structure is characterized by cell (first level) with some openings or windows (second level) on the cell walls as shown in Figure 4.1.1.3 (b). As can be seen from Figures 4.3 (c) and (d), it can be noted that Al matrix of dense cell wall is fabricated using this improved PASDP process.

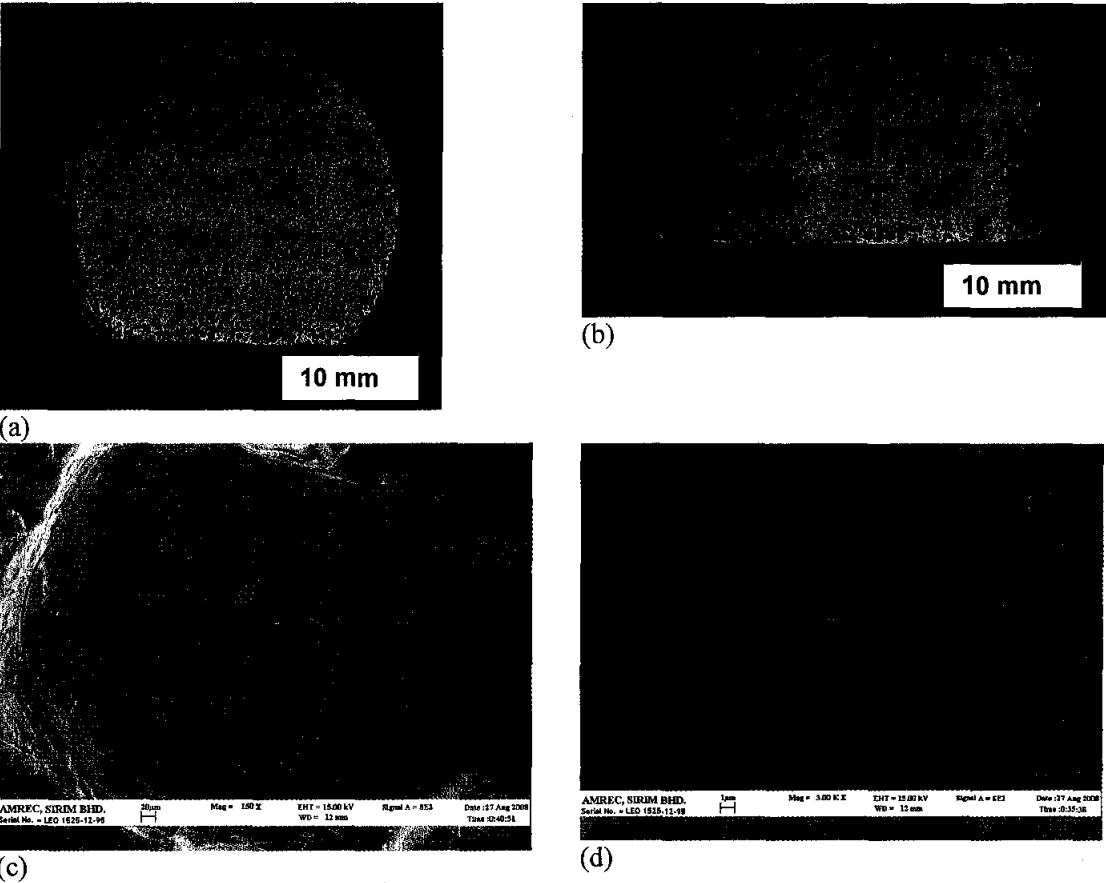


Figure 4.3: Photograph of PASDP Al foam (a) plan view (b) cross section view and SEM images of PASDP Al foam of selected area at (c) x150 showing the cell and window (d) x1000 showing the quality of cell wall

Table 4.1 shows the density and porosity of the compacts with different mode of compaction. It was observed that the compact of sintering dissolution process was

collapsed during subsequent leaching process due to the absence of inter metallic framework between the aluminium particles.

Table 4.1: The physical parameter of the sintered and pressure assisted sintered compacts of Al foam of volume fraction initially at 60 %

Mode of fabrication technique	Density / gcm ⁻³	Porosity / %
Pressure Assisted Sintering (PASDP)	1.132	58.07
Sintering Dissolution Process (SDP)	collapse	collapse

4.2.2 Dissolution characteristic of NaCl/Al compacts, physical behaviour and morphology evolution of PASDP Al foam

Figure 4.4 shows the density and porosity of the pressure assisted sintering compact with different NaCl/Al volume fraction in the compacts. These properties depend on the NaCl/Al volume fraction and it can be observed that the density decrease with increasing NaCl/Al volume fraction. The density of the specimen decreases from 2.465 gcm⁻³ to 2.290 gcm⁻³ when the volume fraction of the specimen is increased from 30 to 60 %. Meanwhile the value of the porosity of the composites increased from 3.25 % to 4.01 % as the volume fraction of the compacts increased from 30% to 60%.

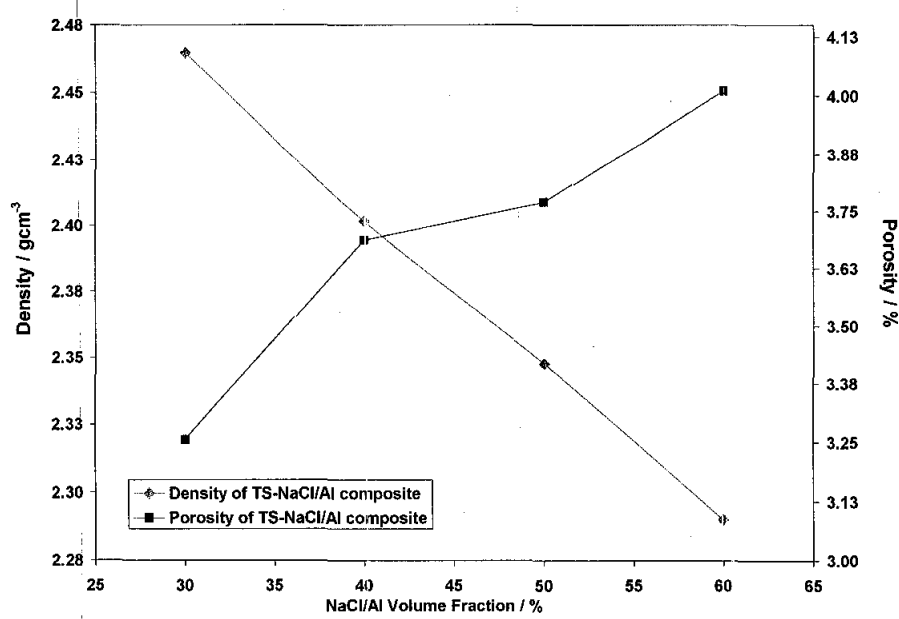


Figure 4.4: Variation of density and porosity of PASDP compact with NaCl volume fraction

Figure 4.12 shows the density of the pressure assisted sintered specimen with different NaCl/Al fraction at various compaction pressures. It was observed that NaCl/Al fraction influences the property and the density decrease with increasing NaCl/Al fraction. At a fixed NaCl/Al volume fraction, the density of the specimen increase with the increasing of the applied pressure.

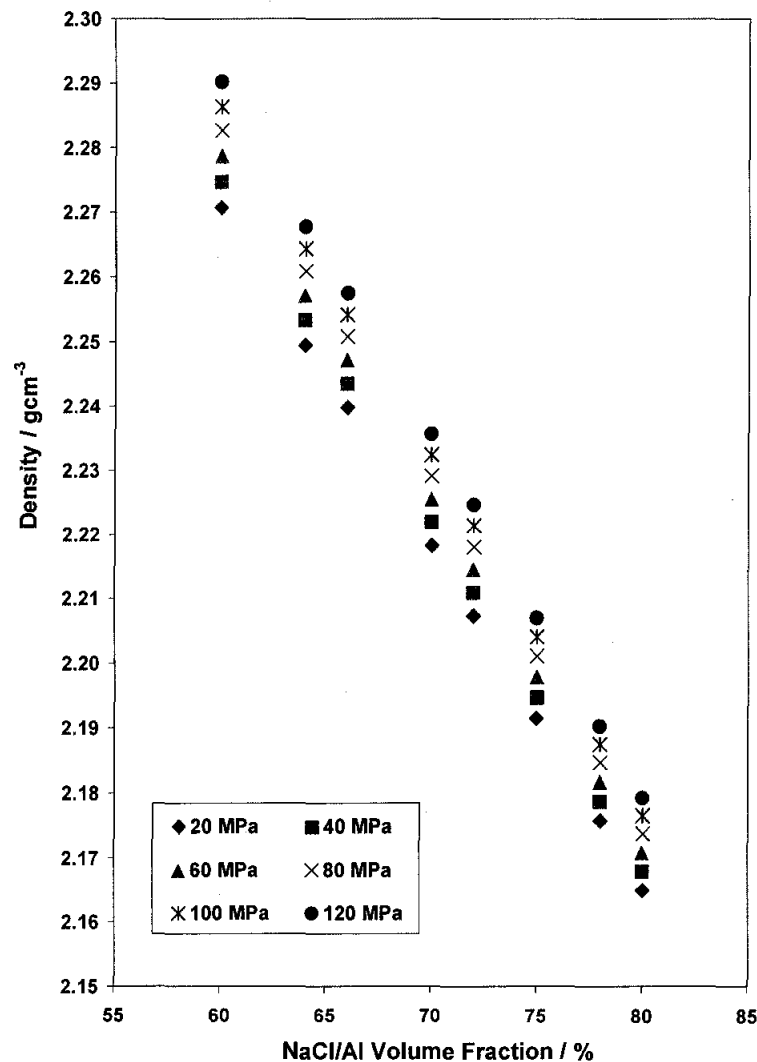


Figure 4.12: Variation of density of pressure assisted sintered NaCl/Al specimen with NaCl/Al volume fraction at different compaction pressure

Figure 4.13 reveals that the pressure assisted sintered compact porosity decreases with increasing compaction pressure. An increase in porosity is observed with the increasing of NaCl/Al volume fraction in the composite which suggests that the

distribution of strain may be not uniform in a compact containing more rigid particles which surround the much softer Al particles. This observation, however contradicts with the findings reported by Zhao *et al.* [8]. They also reported that from the process-control point of view, the compaction pressure needs to be adjusted with NaCl/Al ratio in the compact.

The results obtained under different compaction pressure revealed that compaction pressure does have a determinative influence on the bonding between the Al particles formed in the simultaneous sintering stages. From the work, it was found that the optimum compaction pressures were in the range of 20-120 MPa for the fabrication of the NaCl/Al composites. The metallic contacts between the Al particles could not be formed at lower compaction pressures, meanwhile at higher compaction pressures, the cracks were observed in the composites during pressure assisted sintering process.

In order to study on the densification behaviour of blended powder, equation (2.14) was used to fit experimental data obtained from the density evaluations of samples. The constants of the equation were obtained and are given in Table 4.2.1.1.

The curves in Figure 4.14 are related to Heckel equation which shows that the curves shift down by increasing NaCl content. It can also be observed that the slope of the curves decrease as the content of filler material increase and this behaviour reflects the rate of densification of the homogenously mixture. Similar findings were also observed by Abdoli *et al.* [75] in their work on the study of a nanostructured composite powder.

According to Abdoli *et al.* [75] the values of D_0 in Table 4.3 are related to apparent density at zero compaction pressure. They postulated that the prediction for density in the lack of pressure by this method is reasonable and showing higher density with NaCl content. They also described that due to the arrangement mechanism at the beginning of compaction, i.e. low pressure, D_0 obtained from the equation can be inaccurate.

The K-values obtained from the experiments are tabulated in Table 4.3. It can be observed that the higher the K-value, the higher the plastic deformation ability. So increasing in NaCl content, can result in the lower K-value and restrict the plastic

Table 4.2 shows the variation of the fraction of the dissolved NaCl in the Al foam, $1-\phi$, with the NaCl/Al volume fraction. As described by Zhao *et al.* (2004) in their work of SDP Al foam, a PASDP NaCl/Al compact can be regarded as a composite of Al matrix embedded with NaCl particles. The fraction of the dissolved NaCl increases from 58 to 97% when the volume fraction of NaCl is increased from 30 to 60%. For the composite with volume fraction initially at 60%, most of NaCl particles are in contact with each other and form a continuous three-dimensional network. As water can wash off the NaCl particles in the network, only a small amount of NaCl residue is left in the resultant foam. On the contrary, for composite with volume fraction initially at 30%, some NaCl particles are enclosed completely by the Al matrix. These isolated NaCl particles could not diffuse into the aqueous part and thus trapped in the Al matrix. By decreasing NaCl weight fraction in the NaCl/Al compact, it will increase the Al volume fraction and resulting in the increase amount of residual NaCl in the final Al foam. Similar behaviour was also reported by Zhao *et al.* [8].

Table 4.2: Variation of the fraction of the dissolved NaCl in the Al foam, $1-\phi$, with the NaCl/Al fraction

Specimen	Weight of HPC-BDP* / g	Weight of HPC-ADP^ / g	$1-\phi$
30%NaCl/Al	23.812	17.427	0.5842
40% NaCl/Al	23.602	16.113	0.6241
50% NaCl/Al	22.632	14.254	0.6804
60% NaCl/Al	21.202	9.196	0.9761

*denotes hot pressed compact before dissolution process
^ denotes hot pressed compact after dissolution process

The XRD pattern as shown in Figure 4.5 confirms the non existence of NaCl compound in the compact when the initial volume fraction of the compact is increased to 60%.

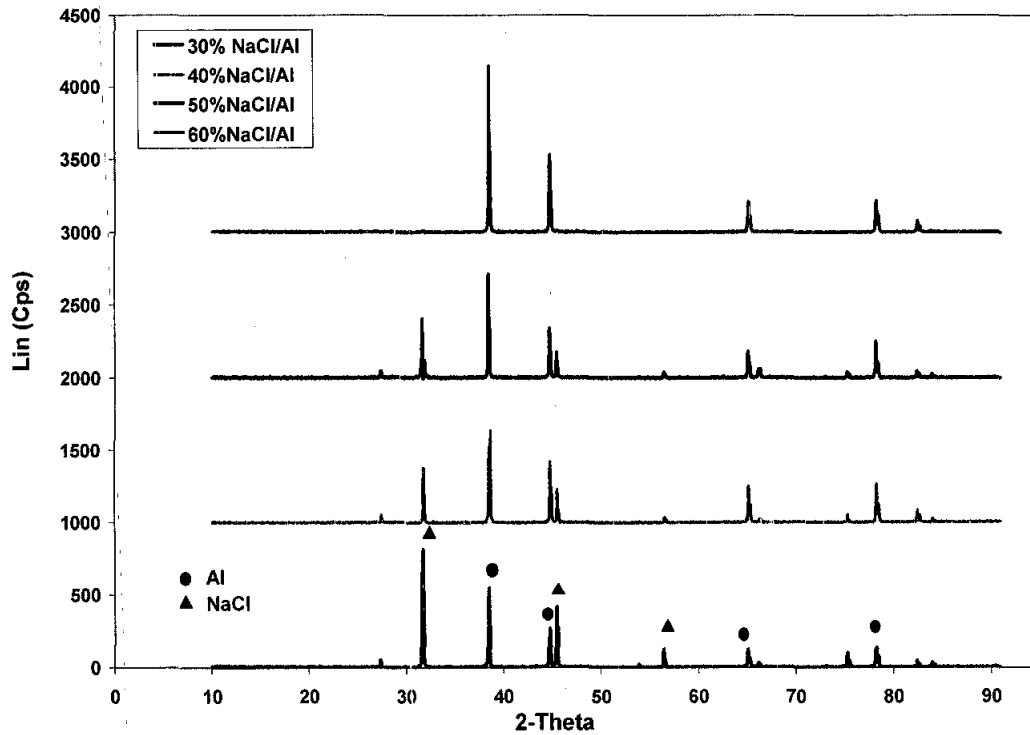


Figure 4.5: XRD spectrum of NaCl/Al compact at different volume fraction after dissolution process

Figure 4.6 shows the density and porosity of the pressure assisted sintering compact after dissolution process with different NaCl/Al volume fraction and it can be deduced that the compact density and porosity depend on the NaCl/Al volume fraction in the composite. The density of the composites decrease from 2.148 to 1.132 gcm^{-3} as the volume fraction of the NaCl is increased from 30 % to 60%. Region A (between 30 to 40% NaCl/Al volume fraction) of this figure shows that most of the NaCl particles are covered entirely by the Al matrix which inhibit them from being into direct contact with the water and hence attributed to the low porosity characteristic of the compact. In region B of the figure, as most NaCl particles are in contact with each other and form a continuous three-dimensional network in the compact, they can be readily be dissolved with water. This behaviour ascribes the higher porosity characteristic of the compact.

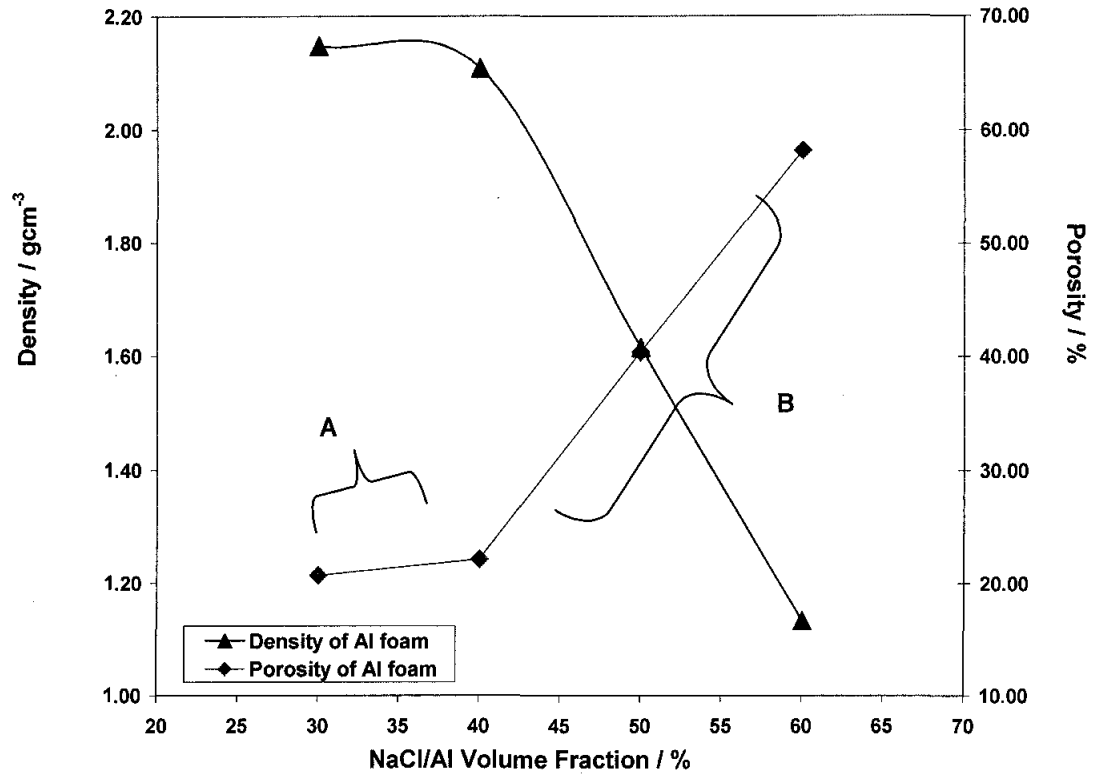


Figure 4.6: Variation of density and porosity of pressure assisted sintered compact with NaCl/Al volume fraction after dissolution process

Figure 4.7 (a)-(d) show the SEM micrographs of with resultant Al foam of volume fraction between 30% to 60% volume fractions of NaCl/Al composites after the dissolution process. The specimens have a homogenous structure with pores of size in the range of 100-400 μm and it can be observed that the structures are mirror images of the NaCl particles and the cell size matches well with the particle size of the filler material. The fabrication of Al foam using PASDP has remarkably pointed to the fact that by varying the local sodium chloride (NaCl) volume fraction in the sodium chloride/aluminium (NaCl/Al) compact, specimen with different densities can be fabricated.

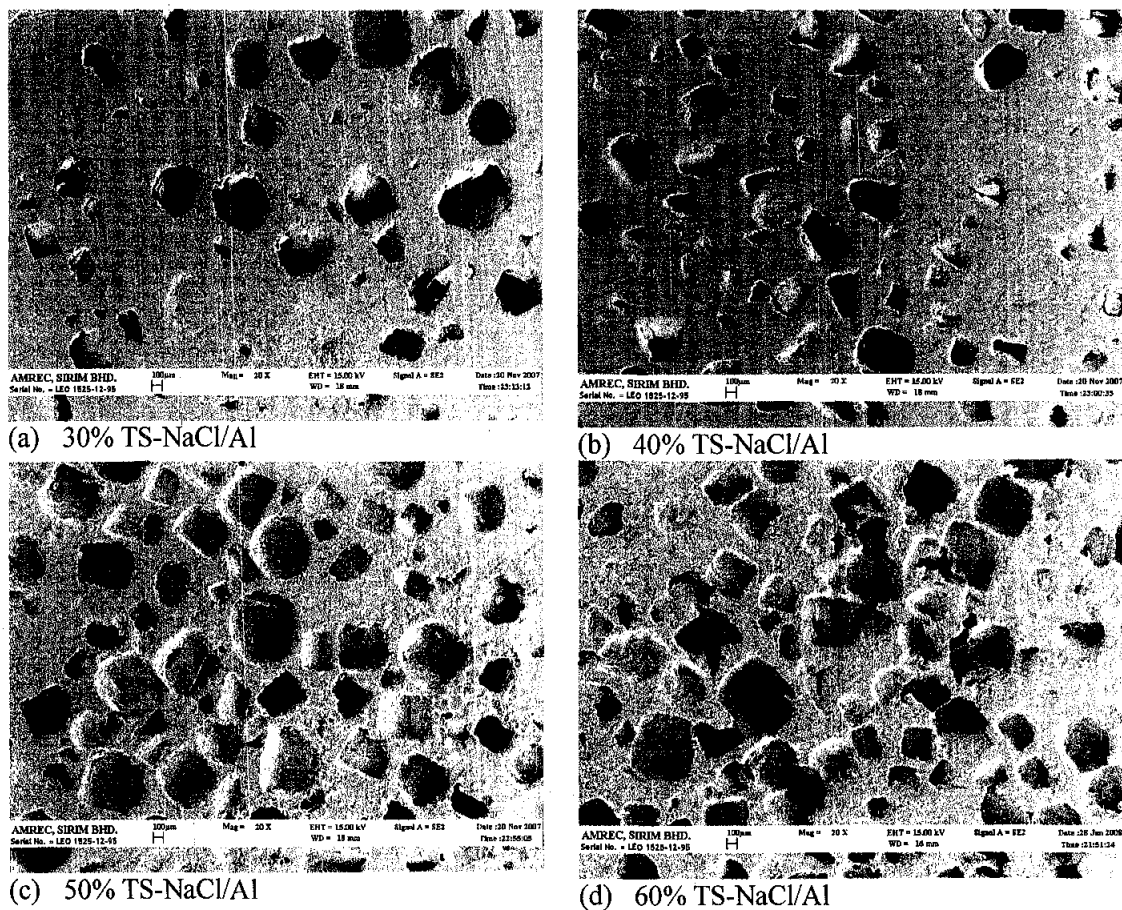


Figure 4.7: Images (SEM) of specimen with different relative density made by pressure assisted sintering technique

4.2.3 Monotonic Compression Test

Figure 4.8 shows the compressive stress-strain curves of the Al specimens with different volume fraction of initial NaCl of 30%, 40%, 50% and 60%, respectively, which correspond to 2.148 gcm^{-3} , 2.109 gcm^{-3} , 1.615 gcm^{-3} and 1.132 gcm^{-3} respectively. The specimens of 30 to 50% volume fraction of NaCl/Al do not exhibit a characteristic of stress-strain foam behaviour when loaded in compression. The typical engineering stress-strain curve of the aluminium is exhibited by specimen of 60% volume fraction of NaCl/Al. The curve is generally characterised by an initial elastic response, followed by a deformation “plateau” with a positive slope and finally a transition to densification [11]. One of the characteristics of the foam manufactured

by PASDP is a very smooth plateau region in the stress-strain curve, as a result of the homogenously distributed pores having a narrow size range.

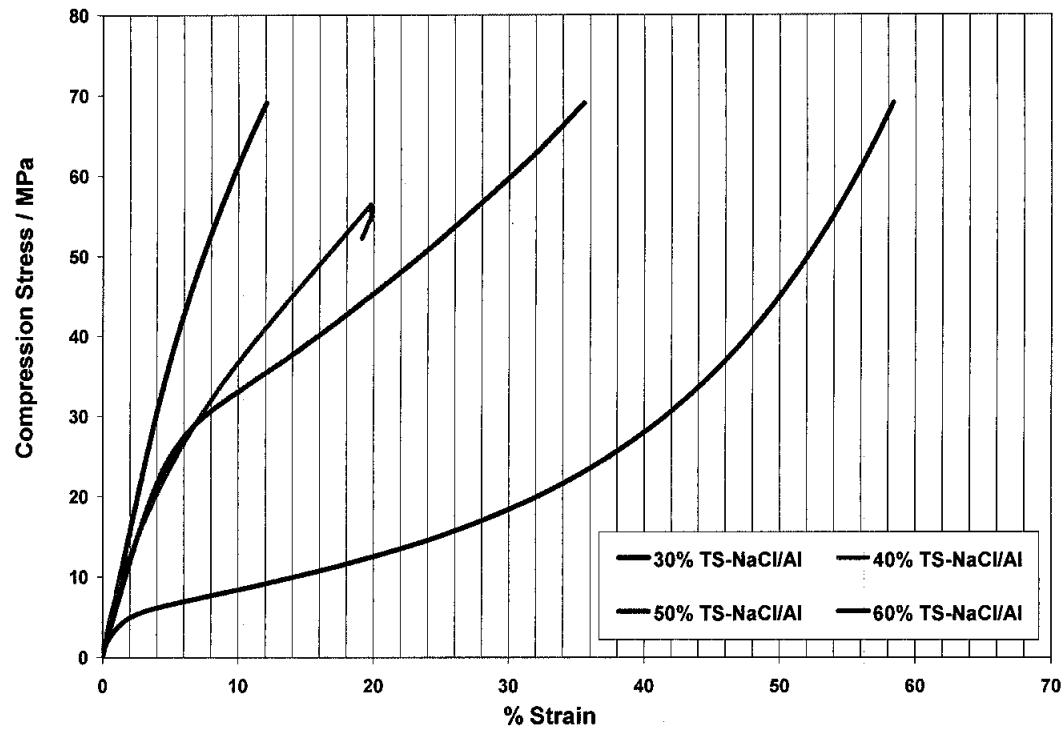


Figure 4.8: Compressive stress-strain curve of the Al specimen with different NaCl/Al volume fraction

From this section, it is demonstrated that the 60%volume fraction of NaCl/Al shows the characteristic of foam specimen and has the little amount of residual NaCl in the resultant foam. Such volume fraction of NaCl in the specimen will be used as the minimum value fraction in the next study to investigate the influence of processing parameters for the fabrication of Al foam through pressure assisted sintering technique. The effect of processing parameters pertaining to the compaction pressure, temperature-time profile and heating rate have to be characterized and optimized in order to achieve the optimum physical and mechanical properties of the foam.

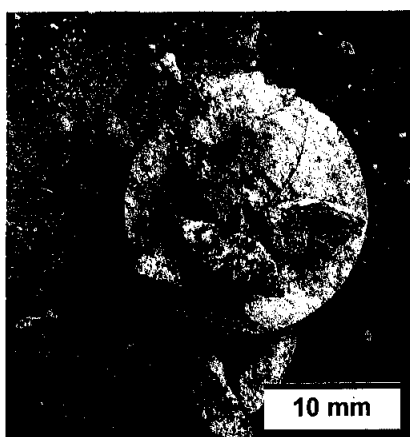
4.3 The influence of processing parameters on the physical and mechanical properties of Al foam fabricated through pressure assisted sintering / dissolution process

This section describes the work carried out to understand the influence of processing parameters on the physical and mechanical properties of Aluminium (Al) foam fabricated through pressure assisted sintering / dissolution (PASDP) technique. The effects of four processing factors: compaction pressure at elevated temperature, sintering temperature, sintering time and heating rate on the properties of final foam were studied. It was found that all the chosen factors have significant effects on the physical and mechanical properties of the aluminium foam and Al volume fraction is the most important parameter affecting the relative density and compressibility behaviour of the resultant foam.

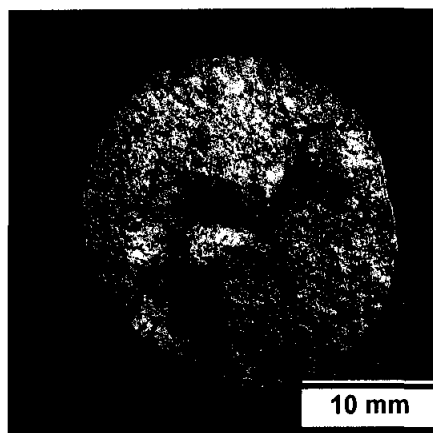
4.3.1 The physical and compressibility behaviour of NaCl/Al compact at elevated temperature

The stability of the NaCl/Al composites in terms of structure rigidity could not be obtained when the compaction pressure applied to homogeneously blended mixture is lower than 20 MPa (Figures 4.9 (a) and (b)). However, when a compaction pressure higher than 120 MPa is applied to the blended mixture, cracks were observed in the fabricated specimen which leads to complete fracture (Figure 4.9 (c) and (d)). The specimen produced under compaction pressure in the range of 20 – 120 MPa exhibited stable original geometry shape (Figure 4.9 (e) and (f)). It should be noted that the value of the compaction pressure employed in the experiment was much lower compared to work by Zhao *et al.* [22] on their the SDP NaCl/Al compact.

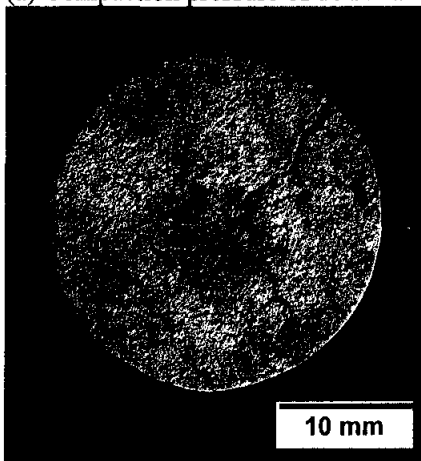
The porosity and density of the pressure assisted sintering specimens as a function of compaction pressure, with different NaCl particles sizes and its width of size distribution and NaCl/Al volume fraction in the compacts is shown in Figures 4.10 and 4.11. The density and porosity of the composites do not depend on the NaCl particle size and its width of size distribution as shown in Figure 4.11.



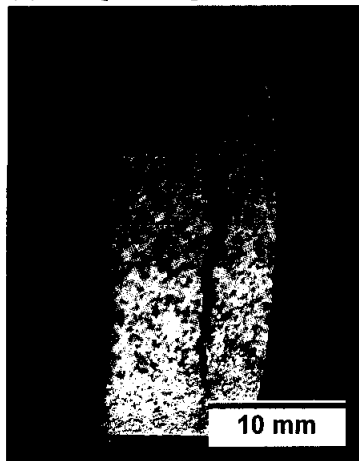
(a) Compaction pressure of 10 MPa



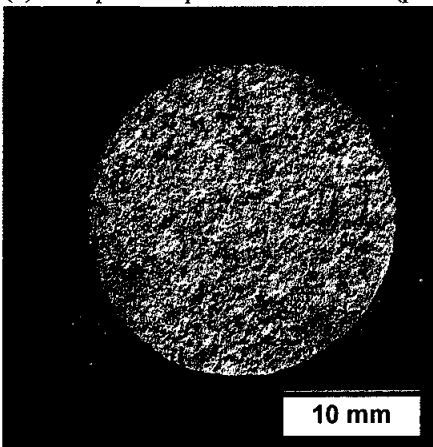
(b) Compaction pressure of 15 MPa



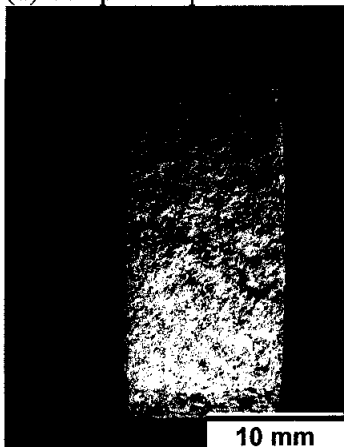
(c) Compaction pressure 130 MPa (plan view)



(d) Compaction pressure 130 MPa (side view)



(e) Compaction pressure 20 MPa (plan view)



(f) Compaction pressure 20 MPa (side view)

Figure 4.9: Photographs of pressure assisted sintered NaCl/Al compact at different compaction pressure

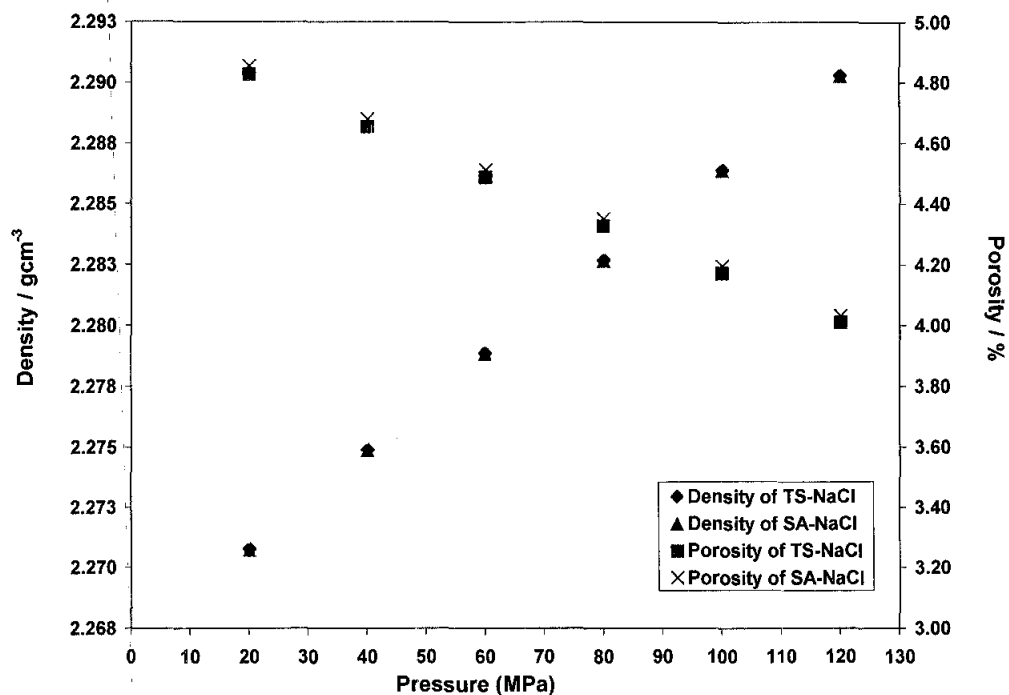


Figure 4.10: Variation of porosity and density of pressure assisted sintered compact with compaction pressure of different NaCl particle size and its width of size distribution

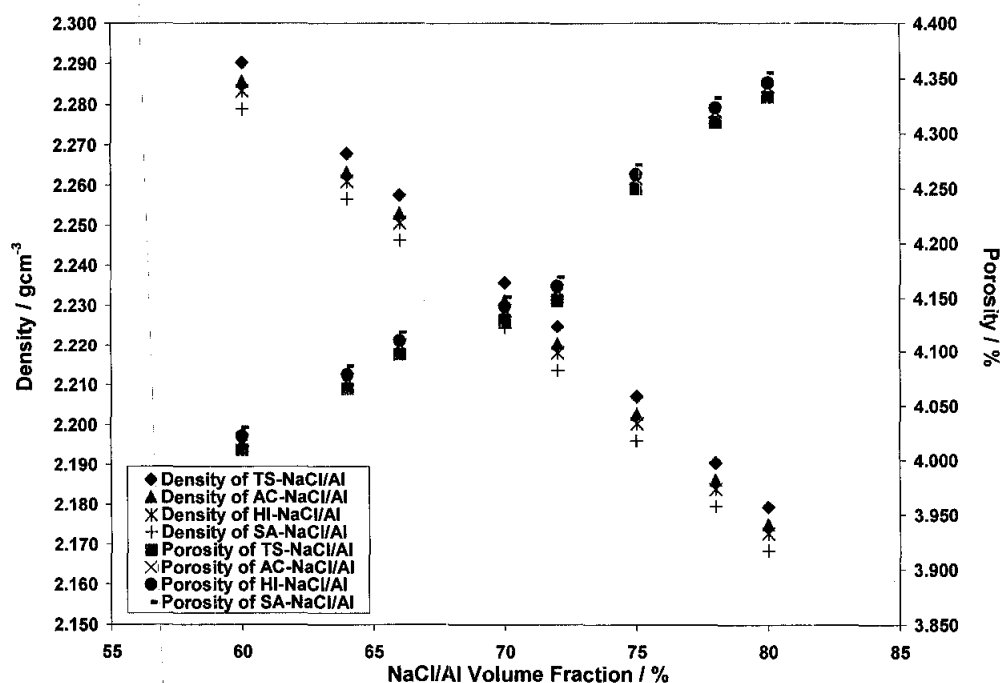


Figure 4.11: Variation of porosity and density of pressure assisted sintered compact with NaCl/Al volume fraction of different NaCl particle size and its width of size distribution

deformation of aluminium matrix. Similar findings were also reported by Abdoli *et al.* [75].

Table 4.4 shows the variation of the fraction of the dissolved NaCl in the Al foam, $1-\phi$, with the NaCl/Al fraction. It can be observed that residual NaCl in the foam was very small when the Al volume fraction in the compact was at and above 60% for all compaction pressure ranges used in the experiment. This behaviour is attributed to the fact that most NaCl particles are in contact with each other and form a continuous three-dimensional network and hence can be dissolved away by water [22].

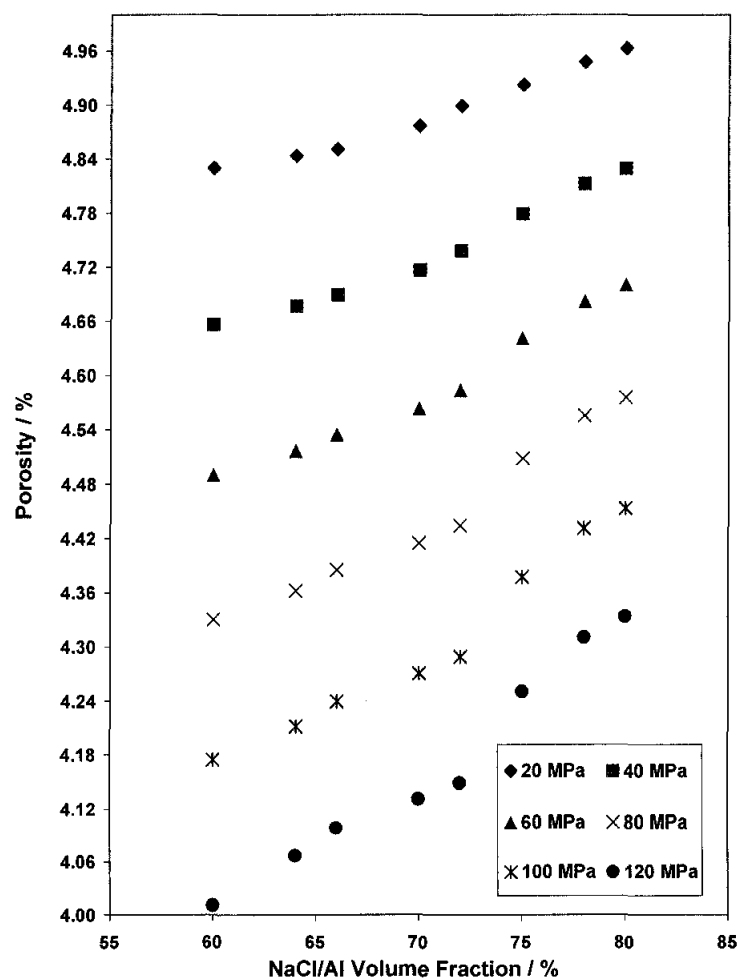


Figure 4.13: Variation of porosity of pressure assisted sintered NaCl/Al specimen with NaCl/Al volume fraction at different compaction pressure

Table 4.3: Fitting constants of the Heckel compaction equation

NaCl/Al	D_0	σ_0 / MPa	$K (X10^{-3})$
60% vol	0.94991	183	1.82
64%vol	0.94984	191	1.74
66%vol	0.94983	198	1.68
70%vol	0.94959	199	1.67
72%vol	0.94935	200	1.66
75%vol	0.94931	228	1.46
78%vol	0.94914	243	1.37
80%vol	0.94901	247	1.35

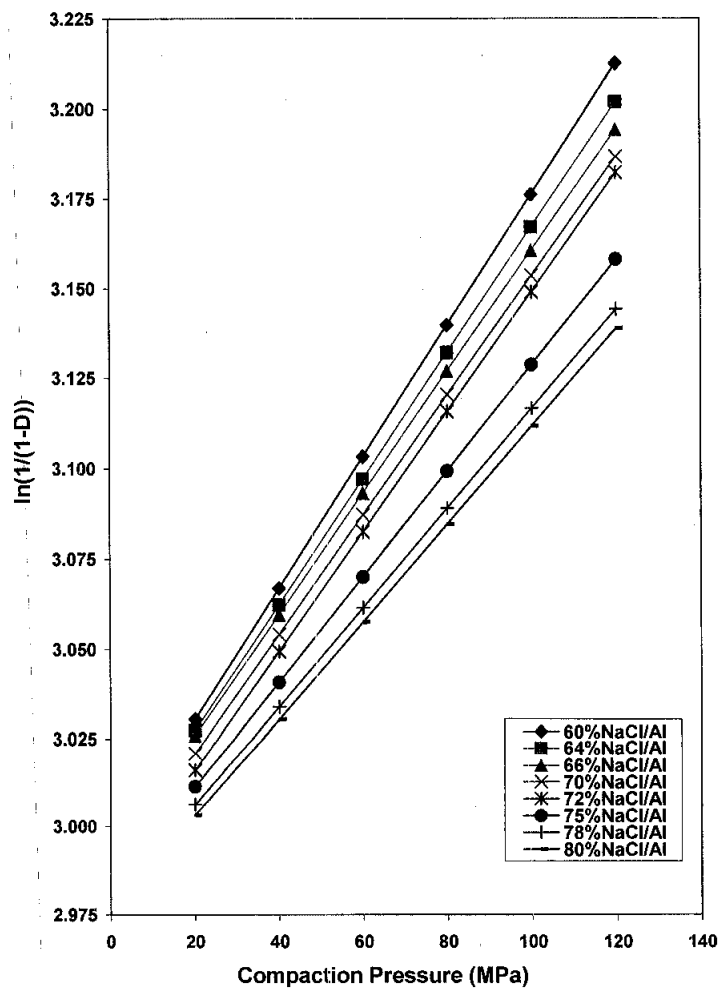


Figure 4.14: Relative density against compaction pressure fitted to Heckel equation for NaCl/Al blended powders with different volume fraction

Table 4.4: Variation of fraction of the dissolved NaCl in the Al foam (1- ϕ) at different compaction pressure

Sample	Weight of HPC-BDP* / g	Weight of HPC-ADP^ / g	1-φ	Pressure / MPa
60%	20.000	10.487	0.87036	
64%	20.000	9.052	0.91233	
66%	20.000	8.679	0.92041	
70%	18.892	7.580	0.94270	
72%	18.121	6.484	0.94610	
75%	18.400	5.980	0.95250	
78%	18.606	5.345	0.96090	
80%	18.304	5.505	0.98152	
60%	23.203	9.845	0.87650	
64%	21.767	8.303	0.92855	
66%	21.871	8.363	0.93160	
70%	21.975	7.462	0.95230	
72%	19.055	6.517	0.96150	
75%	19.295	5.812	0.97703	
78%	19.675	5.487	0.97848	
80%	20.000	4.997	0.98445	
60%	21.692	9.703	0.91940	
64%	19.299	9.140	0.92950	
66%	18.308	8.011	0.94209	
70%	21.601	7.201	0.97297	
72%	18.233	6.536	0.97475	
75%	20.271	5.776	0.97939	
78%	20.000	5.600	0.98097	
80%	20.000	4.988	0.98504	
60%	21.416	9.427	0.91940	
64%	18.843	8.270	0.96734	
66%	19.741	8.011	0.97750	
70%	20.705	7.201	0.97855	
72%	18.310	6.548	0.98017	
75%	17.071	6.300	0.98051	
78%	17.571	5.499	0.98146	
80%	19.654	4.998	0.99030	
60%	20.000	9.409	0.96816	
64%	21.702	8.218	0.97710	
66%	21.433	7.929	0.97855	
70%	21.755	7.213	0.97986	
72%	20.715	6.497	0.98055	
75%	18.569	5.782	0.98060	
78%	20.000	5.459	0.98250	
80%	20.000	5.340	0.99054	
60%	21.202	9.196	0.97610	
64%	20.000	8.261	0.97825	
66%	20.049	7.998	0.97976	
70%	22.051	7.549	0.97986	
72%	20.714	6.496	0.98055	
75%	18.581	5.782	0.98152	
78%	20.268	5.501	0.98668	
80%	18.655	4.965	0.99275	

Figure 4.15 shows the typical macro and microscopic structure of the fabricated foam after undergone leaching process with volume fraction of NaCl/Al initially at 80%. The foam has a homogenous structure with open pores and pore sizes in the range 150-400 μm , which represent the particle characteristics of the original NaCl powder used.

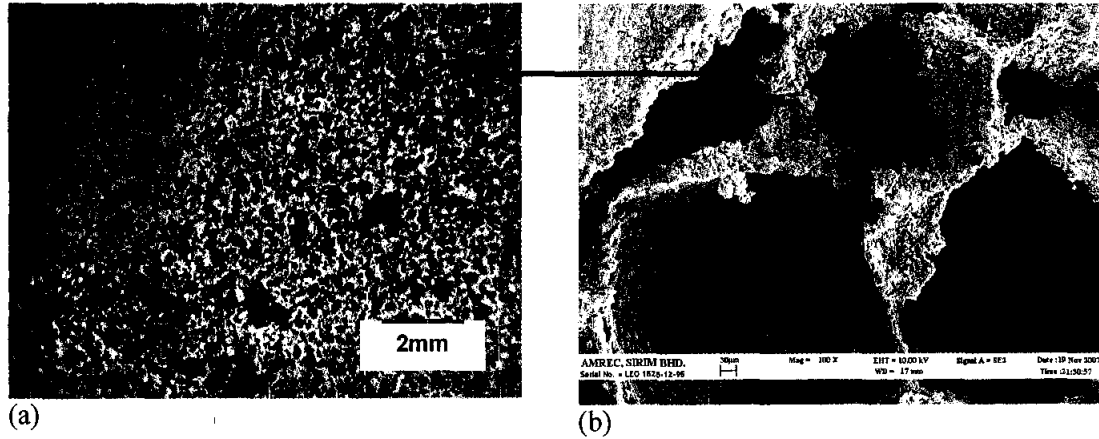


Figure 4.15: (a) Stereomicrograph of Al foam with relative density 0.2 (b) SEM image of PASDP Al foam of selected area at magnification of 100X

It is known [22] that the morphology and size of the pores in the foam can be easily controlled by selecting an appropriate NaCl powder. Figures 4.16 (a)-(d) show that it is also possible to obtain a purposely tailored distribution of pore size in the foam by using NaCl powder with different particle size [8]. Figure 4.17 shows the cell wall of Al foam fabricated under compaction pressure of 120 MPa and it reveals that cell walls are dense and only a few micropores can be seen. Most of Al particles have changed their original shape at compaction pressure of 120 MPa and sintering temperature of 620 $^{\circ}\text{C}$ which leads strong bonding among Al particles as shown in Figures 4.17 (a) and (b). This indicates that simultaneous application of pressure and temperature will result in better binding compared to solid state sintering process.

Figures 4.18 (a) and (b) show the electron micrograph of the Al matrix (compacted at 15 MPa) where several voids are clearly present (see arrows)., Due to the fact that the stress should be the lowest in the regions around the voids, only small amount of deformation can observed [8]. The distributions of stress and strain in the NaCl/Al specimen, and thus the fresh metal contacts, are therefore inhomogenous [8].

Zhao *et al.* [8] reported that very little stress and therefore strain may be present in the Al particles surrounded by touching NaCl particles.

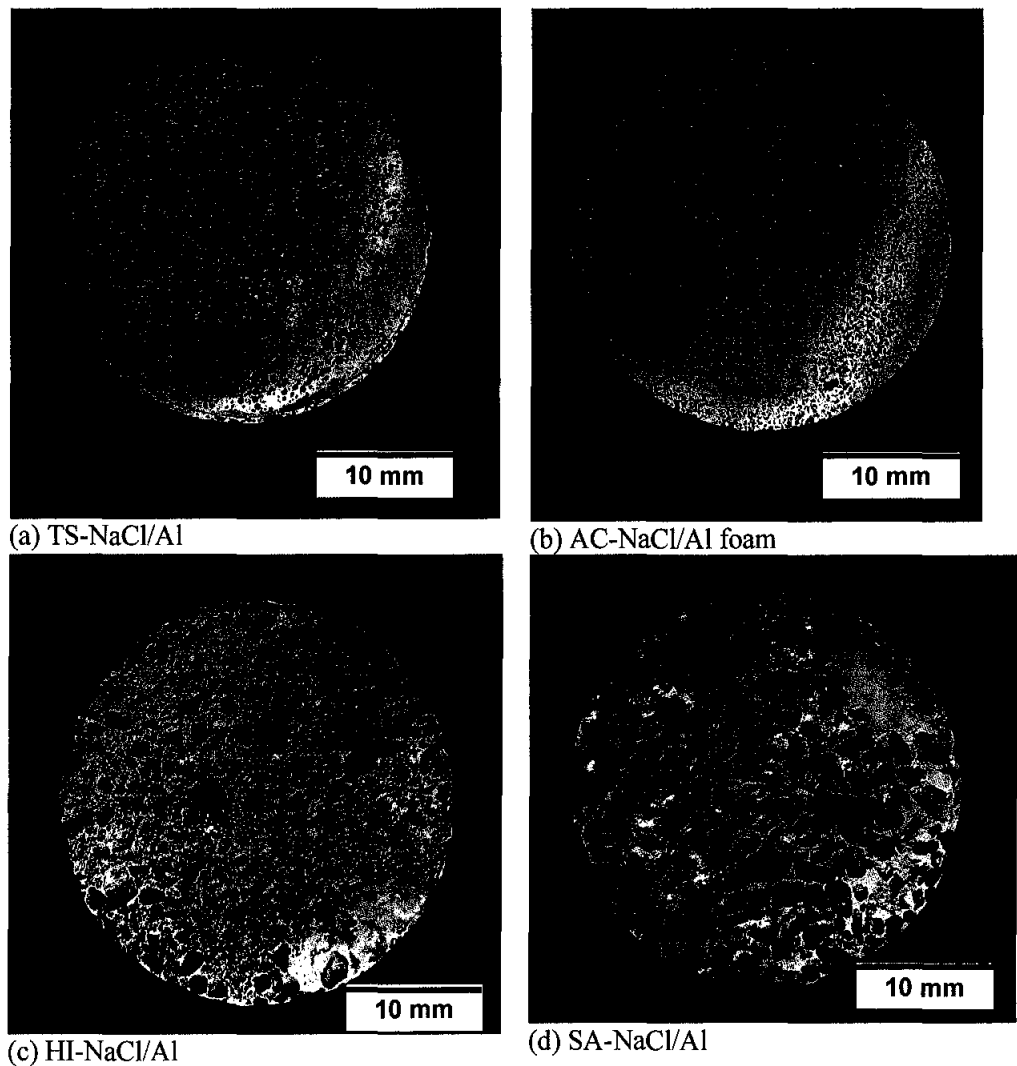


Figure 4.16: Photographs of PASDP Al foam (after dissolution process) using different size and its width of size distribution of filler material (a) TS-NaCl/Al (b) AC-NaCl/Al (c) HI-NaCl/Al (d) SA-NaCl/Al

It was also reported that for SDP Al foam [8], [22], the primitive particles boundaries could not be discerned in the cell walls and the microstructure of the cell walls suggests that a large portion of the oxide film at the Al particles surfaces is broken. The Al and NaCl powders used in this process have different particle morphologies and size. The former is ductile and soft while the latter is brittle and hard. The Al particles close to the NaCl particles are usually subjected to higher strains and the oxide films at their surfaces are disrupted [8]. In SDP process, further

from the NaCl/Al contacts, the strains are lower and the oxide films are likely to remain intact. According to Zhao and Sun [22] in certain extreme conditions, the local Al particles may not subject to much deformation and the destruction of the oxide film may not happen.

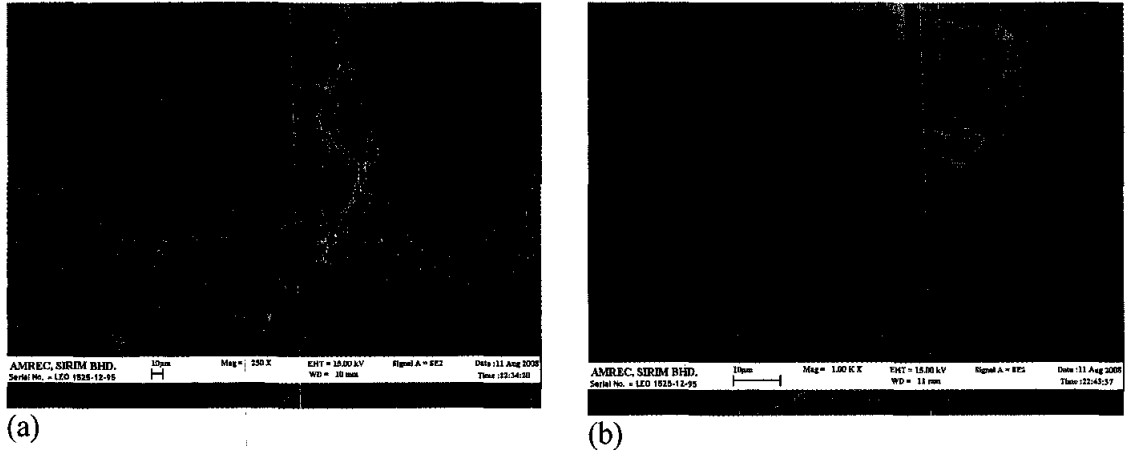


Figure 4.17: SEM images of cell wall of PASDP Al foam with a porosity of 80% at (a) x250 (b) x1000

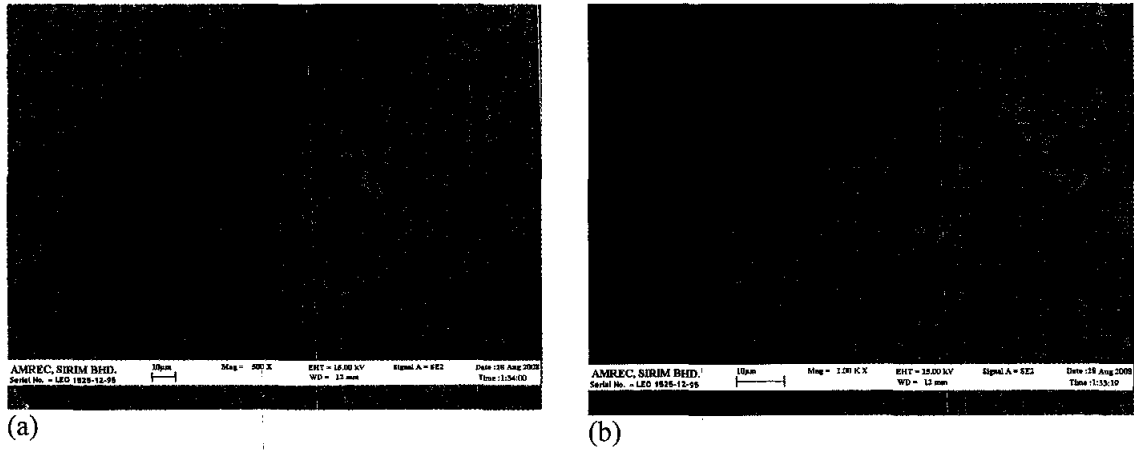


Figure 4.18: Images (SEM) of the Al matrix (compacted at 15 MPa) showing voids between the original Al particles at (a) x500 (b) x1000

Figure 4.19 shows the density and porosity of PASDP specimens with different NaCl/Al volume fraction at different compaction pressure after dissolution process. The result reveals that the density of Al foam with volume fraction initially at 80% increases from 0.533 to 0.545 gcm^{-3} when the pressure is increase from 20 to 120 MPa. The results also reveal a comparison between the final porosity of the Al foam

and the initial volume fraction of the NaCl powder. The foam porosity is 2-4% lower than the initial volume fraction of NaCl, and the higher the NaCl volume fraction, the lower the decrease in foam porosity.

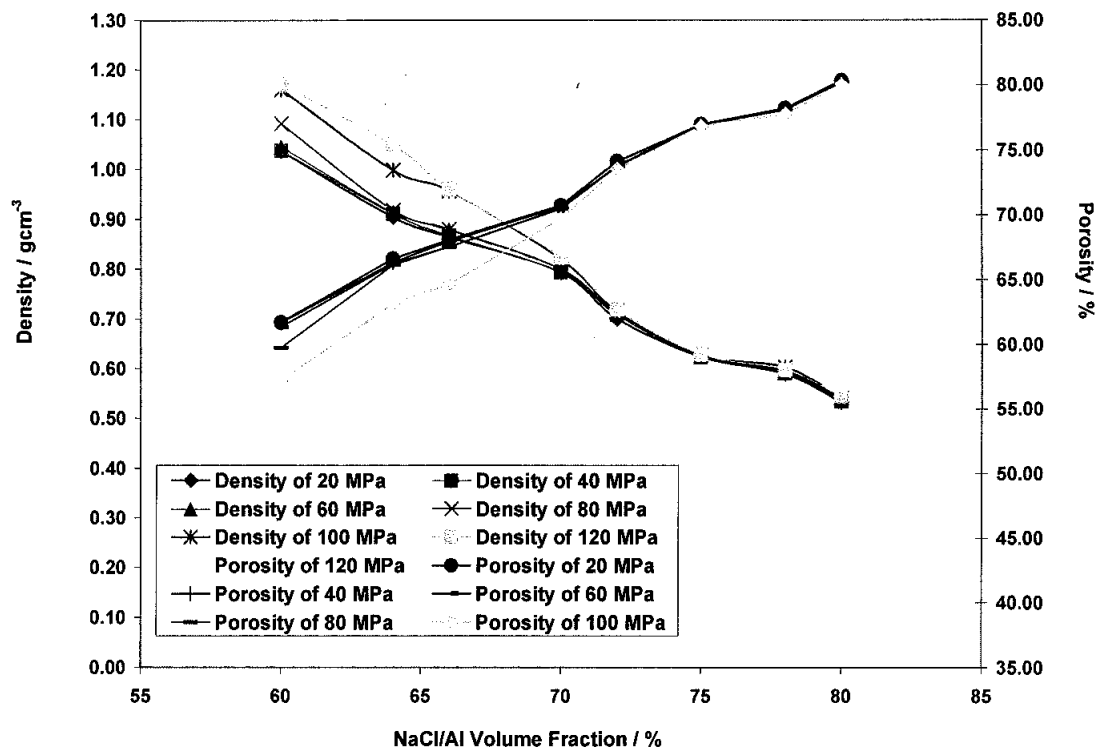


Figure 4.19: Variation of density and porosity of specimens sintered at 620 °C for 30 min with NaCl/Al volume fraction at different compaction pressure after dissolution process

In PASDP technique, increasing compaction pressure can improve the bonding in the Al matrix because of increased fresh metal contacts between the Al particles. Excessively high compaction pressure is not only difficult to achieve in practice but also to bring about undesirable defects in the final Al foam [8]. In addition to the cracking and fracture problems, it can also lead to fragmentation of NaCl particles [22]. This method permits the foam to have variable porosity in a much wider range by adjusting the NaCl to Al volume ratio in the NaCl/Al powder compact, as long as both the NaCl particles and the Al matrix are interconnected in the great majority. Besides that, the foam that fabricated can have a purposely tailored distribution of relative density by varying the local Al volume fraction in the NaCl/Al composites. Similar observation was also reported by Zhao and Sun [22] in their work of SDP Al foam.

The crystallite size D and the microstrain η for the fabricated foam at various NaCl/Al volume fraction specimens after leaching process were calculated from the Williamson-Hall plot (Figure 4.20) and tabulated in Table 4.5. As can be seen from this table, the values of crystallite size tend to decrease with increasing NaCl content. Similar finding is also observed by Abdoli *et al.* [75], which reported that that Al with ductility character possesses more potential to deform plastically leading to grain refining and changing in lattice distortion. They also reported that powders of low stiffness or high work hardening capacity are to densify more effectively. The increase of microstrain with increasing NaCl content can be explained by the fact that in the fabrication process of the foam, they were in a complicated stress strain state after pressure assisted sintering owing to the existence of hard and brittle NaCl particles and even serious stress concentration arisen in the sharp corners of the cell wall [8].

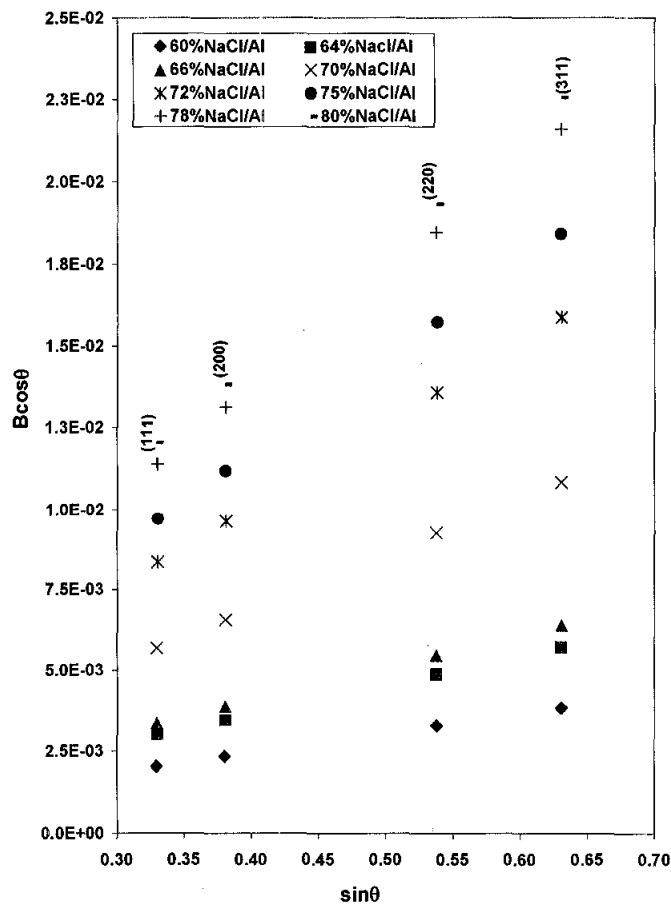


Figure 4.20: Williamson-Hall plot for Al foam with different NaCl/Al volume fraction

Table 4.5: Crystallite size and lattice strain for PASDP Al foam obtained from Williamson-Hall method [128]

NaCl/Al	Al-crystallite size (μm)	Lattice strain (%)
60%vol	2.77	0.006
64%vol	2.76	0.009
66%vol	1.54	0.010
70%vol	1.53	0.017
72%vol	1.26	0.250
75%vol	1.10	0.290
78%vol	0.90	0.340
80%vol	0.30	0.350

4.3.2 The influence of sintering temperature on surface morphology and physical measurement on the fabricated Al foam

Selection of an appropriate sintering temperature is important [8], [22]. The rapid formation of effective bonding between the Al particles in the solid state sintering is fulfilled by the localized fusion of the particles provided that the particles are not completely separated by oxide films. As described above, the number of intimate metal-metal contacts is limited compared with the total interfacial area among the Al particles. Zhao *et al.* [8] proposed that gaps may also form at the fresh metal contacts as a consequence of stress relief after the compaction operation and it is therefore desirable for the Al to have undergone solid state sintering process which occurs by the motion of atoms to form inter-particle bonds. The effectiveness of this process can only be achieved if the oxide film at the surface of the Al particles is destroyed by compaction at elevated temperature [149]. In solid state sintering, effective bonding between the Al particles requires sustained intimate contact between the fresh metal surfaces because the process relies on the diffusion of atoms across the interfaces [23]-[25]. The sintering temperature should therefore be close to the melting temperature of Al. The bonds between particles grow by the motion of individual atoms via solid state events. If the sintering temperature is excessively high, however, some molten Al near the surface of the specimen often oozes out from the compact to form globules and stick at the die, upper and lower punch. The formation of the globules is due to the tendency of separation of molten Al from the NaCl particles, driven by the poor wetting between them, and is facilitated by the low viscosity [8],

[22]. This results in non-uniform distribution of cell size and density in the foam as well as undesired shape distortion. The optimum sintering temperatures falls within 570-620 °C for manufacturing pure Al foams which produce samples of generally preferably quality. Sintering temperatures lower than 570 °C resulted in poor or no bonding between Al particles, leading to foam disintegration during dissolution or subsequent handling. Temperatures higher than 620 °C, however, increased the flowability of molten Al, which resulted in partial separation of the NaCl/Al mixture and hence a non-uniform distribution of local relative density [22]. A foam sample which was simultaneously pressed and sintered at 130 MPa and 630 °C for 45 minutes is showed in Figures 4.21 (a)-(d) and partial melting of cell wall of the foam appears because of high the sintering temperature.

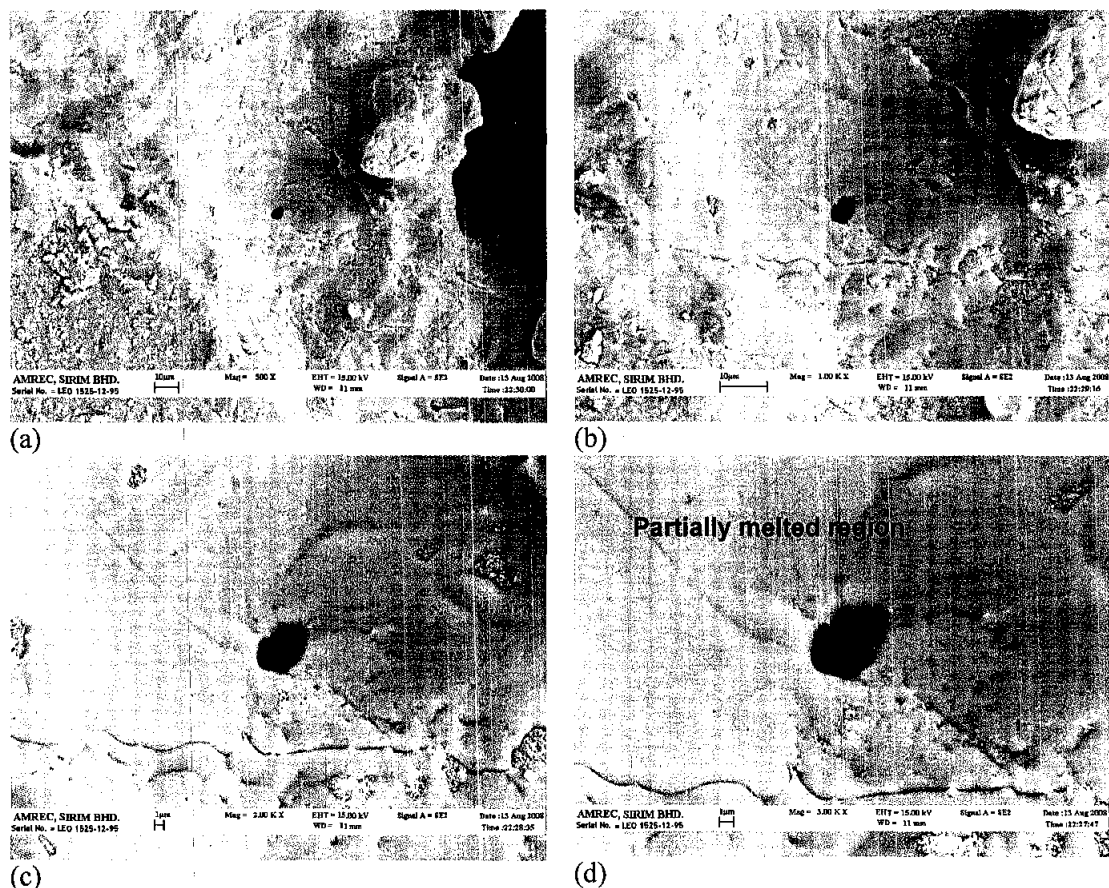


Figure 4.21: Partially melting of the cell wall of Al foam which was pressed at 130 MPa and sintered at 630°C at (a) x500 (b) x1000 (c) x2000 (d) x3000

The variation of the fraction of the dissolved NaCl in the Al foam, $1-\phi$, with the NaCl/Al volume ratio at different sintering temperature is represented in Table 4.6. It can be revealed that residual NaCl in the foam was negligible when the Al volume fraction in perform was 60% for all ranges of sintering temperatures used in the experiment. As most of NaCl particles are in contact with each other and form a continuous three-dimensional network, they can be easily dissolved by leaching process. As a result of this leaching process a highly porous aluminium with the same chemical composition as that of original Al powder is formed and XRD results (Figure 4.22) indicated that the NaCl compound is no longer exist in the foam when the volume fraction of NaCl is increased from 50% to 60%.

The density and porosity of PASDP specimens with different NaCl/Al volume fraction at different sintering temperature after dissolution process is shown in Figure 4.23. The results obtained also presents a comparison between the final porosity of the Al foam and the initial volume fraction of NaCl powder .which reveals that the foam porosity is 2-4% lower than the initial volume fraction of NaCl, and the higher the NaCl volume fraction, the lower the decrease in foam density.

When sintering temperature was below 570 °C, completely intact Al foam could not be produced at the given hold time of 30 minutes. All compacts could not retain their original shape and the structure was collapsed in the subsequent leaching process. When the sintering temperature was above 620 °C, some Al moved out of the surface of the compacts in the form of globules, although effective bonding was achieved. The size of the globules increased with increasing temperature. The loss of Al from the compact led to inhomogenous cell wall structure and cell size distribution. When the sintering temperature was controlled in the range of 570-620 °C, the quality of the samples was generally satisfactory. It can also be observed that when the sintering temperature is increase from 570 to 620 °C, there is more fresh metal-metal contacts during simultaneous pressing and sintering and become effective bonding points between the Al particles. As a consequence, an interconnected metallic framework is formed and the cell wall becomes more dense as evident in the electron micrographs of the matrix as shown in Figure 4.24 (a) to (f).

In Figure 4.25, the variation of crystallite size of Al foams of different relative density with sintering temperature is presented. In general, the crystallite size increases with sintering temperature. In sample 80% NaCl/Al, it increases from 0.06 μm to 0.30 μm when the sintering temperature is increased from 570 to 620 $^{\circ}\text{C}$. This is due to grain growth during pressure assisted sintering process. The crystallite size of 78% NaCl/Al composite increases from 0.18 to 0.90 μm when the temperature is increased from 570 $^{\circ}\text{C}$ to 620 $^{\circ}\text{C}$. For sample 75% NaCl/Al, it increases from 0.22 μm to 1.10 μm when the sintering temperature is increased from 570 $^{\circ}\text{C}$ to 620 $^{\circ}\text{C}$. When the sintering temperature is increased from 570 $^{\circ}\text{C}$ to 620 $^{\circ}\text{C}$, the crystallite size of 72% NaCl/Al composites increase from 0.25 μm to 1.26 μm . The crystallite sizes of 70% NaCl/Al composite increase from 0.31 μm to 1.53 μm when the temperature is increased from 570 $^{\circ}\text{C}$ to 620 $^{\circ}\text{C}$. When the sintering temperature is increased from 570 $^{\circ}\text{C}$ to 620 $^{\circ}\text{C}$, the crystallite size of 66% NaCl/Al composites increase from 0.34 μm to 1.54 μm . For sample 64% NaCl/Al, it increases from 0.55 μm to 2.76 μm when the sintering temperature is increased from 570 $^{\circ}\text{C}$ to 620 $^{\circ}\text{C}$. Lastly for samples 64% NaCl/Al, it increases from 0.61 μm to 2.77 μm when the sintering temperature is increased from 570 $^{\circ}\text{C}$ to 620 $^{\circ}\text{C}$.

The activation energy for grain growth was determined from the crystallite size measurement by constructing an Arrhenius plot for a constant sintering time as shown in Figure 4.26. The best fit line was plotted by using the least min square method. The slope of this line was used to determine the activation energy (Q) from the following equation [164]:

$$D = A \exp[Q / RT] \quad (4.1)$$

where D is the average of crystallite size, T is the temperature and R is the gas constant, i.e. 8.314 Jmol $^{-1}$ K $^{-1}$. The value for Q obtained for diifferent volume fraction of NaCl/Al was tabulated in Table 4.7. As can be seen from the results, the value of the activation energy, Q , tend to be independent on Al content in the composite. These values obtained correspond to the activation energy for the diffusion of Al in the NaCl/Al compact during pressure assisted solid state sintering process.

Table 4.6: Variation of fraction of the dissolved NaCl in the Al foam (1- ϕ) at different sintering temperature

Sample	Weight of HPC-BDP* / g	Weight of HPC-ADP^ / g	1- ϕ	Temperature / °C
60%	19.801	9.949	0.90136	570
64%	20.105	9.148	0.91311	
66%	19.998	8.665	0.92140	
70%	19.821	7.545	0.94138	
72%	19.640	6.463	0.95488	
75%	19.793	5.845	0.96190	
78%	19.862	5.485	0.97143	
80%	19.973	5.005	0.98213	
60%	19.728	9.766	0.91141	580
64%	19.381	8.288	0.92441	
66%	19.505	8.046	0.93163	
70%	20.043	7.584	0.95546	
72%	19.845	6.564	0.96241	
75%	19.940	5.782	0.97642	
78%	20.055	5.534	0.98115	
80%	20.131	5.098	0.98645	
60%	19.494	9.344	0.92861	590
64%	19.358	8.165	0.93272	
66%	19.515	7.896	0.94465	
70%	19.974	7.469	0.95897	
72%	20.345	6.870	0.97642	
75%	19.970	5.678	0.98563	
78%	20.033	5.404	0.98845	
80%	20.016	4.936	0.98952	
60%	20.154	9.882	0.93980	600
64%	19.596	8.285	0.94262	
66%	19.713	7.973	0.95445	
70%	20.011	7.151	0.98617	
72%	20.000	6.378	0.98710	
75%	20.012	5.690	0.98772	
78%	20.025	5.395	0.98854	
80%	20.004	4.920	0.98975	
60%	20.171	9.655	0.96212	610
64%	19.913	8.214	0.97494	
66%	20.051	7.943	0.98442	
70%	20.025	7.136	0.98845	
72%	20.093	6.445	0.98897	
75%	20.059	5.714	0.98928	
78%	20.052	5.398	0.99011	
80%	20.099	4.929	0.99542	
60%	20.327	9.655	0.97643	620
64%	19.955	8.214	0.97845	
66%	20.088	7.943	0.98743	
70%	20.045	7.136	0.98994	
72%	20.107	6.445	0.99002	
75%	20.070	5.714	0.99006	
78%	20.066	5.398	0.99110	
80%	20.066	4.929	0.99321	

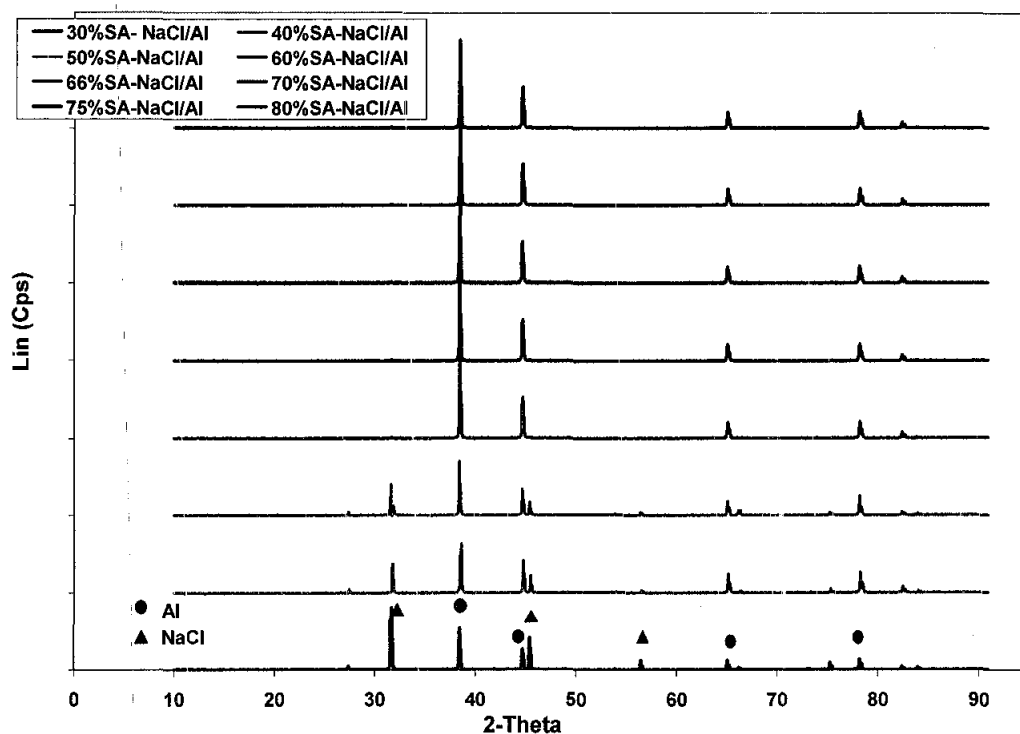


Figure 4.22: XRD spectrum of NaCl/Al specimens at different volume fraction, fabricated at sintering temperature of 620°C for 30 min, after dissolution process

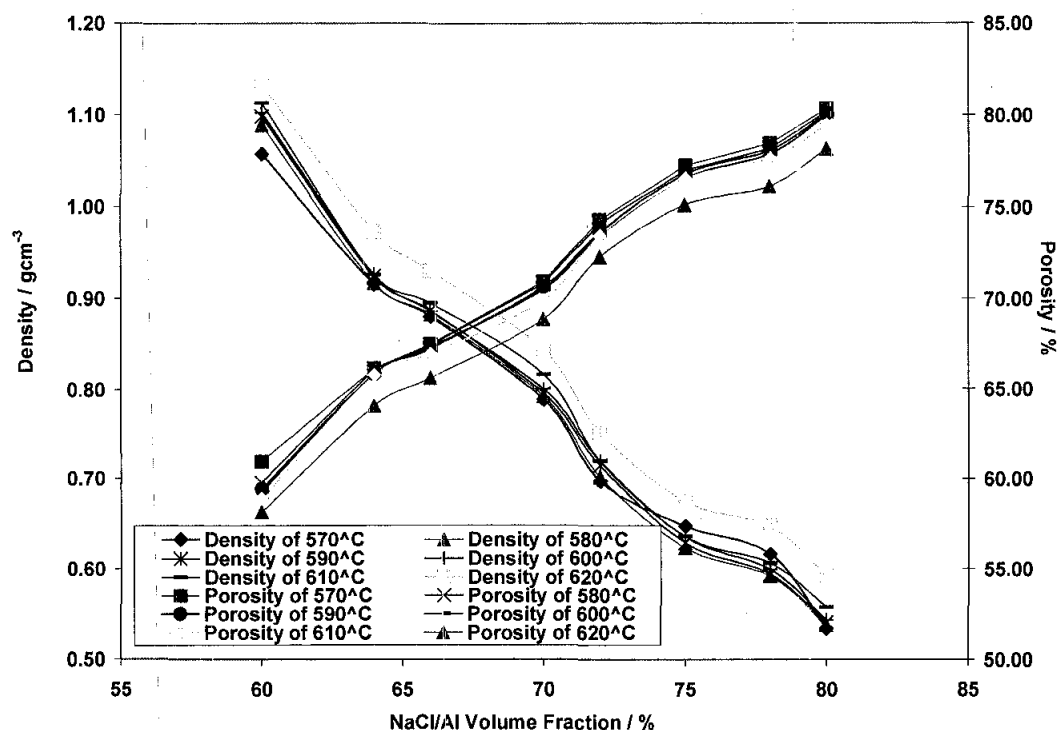
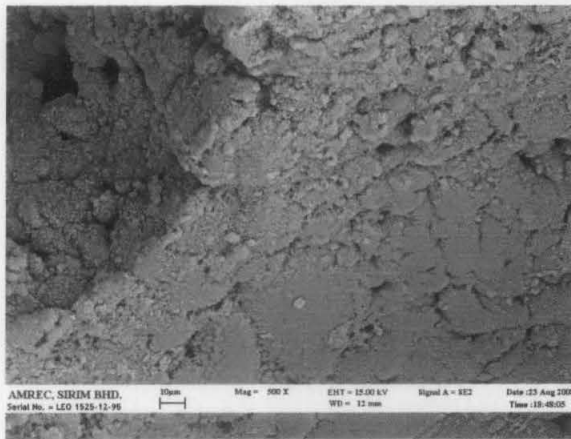
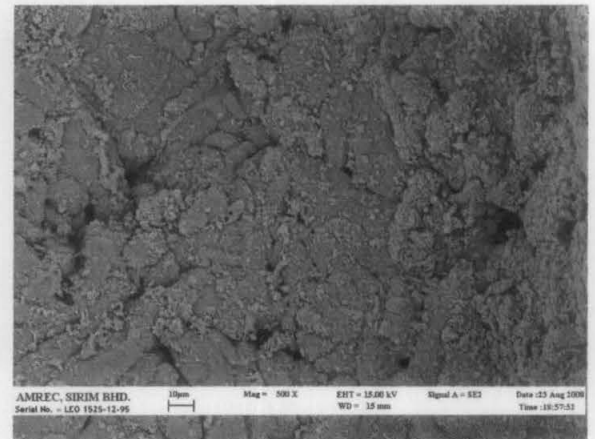


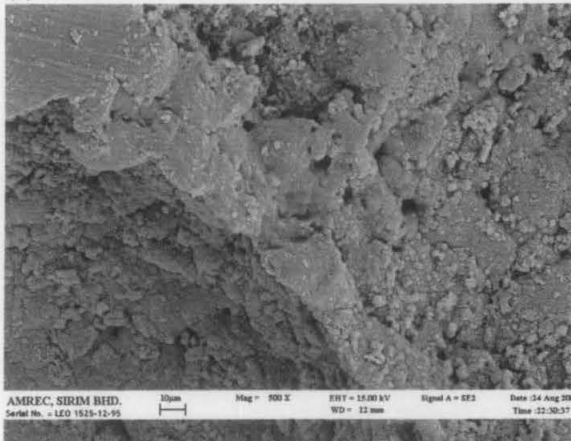
Figure 4.23: Variation of density and porosity of pressure assisted sintered specimens with NaCl/Al volume fraction at various sintering temperature after dissolution process



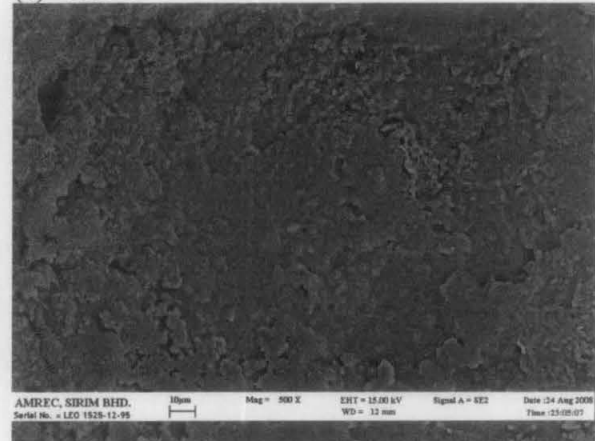
(a) 570 °C



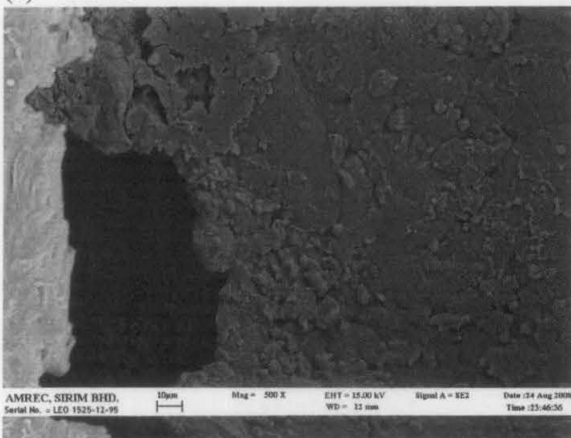
(b) 580 °C



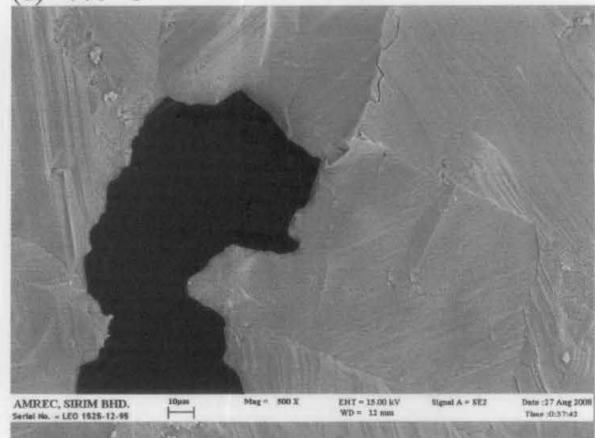
(c) 590 °C



(d) 600 °C



(e) 610 °C



(f) 620 °C

Figure 4.24: Images (SEM) of the formation of the interconnected metallic framework of the Al cell wall, which becomes denser as sintering temperature is increased

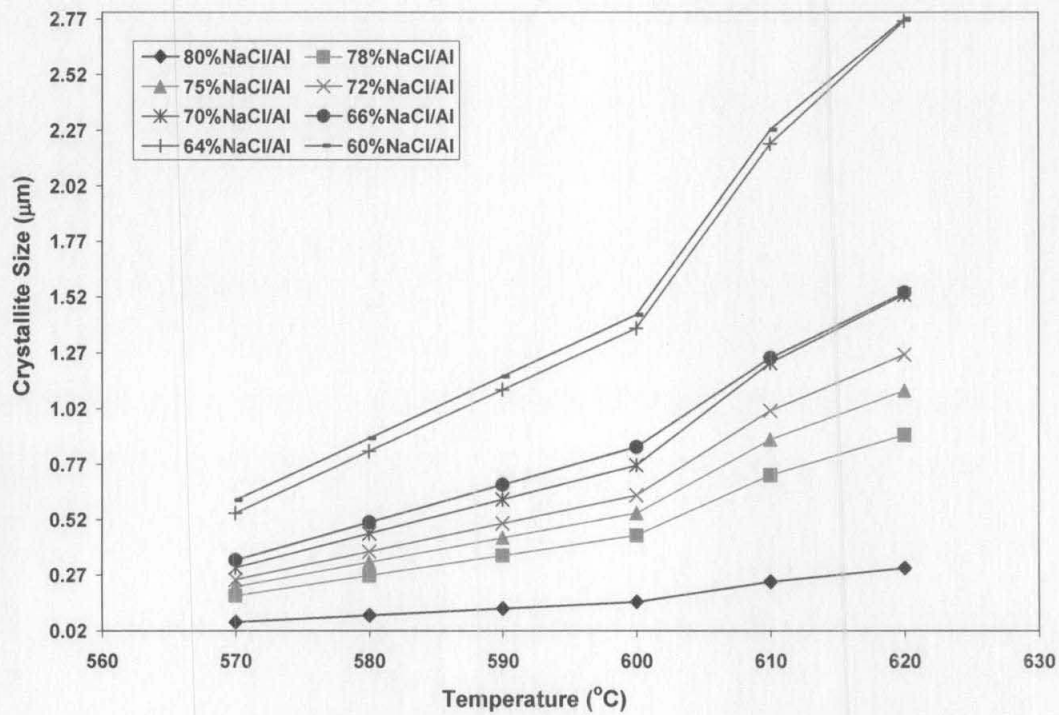


Figure 4.25: The influence of sintering temperature on the crystallite size of Al foams at various volume fractions

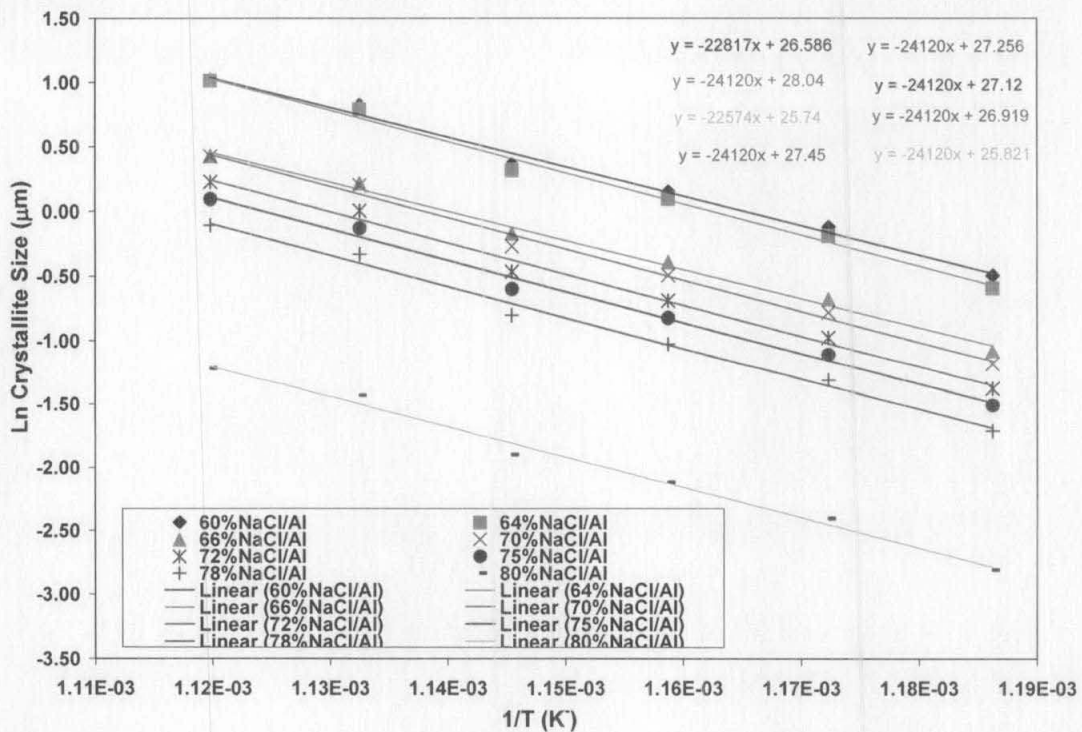


Figure 4.26: Arrhenius plot of log crystallite size against reciprocal of sintering temperature for Al foams at various volume fractions

Table 4.7: The activation energy for the formation of Al foams	
Vol% NaCl/Al	Activation Energy / kJmol ⁻¹
60	22.81
64	24.12
66	22.57
70	24.12
72	24.12
75	24.12
78	24.12
80	24.12

4.3.3 The influence of sintering time on surface morphology and physical measurement on the fabricated Al foam

Table 4.8 presents the variation of the fraction of the dissolved NaCl in the Al foam, (1- ϕ), with the NaCl ratio. With a high volumes fraction of NaCl in the compact, most NaCl particles are in contact with each other and form a continuous three-dimensional network. Due to the fact that all the NaCl particles in the network can be dissolved away by water, there is only a small amount of residual NaCl in the resultant foam. For the composites that was subjected to 5 minutes of PASDP, the, 1- ϕ , increase from 0.90 to 0.98 when the volume fraction of NaCl in the composite is increased from 60 to 80%. The fraction of NaCl dissolved in the composites that was subjected to 10 minutes of PASDP is increased from 0.91 to 0.98 when volume fraction of NaCl increases from 60 to 80%. When the volume fraction of NaCl/Al in the composite was subjected to 30 minutes of PASDP is increased from 60 to 80%, the, 1- ϕ , increases from 0.97 to 0.99. XRD analysis as shown in Figure 4.27 confirms that no phase of NaCl was detected in the composites of 60 % volume fraction when it was subjected to processing time of 5 to 30 minutes of PASDP.

As shown in the analysis of the results, sintering time has a strong effect on the density of the resultant foam. From Figure 4.28, it can be seen that with an increase sintering time, the density of the foam at fixed NaCl/Al ratio increases. For sample 75% NaCl/Al composite, the density increase from 0.628 gcm⁻³ to 0.675 gcm⁻³ when the time is increased from 5 minutes to 30 minutes. Normally a longer sintering time is essential to ensure good bonding between Al particles [8], [22].

Table 4.8: Variation of fraction of the dissolved NaCl in the Al foam (1- ϕ) at different sintering time

Sample	Weight of HPC-BDP* / g	Weight of HPC-ADP^ / g	1-φ	Time / minutes
60%	19.809	9.956	0.90148	
64%	20.127	9.156	0.91422	
66%	19.893	8.548	0.92236	
70%	19.892	7.561	0.94560	
72%	19.621	6.468	0.95311	
75%	19.881	5.921	0.96279	
78%	19.822	5.452	0.97095	
80%	19.984	5.012	0.98244	
60%	19.779	9.741	0.91842	
64%	19.273	8.197	0.92304	
66%	19.626	7.985	0.94648	
70%	20.039	7.562	0.95684	
72%	19.789	6.425	0.96844	
75%	19.984	5.796	0.97849	
78%	20.045	5.526	0.98098	
80%	20.085	5.102	0.98311	
60%	19.460	9.302	0.92941	
64%	19.322	8.142	0.93168	
66%	19.379	7.694	0.95001	
70%	19.622	7.104	0.95994	
72%	20.131	6.672	0.97531	
75%	19.970	5.694	0.98455	
78%	19.737	5.122	0.98753	
80%	19.941	4.886	0.98786	
60%	19.968	9.752	0.93465	
64%	19.668	8.316	0.94596	
66%	19.575	7.782	0.95876	
70%	19.912	7.046	0.98669	
72%	19.990	6.362	0.98756	
75%	20.068	5.742	0.98802	
78%	19.960	5.325	0.98889	
80%	20.010	4.924	0.98988	
60%	19.982	9.436	0.96489	
64%	20.069	8.314	0.97961	
66%	19.978	7.861	0.98516	
70%	20.085	7.208	0.98753	
72%	20.026	6.378	0.98901	
75%	20.059	5.708	0.98974	
78%	19.951	5.296	0.99022	
80%	20.111	4.974	0.99321	
60%	20.229	9.554	0.97668	
64%	19.772	8.006	0.98054	
66%	20.010	7.846	0.98892	
70%	20.117	7.208	0.98997	
72%	20.212	6.545	0.99038	
75%	19.992	5.623	0.99099	
78%	19.962	5.279	0.99208	
80%	20.135	4.956	0.99602	

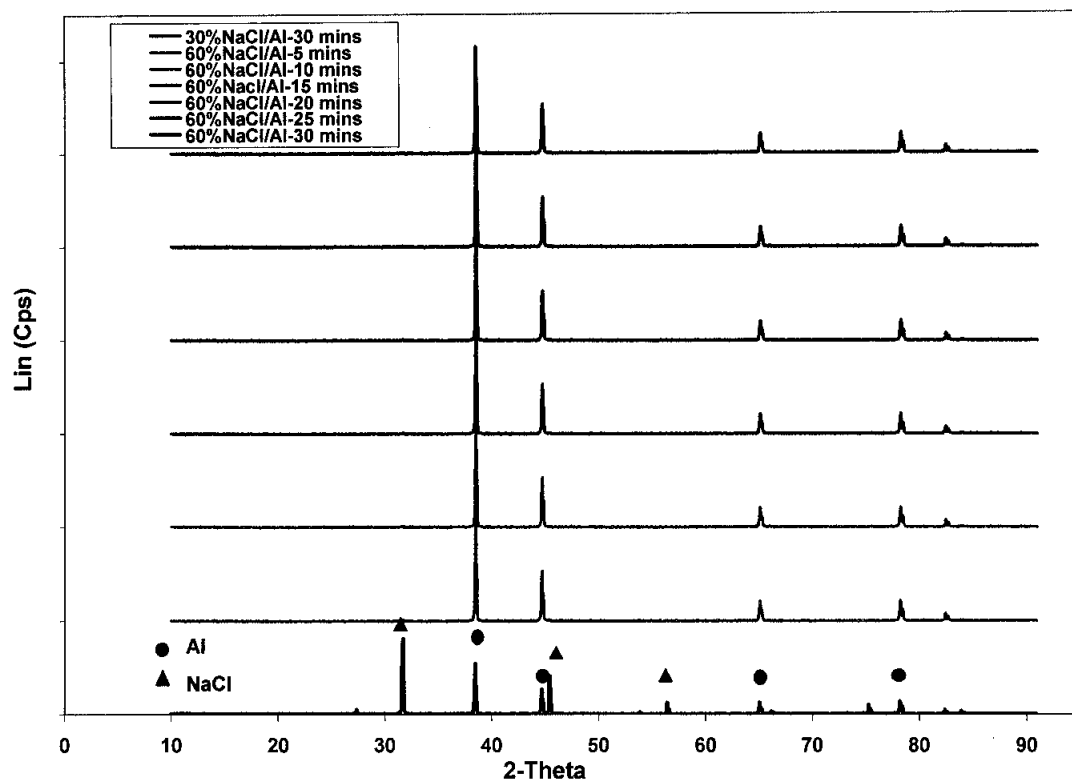


Figure 4.27: XRD spectrum of NaCl/Al specimen at different sintering time after the dissolution process

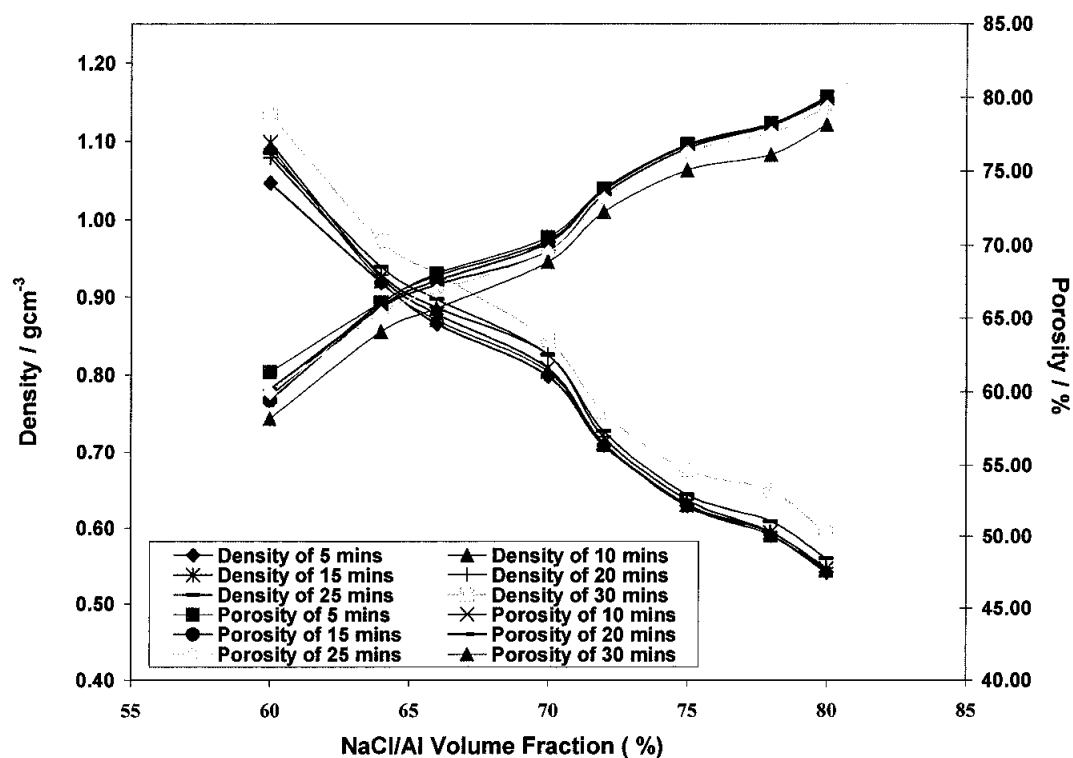


Figure 4.28: Variation of density and porosity of specimens with NaCl/Al volume fraction at various sintering time after dissolution process

In Figure 4.29, the variation of crystallite size of Al foams of different relative density with sintering time is presented. In general, the crystallite size increases with sintering time.

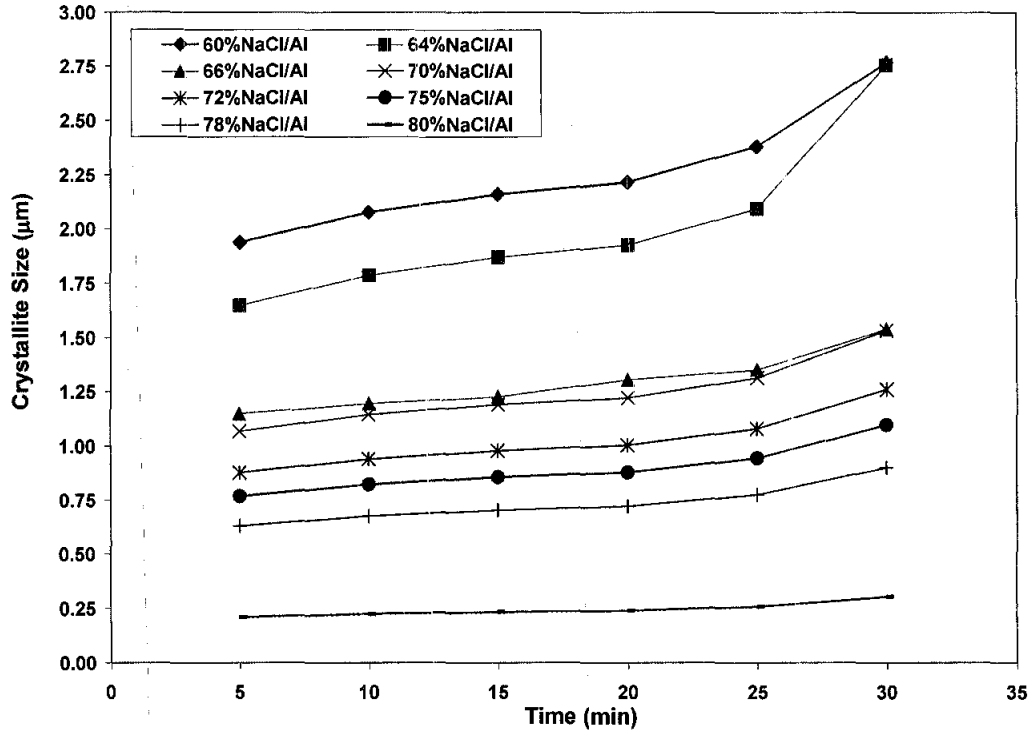
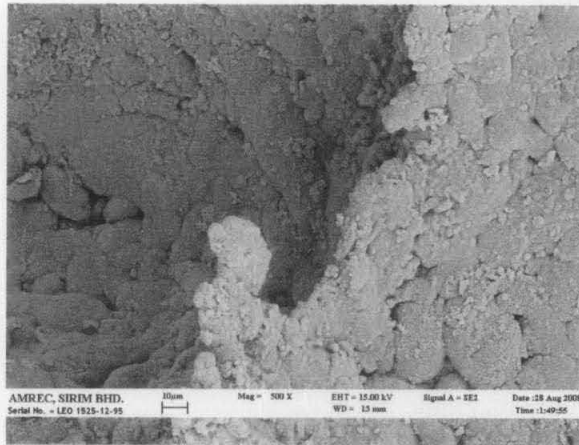


Figure 4.29: The influence of sintering time on the crystallite size of Al foams at various volume fractions of NaCl/Al

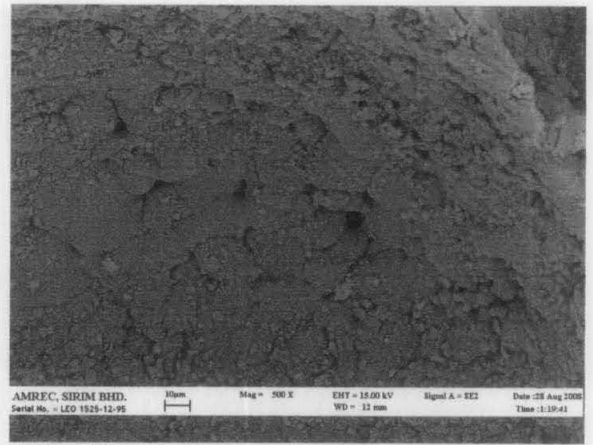
From the analysis of the above result, it can be shown that sintering time has a significant effect on the final density. The effect of sintering time on the final density can be explained by the following equation as proposed by German [24], [25]:

$$F_s = f_i + B_o \exp\left(-\frac{Q}{kT}\right) \ln t \quad (4.2)$$

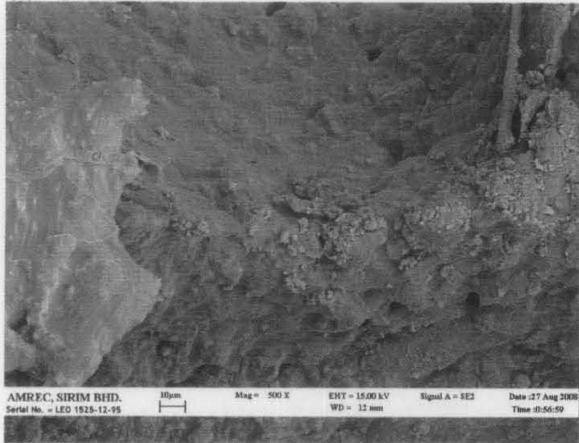
where F_s is the sintered fractional density, f_i is the fractional density at the beginning of the second sintering stage, k is Boltzmann's constant, T is the absolute temperature, B_o is a collection of constants that depend on surface energies, atomic size, atomic vibration frequencies and system geometry, and t is the time. With the increase of sintering time, the degree of formation of interconnected metallic framework of the Al cell wall will also improved as shown in Figure 4.30 (a)-(f).



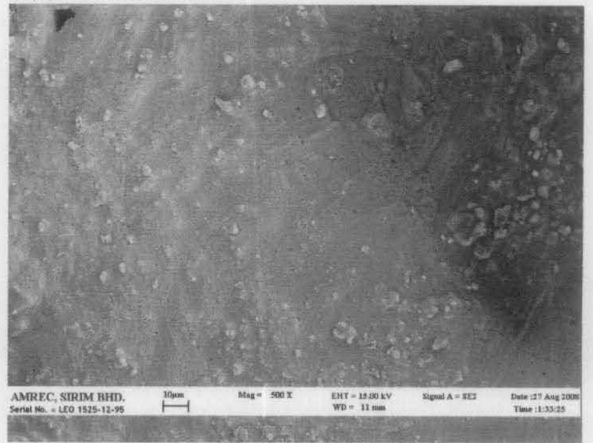
(a) 5 minutes



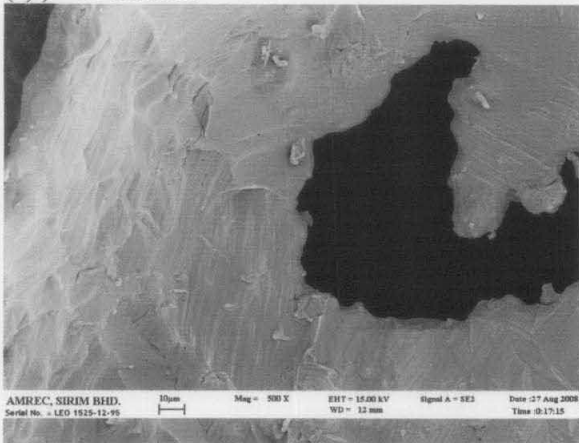
(b) 10 minutes



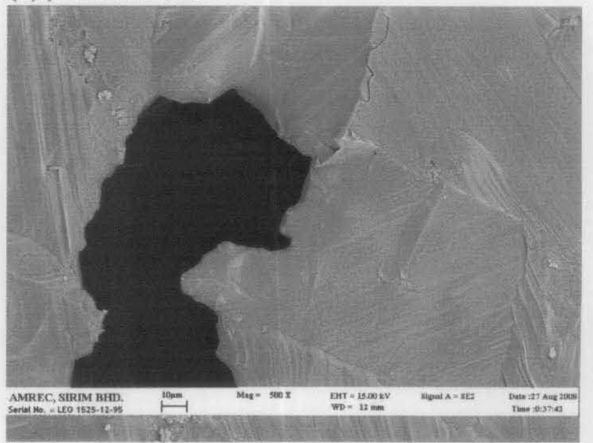
(c) 15 minutes



(d) 20 minutes



(e) 25 minutes



(f) 30 minutes

Figure 4.30: Images (SEM) of the formation of the interconnected metallic framework of the Al cell wall, which becomes denser as sintering time is increased

4.3.4 The influence of heating rate on the physical properties of fabricated Al foam

As shown in the analysis of the previous results, heating rate has also have an influential effect on the density of the foam. At a heating rate greater than 30 °C/min, cracks were often observed in the samples. The sample fabricated under heating rate in the range of 5–30 °C/min produced the acceptable qualities.

Table 4.9 presents the variation of the fraction of the dissolved NaCl in the Al foam, $(1-\phi)$, with the NaCl ratio. With a high volumes fraction (60% to 80%) of NaCl in the compact, most NaCl particles are in contact with each other and form a continuous three-dimensional network. Due to the fact that all the NaCl particles in the network can be dissolved away by water, there is only a small amount of residual NaCl in the resultant foam. For the compact that was subjected to 10 °C/min of PASDP, the, $1-\phi$, increase from 0.90 to 0.98 when the volume fraction of NaCl in the compact is increased from 60 to 80%. The fraction of the dissolved NaCl in the composites that was subjected to 15 °C/min of PASDP is increased from 0.93 to 0.98 when the volume fraction of NaCl/Al increases from 60 to 80%. When the volume fraction of NaCl is increased from 60 to 80% in the NaCl/Al compact, which was subjected to 30 °C/min of PASDP, the, $1-\phi$, increase from 0.97 to 0.99. XRD analysis as shown in Figure 4.31 confirms that no phase of NaCl was detected in the compacts of 60 % volume fraction when it was subjected to heating rate of 5–30 °C/min of processing time.

From Figure 4.32, it can be seen that with an increase heating rate, the density of the foam at fixed NaCl/Al ratio increases. According to German and Zhao *et al.* [24], [8] a higher heating rate induces large thermal stress that highlight sintering beyond that found in isothermal sintering. They also reported that higher heating rate demonstrated an ability to reduce grain growth while achieving high final density. There is an added driving force for sintering in temperature gradient. Since heat transport is poor in a porous material, such gradients are expected during heating to the sintering temperature [8], [22].

Table 4.9: Variation of fraction of the dissolved NaCl in the Al foam (1-φ) at different heating rate

Sample	Weight of HPC-BDP* / g	Weight of HPC-ADP^ / g	1-φ	Heating Rate / °C/min						
60%	19.842	9.942	0.90578	5						
64%	20.036	9.002	0.91954							
66%	19.859	8.412	0.93062							
70%	19.821	7.452	0.94856							
72%	19.708	6.489	0.95788							
75%	19.859	5.808	0.96902							
78%	19.897	5.394	0.97994							
80%	19.964	5.028	0.98006							
60%	19.779	9.724	0.91996	10						
64%	19.336	8.204	0.92764							
66%	19.511	7.840	0.94886							
70%	19.778	7.361	0.95224							
72%	19.710	6.325	0.96992							
75%	19.746	5.646	0.97244							
78%	19.958	5.424	0.98204							
80%	20.136	5.116	0.98556							
60%	19.289	9.124	0.93001	15						
64%	19.366	8.104	0.93846							
66%	19.275	7.567	0.95189							
70%	19.750	7.246	0.95889							
72%	20.091	6.568	0.97990							
75%	19.973	5.684	0.98546							
78%	19.766	5.167	0.98641							
80%	19.940	4.884	0.98791							
60%	20.062	9.801	0.93877	20						
64%	19.690	8.304	0.94887							
66%	19.549	7.689	0.96420							
70%	19.813	7.002	0.98245							
72%	20.000	6.376	0.98725							
75%	20.074	5.734	0.98896							
78%	19.961	5.326	0.98891							
80%	20.013	4.928	0.98982							
60%	20.046	9.444	0.97002	25						
64%	20.027	8.268	0.97989							
66%	19.844	7.764	0.98209							
70%	20.149	7.286	0.98643							
72%	19.964	6.304	0.98986							
75%	20.044	5.689	0.98998							
78%	19.936	5.284	0.99002							
80%	20.093	4.988	0.99115							
60%	20.169	9.468	0.97903	30						
64%	19.820	8.045	0.98126							
66%	19.934	7.768	0.98909							
70%	20.113	7.204	0.98992							
72%	20.277	6.589	0.99189							
75%	20.002	5.611	0.99248							
78%	19.969	5.268	0.99334							
80%	20.124	4.948	0.99578							

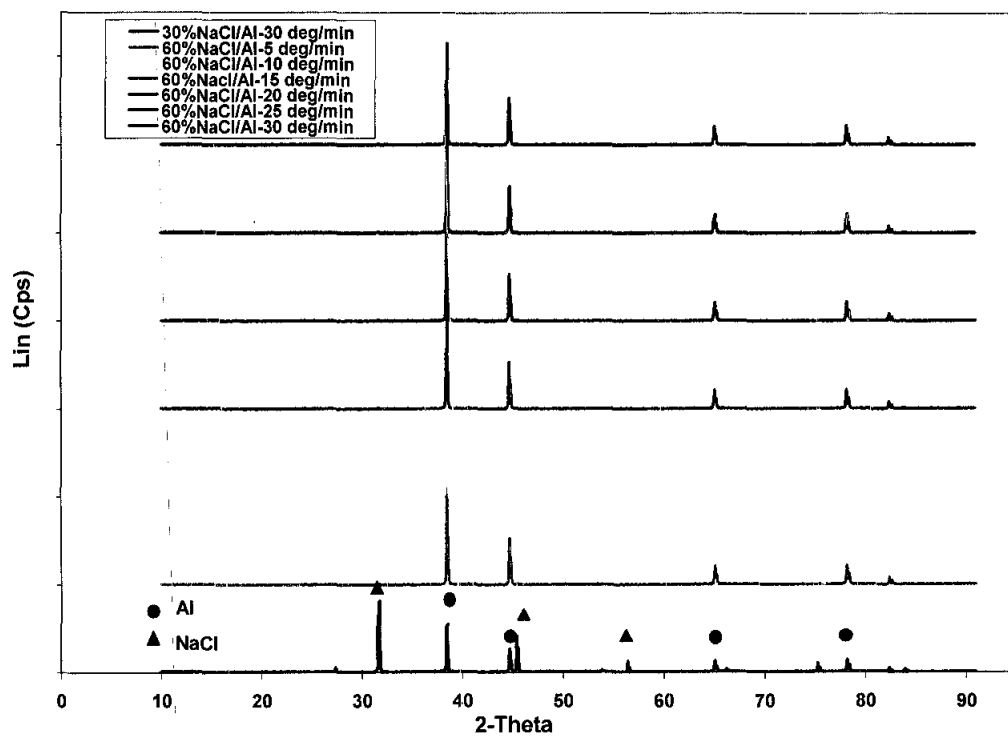


Figure 4.31: XRD spectrum of 60% vol NaCl/Al composites at different heating rate after the dissolution process

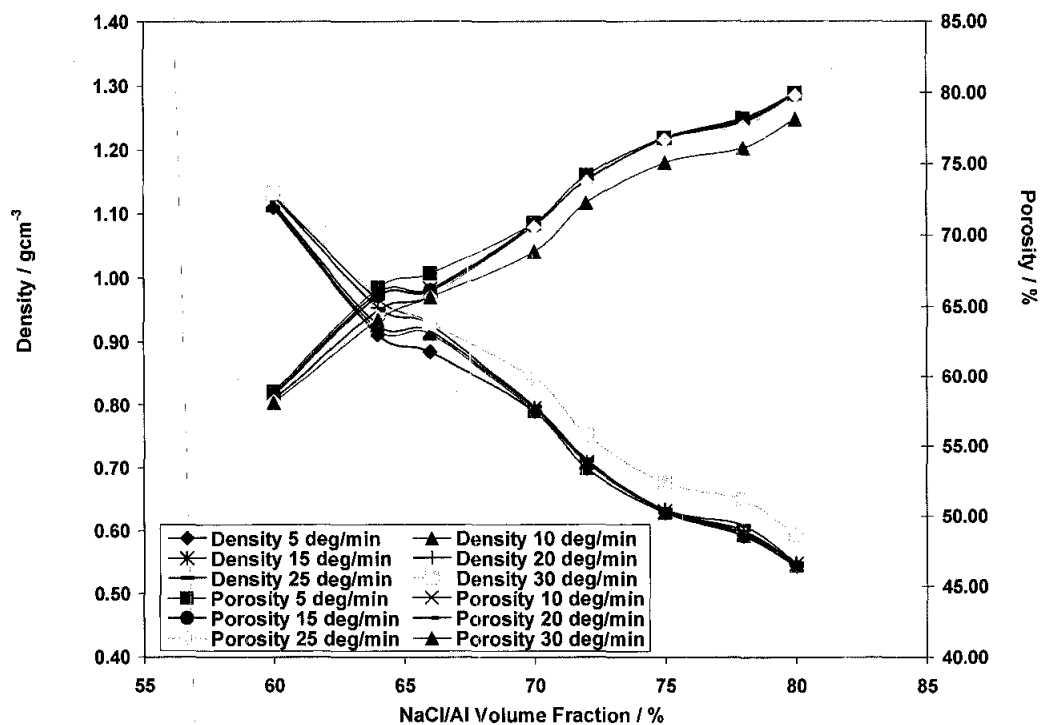


Figure 4.32: Variation of density and porosity of specimens with NaCl/Al volume fraction at various heating rate after dissolution process

4.4 The monotonic compression properties of aluminium foam produced by pressure assisted sintering process

In compression, cellular metals show a unique stress-strain response with a plateau region in which the stress is nearly constant over a wide range of strain (Figure 4.33). This behaviour makes cellular metals interesting for energy absorbing applications where at a relatively low constant stress a large amount of deformation can be absorbed [29-31]. The compressive stress-strain curves of the Al foams with different volume fraction of initial NaCl of 30%, 40%, 50%, 60%, 64%, 66%, and 70% respectively, which correspond to 2.148 gcm^{-3} , 2.109 gcm^{-3} , 1.615 gcm^{-3} , 1.132 gcm^{-3} , 1.015 gcm^{-3} , 0.952 gcm^{-3} and 0.815 gcm^{-3} respectively is presented in Figure 4.33.

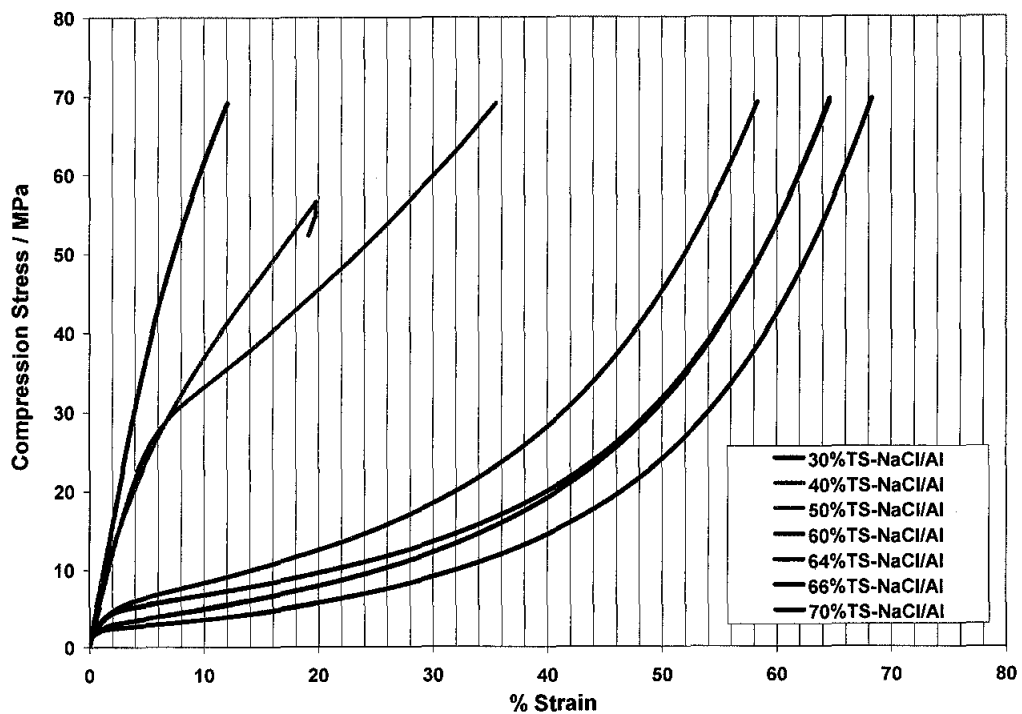


Figure 4.33: Compressive stress-strain curve of the Al foam with different NaCl/Al volume fraction

When loaded in compression, the characteristic of stress-strain foam behaviour are not exhibited by specimens of 30 to 50% volume fraction of NaCl/Al. The typical engineering stress-strain curve of the aluminium is exhibited by specimen of 60% to 70% volume fraction of NaCl/Al. The compressive stress, which is defined as the

mean value of constant flow stress is 2.13 MPa, 1.86 MPa, 1.77 MPa and 1.69 MPa for the porous Al specimen with the porosity of 58.07%, 62.41%, 64.74% and 69.81%.

4.4.1 The influence of compaction pressure on the compressive properties of Al foam

The compressive stress-strain curves for Al foams of 66% NaCl/Al volume fraction is shown in Figures 4.34 and 4.35. The samples were sintered at different pressures in a vacuum hot press machine for 30 minutes. Higher plateau stress is observed when the compaction pressure is increased from 20 to 120 MPa. This indicates that at higher compaction pressure will result better binding among Al particles. But a higher compaction pressure which was above 120 MPa should be avoided because of the increasing tendency of cracking in the samples.

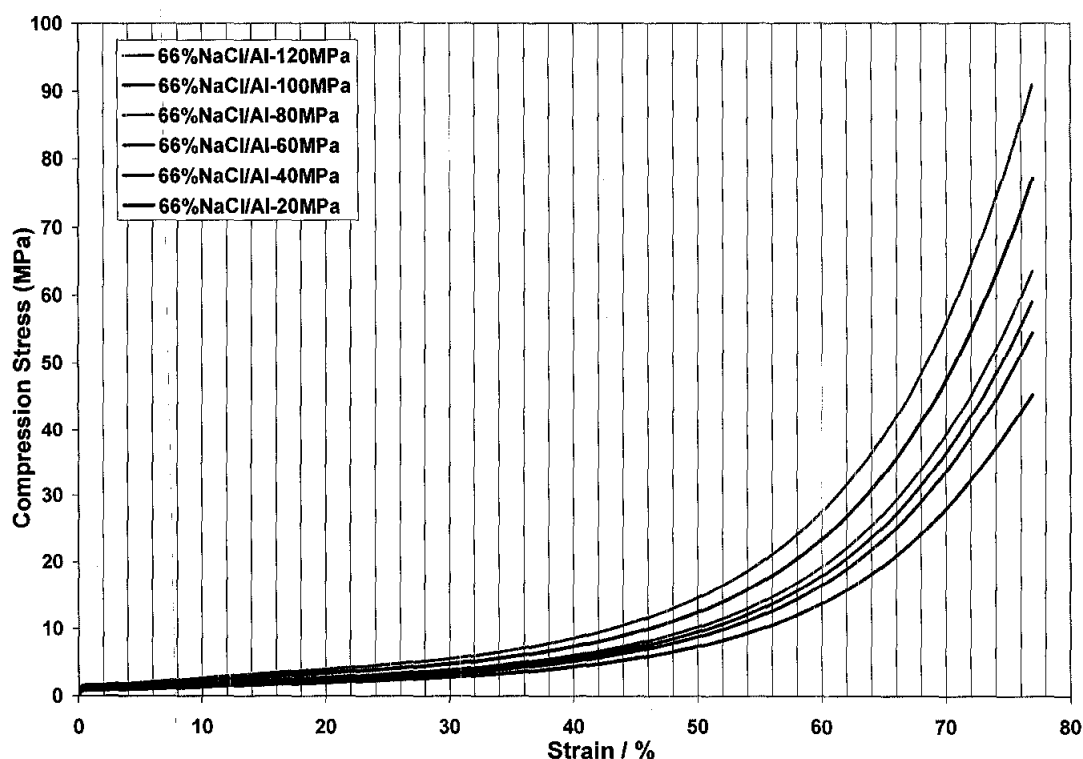


Figure 4.34: Compressive stress-strain curves of Al foam at different compaction pressure sintered at 620 °C for 30 minutes

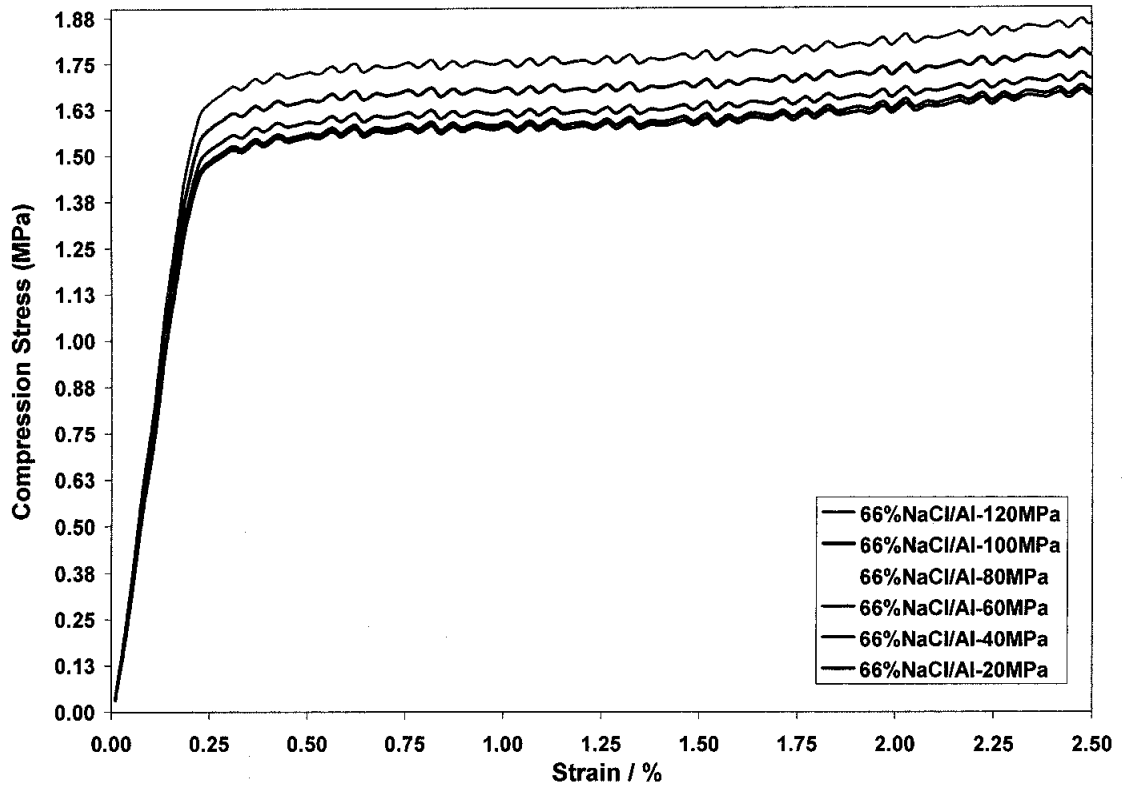


Figure 4.35: Enlarge portion of the beginning of the compressive stress-strain curves of Al foam at different compaction pressure sintered at 620 °C for 30 minutes

Figure 4.36 shows the compressive strength of the foam with different compacting pressure at various NaCl/Al ratios. It was found that this property depends on the compacting pressure and compressive strength increase with increasing pressure at fixed NaCl/Al ratio. The value of the compressive strength of 66% NaCl/Al composites after leaching process increase from 1.54 MPa to 1.77 MPa when the pressure is increased from 20 MPa to 120 MPa. Meanwhile, at a fixed compacting pressure, the compressive strength decrease with increasing NaCl/Al ratio. The compressive strength decreases from 2.13 MPa to 0.75 MPa when the volume fraction of NaCl is increased from 60% to 80% at fixed compaction pressure of 120 MPa.

The influence of compacting pressure on the modulus is also noticeable and the modulus increase when the pressure is increased for all different volume fraction of NaCl/Al (Figure 4.37). The compressive modulus of 60% NaCl/Al foam increases from 0.62 GPa to 0.66 GPa when the compaction pressure is increased from 20 MPa to 120 MPa. The compressive modulus of the foam decrease from 0.66 MPa to 0.33

MPa when the volume fraction of the composite is increased from 60% to 80% at a compaction pressure of 120 MPa. Clearly the effect of density and hence the modulus of the specimens is governed by the scaling law of Gibson and Ashby [1].

The influence of density (varying the volume fraction of NaCl) on the compressive strength at densification (σ_{dens}) is obvious as shown in Figure 4.38. At fixed pressure (120 MPa), it decreases from 19.18 MPa to 3.34 MPa when the volume fraction of NaCl in NaCl/Al is increased from 60% to 80%. The σ_{dens} shows an increase in value when the compaction pressure is increased at fixed volume fraction of NaCl/Al. For sample 60% volume fraction of NaCl, σ_{dens} increases from 16.60 MPa to 19.12 MPa when the pressure is increased from 20 MPa to 120 MPa. The σ_{dens} increased from 13.02 MPa to 15.98 MPa when the pressure is increased from 20 MPa to 120 MPa for sample 64% volume fraction of NaCl. When the pressure is increased from 20 MPa to 120 MPa, the σ_{dens} of sample 66% volume fraction of NaCl increases from 11.95 MPa to 14.28 MPa. For sample 70% volume fraction of NaCl, σ_{dens} increases from 10.03 MPa to 10.60 MPa when the pressure is increased from 20 MPa to 120 MPa.

The deformation at densification (ϵ_{dens}) is highly affected either by pressure or the density of the foams. The porosity of the foams does have a positive effect on the deformation mechanisms in compression, similar to springs that can accommodate larger deformation than the materials they are made of [30]. Moreover, the effect of density on the deformation at densification is very significant when density increases. From Figure 4.39, it can be observed that the ϵ_{dens} increases from 31.47 % to 56.19 % when the volume fraction of NaCl is increased from 60% to 80% at fixed compaction pressure of 120 MPa. The ϵ_{dens} shows a decrease in value when the compaction pressure is increased at fixed volume fraction of NaCl/Al. For sample 60% volume fraction of NaCl, ϵ_{dens} decreases from 35.40 % to 31.44 % when the pressure is increased from 20 MPa to 120 MPa. The ϵ_{dens} decreases from 41.00 % to 36.37 % when the pressure is increased from 20 MPa to 120 MPa for sample 64% volume fraction of NaCl. When the pressure is increased from 20 MPa to 120 MPa, the ϵ_{dens} of sample 66% volume fraction of NaCl decreases from 42.68 % to 39.02 %.

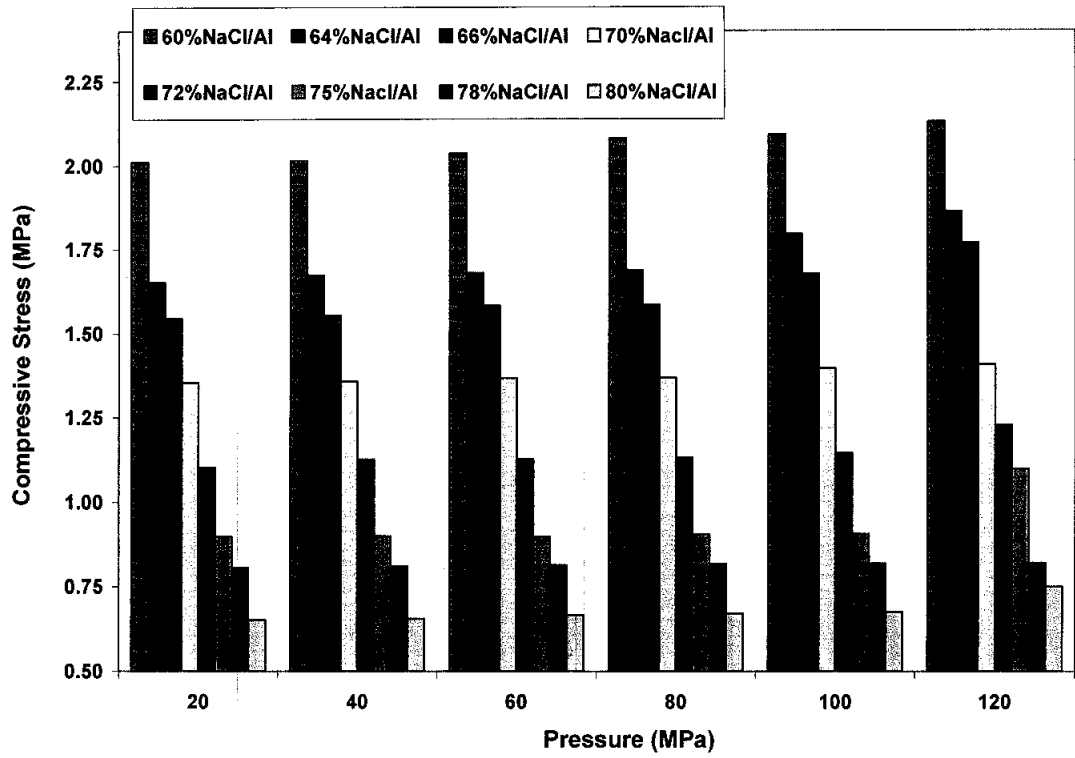


Figure 4.36: Variation of compressive strength of Al foam with compaction pressure at different NaCl/Al volume fractions

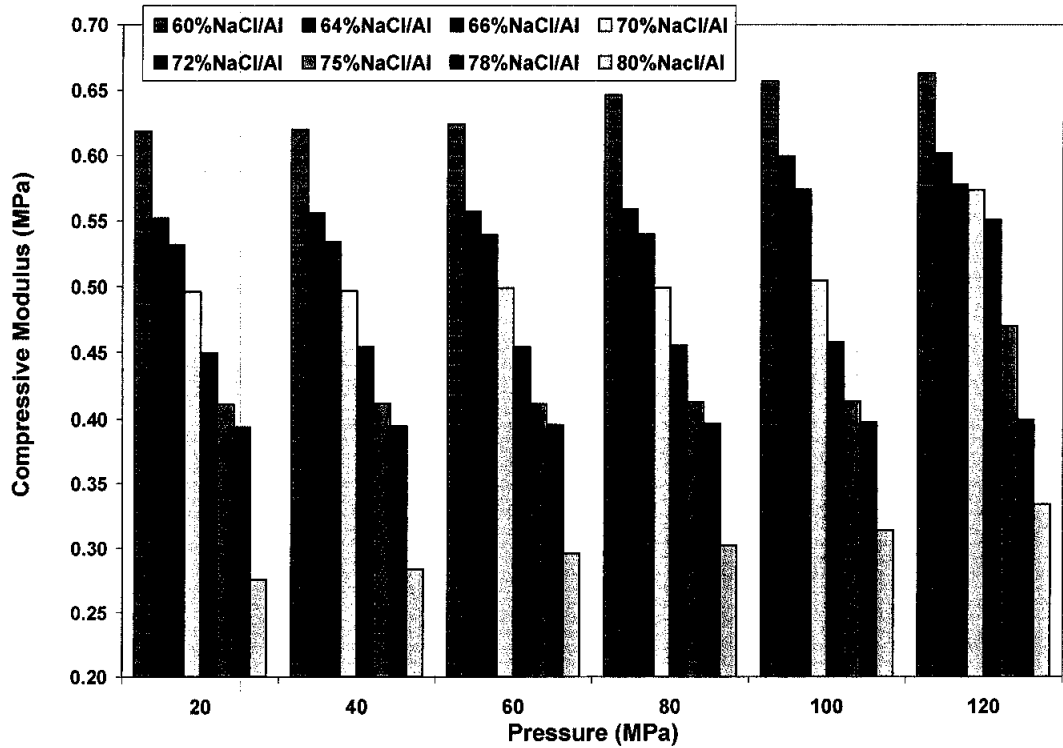


Figure 4.37: Variation of compressive modulus of Al foam with compaction pressure at different NaCl/Al volume fractions

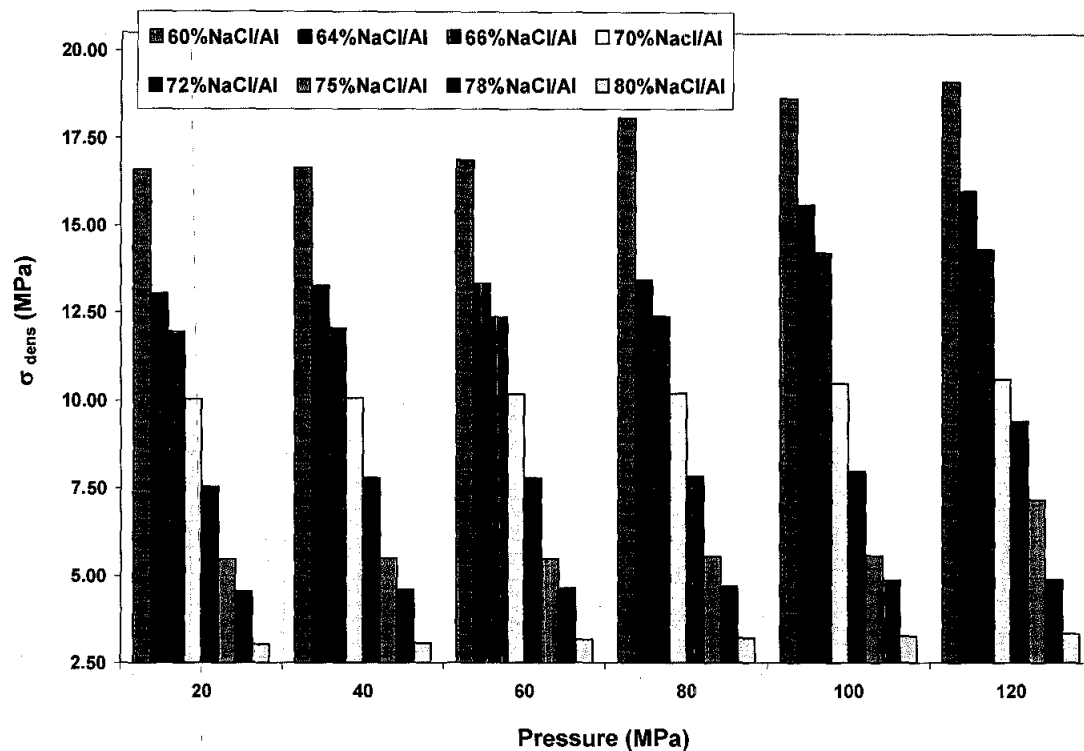


Figure 4.38: Variation of strength at densification of Al foam with compaction pressure at different NaCl/Al volume fraction

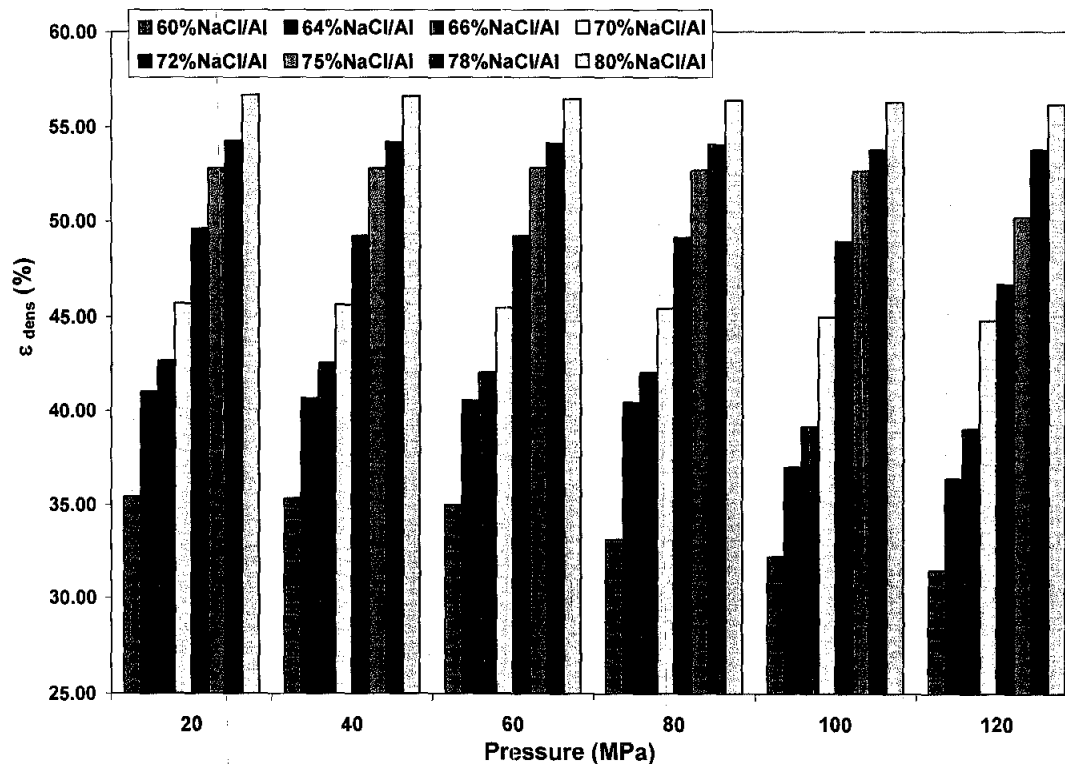


Figure 4.39: Variation of deformation at densification of Al foam with compaction pressure at different NaCl/Al volume fraction

4.4.2 The influence of sintering temperature on the compressive properties of Al foam

One of the formulation (66% NaCl/Al) was selected and sintered at different temperatures in a vacuum hot press machine for 30 minutes at a compaction pressure of 120 MPa and all the samples show a characteristic of stress-strain behaviour of metallic foam when loaded in compression (Figures 4.40 and 4.41). It should be noted that the compressive loads were applied along directions parallel to the compacting directions. The response typically included a distinct knee at a critical stress where the slope of the stress-strain curve changed from a high value to zero. The critical stress, which marks the end of linear elastic deformation and the beginning of foam collapse, was taken to be the compression strength. A long deformation plateau of almost constant stress ensued, during which the cell walls buckled and collapsed [116-118]. Finally, the plateau ended and the stress begins to rise sharply, as the flattened cell wall completely collapsed and impinged [119]-[122]. Figure 4.40 presents the compressive stress-strain curves of the Al foams with volume fraction of initial 66% NaCl at various sintering temperatures of 570 °C, 580 °C, 590 °C, 600 °C, 610 °C and 620 °C respectively which corresponds to 0.880 gcm⁻³, 0.883 gcm⁻³, 0.886 gcm⁻³, 0.887 gcm⁻³, 0.895 gcm⁻³ and 0.952 gcm⁻³ respectively. It seems that the property depends on the sintering temperature and compressive strength increases with increasing sintering temperature at fixed NaCl/Al ratio.

The compressive strength is 1.58 MPa, 1.59 MPa, 1.60 MPa, 1.61 MPa, 1.62 MPa and 1.77 MPa for the porous Al specimens with the porosity of 67.40%, 67.29%, 67.18%, 67.14%, 66.86% and 64.74% respectively. Higher plateau stress is observed when the sintering temperature is increased from 570 to 620°C. This indicates that at higher sintering temperature will result better binding among al particles. But a higher sintering temperature which was above 620 °C should be avoided because of the increasing tendency of some Al drained out of the surface of the compacts and melted at the upper punch and the die wall.

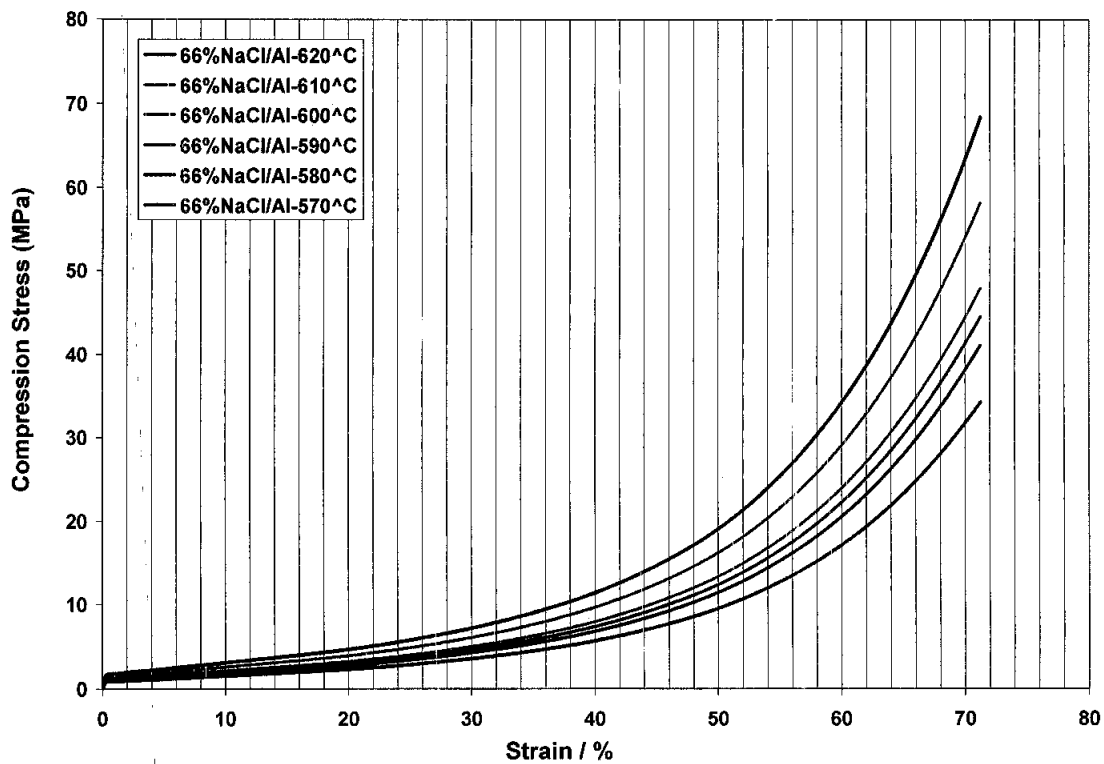


Figure 4.40: Compressive stress-strain curves of Al foam at different sintering temperature

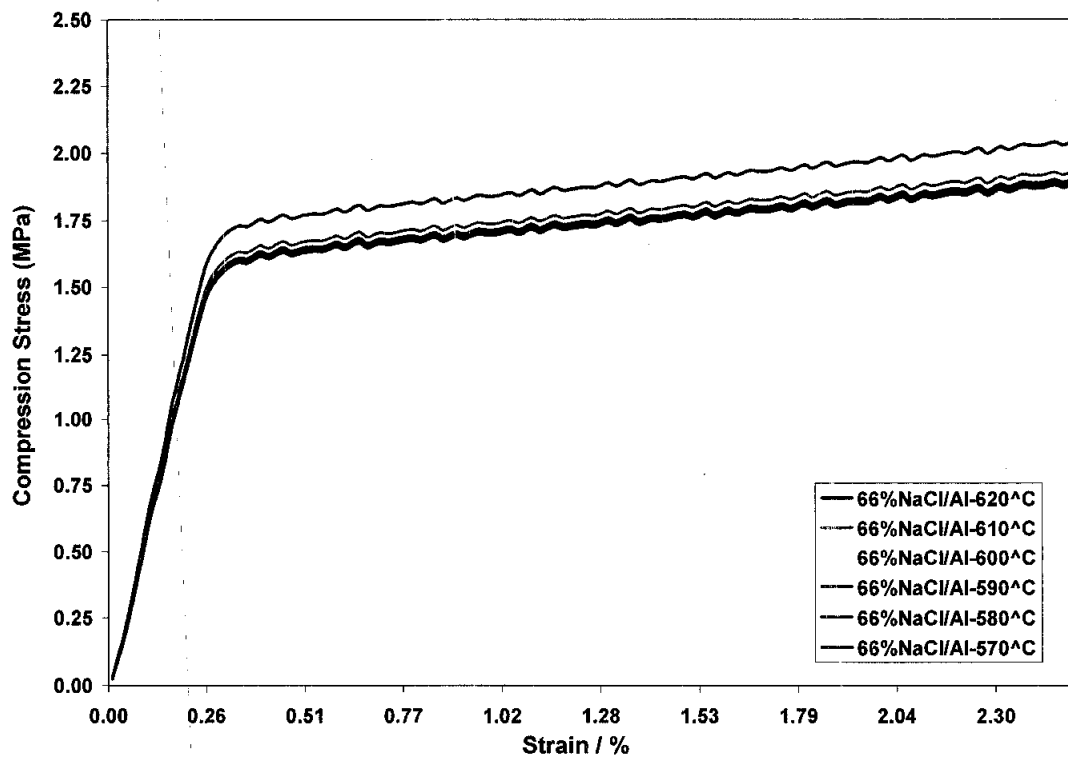


Figure 4.41: Enlarge portion of the beginning of the compressive stress-strain curves of Al foam at different sintering temperature

The compressive strength with different sintering temperature at various NaCl/Al ratio is shown in Figure 4.42. It can be observed that the property depends on the sintering temperature and compressive strength increases from 2.06 MPa to 2.13 MPa with the increasing temperature of the PASDP process from 570 to 620°C at fixed initial volume fraction of 66 % NaCl/Al. Meanwhile, at a fixed sintering temperature, the compressive strength of the specimen decreases with increasing NaCl/Al ratio. The compressive strength decreases from 2.13 MPa to 0.75 MPa when the volume fraction of NaCl is increased from 60% to 80% at fixed sintering temperature of 620°C.

Figure 4.43 reveals that the influence of sintering temperature on the modulus of the foam is significant and the modulus increases when the sintering temperature is increased for all different volume fraction of NaCl/Al. The scaling law of Gibson and Ashby clearly governs the effect of sintering temperature on the modulus properties of the specimens [1]. The compressive modulus of initial volume fraction of 60% NaCl/Al foam increases from 0.64 GPa to 0.66 GPa when the sintering temperature is increased from 570 °C to 620 °C. For the initial volume fraction of 64% NaCl/Al foam, the value of the compressive modulus increases from 0.56 GPa to 0.60 GPa as the sintering temperature is increased from 570 °C to 620 °C. When the sintering temperature is increased from 570 °C to 620 °C, the compressive modulus increases from 0.50 GPa to 0.57 GPa for the initial volume fraction of 70% NaCl/Al foam. The compressive modulus of the foam decreases from 0.66 GPa to 0.33 GPa when the initial volume fraction of the NaCl/Al is increased from 60% to 80% at a sintering temperature of 620 °C.

The influence of density (varying the volume fraction of NaCl) on the compressive strength at densification (σ_{dens}) is obvious as presented in Figure 4.44. At fixed sintering temperature (620 °C), it decreases from 19.12 MPa to 3.34 MPa when the initial volume fraction of NaCl is increased from 60% to 80%. The σ_{dens} show an increase in value when the sintering temperature is increased at fixed initial volume fraction of NaCl/Al. For sample of initial 60% volume fraction of NaCl, σ_{dens} increases from 17.11 MPa to 19.12 MPa when the sintering temperature is increased from 570 °C to 620 °C. The σ_{dens} increased from 13.32 MPa to 15.98 MPa when the pressure is increased from 570 °C to 620 °C for sample of initial 64% volume fraction

of NaCl. When the sintering temperature is increased from 570 °C to 620 °C, the σ_{dens} of sample initial volume fraction of 66%NaCl increases from 12.35 MPa to 14.28 MPa..

The sintering temperature or the densities of the foams affect the deformation at densification properties. From Figure 4.45, it can be observed that the $\varepsilon_{\text{dens}}$ increases from 34.59 % to 56.17 % when the volume fraction of NaCl is increased from 60% to 80% at fixed sintering temperature of 620 °C. The $\varepsilon_{\text{dens}}$ show a decrease in value when the sintering temperature is increased at fixed volume fraction of NaCl/Al. For sample of initial 60% volume fraction of NaCl, $\varepsilon_{\text{dens}}$ decreases from 34.59 % to 31.44 % when the sintering temperature is increased from 570 °C to 620 °C. The $\varepsilon_{\text{dens}}$ decrease from 40.54 % to 36.37 % when the sintering temperature is increased from 570 °C to 620 °C for sample of initial 64% volume fraction of NaCl. When the sintering temperature is increased from 570 °C to 620 °C, the $\varepsilon_{\text{dens}}$ of sample of initial volume fraction of 66% NaCl decreases from 42.05 % to 39.02 %.

Gibson and Ashby [1] have postulated that the densification strain for open cell plastic foams can be described by the following equation:

$$\varepsilon_d = \alpha \left(1 - (1.4 \frac{\rho^*}{\rho}) + 0.4(\frac{\rho^*}{\rho})^3 \right) \quad (4.3)$$

where ε_d is the densification strain, ρ^* is the apparent density of the foam, ρ is the density of cell wall and α is a material constant, being between 0.8 and 1.0 for open cell aluminium foams. The data that obtained from experiments for 80% volume ratio NaCl/Al which was produced at sintering temperature of 620 °C and compacted at 120 MPa and inserted in equation (4.3), the following value will be obtained:

$$\varepsilon_d = 0.8 \left(1 - 1.4(\frac{0.545}{2.71}) + 0.4(\frac{0.545}{2.71})^3 \right) = 0.58$$

According to equation (4.3), ε_d of the present aluminium foam is 58% if α is chosen to be 0.8 and the aluminium foam produced by pressure assisted sintering has the value of 56%. There is a fair good agreement between the experimental data and the theoretical value of strain at densification.

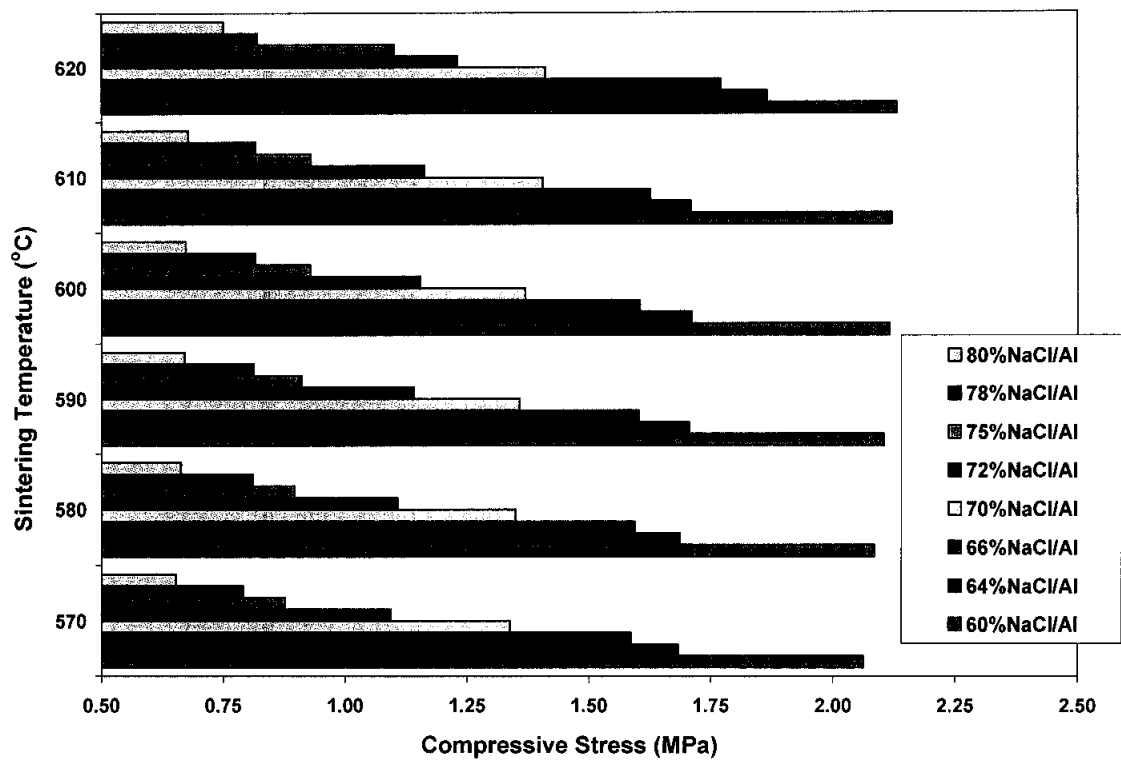


Figure 4.42: Variation of compressive strength of Al foam with sintering temperature at different NaCl/Al volume fraction

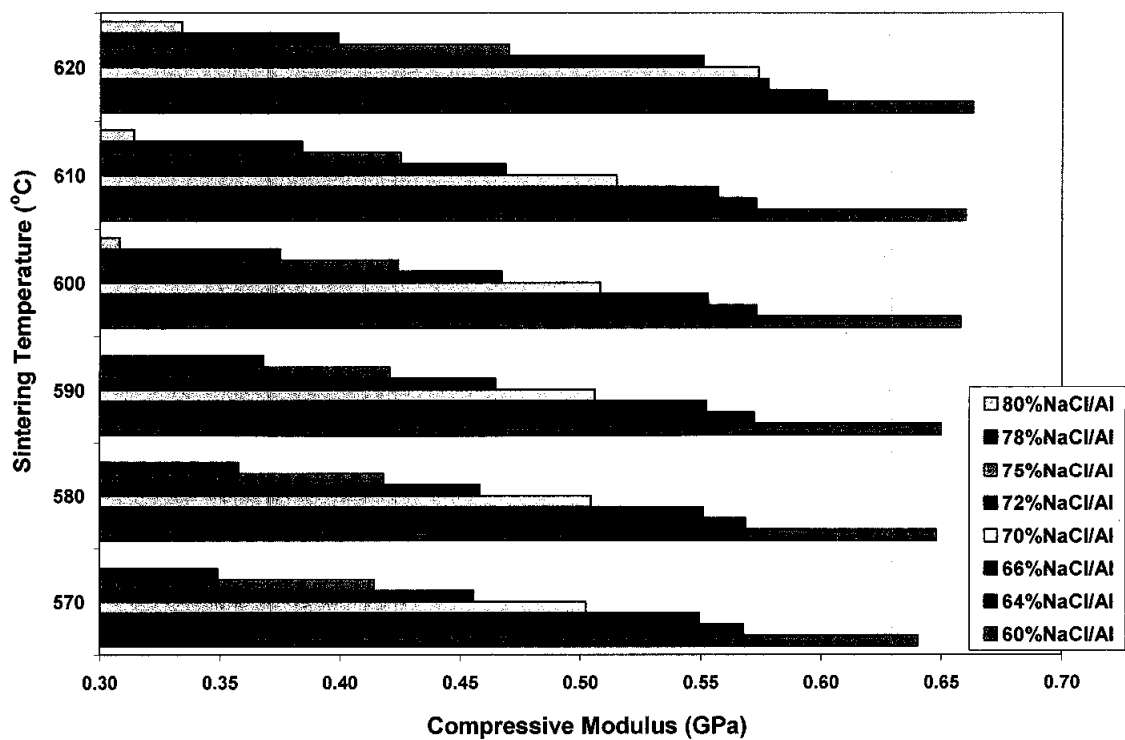


Figure 4.43: Variation of compressive modulus of Al foam with sintering temperature at different NaCl/Al volume fraction

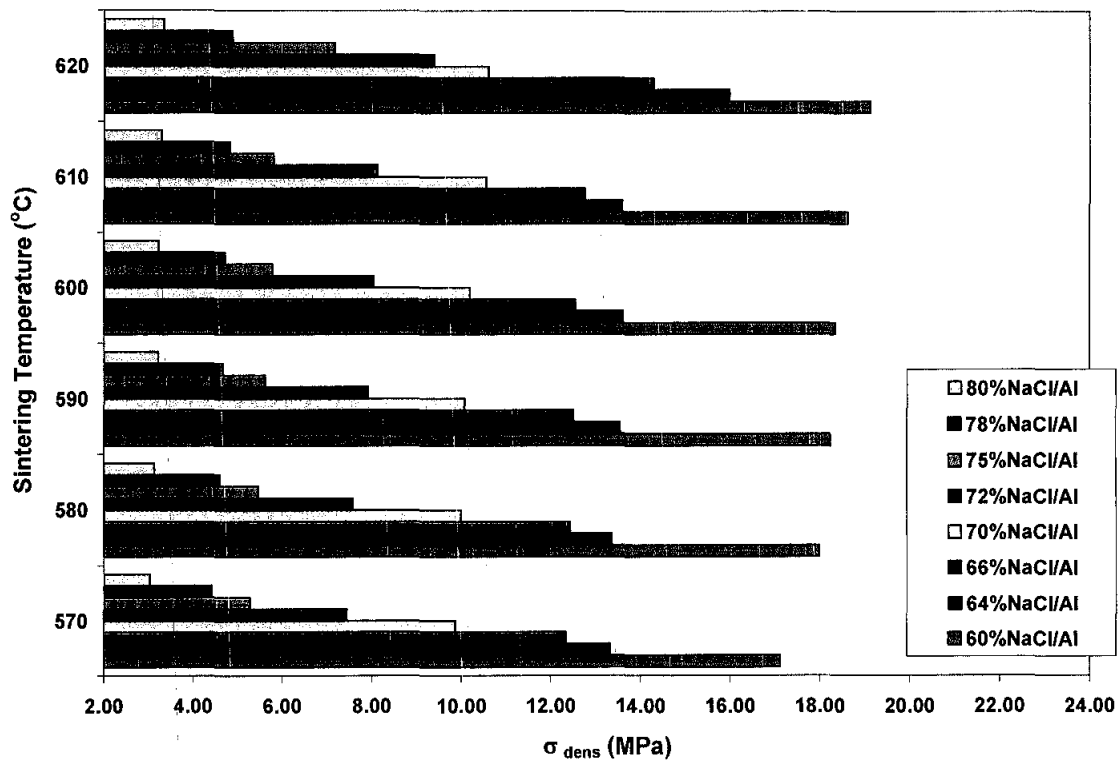


Figure 4.44: Variation of strength at densification of Al foam with sintering temperature at different NaCl/Al volume fraction.

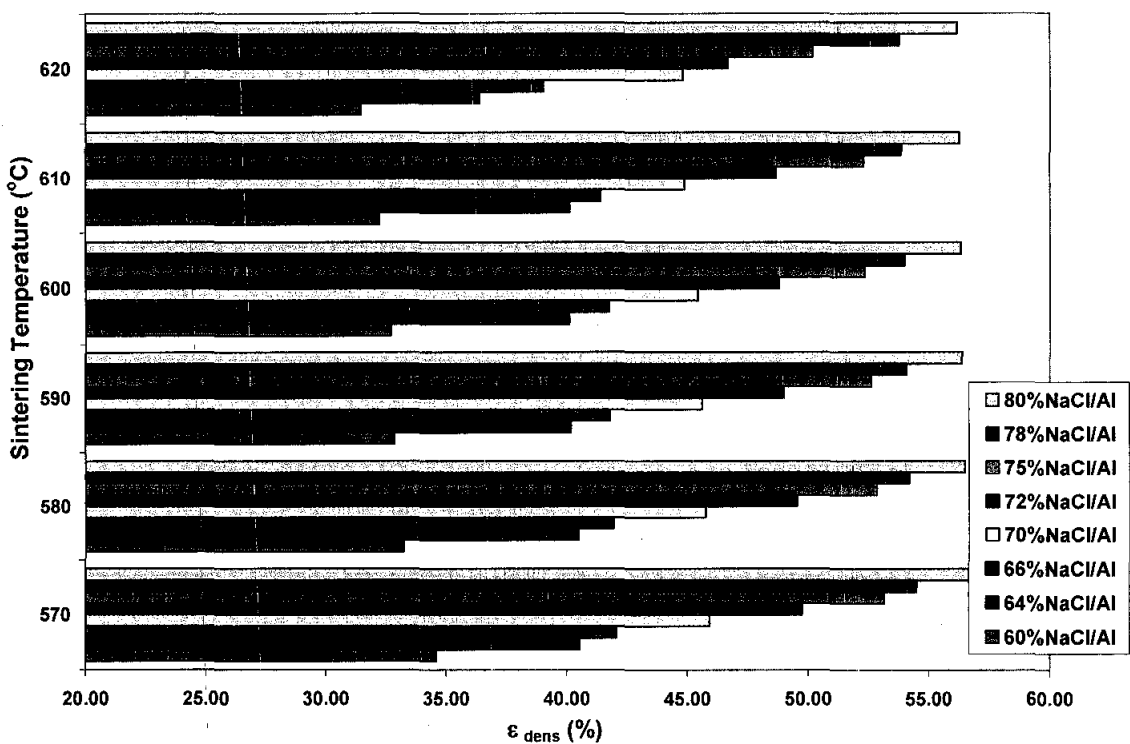


Figure 4.45: Variation of deformation at densification of Al foam with sintering temperature at different NaCl/Al volume fraction.

4.4.3 The influence of sintering time on the compressive properties of Al foam

Figure 4.46 shows typical stress-strain curves under monotonic compression for initial volume fraction of 66% NaCl/Al produced by pressure assisted sintering process (PASDP). The curve shows an elastic region at the initial stage of deformation, then a plateau region where the specimen deforms under a nearly constant flow stress (plateau stress) and finally a densification region where the flow stress steeply increased at high strain. Figure 4.46 (a) presents the compressive stress-strain curves of the Al foams with volume fraction of initial 66 % NaCl at various sintering times of 5 min, 10 min, 15 min, 20 min, 25 min and 30 min respectively which corresponds to 0.865 gcm^{-3} , 0.870 gcm^{-3} , 0.878 gcm^{-3} , 0.886 gcm^{-3} , 0.897 gcm^{-3} and 0.952 gcm^{-3} respectively. It seems that the property depends on the sintering temperature and compressive strength increases with increasing sintering temperature at fixed NaCl/Al ratio.

The plateau stress, which is defined as the mean value of constant flow stress is 1.54 MPa, 1.55 MPa, 1.58 MPa, 1.60 MPa, 1.63 MPa and 1.77 MPa for the porous Al specimens with the porosity of 67.96%, 67.77%, 67.48%, 67.18%, 66.77% and 64.74% respectively. Higher plateau stress is observed when the sintering time is increased from 5 to 30 min. This indicates that at higher sintering time will result better binding among aluminium particles.

The influence of sintering time on the compressive strength is significant and the property increases when the time is increased for all different volume fraction of NaCl/Al (Figure 4.47). It can be observed that the property depends on the sintering time and compressive strength increases from 1.54 MPa to 1.77 MPa with the increasing time of the PASDP process from 5 min to 30 min at fixed initial volume fraction of 66 % NaCl/Al. Meanwhile, at a fixed sintering time, the compressive strength of the specimen decreases with increasing NaCl/Al ratio. The compressive strength decreases from 2.13 MPa to 0.75 MPa when the volume fraction of NaCl is increased from 60% to 80% at fixed sintering time of 30 min.

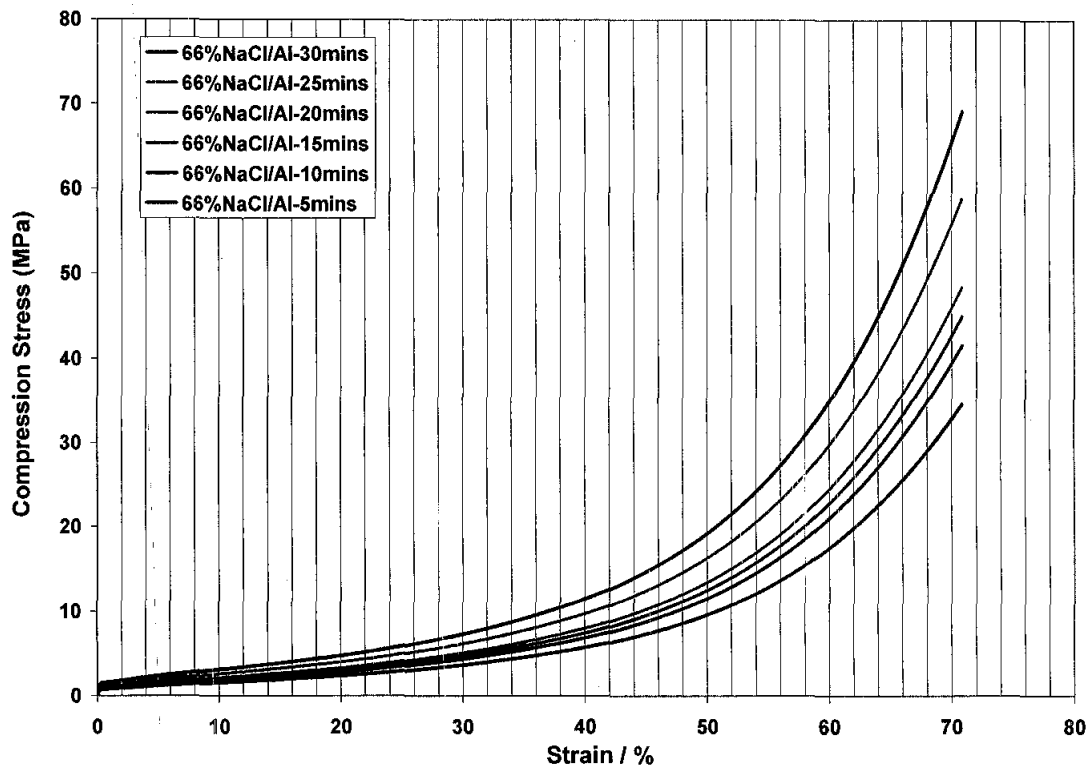


Figure 4.46 (a): Compressive stress-strain curves of Al foam at different sintering time

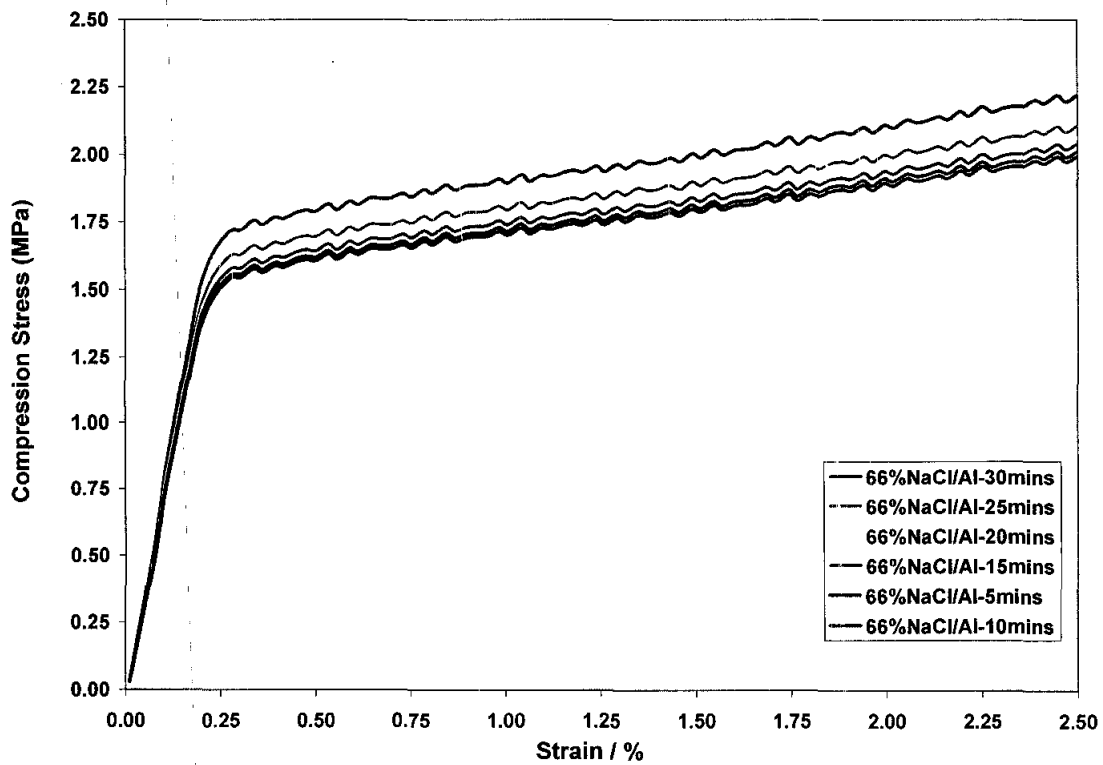


Figure 4.46 (b): Enlarge portion of the beginning of the compressive stress-strain curves of Al foam at different sintering time

Figure 4.48 reveals that the influence of sintering temperature on the modulus of the foam is noticeable and the modulus increase when the sintering time is increased for all different volume fraction of NaCl/Al. The compressive modulus of initial volume fraction of 60% NaCl/Al foam increases from 0.63 GPa to 0.66 GPa when the sintering time is increased from 5 to 30 min.

The influence of density (varying the volume fraction of NaCl) on the compressive strength at densification (σ_{dens}) is obvious as presented in Figure 4.49. At fixed sintering time (30 min), it decreases from 19.12 MPa to 3.34 MPa when the initial volume fraction of NaCl is increased from 60% to 80%. The σ_{dens} shows an increase in value when the sintering time is increased at fixed initial volume fraction of NaCl/Al. For sample 60% volume fraction of NaCl, σ_{dens} increases from 16.84 MPa to 19.12 MPa when the sintering time is increased from 5 min to 30 min. The σ_{dens} increased from 13.40 MPa to 15.98 MPa when the time is increased from 5 min to 30 min for sample 64% volume fraction of NaCl. When the time is increased from 5 min to 30 min, the σ_{dens} of initial volume fraction of 66% NaCl increases from 11.95 MPa to 14.28 MPa. For sample 70% volume fraction of NaCl, σ_{dens} increases from 10.14 MPa to 10.60 MPa when the pressure is increased from 5 min to 30 min.

The sintering time or the densities of the foams influence the deformation at densification properties. From Figure 4.50, it can be observed that the ϵ_{dens} increases from 31.44% to 56.16% when the initial volume fraction of NaCl is increased from 60% to 80% at fixed sintering time of 30 min. The ϵ_{dens} shows a decrease in value when the sintering time is increased at fixed volume fraction of NaCl/Al. For sample 60% volume fraction of NaCl, ϵ_{dens} decreases from 35.02% to 31.44% when the sintering time is increased from 5 min to 30 min. The ϵ_{dens} decrease from 40.41% to 36.37% when the sintering time is increased from 5 min to 30 min for sample 64% volume fraction of NaCl. When the sintering time is increased from 5 min to 30 min, the ϵ_{dens} of sample 66% volume fraction of NaCl decreases from 42.69% to 39.02%. For sample 70% volume fraction of NaCl, ϵ_{dens} decreases from 45.52% to 44.79% when the sintering time is increased from 5 min to 30 min.

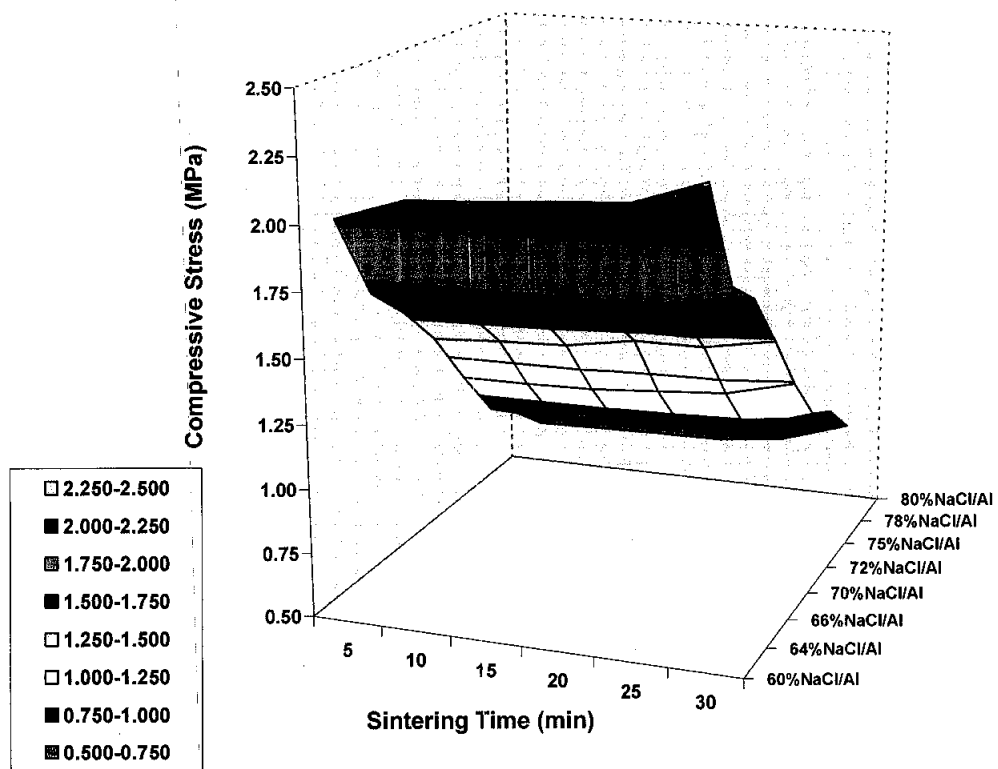


Figure 4.47: Variation of compressive strength of Al foam with sintering time at different NaCl/Al volume fraction

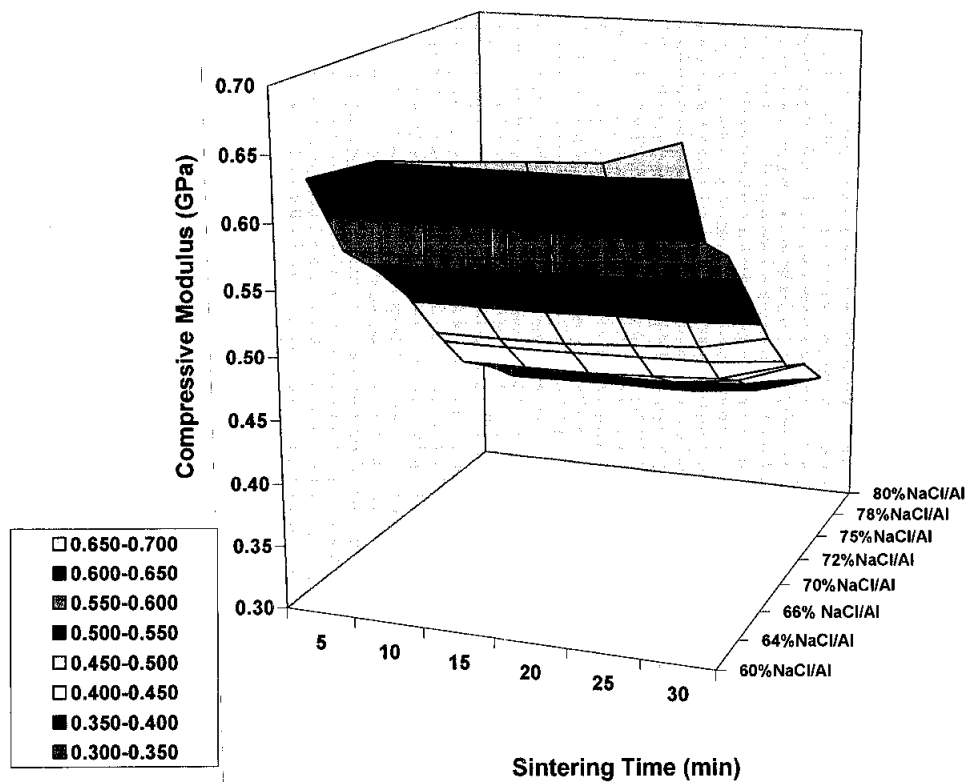


Figure 4.48: Variation of compressive modulus of Al foam with sintering time at different NaCl/Al volume fraction

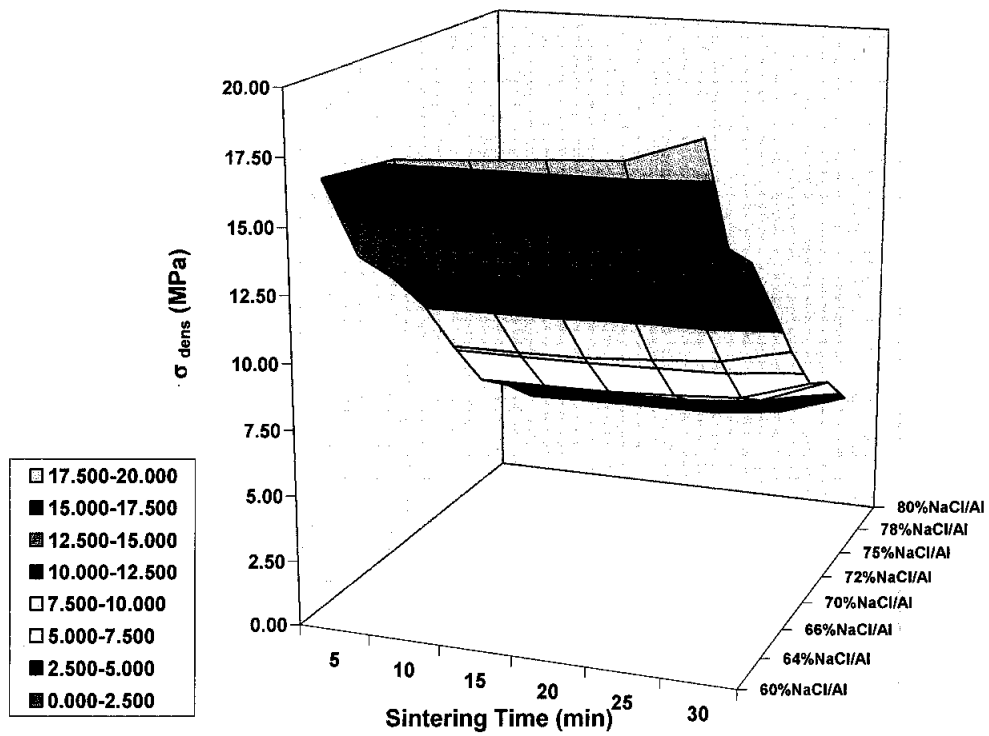


Figure 4.49: Variation of strength at densification of Al foam with sintering time at different NaCl/Al volume fraction

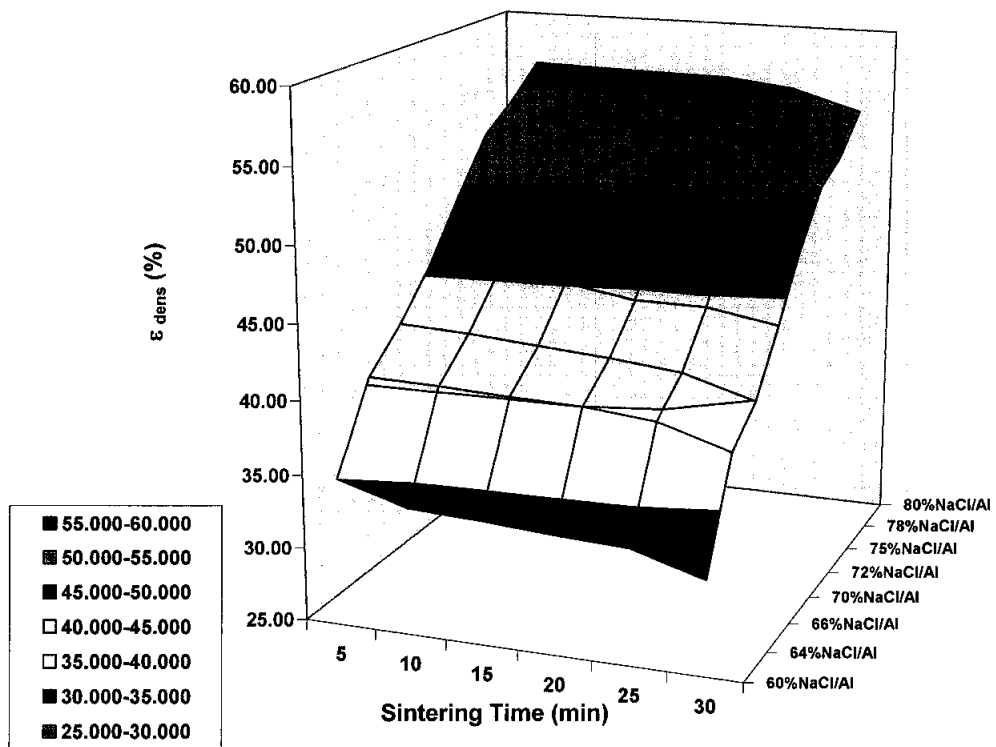


Figure 4.50: Variation of deformation at densification of Al foam with sintering time at different NaCl/Al volume fraction

4.4.4 The influence of heating rate on the compressive properties of Al foam

The engineering stress-strain curve of the 66% NaCl/Al foam which was manufactured at 30°C/min heating rate and simultaneously sintered and pressed at 620 °C and 120 MPa for 30 minutes is shown in Figure 4.51. The present aluminium foam shows a similar stress-strain behaviour compared with other metallic foams, characterized by three distinct regions, i.e. linear elastic deformation, collapse plateau and densification region.

Figure 4.52 presents the compressive stress-strain curves of the Al foams with volume fraction of initial 66 % NaCl at various heating rate of 5°C/min, 10°C/min, 15°C/min, 20 °C/min, 25°C/min and 30°C/min respectively which corresponds to 0.885 gcm⁻³, 0.914 gcm⁻³, 0.918 gcm⁻³, 0.928 gcm⁻³, 0.929 gcm⁻³, 0.930 gcm⁻³ respectively. It seems that the property depends on the heating rate and compressive strength increases with increasing sintering temperature at fixed NaCl/Al ratio.

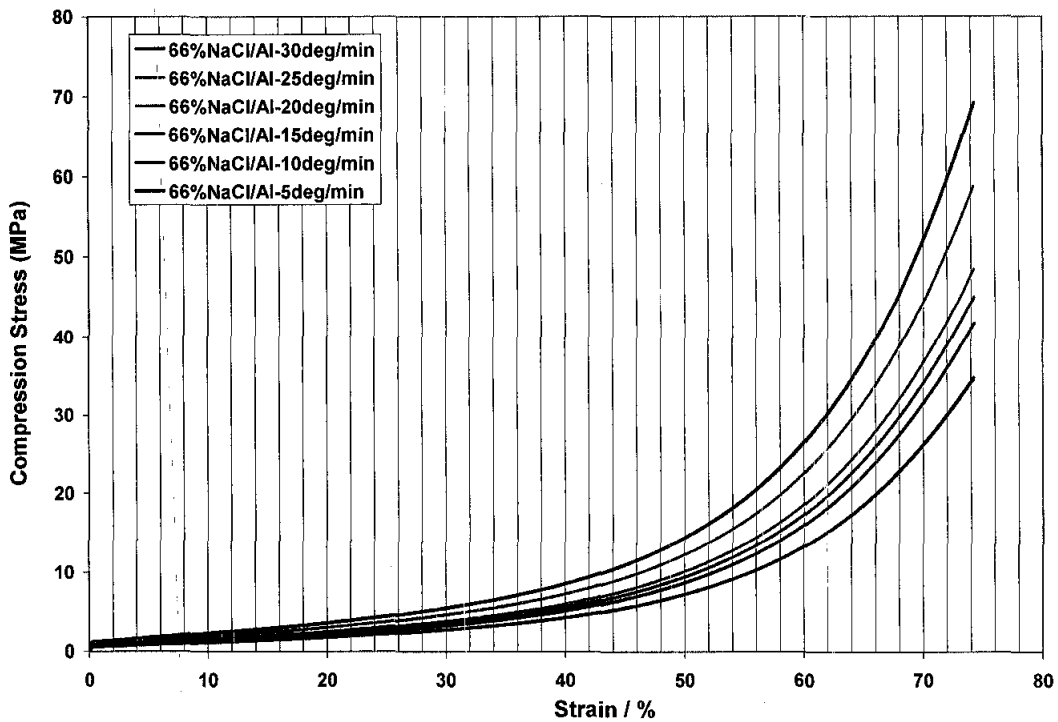


Figure 4.51: Compressive stress-strain curves of Al foam at different heating rate

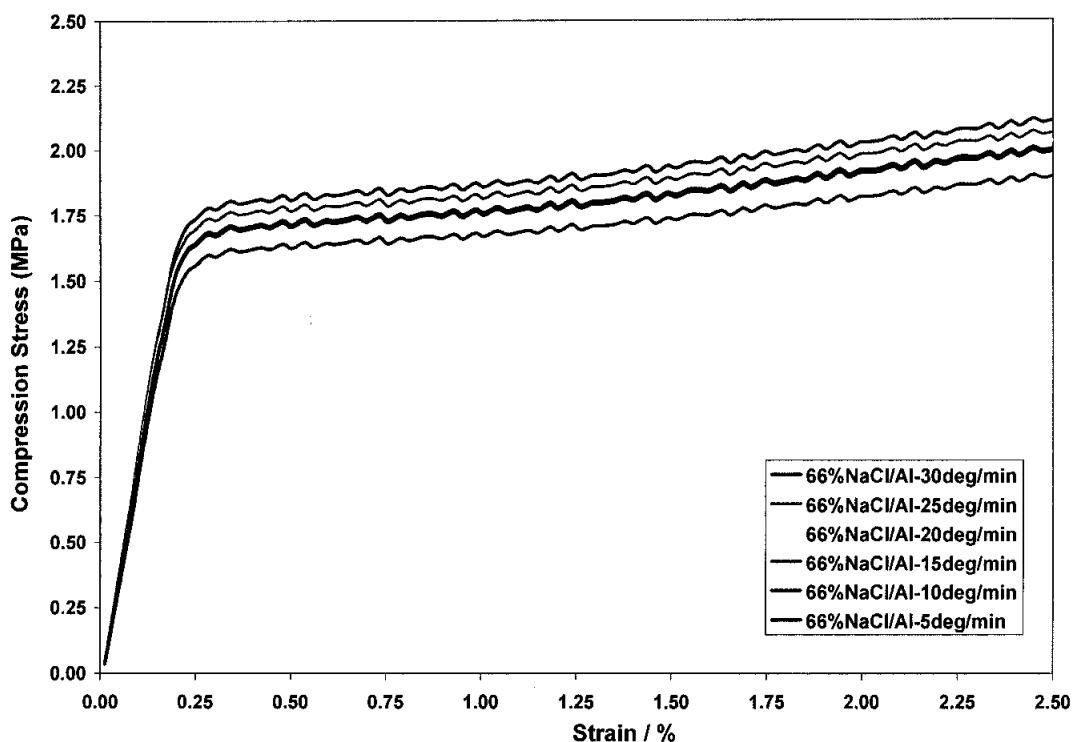


Figure 4.52: Enlarge portion of the beginning of the compressive stress-strain curves of Al foam at different heating rate.

From Figure 4.52, it can be seen that with an increase heating rate, the compressive properties of foam increase at fixed NaCl/Al volumr fraction. The grain growth of the samples will be reduced at high heating rate which lead to high final density and hence the compressive properties of the samples.

The influence of heating rate on the compressive strength is significant and the property increases when the heating rate is increased for all different volume fraction of NaCl/Al (Figure 4.53). It can be observed that the property depends on the heating rate and compressive strength increases from 1.59 MPa to 1.77 MPa with the increasing of heating rate of the PASDP process from 5 °C/min to 30 °C/min at fixed initial volume fraction of 66 % NaCl/Al. Meanwhile, at a fixed heating rate, the compressive strength of the specimen decreases with increasing NaCl/Al ratio. The compressive strength decreases from 2.05 MPa to 0.65 MPa when the initial volume fraction of NaCl/Al is increased from 60% to 80% at fixed heating rate of 20 °C/min.

Figure 4.54 reveals that the influence of heating rate on the modulus of the foam is significant and the modulus increase when the heating rate of the process is

increased for all different volume fraction of NaCl/Al. The scaling law of Gibson and Ashby clearly governs the effect of heating rate on the modulus properties of the specimens [8]. The compressive modulus of initial volume fraction of 64% NaCl/Al foam increases from 0.56 GPa to 0.60 GPa when the heating rate is increased from 5 °C/min to 30 °C/min.

The influence of density (varying the volume fraction of NaCl) on the compressive strength at densification (σ_{dens}) is obvious as presented in Figure 4.55. At (20 °C/min), it decreases from 19.02 MPa to 3.04 MPa when the initial volume fraction of NaCl is increased from 60% to 80%. The σ_{dens} shows an increase in value when the heating rate is increased at fixed initial volume fraction of NaCl/Al. For sample 60% volume fraction of NaCl, σ_{dens} increases from 18.53 MPa to 19.12 MPa when the heating rate is increased from 5 °C/min to 30 °C/min. The σ_{dens} increased from 13.02 MPa to 15.98 MPa when the heating rate is increased from 5 °C/min to 30 °C/min for sample 64% volume fraction of NaCl. When the heating rate is increased from 5 °C/min to 30 °C/min, the σ_{dens} of sample 66% volume fraction of NaCl increases from 12.47 MPa to 14.28 MPa. For sample 70% volume fraction of NaCl, σ_{dens} increases from 9.91 MPa to 10.60 MPa when the heating rate is increased from 5 °C/min to 30 °C/min.

The heating rate or the densities of the foams affect the deformation at densification properties. From Figure 4.56, it can be observed that the ϵ_{dens} increase from 31.44% to 56.16% when the volume fraction of NaCl is increased from 60% to 80% at fixed heating rate of 30 °C/min. The ϵ_{dens} show a decrease in value when the heating rate is increased at fixed volume fraction of NaCl/Al. For sample 60% volume fraction of NaCl, ϵ_{dens} decreases from 32.37% to 31.44% when the heating rate is increased from 5 °C/min to 30 °C/min. The ϵ_{dens} decrease from 40.72% to 36.37% when the heating rate is increased from 5 °C/min to 30 °C/min for sample 64% volume fraction of NaCl. When the heating rate is increased from 5 °C/min to 30 °C/min, the ϵ_{dens} of NaCl/Al foam with initial volume fraction of 66% decreases from 41.86% to 39.02%. For sample of 70% volume fraction of NaCl, ϵ_{dens} decreases from 45.87% to 44.79% when the heating rate is increased from 5 °C/min to 30 °C/min.

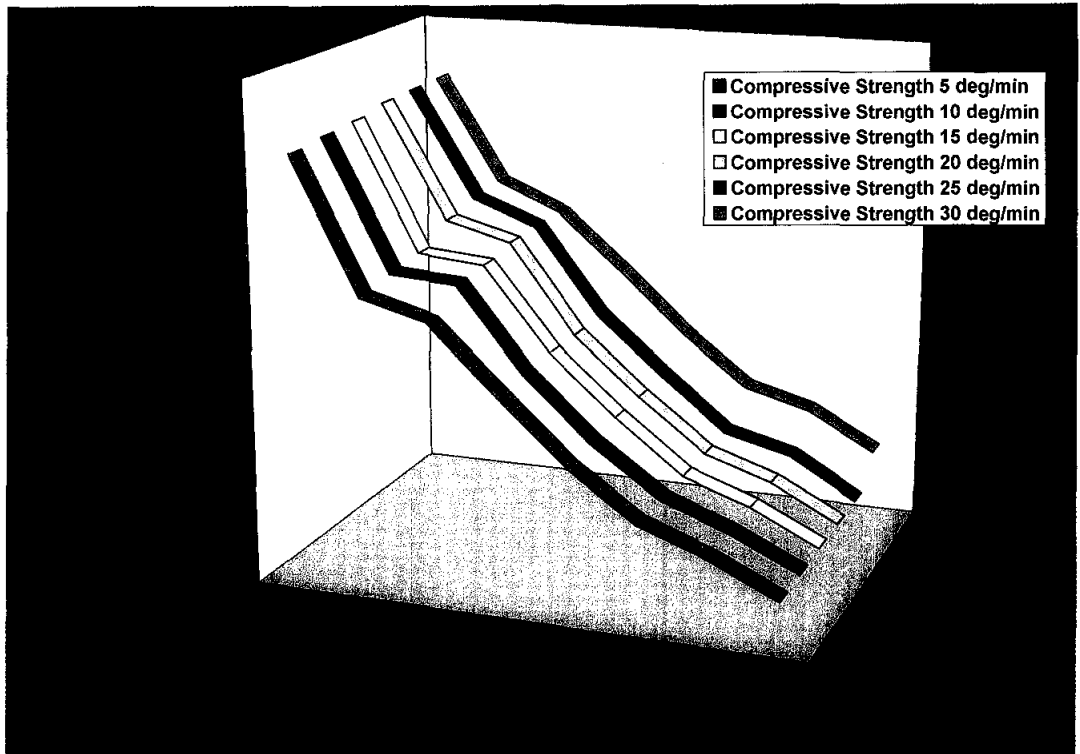


Figure 4.53: Variation of compressive strength of Al foam with heating rate at different NaCl/Al volume fraction

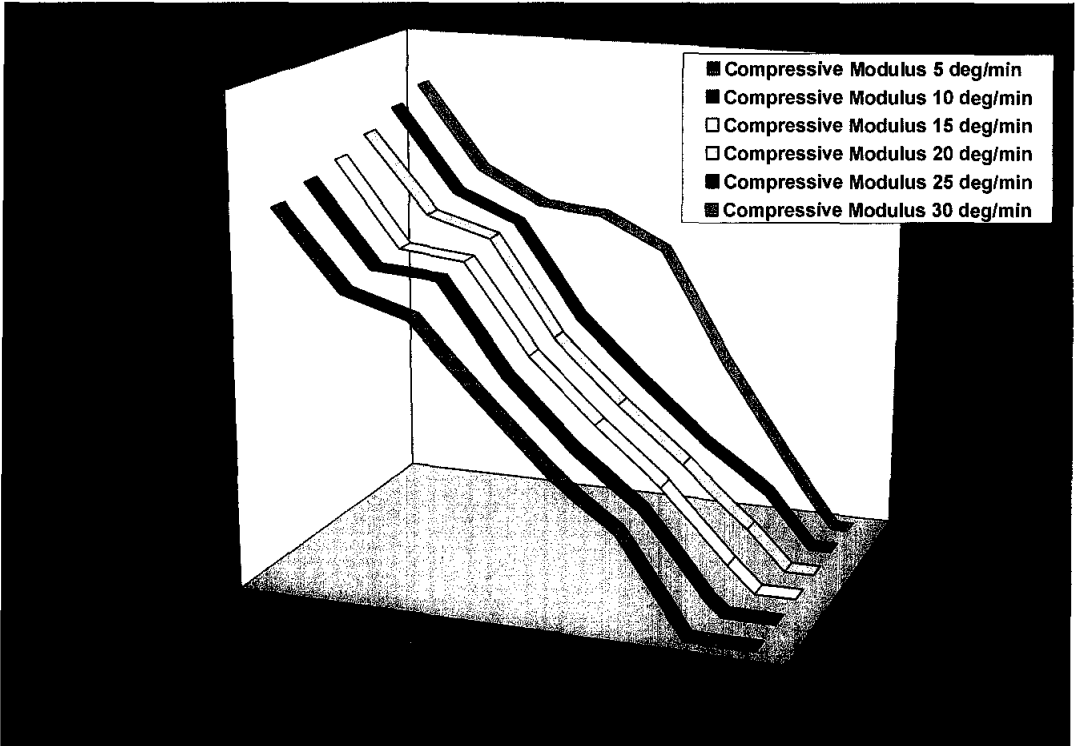


Figure 4.54: Variation of compressive modulus of Al foam with heating rate at different NaCl/Al volume fraction

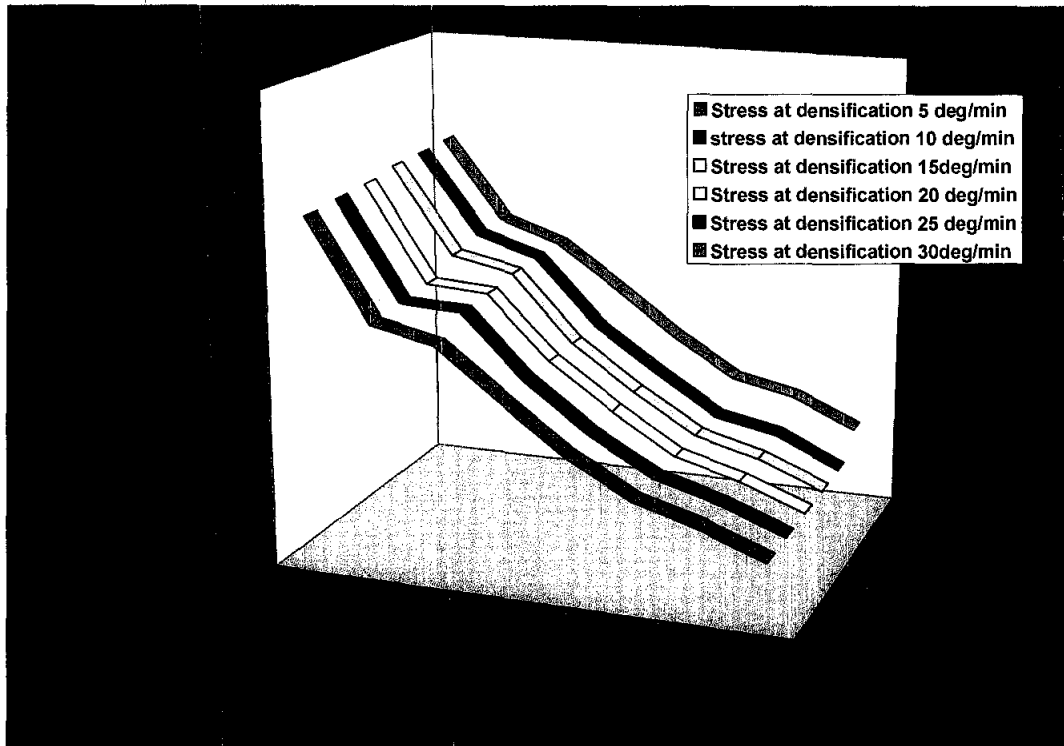


Figure 4.55: Variation of strength at densification of Al foam with heating rate at different NaCl/Al volume fraction

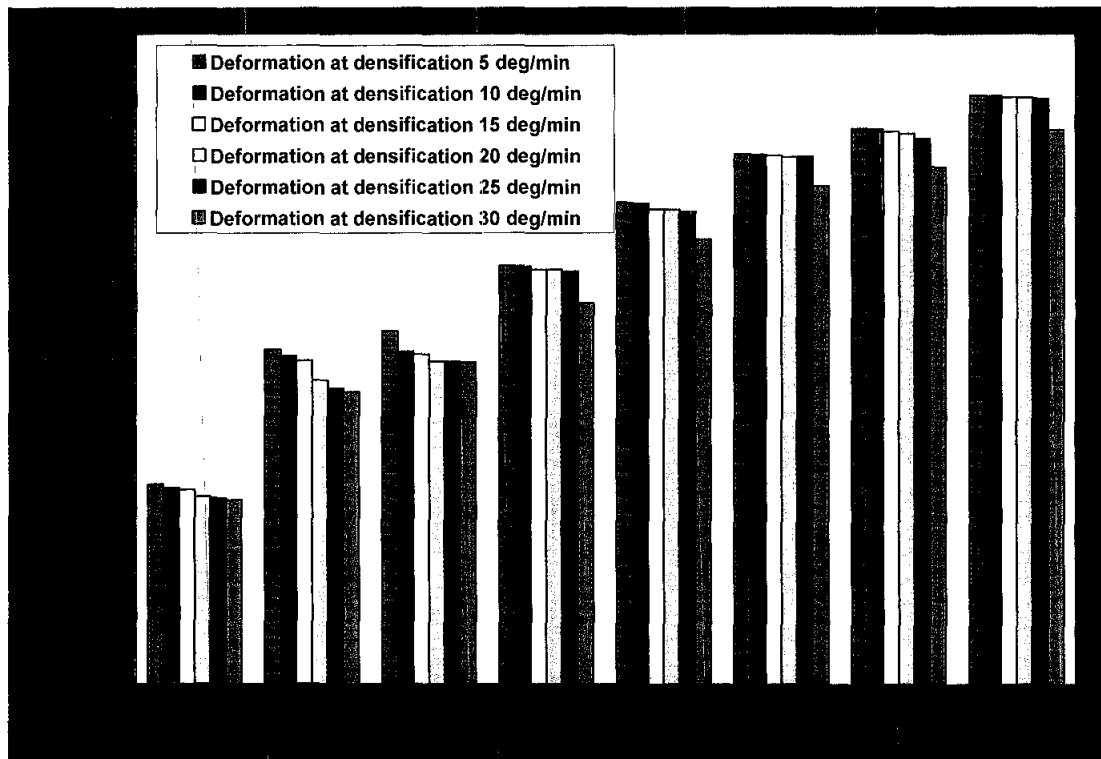


Figure 4.56: Variation of deformation at densification of Al foam with heating rate at different NaCl/Al volume fraction

4.4.5 The modulus and compressive strength of aluminium foam

The effect of density on the modulus and compressive strength of metallic foams has been widely reported and models have been proposed to describe the yield strength and modulus as a function of density such as Gibson and Ashby scaling laws [1]:

$$E_f = \alpha E_s \left(\frac{\rho_f}{\rho_s} \right)^n \quad (4.4)$$

and

$$\sigma_f = \beta \sigma_s \left(\frac{\rho_f}{\rho_s} \right)^m \quad (4.5)$$

where α and β are the scaling law coefficients for the compressive modulus and yield strength, E_s and σ_s are respectively the compression modulus and compressive yield stress of the dense metal and ρ_f and ρ_s are the density of foam and dense metal respectively.

The value of n which is the value of the slope by plotting logarithm of relative compressive modulus with logarithm of relative density for compaction pressure of 20, 40, 60, 80, 100 and 120 MPa is 0.7943, 0.7949, 0.7960, 0.7989, 0.8013 and 0.8256 (Figures 4.57 (a)-(f)) respectively. The value of α attained from the experiment is 0.0191, 0.0192, 0.0192, 0.0193, 0.0193 and 0.0199 respectively. Although equation (4.4), as described by Kriszt [150], is based on a simple model of cubic foam structure, which considerably deviates from real foam, it exhibits fair agreement with experimental results. According to him, this equation is valid as long as the main deformation mechanism is the bending of cell edges and, for high density foam, extension and compression of cell edges become more important and therefore, a deviation from these relations should become apparent.

By plotting logarithm of relative compressive modulus with logarithm of relative density for sintering temperature of 570, 580, 590, 600, 610 and 620°C, the obtained slope which is the value of n is 0.8457, 0.7743, 0.7985, 0.7993, 0.8016 and 0.8256

(Figures 4.58 (a)-(f)) respectively. The value of α attained from the experiment is 0.0207, 0.0186, 0.0193, 0.0193, 0.0193 and 0.0199 respectively.

The value of n which is the value of the slope by plotting logarithm of relative compressive modulus with logarithm of relative density for sintering time of , 5, 10, 15, 25 and 30 min is 0.7953, 0.7974, 0.7982, 0.7987, 0.8012 and 0.8256 (Figures 4.59 (a)-(f)) respectively. The value of α attained from the experiment is 0.0191, 0.0192, 0.0192, 0.0193, 0.0193 and 0.0199 respectively.

By plotting logarithm of relative compressive modulus with logarithm of relative density for heating rate of 5, 10, 15, 20, 25 and 30°Cmin⁻¹, the obtained slope which is the value of n is 0.7944, 0.8001, 0.8006, 0.8018, 0.8087 and 0.8256 (Figures 4.60 (a)-(f)) respectively. The value of α attained from the experiment is 0.0193, 0.0193, 0.0193, 0.0193, 0.0195 and 0.0199 respectively.

In Figures 4.61 (a)-(f), data for logarithm of relative compressive strength with logarithm of relative density for compaction pressure of 20, 40, 60, 80, 100 and 120 MPa is plotted to test the relation equation (4.5) and to determine the exponent value m . The set of data appears to be linear. The exponent m which is determined by linear regression is 1.64, 1.67, 1.66, 1.64, 1.63 and 1.49 respectively for the foam sample. From the results obtained, there is good agreement between the experimental data and the theoretical yield strength. The value of C obtained from this experiment is 0.33, 0.34, 0.34, 0.33, 0.32 and 0.26 respectively and is in good agreement with the value obtained by Gibson and Ashby [1].

Figures 4.62 (a)-(f) reveal the plotted data for logarithm of relative compressive strength with logarithm of relative density of sintering temperature for 570, 580, 590, 600, 610 and 620°C according to equation (4.5), which also determines the exponent, m , of this equation. The set of data appears to be linear and the exponent determined by linear regression is 1.67, 1.65, 1.65, 1.64, 1.63 and 1.48 for foam sample. There is a fair compliance between the experimental data and the theoretical yield strength.

In Figures 4.63 (a)-(f), data for logarithm of relative compressive strength with logarithm of relative density for sintering time of , 5, 10, 15, 25 and 30 min is plotted to test the relation equation (4.5) and to determine the exponent value m . The set of

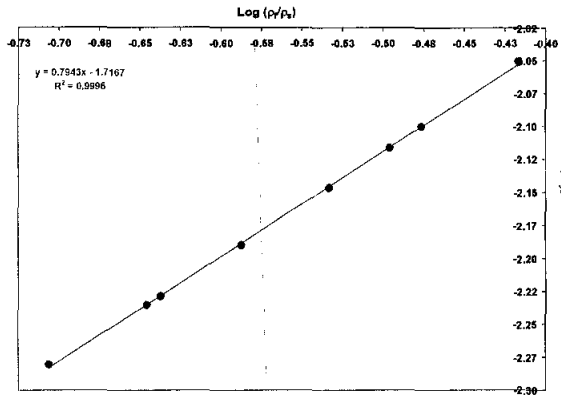
data appears to be linear. The exponent m which is determined by linear regression is 1.67, 1.65, 1.65, 1.64, 1.63 and 1.49 respectively for the foam sample. From the results obtained, there is good agreement between the experimental data and the theoretical yield strength. The value of C obtained from this experiment is 0.33, 0.32, 0.32, 0.33, 0.32 and 0.26 respectively and is in good agreement with the value obtained by Gibson and Ashby [1].

In Figures 4.64 (a)-(f), data for logarithm of relative compressive strength with logarithm of relative density for heating rate of 5, 10, 15, 20, 25 and 30°Cmin⁻¹ is plotted to test the relation equation (4.5) and to determine the exponent value m . The set of data appears to be linear. The exponent m which is determined by linear regression is 1.64, 1.64, 1.63, 1.63, 1.62 and 1.49 respectively for the foam sample. From the results obtained, there is good agreement between the experimental data and the theoretical yield strength. The value of C obtained from this experiment is 0.33, 0.34, 0.34, 0.33, 0.32 and 0.26 respectively and is in good agreement with the value obtained by Gibson and Ashby [1].

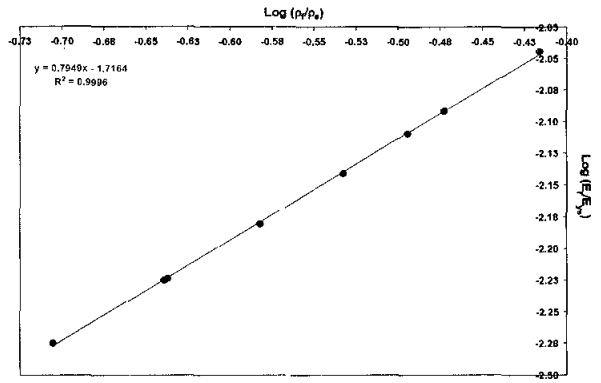
From the experimental results of various processing parameters, the number of specimens and the range of densities obtained in the study were sufficient to obtain good correlations. As can be seen from the data gathered, the values obtained fit the scaling laws, as indicated in figure. The coefficients estimated with these scaling laws are summarised in Table 4.10.

Table 4.10: Correlation coefficients of equations. (4.4) and (4.5) for the Al foams at different processing parameters

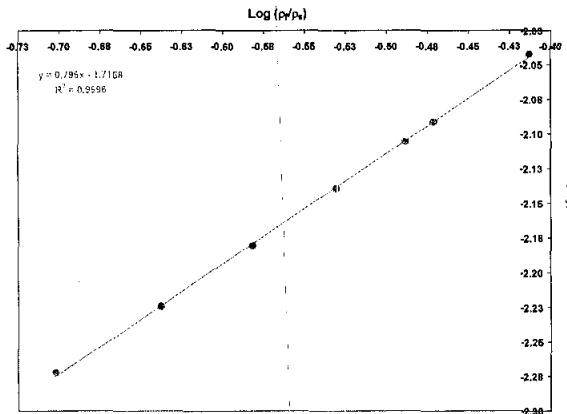
Pressure (MPa)	α	n	m	β
100	0.0193	0.8013	0.3274	1.6353
120	0.0199	0.8256	0.2671	1.4820
Sintering Temperature (°C)				
610	0.0193	0.8016	0.3260	1.6304
620	0.0195	0.8087	0.3085	1.5823
Sintering time (min)	n	α	m	β
25	0.0193	0.8012	0.3267	1.6317
30	0.0195	0.8087	0.3085	1.5823
Heating rate (°C/min)				
25	0.0195	0.8087	0.3235	1.6272
30	0.0194	0.8024	0.3085	1.5823



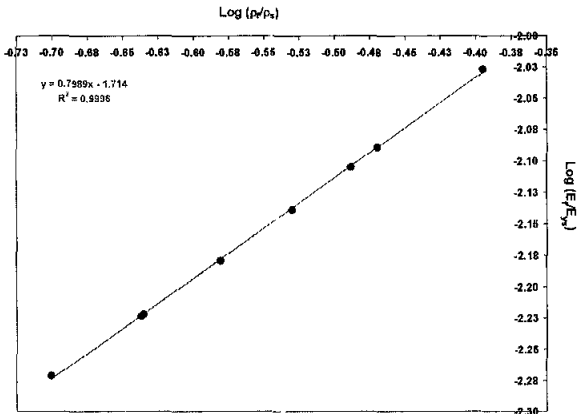
(a) Pressure : 20 MPa



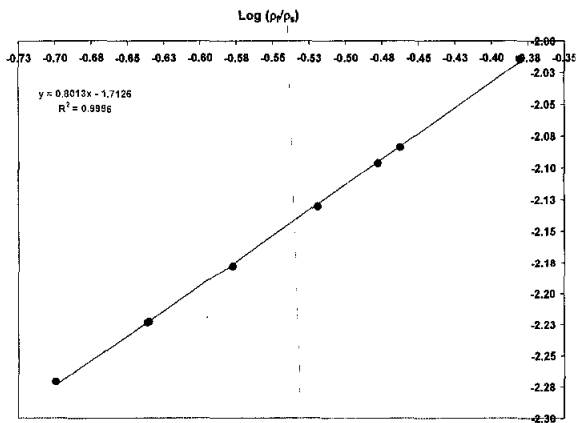
(b) Pressure : 40 MPa



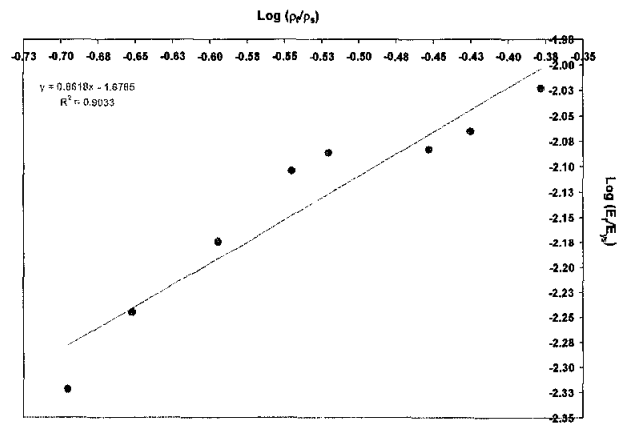
(c) Pressure : 60 MPa



(d) Pressure : 80 MPa

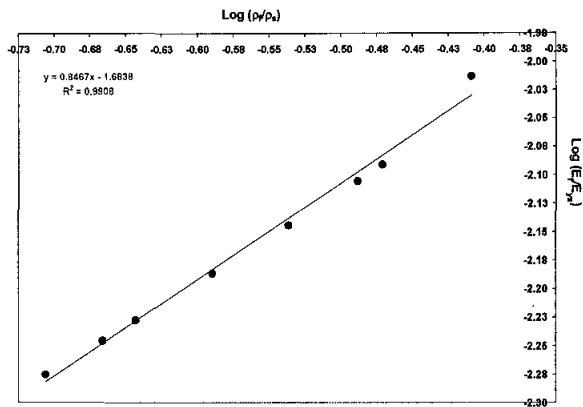


(e) Pressure : 100 MPa

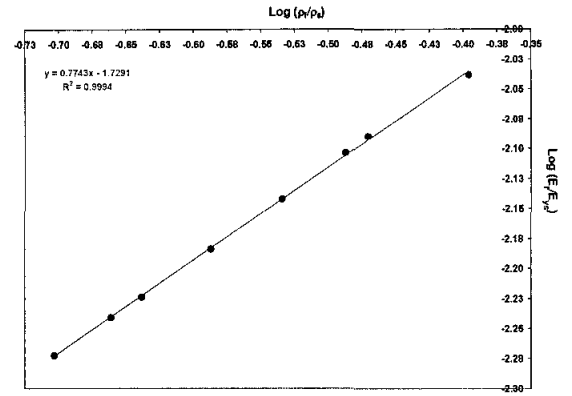


(f) Pressure : 120 MPa

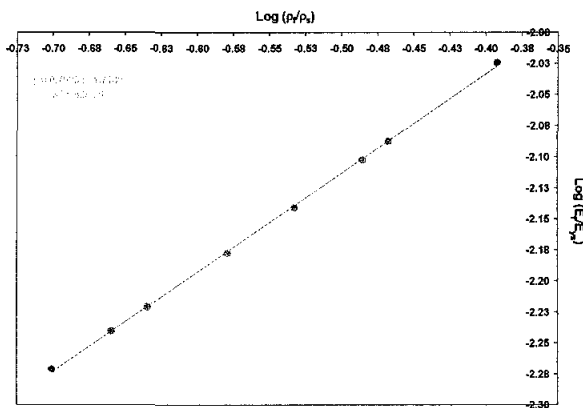
Figure 4.57: Relative Young's modulus of Al foam as function of relative density at various compaction pressures



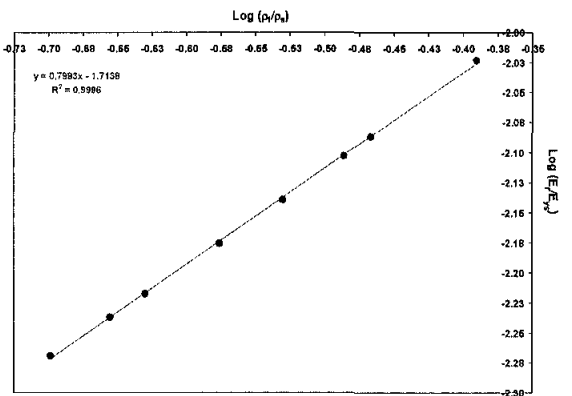
(a) Sintering temperature : 570 °C



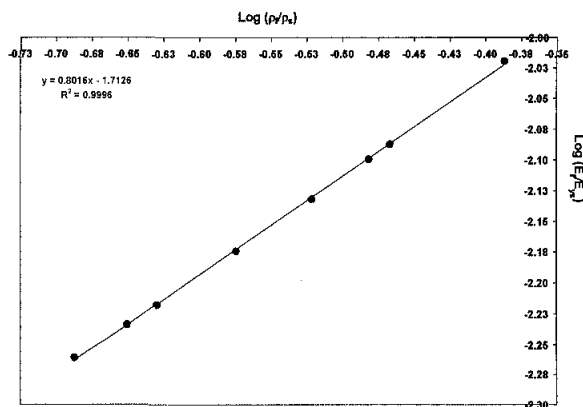
(b) Sintering temperature : 580 °C



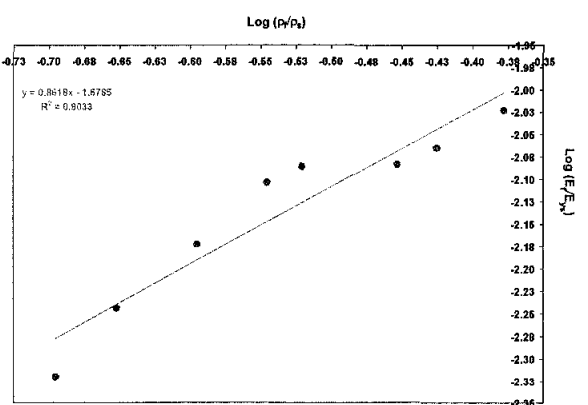
(c) Sintering temperature : 590 °C



(d) Sintering temperature : 600 °C

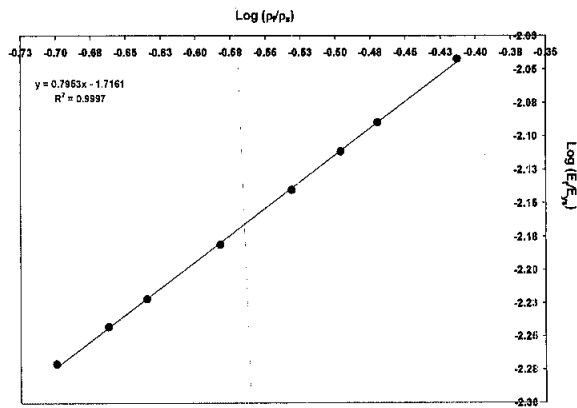


(e) Sintering temperature : 610 °C

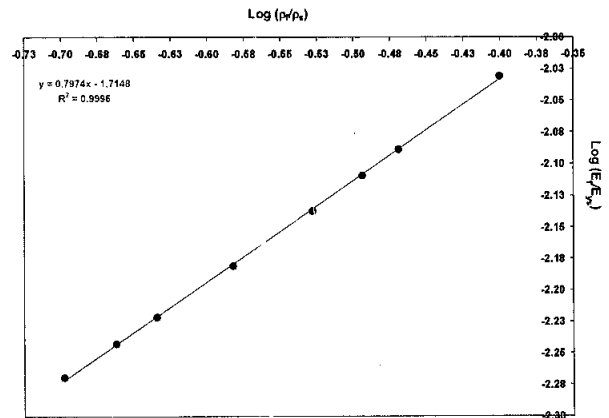


(f) Sintering temperature : 620 °C

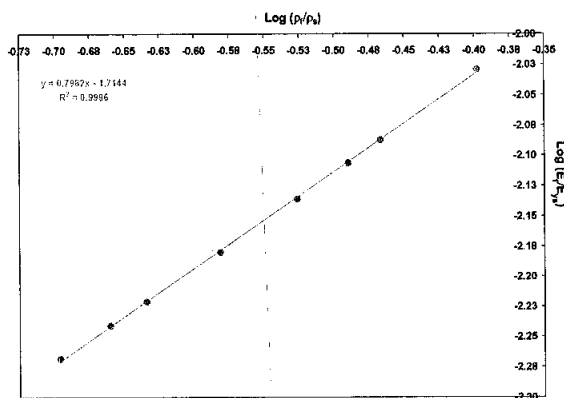
Figure 4.58: Relative Young's modulus of Al foam as function of relative density at various sintering temperatures



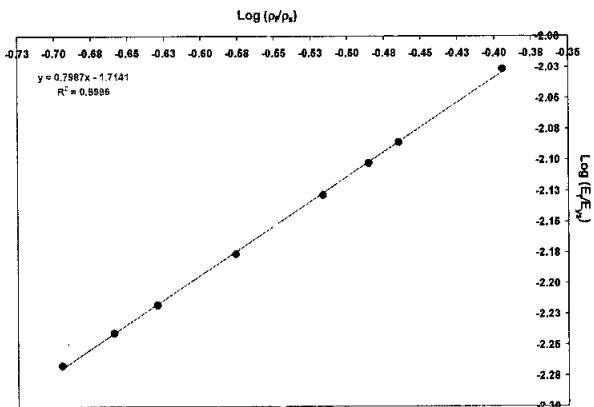
(a) Sintering time : 5 minutes



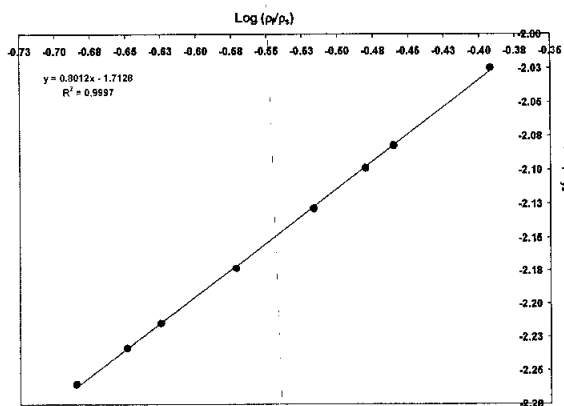
(b) Sintering time: 10 minutes



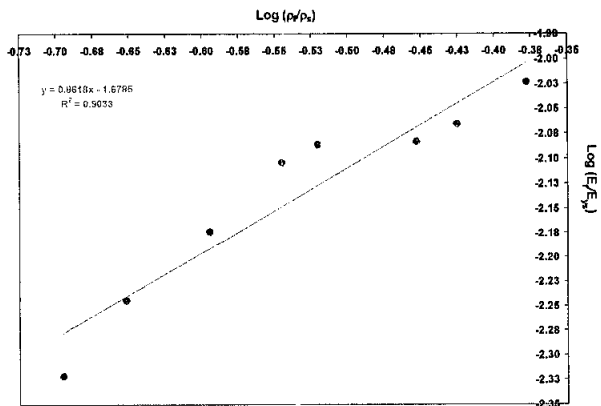
(c) Sintering time: 15 minutes



(d) Sintering time: 20 minutes

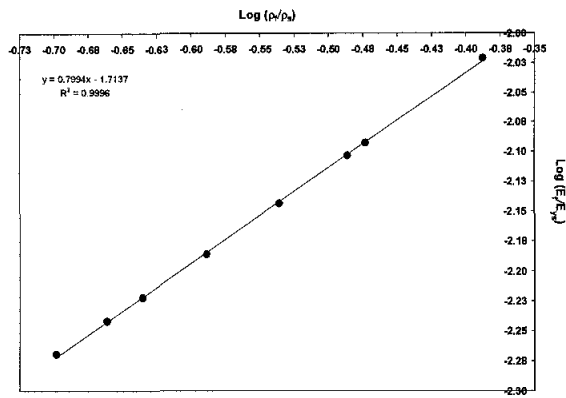


(e) Sintering time: 25 minutes

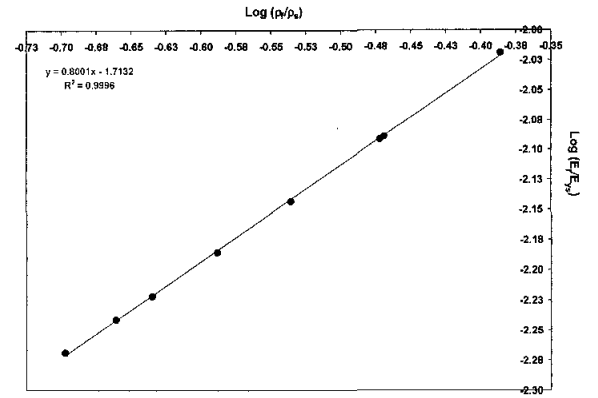


(f) Sintering time : 30 minutes

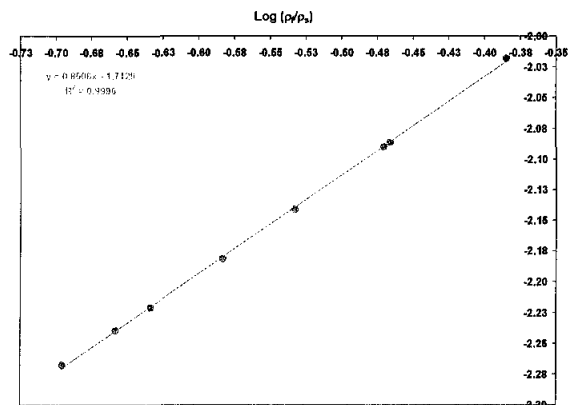
Figure 4.59: Relative Young's modulus of Al foam as function of relative density at various sintering time



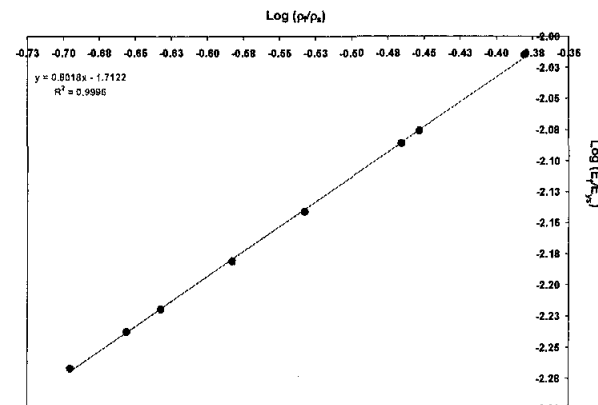
(a) Heating rate : 5 °C/min



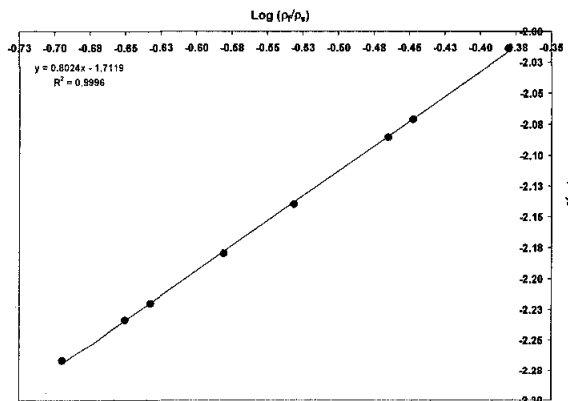
(b) Heating rate : 10 °C/min



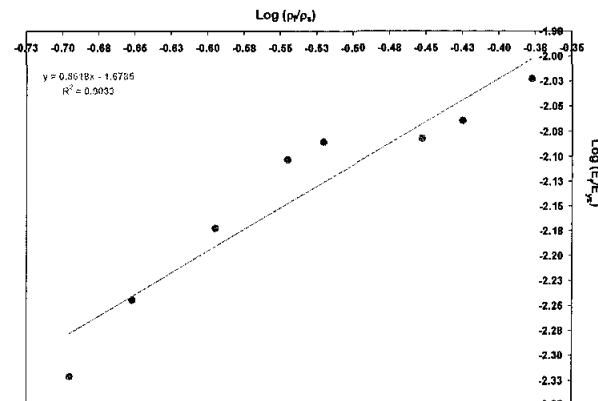
(c) Heating rate : 15 °C/min



(d) Heating rate : 20 °C/min

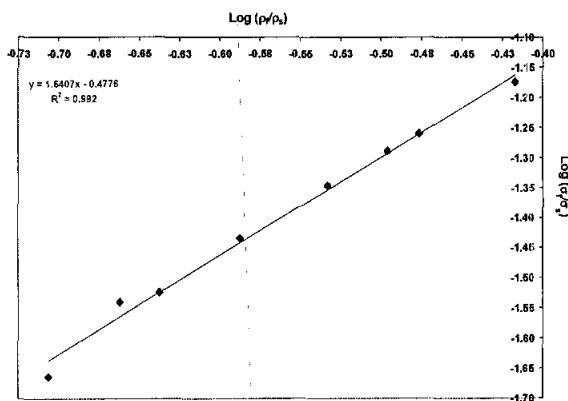


(e) Heating rate : 25 °C/min

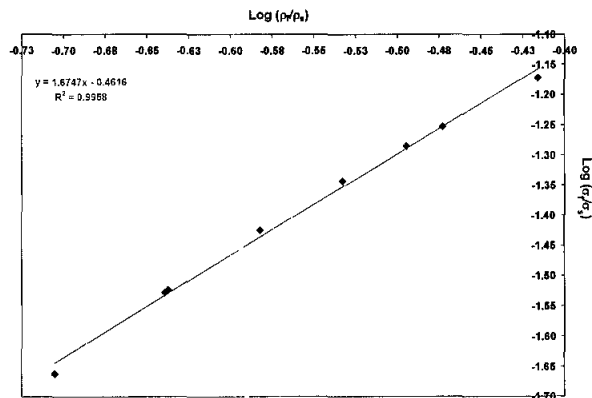


(f) Heating rate : 30 °C/min

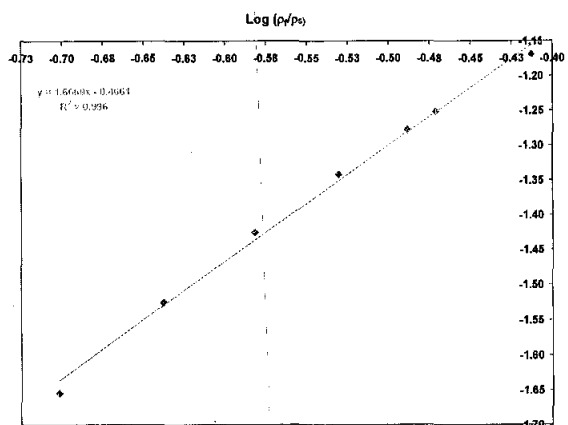
Figure 4.60: Relative Young's modulus of Al foam as function of relative density at various heating rate



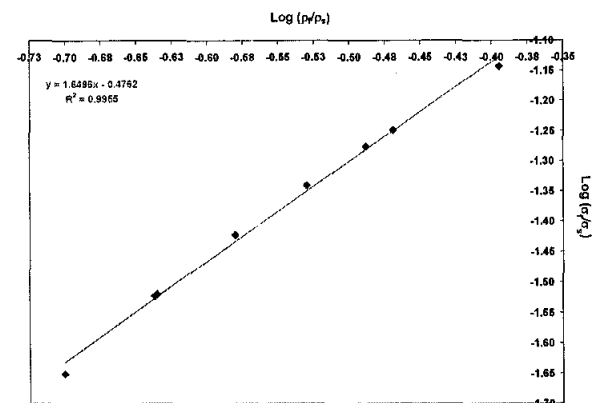
(a) Pressure : 20 MPa



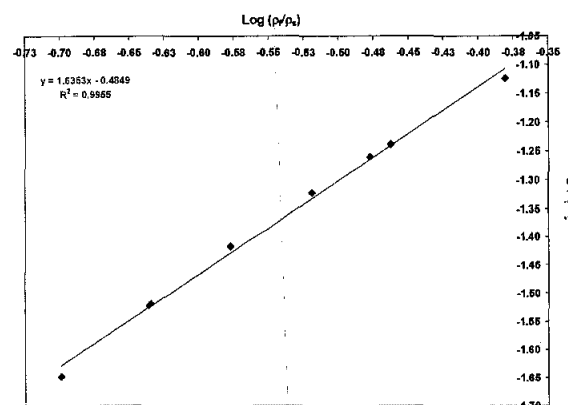
(b) Pressure : 40 MPa



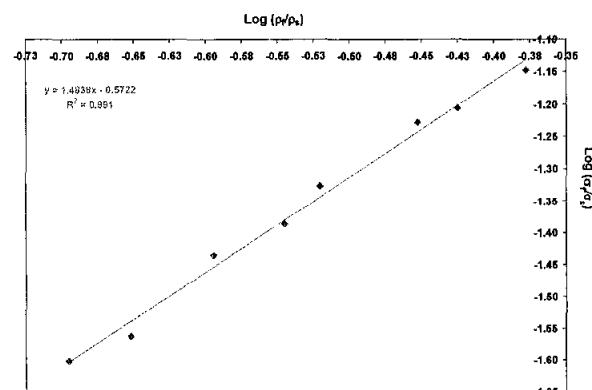
(c) Pressure : 60 MPa



(d) Pressure : 80 MPa

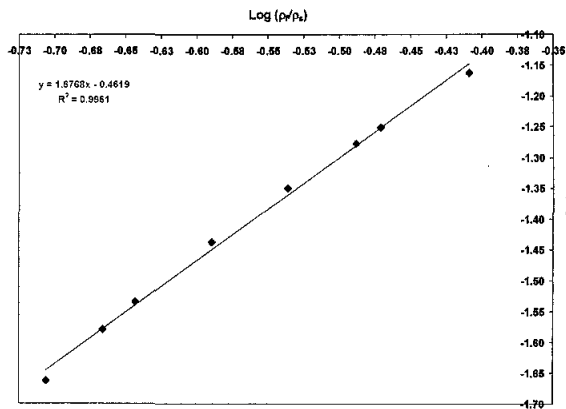


(d) Pressure : 100 MPa

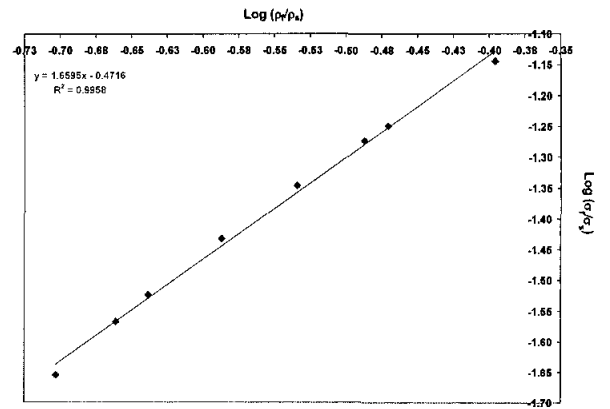


(e) Pressure : 120 MPa

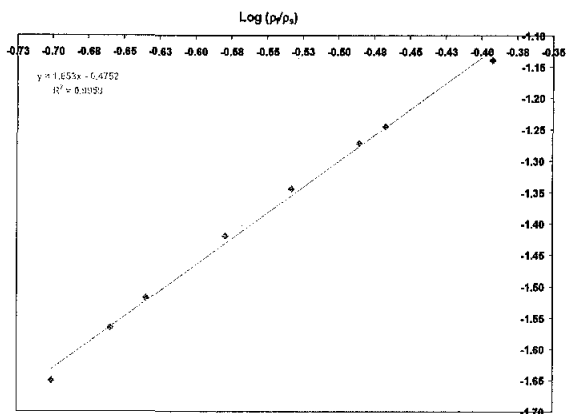
Figure 4.61: Relative compressive strength of Al foam as function of relative density at various compaction pressures



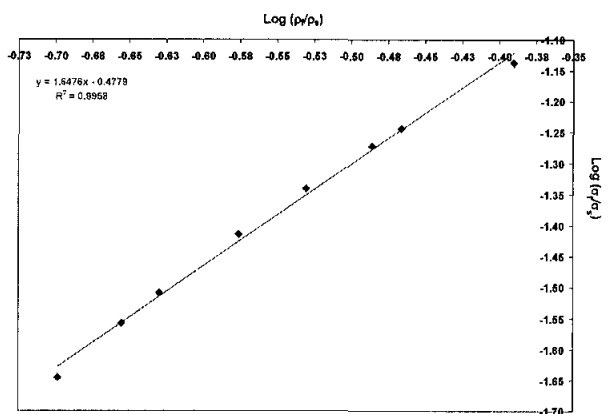
(a) Sintering temperature : 570 °C



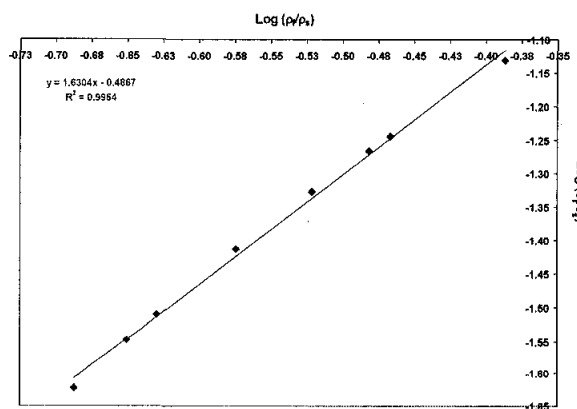
(b) Sintering temperature : 580 °C



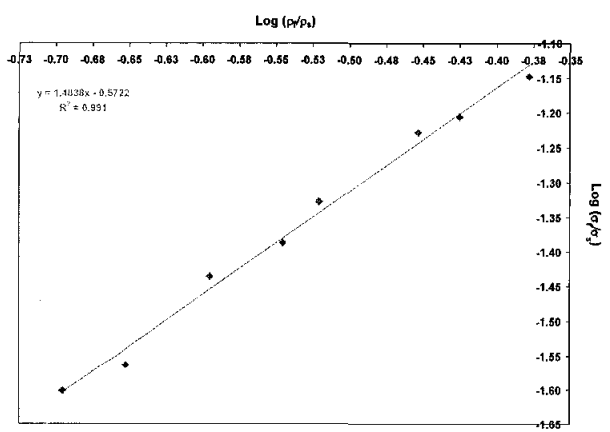
(c) Sintering temperature : 590 °C



(d) Sintering temperature : 600 °C

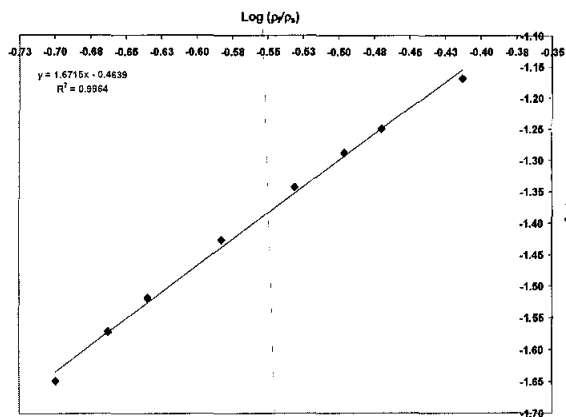


(d) Sintering temperature : 610 °C

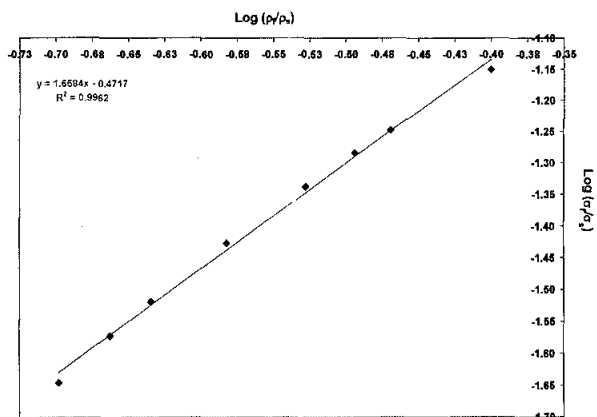


(f) Sintering temperature : 620 °C

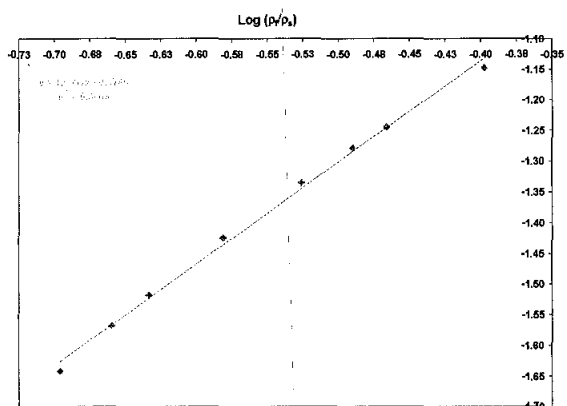
Figure 4.62: Relative compressive strength of Al foam as function of relative density at various sintering temperatures



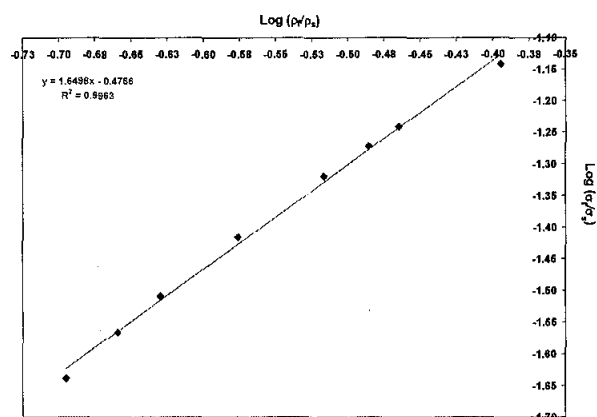
(a) Sintering time : 5 minutes



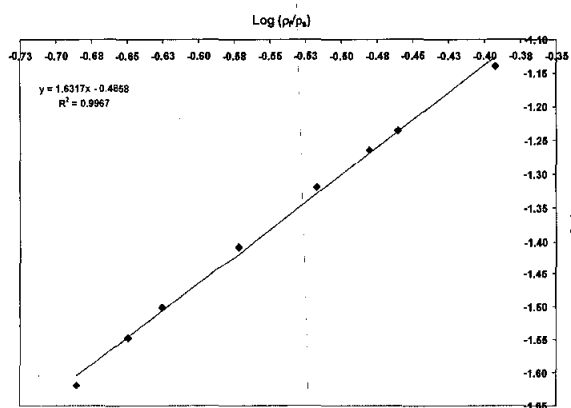
(b) Sintering time: 10 minutes



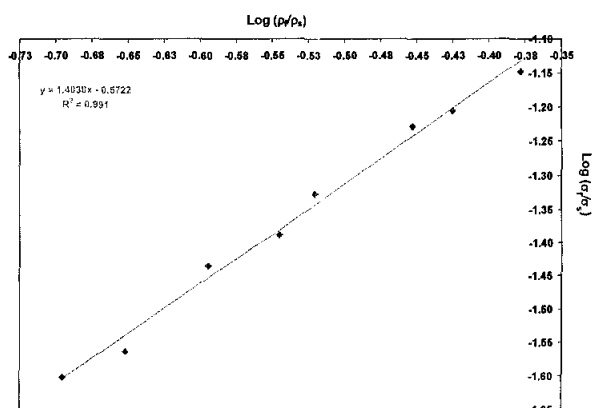
(c) Sintering time: 15 minutes



(d) Sintering time: 20 minutes

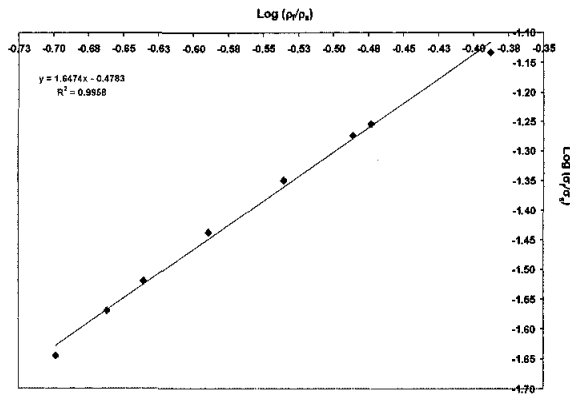


(e) Sintering time: 25 minutes

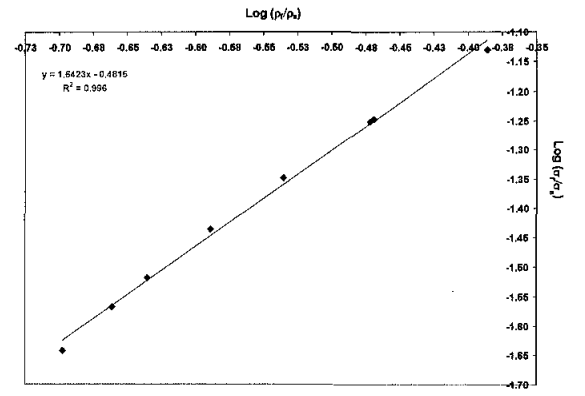


(f) Sintering time : 30 minutes

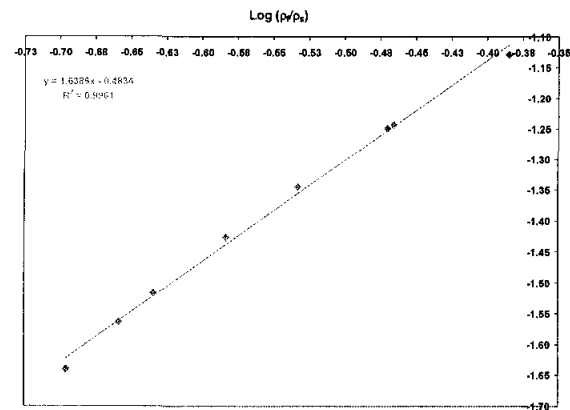
Figure 4.63: Relative compressive strength of Al foam as function of relative density at various sintering time



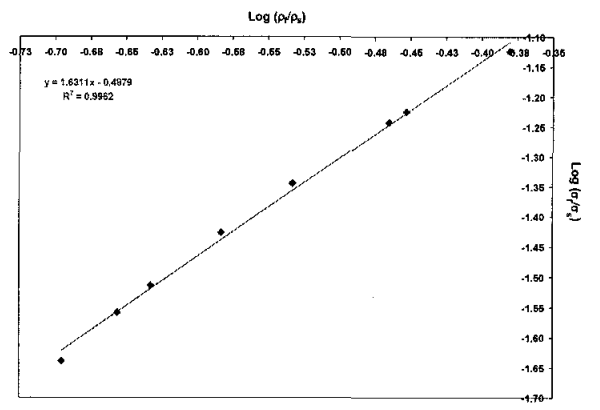
(a) Heating rate : 5 °C/min



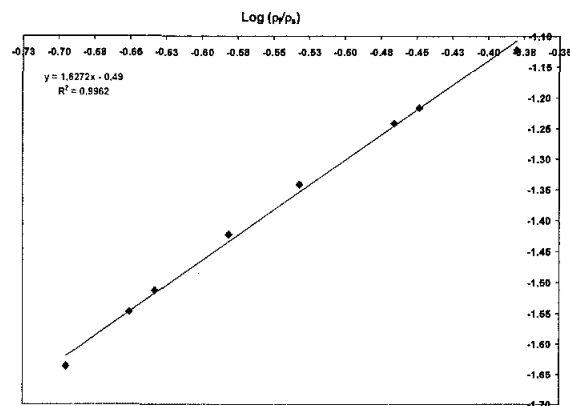
(b) Heating rate : 10 °C/min



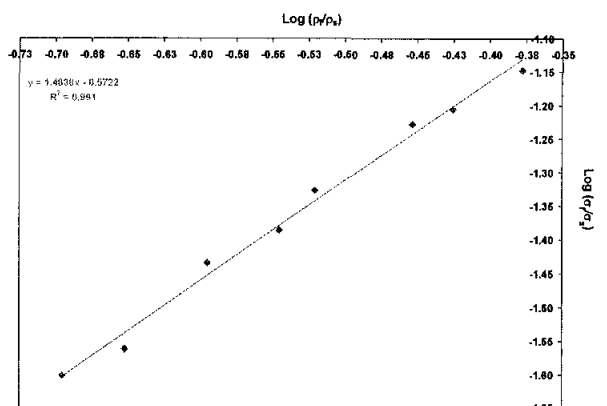
(c) Heating rate : 15 °C/min



(d) Heating rate : 20 °C/min



(e) Heating rate : 25 °C/min



(f) Heating rate : 30 °C/min

Figure 4.64: Relative compressive strength of Al foam as function of relative density at various heating rate

4.4.6 The energy absorbing capabilities

The majority of the absorbed energy is irreversibly converted into plastic deformation energy [54]. This occurs primarily in the broad stress plateau, which is typical of most metallic foams under compression loading and imparts a large capacity for energy absorption. During the stress plateau, energy is absorbed largely by the bending and collapse of cell walls in the foam. When the mechanism is exhausted, the stress begins to rise and the material is densified. The magnitude (or 'height') of the stress plateau is strongly affected by the intrinsic yield strength of the metal [54]-[56].

The energy absorbed per unit volume, W , defined as the area under the stress-strain curve obtained prior to the onset of densification, was estimated from the compression stress-strain data up to the onset of densification strain, ε_D , using the following relation:

$$W = \int_{\varepsilon_1}^{\varepsilon_2} \sigma(\varepsilon) d\varepsilon \quad (4.6)$$

The energy absorption efficiency for a given strain value is defined as the ratio of the deformation energy absorbed by a real material to the deformation energy absorbed by an ideal energy absorber [1], [54]. In Figure 4.65, the area under the stress-strain curve represents the real amount of energy, which is converted into deformation work. An ideal absorber shows a rectangular stress-strain curve, the area of which is defined by the maximum stress and strain values (as perfectly plastic behaviour). Therefore the efficiency η is given by the real absorbed energy after a compression strain s divided by the energy absorption of the ideal absorber:

$$\eta = \frac{\int_{\varepsilon_1}^{\varepsilon_2} \sigma(\varepsilon) d\varepsilon}{\sigma_o(\varepsilon_2 - \varepsilon_1)} \quad (4.7)$$

The plastic collapse of cells can be considered to occur at a constant stress until densification and neglecting the initial elastic contribution; equation. (4.6) can be written as:

$$W = \sigma^* \varepsilon_D \quad (4.8)$$

which indicates that W is largely determined by the inherent deformation characteristic of the materials through σ^* [54]. Since the value of W have been computed at a fixed ε_D of 57%, equation (4.8) implies that the variability in W should be similar to the variability in σ^* , and is consistent with the experimental observation.

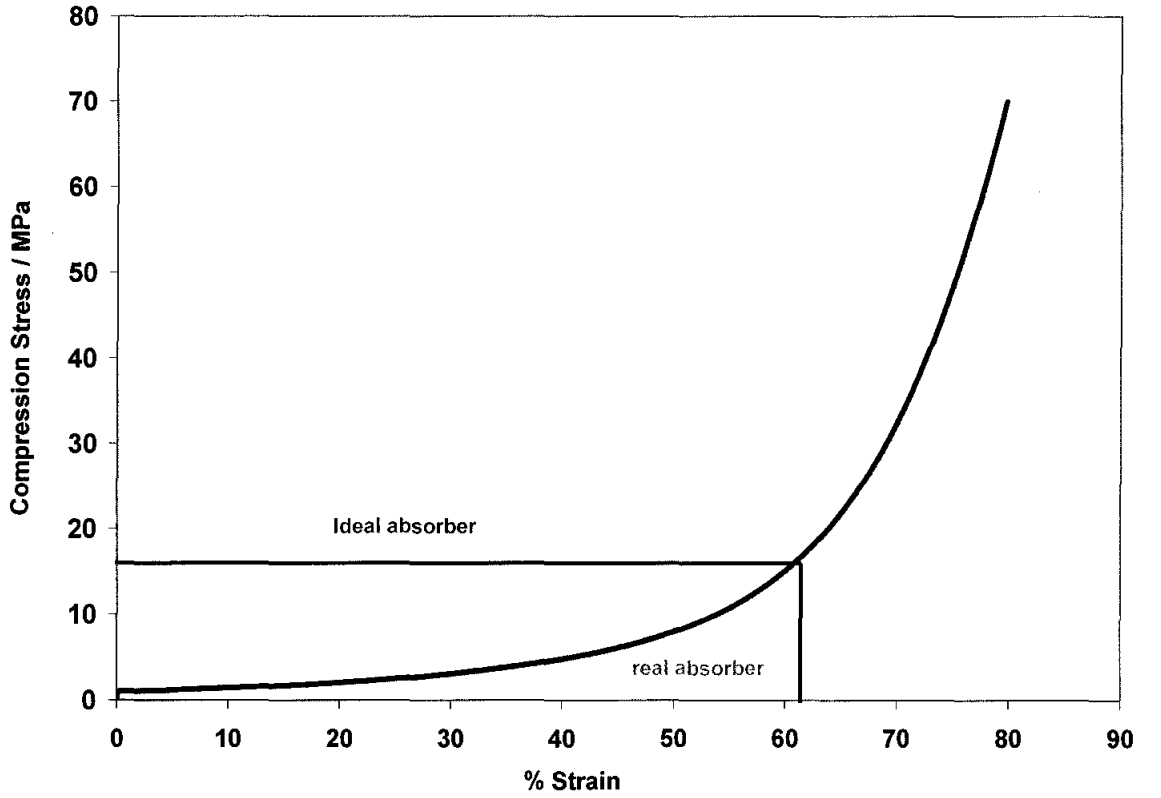


Figure 4.65: The energy absorbing efficiency, η , is the ratio between absorbed energy of the material and absorbed energy of an ideal plastic material in a certain strain range

To examine the validity of equation (4.8), W is plotted against σ^* in Figures 4.66 to 4.69 for all processing parameters used in the fabrication of Al foams. As expected, a linear trend between W and σ^* was obtained. Curve-fitting a linear equation to the entire data yields the ε_D of 56%, very close to that used in experimentally evaluating W .

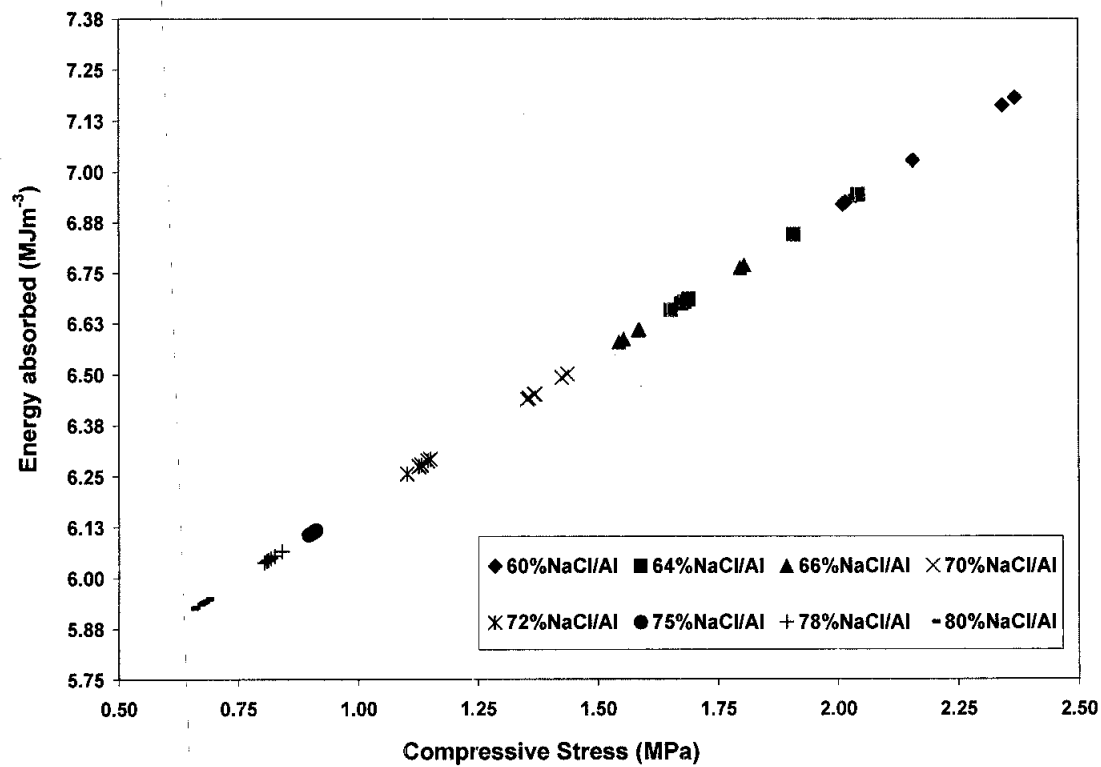


Figure 4.66: Variation of energy absorbed with compressive strength of different NaCl/Al volume fraction at different compaction pressure

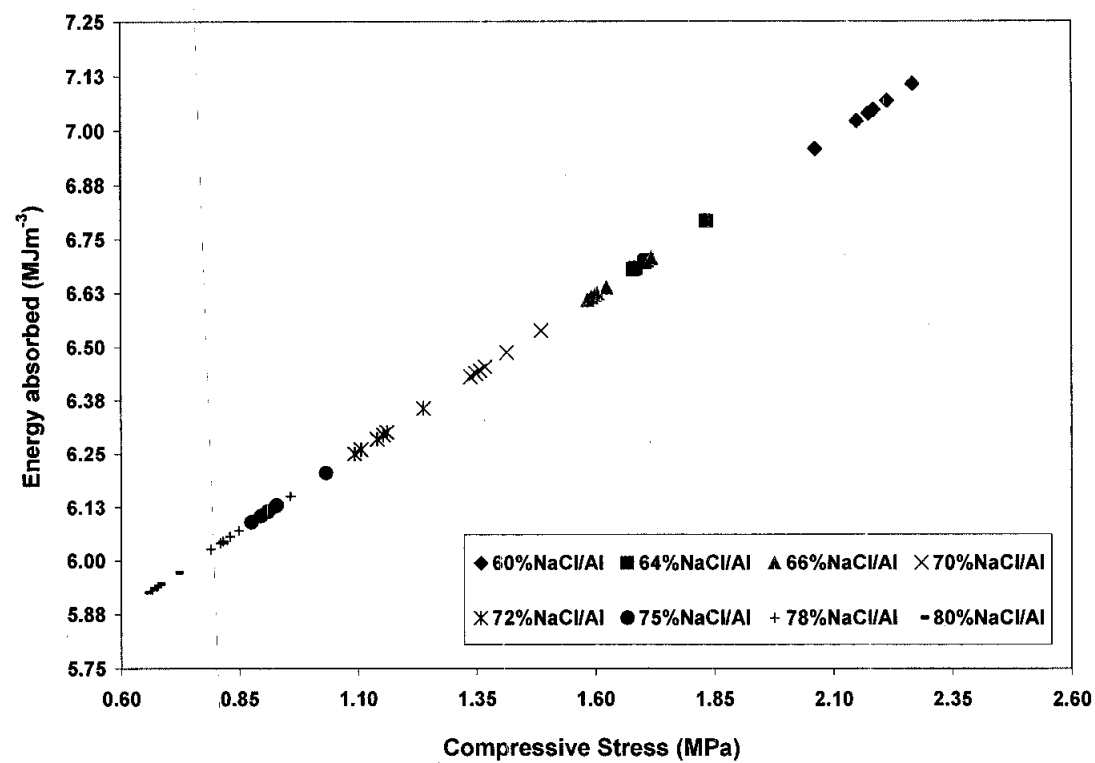


Figure 4.67: Variation of energy absorbed with compressive strength of different NaCl/Al volume fraction at different sintering temperature

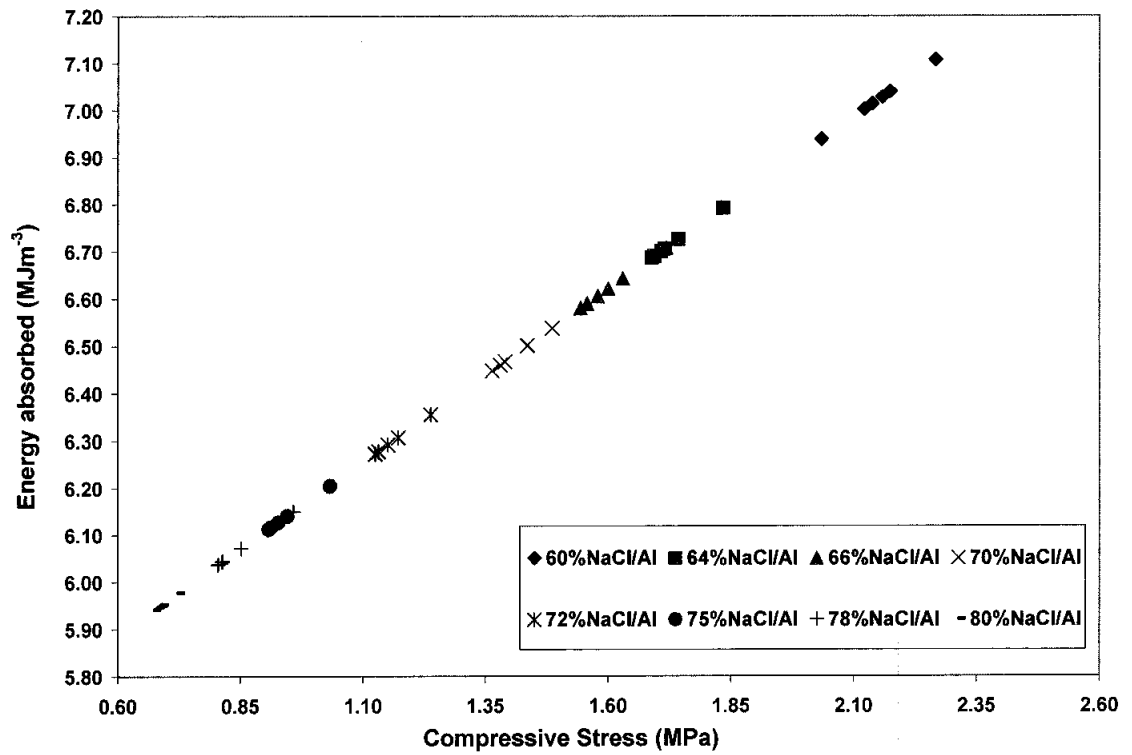


Figure 4.68: Variation of energy absorbed with compressive strength of different NaCl/Al volume fraction at different sintering time

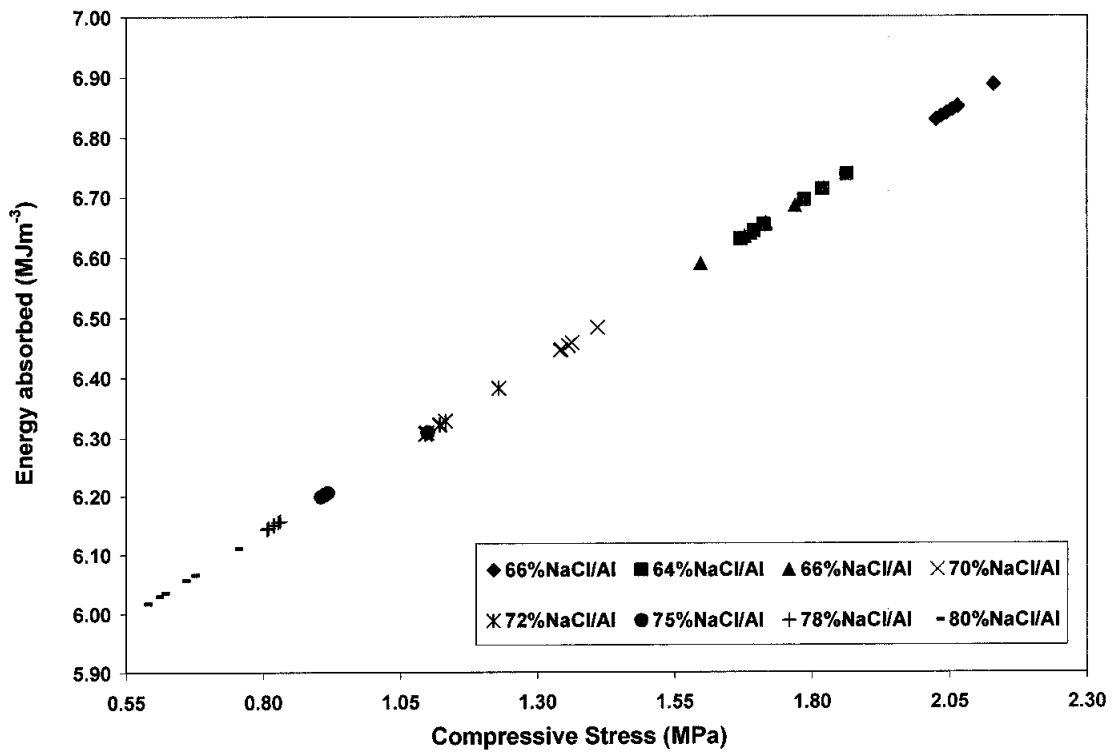


Figure 4.69: Variation of energy absorbed with compressive strength of different NaCl/Al volume fraction at different heating rate

4.5 Determination of the optimum processing parameters for the fabrication aluminium foam using Taguchi method

Considering all contributing factors from previous section in forming the Al foam using PASDP method, statistical evaluation utilizing the Taguchi's Design of Experiments were carried out extensively to predict the optimum processing parameters in this work. This principal of Taguchi method were employed in characterizing and optimizing the processing parameters for the fabrication of Al foams. The effects of four processing parameters: sintering time, sintering temperature, heating rate and compaction pressure at elevated temperature on the properties of final foam were studied. Results were analysed based on Taguchi's signal to noise ratio (S/N) and analysis of variance (ANOVA) techniques in order to obtain the optimum combination of the process parameters setting. Results indicate that the most notable factor influencing the fabrication of Al foam was the compaction at elevated temperature, followed by temperature, time and the process heating rate.

It is obvious that NaCl/Al volume fraction is the most important parameter affecting relative density and compressive strength of the foam. As compressive strength depends on the foam density, in this section (on statistical optimization of processing parameters), the composition of the NaCl/Al composite is kept constant, hence the foam properties are only attributed to the effects of processing parameters, and not caused by the specimen composition. It was also demonstrated that the Al foam with an initial volume fraction of 60% exhibits typical metallic foam characteristics when subjected to compression mode loading, and contains only a small amount of NaCl residue in the resultant foam. This volume fraction of NaCl will be used as the minimum volume fraction of the specimens in the next study, to investigate the influence of processing parameters on the physical and mechanical properties of Al foam fabricated through the PASDP technique.

The results of the nine trial conditions, with three run per trial condition are shown in Table 4.11. It was described [92], [93] that three types of quality characteristics with respect to the target in Taguchi's analysis method, i.e. 'smaller is

better', 'nominal is better' and 'bigger is better'. In this study, higher compressive strength is desirable qualities, and thus, were categorized in the 'bigger is better' quality characteristic. Column four in Tables 4.11 gives the Mean Squared Deviation (MSD). These were transformed into the respective signal to noise ratios (S/N), the values of which are given in the last column of Tables 4.11.

The mean squared deviation for the 'bigger is better' quality characteristic is given by:

$$MSD = \frac{\left(\frac{1}{R_1^2} + \frac{1}{R_2^2} + \frac{1}{R_3^2} \right)}{3} \quad (4.9)$$

The signal to noise ratio was computed as follow:

$$S / N = -10\log(MSD) \quad (4.10)$$

Table 4.11: Experimental results and their S/N ratios

Trial No.	Compressive strength (MPa)			MSD	S/N
	R ₁	R ₂	R ₃		
1	1.035	1.035	1.034	0.934	0.299
2	1.102	1.102	1.102	0.823	0.844
3	1.691	1.691	1.690	0.350	4.563
4	1.710	1.710	1.711	0.342	4.660
5	1.006	1.004	1.004	0.990	0.043
6	1.750	1.750	1.752	0.327	4.861
7	1.163	1.164	1.163	0.739	1.315
8	1.802	1.800	1.800	0.308	5.110
9	1.610	1.611	1.610	0.386	4.139
Mean					2.870

The average effects of the factors for each level were shown in Table 4.12. For an example, the compaction pressure was at level three for trial condition 3, 4 and 8 in the array.

Table 4.12: The average effects on compressive strength of factors at each level

Column	Factors	Average Effects		
		Level 1	Level 2	Level 3
1	Time	1.90	3.19	3.52
2	Temperature	2.09	2.00	4.52
3	Heating Rate	3.42	3.21	1.97
4	Compaction Pressure	1.49	2.34	4.78

In other words, number 3 appeared at trial 3, 4 and 8 in column 4 of Table 3.6 Computation for average effect of compaction pressure at level 3, which denoted by m_{D3} is shown below:

$$\begin{aligned}
 m_{D3} &= 1/3 (S/N_3 + S/N_4 + S/N_8) \\
 &= 1/3 (4.563 + 4.660 + 5.110) \\
 &= 4.78
 \end{aligned}
 \tag{4.11}$$

where S/N_3 , S/N_4 and S/N_8 were the signal to noise ratio values listed in the last column of Table 4.11 corresponding to their trial number. The others were computed in the same manner as m_{D3} . From Table 4.12, it can be noted that there is a gradual increase in average effects starting from level 1 to level 3 for three factors: time, temperature and compaction at elevated temperature. These observations indicate that the compressive strength and density of the resultant foam would increase when these three factors are increased. On the contrary, when the heating rate is increased, the compressive strength of the resultant foam decreases.

Different factors affect the compressive strength and density of the resultant foam to different degrees. According to Ibrahim *et al.* [92] and Kishore *et al.* [93], the relative effects of different factors can be obtained by decomposing the total variation into appropriate components, commonly called analysis of variance (ANOVA). ANOVA is also needed for estimating the error variance, and the results on compressive strength from the study is shown in Table 4.13.

Table 4.13: ANOVA table

Column	Factors	DOF	SS	Variance	F	%
1	Time	2	4.390	2.195	-	11.617
2	Temperature	2	9.07	6.136	-	32.475
3	Heating rate	2	2.68	1.842	-	9.747
4	Compaction pressure	2	17.43	8.721	-	46.161
All Others / Error		0	-	-		-
Total		8	37.787			100.00

Coloumn 4 in the ANOVA table was defined as Sum of Squares. For example, sum of squares due to compaction pressure factor was computed using the following formula:

$$\begin{aligned}
 SS_{\text{compaction pressure}} &= 3(m_{D1} - m)^2 + 3(m_{D2} - m)^2 + 3(m_{D3} - m)^2 \\
 &= 3(1.49 - 2.87)^2 + 3(2.34 - 2.87)^2 + 3(4.78 - 2.87)^2 \\
 &= 17.43
 \end{aligned}
 \tag{4.12}$$

where m_{D1} , m_{D2} and m_{D3} refer to average effects correspond to compaction pressure factor for each level as listed in Table 4.12. Sum of squares of other factors were computed in the same manner and respectively tabulated in the same column. Ibrahim *et al.* [92] reported that the variance of each factor is determined by dividing the sum of squares for each factor with its degree of freedom (DOF). They also mentioned that the degree of freedom associated with a factor equals to one less than the number of levels. According to them, for a factor with 3 levels, level 1 data can be compared with level 2 and level 3 data but not with level 1 itself. Thus the 3 level factors have 2 DOF. They also described that the variance ratio (F) is the ratio of variance due to the effects of a factor, to the variance due to the error term. This approach was used and explained in detail by Ibrahim *et al.* [92]

A review of the “Percent” column in Table 4.13 showed that compaction pressure contributed the highest percentage (46.16%), followed by temperature (32.47%), time (11.61%) and heating rate (9.74%). Since the contribution of heating rate was the smallest, and at less than 10%, it was considered insignificant and this factor was

pooled (combined) with the error term. Pooling as described by Ibrahim *et al.* [92] is the process of ignoring the contribution of a selected factor and subsequently adjusting the contribution of the other factors. Hence, the new ANOVA results after pooling are as tabulated in Table 4.14.

Table 4.14: Pooled ANOVA table

Column	Factors	DOF	SS	Variance	F	%
1	Time	2	4.390	2.195	1.192	1.869
2	Temperature	2	12.271	6.136	3.332	22.728
3	Heating rate	{2}	{3.683}			
4	Compaction pressure	2	17.443	8.721	4.736	36.414
All Others / Error		2	3.683	1.842		38.989
Total		8	37.787			100.00

It was observed that after the small factor (effect of heating rate) was pooled, percentage contributions of the remaining factors decreased slightly, but the factor effects ranking remain unchanged. The average performance of effects indicates that level 3 for the factors compaction pressure at elevated temperature, temperature and time gives the optimal condition for compressive strength and density of the foam. As shown in Table 4.15 for compressive strength, the expected improvement is 4.21 over the current average performance of 2.87. Since heating rate is of little significance, it was omitted from the selection of levels for the optimum condition as described by Ibrahim *et al.* [92], Kishore *et al.* [93] and Kumar *et al.* [94].

The contributions from these factors were calculated by subtracting the current grand average of performance value from the values listed in the last column of Table 5.4.2 (Level 3) that correspond to each factor. For an example, the contribution of time factor was 0.651, which was obtained by subtracting 2.87 (Mean value) from 3.52 (value of the last column and first row of Table 4.11).

Based on these results, the highest compressive strength and density of the resultant foam could be attained at the combination setting of A₃, B₃, C₁ and D₃, i.e. sintering time of 30 min, sintering temperature of 620°C, processing heating rate of

30°Cmin⁻¹ and compaction pressure at elevated temperature of 120 MPa. This combination of settings was not used in the experiments. Hence, according to Ji *et al.* [95] the orthogonal array is capable of identifying optimum factors in a multidimensional factor space.

Table 4.15: Estimate of the optimum condition of design

Factors	Level Description	Level	Contribution
Time	30 min	3	0.651
Temperature	620 °C	3	1.650
Compaction pressure	120 MPa	3	1.907
Contributions from all factors (total)			4.209
Current grand average of performance or Mean			2.870
Expected results at optimum condition			7.079

The expected results (R_{expected}) at optimum condition in term of S/N ratio can be converted back to scale of units of the original observations by the following steps:

$$7.08 = -10 \log (\text{MSD})$$

$$\text{MSD} = 10^{-7.08/10} = 0.196$$

$$R_{\text{expected}} = (\text{MSD})^{-1/2} = 2.25$$

Confirmation experiments were conducted by running another three replications at the combined setting of A₃, B₃, C₁ and D₃. The average compressive strength was found to be 2.26 MPa which was within the confidence interval of the predicted optimal of compressive strength. However this prediction just considered the compressive strength value, as the “bigger is better” quality characteristic.

4.6 The electrical conductivity behaviour of aluminium foam

In this section the electrical conductivity measurement as a tool for describing the surface morphology and mechanical properties of pressure assisted sintering foam specimen was presented. The relationship between formation of sintered contacts and mechanical properties were evaluated through determination of electrical conductivity [135]-[137].

The influence of compacting pressure on the relative electrical conductivity of foam specimen is shown in Figure 4.70. This indicates that high compaction pressure promotes better binding among Al particles in the Al matrix because of fresh metal contacts between the Al particles. In other words, electrical resistivity decreased with high pressure as a consequence of more interparticle contact regions being formed.

The effect of the sintering temperature and time on the relative electrical conductivity of foam specimen is shown in Figures 4.71.-4.72. It is obvious that formation of sintered contacts should result in higher electrical conductivity (see Figures 4.71 and 4.72.). This relationship is comparable to the mechanical properties of Al foam at various sintering temperature and time as shown in Figures 4.42 – 4.45 and Figures 4.47 – 4.50. Thus, it is evident that at high sintering temperature and longer time result in lower electrical resistivity and higher strength.

As shown in the analysis of previous results (Figures 4.53 – 4.56), heating rate has had an influential effect on the mechanical properties of the Al foam. From Figure 4.73, it can be seen that with an increase in heating rate, the relative electrical conductivity of the foam at fixed NaCl/Al ratio increases.

It is evident that the present of pores will significantly affect the electrical properties of the specimen [136]. A decrease in the conductivity is visible as the volume fraction of specimen is increased. An increase in conductivity is observed when the processing parameters (compaction pressure, sintering temperature, time and heating rate) are increase. This behaviour is due to the fact that these optimum conditions will lead to better binding among the aluminium particles when they are simultaneously sintered and pressed. It is obvious that formation of pores should result in higher electrical resistivity [137]-[139].

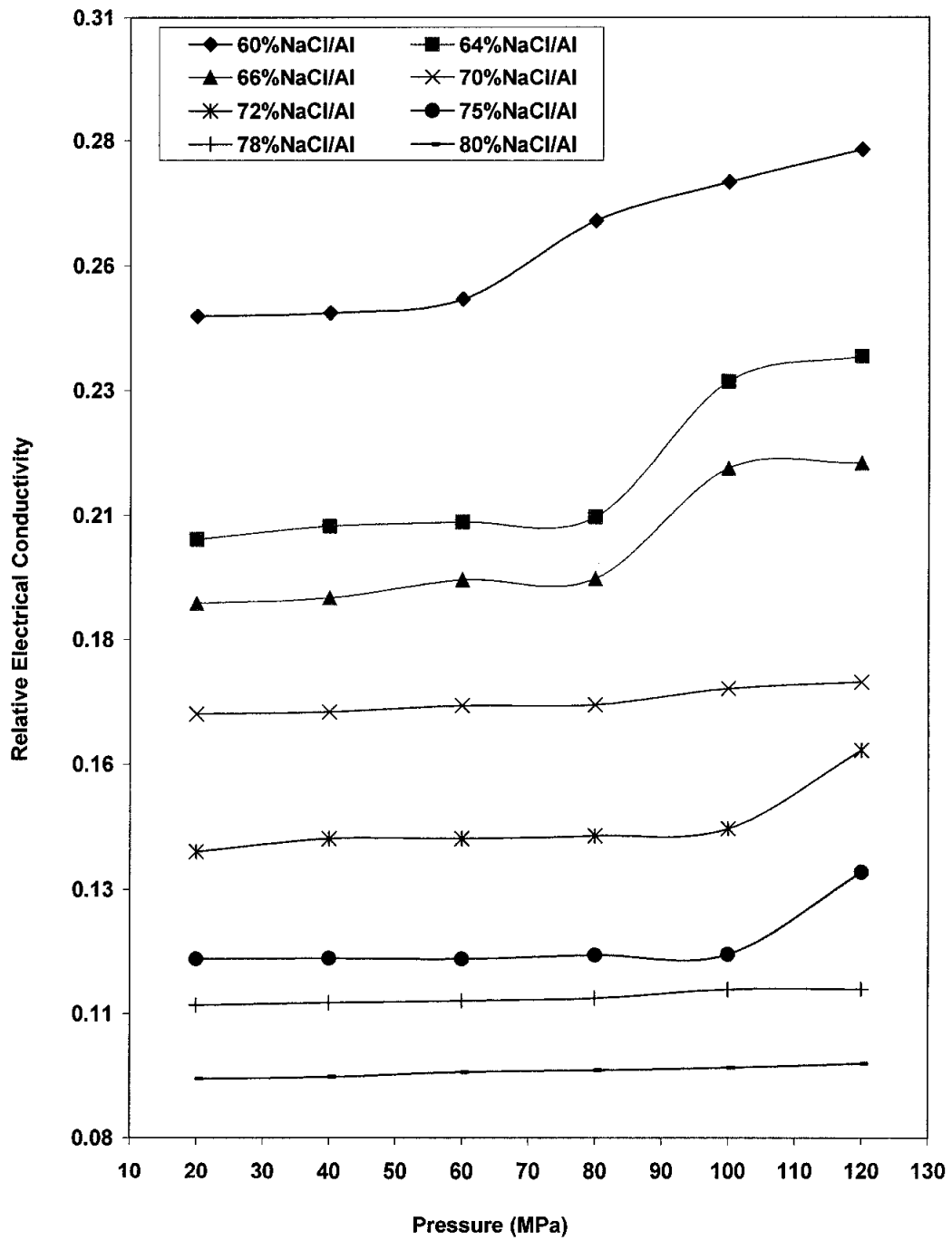


Figure 4.70: Variation of relative electrical conductivity of pressure assisted sintering Al foams (at 620 °C for 30 min) with compaction pressure at different NaCl/Al volume fraction

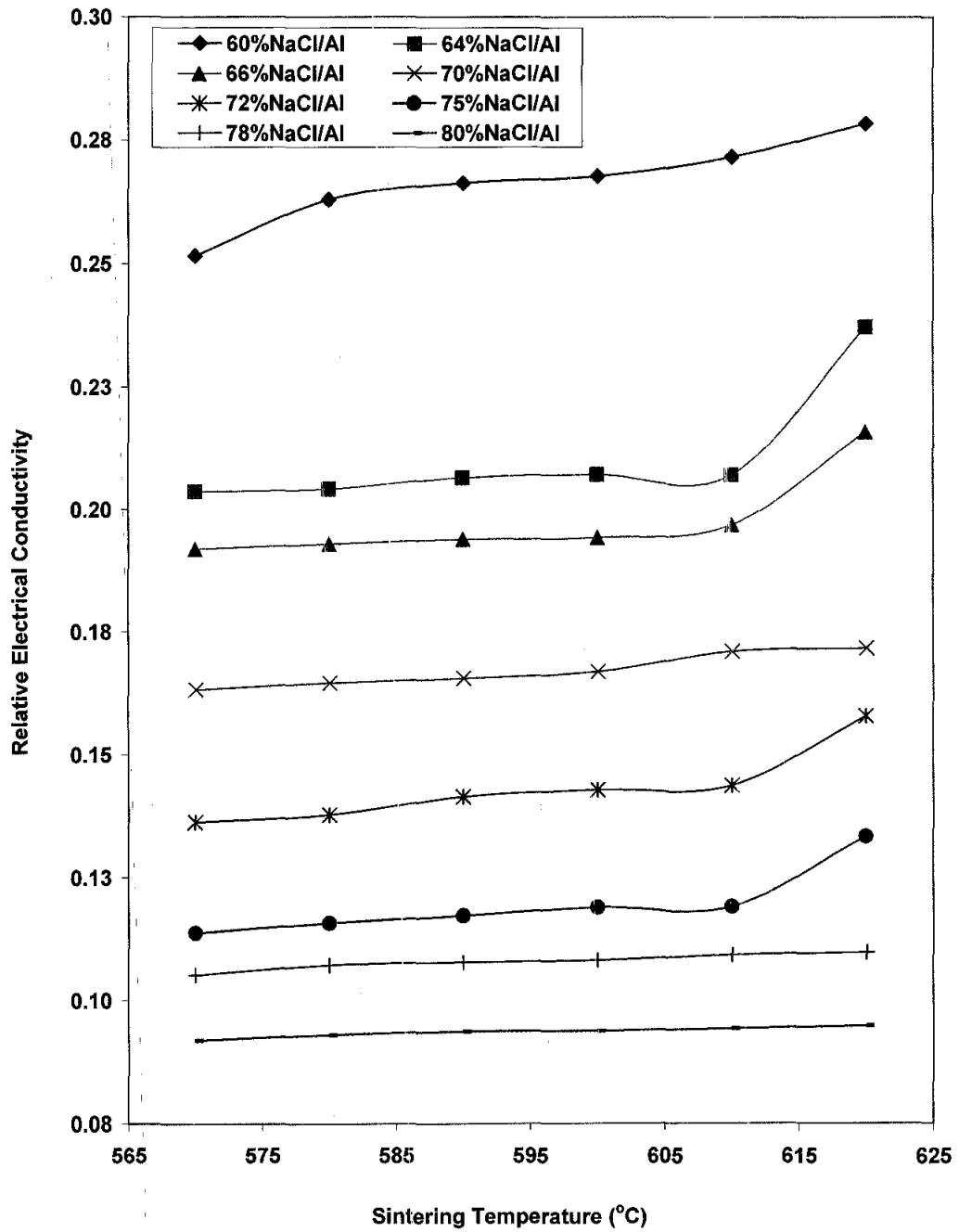


Figure 4.71: Variation of relative electrical conductivity of pressure assisted sintering Al foams (at compaction pressure of 120 MPa for 30 min) with sintering temperature at different NaCl/Al volume fraction

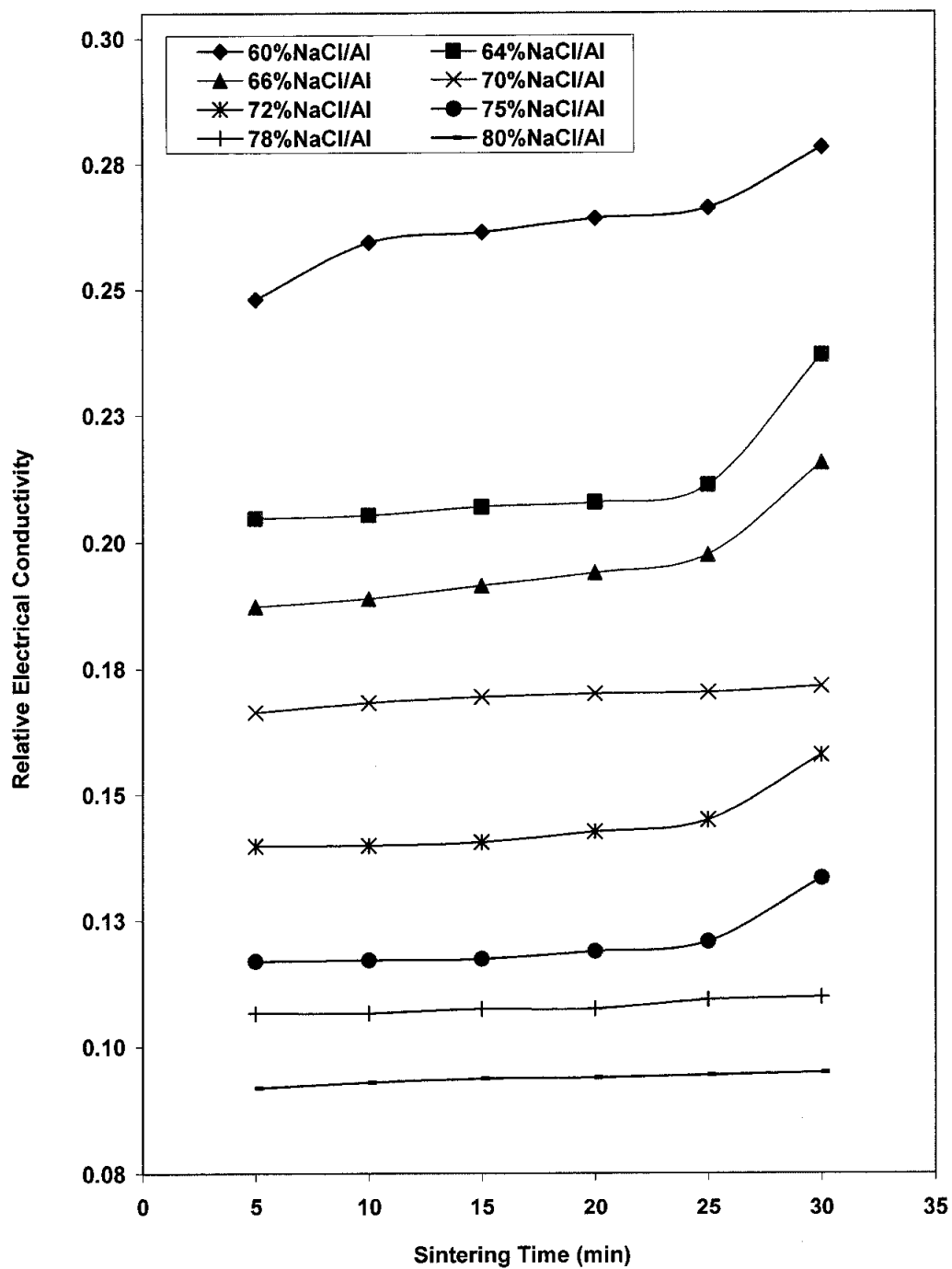


Figure 4.72: Variation of relative electrical conductivity of pressure assisted sintering Al foams (at compaction pressure of 120 MPa and at 620 °C) with sintering time at different NaCl/Al volume fraction

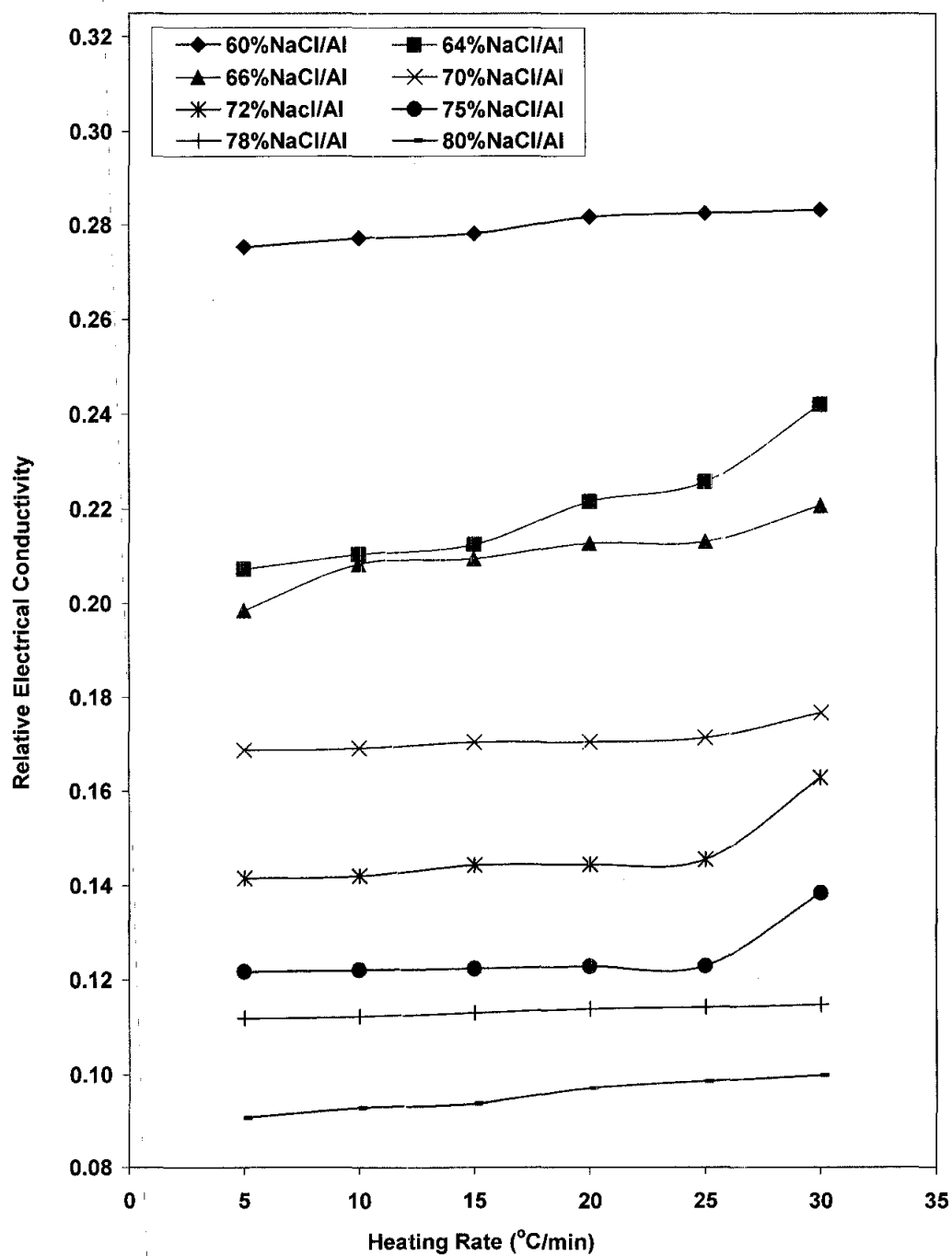


Figure 4.73: Variation of relative electrical conductivity of pressure assisted sintering Al foams (at compaction pressure of 120 MPa and at 620 °C) with heating rate at different NaCl/Al volume fraction

The results obtained revealed that the electrical conductivity of pressure assisted sintering foams is closely related to their porosity level which has a significant influence on the resistivity. An attempt was made to find the possible applicability of this physical property by relating it to mechanical properties. In Figures 4.74 – 4.77, the relationship between relative electrical conductivity and total porosity according to different experimental processing parameters are shown for the foam specimens. The mathematical description given by Skorohod and Solonin was also tested with the experimental data obtained. It was observed that the relationship does not follow this empirical equation.

The relationship between relative electrical conductivity and density is shown in Figures 4.78 – 4.81. The results reveal that the electrical conductivity of foam increases with the increase of density. The behaviour can be qualitatively understood by noting that, as relative density decreases, the average cross-section available for conduction decreases and the tortuosity of the current path increases, thus the resistivity increases.

One of the approaches of finding the empirical relationship between relative density and selected physical property in this case, relative electrical conductivity, is to use the principles of percolation theory [138], [139] which covers the whole density range. According to percolation theory the effective property near the connectivity threshold (in this case set to zero) behaves like a power-law function of a relative density:

$$\frac{\sigma}{\sigma_o} = z \left(\frac{\rho}{\rho_o} \right)^t \quad (4.12)$$

where σ and ρ are the effective property and density of foam respectively, while σ_o and ρ_o are the corresponding properties of the cell-wall material. Constant t (often called as a critical exponent) can be theoretically predicted for the specific property.

Figures 4.82 – 4.85 show that the experimental results of electrical conductivity are fundamentally consistent with the calculation results of Eqn. (4.12). That is to say, the relationship between electrical conductivity and relative density for the aluminium foams is in agreement with the percolation theory [139].

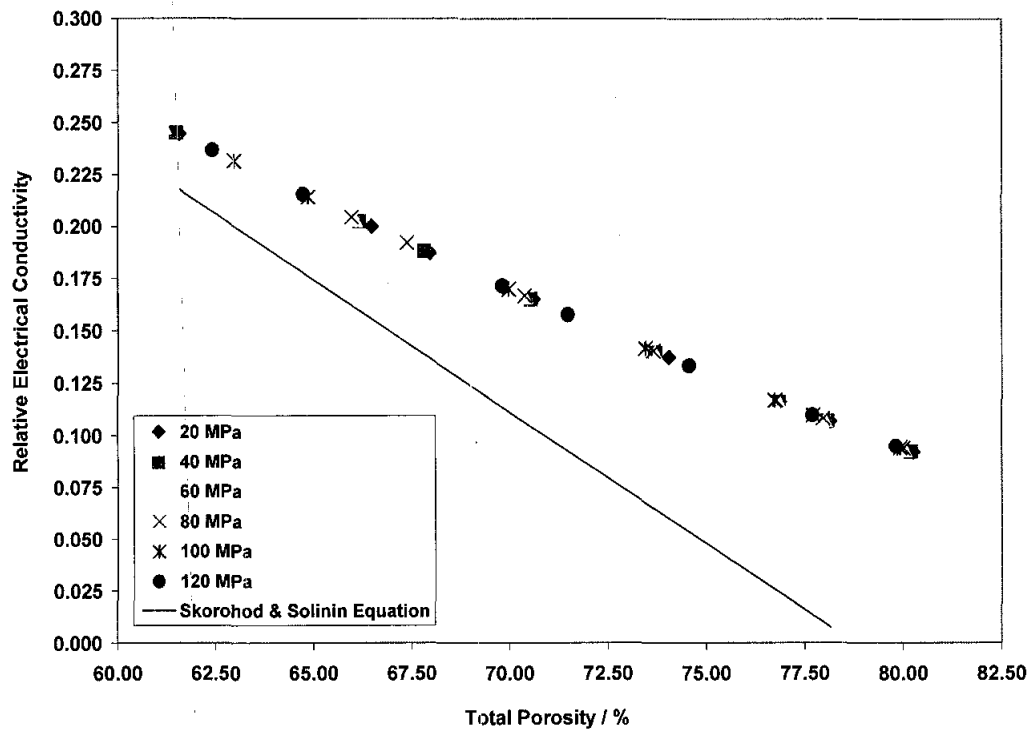


Figure 4.74: Relative electrical conductivity of foam specimens as a function of total porosity at different compaction pressure

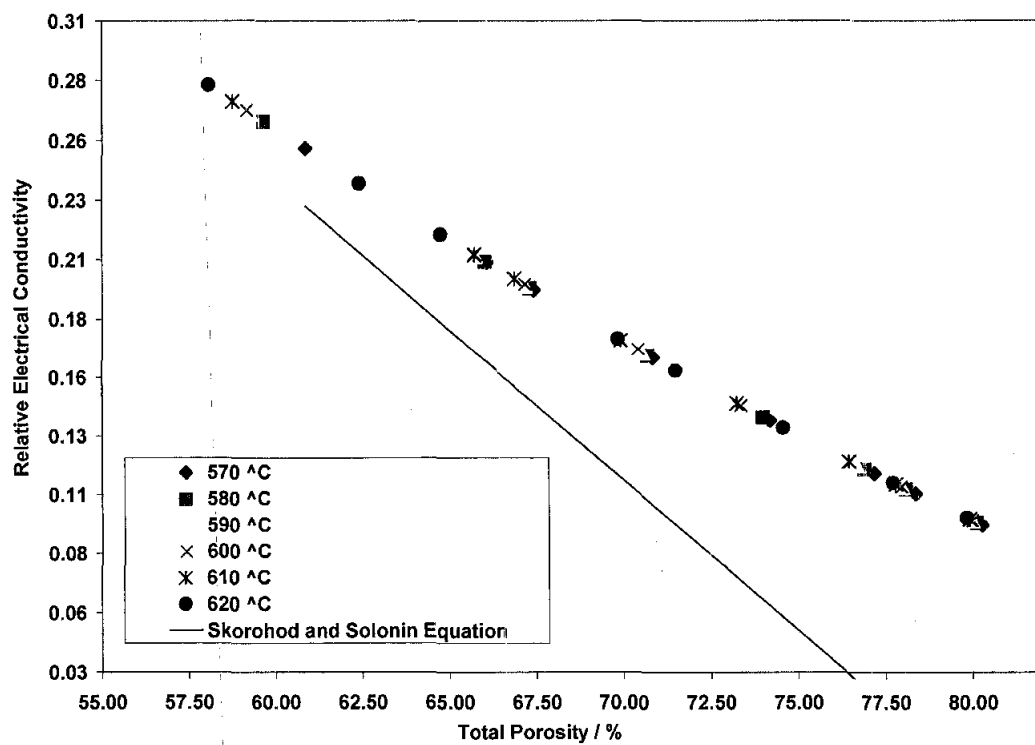


Figure 4.75: Relative electrical conductivity of foam specimens as a function of total porosity at different sintering temperature

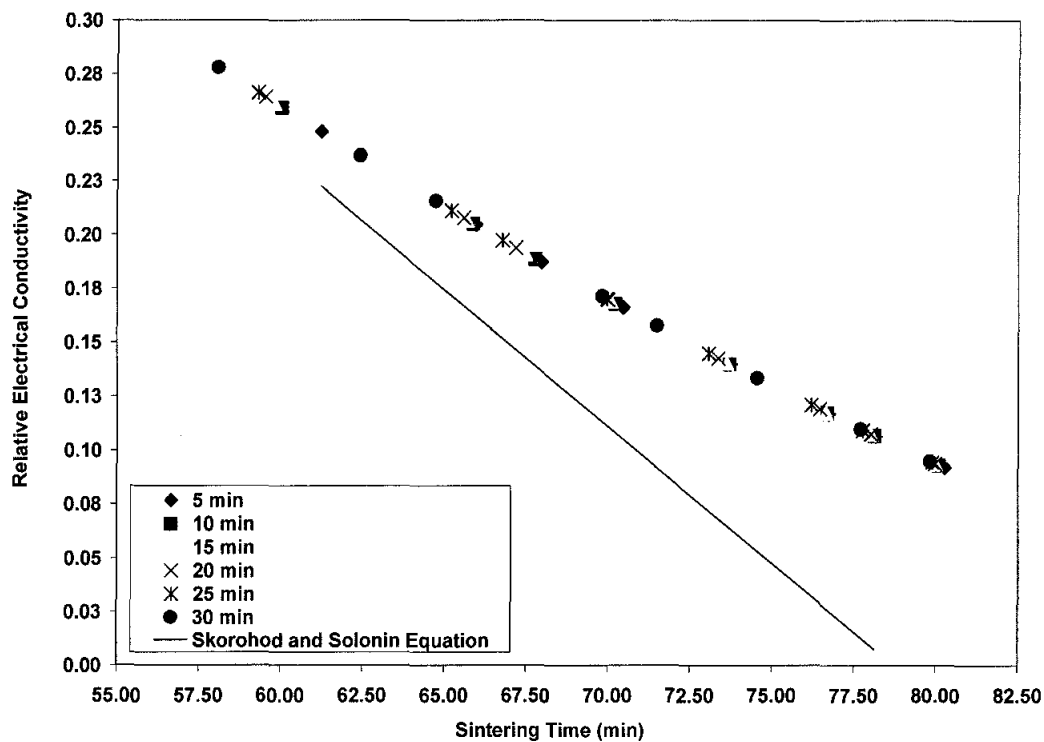


Figure 4.76: Relative electrical conductivity of foam specimens as a function of total porosity at different sintering time

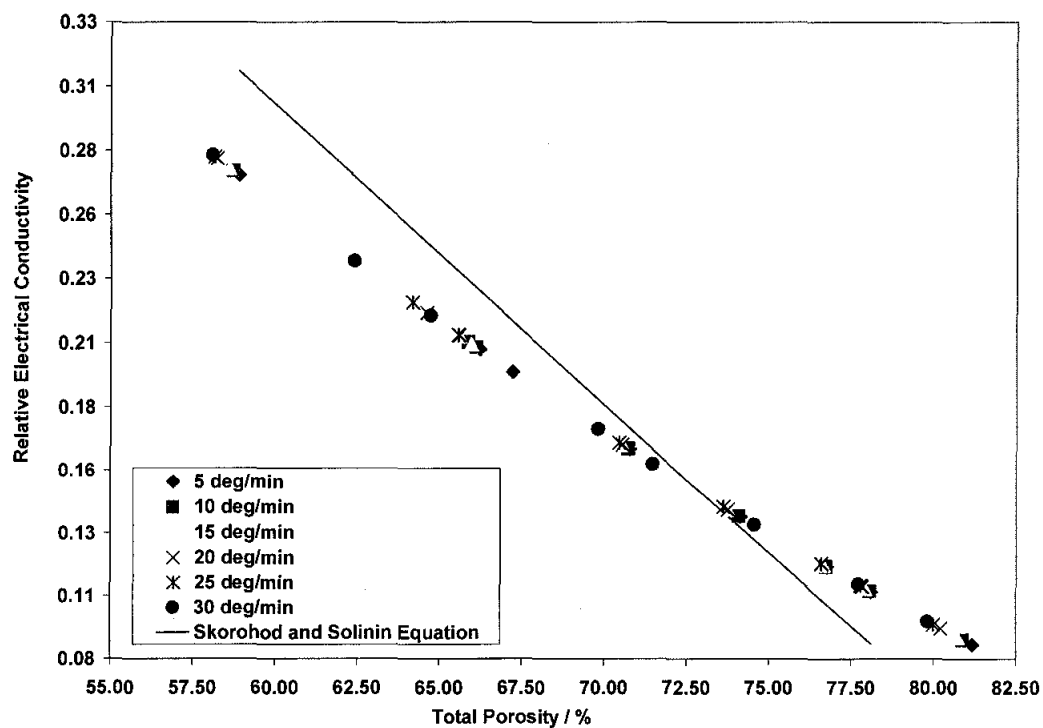


Figure 4.77: Relative electrical conductivity of foam specimens as a function of total porosity at different heating rate

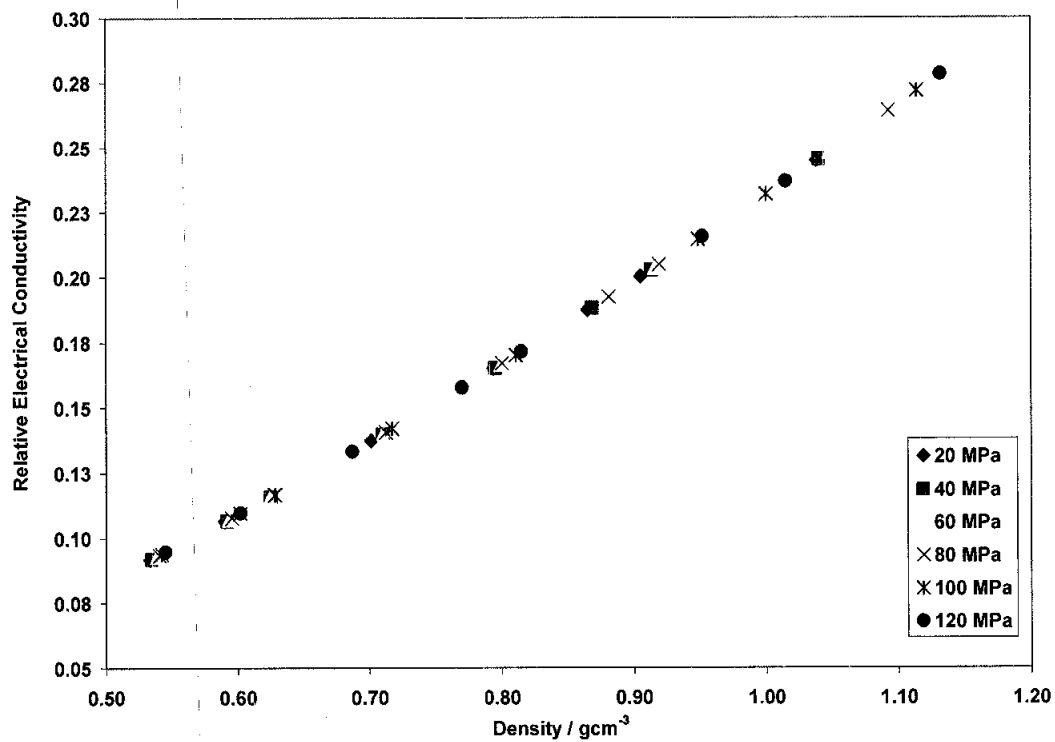


Figure 4.78: Relative electrical conductivity of foam specimens as a function of density at different compacting pressure

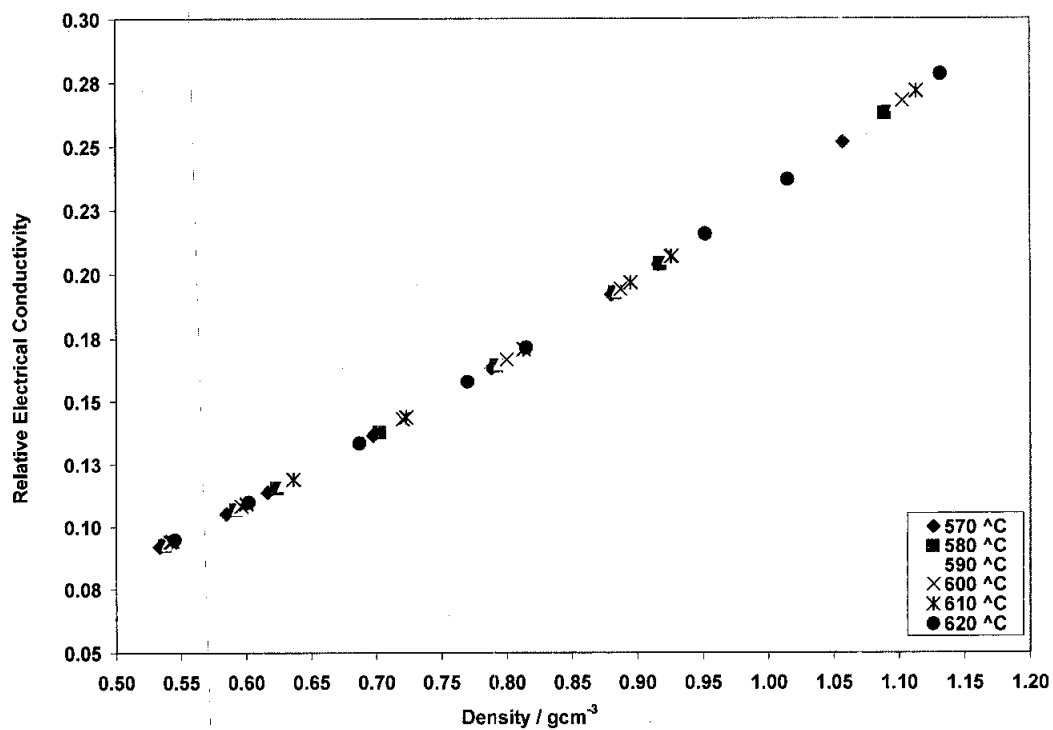


Figure 4.79: Relative electrical conductivity of foam specimens as a function of density at different sintering temperature

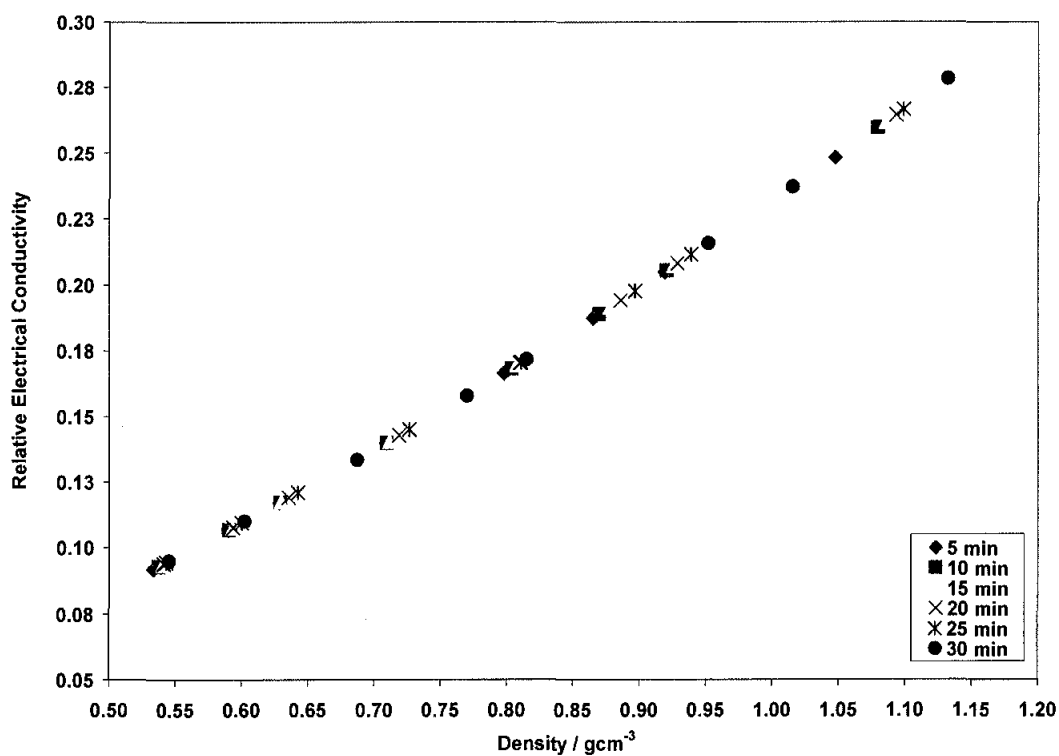


Figure 4.80: Relative electrical conductivity of foam specimens as a function of density at different sintering time

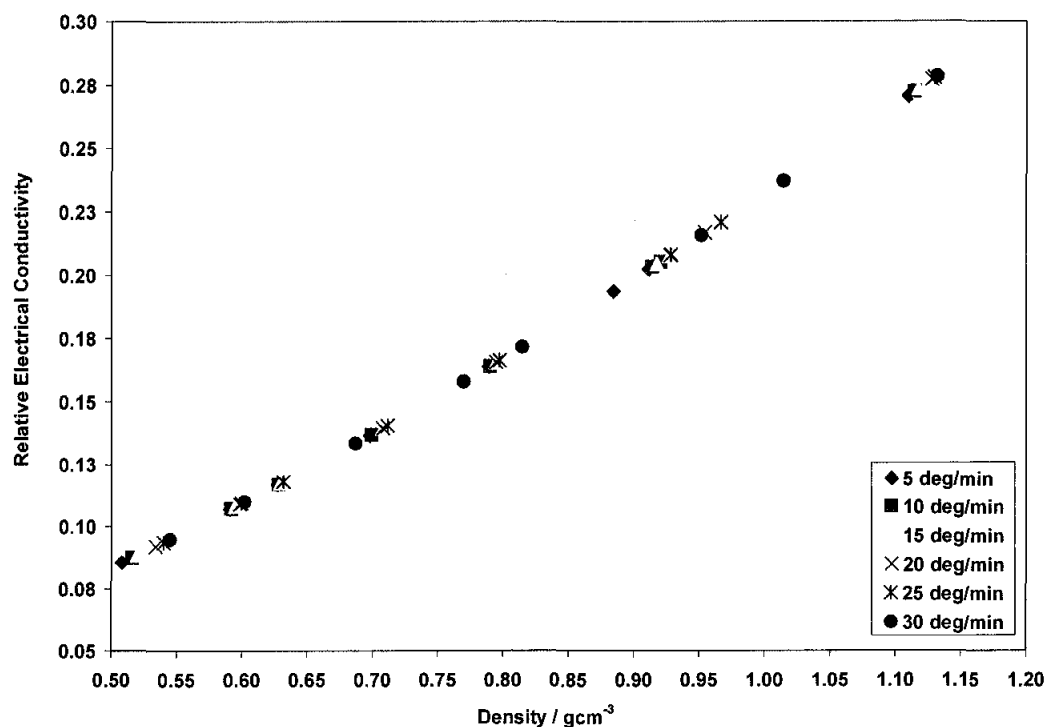


Figure 4.81: Relative electrical conductivity of foam specimens as a function of density at different heating rate

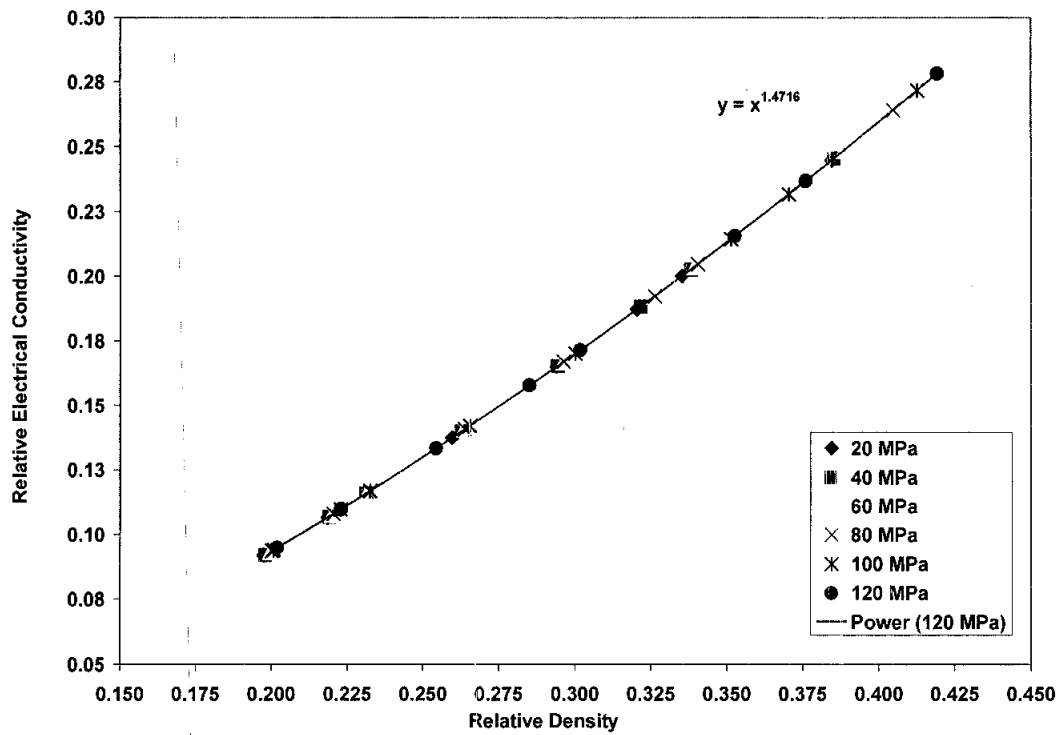


Figure 4.82: Relative electrical conductivity of foam specimens as a function of density at different compaction pressure

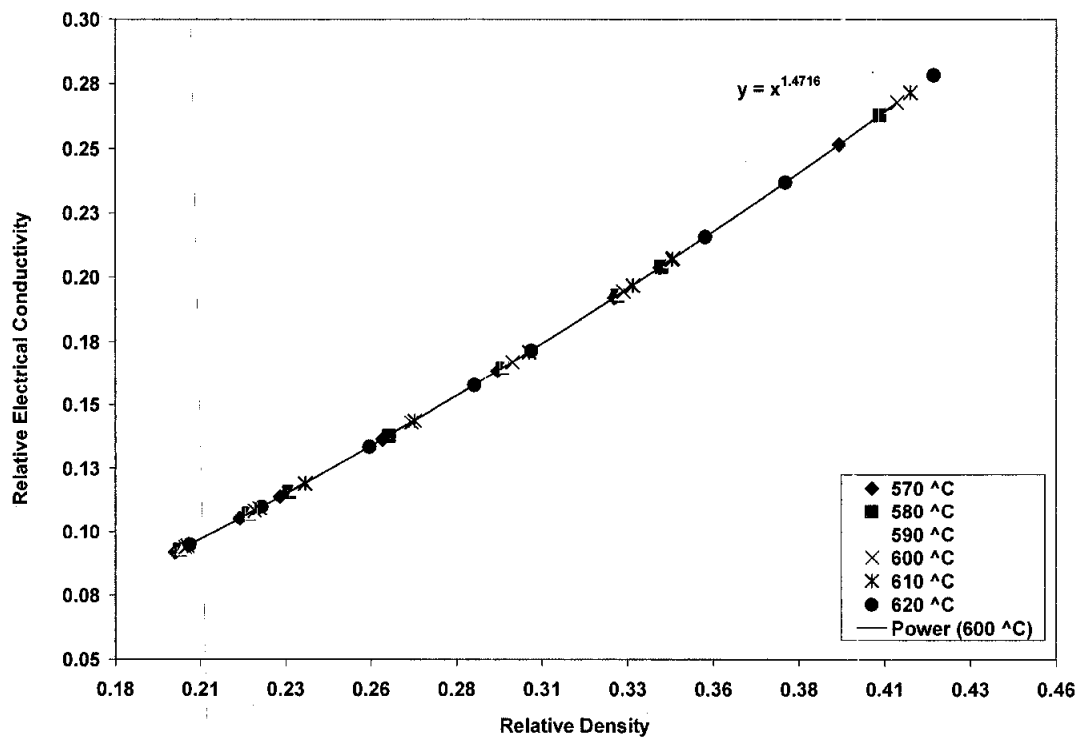


Figure 4.83: Relative electrical conductivity of foam specimens as a function of density at different sintering temperature

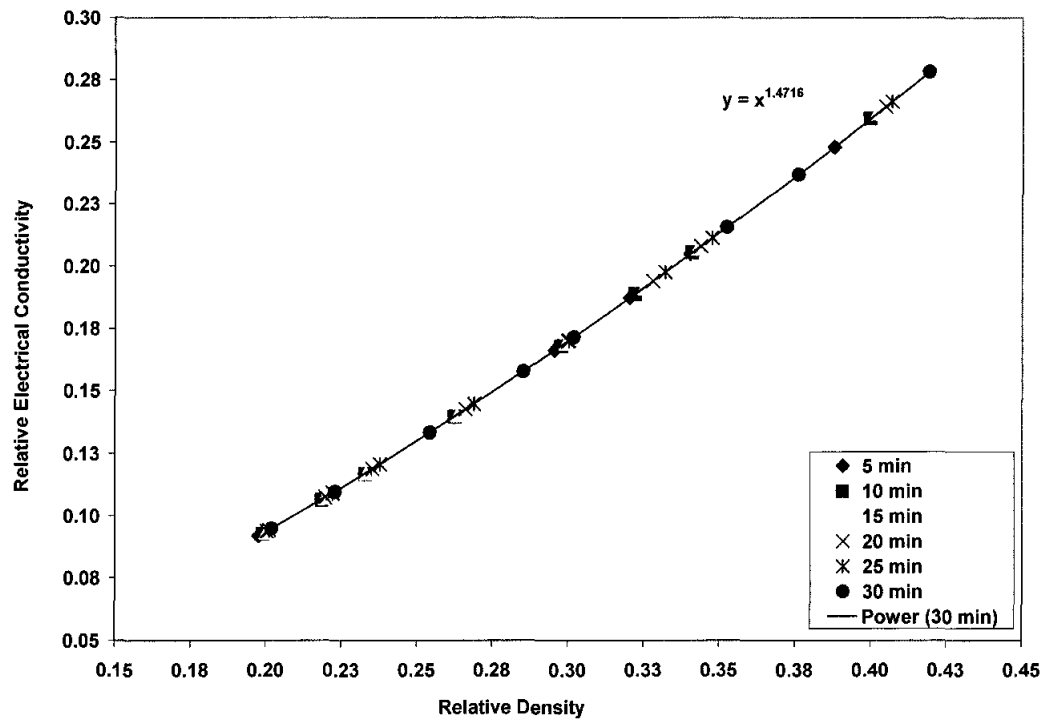


Figure 4.84: Relative electrical conductivity of foam specimens as a function of density at different sintering time

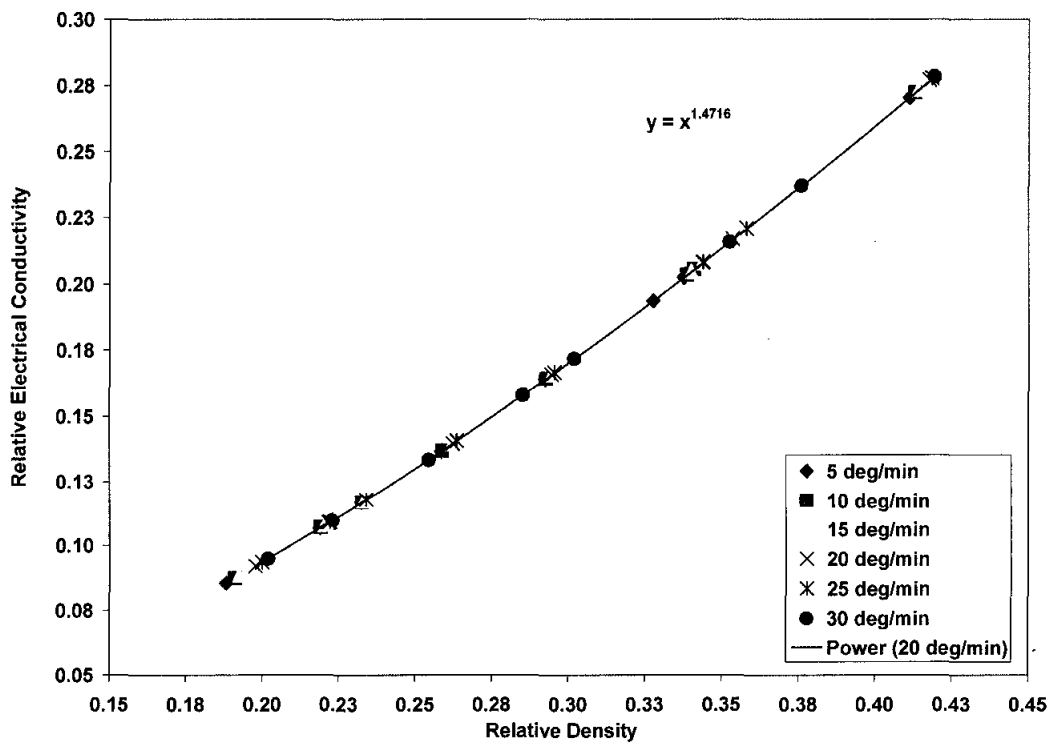


Figure 4.85: Relative electrical conductivity of foam specimens as a function of density at different heating rate

4.7 The influence of pore shape and its width of size distribution on the empirical relationship between physical and mechanical properties of Al foam

Aluminium foam is characterized structurally by its cell topology, relative density, cell size and shape. Current work on the improvement of the fabrication process concentrates on improving process control to produce higher quality materials and to achieve a better reproducibility and predictability of their properties. "Better quality" usually means a good morphological and structural homogeneity of the cellular materials. In this section, the reproducibility and predictability of pore size of the Al foam synthesized by the PASDP were studied and the mechanical properties of the foam investigated in light of its pore size and its widths of size distribution and relative density [10], [13], [15], [22], [66].

4.7.1 The dissolution characteristic of the NaCl in the NaCl/Al compact during leaching process

Figures 4.86 – 4.89 show the variation of the fraction of the dissolved NaCl of different size and its widths of size distribution, used as filler material in the Al foam, $1-\phi$, with the NaCl/Al volume fraction. It can be observed that the dissolution of NaCl from the compact does not depend on the particle size of the filler material used. In most cases, the NaCl particles in the sintered composites could not be dissolved completely [10]. A PASDP NaCl/Al compact consists of sintered aluminium particles which are surrounded by NaCl particles [10]. With a high volume fraction of NaCl in the compact, most NaCl particles are in contact with each other and form a continuous three-dimensional network. Because all the NaCl particles in the network can be dissolved away by water, there is only a small amount of residual NaCl in the resultant foam. It is possible to fabricate Al foam with a designed classification of pore size by using NaCl particles of different size and its width of size distribution and the morphology of resultant foam is shown in Figures 4.90 (a)-(d).

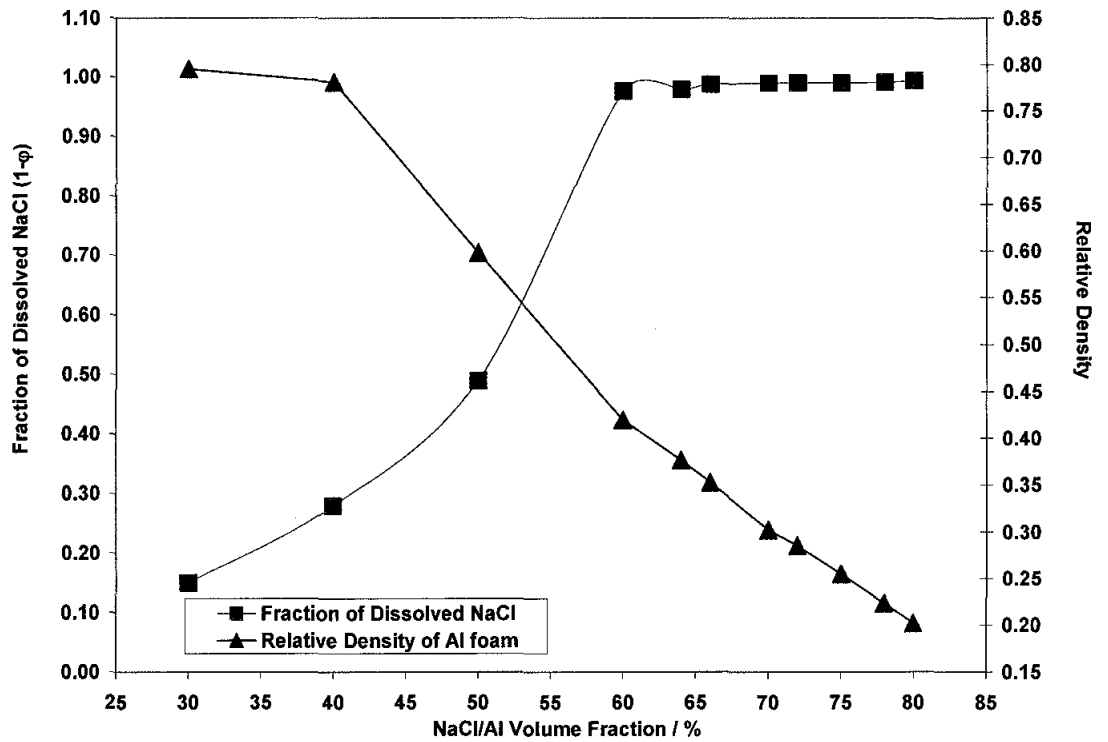


Figure 4.86: Relationship between fraction of dissolved NaCl, relative foam density and NaCl/Al volume fraction for TS-NaCl/Al

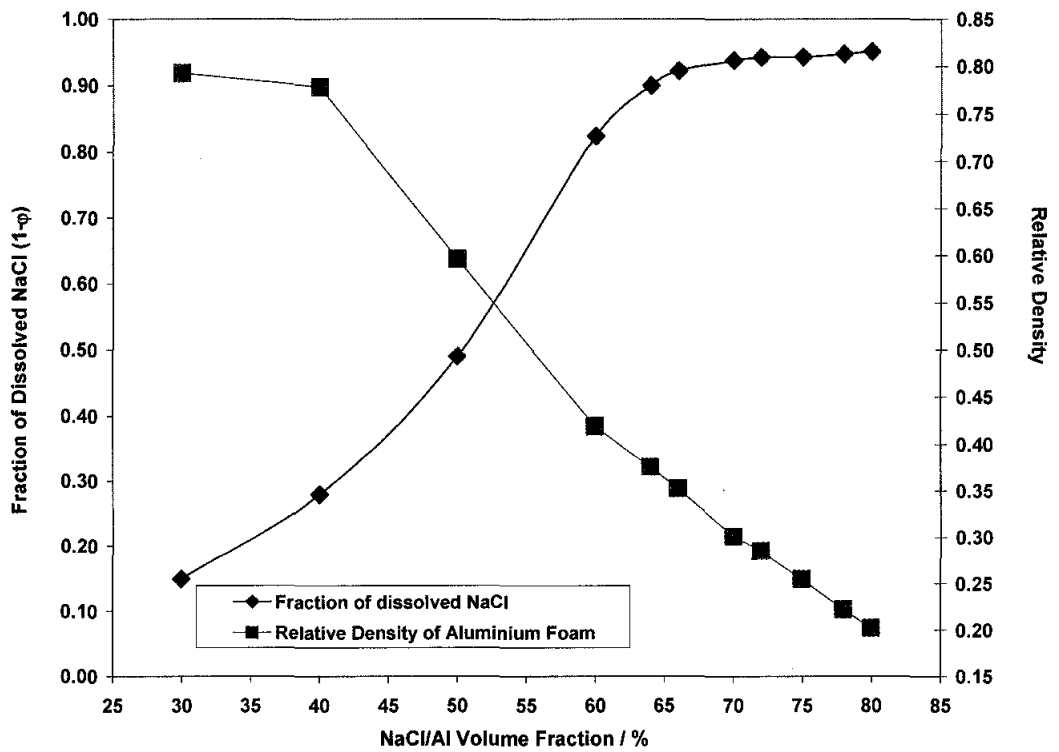


Figure 4.87: Relationship between fraction of dissolved NaCl, relative foam density and NaCl/Al volume fraction for AC-NaCl/Al

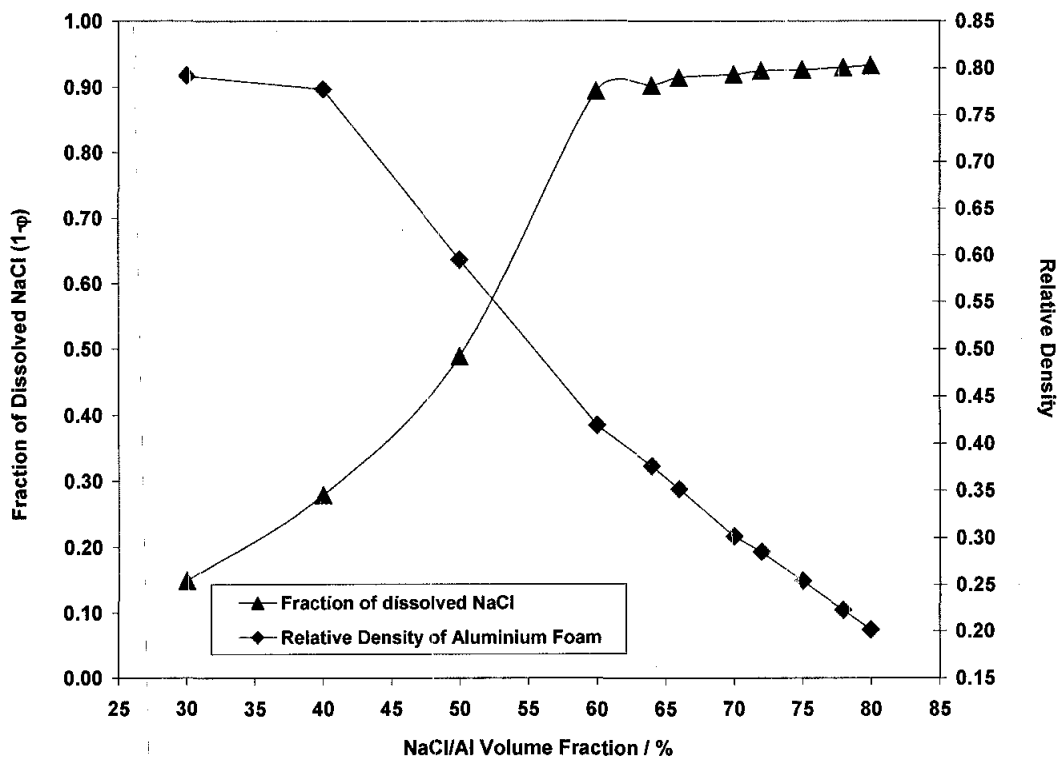


Figure 4.88: Relationship between fraction of dissolved NaCl, relative foam density and NaCl/Al volume fraction for HI-NaCl/Al

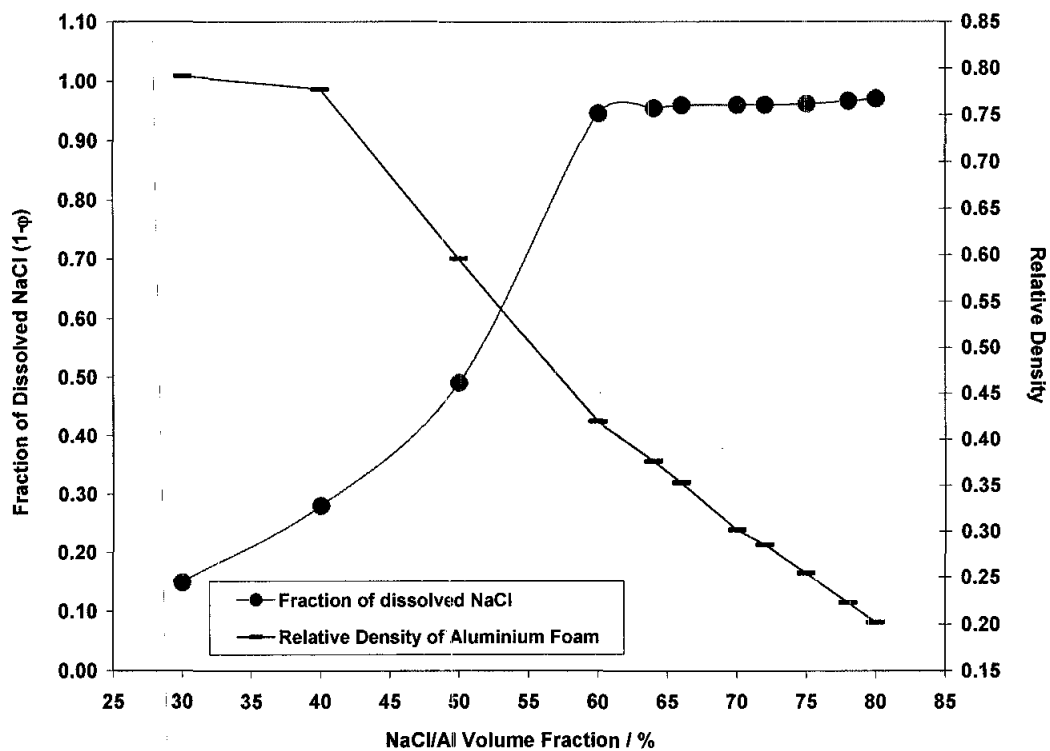


Figure 4.89: Relationship between fraction of dissolved NaCl, relative foam density and NaCl/Al volume fraction for SA-NaCl/Al

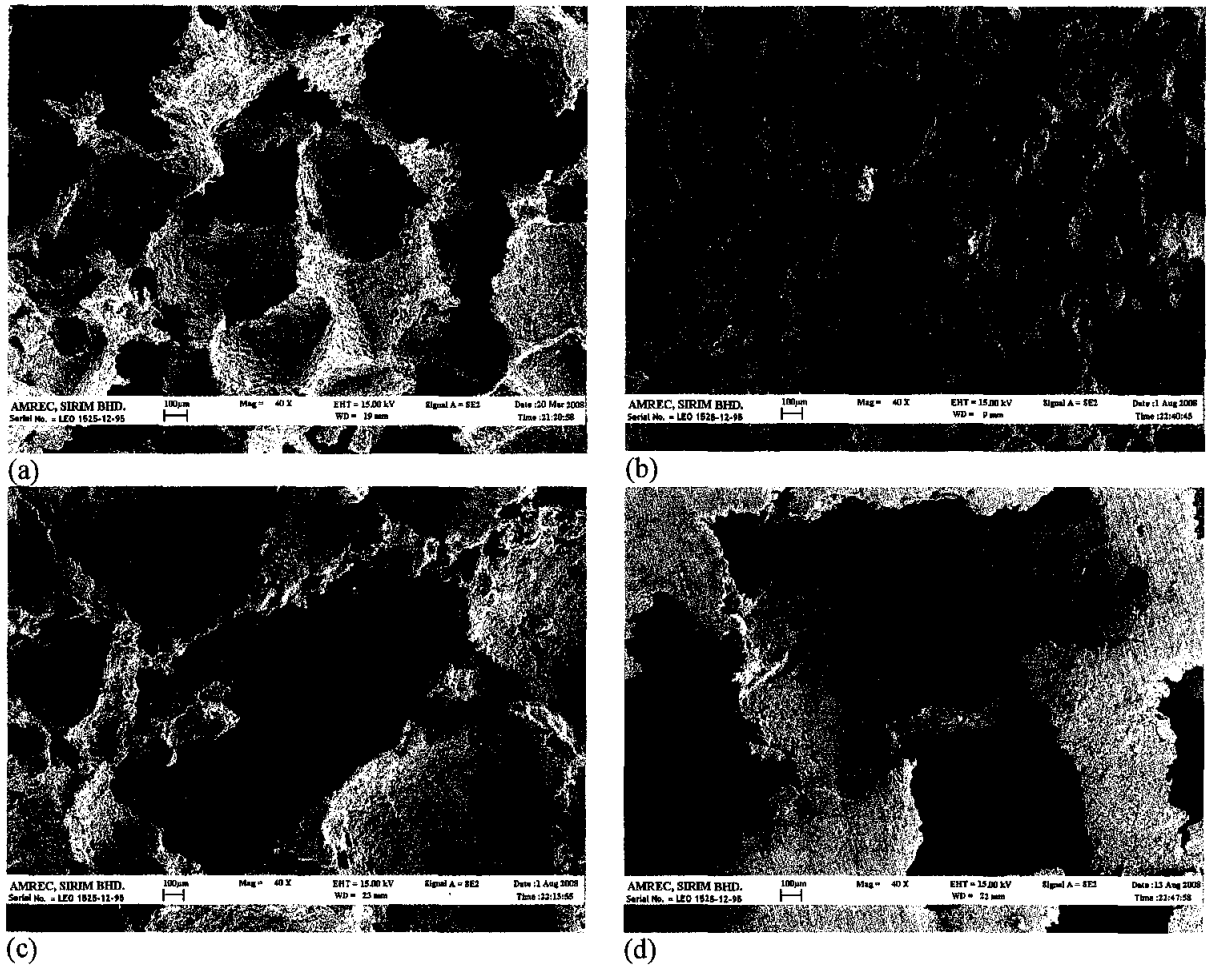


Figure 4.90: SEM images of PASDP Al foam with volume fraction initially at 80% volume fraction using different size and its width of size distribution of filler material
(a) TS-NaCl (b) AC-NaCl (c) HI-NaCl (d) SA-NaCl

In contrast, with a low volume fraction of NaCl in the preform some NaCl particles are enclosed completely by the Al matrix [22]. These isolated NaCl particles cannot be dissolved away and remain in the foam. Decreasing NaCl weight fraction in the NaCl/Al compact increase the Al volume fraction and therefore increases the amount of residual NaCl in the final Al foam. It can be observed from Figures 4.86 – 4.89 that the residual of NaCl of different size and its width of size distribution in the foam was very small when Al volume fraction in the compacts was below 40% [10], [22]. When the Al volume fraction was increased to 60% and above the fraction of dissolved NaCl in the foam with respect to the total NaCl in the initial composite is decrease. The XRD pattern (Figure 4.91 (a)-(d)) reveals that as NaCl of different size and its width size distribution content is increased to 60% volume fraction, no

compound of NaCl present in the compact after leaching process. The relative density foam of the foam with a high Al volume fraction in the initial compact was therefore expected to be higher than the theoretical value [15]. The measured relative densities of the foam at Al volume fraction $> 40\%$, however were not always higher than the calculated ones and showed greater variation between individual measurements [10], [13]. This might be because the Al distributions in the NaCl/Al composites were not uniform and consequently the local Al volume fractions of the samples were somewhat different from those of the whole specimens from which the samples were cut [10].

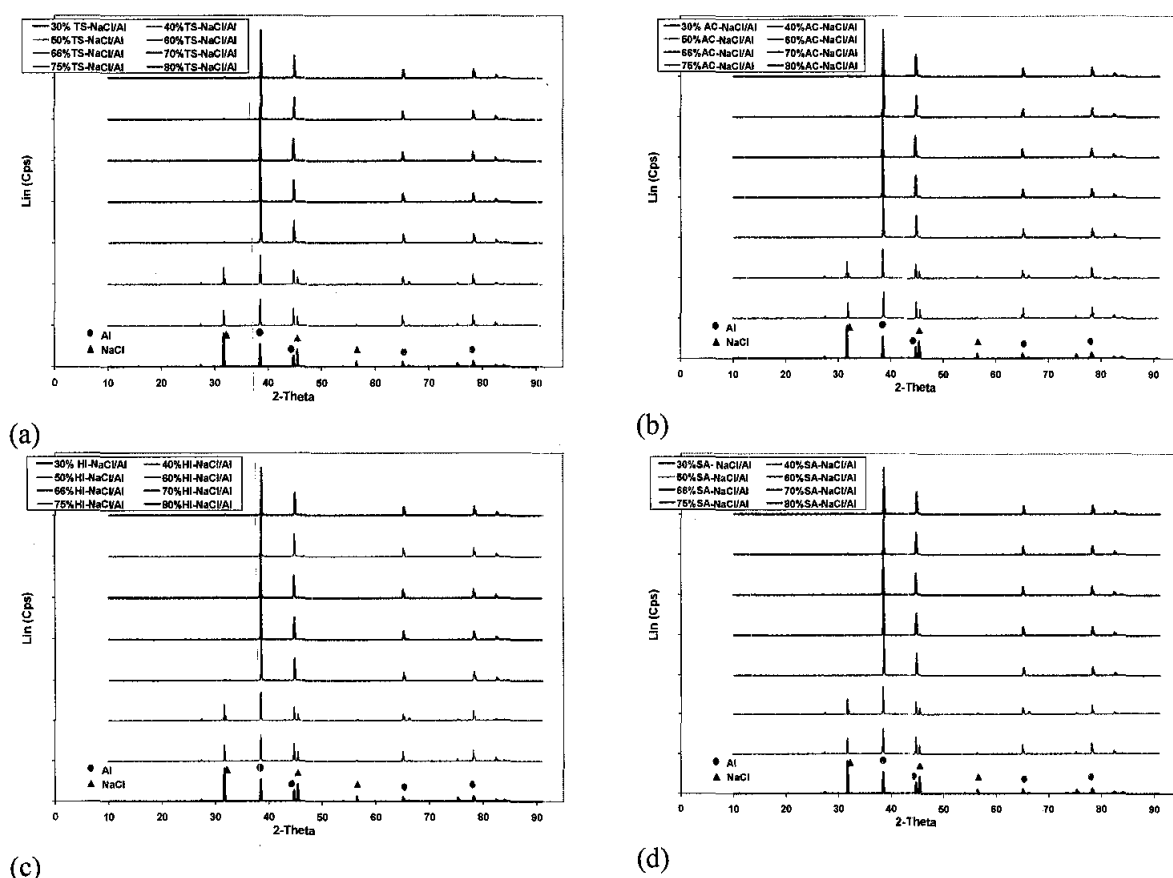


Figure 4.91: XRD spectrum of different size and its width of size distribution of filler material at different volume fraction (a) TS-NaCl (b) AC-NaCl (c) HI-NaCl (d) SA-NaCl

Figures 4.92 (a)-(h) show the typical macro and microscopic structure of the fabricated foam after undergone leaching process using different size and shape of NaCl with volume fraction initial at 80%.

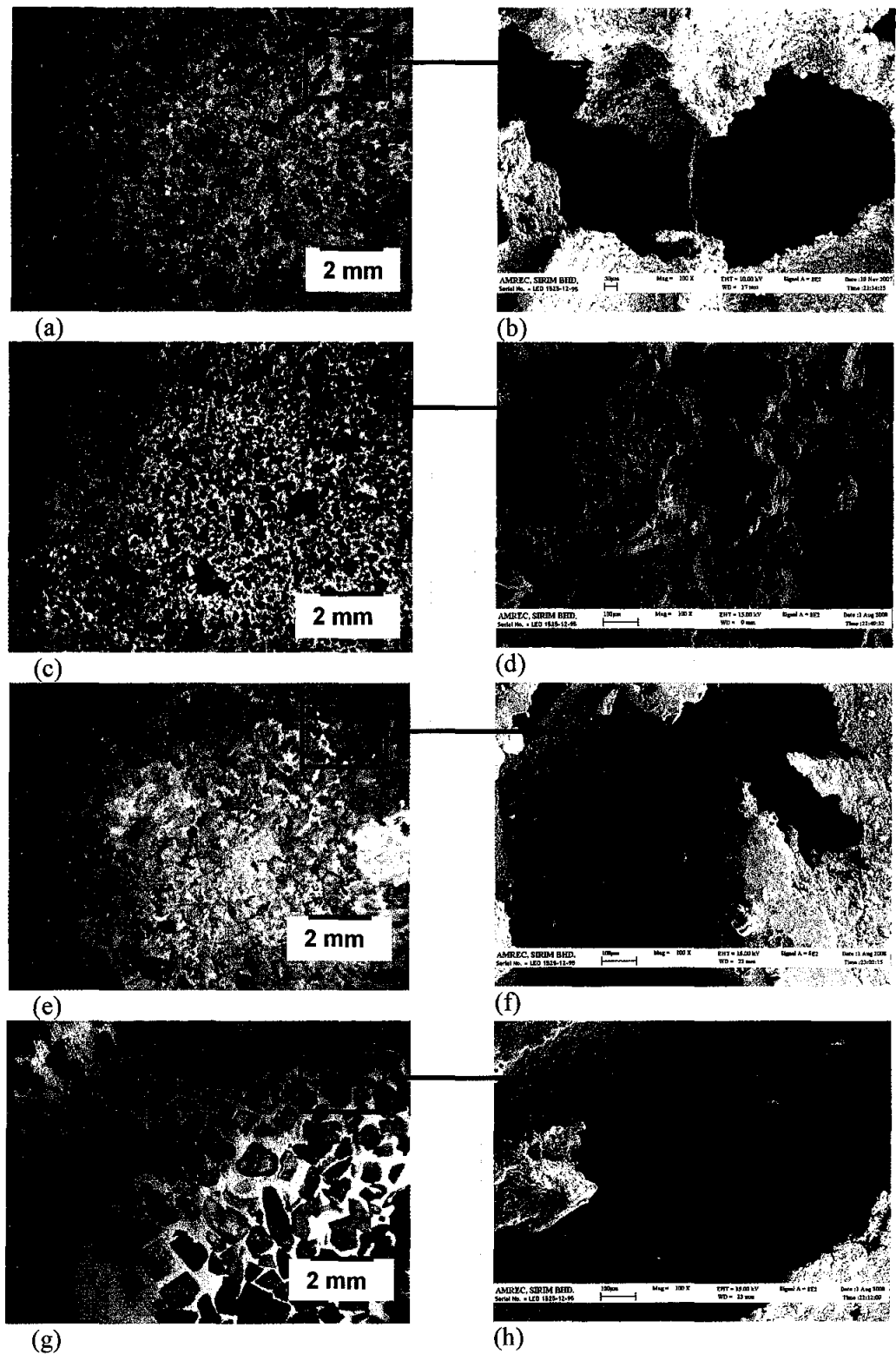


Figure 4.92: Streamicrographs of Al foam with relative density of 0.2 for different size of filler material (a) TS-NaCl(c) AC-NaCl (e) HI-NaCl (h) SA-NaCl. SEM images of selected area at x100 for (b) TS-NaCl (d) AC-NaCl (f) HI-NaCl (h) SA-NaCl

Figures 4.93 (a)–(d) present the density of the pressure assisted sintering specimens after dissolution process with different size and its width of size distribution of leaching agent at different volume fraction. It can be observed the compact density seems to be dependent on the NaCl/Al volume fraction in the compacts. The figures also show a comparison between the final porosity of the Al foam and the initial volume fraction of the NaCl/Al powder mixture. The foam porosity is 0.2-2% lower than the initial volume fraction of NaCl, and the higher the NaCl volume fraction, the lower the decrease in foam porosity.

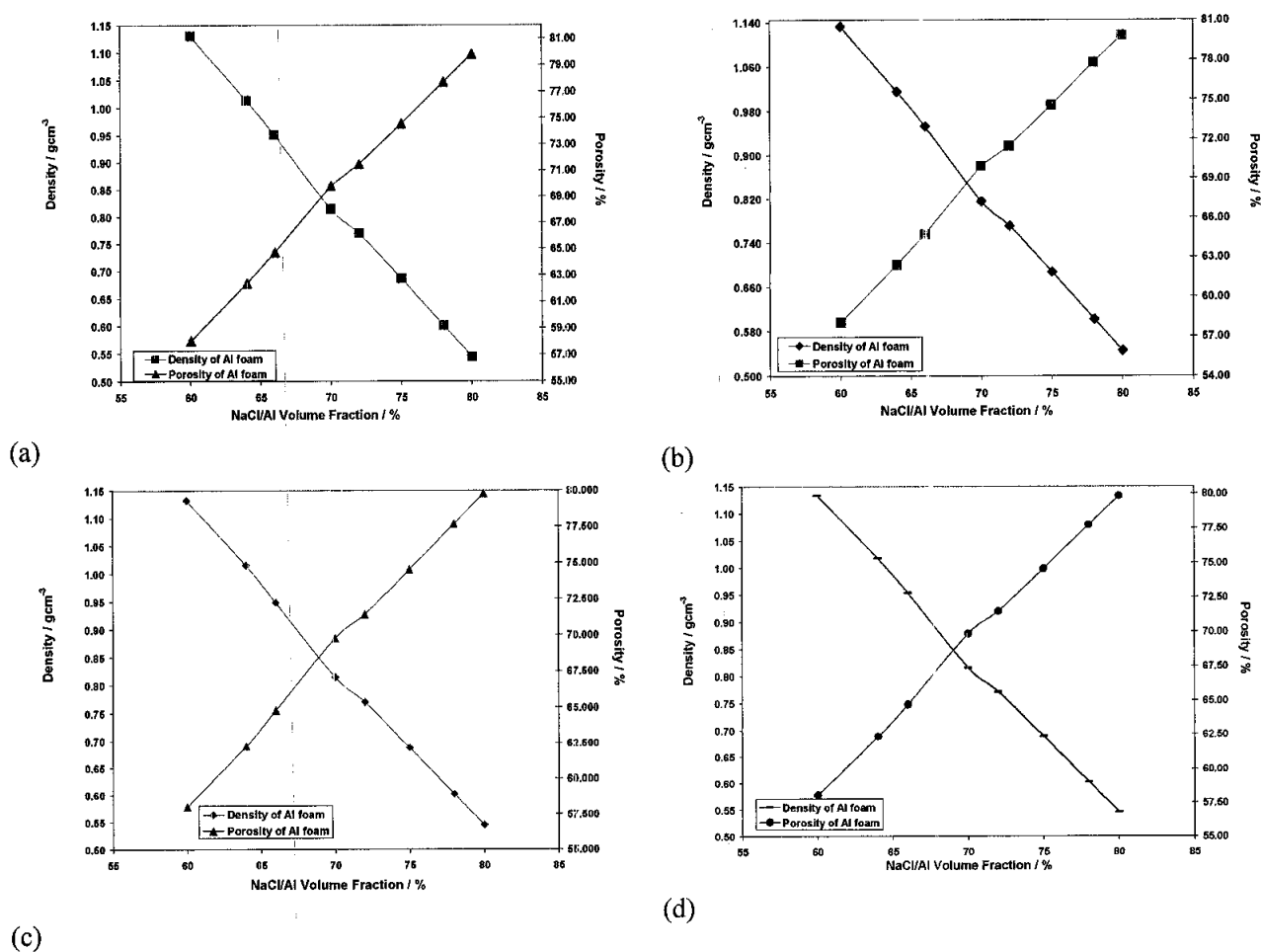


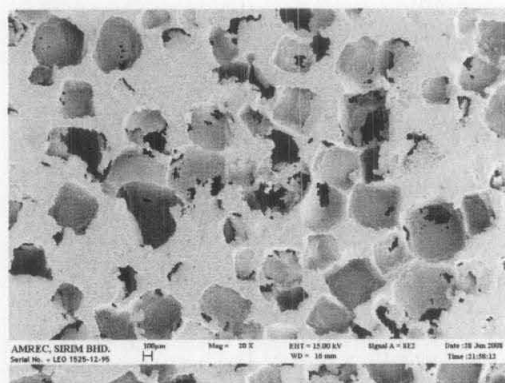
Figure 4.93: Variation of density and porosity of pressure assisted sintering foam with NaCl/Al volume fraction after dissolution process for (a) TS-NaCl (b) AC-NaCl (c) HI-NaCl (d) SA-NaCl

In PASDP the foam porosity can be varied in a much wider range by adjusting the NaCl-to-Al volume fraction in the NaCl/Al powder compact, as long both the NaCl particles and the Al matrix are interconnected in the great majority [10]. PASDP can use finer NaCl particles to produce fine-celled foams because the interstices between the NaCl particles are filled with Al particles in the solid state [13]. Consequently, the Al foams produced by PASDP are expected to be able to meet the property requirements in a wide range of applications [10], [13], [22].

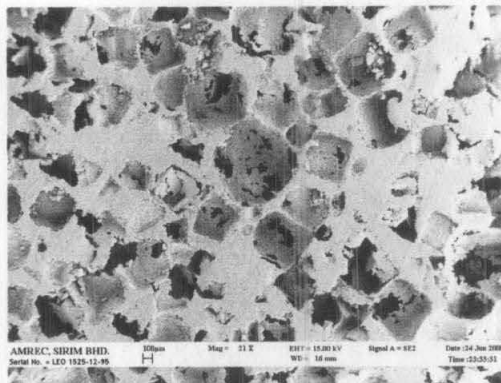
PASDP is most suitable for manufacturing Al foams with relative densities between 0.15 and 0.4. It is difficult to obtain a relative foam density below 0.15 by PASDP because the Al particles in the NaCl/Al perform with a low Al weight fraction are largely separated between each particle rather than forming a continuous network between them [10], [13], [22].

Figures 5.94 – 5.97 show the SEM micrograph of typical Al foam with Al volume fraction between 60 % and 80 % in the initial of different particle size and its widths of size distribution of leaching agent in NaCl/Al composites. The foam has a homogenous structure with open pores and pore sizes in the range 200-1000 μm , which represent the particle characteristics of the original NaCl powder. It is demonstrated that the morphology and sizes of the pores in the foam can be easily controlled by selecting an appropriate NaCl powder [10]. It is also possible to obtain a purposely tailored distribution of pore size or relative density in the foam by using NaCl powders with different particle size ranges or by varying the local Al volume fraction in the NaCl/Al composites [13].

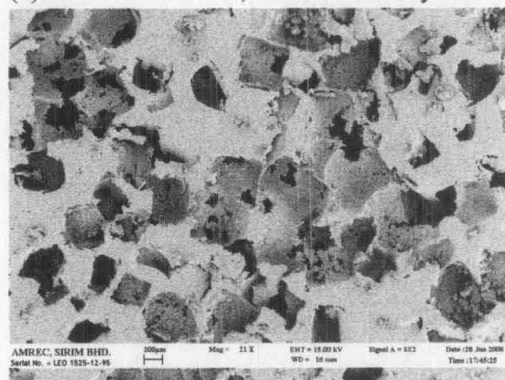
All the type of foams which have produced by different shape and size of leaching agent posses an open-pore structure featuring three level of porosity (Figures 4.98 – 4.101). The structure is characterized by cell (1st level) with some openings or windows (2nd level) on the cell walls. The third level of porosity, visible at higher magnification, results from the voids between the pressure assisted sintering metallic particles. The pore size distribution evaluated by image analysis shows that most of pores fit into the range of 150-2500 μm which reflect the original size of NaCl used.



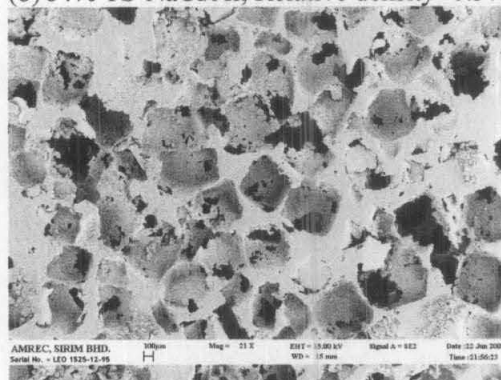
(a) 60% TS-NaCl/Al; Relative density=0.419



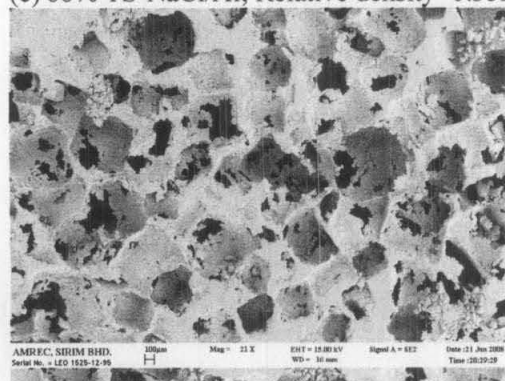
(b) 64% TS-NaCl/Al; Relative density=0.376



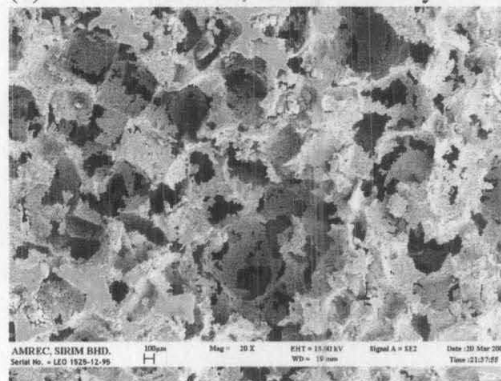
(c) 66% TS-NaCl/Al; Relative density=0.352



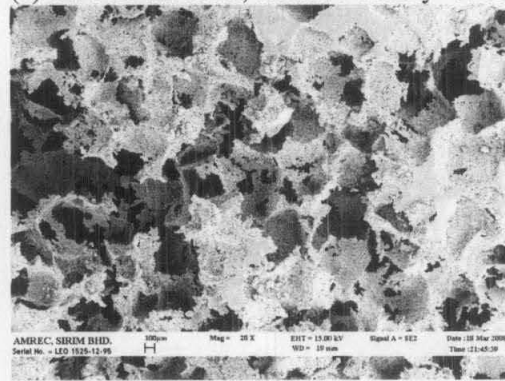
(d) 70% TS-NaCl/Al; Relative density=0.301



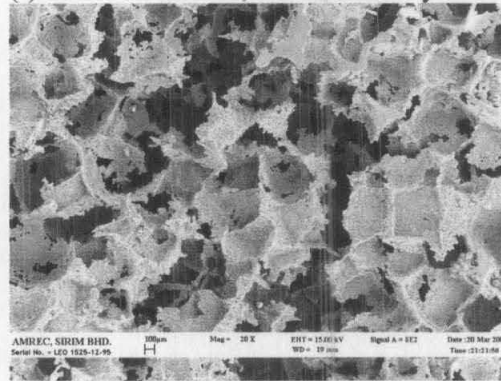
(e) 72% TS-NaCl/Al; Relative density=0.285



(f) 75% TS-NaCl/Al; Relative density=0.254

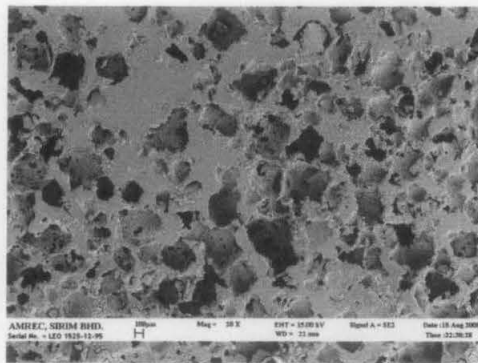


(g) 78% TS-NaCl/Al; Relative density=0.222

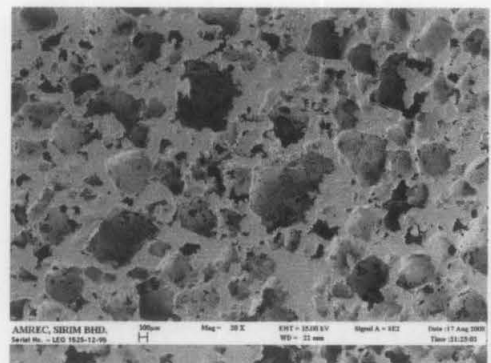


(h) 80% TS-NaCl/Al; Relative density=0.201

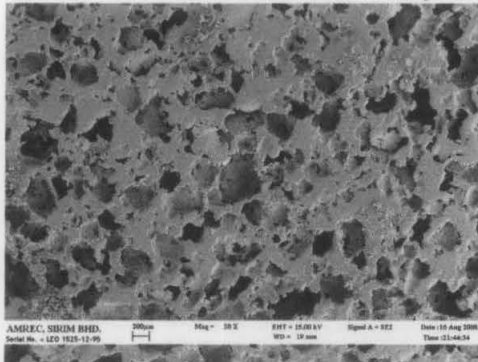
Figure 4.94: Images (SEM) of TS-NaCl/Al foams with different relative densities made by PASDP



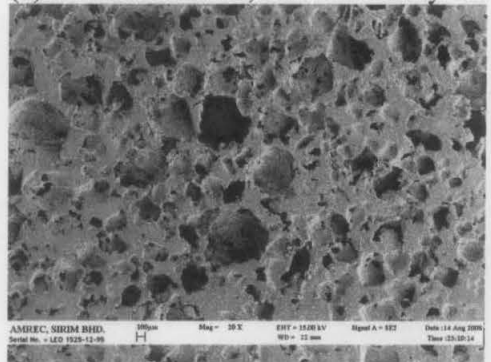
(a) 60% AC-NaCl/Al; Relative density=0.420



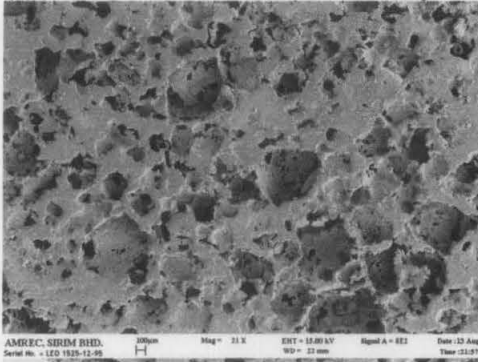
(b) 64% AC-NaCl/Al; Relative density=0.376



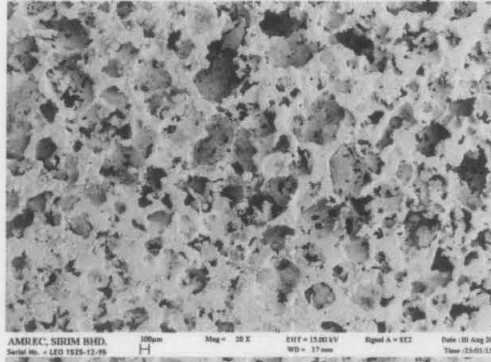
(c) 66% AC-NaCl/Al; Relative density=0.353



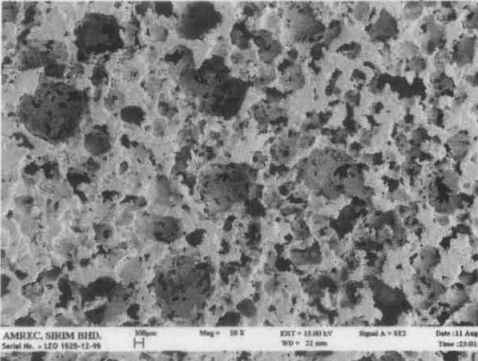
(d) 70% AC-NaCl/Al; Relative density=0.301



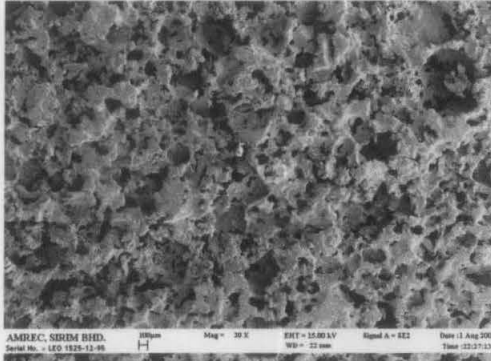
(e) 72% AC-NaCl/Al; Relative density=0.285



(f) 75% AC-NaCl/Al; Relative density=0.254

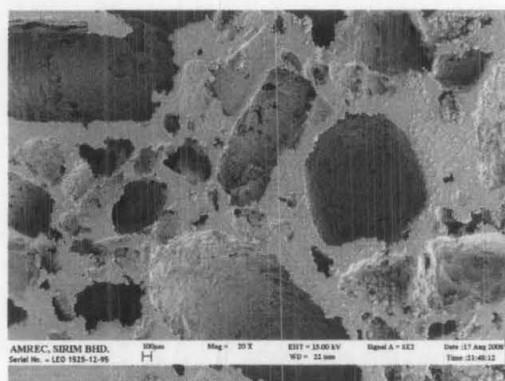


(g) 78% AC-NaCl/Al; Relative density=0.222

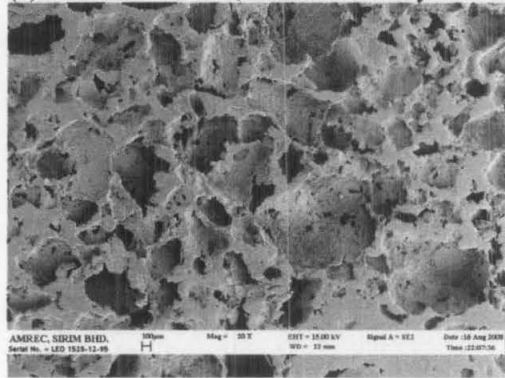


(h) 80% AC-NaCl/Al; Relative density=0.202

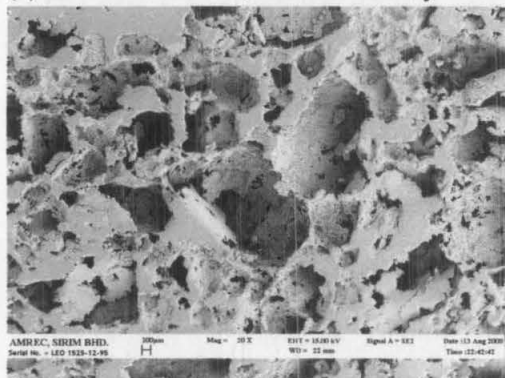
Figure 4.95: Images (SEM) of AC-NaCl/Al foams with different relative densities made by PASDP



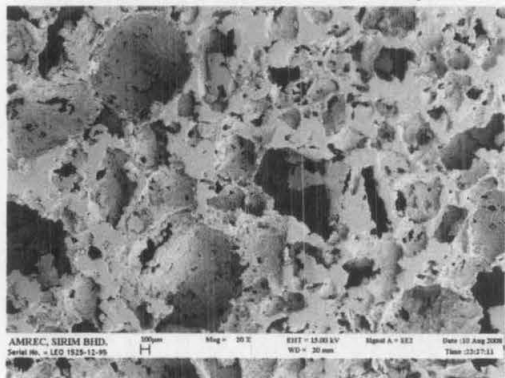
(a) 60% HI-NaCl/Al; Relative density=0.420



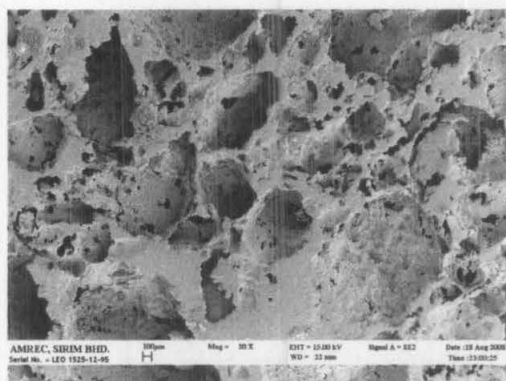
(c) 66% HI -NaCl/Al; Relative density=0.352



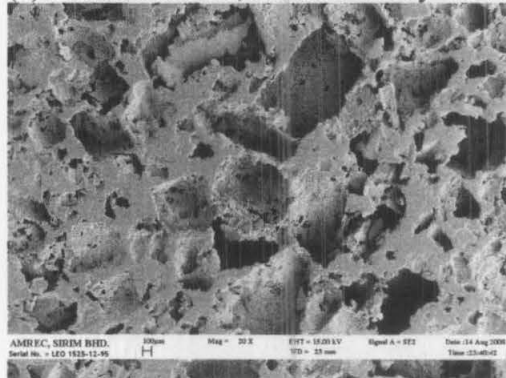
(e) 72% HI-NaCl/Al; Relative density=0.285



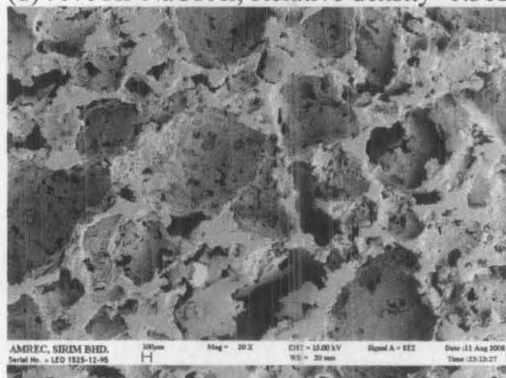
(g) 78% HI-NaCl/Al; Relative density=0.223



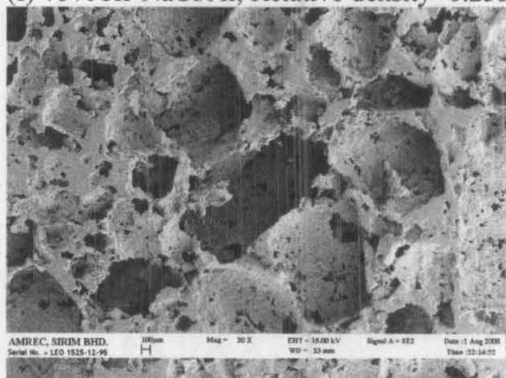
(b) 64% HI-NaCl/Al; Relative density=0.377



(d) 70% HI-NaCl/Al; Relative density=0.302

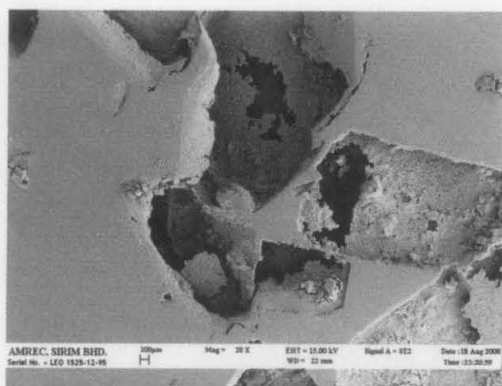


(f) 75% HI-NaCl/Al; Relative density=0.255

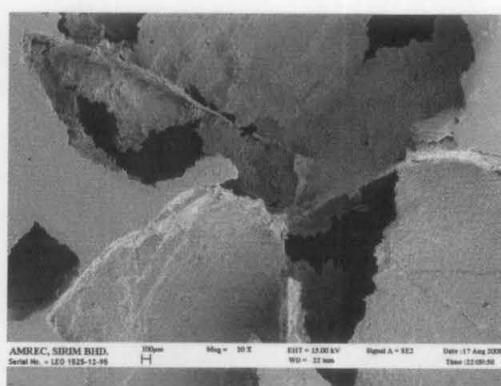


(h) 80% HI-NaCl/Al; Relative density=0.202

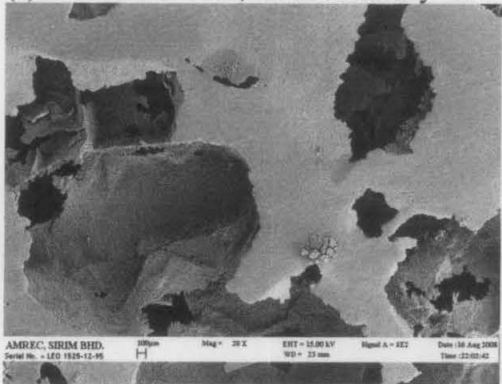
Figure 4.96: Images (SEM) of HI-NaCl/Al foams with different relative densities made by PASDP



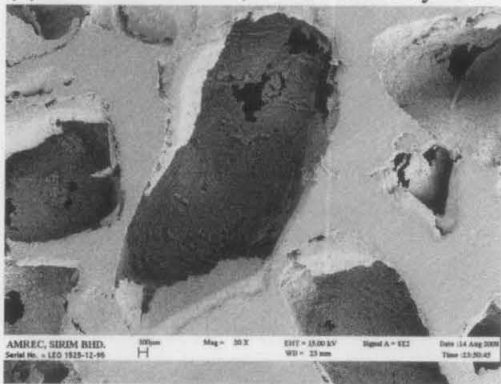
(a) 60% SA-NaCl/Al; Relative density=0.419



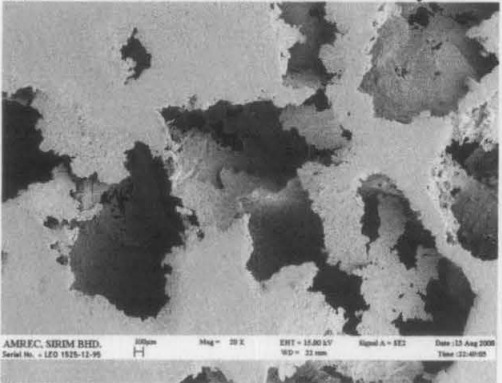
(b) 64% SA-NaCl/Al; Relative density=0.376



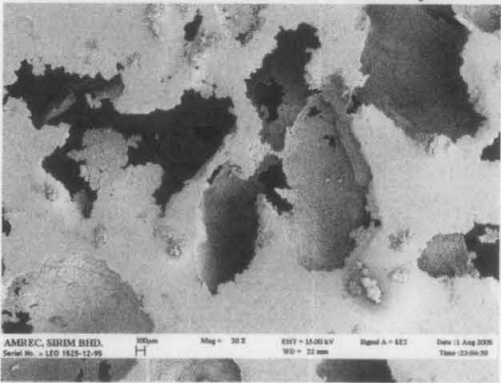
(c) 66% SA-NaCl/Al; Relative density=0.353



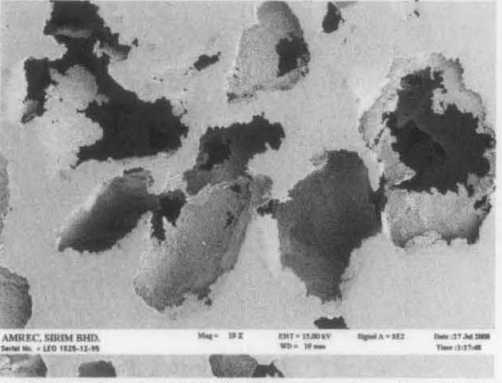
(d) 70% SA-NaCl/Al; Relative density=0.302



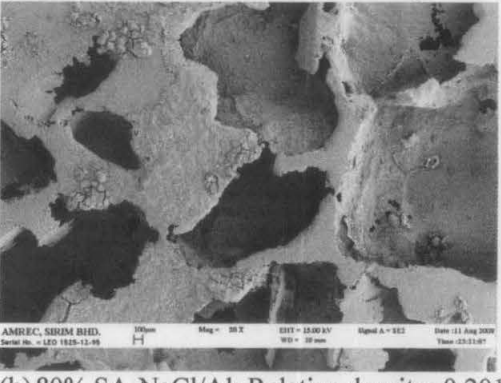
(e) 72% SA-NaCl/Al; Relative density=0.285



(f) 75% SA-NaCl/Al; Relative density=0.254

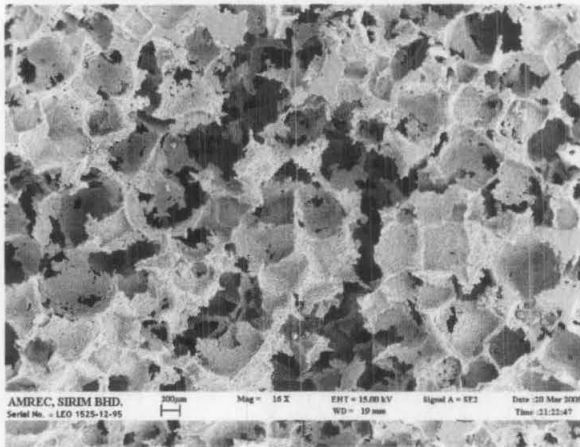


(g) 78% SA-NaCl/Al; Relative density=0.222

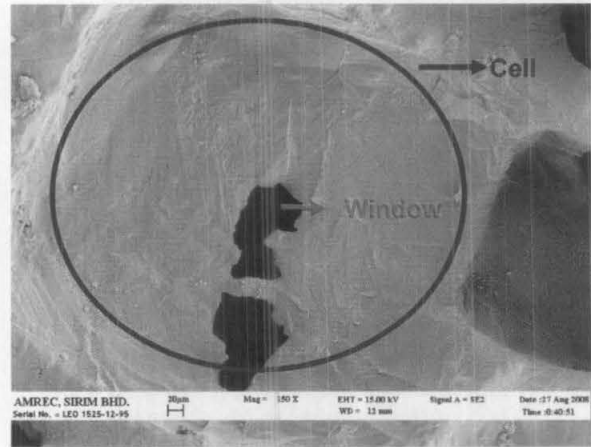


(h) 80% SA-NaCl/Al; Relative density=0.201

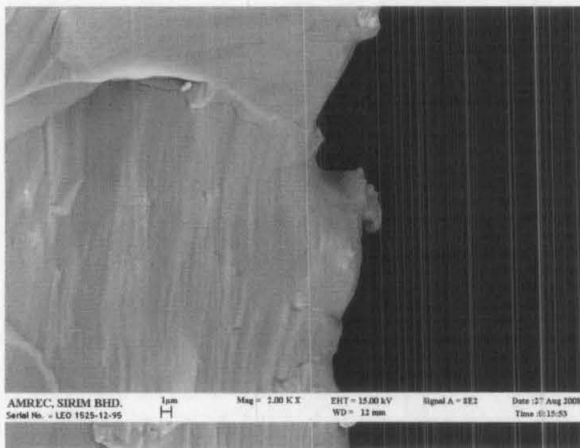
Figure 4.97: Images (SEM) of SA-NaCl/Al foams with different relative densities made by PASDP



(a)



(b)

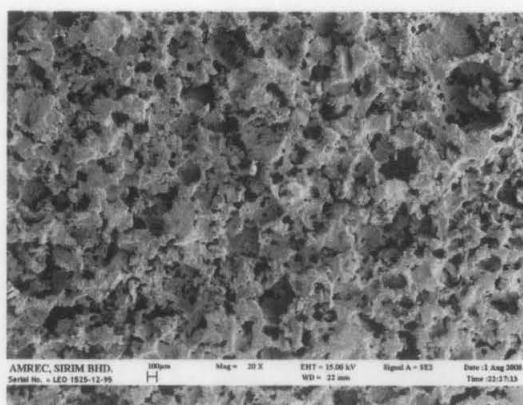


(c)

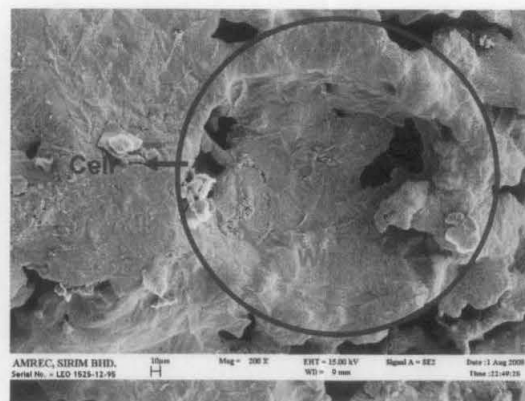


(d)

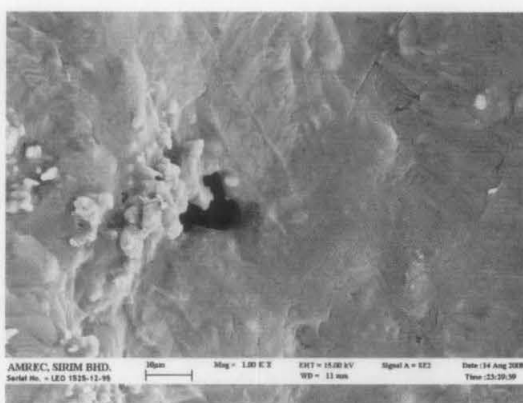
Figure 4.98: Images (SEM) of pressure assisted sintering aluminium foam using 80% TS-NaCl filler material (a),(b) showing the cells and windows (a x20 and b x50); (c),(d) showing the quality of cell wall (c x1000X and d x2000)



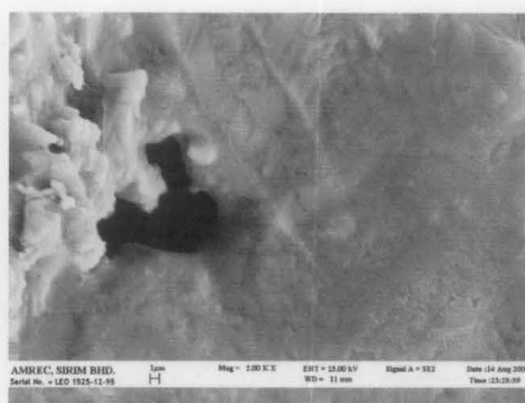
(a)



(b)



(c)



(d)

Figure 4.99: Images (SEM) of pressure assisted sintering aluminium foam using 80% AC-NaCl filler material (a),(b) showing the cells and windows (a x20 and b x50); (c),(d) showing the quality of cell wall (c x1000X and d x2000)

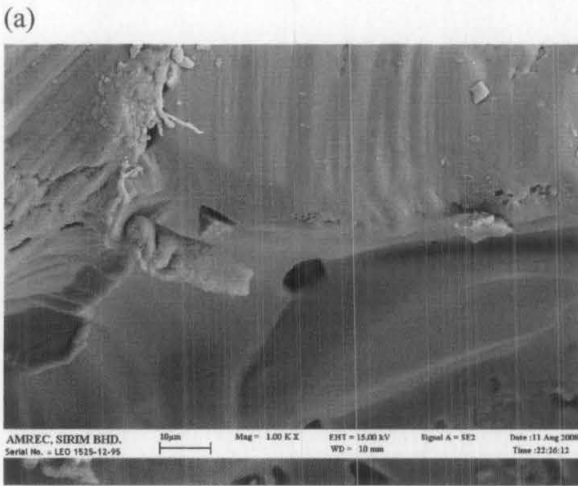
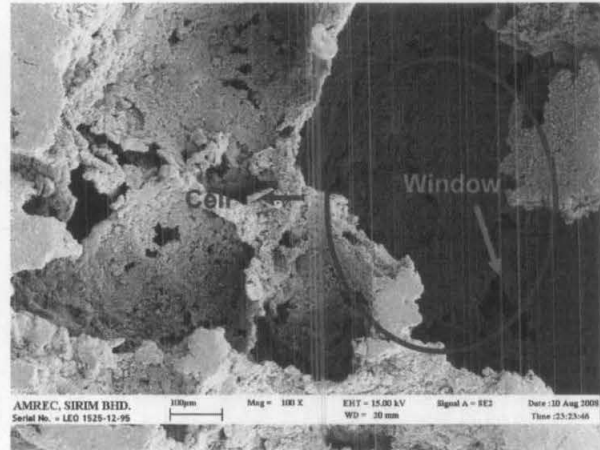
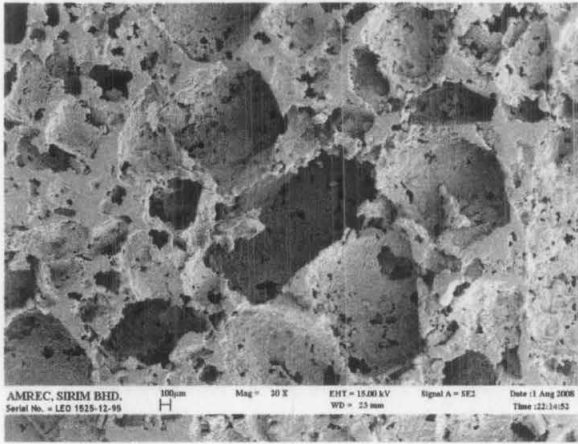
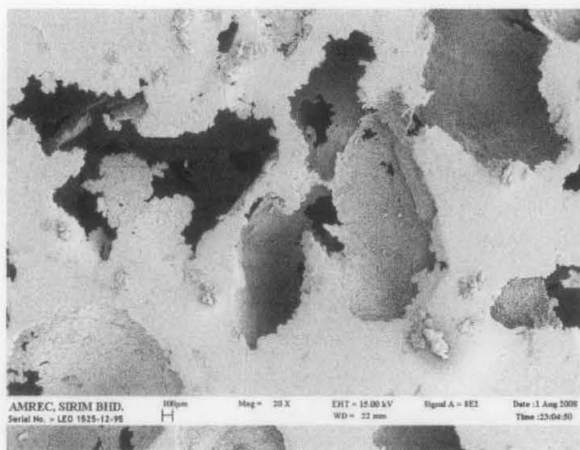
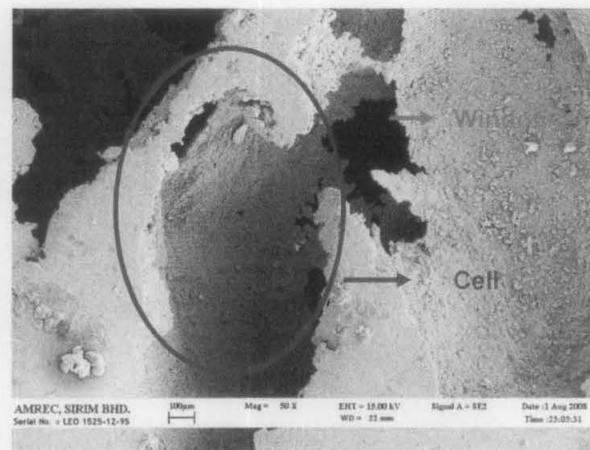


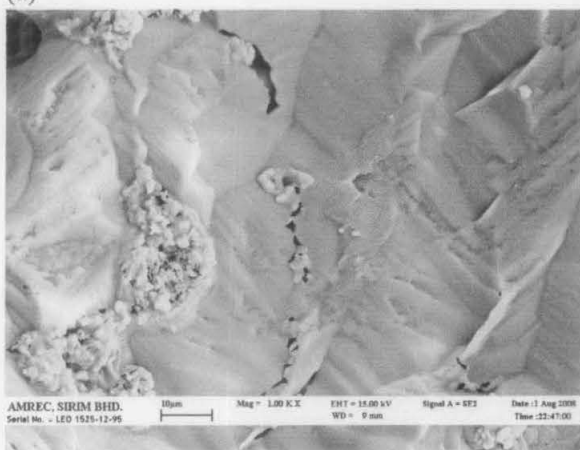
Figure 4.100: Images (SEM) of pressure assisted sintering aluminium foam using 80% HI-NaCl filler material (a),(b) showing the cells and windows (a x20 and b x50); (c),(d) showing the quality of cell wall (c x1000X and d x2000)



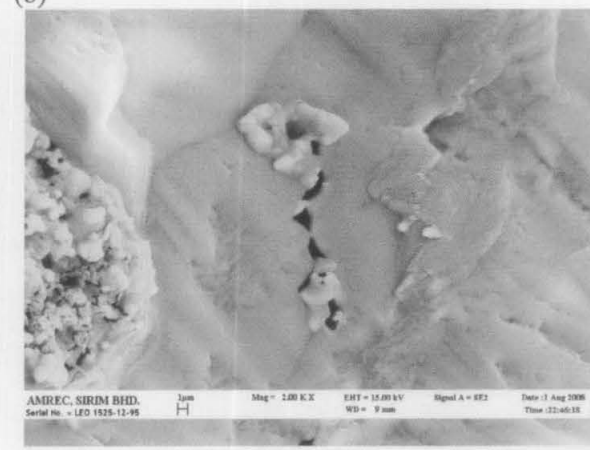
(a)



(b)



(c)



(d)

Figure 4.101: Images (SEM) of pressure assisted sintering aluminium foam using 80% SA-NaCl filler material (a),(b) showing the cells and windows (a x20 and b x50); (c),(d) showing the quality of cell wall (c x1000X and d x2000)

4.8 The effect of pore size on the electrical conductivity of aluminium foam

Aluminium foam is an isotropic, highly porous aluminium in which the pores create a cellular structure [135]. It is obvious that the properties of the foams are significantly affected by their porosity level. On the macroscopic level, aluminium foam can be approximately characterized by the effective mechanical and physical properties, considering the foam as a homogenous bulk body with a certain apparent density.

The dependence of these effective properties on the pore structure has been explained by various approximate methods [135]-[137], originally developed for composite materials. The problem relating the conductivity in a two-phase composite to the conductivity of the component phase-a continuous solid phase and a continuous or discontinuous pore phase- has been approached in a number of ways by different authors [135], [137]-[139]. Some expressions are empirical generalization, while others emerge from consideration of the structure of foam. However, the data and formulae that described the dependence of electrical properties on the cell structure and on the porosity are still limited. Based on the equations derived for modeling the electrical conductivity of sintered compacts, Skorohod and Solonin [136] found the empirical formula for the specimens of porosity above 40%:

$$(1 - \theta)^{5/2} \quad (4.13)$$

where θ is the mean porosity of the foam.

A theoretical model based on the electrodeposition nickel foams (open cell), Langlois and Coeuret [143] found the empirical formula connecting electrical conductivity with porosity for porous nickel:

$$\lambda_f = \frac{1}{4}(1 - \theta)\lambda_s \quad (4.14)$$

where λ_f and λ_s are the electrical conductivity of foam and solid, respectively, and θ is the mean porosity of the foam.

A theoretical model based on octahedral arrays of wires has been proposed by Liu and Liang [141]:

$$\lambda_f = \frac{1-\theta}{3[1-0.121(1-\theta)^{1/2}]} \lambda_s \quad 4.15)$$

where the symbols have the same meaning as above. All of these formulae are based on the perquisite that the cells of the porous body are the open-type.

As summarized above, the dependence of electrical properties on the cell structure and the relative density that characterizes the metal foam is lacking. The value of the effective electrical conductivity proves to be useful and of critical importance in structural foam.

The relationship between relative electrical conductivity and total porosity according to different pore size and its width of size distribution are shown for the foam specimen is shown in Figure 4.102. The mathematical description given by Skorohod and Solonin was also tested with the experimental data obtained and it was revealed that the relationship does not follow this equation.

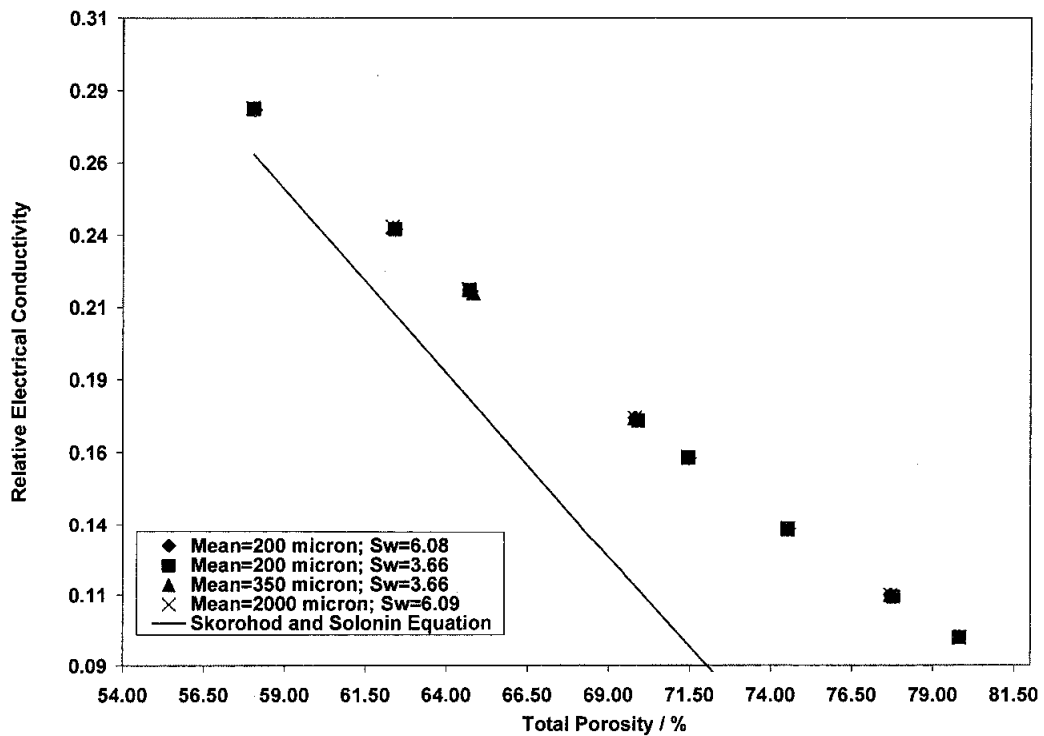


Figure 4.102: Relative electrical conductivity of foam specimens as a function of total porosity at different pore size and the width of pore size distribution

The relationship between relative electrical conductivity and density is shown in Figure 4.103. It was found that a simple linear correlation dependent on pore size and its width of size distribution reasonably fits the experimentally measured data.

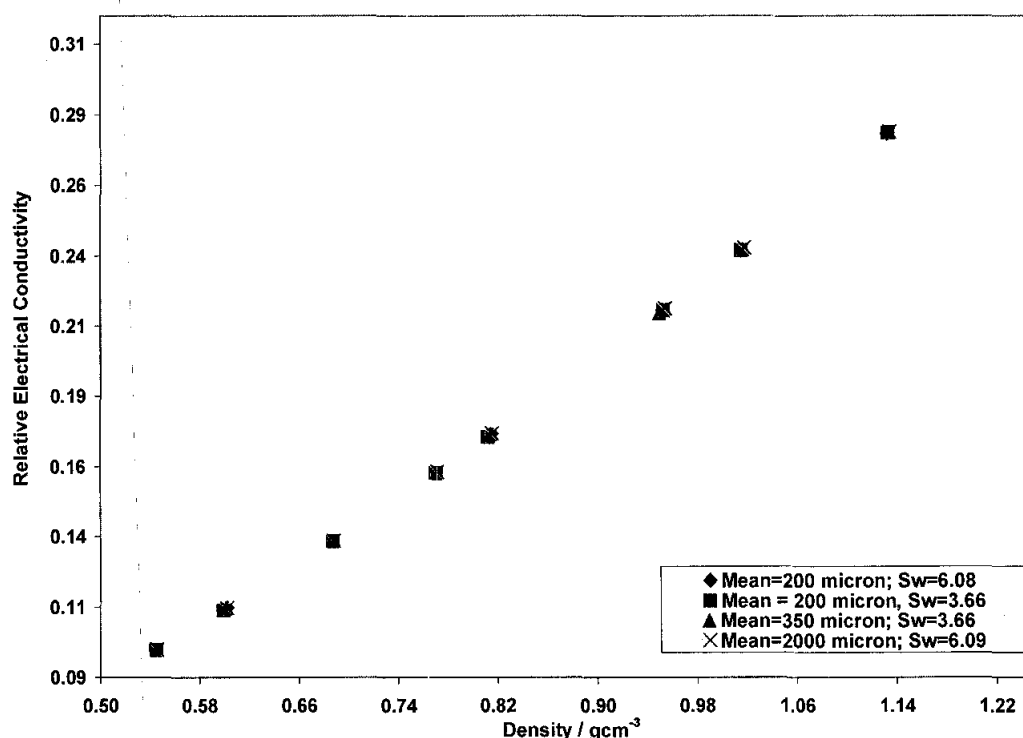


Figure 4.103: Relative electrical conductivity of foam specimens as a function of density at different pore size and the width of pore size distribution

As mentioned earlier, the foam is created by an “infinite” aluminium cluster [135] as presented in Figure 4.92. The cluster has a homogenous structure with open pores and pore size is in the range 150 – 2500 μm , which represents the particles characteristic of the original NaCl powder. It is shown that the cells in the structures are virtually negative replica of the NaCl particles and the cell size matches closely with the particle size. The presence of such cluster is essential for the existence of the foam [22]. If the cluster does not exist the foam disintegrates and the effective properties are zero. This situation agrees well with the behaviour of the effective properties according to the percolation theory [135]-[138]. The effective property becomes zero at the percolation threshold ρ_c while near ρ_c it behaves as a power of $\rho - \rho_c$:

$$\pi \propto (\rho - \rho_c)^t \quad (4.16)$$

where π is the effective property and ρ is the volume fraction of the relevant component, the constant t is often called the critical exponent [136].

The power law seems to be a good characterization of the relationship between experimental data of relative electrical conductivity and relative density of the foam specimens fabricated from PASDP technique as shown in Figure 4.104. The characteristic exponents of z and t of percolation theory [137], which was obtained experimentally are tabulated in Table 4.16.

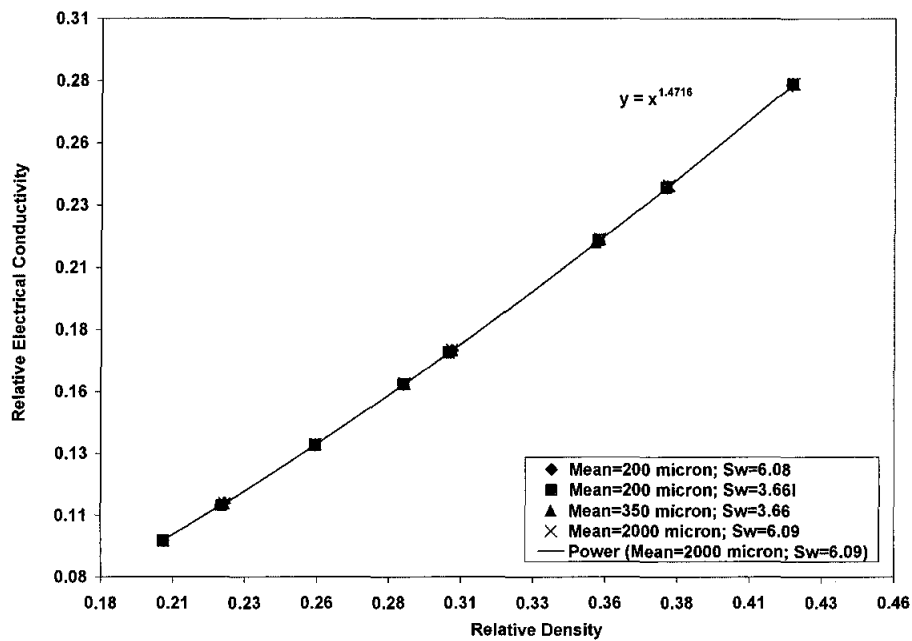


Figure 4.104: Relative electrical conductivity of foam specimens as a function of relative density at pore size and the width of its size distribution

Table 4.16: The obtained fitting parameters for the dependence of relative electrical conductivity on the relative density for different pore size and distribution

Pore size and distribution	z	t
Mean=200 μm ; $S_w=6.08$	1.0000	1.4716
Mean=200 μm ; $S_w=3.66$	1.0000	1.4716
Mean=350 μm ; $S_w=3.66$	1.0000	1.4716
Mean=2000 μm ; $S_w=6.09$	1.0000	1.4716

4.9 The compressive properties of Aluminium foam of different pore size and the width of pore size distribution

Figure 4.105 shows the compressive stress-strain curves of the Al foams with different volume fraction of initial TS-NaCl of 30%, 40%, 50% and 60 respectively, which correspond to porosity of 20.44%, 21.89%, 40.19% and 58.07% respectively. The specimens of 30 to 50% volume fraction of TS-NaCl/Al do not exhibit a characteristic of stress-strain foam behaviour when loaded in compression. The typical engineering stress-strain curve of the aluminium is exhibited by specimen of 60% volume fraction of TS-NaCl/Al. The compressive stress-strain curves of the Al foams with different volume fraction of initial AC-NaCl of 30%, 40%, 50% and 60 respectively is shown in Figure 4.106. These stress-strain curves correspond to porosity of 20.73%, 22.17%, 40.40% and 58.04% respectively. The specimens of 30 to 50% volume fraction of AC-NaCl/Al do not possess the stress-strain characteristic of metallic foam behaviour when subjected to compression. The specimen of 60% volume fraction of AC-NaCl/Al shows the characteristic engineering stress-strain curve of metallic foam.

The initial volume fraction of HI-NaCl of 30%, 40%, 50% and 60 respectively have the compressive stress-strain curves behaviour as presented in Figure 4.107 which relates to porosity of 20.70%, 22.10%, 40.30% and 58.03% respectively. The specimens of 30 to 50% volume fraction of AC-NaCl/Al do not exhibit a characteristic of stress-strain foam behaviour when loaded in compression. The typical engineering stress-strain curve of the aluminium is exhibited by specimen of 60% volume fraction of HI-NaCl/Al. The engineering compressive stress-strain curves of the Al foams with different volume fraction of initial SA-NaCl of 30%, 40%, 50% and 60 respectively, is shown in Figure 4.108 shows which correspond to porosity of 20.60%, 22.00%, 40.20% and 58.00% respectively. The specimens of 30 to 50% volume fraction of AC-NaCl/Al do not exhibit a characteristic of stress-strain foam behaviour when loaded in compression. The typical engineering stress-strain curve of the aluminium is exhibited by specimen of 60% volume fraction of SA-NaCl/Al.

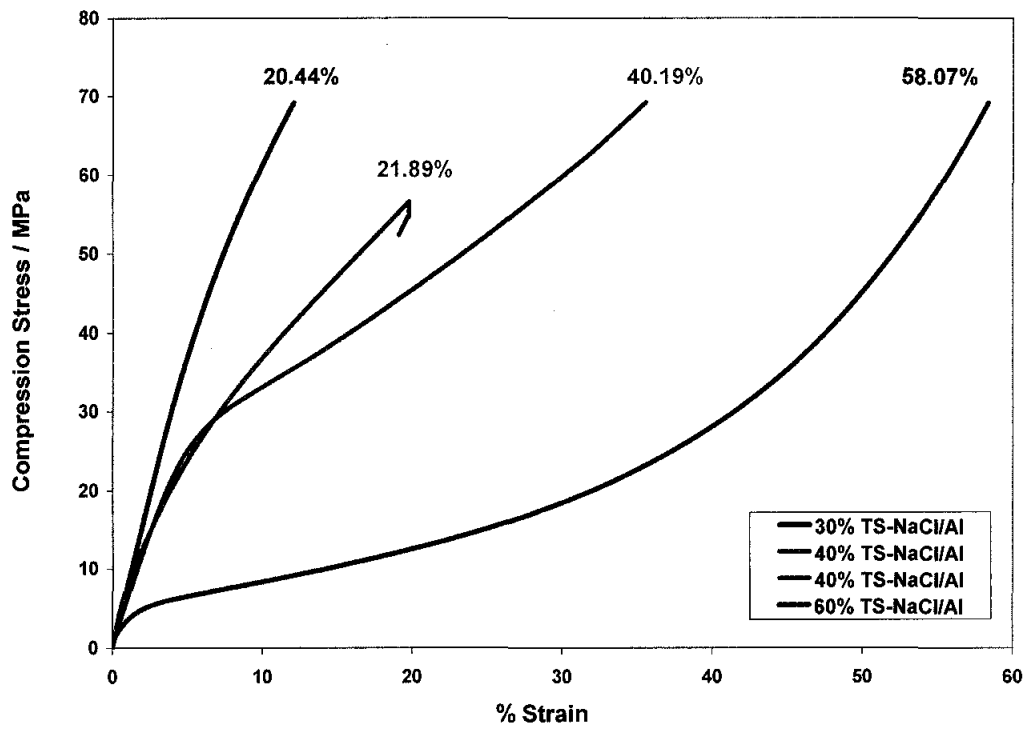


Figure 4.105: Compressive stress-strain curves of the TS-NaCl/Al for highly porous specimens

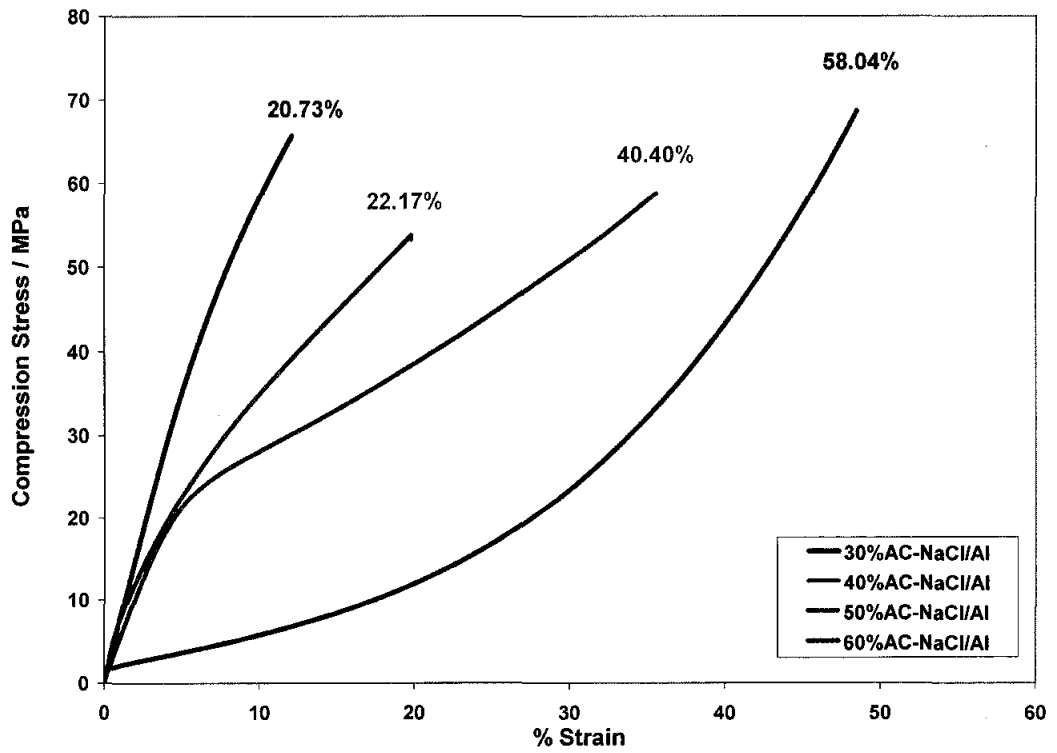


Figure 4.106: Compressive stress-strain curves of the AC-NaCl/Al for highly porous specimens

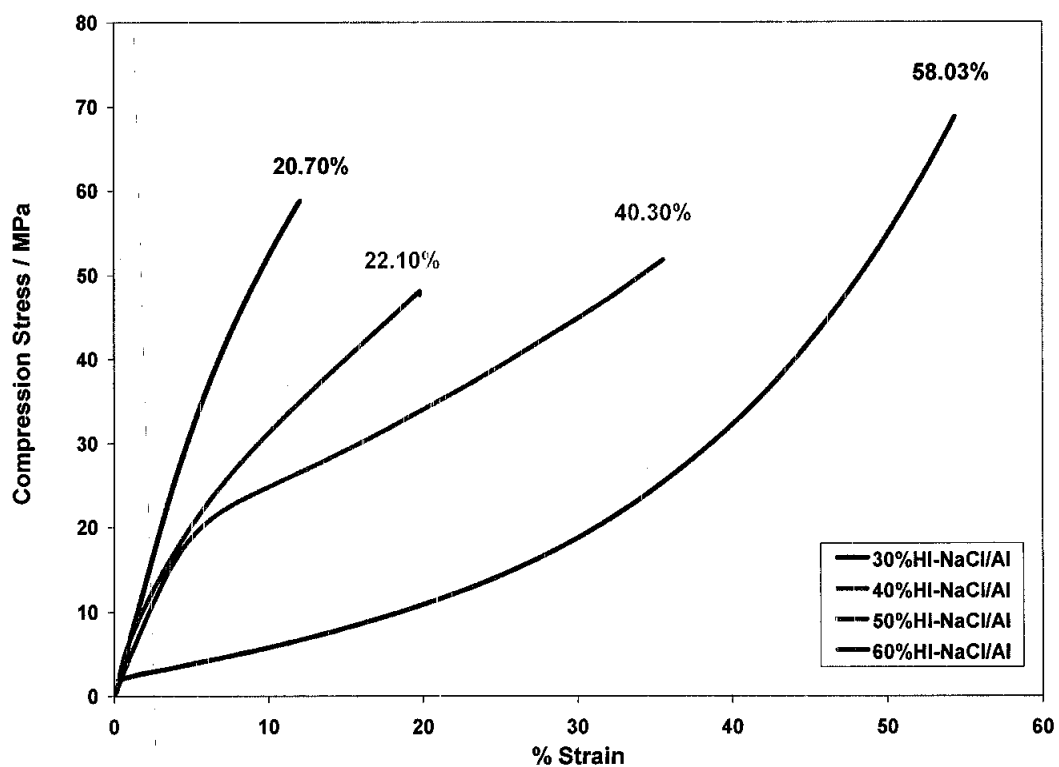


Figure 4.107: Compressive stress-strain curves of the HI-NaCl/Al for highly porous specimens

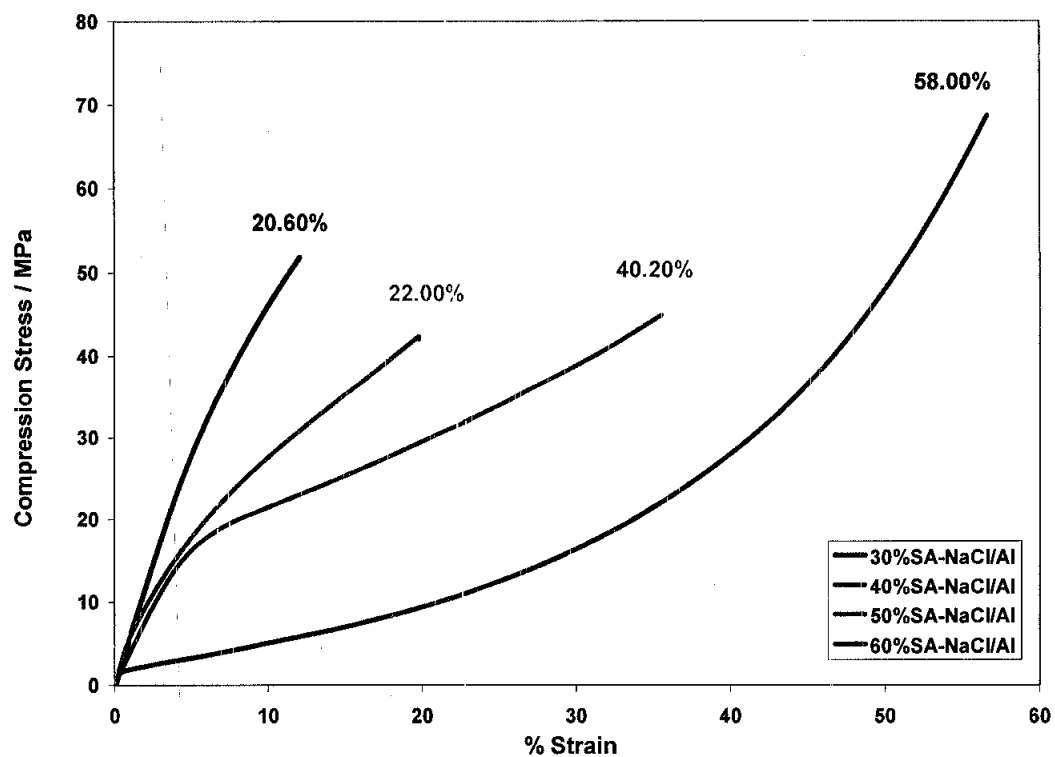


Figure 4.108: Compressive stress-strain curves of the SA-NaCl/Al for highly porous specimens

The typical engineering stress-strain curve of the aluminium is exhibited by specimen of 60% to 80% volume fraction of all types of NaCl/Al. The curves are generally characterised by an initial elastic response, followed by a deformation “plateau” with a positive slope and finally a transition to densification [1], [10], [13], [22]. The plateau stress, which is defined as the mean value of constant flow stress is 2.13 MPa, 1.86 MPa, 1.77 MPa and 1.41 MPa, 1.23 MPa, 1.11 MPa, 0.82 MPa and 0.75 MPa for the Al foam specimen of TS-NaCl type with the porosity of 58.06%, 62.42%, 64.75%, 69.82%, 71.47%, 74.55%, 77.17% and 79.82% respectively (Figure 4.109).

For the Al foam specimen of AC-NaCl type with the porosity of 54.04%, 62.40%, 64.72%, 69.81%, 71.47%, 74.55%, 77.71% and 79.81% has the plateau stress of 1.98 MPa, 1.57 MPa, 1.55 MPa, 1.53 MPa, 1.17MPa, 1.00 MPa, 0.78 MPa and 0.73 MPa respectively (Figure 4.110). The plateau stress is 1.75 MPa, 1.50 MPa, 1.37 MPa, 1.34 MPa, 1.14 MPa, 0.96 MPa, 0.75 MPa and 0.73 MPa for the porous Al specimen of HI-NaCl type with the porosity of 58.03%, 62.35%, 64.83%, 69.82%, 71.47%, 74.55%, 77.71% and 79.81% respectively (Figure 4.111). For the porous Al specimen of SA-NaCl type with the porosity of 58.01%, 62.32%, 64.68%, 69.82%, 71.45%, 74.54%, 77.71% and 79.81% has the plateau stress is 1.62 MPa, 1.42 MPa, 1.33 MPa, 1.26 MPa, 0.97 MPa, 0.83 MPa, 0.71 MPa and 0.60 MPa respectively (Figure 4.112).

Compression test data from both types of foams provided insight into the mechanism of cell collapse, an important indicator for aluminium foam applications [118]. Both types of foam deformed smoothly throughout the entire compression range (samples of 60 to 80 volume fraction of NaCl). Cell walls buckled continuously during compression, providing the main structural collapse mechanism throughout the entire deformation range, and the buckling appeared to be uniformly distributed through the sample [118]-[120]. The majority of the absorbed energy (in Figures 4.109 – 4.112), the area under the stress-strain curve represents the real amount of energy) which is irreversibly converted into plastic deformation energy [121]. This occurs primarily in the broad stress plateau, which is typical of most metallic foams under compression loading and imparts a large capacity for energy absorption [118].

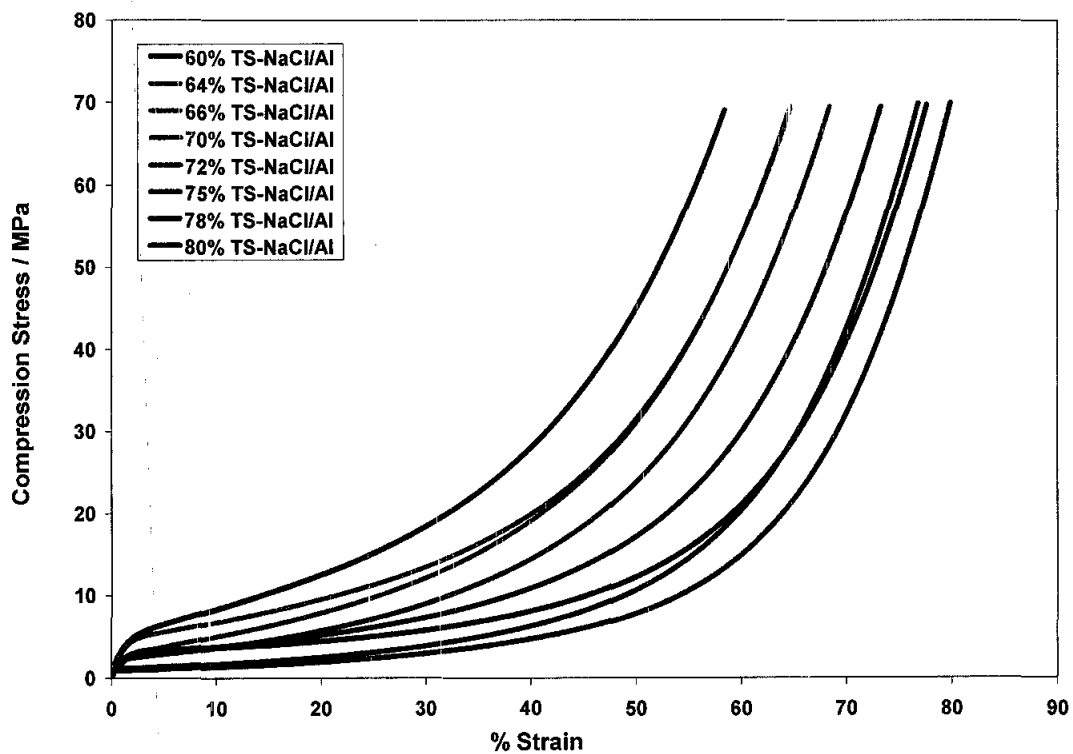


Figure 4.109: Compressive stress-strain curves of the Al foam with different volume fraction for TS-NaCl.

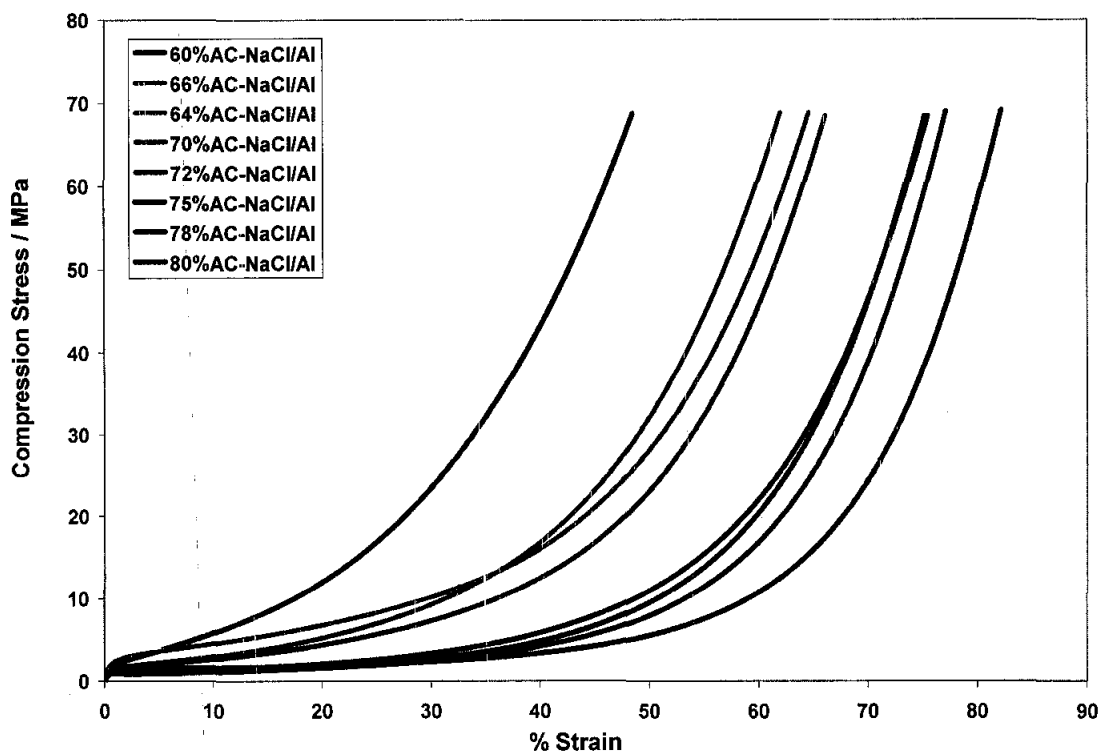


Figure 4.110: Compressive stress-strain curves of the Al foam with different volume fraction for AC-NaCl.

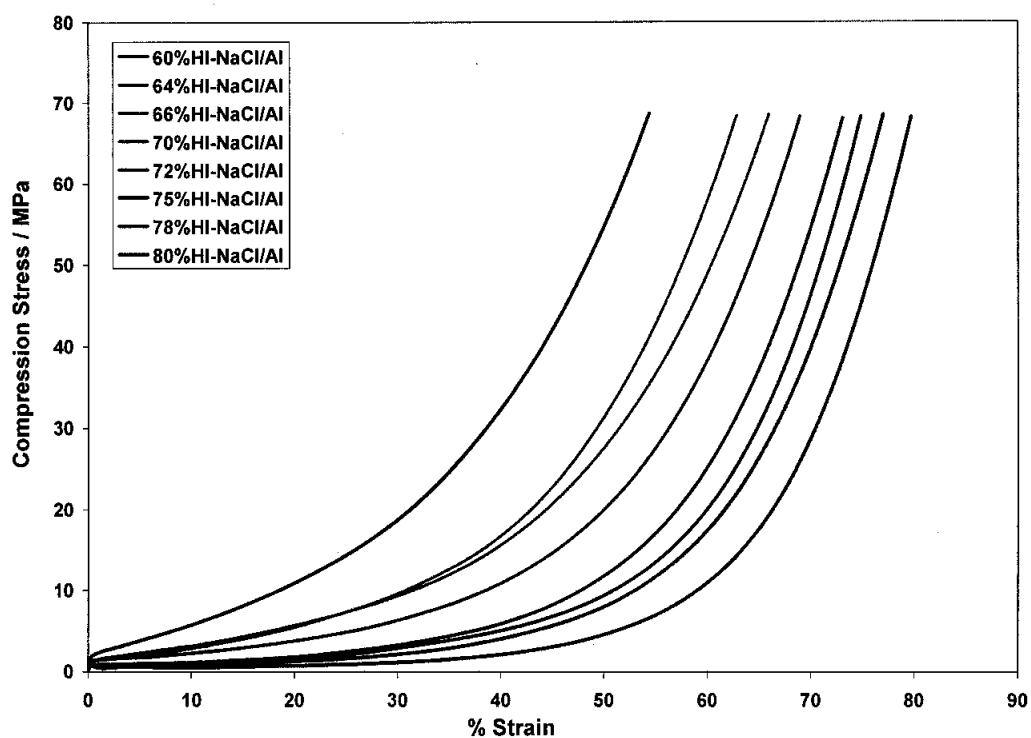


Figure 4.111: Compressive stress-strain curves of the Al foam with different volume fraction for HI-NaCl.

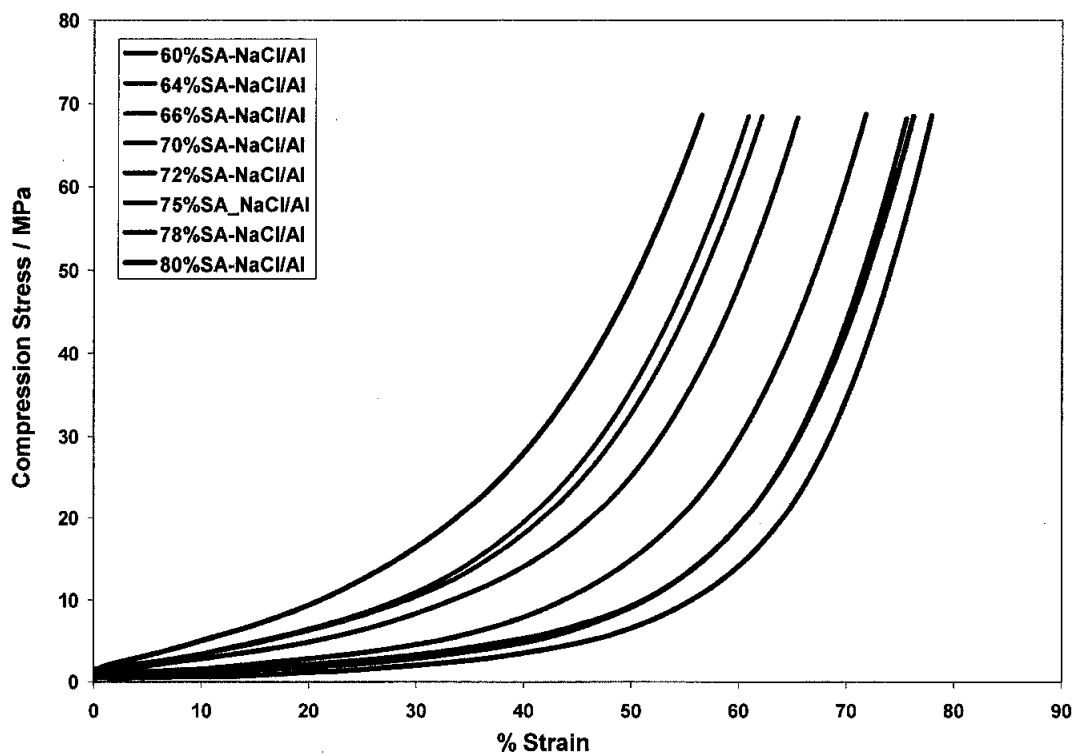


Figure 4.112: Compressive stress-strain curves of the Al foam with different volume fraction for SA-NaCl.

It has been known that the pore size has an influence effect on the mechanical properties of Al foams [9, 13, 15]. Figure 4.113 – 4.116 show that there are differences between compressive stress-strain curves of specimens with similar initial volume fraction of NaCl (relative densities). The variations in compressive stress-strain as a function of pore size are also shown in the figures. The value of the compressive strength of initial 72% NaCl/Al composites after leaching process decrease from 1.23 MPa to 0.97 MPa when the mean pore size is increased from 200 μm to 2000 μm . For sample of initial 75% volume fraction of NaCl, the compressive strength decreases from 1.11 MPa to 0.83 MPa when the pore size is increased from 200 μm to 2000 μm . When the pore size is increased from 200 μm to 2000 μm , the compressive strength of initial volume fraction of 78% NaCl/Al composite after leaching process decreases from 0.82 MPa to 0.71 MPa. For sample of initial 80% volume fraction of NaCl, the compressive strength decrease from 0.75 MPa to 0.60 MPa when the pore size is increased from 200 μm to 2000 μm .

The compressive strength shows an increase in value when the width of size distribution of the pore is altered from narrow to broad at fixed volume fraction of NaCl/Al (relative density) and mean pore size. For the sample of 72% initial volume fraction, it increases from 1.17 MPa to 1.23 MPa when the width of size distribution of the pore is increased from 3.6 to 6.1. The value of the compressive strength is increased from 1.00 MPa to 1.11 MPa when the width of size distribution of the pore is increased from 3.6 to 6.1 for sample of 75% initial volume fraction. Gibson and Ashby [1] analysed the collapse stress of a porous metal using a simple model and noted that the collapse stress is not affected by pore size. Generally, the results in the present investigation show that the compressive stress-strain curve increased with increasing pores size. If the foam density is high, then the constant-stress plateau is short [15]. On the other hand, Al foam of lower density exhibited longer, flatter plateau because the structure affords more opportunity for cell walls to collapse and deform [1], [13]. The compressive stress increased with increasing relative density.

As shown in Figure 4.113 – 4.116, it can be seen that the compressive strength increase with decreasing pore size. As mentioned before, the shape and size of the pores are virtually the replicas of the NaCl particles.

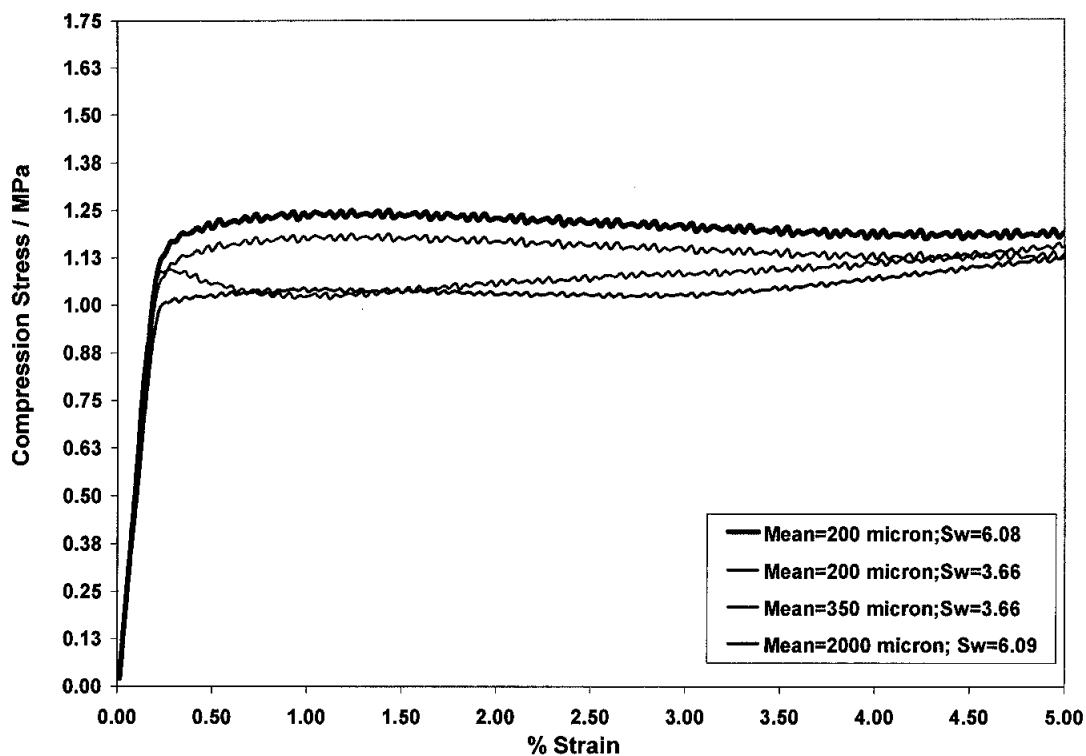


Figure 4.113: The influence of pore size and the width of pore size distribution on compressive stress-strain behaviour of 72% volume fraction of NaCl/Al

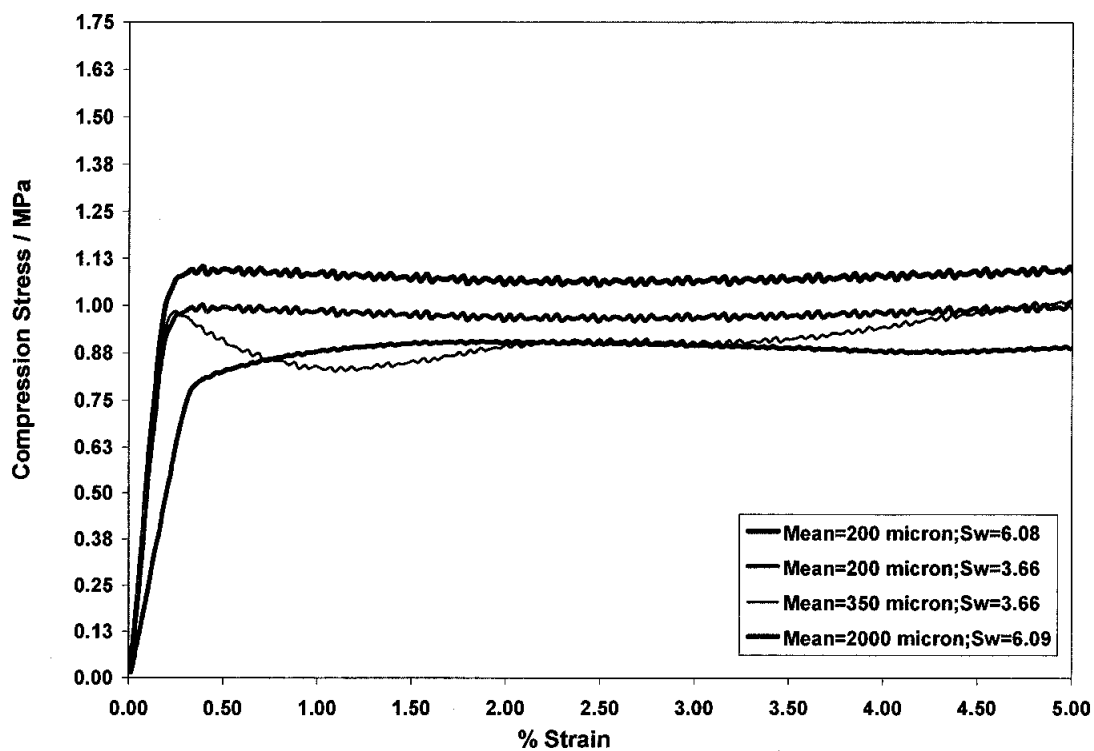


Figure 4.114: The influence of pore size and the width of pore size distribution on compressive stress-strain behaviour of 75% volume fraction of NaCl/Al

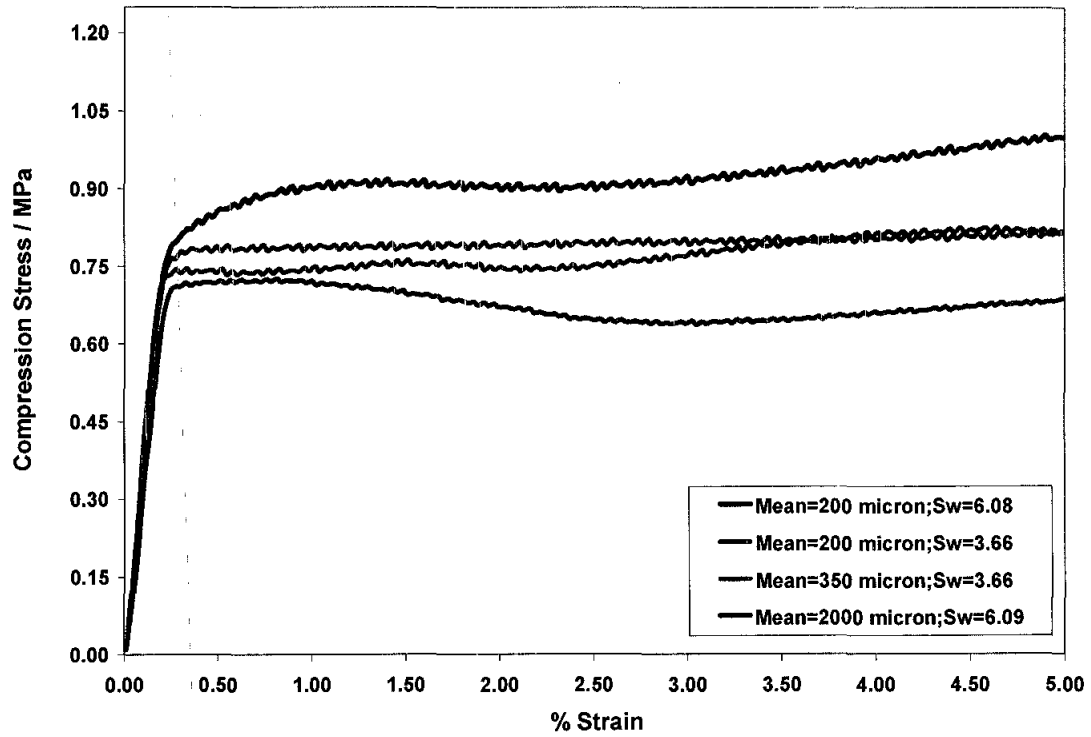


Figure 4.115: The influence of pore size and the width of pore size distribution on compressive stress-strain behaviour of 78% volume fraction of NaCl/Al

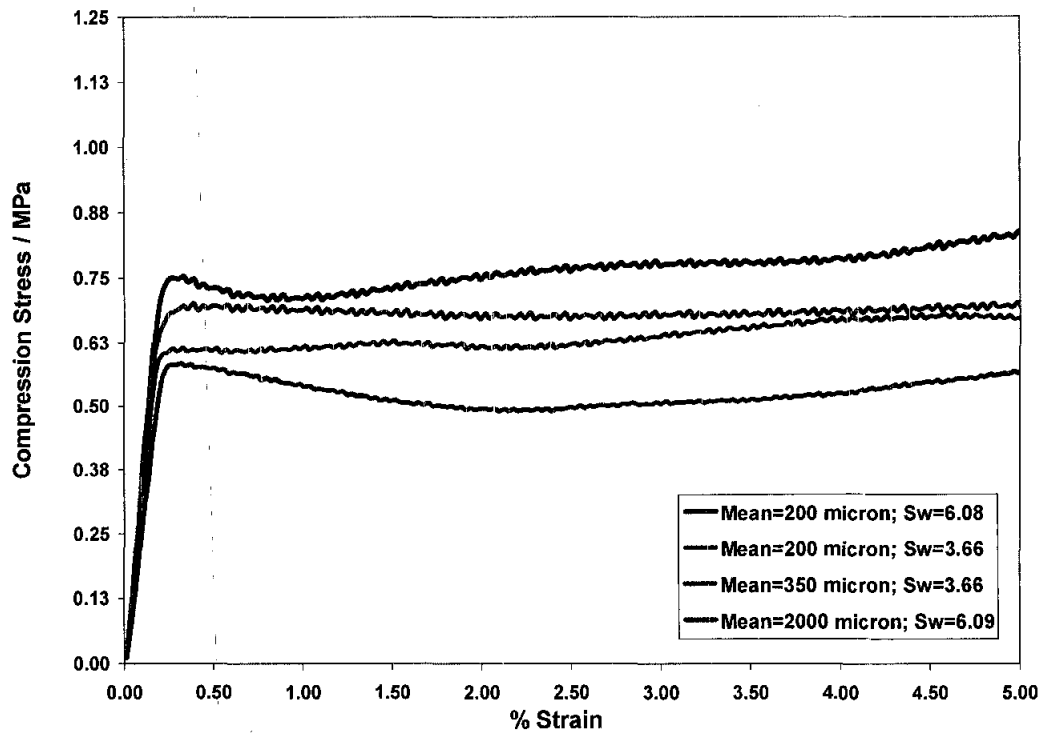


Figure 4.116: The influence of pore size and the width of pore size distribution on compressive stress-strain behaviour of 80% volume fraction of NaCl/Al

Extensive analytical, numerical and experimental works [1], [7], [9], [10] show that the Young's modulus, E , can be written as equation. (4.4). The relationships among the compressive strength of the foam, the yield strength of the cell wall material and the relative density which have been explained in the previous section according to equation (4.5) will be used to determine the value of the exponent for different pore size and its width of distribution.

In Figures 4.117 – 4.124, data for Al foam with different pore size and its width of distribution is plotted to test the relation and to determine the exponent. The set of data appear to be linear. The exponent m is determined by linear regression to be 1.48, 1.37, 1.23 and 1.36 for TS, AC, HI and SA-NaCl samples respectively. From the results obtained, there is a good agreement between the experimental data and the theoretical yield strength. The m values differ from the value of 1.5 predicted by the cubic model for open cell foams. Because the model assumes cubic cell geometry and the aluminium foam fabricated by this process are more irregular, some deviation between measured and predicted behaviour is expected [1]-[3], [11], [31]. Nevertheless, the cubic model describes with reasonable accuracy the relative variation of compressive strength with density. These findings suggest that the n coefficient could be affected by the pore size and shape of the foams. The value of α obtained from this experiment is to be 0.26, 0.22, 0.17 and 0.18 for TS, AC, HI and SA-NaCl samples respectively. The α value obtained is in a good agreement the value obtained by Ashby of between 0.1 and 1 [1], [9], [31]. The values of n which are the values of the slopes by plotting the data as in Figures 4.125 – 4.131 is 0.82, 0.84, 1.02 and 1.16 for TS, AC, HI and SA-NaCl samples respectively. Although the equation (4.8) is based on a simple model of a cubic foam structure, which considerably deviates from Al foam, there is a fair agreement with experimental results. This equation is valid as long as the main deformation mechanism is bending of cell edges [1], [118]. For a high density foam extension and compression of cell edges becomes more important and therefore a deviation from these relations should be observed [22]. The value of β obtained from this experiment is to be 0.0199, 0.0195, 0.0215 and 0.0281 for TS, AC, HI and SA-NaCl samples respectively. The β value obtained is in a good agreement the value obtained by Gibson and Ashby [1] of between 0.01 and 0.09.

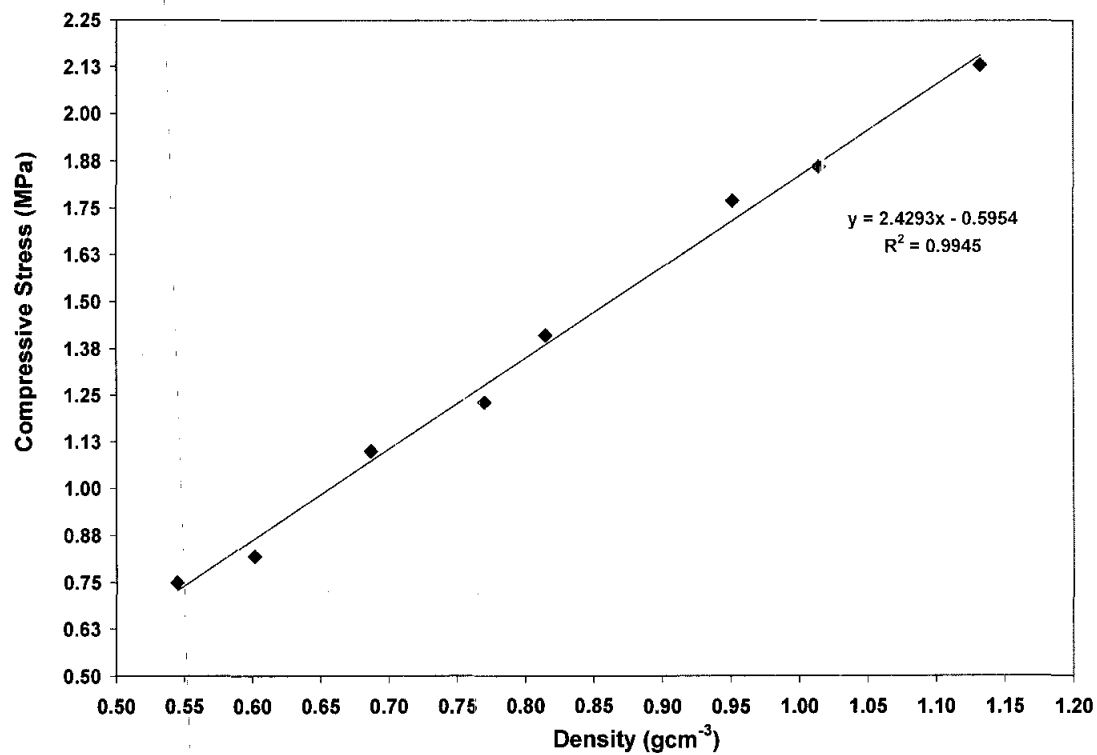


Figure 4.117: Compressive strength of TS-NaCl/Al foam as a function of density

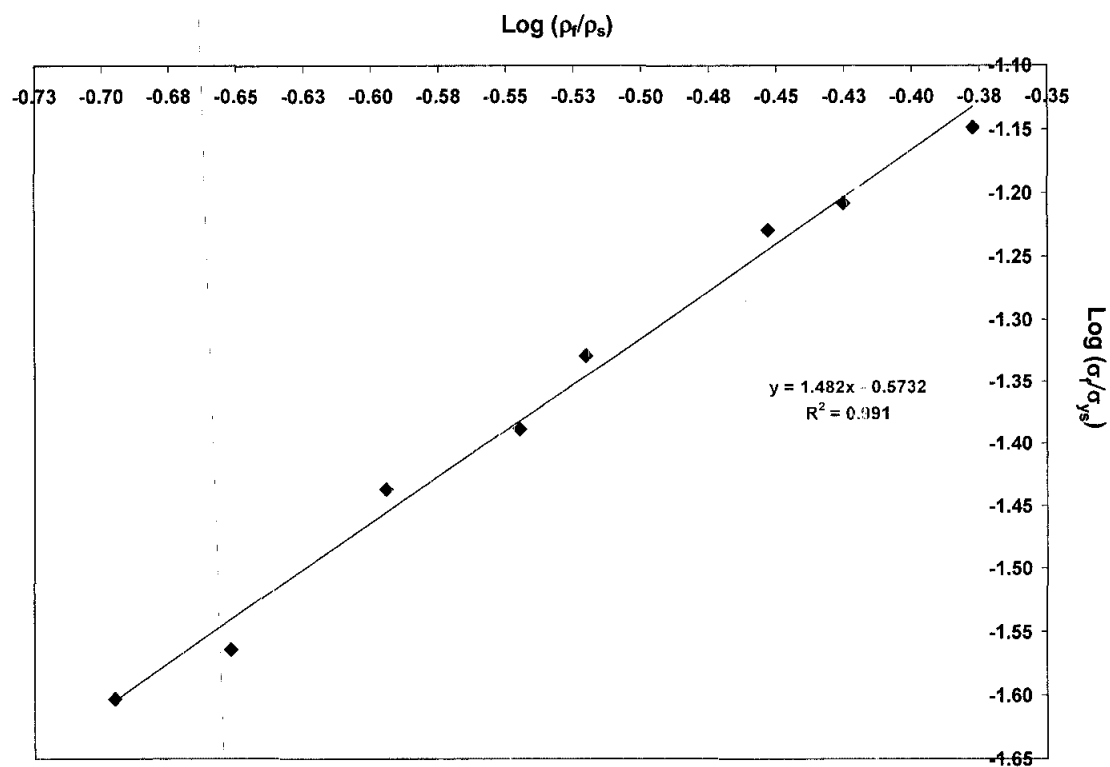


Figure 4.118: Relative compressive strength of TS-NaCl/Al foam as a function of relative density

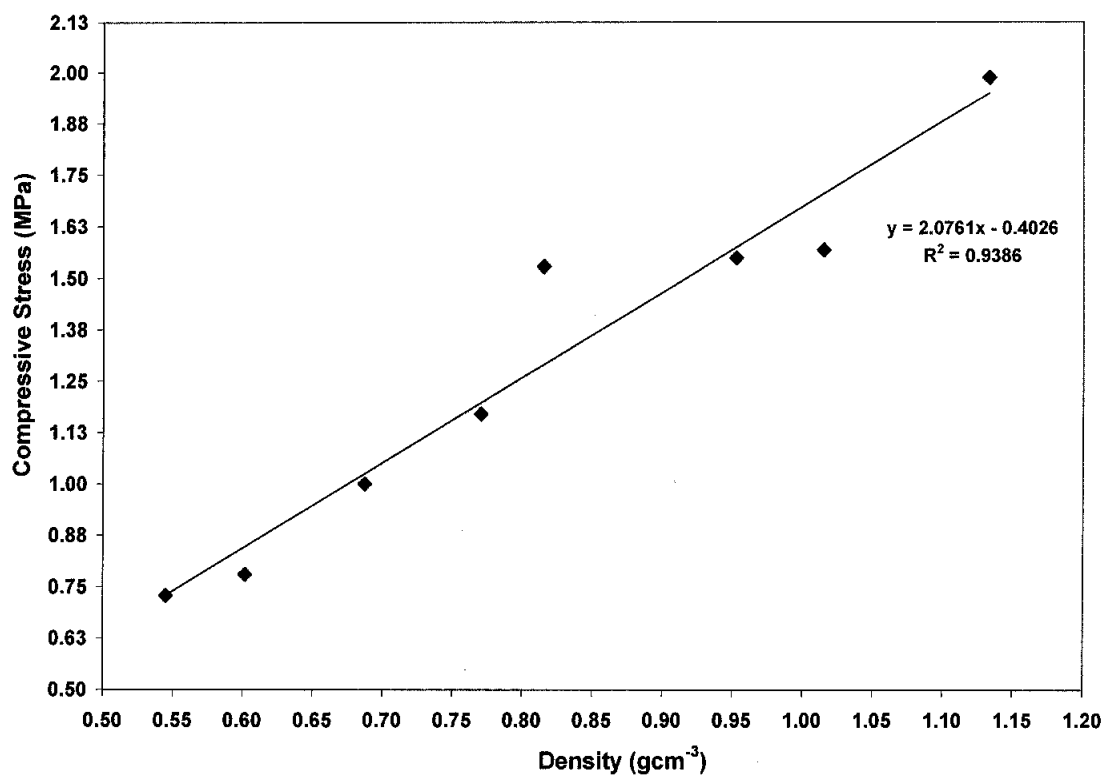


Figure 4.119: Compressive strength of AC-NaCl/Al foam as a function of density

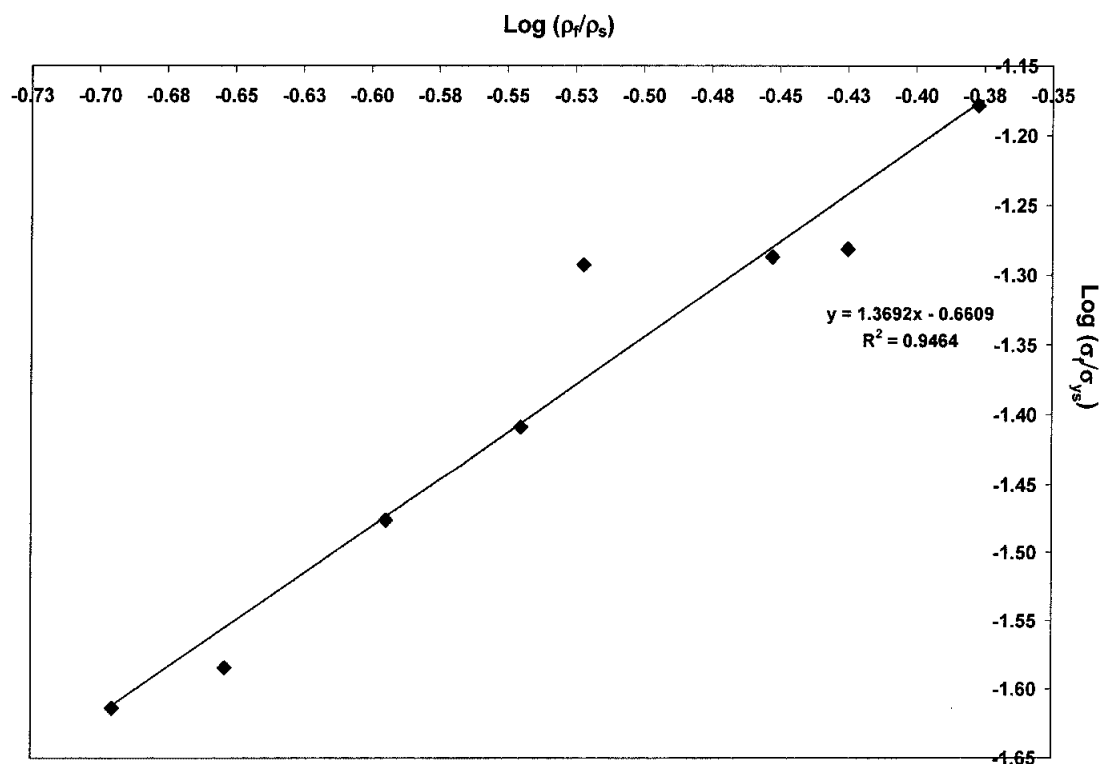


Figure 4.120: Relative compressive strength of AC-NaCl/Al foam as a function of relative density

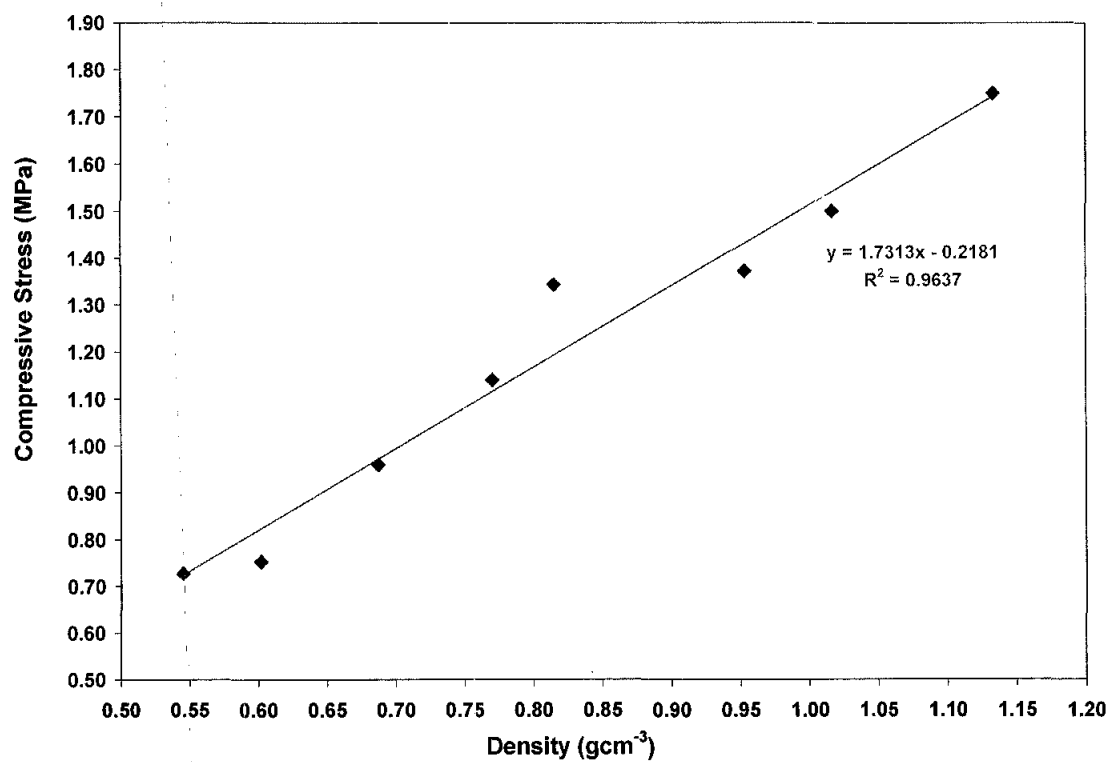


Figure 4.121: Compressive strength of HI-NaCl/Al foam as a function of density

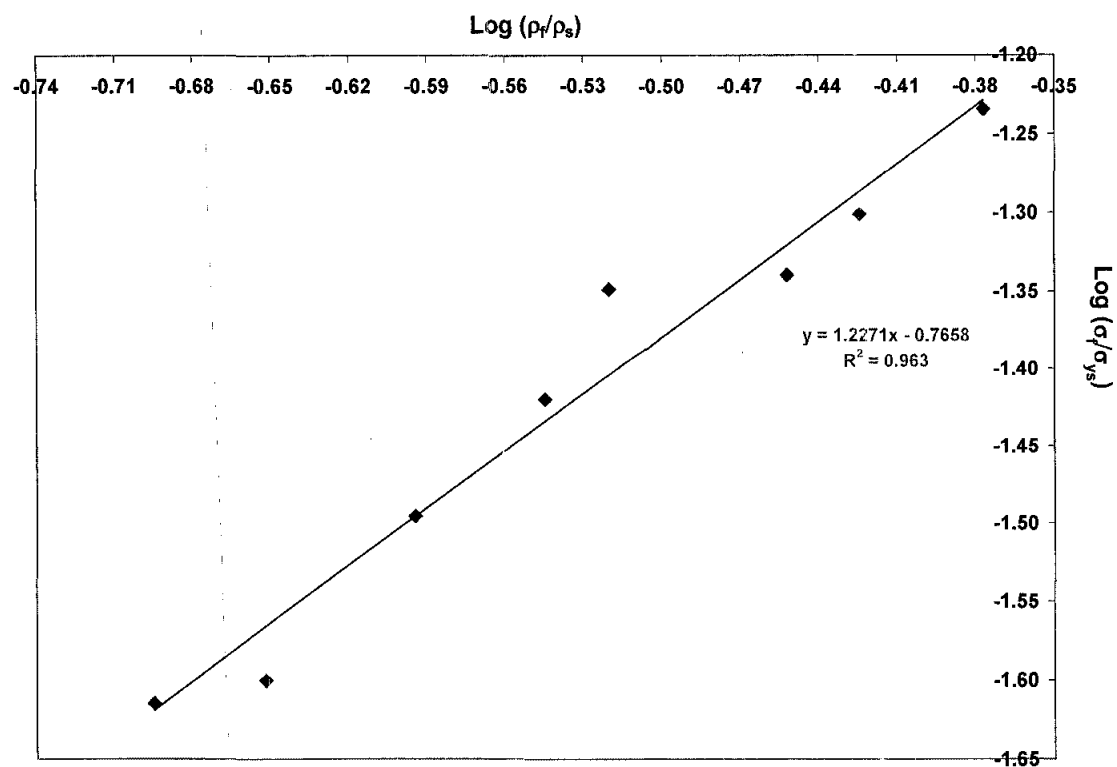


Figure 4.122: Relative compressive strength of HI-NaCl/Al foam as a function of relative density

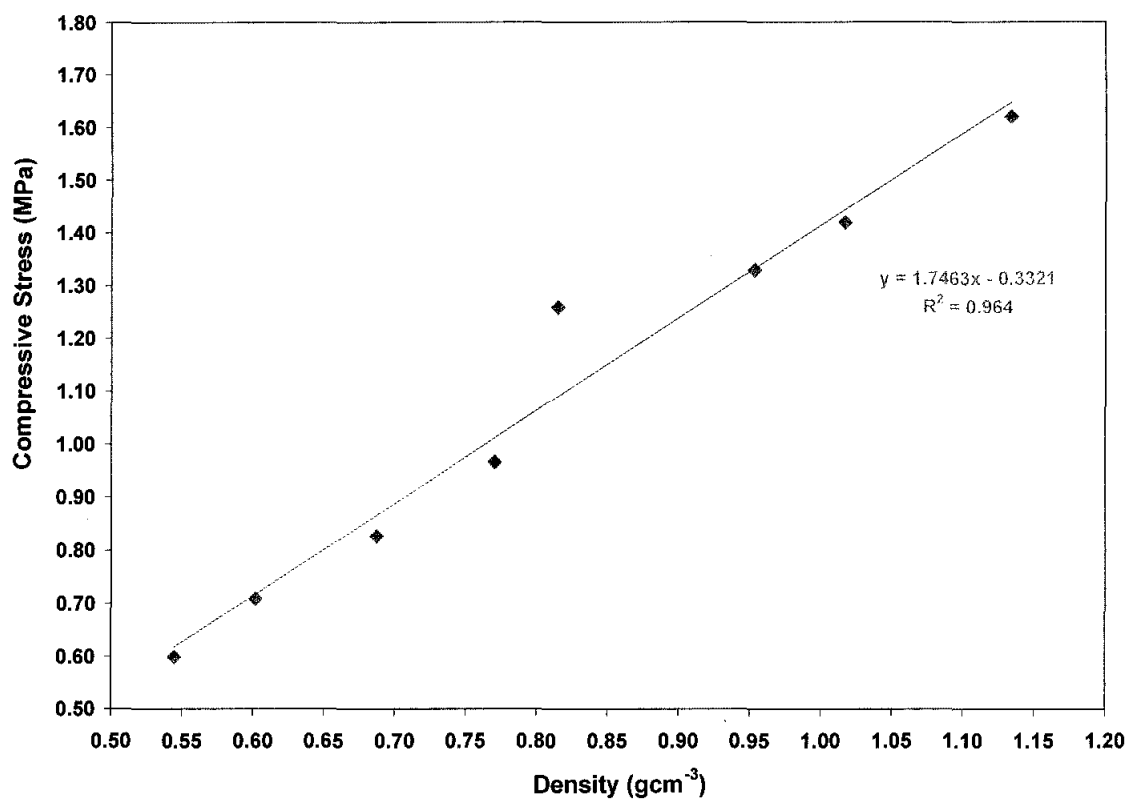


Figure 4.123: Compressive strength of SA-NaCl/Al foam as a function of density

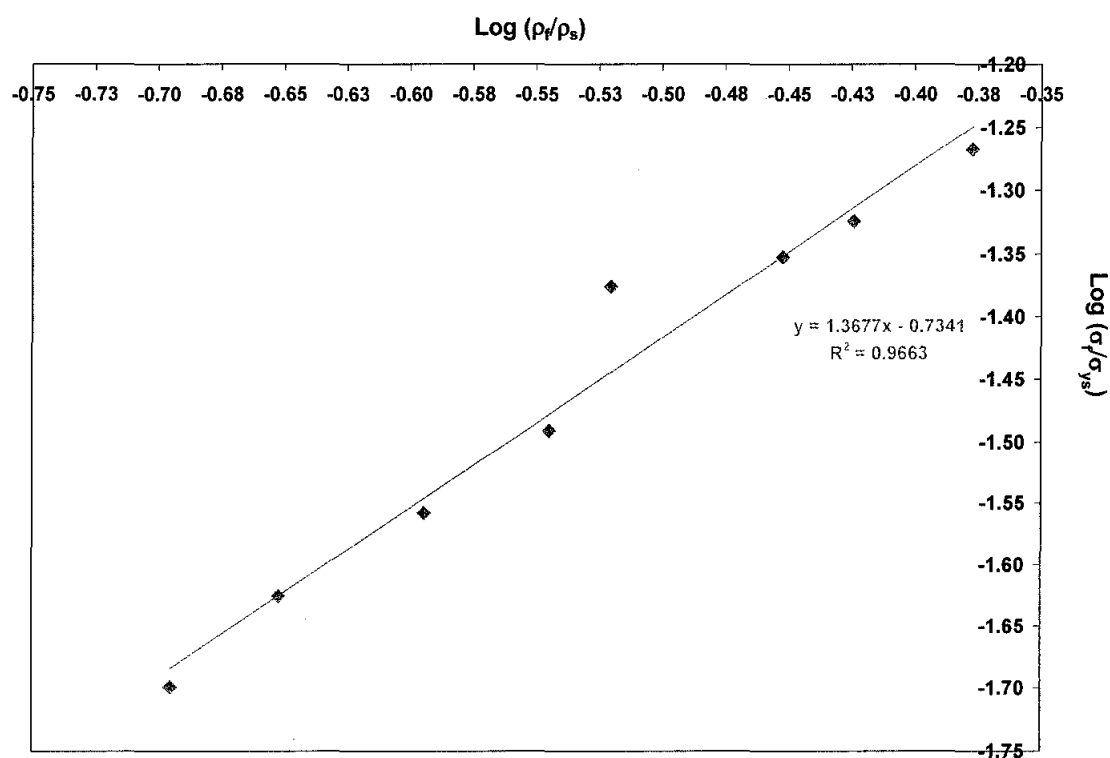


Figure 4.124: Relative compressive strength of SA-NaCl/Al foam as a function of relative density

According to Park and Nutt [118] compression test data from the foams provided insight into the mechanism of cell collapse, an important indicator for all foam applications. They postulated that the foam deformed smoothly throughout the entire compression range in which the cell wall buckled continuously during compression, providing the main structure collapse mechanism throughout the entire deformation range, and the buckling appeared to be uniformly distributed throughout the sample.

The energy absorbed per unit volume, defined as the area under the stress-strain curve obtained prior to the onset of densification, was estimated from the compression stress-strain data up to the onset of densification strain using equation (4.10). The plastic collapse of cells can be considered to occur at a constant stress until densification and neglecting the initial elastic contribution which indicates that W is largely determined by the inherent deformation characteristic of the materials through σ^* [1], [22], [34]. In order to calculate the ε_D for evaluating the value of energy absorption per unit volume, W is plotted against σ^* as shown in Figure 4.132. Since the value of W has been computed at a fixed ε_D of 57%, equation (4.12) implies that the variability in W should be similar to the variability in σ^* , and a linear trend between W and σ^* was obtained. Curve-fitting a linear equation to the entire data yields the ε_D of 57% for TS, AC, HI and SA-NaCl samples. The value obtained is then used as ε_D in experimentally evaluating W .

The influence of pore size on the compressive strength is significant and the compressive strength increases with the decrease of the pore size as presented in Figure 4.131. The value of the compressive strength of initial 80% NaCl/Al composites after leaching process increases from 0.60 MPa to 0.75 MPa when the mean pore size is decreased from 2000 μm to 200 μm . For sample of initial 78% volume fraction of NaCl, the compressive strength decreases from 0.65 MPa to 0.56 MPa when the pore size is increased from 200 μm to 2000 μm . When the pore size is decreased from 2000 μm to 200 μm , the compressive strength of initial volume fraction of 75% NaCl/Al composites after leaching process increases from 0.61 MPa to 0.67 MPa. For sample of initial 72% volume fraction of NaCl, the compressive strength increases from 0.69 MPa to 0.75 MPa when the pore size is increased from 200 μm to 2000 μm .

The influence of pore size on the modulus is also noticeable and generally, it can be observed that the modulus increase when the pore size is decreased for all different volume fraction of NaCl/Al (Figure 4.132). It reveals that the compressive modulus of initial 80% NaCl/Al foam increases from 0.60 GPa to 0.75 GPa when the pore size is increased from 200 μm to 2000 μm . The compressive modulus of the foam decrease from 0.75 GPa to 0.72 GPa when the width of pore distribution is tailored from narrow to broad at fixed mean pore size of 200 μm for sample of initial 80% volume fraction NaCl/Al foam. Clearly the effect of density and hence the modulus of the specimens is governed by the scaling law of Gibson and Ashby [1].

The compressive strength at densification is influenced by the pore size of the foam, as shown in Figure 4.133. The σ_{dens} shows a decrease in value when the pore size is increased from 200 μm to 2000 μm . For sample of initial 60% volume fraction of NaCl, σ_{dens} decrease from 19.16 MPa to 12.00 MPa when the pore size is increased from 200 μm to 2000 μm . The σ_{dens} decreased from 14.84 MPa to 9.06 MPa when the pore size is increased from 200 μm to 2000 μm for sample 64% volume fraction of NaCl. When the the pore size is increased from 200 μm to 2000 μm , the σ_{dens} of sample 66% volume fraction of NaCl decreases from 13.69 MPa to 8.24 MPa. For sample of initial 70% volume fraction of NaCl, σ_{dens} decreases from 11.37 MPa to 6.04 MPa when the pore size is increased from 200 μm to 2000 μm .

The deformation at densification is highly affected either by pore size or the density of the foams. From Figure 4.134, it can be observed that the ϵ_{dens} shows an increase in value when the pore size is increased from 200 μm to 2000 μm . For sample 72% volume fraction of NaCl, ϵ_{dens} increases from 47.48 % to 49.66 %. The ϵ_{dens} increases from 50.69 % to 52.76 % when the the pore size is increased from 200 μm to 2000 μm for sample of initial 75% volume fraction of NaCl. When the pore size is increased from 200 μm to 2000 μm , the ϵ_{dens} of sample of initial 78% volume fraction of NaCl increases from 51.86 % to 54.29 %. For sample of initial 80% volume fraction of NaCl, ϵ_{dens} increases from 54.17 % to 60.77 % when the pore size is increased from 200 μm to 2000 μm .

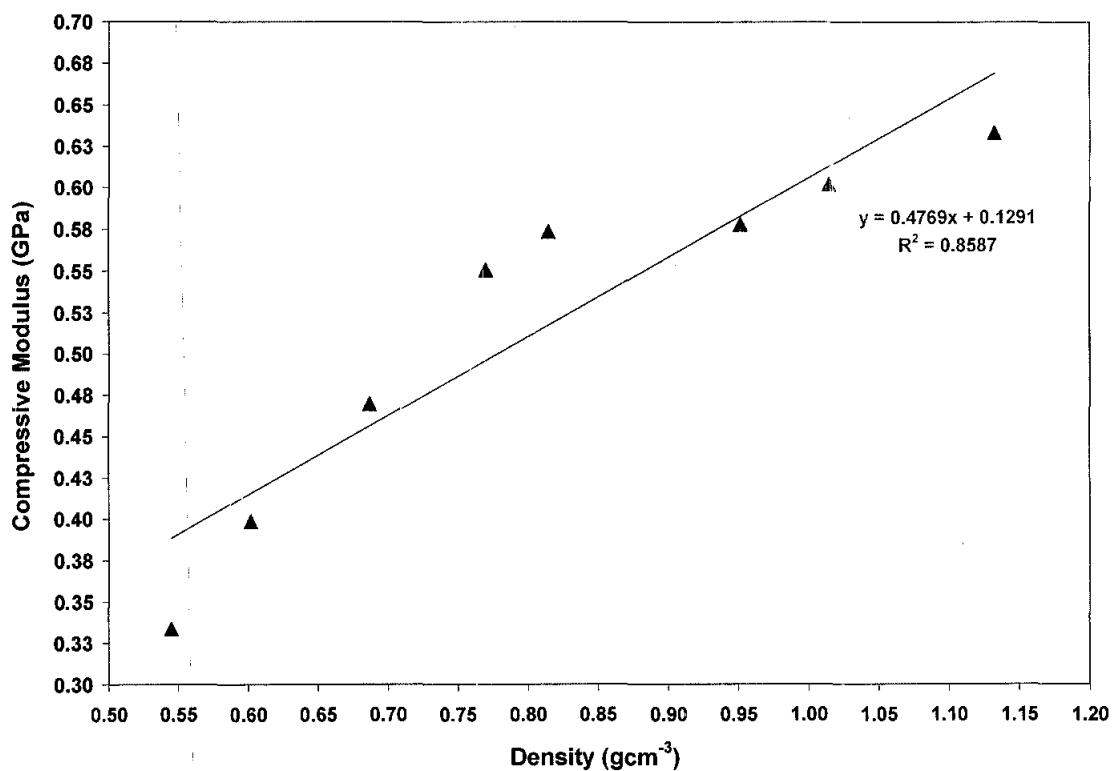


Figure 4.125: Compressive modulus of TS-NaCl/Al foam as a function of density

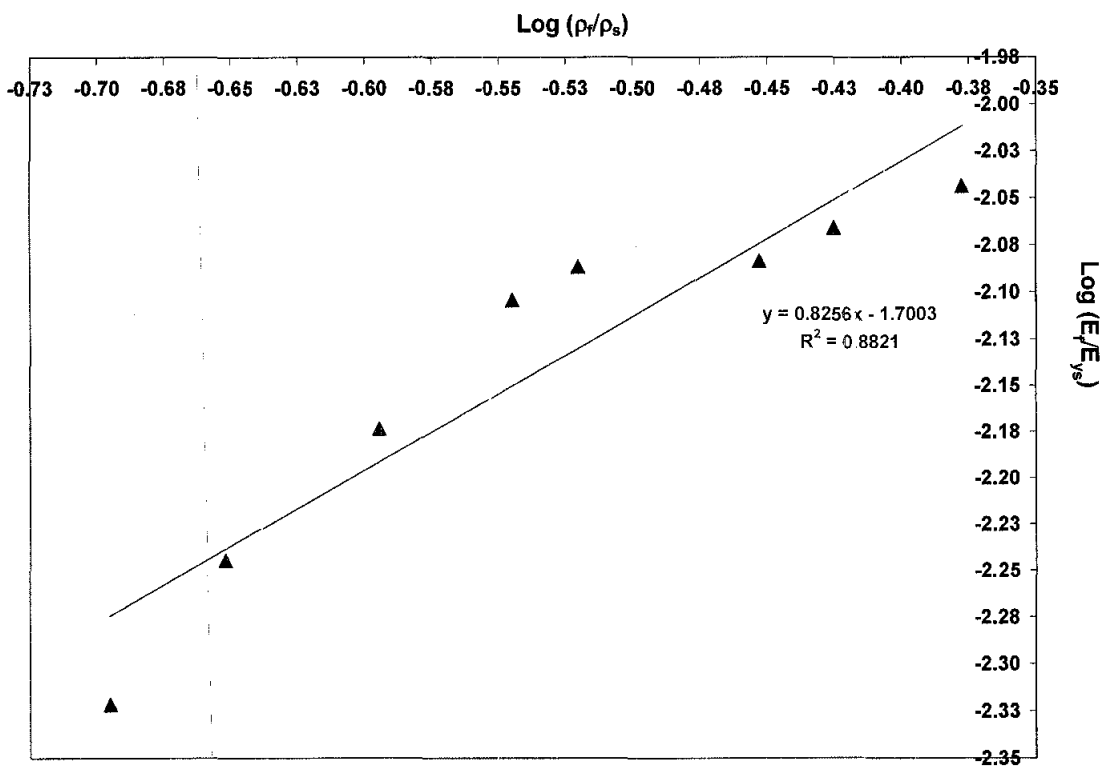


Figure 4.126: Relative compressive modulus of TS-NaCl/Al foam as a function of relative density

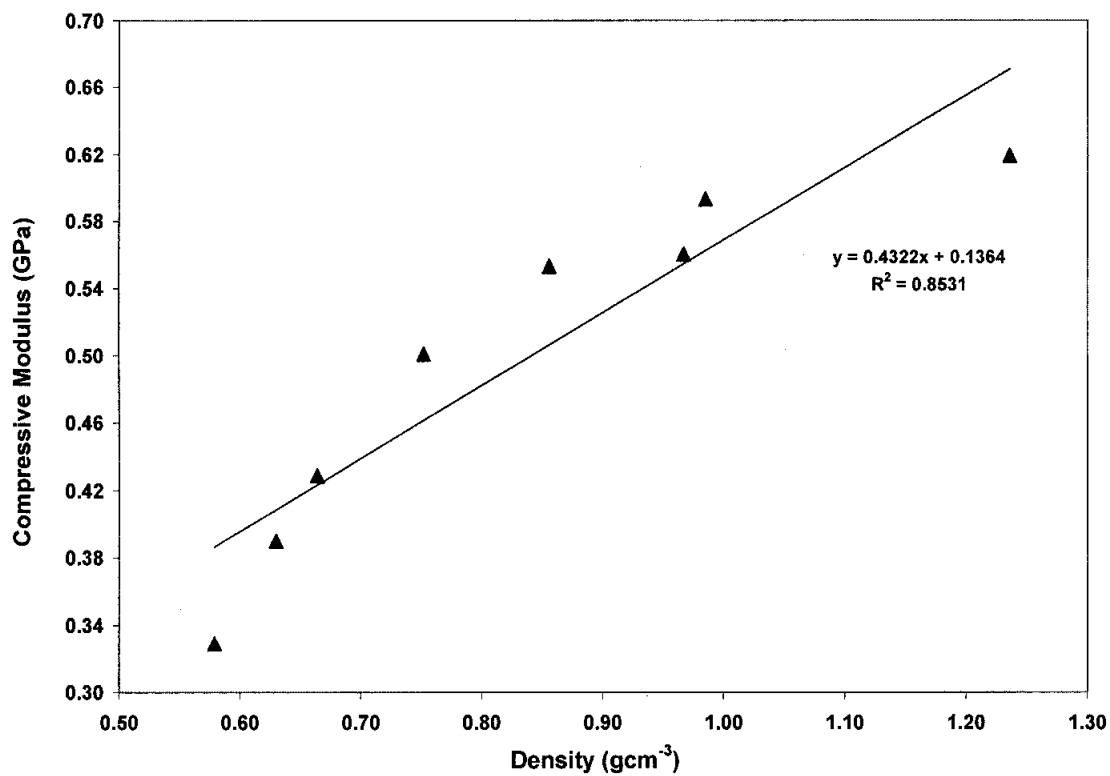


Figure 4.127: Compressive modulus of AC-NaCl/Al foam as a function of density

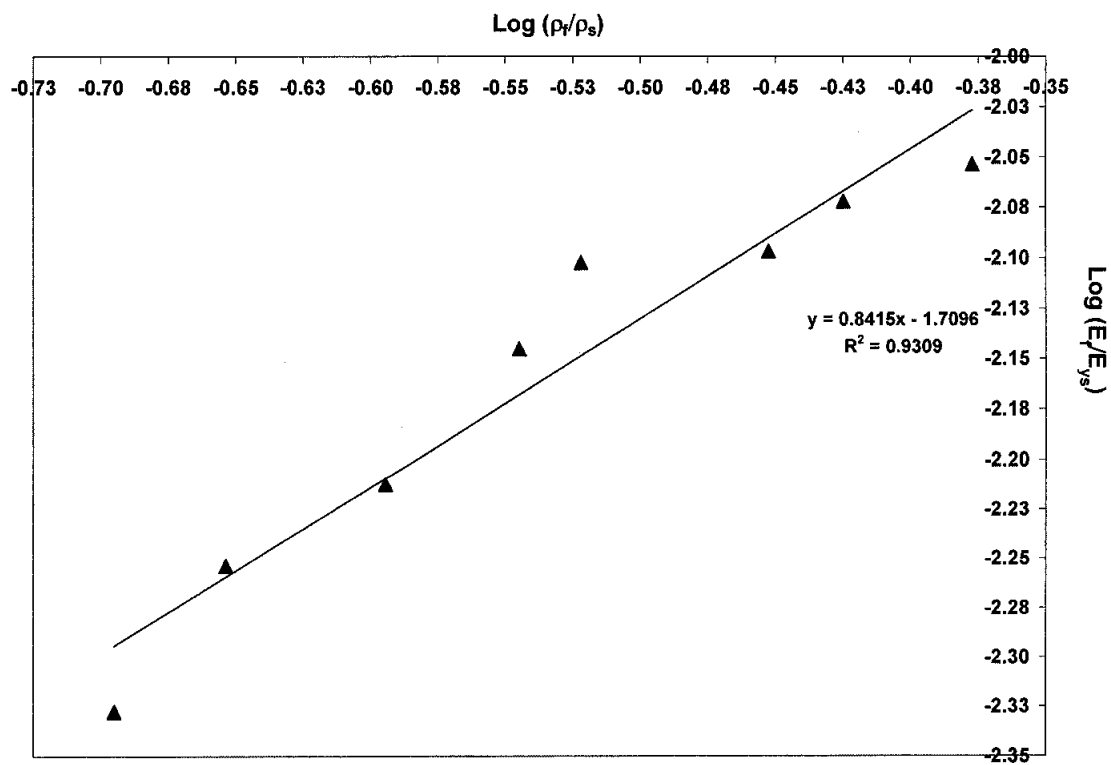


Figure 4.128: Relative compressive modulus of AC-NaCl/Al foam as a function of relative density

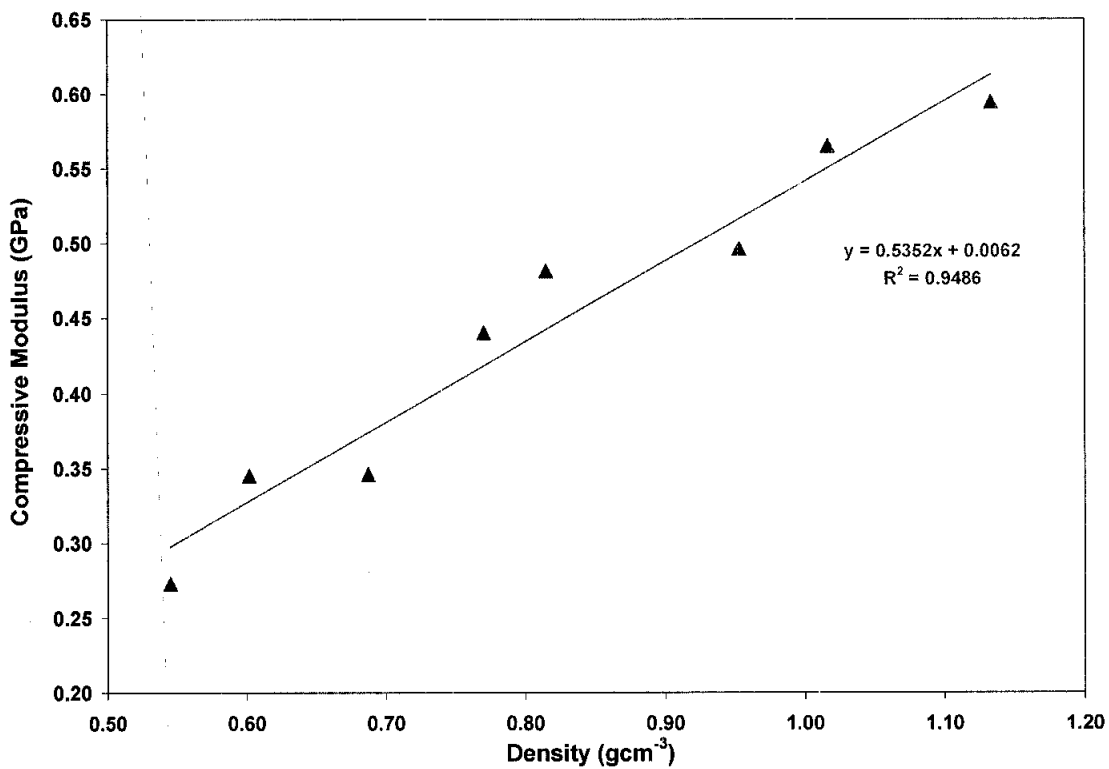


Figure 4.129: Compressive modulus of HI-NaCl/Al foam as a function of density

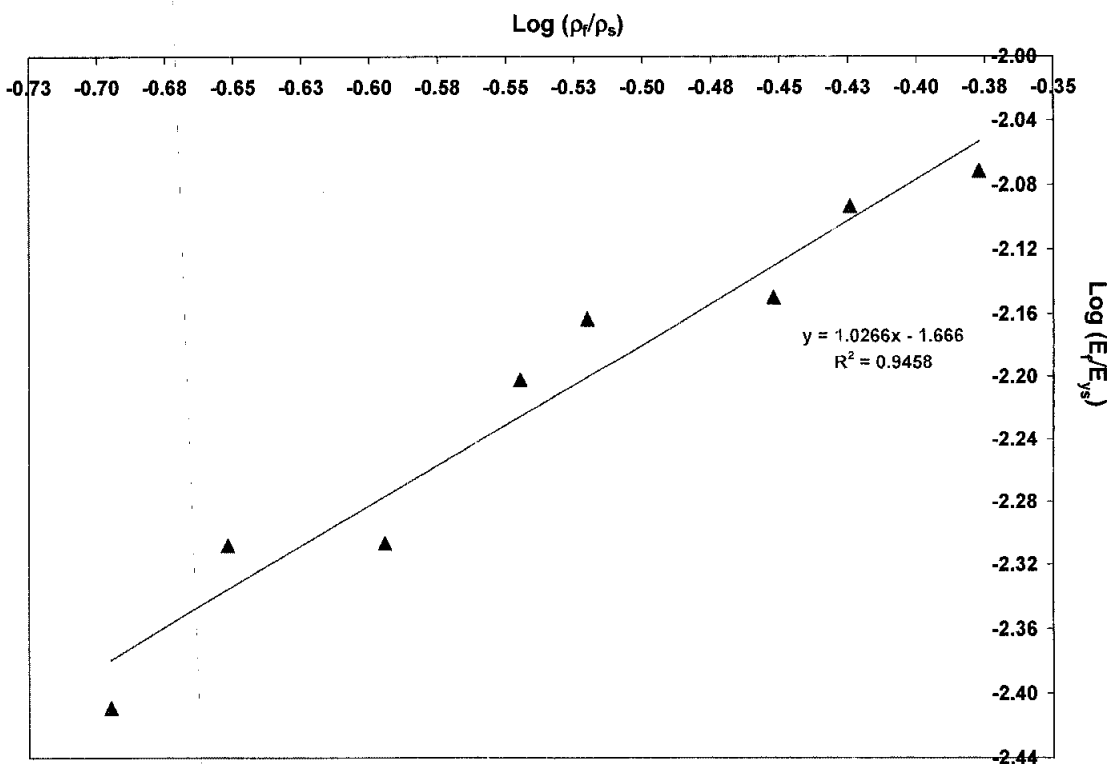


Figure 4.130: Relative compressive modulus of HI-NaCl/Al foam as a function of relative density

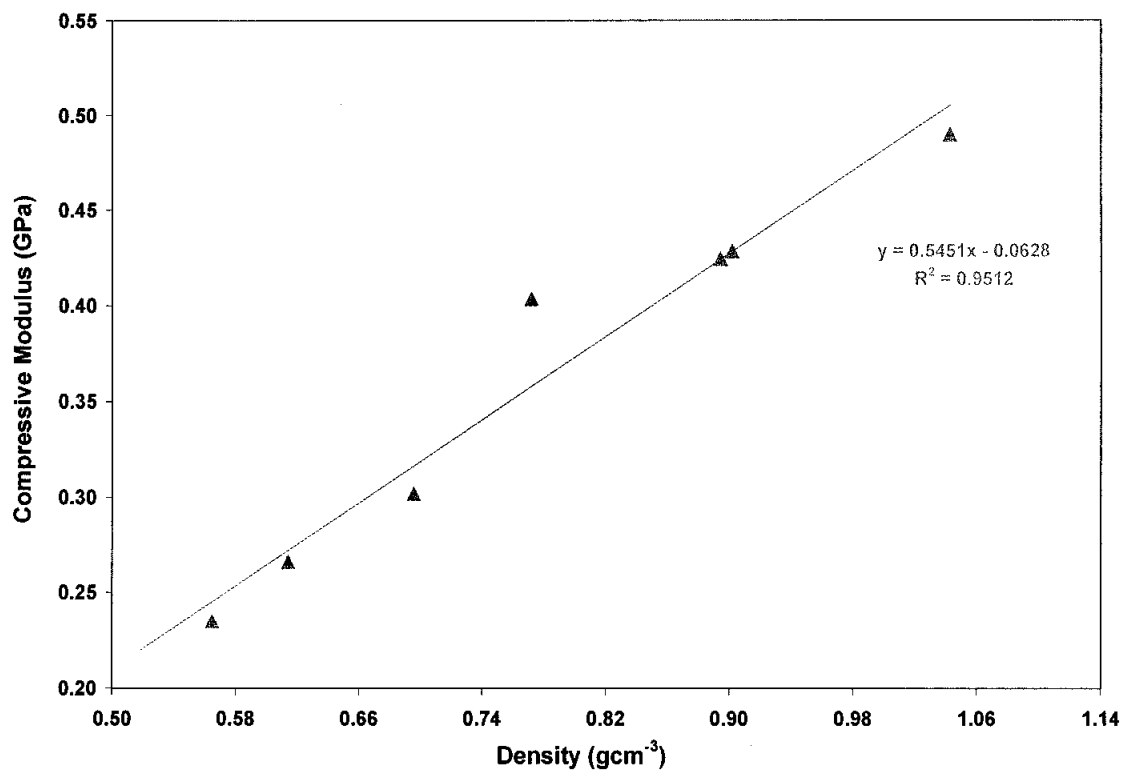


Figure 4.131: Compressive modulus of SA-NaCl/Al foam as a function of density

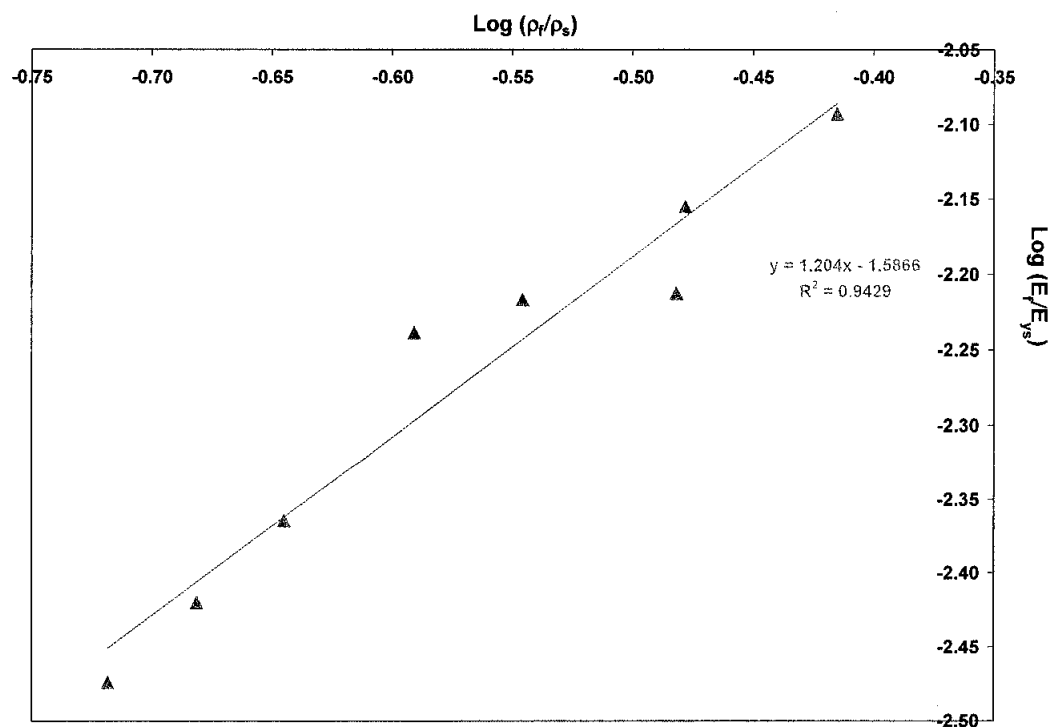


Figure 4.131: Relative compressive modulus of AC-NaCl/Al foam as a function of relative density

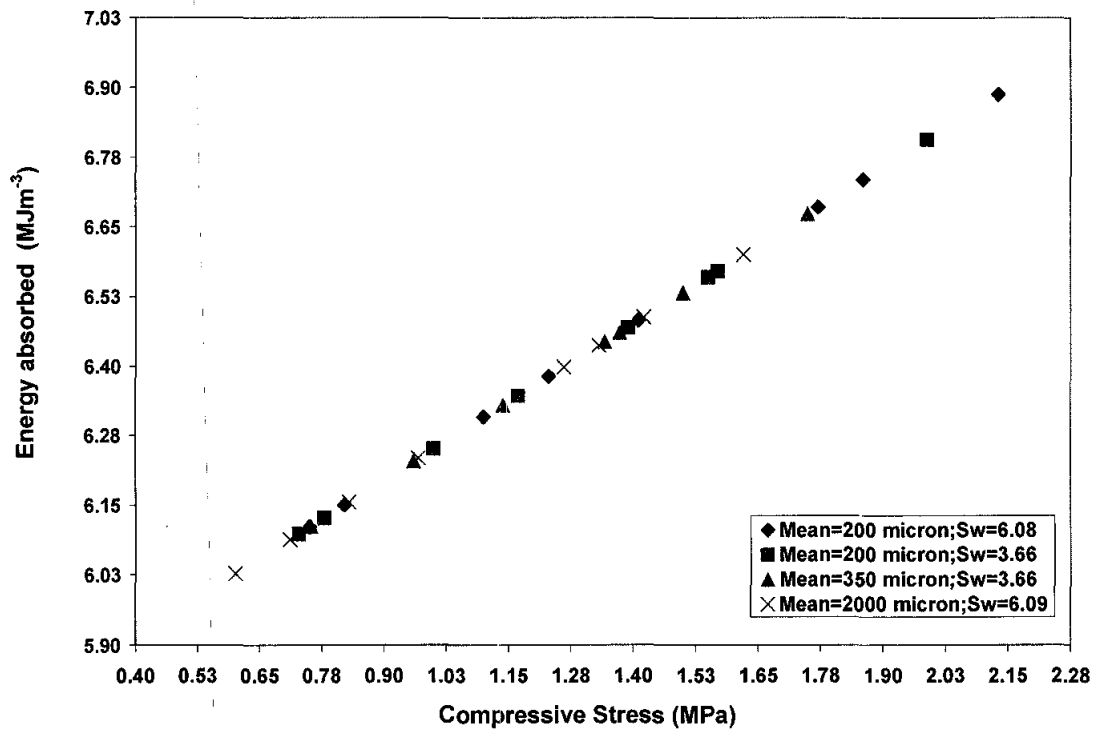


Figure 4.132: Variation of energy absorbed with compressive strength at different volume fraction of foam for different pore size and its width of size distribution.

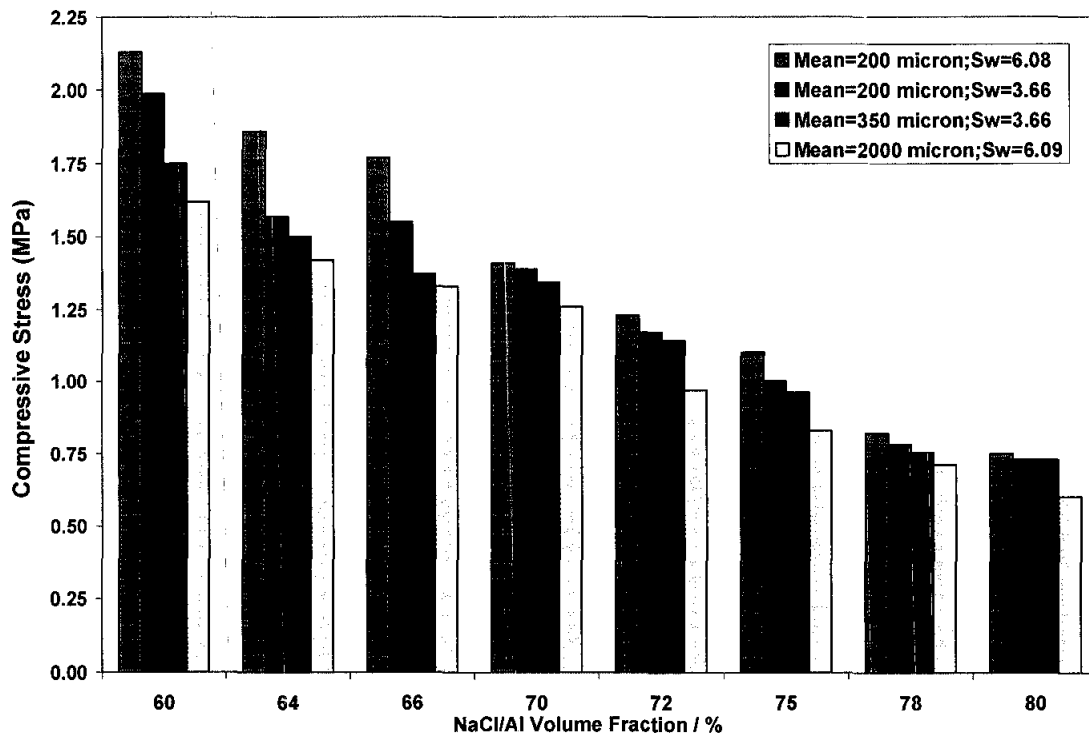


Figure 4.133: Variation of compressive strength of different pore size and its width of size distribution of Al specimens at different NaCl/Al volume fractions

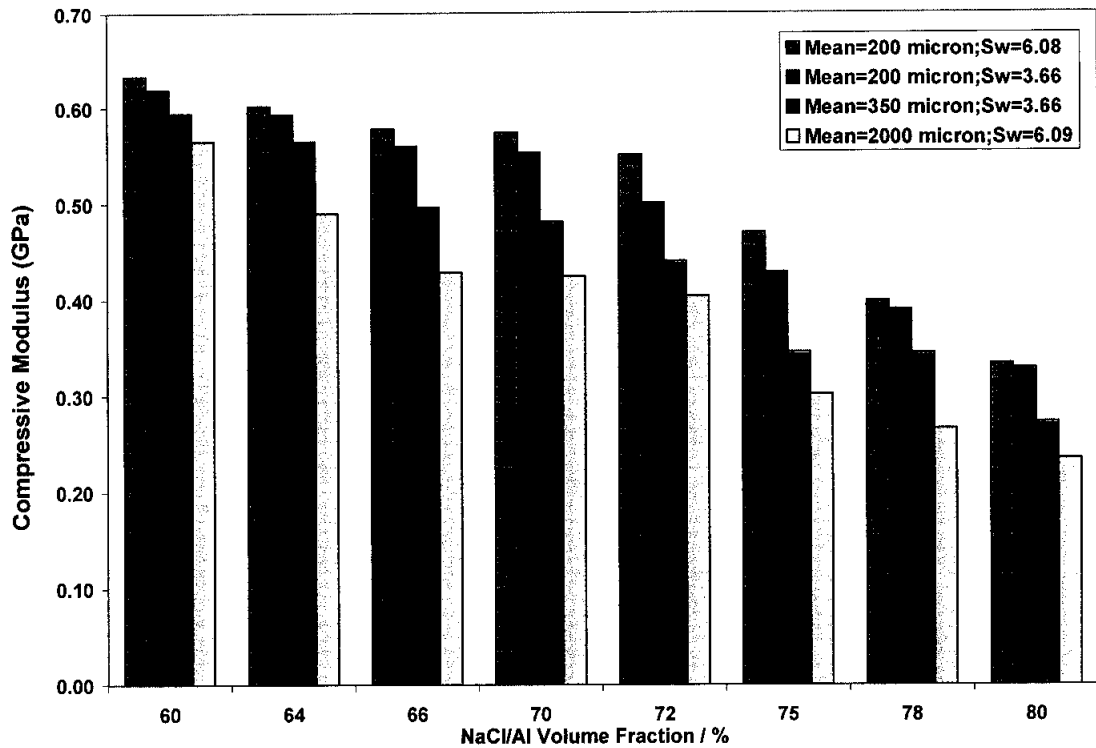


Figure 4.134: Variation of compressive modulus of different pore size and its width of size distribution of Al specimens at different NaCl/Al volume fractions.

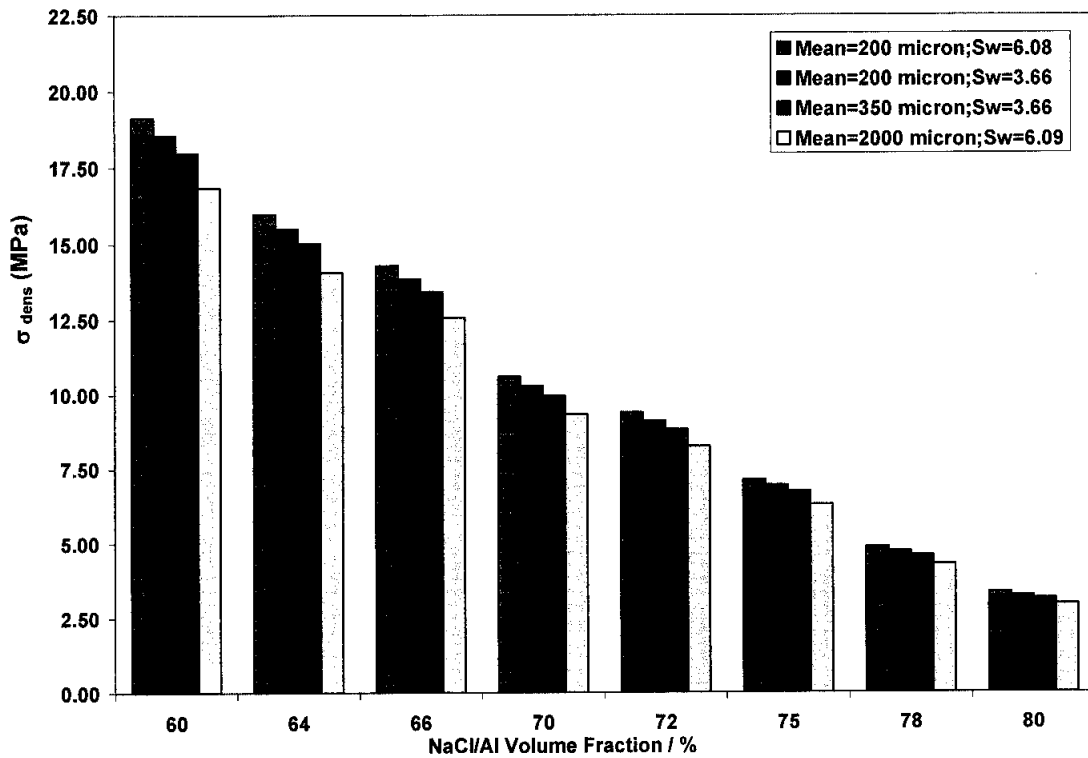


Figure 4.135: Variation of strength at densification of different pore size and its width of size distribution of Al specimens at different NaCl/Al volume fractions

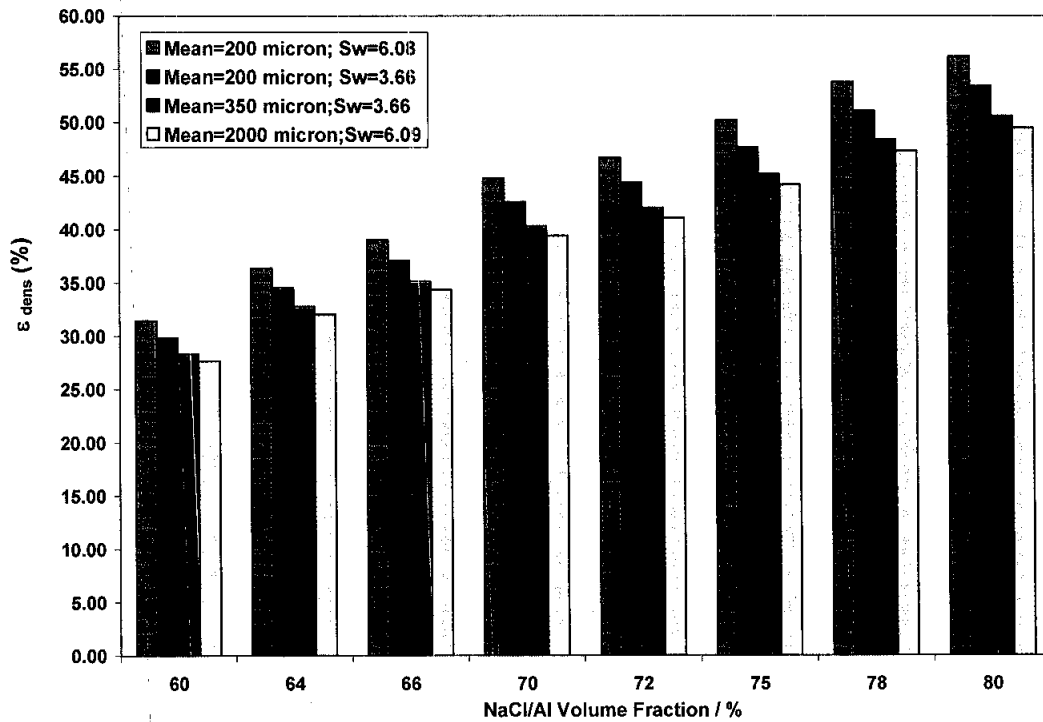


Figure 4.136: Variation of deformation at densification of different pore size and its width of size distribution of Al specimens at different NaCl/Al volume fractions

4.9.1 Energy absorption capacity

The energy absorption capacity is defined as the energy necessary to deform a given specimen to specific strains, and is used to compare foams of different density. Generally, a substantial increase in energy absorption is observed as the foam density is varied from low to high. Furthermore, the rate at which energy absorption increases with density increase with increasing strain. Figure 4.137 – 4.140 show the energy absorption after compression strains of 20, 30 and 50% for different pore shape and size. The energy absorption data for all specimens show a dependence on density that ranges from weak to strong as the strain increases from 20 to 50%.

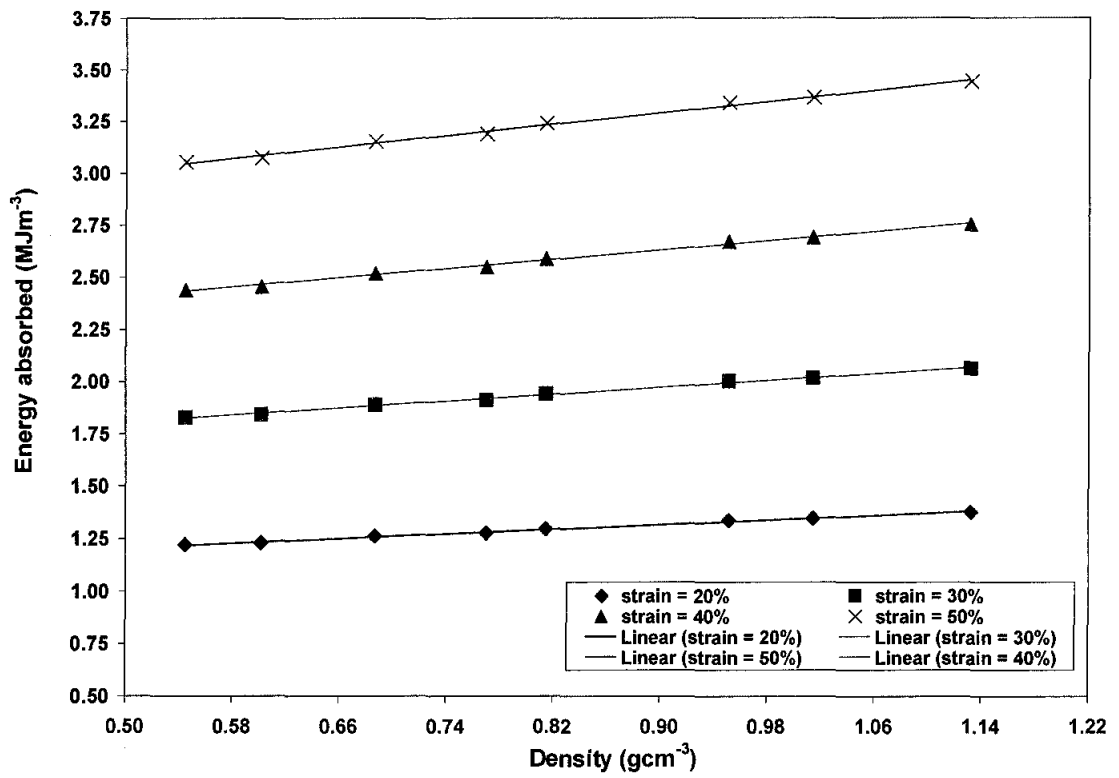


Figure 4.137: Energy absorbed by TS-NaCl/Al foams after compression strains of 20, 30, 40 and 50%

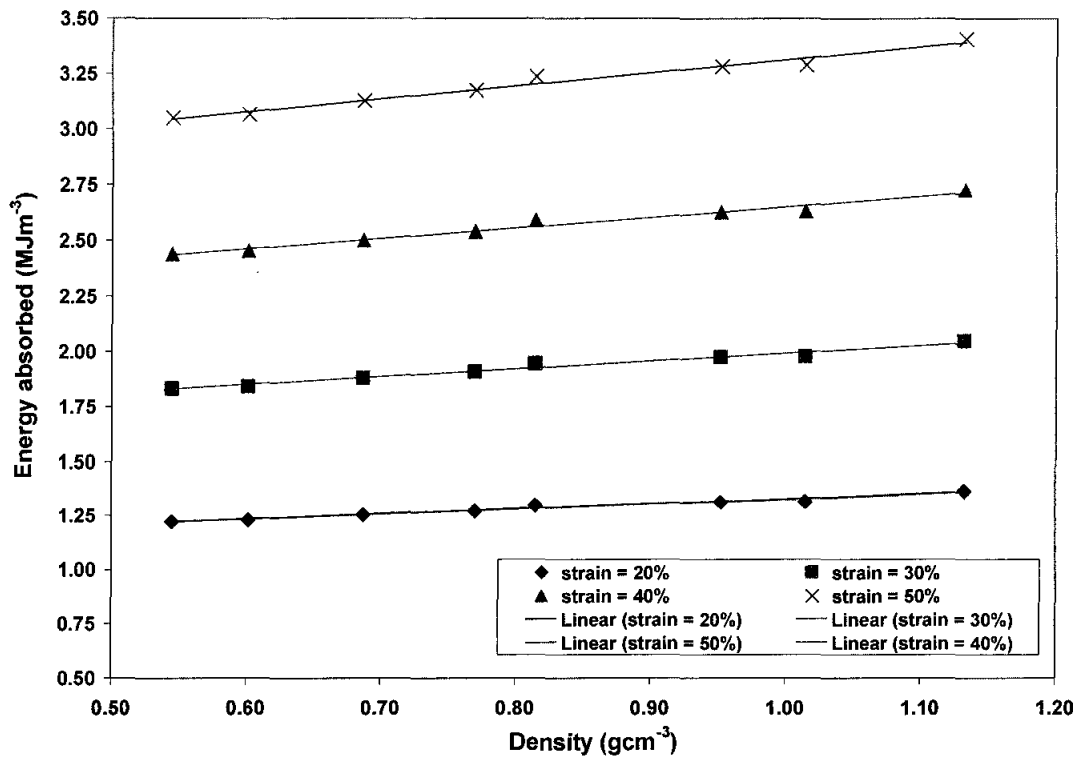


Figure 4.138: Energy absorbed by AC-NaCl/Al foams after compression strains of 20, 30, 40 and 50%

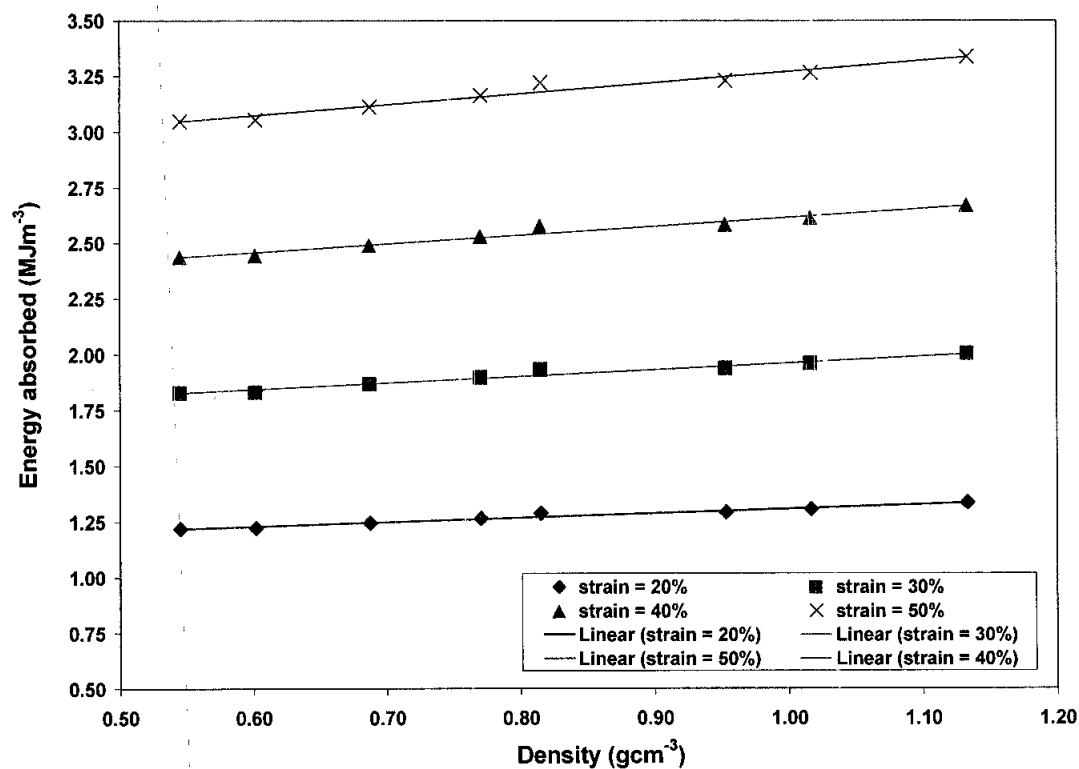


Figure 4.139: Energy absorbed by HI-NaCl/Al foams after compression strains of 20, 30, 40 and 50%

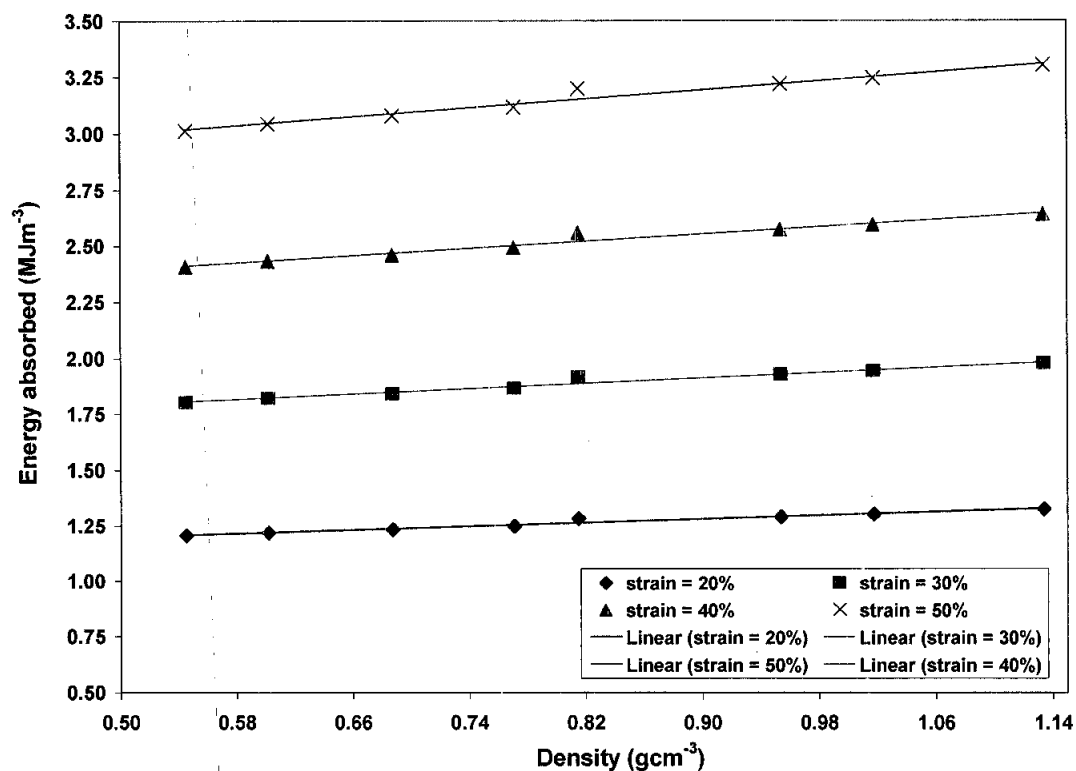


Figure 4.140: Energy absorbed by HI-NaCl/Al foams after compression strains of 20, 30, 40 and 50%

4.10 The synthesis of ceramic reinforcement materials for Al foam from the carbothermal nitridation process using structured alteration silica sand

This section discusses an improved method of synthesis silicon carbide whisker from milled silica sand under gaseous 5% H₂ + 95% N₂ environment with the addition of carbon in dry mixing method which could overcome the need of high temperature reaction. Planetary Ball Mill method (based on impact and friction among particles) was then employed in order to alter the regularity of the crystalline network in the silica used. The silica sand materials was primarily crushed by the high-energy impact of grinding balls together with friction between the balls and the wall of grinding bowl. The centrifugal forces caused by rotation of the grinding bowls and supporting disc work on the contents of the grinding bowl. The force resulting from rotation of the grinding bowl when the mill was started causes the rotating balls to rub against the inside wall of the bowl thus crushing the silica sand. At a certain point in time the stronger centrifugal force of the supporting disc caused the grinding silica sand and balls to separate from the inner wall of the grinding bowls. The grinding balls crossed the bowl at high speed impacting with the silica sand on the opposite wall creating size reduction by impact.

As a result of low conductivity characteristic of silica sand, the energy delivered by the mill is not stored in the particle as thermal energy, but applied to bending and/or breaking of the crystal. This kind of treatment apart from producing important changes in the physio chemical properties of solid, leads to structural alteration by loss of regularity in the crystalline network. This empirical of crystallinity has been established by characterization mainly based on XRD measurement. The presence of defects or random disorder in the silica sand is evident by the loss or reduction of peak intensity along the whole diffractograms with the broadening effect at the base of the peak. This mechanical milling process which based on impact and friction among particles not only causes size reduction but also structural changes from crystalline phase to amorphous. These structurally distorted silica sand particles are activated due to the high surface energy and will be used as precursors for the following reaction.

4.10.1 The effect of mechanical milling treatment on silica sand

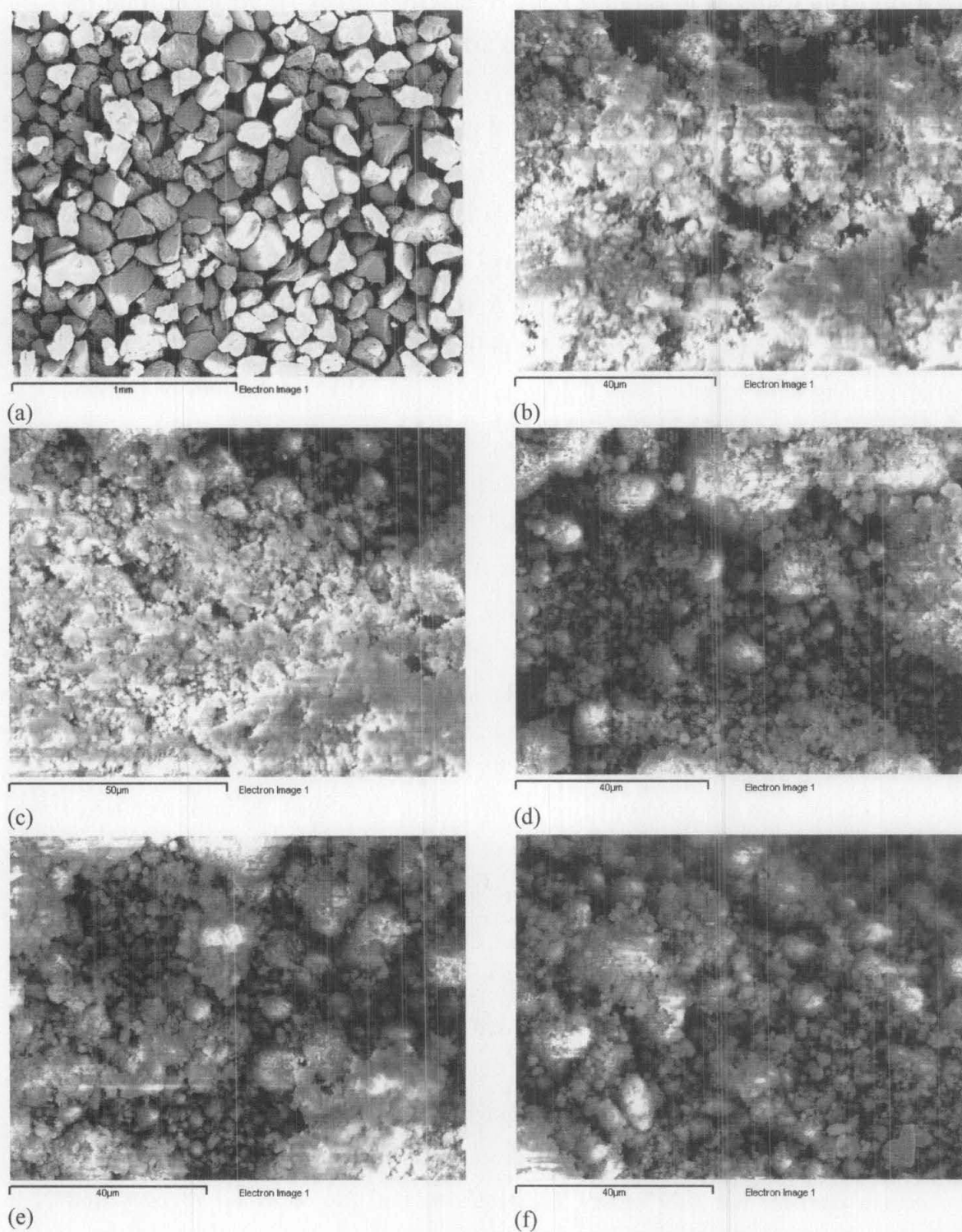


Figure 4.141: The surface morphology of SiO_2 sand after undergoing mechanical treatment at various grinding times: (a) as-received (b) 20 hrs (c) 40 hrs (d) 60 hrs (e) 80 hrs (f) 100 hrs

The surface morphology of the silica sand which is subjected to various milling time is shown in Figure 4.141 (a) – (f). The XRD patterns shown in Figure 4.142 (a) had different grinding periods ranging from 0 hour to 100 hour. The highest peak for Un-MM silica sand is at 26.2° (2θ angle) and this peak was taken as reference. The intensity of the peak after 20 hour of grinding was reduced to by 87%. A great intensity reduction up to 97% was observed after 100 hour of grinding.

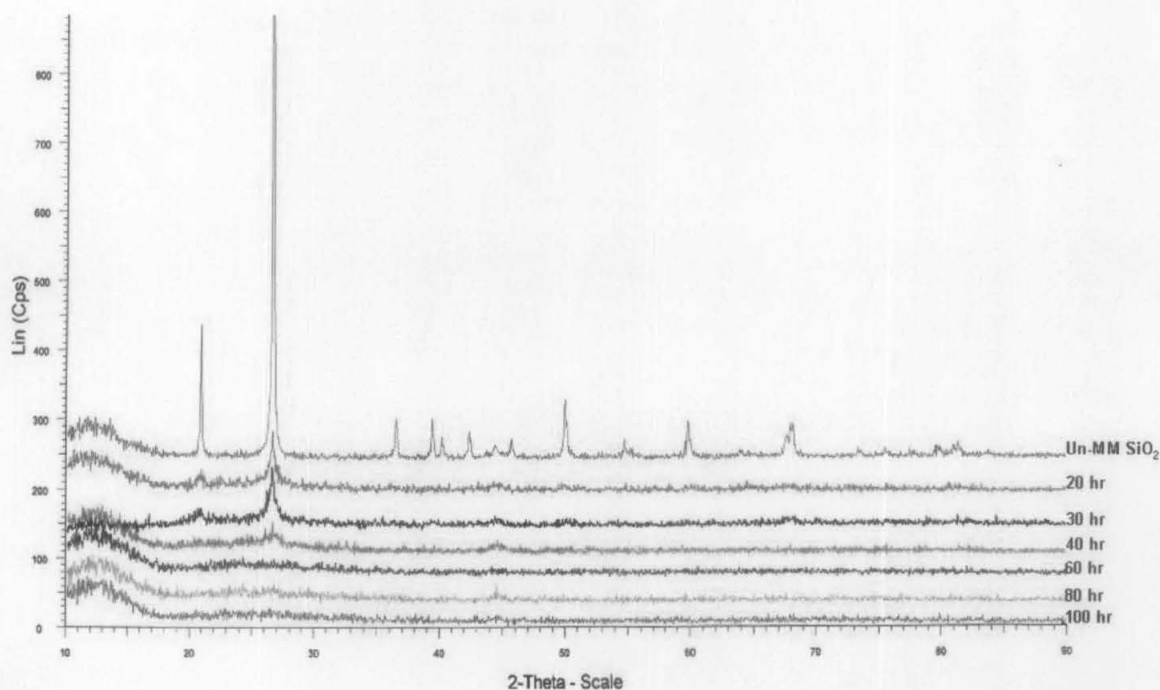


Figure 4.142: X-ray diffractograms of milled silica at different milling time

As particle size of (MM) silica sand is reduced by mechanical milling process using longer milling time, the broadening effect at the peak base of the spectrum is increase (see Table 4.17). This observation would be in agreement with the studies of Suryanarayana [108] who found the same XRD pattern for the talc sample where the reduction of peak intensity and the broadening effects were observed. Szewezak et al [109] have reported that the maximum size reduction limit for a particle is equivalent to the size of tough-brittle transition which lead to plastic deformation rather than breakage of particle and it is accompanied by the growth of structure distortion. Table 4.17 shows that the degree of random disorder in (MM) silica sand increases as milling time increases. The degree of random disorder is about 80% after milling time of 100 hour. This show that the mechanical milling process which based on impact and friction among particles not only causes size reduction but also produces

important changes in the physio chemical properties of solid, leads to structural alteration by loss of regularity in the crystalline network. An important method employed for the investigation of distortion is the observation of line broadening in the X-Ray diffraction spectra. The intensity and half width of the X-Ray lines in different pattern reflect the degree of random disorder and lattice distortion of the particles.

Table 4.17: Intensity value and d₅₀ at various milling time

Sample	Milling Time / hour	Intensity / counts	d ₅₀ / μm	Random Disorder / %
Un-MM	0	800	64.00	
MM1	20	100	3.46	87.5
MM2	30	80	3.38	90.0
MM3	40	45	2.61	94.0
MM4	60	40	2.58	95.0
MM5	80	30	1.26	96.0
MM6	100	20	1.18	97.0

4.10.2 Carbothermal nitridation process of structured silica sand

The mixture after carbothermal reduction at 1350 °C under 5% H₂ + 95% N₂ atmosphere for 1.5 hour

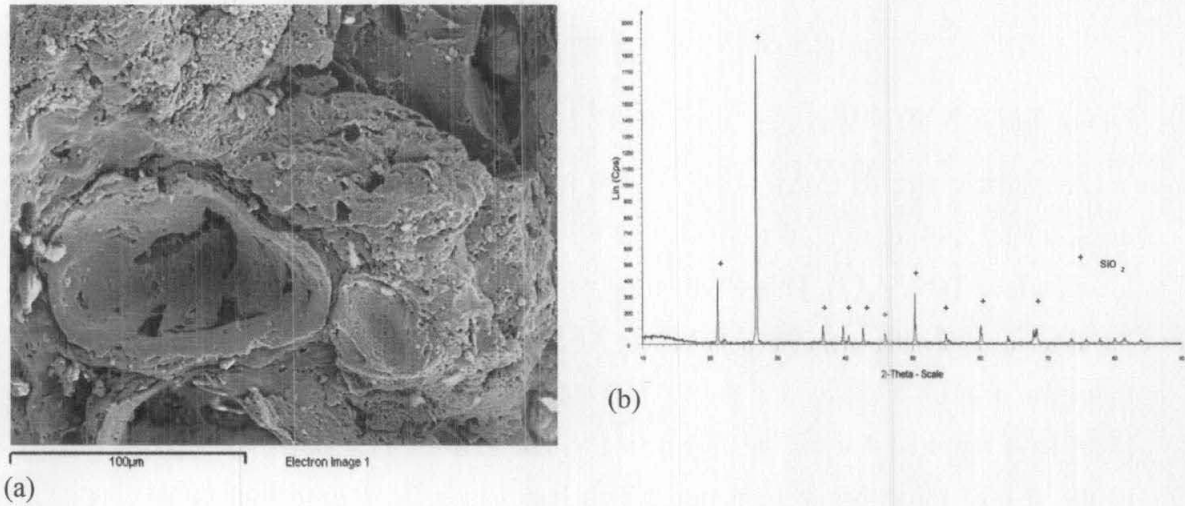


Figure 4.143: (a) SEM micrograph of Un-MM mixture at 1350 °C (b) XRD spectrum of Un-MM mixture at 1350 °C

The surface morphology of the Un-MM mixture after the carbothermal reduction process is shown in Figure 4.143 (a). No formation of silicon nitride or silicon carbide compound can be detected. The XRD spectrum of Figure 4.143 (b) indicated that the presence of unreacted silica. The formation of silicon nitride was visible on the mixture of MM mixture at 1350 °C (Figure 4.144 (a)). At this temperature, the compound present as non-filamentary, although some primitive fibrous structures can be observed. The presence of silicon nitride compound was shown by XRD spectrum (Figure 4.144 (b)). This shows that the mechanical milling treatment on the silica sand not only causes size reduction but also structural changes from crystalline phase to distorted structure which are activated due to the high surface energy. Alcala et al [90] explained that the formation of this compound is formed through vapour-solid-liquid (VSL) mechanism. The VLS mechanism is characterised by the existence of impurity that acts as a preferred site for the deposition of gaseous intermediate leading to supersaturation of the liquid in the elements forming the crystal.

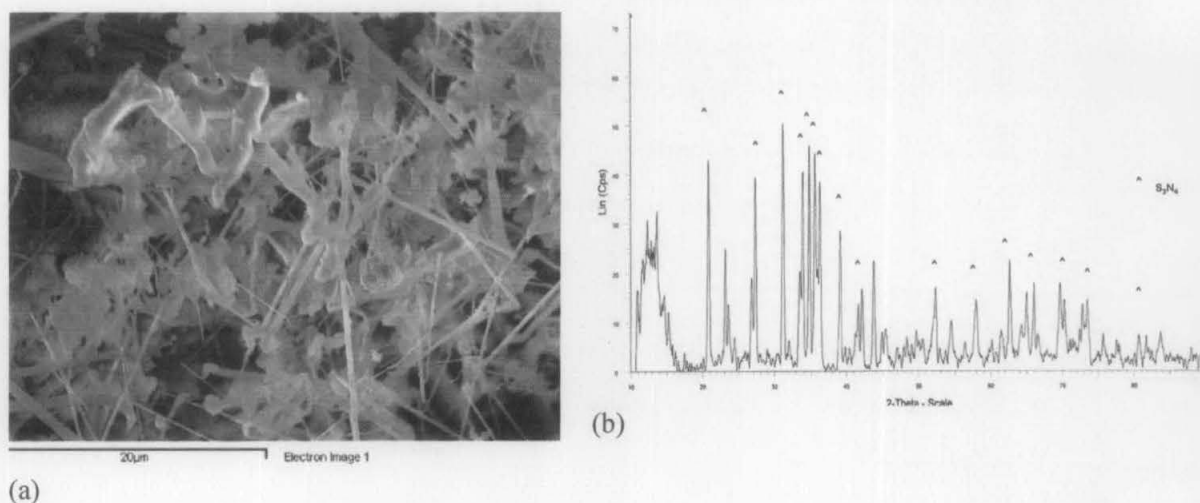


Figure 4.144: (a) SEM micrograph of MM mixture at 1350 °C (b) XRD spectrum of MM mixture at 1350 °C

The mixture after carbothermal reduction at 1450 °C under 5% H₂ + 95% N₂ atmosphere for 1.5 hour

Figure 4.145 (a) shows the surface morphology of the Un-MM mixture at 1450 °C and show no formation of silicon nitride compound. X-ray diffractometry spectrum reveals no indication of formation of silicon nitride on the structure as shown in Figure 4.145 (b).

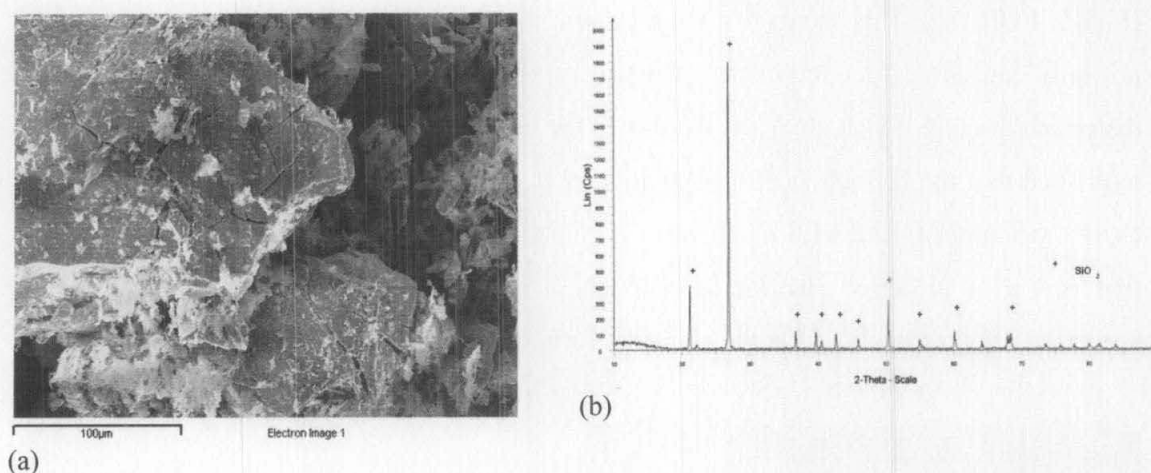


Figure 4.145: (a) SEM micrograph of Un-MM mixture at 1450 °C (b) XRD spectrum of Un-MM mixture at 1450 °C

The crystalline nature of Un-MM silica, makes it very stable even at 1450 °C and prohibited them from becoming gaseous intermediate in this reaction. This reaction occurs via a gas-solid mechanism, with silicon monoxide produced as an intermediate.

The SEM micrograph shown in Figure 4.146 (a) point out that the MM mixture has a homogenous composition being constituted by whisker shape compound of silicon nitride as indicated by XRD spectrum of Figure 146 (b). Considering the previous observation of other authors [91]-[95], the formation of whisker silicon nitride could be associated with the formation of β -Si₃N₄. This crystal grows by precipitation from the liquid at the liquid-solid interface, originating a whisker that carries the particle from which it was formed on top [94].

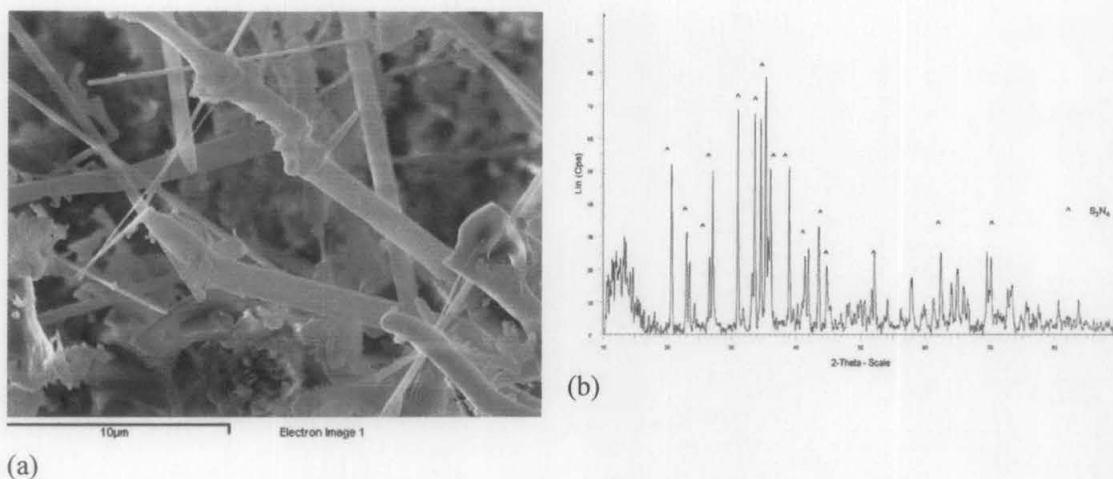


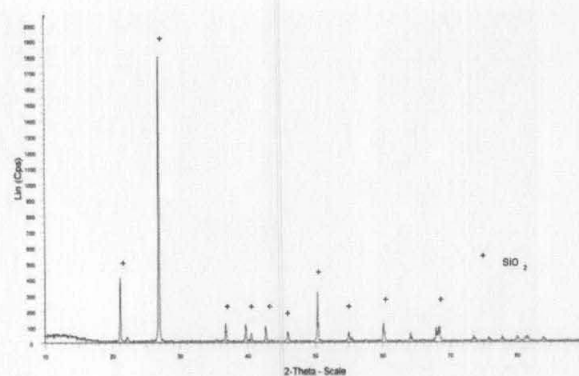
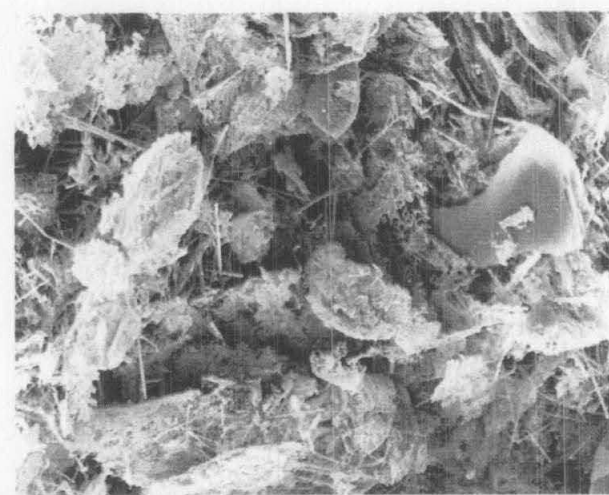
Figure 4.146: (a) SEM micrograph of MM mixture at 1450 °C (b) XRD spectrum of MM mixture at 1450 °C

The mixture after carbothermal reduction at 1550 °C under 5% H₂ + 95% N₂ atmosphere for 1.5 hour

The surface morphology of the mixture after carbothermal reduction process at 1550°C is shown in Figure 4.147. The presence of spiky-like compound was observed. X-ray diffractometry spectrum reveals no indication of formation of silicon carbide on the structure as shown in Figure 4.147 (b). From the results obtained, the formation of SiC was not favourable due to the crystallinity characteristic of the silica used in the experiment.

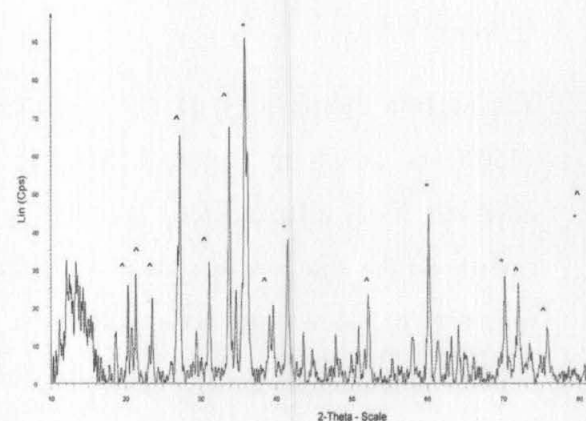
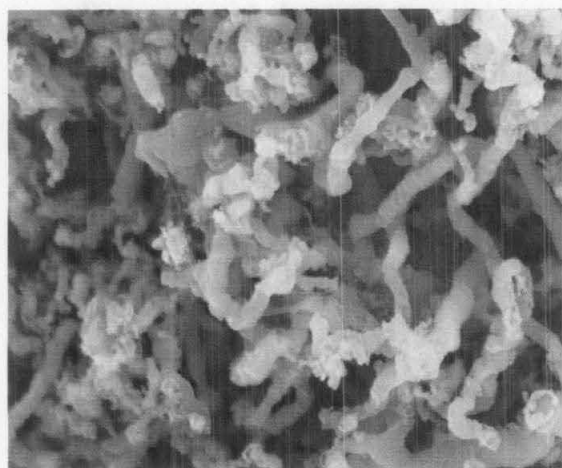
The morphology characteristic of the product of MM mixture obtained at this temperature (1550 °C) consists of mainly silicon carbide whisker and some silicon nitride compound which was identified by xray diffraction analysis (see Figure 4.8.2.6 (a) and (b)).

This means that, at this temperature the formation of silicon carbide is more favourable compared to silicon nitride, as predicted by thermodynamic calculation. The increase in temperature to 1550 °C favours silicon carbide formation and increase the yield to large extent.



(b)

Figure 4.147: (a) SEM micrograph of Un-MM mixture at 1550 °C (b) XRD spectrum of Un-MM mixture at 1550 °C



(b)

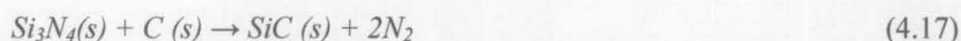
Figure 4.148: (a) SEM micrograph of MM mixture at 1550 °C (b) XRD spectrum of MM mixture at 1550 °C

The mixture after carbothermal reduction at 1650 °C under 5% H₂ + 95% N₂ atmosphere for 1.5 hour

The surface morphology of the mixture after carbothermal reduction at 1650°C is shown in Figure 4.149 (a) and the presence of spiky-like compound was observed. X-ray diffractometry spectrum reveals no indication of formation of either silicon

carbide or silicon nitride compound on the structure as shown in Figure 149 (b). Since silica firstly decomposes into silicon monoxide vapour, the SiC formation will be dominantly controlled by diffusion of silicon monoxide into the carbon structure [95]. Therefore, this formation could be facilitated by using distorted structure of silica sand and the use of iron element or compound as effective agent for catalysis.

The morphology characteristic of the product obtained at 1650 °C is dominated by the presence of silicon carbide whisker (see Figure 4.150 (a) and (b)). At this higher temperature, the formation of silicon carbide is more favourable than silicon nitride. There is no silicon nitride present. With the presence of carbon, silicon nitride will convert to silicon carbide with the release of nitrogen gas according to reaction (4.17) at high temperature.



According to thermodynamic calculation, free energy (ΔG°) for reaction (4.17) become negative at temperature of 1450 °C therefore the formation of silicon carbide becomes favourable.

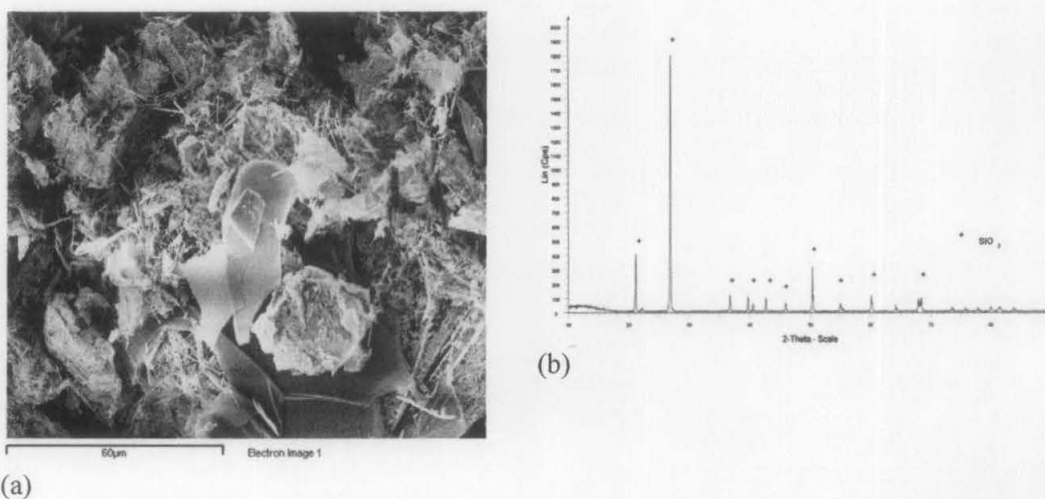


Figure 4.149: (a) SEM micrograph of Un-MM mixture at 1650 °C (b) XRD spectrum of Un-MM mixture at 1650 °C

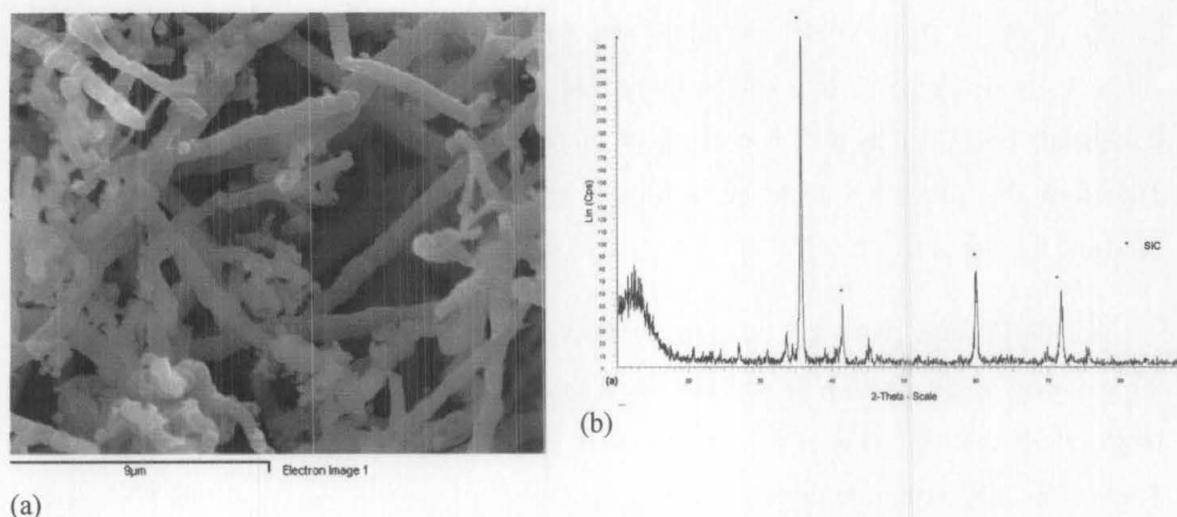


Figure 4.150: (a) SEM micrograph of MM mixture at 1650 °C (b) XRD spectrum of MM mixture at 1650 °C

The following Table 4.18 and Figure 4.151 summarize the effect of increasing the temperature on the products composition and reaction yields both for Un-MM and MM mixture. For the MM-mixture, an increase in temperature from 1350 °C to 1450 °C leads to increase of formation of silicon nitride by 30%. This shows that the increase in temperature favours the formation of silicon nitride and increase the reaction yield to large extent. However at this temperature the formation of silicon carbide starts to be detected. The quantity of silicon carbide formed increase with the increase of temperature. It is believed that the silicon carbide formed from the reaction of silicon nitride and carbon via reaction (4.17) mechanism.

Table 4.18: The influence of temperature on the reaction yield and the product composition

Temperature	MM-Mixture			Un-MM Mixture		
	% Yields	% of Si ₃ N ₄	% of SiC	% Yields	% of Si ₃ N ₄	% of SiC
1350 °C	25.46	25.46	-	-	-	-
1450 °C	82.59	76.48	6.11	-	-	-
1550 °C	54.80	19.56	35.24	-	-	-
1650 °C	74.58		74.58	1.54	-	1.54

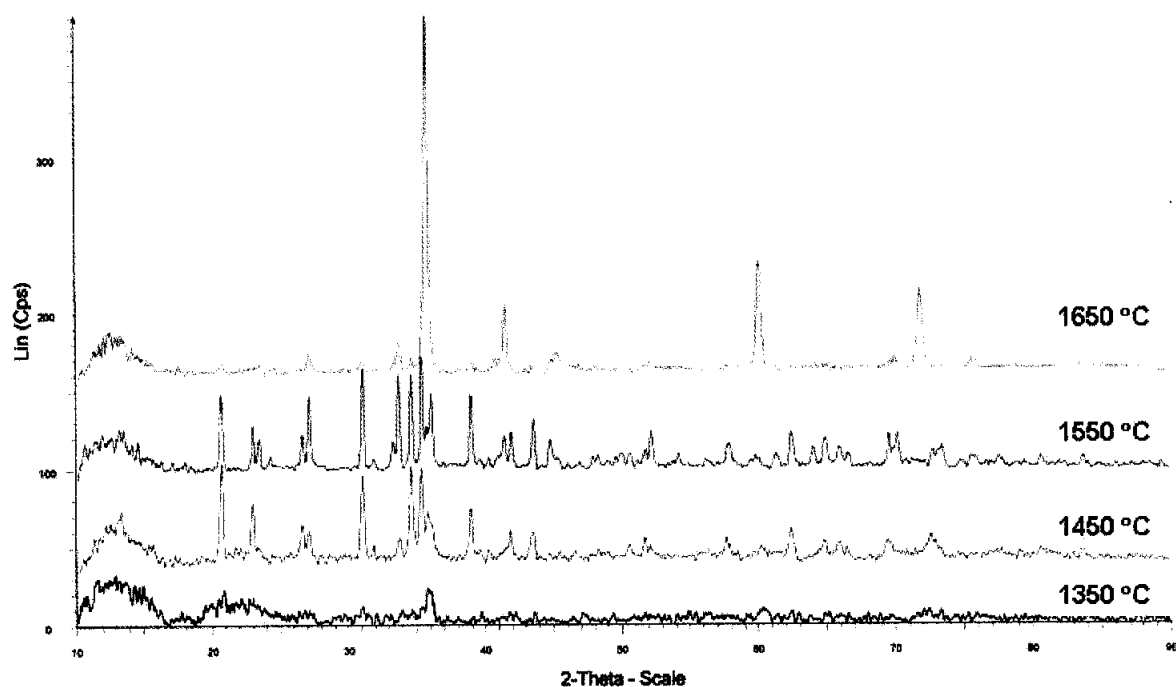


Figure 4.151: X-ray diffractograms of carbon mixture after carbothermal nitridation process at various temperatures

4.10.3 Statistical optimization for the carbothermal nitridation process of structured alteration silica sand using Taguchi's method

There are three categories of performance characteristics, i.e. the lower-the-better, the higher-the-better, and the nominal-the-better [29]. Table 4.19 presented the results of the overall experimental results and in this studies, the higher value of silicon carbide formation is desirable. Column four was assigned as the Mean Squared Deviation (MSD). All of the results were transformed into signal to noise ratio (S/N) in the last column of Table 4.19.

Table 4.19: Experimental results and their S/N ratios

Trial No.	Weight of SiC _w (g)		MSD	S/N
	R ₁	R ₂		
1	5.300	5.160	3.658E-02	14.36
2	6.310	6.490	2.443E-02	16.12
3	9.000	8.770	1.267E-02	18.97
4	9.660	9.850	1.051E-02	19.78
5	5.150	4.940	3.934E-02	14.05
6	9.840	9.540	1.066E-02	19.72
7	7.820	7.810	1.637E-02	17.85
8	11.200	11.400	7.833E-03	21.06
9	8.540	8.480	1.381E-02	18.59
Mean				17.83

This transformation consolidates the repeated response (raw data) in each trial condition into a single number. Thus, 9 S/N ratios were calculated which in turn also reduced the total DOF of the experiments. The quality characteristic for the % yield of SiC_w formation (weight of SiC_w obtained) is of the higher-the-better type.

From Table 4.20 it can be noted that there had been gradually increased in average effects started from level 1 to level 3 for factors temperature, time and duration of mechanical milling process for silica sand. These observations indicated that the % yield of SiC_w (in terms of the weight of product obtained) formation would be increased when the temperature, time, and duration of mechanical milling process for silica sand becomes higher. On the contrary, when the heating rate increased, the % yield of SiC_w formation will become lower.

Different factors affect the formation of SiC_w to different degrees. According to Ibrahim *et al.* and Kishore *et al.* [25], [26] the relative effect of the different factors can be obtained by the decomposition of total variation into appropriate components, which is commonly called analysis of variance (ANOVA). The purpose of ANOVA is to investigate which of the operation parameters significantly affect the performance characteristic. ANOVA is also needed for estimating the error variance. The ANOVA results from the study are shown in Table 4.20.

Table 4.20: The average effects of factors for each level

Column	Factors	Average Effects		
		Level 1	Level 2	Level 3
1	Temperature	16.49	17.85	19.17
2	Time	17.34	17.08	19.10
3	Heating Rate	18.38	18.17	16.96
4	Duration of mechanical milling process of silica sand	15.67	17.90	19.94

Table 4.21: ANOVA table

Column	Factors	DOF	SS	Variance	F	%
1	Temperature	2	10.823	5.411	-	22.126
2	Time	2	7.248	3.624	-	14.818
3	Heating rate	2	3.530	1.765	-	7.218
4	Duration of mechanical milling process of silica sand	2	27.313	13.656	-	55.835
All Others / Error		0	-	-		-
Total		8	48.914			100.00

Ibrahim *et al.* [24] reported that the variance of each factor is determined by dividing the sum of squares for each factor with its degree of freedom (DOF). They also mentioned that the degree of freedom associated with a factor equals to one less than the number of levels. According to them, for a factor with 3 levels, level 1 data can be compared with level 2 and level 3 data but not with level 1 itself. Thus the 3 level factors have 2 DOF. They also described that the variance ratio (F) is the ratio of variance due to the effect of a factor to the variance due to the error term. This approach was used and explained in detail by Ibrahim *et al.* [24].

The “Percent” column in Table 4.8.3.3 shows that the factor duration of mechanical milling for silica sand contributed the highest percentage (55.83%),

followed by temperature (22.12%), time (14.81%) and heating rate (7.21%). Since the contribution of heating rate was smallest, and at less than 10%, it was considered insignificant and this factor was pooled (combined) with the error term. Pooling as described by Ibrahim *et al.* [24] is the process of ignoring the contribution of a selected factor and subsequently adjusting the contribution of the other factors. Hence, the new ANOVA result after pooling is as tabulated in Table 4.22.

Table 4.22: Pooled ANOVA table

Column	Factors	DOF	SS	Variance	F	%
1	Temperature	2	10.823	5.411	3.065	14.908
2	Time	2	7.248	3.624	2.053	7.600
3	Heating rate	{2}	{3.530}	-	-	-
4	Duration of mechanical milling process of silica sand	2	27.313	13.656	7.736	48.620
All Others / Error		2	3.530	1.765		28.871
Total		8	48.914			100.00

It was observed that as the small factor effect of heating rate was pooled, percentage contributions of the remaining factors decreased slightly, but ranking of the factor effects still remained. The average performance of effects indicates that level 3 for factors duration of mechanical milling for silica sand, temperature and time gives the optimal condition. As shown in Table 4.23, the expected improvement is 4.69 over the current average performance of 17.83. Since heating rate had little significance, it was omitted in the selection of levels for the optimum condition [24]-[28].

Table 4.23: Estimate of the optimum condition of design

Factors	Level Description	Level	Contribution
Temperature	1650 °C	3	1.335
Time	180 minutes	3	1.260
Duration of mechanical milling process of silica sand	100 hours	3	2.101
Contributions from all factors (total)			4.697
Current grand average of performance or Mean			17.837
Expected results at optimum condition			22.534

Based on these results, the highest % yield of SiC_w formation could be attained at the combination setting of A₃, B₃, C₁ and D₃, i.e. processing temperature of 1650 °C, processing time of 180 min, heating rate of 5 °Cmin⁻¹ and duration of mechanical milling for silica sand of 100 hours. This combination of settings was not used in the experiments. Hence, according to Ji *et al.* [26] the orthogonal array is capable of identifying optimum factors in a multidimensional factor space.

The expected results (R_{expected}) at optimum condition in terms of S/N ratio can be converted back to the scale of units of the original observations as follows:

$$22.53 = -10 \log (\text{MSD})$$

$$\text{MSD} = 10^{-22.53/10} = 5.53 \times 10^{-3}$$

$$R_{\text{expected}} = (\text{MSD})^{-1/2} = 13.387 \text{ g}$$

Verification experiments were conducted by running another three replications at the combined setting of A₃, B₃, C₁ and D₃. The average yield of SiC was found to be 12.824 g which is within the confidence interval of the predicted optimal yield formation of SiC.

4.11 The influence of silicon carbide particulate addition on the physical and mechanical properties of fabricated Al foam

This section presents the work that has been carried out to study the influence of silicon carbide addition on the physical and mechanical properties of the fabricated Al foam.

4.11.1 Surface morphology of the reinforcement Al foam

The typical microstructure of the cell wall of the aluminium foam is shown in Figure 4.152 (a) – (c). It can be observed that the cell wall of the pure aluminium is very dense and only a few numbers of micro pores can be seen. Figure 4.152 (d) shows the energy dispersive spectrum of the cell wall and the chemical composition of the cell wall is tabulated in Table 4.24. Most of the aluminium particles have changed their original shape at a compaction of 120 MPa and the strong bonding between the aluminium particles have been achieved after pressure assisted solid state sintering at 620 °C for 30 minutes there is no boundaries between the aluminium particles.

After adding 1 wt.% SiC_p, the surface of the cell wall is covered with some materials, which is shown in Figure 4.153 (a). The composition of the particles (point A) in the foam was characterized by energy dispersive spectrum (EDS). Figure 4.153 (b) shows the presence of SiC particles and the results is tabulated in Table 4.25. Meanwhile, the EDS and the chemical composition on the cell wall were also characterized and the result is shown in Figure 4.153 (c) and Table 4.25. The results reveal that a great deal of SiC exists on the cell wall of aluminium foam. No SiC was detected at point B of the cell wall. The results demonstrate that the aluminium powders were coated with SiC after mixing in a three dimensional mixer for 1 hour.

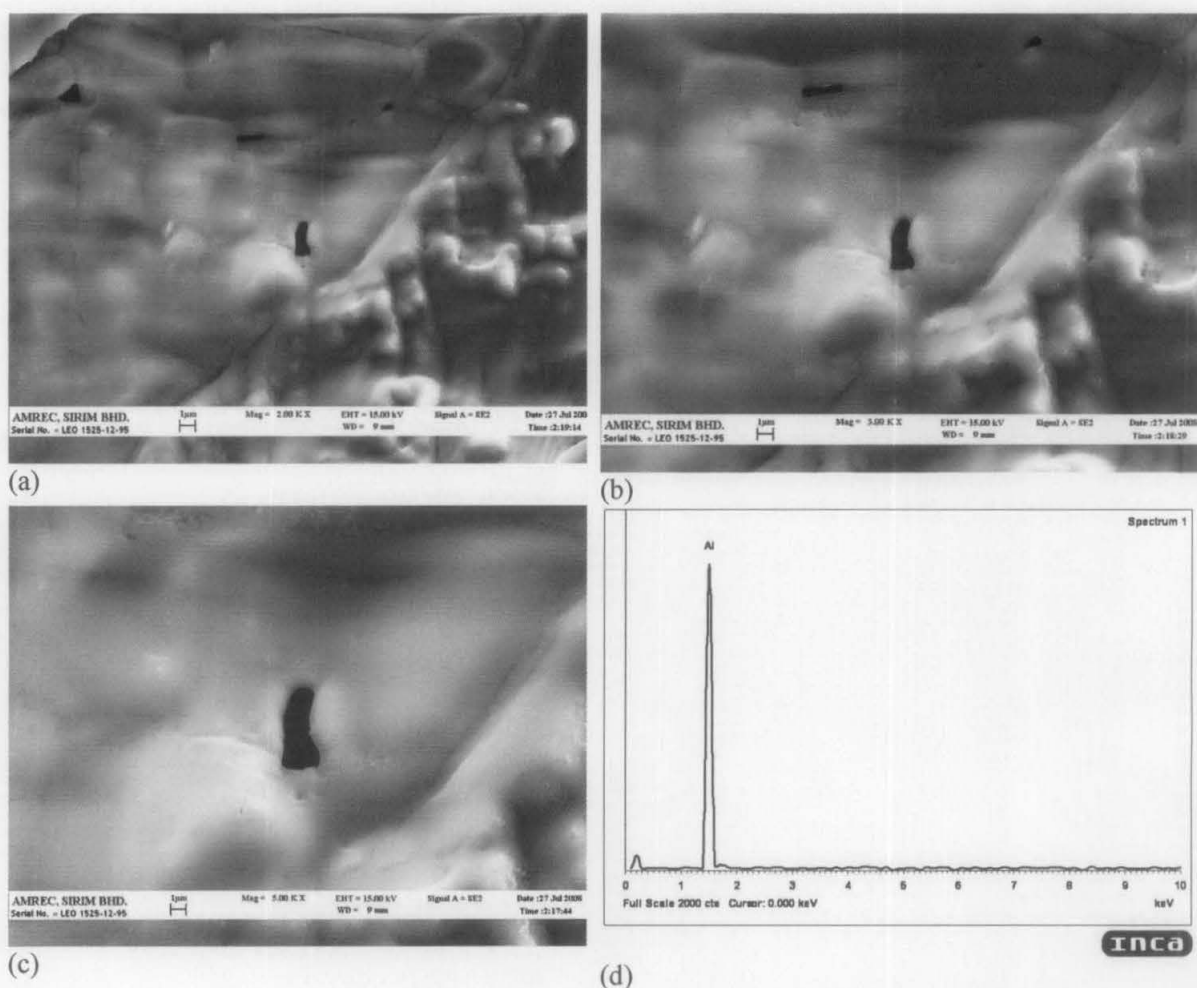


Figure 4.152: Electron micrographs of the cell walls of aluminium foam at different magnification (a) 2kX (b) 3kX (c) 5kX (d) EDX of the cell wall aluminium

Table 4.24: Chemical composition of the cell wall of aluminium foam

Element	Weight %	Atomic %
C	4.43	7.25
Al	95.57	92.75
Total	100.00	

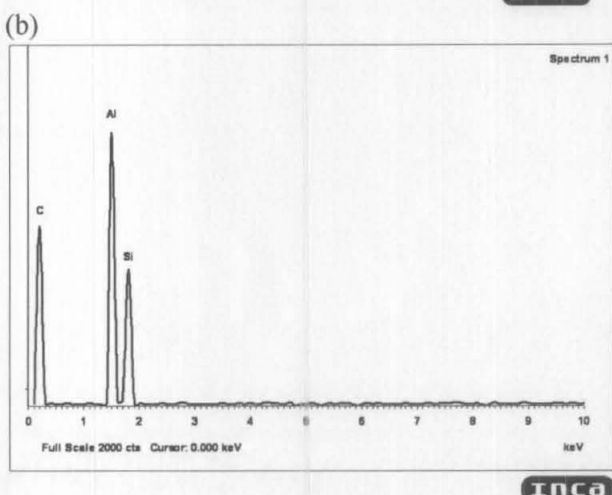
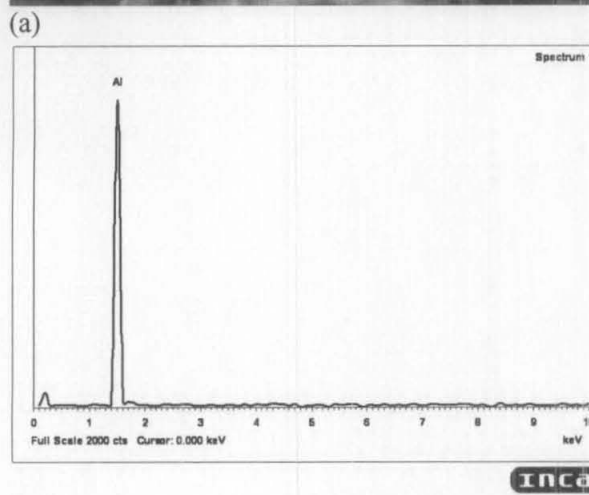
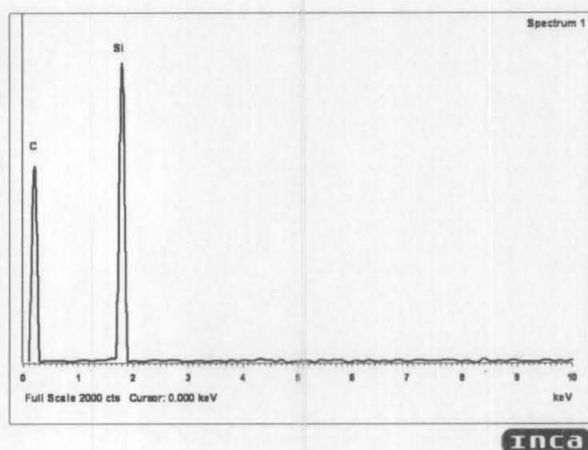
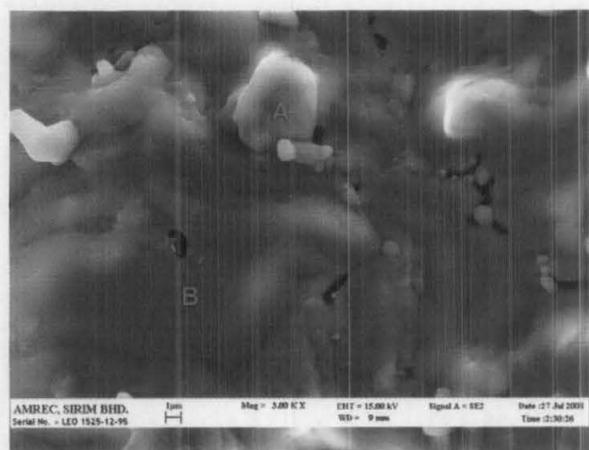


Figure 4.153: (a) Electron micrographs of the cell walls of reinforced aluminium foam (b) EDS analysis result taken from point A (c) EDS analysis result taken from point B (d) EDX of the cell wall of reinforced aluminium foam

Table 4.25: Chemical composition of the cell wall of reinforced aluminium foam at point A

Element	Weight %	Atomic %
Carbon	38.56	54.71
Silicon	61.44	45.29
Total	100	

4.10.2 Mechanical properties

Figure 4.154 presents examples of compression curves of Al and Al-1% wt. SiC foams. The curves show the typical compression deformation behaviour of ductile metallic foams. As expected, the Al-1% wt. SiC foam has higher compressive strength and absorbs more energy during densification (area under the curve up to densification). However, the Al-1% wt. SiC shows some disintegration during the compression tests, indicating its lower ductility. In both cases, the materials show a long and flat stress-strain plateau for energy absorption applications.

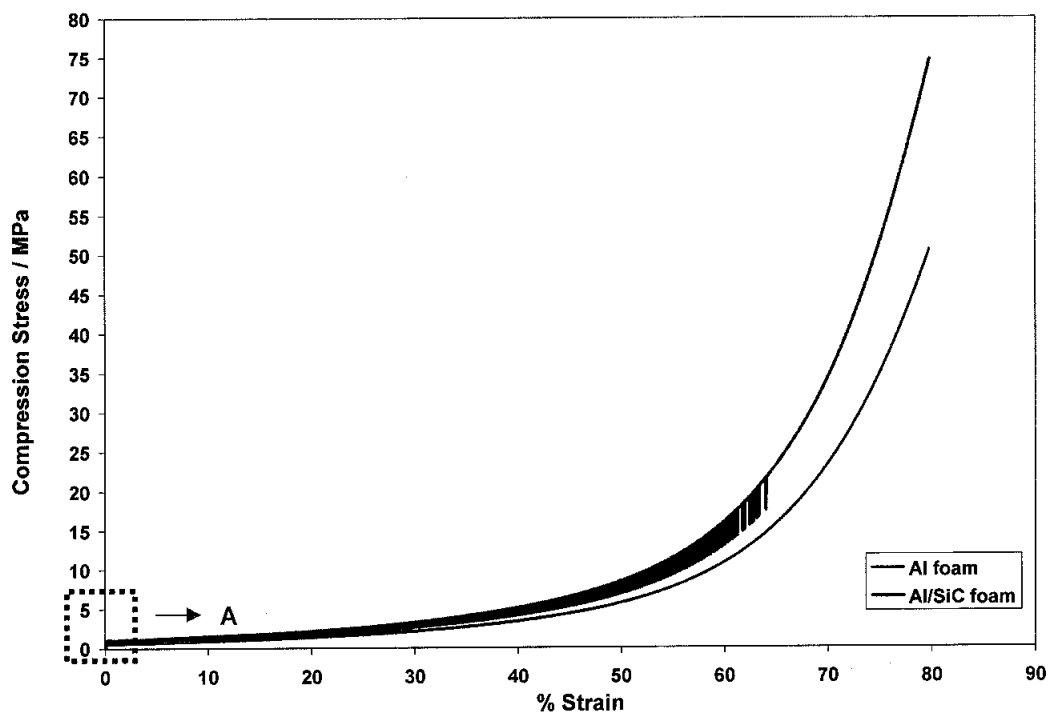


Figure 4.154: Compression curves of Al and Al-1% wt. SiC foams

The compressive yield strength of the of the pure Al foams varies from 0.75 to 2.13 MPa when the density increases from 0.545 to 1.132 gcm^{-3} while that of the Al-1% wt. SiC foam varies from 1.12 to 3.19 MPa when the density increases from 0.588 to 1.223 gcm^{-3} . The differences between the yield strength of pure Al and Al-1% wt. SiC foam increases with foam density.

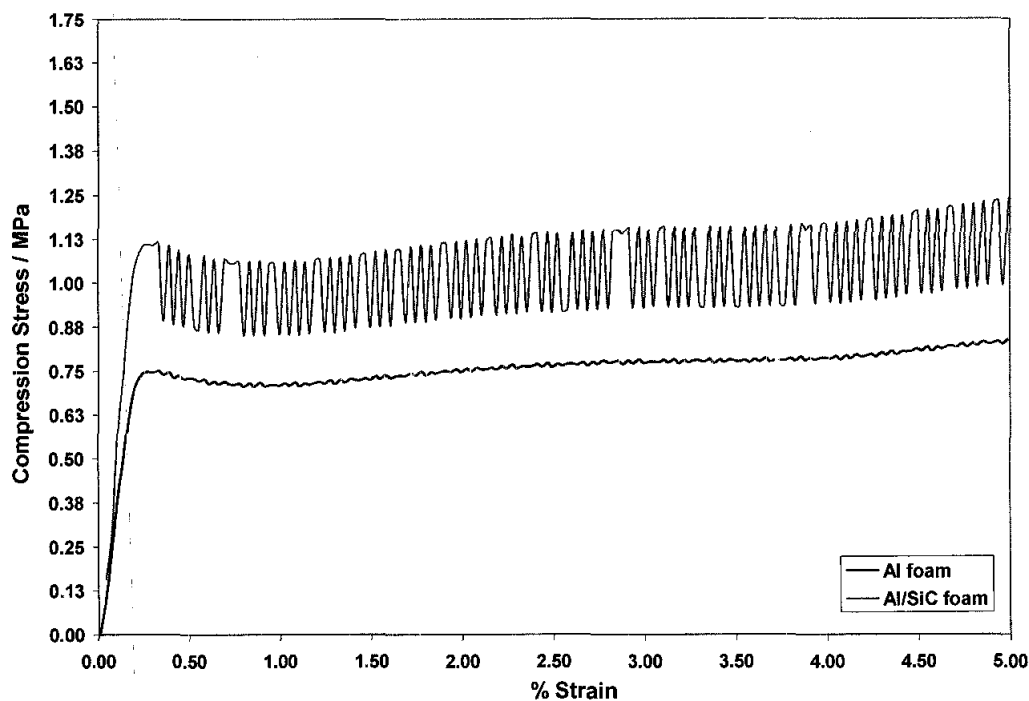


Figure 4.155: Enlarge portion of the beginning of the curve of point A of the compression graphs pure Al and Al-1% wt. SiC foams.

The addition of SiC of 1% wt. has much less impact on the modulus of the foams. Moreover, the effect of density on the modulus of both foams is significant and the value of modulus increases when the density increases. As shown above, the compressive strength and modulus Al foam depends strongly on the relative density, defined as the ratio of the foam density to the material density. The compression strength and modulus of foams can be predicted from a simple theory based on cubic unit cells as equations. (4.4) and (4.5) respectively. The values obtained are directional proportional to the relative density of the foam and the yield strength and modulus of the cell wall material and fit the scaling law as indicated in Figures 4.156 – 4.159. The coefficients estimated with these scaling laws are listed in Table 4.26. The m coefficient obtained is nearly similar for the two types of foam. According to the literature, this coefficient is structure dependent and the structure of the Al and Al-1% wt. SiC foams investigated in this study are similar. This finding suggests that the m coefficient is only affected by the structure of the foam.

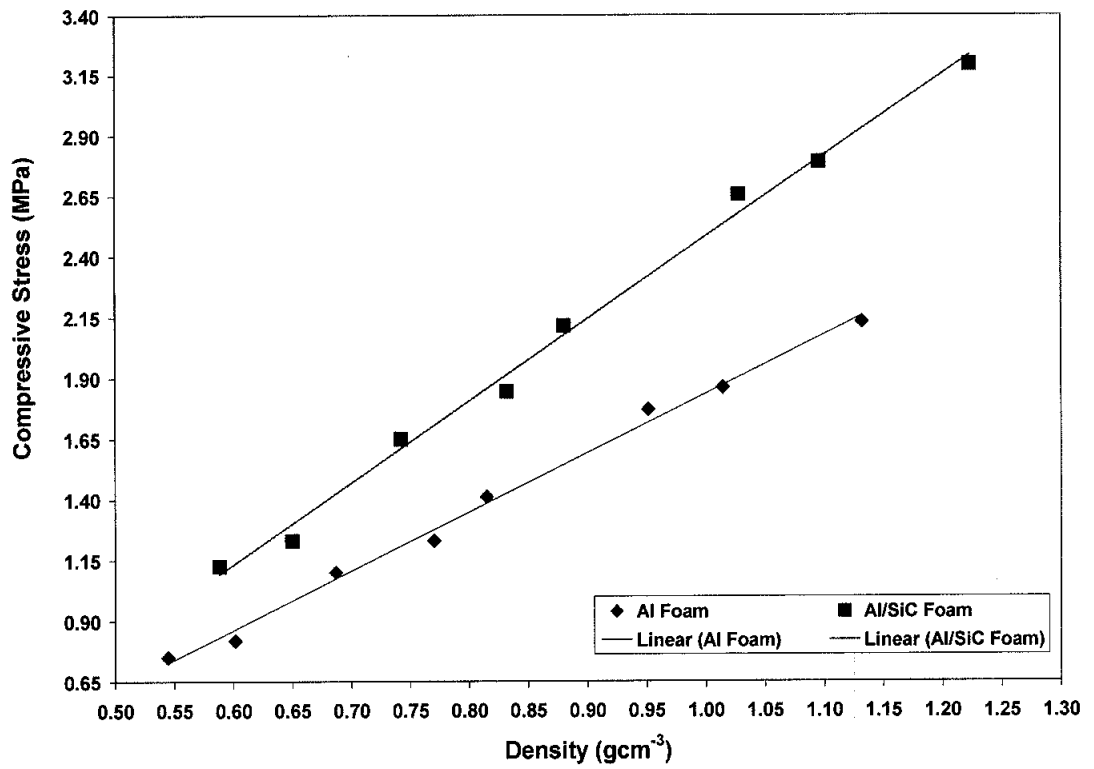


Figure 4.156: Compressive strength of pure Al and Al-1% wt. SiC foams as a function of density

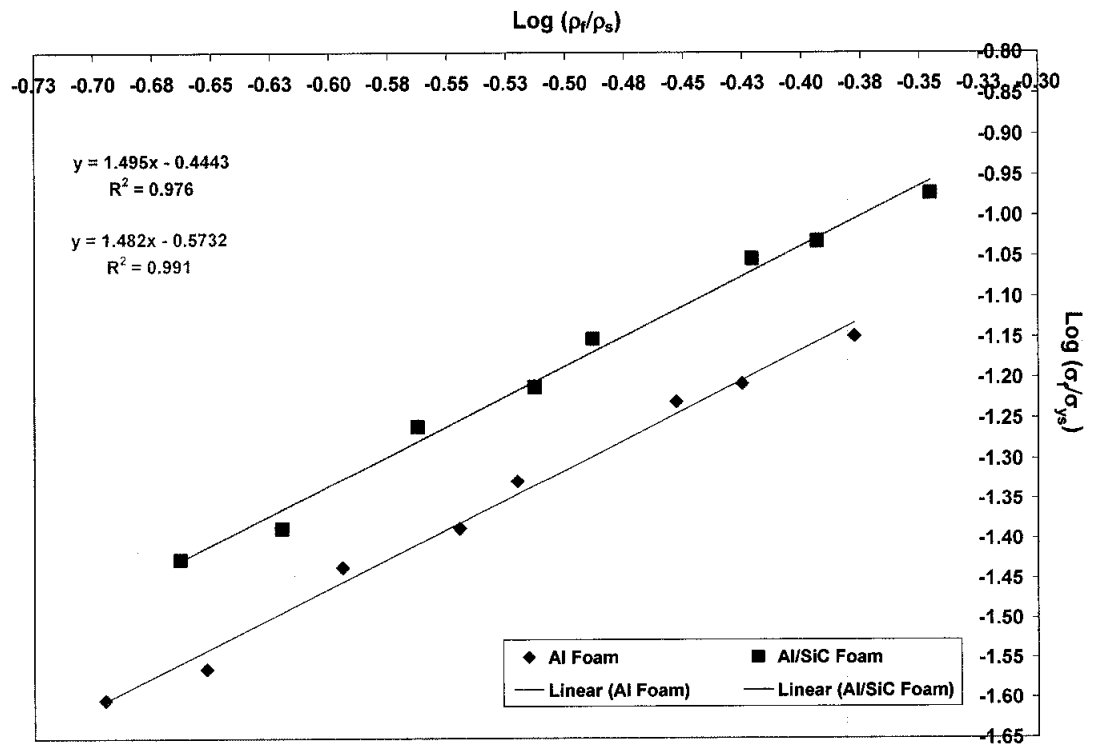


Figure 4.157: Relative compressive strength of pure Al and Al-1% wt. SiC foams as a function of relative density

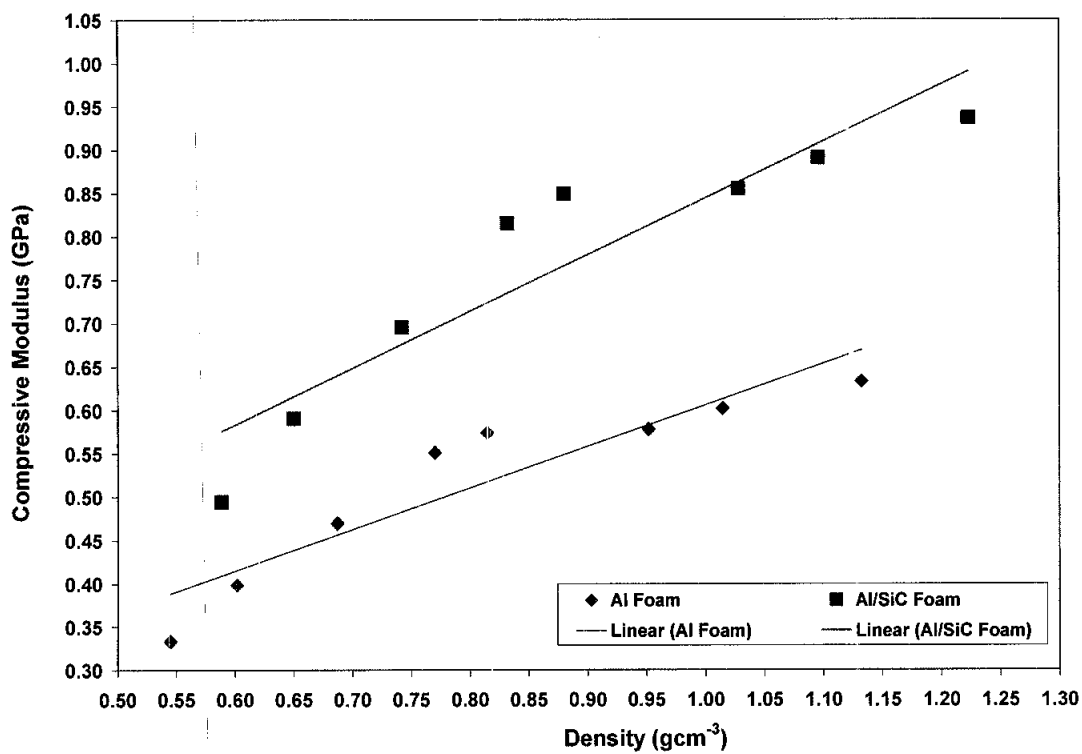


Figure 4.158: Compressive modulus of pure Al and Al-1% wt. SiC foams as a function of density

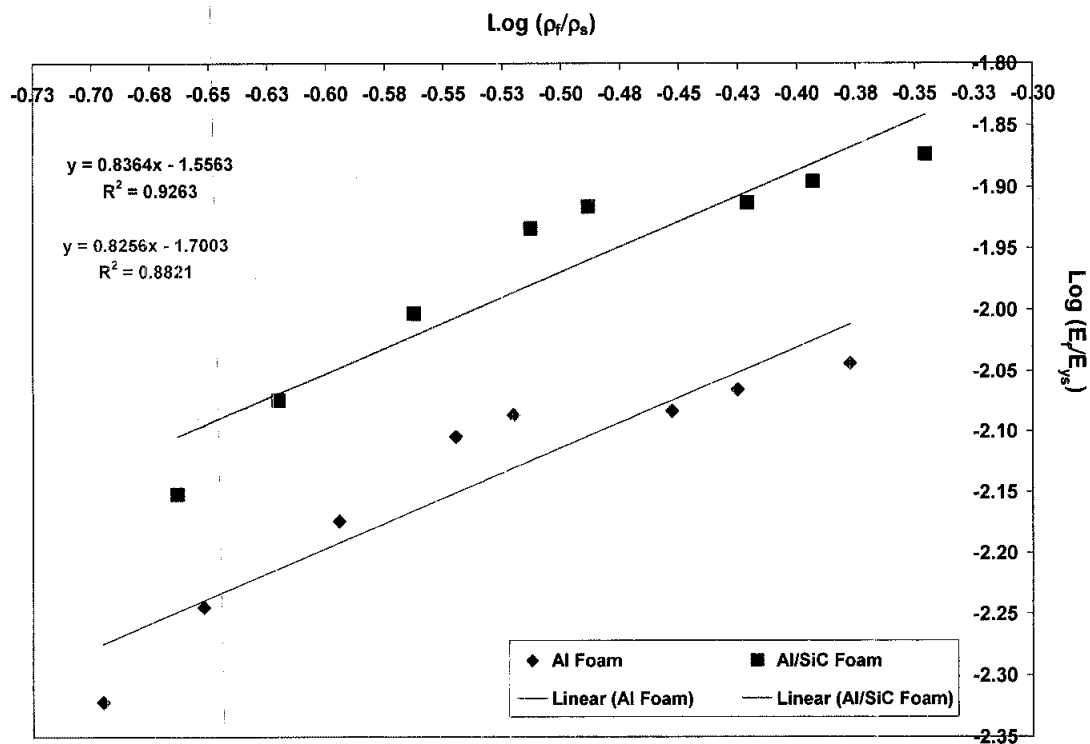


Figure 4.159: Relative compressive modulus of pure Al and Al-1% wt. SiC foams as a function of relative density

Table 4.26: Correlation coefficients equations (4.4) & (4.5) for the Al and Al-1% wt.

SiC foam

	β	m	α	n
Al foam	0.267	1.482	0.019	0.825
Al-1%SiC foam	0.359	1.495	0.027	0.836

The n coefficient obtained fits in the range 0.80-1.50 obtained with other commercial metallic foams and the α coefficient obtained also fits in the range obtained with other foams.

The effect of density on the compressive strength at densification is clearer. It increases from 5.0 to 20.5 MPa for the pure Al foams and 7.4 to 30.3 MPa for the Al-1% wt. SiC foams, when density increase for both types of foams.

The deformation at densification is affected either by the density and composition of the foams characterized in this study due to the fact that the ductility of the materials is different (Figure 4.161). The effect of density on the deformation at densification is significant when density increases.

The energy absorbed by the foams, represented by the area under the curve up to densification, varies from 9.04 to 10.19 MJm⁻³ when the density increases from 0.588 to 1.223 gcm⁻³ for Al-1% wt. SiC (Figure 4.163).

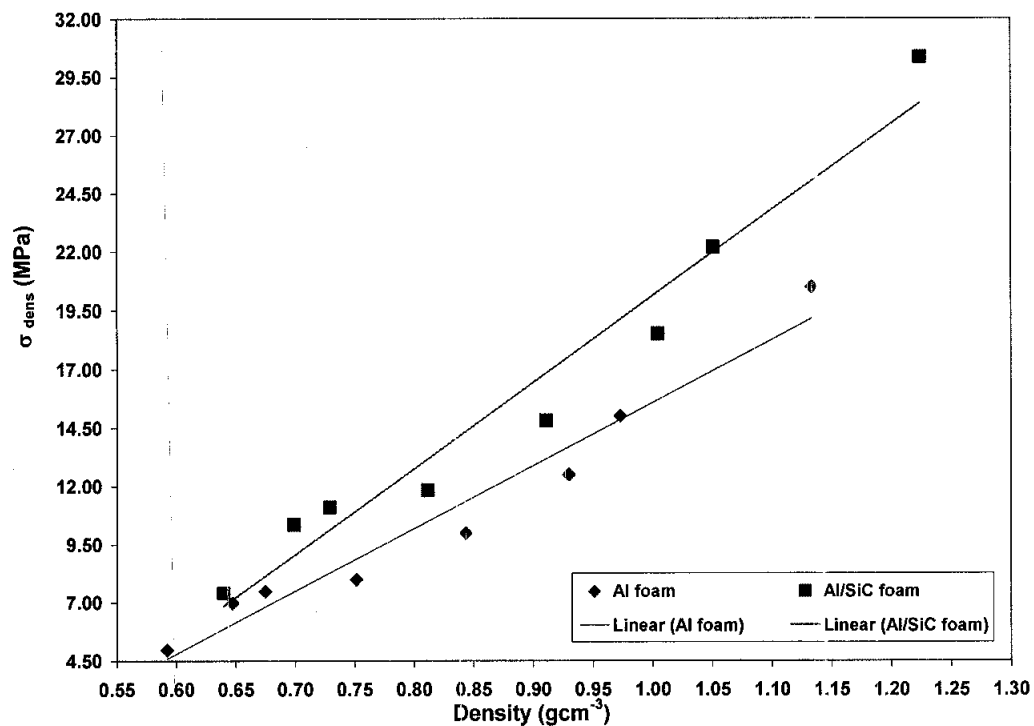


Figure 4.160: Strength at densification of pure Al and Al-1% wt. SiC foams as a function of density

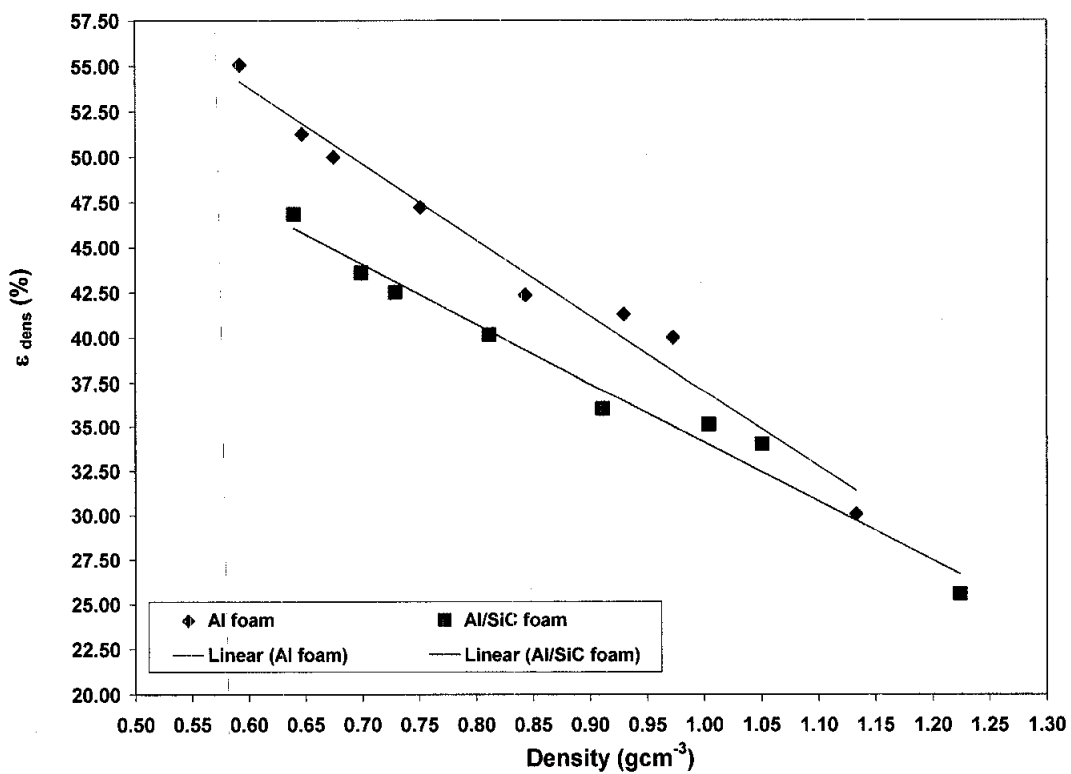


Figure 4.161: Deformation at densification of pure Al and Al-1% wt. SiC foams as a function of density

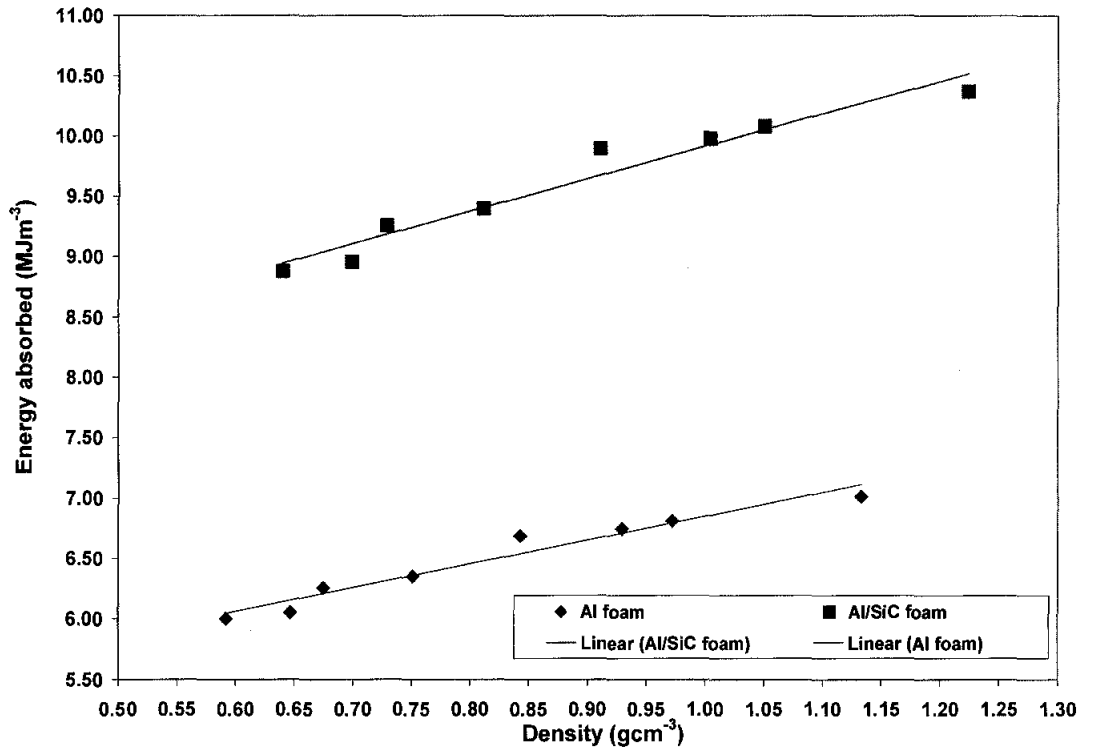


Figure 4.162: Energy absorbed at densification of pure Al and Al-1% wt. SiC foams as a function of density

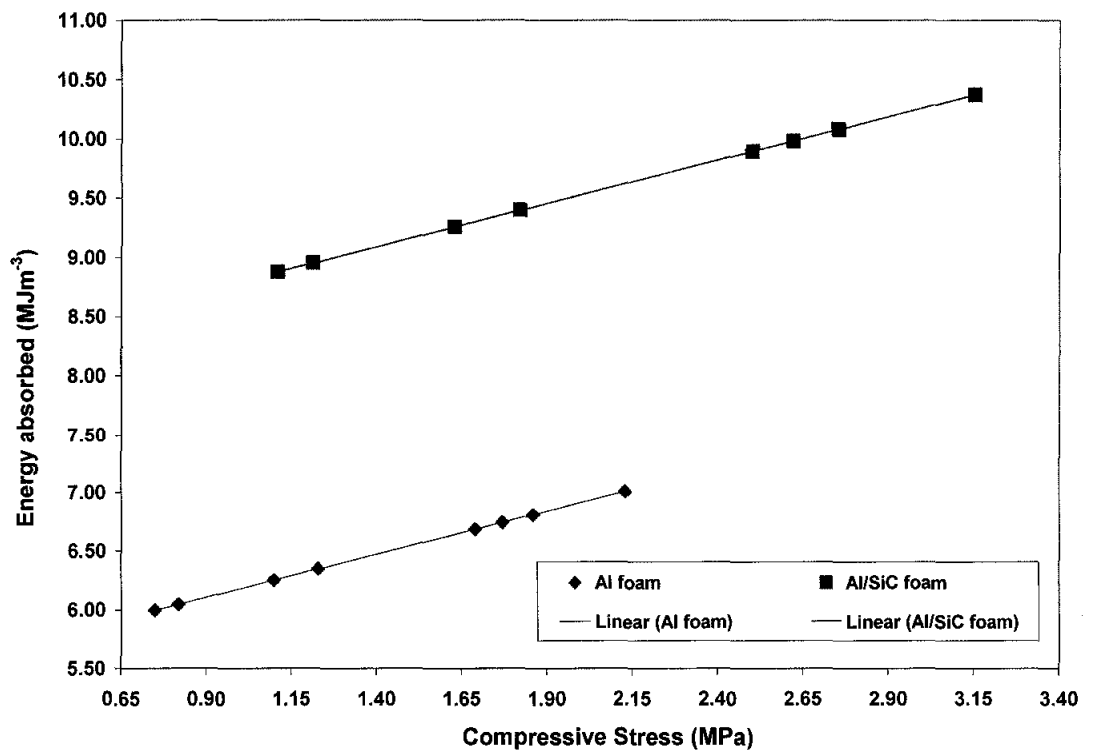


Figure 4.163: Energy absorbed at densification of pure Al and Al-1% wt. SiC foams as a function of compressive strength

4.12 Summary of findings

It was demonstrated in this experiment that net-shape aluminium foam can be produced by pressure assisted solid state sintering and dissolution process. The study revealed that compaction at elevated temperature favours the metallic framework of Aluminium matrix. The bonding between Aluminium particles is facilitated by the localised fusion of the particles through metal-metal contacts. In contrast to foams made by SDP, Al foams made by PASDP have highly dense of cell wall which can be attained in a much shorter time and possess superior mechanical properties. The PASDP Al foam has an open-pore structure featuring three level of porosity. The structure is characterized by cell (1st level) with some openings or windows (2nd level) on the cell walls. The third level of porosity, is only visible at higher magnification. In this process the foam porosity can be varied in a much wider range by adjusting the NaCl-to-Al volume ratio in the NaCl/Al powder compact, as long as both the NaCl particles and the Al matrix are interconnected in the great majority. PASDP can use finer NaCl particles to produce fine celled foams because the interstices between the NaCl particles are filled with Al particles in the solid state.

A PASDP NaCl/Al compact can be seen as a compact of Al matrix with embedded NaCl particles. With a high volume fraction of NaCl in the compact, most NaCl particles are in contact with each other and form a continuous three-dimensional network. Because all the NaCl particles in the network can be dissolved away by water, there is only a small amount of residual NaCl in the resultant foam. In contrast, with a low volume fraction of NaCl in the preform some NaCl particles are enclosed completely by the Al matrix. These isolated NaCl particles cannot be dissolved away and remain in the foam. Decreasing NaCl weight fraction in the NaCl/Al compact increases the Al volume fraction and therefore increases the amount of residual NaCl in the final Al foam.

At a compaction pressure lower than 20 MPa, there was severe spalling of Al particles yielding an imperfect geometry. The sample produced under compaction pressure in the range 20 – 120 MPa exhibited acceptable qualities. The compressibility behaviour of NaCl/Al compact at elevated temperature was found to

be dependant on the amount of filler agent content. Due to lower plastic deformation capacity, the composite with higher content of leaching agent exhibited lower compressibility. The values of the Al-crystallite size tend to decrease with increasing NaCl content. Whereas, the lattice strain of Al increases with increasing NaCl content. It reveals that Al with ductility character possesses more potential to deform plastically leading to grain refining and changing in lattice distortion. In other words, powders of low stiffness or high work hardening capacity are be able to densify more effectively.

The optimum sintering temperatures falls within 570-620 °C for manufacturing pure Al foams which produce samples of generally preferably quality. Sintering temperatures lower than 570 °C results in poor or no bonding between Al particles, leading to foam disintegration during dissolution or subsequent handling. Temperatures higher than 620 °C, however, increased the flowability of molten Al, which resulted in partial separation of the NaCl/Al mixture and hence a non-uniform distribution of local relative density. Sintering times shorter than 5 minutes were not sufficient to ensure good bonding between aluminium particles. Heating rate higher than 30 °C/min should be avoided in the process in order to avoid the cracking of the specimens.

By using Taguchi's method and ANOVA which is a major improvement from the conventional Full factorial Design of Experiment statistical method, the influence of processing parameters on the physical and mechanical properties of the PASDP foams have been optimized. The optimum parameters and their levels were found to be A₃, B₃, C₁, D₃, i.e., sintering time of 30 min, sintering temperature of 620 °C, heating rate of 30 °C/min and compaction pressure of 120 MPa.

The specimens of 30% to 50% volume fraction of NaCl/Al do not exhibit a characteristic of stress-strain foam behaviour when loaded in compression. The typical engineering stress-strain curve of the aluminium is exhibited by specimen of 60 to 80 % volume fraction of NaCl/Al. The curve is generally characterised by an initial elastic response, followed by a deformation "plateau" with a positive slope and finally a transition to densification. One of the characteristics of the foam

manufactured by PASDP is a very smooth plateau region in the stress-strain curve, as a result of the homogenously distributed pores having a narrow size range.

The mechanical properties of the foam were dependant on the pore size and its width of size distribution. It can be seen that the compressive strength, compressive modulus and stress at densification increase with decreasing of the pore size.

It is evident that the present of pores will significantly affect the electrical properties of the specimen. A decrease in the conductivity is visible as the volume fraction of specimen is increased. An increase in conductivity is observed when the processing parameters (compaction pressure, sintering temperature, time and heating rate) are increase. This behaviour is due to the fact that these optimum conditions will lead to better binding among the aluminium particles when they were simultaneously sintered and pressed. It is obvious that formation of pores should result in higher electrical resistivity. Thus the behaviour of the resistivity as a function of the manufacturing parameters should be similar to the properties such as density. It was shown that the relative density is the most important variable and the power law function can be successfully applied to describe the dependence of electrical conductivity of aluminium foam on the relative density, confirming the suitability of the percolation theory approach.

PASDP is most suitable process for manufacturing Al foams with relative densities between 0.15 and 0.4. Within this range, the residual NaCl in the foam is less than 10% of the total NaCl in the initial perform. The relative foam density can be controlled with reasonable accuracy by mixing NaCl and Al powders at a pre-specified volume ratio. It is difficult to obtain a relative foam density below 0.15 by PASDP because the Al particles in the NaCl/Al perform with a low Al weight fraction are largely isolated patches rather than a continuous network. At a relative density greater than 0.5, the Al foam contains more than 10% of the initial NaCl. The residual NaCl may result in undesirable effect of the Al matrix, degrading the mechanical and chemical properties of the foam.

By using Taguchi's method and ANOVA, the influence of processing parameters on the yield formation of silicon carbide, which will be acting as reinforcement material, from the carbothermal nitridation process of using structured alteration silica

sand have been optimized. The optimum parameters and their levels were found to be A_3, B_3, C_1, D_3 , i.e., temperature of 1650 °C, time of 180 minutes, heating rate of 5 °C/min and duration of milling process of silica sand of 100 hour. Silicon carbide and silicon nitride whiskers were produced in silica and carbon solid mixtures under nitrogen-containing atmosphere. It was observed that the use of structurally distorted silica sand will lower the temperature formation of silicon carbide and at high process temperature of 1550 °C, the formation of silicon carbide whisker is more favourable. The morphological characteristics of whisker, which are of major importance for applications in composite materials, are significantly improved by the use of structurally distorted silica sand in the carbothermal nitridation process.

The study also indicates that the addition of SiC in the Al foam has noticeable effect in improving its mechanical properties which degrade with the increase of porosity. The compressive strength and energy absorbed at densification are significantly affected by the reinforcement addition.

CHAPTER 5

CONCLUSION AND SUGGESTION FOR FUTURE WORK

From the results of the experiments and observation made in the present study, the following conclusions were deduced:

- An improved method known as pressure assisted sintering and dissolution process (PASDP) was successfully developed to fabricate open-celled Al foams with superior morphological, physical and mechanical properties. The study revealed that compaction at elevated temperature favours the metallic framework of Aluminium matrix. The bonding between Aluminium particles is facilitated by the localised fusion of the particles through metal-metal contacts. In contrast to foams made by SDP, Al foams made by PASDP have highly dense cell wall, which can be attained in a much shorter time and possess superior mechanical properties.
- The four processing parameters of PASDP (compaction pressure at elevated temperature, sintering temperature, sintering time, sintering and heating rate) have an influential effect on the properties of the fabricated Al foam.
- By manipulating the NaCl-to-Al volume fraction in the compact according to the rule of mixture, the density and hence the porosity of the foam can be varied according to the need of the application for density graded material.
- The values of the crystallite size tend to decrease with increasing filler agent content. However the value of the micro strain of the Al foam increase with the increase of filler agent content.

- The study reveals that relative density is the important factor that affects the electrical conductivity behaviour of the PASDP Al foam. The findings highlighted that the relationship between relative electrical conductivity and density of the specimen does not follow the mathematical description given by Skorohod and Solonin, instead the power law seems to be a good characterization of the relationship between experimental data of electrical conductivity and density of the resultant foams.
- The Taguchi's Design of Experiment and ANOVA demonstrated that the optimization of the influence of the processing parameters on the physical and mechanical properties of the Al PASDP foams can be predicted using the minimum numbers of experiments needed in order to produce relevant information for a given set of factors.
- The results revealed that the compressive properties of the foams increase with the increase of relative density and decrease with the increase of pore size. The pore size however has a negligible effect on the electrical conductivity of the foam.
- An improved process for producing silicon carbide for the reinforcement material has been successfully synthesised using simple set up that can be worked without high conversion engineering cost and using distorted structure silica sand as cheap precursor materials.
- Addition of silicon carbide materials will improve the mechanical properties of the fabricated foam that degraded with increasing porosity.

5.1 SUGGESTION FOR FUTURE WORK

It has been found that the dense cell wall of Al foam can be achieved using pressure assisted sintering process and it would be worthwhile investigating of using pressure isostatic pressing technique in which high isostatic pressure is applied to a powder at elevated temperature to produce particle bonding. This process usually results in the

manufacture of a fully dense body. During processing, the compact is subjected to equal pressure from every side. The selection of process parameters, such as temperature, time, pressure and heating rate, to achieve material property and dimensional requirements usually is verified by processing through a matrix and testing. Guidelines to process temperature for isostatic pressing at elevated temperature of P/M parts which may be obtained from published literature may be useful in fabricating the NaCl/Al compact. This process also allows in using much finer Al powder of submicron size (0.1 to 1.0 μm) which can be densified at approximately 100 to 200 $^{\circ}\text{C}$ below coarser powders at equivalent pressure and time.

Changing the shape of the filler agent to spherical shape provides a pathway for the exploration of microstructure/property relations in open cell aluminium foams. In order to manufacture spherical particles the as-received NaCl were melted using propane gas torches in a method capable of producing a considerably large quantity of particles. It was found that for successful production of spherical particles of 400 μm diameter, a preheating stage is necessary, without which the particles could not be melted by passing through propane torches. To achieve this, a tube furnace set a constant temperature of 775 $^{\circ}\text{C}$ which is slightly lower than the melting point of NaCl, 800 $^{\circ}\text{C}$ is used. Particles pass through the furnace in an inclined steel channel, which is vibrated to cause the particles to move gradually through the furnace. The channel rests on a copper block to spread and retain heat along the whole length. Preheating was not found to be necessary for the smaller 75 μm particles to be melted using the same apparatus with a continuous and controlled powder feed. As soon as the particles exit the furnace they fall into the first of two propane torches. This is fitted with an attachment that spreads the flame along the direction of salt travel and inclined to maximise the time the particles stay in the hottest part of the flame. Subsequently the particles pass into the second torch which is angled upwards to prolong their time in the air. After leaving the torches the particles are molten, and will have adopted a spherical shape due to surface tension of the liquid. The particles then fall through a distance of approximately 40 cm, during which time they cool and solidify.

The use of aluminium alloy powder such Al 6061 which is more suitable in engineering application can be investigated further by blending it with the leaching

agent. Al 6061 alloys contain Si and Mg as main alloying elements with other elements such as Cu and Mn for improving mechanical properties.

The influence of heat treatment on the structure and mechanical properties of the foams should be investigated. The objective of the heat treatment is to produce a uniform distribution of coherent or semi coherent precipitates while avoiding the development of larger equilibrium structures without coherence with the matrix lattice. The physical process effective in heat treating Al 6061 alloys is precipitation hardening and can be divided into three steps: During solution heat treatment (SHT) at a temperature T_s for period t_s a solid solution of the alloying elements is formed. Quenching at a rate $(dT/dt)_q$ allows for stabilising this state at room temperature, thus leading to a supersaturated solid solution. After an optional delay time t_d , ageing at temperature T_a for a period t_a leads to the formation of precipitates in fine dispersion within the supersaturated regions.

REFERENCES

- [1] L.J. Gibson, M.F. Ashby, *Cellular Solid: Structure and Properties*, 2nd Edn., Cambridge, UK, *Cambridge University Press*, 1997.
- [2] J. Banhart and H. Eifert, *Metal Foams*, *Verlag MIT Publishing, Bremen*, 1997.
- [3] J. Banhart, M.F. Ashby and N.A. Fleck, *Metal Foams and Porous Metal Structures*, *Verlag MIT Publishing, Bremen*, 1997.
- [4] I. Duarte, J. Banhart, "A study of aluminium foam formation – Kinetics and Microstructure", *Acta mater.*, 48, pp. 2349-2362, Jan. 2000
- [5] R. Goodall, J. Despois and A. Marmottant, "The effect of preform processing on replicated aluminium foam structure and mechanical properties", *Scripta Mater.*, 54, pp.2069-2073, Oct. 2006.
- [6] D. Lehmhus and J. Banhart, "Properties of heat-treated aluminium foams", *Mater. Sci. Eng. A* 349, pp 98-110, Nov. 2003.
- [7] K. Chou and M. Song "A novel method for making open-cell aluminium foams with soft ceramic balls", *Scr. Mater.*, 46, pp. 379-382, Dec. 2002.
- [8] Y. Zhao, F. Han and T. Fung "Optimisation of compaction and liquid-state sintering in sintering and dissolution process for manufacturing Al foams", *Mater. Sci. Eng. A* 3364: 117-125, Nov. 2004.
- [9] D.P. Kou and J.R. Li, "Mechanical behaviour of open-cell metallic foams with dual-size cellular structure", *Scripta Mater.*, 59, pp. 483-486, Jan. 2008.
- [10] B. Jiang, N.Q. Zhao, C.S. Shi and J.J. Li, "Processing of open cell aluminium foams with tailored porous morphology", *Scripta Mater.*, 53, pp. 781-785, Jul. 2005.
- [11] B. Jiang, N.Q. Zhao, C.S. Shi and H.C. Man, "A novel method for making open cell Aluminium foams by powder sintering process", *Mater. Lett.*, 59, pp. 3333-3336, Dec. 2005.
- [12] A.H. Brothers and D.C. Dunand, "Mechanical properties of a density-graded replicated aluminium foam", *Mater. Sci. Eng., A* 489, pp 439-443, Apr. 2008.
- [13] B. Jiang, Z. Wang, and N. Zhao, "Effect of pore size and relative density on the mechanical properties of open cell aluminium foams" *Scripta Mater.*, 56 pp. 169-172, Jun 2006.
- [14] N.Q. Zhao, B. Jiang, X.W. Du and C.S. Shi, "Effect of Y_2O_3 on the mechanical properties of open cell aluminium foams", *Mater. Lett.*, 60, pp. 1665-1668, Dec. 2005.
- [15] J. Bin, W. Zejun and Z. Naiqin, "Effect of pore size and relative density on the mechanical properties of open cell aluminium foams", *Scripta Mater.*, 56, pp. 169-172, 2007.
- [16] Y.J. Yang, F.S. Han, D.K. Yang, J. Wu, G.L. Hao and Q.Z. Wang, "Effect of heat treatment on compressive properties of open cell Al/ Al_2O_3 composite foams", *Powder Metall.*, 50, pp. 50-53, 2007.

- [17] M. Hakamada, T. Kuromura, Y. Chino, Y. Yamada, Y. Chen, H. Kusuda and M. Mabuchi, "Monotonic and cyclic compressive properties of porous aluminium fabricated by spacer method", *Mater. Sci. Eng., A* 459, pp 286-293, Mar. 2007.
- [18] E. Amsterdam, J. Hosson and P.R. Onck, "On the plastic collapse stress of open-cell aluminium foam", *Scripta Mater.*, 59, pp 653-656, 2008.
- [19] R. Goodall, A. Marmottant, L. Salvo and A. Mortensen, "Spherical pore replicated microcellular aluminium: Processing and influence of properties", *Mater. Sci. Eng., A* 465, pp. 124-135, 2007.
- [20] S. Asavavisithchai and A.R. Kennedy, "The effect of Mg addition on the stability of Al-Al₂O₃ foams made by a powder metallurgy route", *Scripta Mater.*, 54, pp. 1331-1334, 2006.
- [21] A.R. Kennedy and S. Asavavisithchai, "Effects of TiB₂ particle addition on the expansion, structure and mechanical properties of PM Al foams", *Scripta Mater.*, 50, pp. 115-119, 2004.
- [22] Y. Zhao. and D.X. Sun, "A novel sintering-dissolution process for manufacturing Al foams", *Scripta Mater.*, 44, pp.105-110, 2000.
- [23] M. Mazli and M. Othman, "The formability of Aluminium foam using pressure assisted sintering technique". *National Postgraduate Symp. (UTP)*, 2008.
- [24] R.M. German, *Sintering Theory and Practice*, John Wiley & Sons, Inc., 1996.
- [25] R.M. German, *Powder Metallurgy Science*, Metal Powder Industries Federation, Second Edition, 1994.
- [26] ASM Handbook, *Powder Metallurgy*, 9th edition, volume 7 American Society for Metals, 1993.
- [27] P.C. Silva and J.L. Figueiredo, "Production of SiC and Si₃N₄ whiskers in C + SiO₂ solid mixtures", *Mater. Chem. Phys.*, 72, pp. 326-331, 2001.
- [28] Mohd A.A., "SIRIM Berhad: Spearheading Malaysia's Industrialization and Raising Her Global Competitiveness", *Technology Business Review*, 9, pp. 49-58, 2005.
- [29] Ninth Malaysia Blueprint.
- [30] J. Banhart, "Manufacture, characterization and application of cellular metals and metal foams", *Pror. Mater. Sci.*, 46, pp. 559-632, 2001.
- [31] M.F. Ashby, A.G. Evans, N.A. Fleck, L.J. Gibson and J.W. Hutchinson, *Metal Foams: A design guide*, Butterworth-Heinemann, Oxford, 2000.
- [32] F. Simancik, "Introduction: The strange world of cellular metals", *Handbook of Cellular Metals*, Wiley-Vch Verlag, 2002, pp. 1-4.
- [33] Q. Cheng, W. Altenhol, S.Y. Jin and C. Powell, "Energy absorption of aluminium foam filled braided stainless steel tubes under quasi-static tensile loading conditions", *International J. Mech. Sci.*, 48, pp. 1223-1233, 2006.
- [34] Z. Wang, Z. Li, J. Ning and L. Zhao, "Effect of heat treatments on the crushing behaviour and energy absorbing performance of aluminium alloys foam", *Mater. Des.*, 48, pp. 167-175, 2008.
- [35] B.V. Krishna, S. Bose and A. Bandyopadhyay, "Strength of open-cell 6101 aluminium foams under free and constrained compression", *Mater. Sci. Eng., A* 387, pp. 289-295, 2006.

- [36] D.X. Sun and Y.Y. Zhao, "Phase changes in sintering of Al/Mg/NaCl compacts for manufacturing Al foams by the sintering and dissolution process", *Mater. Lett.*, 59, pp. 6-10, 2005.
- [37] A. Bhattacharya, V.V. Calmide and R.L. Mahajan, "Thermophysical properties of high porosity metal foams", *Int. J. Heat Mass Transfer*, 45, pp. 1017-1031, 2002.
- [38] A.E. Markaki and T.W. Clyne, "The effect of cell wall microstructure on the deformation and fracture of aluminium-based foams", *Acta Mater.*, 49, pp. 1677-1686, 2001.
- [39] O. Prakash, H. Sang and J.D. Embury, "Structure and properties of Al-SiC foam", *Mater. Sci. Eng.*, A199, pp. 195-203, 1995.
- [40] A.G. Hanssen, O.S. Hopperstad, M. Langseth and H. Ilstad, "Validation of constitutive models applicable to aluminium foams", *International J. Mech. Sci.*, 44, pp. 359-406, 2002.
- [41] Dave Curran – Metal Foams at www.swissdave.co.uk
- [42] A.G. Hanssen, L. Enstock, M. Langseth, "Close-range blast loading of aluminium foam panels", *Int. J. Impact Eng.*, 27, pp. 593-618, 2002.
- [43] J. Banhart and F. Baumgartner, "Industrialization of powder-compact-foaming technique", *Handbook of Cellular Metals*, Wiley-Vch Verlag, 2002, pp. 14-21.
- [44] J. Banhart, "Foam metal: the recipe", *Europhysics News*, 1999, 30, pp. 17.
- [45] J. Baumeister, J. Banhart and M. Weber, German Patent DE 4426627, 1994.
- [46] J. Baumeister, German Patent DE 4018360, 1990.
- [47] B. Matijasevic, J. Banhart, S. Fiechter, O. Gorke and N. Wanderka, "Modification of titanium hydride for improved aluminium foam manufacture", *Acta Mater.*, 48, pp. 558-568, 2006.
- [48] K. Kitazono, E. Sato and K. Kuribayashi, "Novel manufacturing process of closed-cell aluminum foam by accumulative roll-bonding", *Scripta Mater.*, 50, pp. 495-498, 2004.
- [49] U. Ramamurty and A. Paul, "Variability in mechanical properties of a metal foam" *Acta Mater.*, 52, pp. 181-189, 2003.
- [50] U. Ramamurty, M.C. Kumaran, "Mechanical property extraction through conical indentation of a closed-cell aluminum foam", *Acta Mater.*, 52, pp. 181-189, 2004.
- [51] A.R. Kennedy, "The effect of TiH₂ heat treatment on gas release and foaming in Al-TiH₂ preforms", *Scripta Mater.*, 47, pp. 763-767, 2002.
- [52] K. Kitazono, A. Kitajima, E. Sato, J. Matsushita and K. Kuribayashi, "Solid-state diffusion bonding of closed-cell aluminum foams", *Mater. Sci. Eng.*, A327, pp. 128-132, 2002.
- [53] U. Ramamurty and M.C. Kumaran, "Mechanical property extraction through conical indentation of a closed-cell aluminum foam", *Acta Mater.*, 52, pp. 181-189, 2004.
- [54] C. Park and S.R. Nutt, "PM synthesis and properties of steel foams", *Mater. Sci. Eng.*, A288, pp. 111-118, 2000.
- [55] D.P. Mondal, M.D. Goel and S. Das, "Effect of strain rate and relative density on compressive deformation behaviour of closed cell aluminium-fly ash composite foam", *Mater. Sci. Eng.*, A 359, pp 203-211, 2008.
- [56] J.F. Despois, R. Mueller and A. Mortensen, "Uniaxial deformation of microcellular metals", *Acta Mater.*, 54, pp. 4129-4142, 2006.

- [57] M. Guden, S. Yuksel, A. Tasdemirci, M. Tanoglu, "Effect of aluminium closed-cell foam filling on the quasi-static axial crush performance of glass fibre reinforced polyester composite and aluminium/composite hybrid tubes", *Composite Structures*, 81, pp. 480-490, 2007.
- [58] G. Kaptay, "Interfacial criteria for stabilization of liquid foams by solid particles", *Colloids and Surfaces A: Physicochem. Eng. Aspects*, 230, pp. 67–80, 2004.
- [59] C.C. Yanga and H. Nakae, "The effects of viscosity and cooling conditions on the foamability of aluminum alloy", *J. Mater. Process Technol.*, 141, pp. 202–206, 2003.
- [60] V. Gergely, D.C. Curran and T.W. Clyne, "The FOAMCARP process: foaming of aluminium MMCs by the chalk-aluminium reaction in precursors", *Composites Science and Technology*, 63, pp. 2301–2310, 2003.
- [61] S. Ramachandra, P. S. Kumar and U. Ramamurty, "Impact energy absorption in an Al foam at low velocities", *Scripta Mater.*, 49, 2003, pp. 741–745.
- [62] Y. Fenga, N. Taob, Z. Zhuc, S. Hub and Y. Pan, "Effect of aging treatment on the quasi-static and dynamic compressive properties of aluminum alloy foams", *Mater. Lett.* 57, pp. 4058–4063, 2003.
- [63] P.S. Kumar, S. Ramachandra and U. Ramamurty, "Effect of displacement-rate on the indentation behavior of an aluminum foam", *Mater. Sci. Eng.*, A347, 2003, pp. 330- 337, 2004.
- [64] S.M. Oak, B.J. Kim, W.T. Kim, M.S. Chun and Y.H. Moon, "Physical modeling of bubble generation in foamed-aluminum", *J. Mater. Process. Technol.*, 130–131, pp. 304–309, 2002.
- [65] O. Andersen and G. Stephani, "Solid state and deposition methods", *Handbook of Cellular Metals*, Wiley-Vch Verlag, 2002, pp. 14-21.
- [66] F. Han, H. Cheng, J. Wang and Q. Wang, "Effect of pore combination on the mechanical properties of an open cell aluminum foam", *Scripta Mater.*, 50, pp. 13–17, 2004.
- [67] W. Deqing and S. Ziyuan, "Effect of ceramic particles on cell size and wall thickness of aluminum foam", *Mater. Sci. Eng.*, A361, pp. 45–49, 2003.
- [68] F. Diologent, R. Goodall and A. Mortensen, "Creep of aluminium-magnesium open cell foam", *Acta Mater.*, 57, pp. 830-837, 2009.
- [69] E. Amsterdam, R. Goodall, A. Mortsen and P.R. Onck, "Fracture behaviour of low-density replicated aluminium alloy foams", *Mater. Sci. Eng.*, A 449, pp 186-191, 2008.
- [70] E. Kozaa, M. Leonowicza, S. Wojciechowska, F. Simancik, "Compressive strength of aluminium foams", *Mater. Lett.*, 58, pp. 132– 135, 2003.
- [71] H.F. Cheng and F.S. Han, "Compressive behavior and energy absorbing characteristic of open cell aluminum foam filled with silicate rubber", *Scripta Mater.*, 49, pp. 583–586, 2003.
- [72] W.M. Long, "Theory of hysteresis of the radial pressure", *Powder Metall.*, 6, 1960.
- [73] U. Engstrom, B. Johansson and O. Jacobson, "Properties and tolerances of warm compacted PM materials", *Euro PM 95, Birmingham*, 1995.
- [74] B. Johansson, H. Rutz, F. Hanejlo, S. Luk and U. Engstrom, "High density PM materials for future application", *Euro PM 94, Paris*, 1994.

- [75] H. Abdoli, H. Farnoush, E. Salahi and K. Pourazrang, "Study of the densification of a nanostructured composite powder", *Mater. Sci. Eng., A* 486, pp. 580-584, 2008.
- [76] R.L. Hewitt, W. Wallace, M.C. Malherbe, *Powder Metall.*, 17, 1974.
- [77] P.R. Seeling, J. Wulff, *Trans. AIME*, 166, pp. 492-500, 1946.
- [78] D. Poquillon, J. Lemaitre and J. Lacaze, *Powder Technol.*, 126, pp. 65-74, 2002.
- [79] I.M. Moon and J.S. Choi, *Powder Metall.*, 28, pp. 21-28, 1985.
- [80] M.L. Hentschel and N.W. Page, *J. Mater. Sci.*, 42, pp. 1261-1268, 2007.
- [81] K.T. Kim, J.H. Chao and J.S. Kim, *ASME J. Eng. Mater. Technology*, 122, pp. 119-128, 2000.
- [82] R.A. Thomson, *Ceramic Bulletin*, 60, pp. 237, 1982.
- [83] J. Gil Sevillano, *J. Mater. Res.*, 16, pp. 1238-1240, 2001.
- [84] C.D. Turner, M.F. Ashby, *Acta Mater.*, 44, pp. 4521-4530, 1996.
- [85] A. Simichi, *Mater. Des.*, 24, pp. 585-594, 2003.
- [86] P.J. Denny, *Powder Technol.*, 127, pp. 162-172, 2002.
- [87] R.W. Heckel, *Trans. Metall. Soc. AIME*, 221, pp. 671-675, 1961.
- [88] L.P. Martin, A.M. Hodge, *Scripta Mater.* 57, pp. 229-232, 2007.
- [89] R. Panelli, F.A. Filho, *Powder Technol.*, 114, pp. 255-261, 2000.
- [90] J.B. Fogagnolo, M.H. Roberta, *Mater. Sci. Eng., A* 48, pp. 50-55, 2003.
- [91] R. Panelli, F.A. Filho, *Mater. Sci. Forum*, 299/300, pp. 463-469, 1999.
- [92] M.N. Ibrahim, C.W. Sia and Z.A. Ahmad, "Preliminary step in formulating the optimum electroless nickel bath using Taguchi's method", *Journal Technology(c)*, 37, 2002, pp. 64-67.
- [93] R.A. Kishore, R. Tiwari, A. Dvivedi and I. Singh, "Taguchi analysis of the residual tensile strength after drilling in glass fibre reinforced epoxy composites", *Mater. Sci. Eng., A* 311, pp. 74-82, 2001.
- [94] S.S. Mahapatra, A. Patnaik and A. Satapathy, "Taguchi method applied to parametric appraisal of erosion behaviour of GF-reinforced polyester composites", *Wear*, 265, pp. 214-222, 2008.
- [95] E. Ozbay, A. Oztas, A. Baykasoglu and H. Ozbebek, "Investigating mix proportions of high strength self compacting concrete by using Taguchi method", *Construction and Building Mater.*, 23, pp. 694-702, 2009.
- [96] H. Tanyidli and A. Coskum, "The effect of high temperature on compressive strength and splitting tensile strength of structural lightweight concrete containing fly ash", *Construction and Building Materials*, 22, pp. 2269-2275, 2008.
- [97] C. Falamaki and J. Veysizadeh, "Taguchi design of experiments approach to the manufacture of one-step alumina micro filter/membrane supports by the centrifugal casting technique" *Ceramics Int.*, 34, pp. 1653-1659, 2008.
- [98] J. Banhart, "Service properties and exploitability", *Handbook of Cellular Metals*, Wiley-Vch Verlag, 2002, pp. 313-320.
- [99] T. Wierzbicki, "Crushing behaviour of box coloumn filled with honeycomb or foams", *Proc. Fraunhofer USA Metal Foam Symp.*, 1997.

- [100] C. Haberling, "The range of applications of structural foams based on cellular metals and alternative polymer solutions", *Handbook of Cellular Metals*, Wiley-Vch Verlag, 2002, pp. 299-311.
- [101] R. Kretz, "Prototype by powder compacting foaming", *Handbook of Cellular Metals*, Wiley-Vch Verlag, 2002, pp. 330-337.
- [102] H.P. Degischer, H. Worz, German Patent DE 4206303, 1992.
- [103] H. Martin, R. Ecke, E. Muller, "Synthesis of nanocrystalline silicon carbide powder by carbothermal reduction", *J. Euro. Ceram. Society*, 18, pp. 1737, 1998.
- [104] I.W.M. Brown, K.J.D. Mackenzie, G.V. White, NZ Patent 229777, 1990.
- [105] W.R. Owners, NZ Patents 227753, 237831 and 240953.
- [106] D.S. Perera, "Conversion of precipitated silica from geothermal water to silicon nitride", *J. Mater. Sci.*, 22, pp. 2411-2415, 1987.
- [107] D.S. Perera, "Silicon nitride and β -sialon made from New Zealand raw materials", *J. Aust. Ceram. Society*, 23, pp. 11-20, 1987.
- [108] G.C. Barris, I.W.M. Brown and J.E. Patterson, "Synthesis of submicron β -SiC from colloidal silica precipitated from geothermal discharge water", *Proceeding of the International Ceramic Conference*, 1992, pp. 481-486.
- [109] C.V. Guterl, I. Alix and P. Ehrburger, "Synthesis of tubular silicon carbide (SiC) from a carbon-silica material by using a reactive replica technique: mechanism of formation of SiC", *Acta Mater.*, 52, pp. 1639-1651, 2004.
- [110] Y. Yao, S.T. Lee and F.H. Li, "Direct synthesis of 2H-SiC nanowhiskers", *Chem. Phys. Lett.*, 381, pp. 628-633, 2003.
- [111] D.F. Liu, S.S. Xie, X.Q. Yan, L.J. Ci, F. Shen, J.X. Wang, Z.P. Zhou, H.J. Yuan, Y. Gao, L. Song, L.F. Liu, W.Y. Zhou and G. Wang, "A simple large-scale synthesis of coaxial nanocables: silicon carbide sheathed with silicon oxide", *Chem. Phys. Lett.*, 375, 2003, pp. 269-272.
- [112] A.K. Ray, S.K. Das and L.C. Pathak, "Synthesis of silicon carbide mats using natural fibers", *Mater. Lett.*, 57, pp. 1120-1123, 2003.
- [113] P.C. Silva and J.L. Figueiredo, "Production of SiC and Si₃N₄ whiskers in C + SiO₂ solid mixtures", *Mater. Chem. Phys.*, 72, pp. 326-331, 2001.
- [114] Z. Ryu, J. Zheng, M. Wang and B. Zhang, "Synthesis and characterization of silicon carbide whiskers", *Carbon*, 39, pp. 1929-1941, 2001.
- [115] H. Martin, R. Ecke and E. Muller, "Synthesis of nanocrystalline silicon carbide powder by carbothermal reduction", *J. Euro. Ceram. Society*, 18, pp. 1737, 1998.
- [116] A.G. Turnbull, M.W. Wadsley, CSIRO Thermochemistry System, version 5.1.
- [117] M.E. Bowden, "Carbothermal synthesis of β '-sialon from New Zealand Halloysite", BSc (Hons), Victoria University of Wellington, New Zealand, 1987.
- [118] M.D. Alcala, J.M. Criado and C. Real, "Influence of the experimental conditions and the grinding of the starting materials on the structure of silicon nitride synthesized by carbothermal reduction", *Solid State Ionics*, 141-142, pp. 657-661, 2001.

- [119] A. Pawelec, B. Strojek, G. Weisbrod and S. Podsiadlo, "Preparation of silicon nitride powder from silica and ammonia", *Ceram. Int.*, 28, pp. 495-501, 2002.
- [120] J. Bermudo and M.I. Osendi, "Study of AlN and Si₃N₄ powders synthesized by SHS reactions", *Ceram. Int.*, 25, pp. 607-612, 1999.
- [121] G.C. Barris, I.W.M. Brown and J.E. Patterson, "Synthesis of submicron β -SiC from colloidal silica precipitated from geothermal discharge water", *Proceeding of the International Ceramic Conference*, 1992, pp. 481-486.
- [122] M.E. Bowden, K.J.D. Mackenzie and J.H. Johnston, "Reaction sequence during carbothermal synthesis of β "-sialon from raw materials", *Mater. Science Forum*, 34-36, pp. 599-603, 1988.
- [123] H. Martin, R. Ecke and E. Muller, "Synthesis of nanocrystalline silicon carbide powder by carbothermal reduction", *J. Euro. Ceram. Society*, 18, pp. 1737, 1998.
- [124] G.J. Zhang, J.F. Yang and T. Ohji, "In situ Si₃N₄-SiC-BN composites: preparation, microstructures and properties", *Mater. Sci. Eng.*, A328, 2002, pp.201-205.
- [125] J.S. Benjamin, "Fundamentals of mechanical alloying", *Mater. Science Forum*, 88-90, 1992, pp. 1-18.
- [126] P. Bhattacharya, P. Bellon and R.S. Averback, "Nanocrystalline TiAl powders synthesized by high-energy ball milling: effects of milling parameters on yield and contamination", *J. Alloys Compd.*, 368, pp. 187-196, 2004.
- [127] L. Lu and M.O. Lai, *Mechanical Alloying*, 1998, Boston: Kluwer Academic Publisher.
- [128] C. Suryanarayana, "Mechanical alloying and milling", *Progress in Material Science*, 46, 2001, pp. 1-184.
- [129] E. Szezewak and J.W. Wyrzykowski, "Influence of the mechanical alloying parameters on crystallite size of TiAl powders", *Nanostructured Mater.*, 12, pp. 171-174, 1999.
- [130] F. Charlot, E. Gaffet and B. Zeghami, "Mechanically activated synthesis studied by X-Ray diffraction in the Fe-Al system", *Mater. Sci. Eng.*, A 262, pp. 279-288, 2000.
- [131] M.K. Datta, S.K. Pabi and B.S. Murty, "Thermal stability of Ni Silicides synthesized by mechanical alloying", *Mater. Sci. Eng.*, A 284, pp. 219-225, 2000.
- [132] G. Gonzalez, J. Lara and E. Rodriguea, "The influence of milling intensity on mechanical alloying", *Material Science Forum*, 386-388, 2002, pp. 159-164.
- [133] G.F. Bocchini, R. Esposito, "Influence of operating temperature on shrink fitting pressure of PM dies", *Powder Metall.*, 39-3, pp. 195-206, 1996.
- [134] K.J. Laidler and J.H. Meiser: 'Physical chemistry: reaction in solutions'; 1982, California, The Benjamin Publishing Company.
- [135] A. Simchi, H. Danninger, "Electrical conductivity and microstructure of sintered ferrous materials: sintered iron", *Powder Metall.*, 43, pp. 209-218, 2000.
- [136] A. Simchi, H. Danninger, B. Weiss, "Microstructural modeling of electrical conductivity and mechanical properties of sintered ferrous materials", *Powder Metall.*, 43, pp. 219-227, 2000.

- [137] A. Simchi, H. Danninger, C. Gierl, "Electrical conductivity and microstructure of sintered ferrous materials: iron-graphite compacts", *Powder Metall.*, 44, pp. 148-156, 2001.
- [138] J. Kovacik and F. Simancik, "Aluminium Foam – Modulus of elasticity and electrical conductivity according to percolation theory", *Scripta Mater.*, 39, pp. 239-246, 1998.
- [139] Yi. Feng, H. Zheng, Z. Zhu and F. Zu, "The microstructure and electrical conductivity of aluminum alloy foams", *Mater. Chem. Physc*, 78, pp. 196-201, 2002.
- [140] Y. Sugimura, J. Meyer, A.G. Evans, *Acta Mater.*, 45, pp. 245, 1997.
- [141] H. Kanahasni, T. Mukai, Y. Yamada, K. Higashi, *Mater. Sci. Eng.*, A 308, pp. 287, 2001.
- [142] G.J. Davies and S. Zhen, *J. Mater. Sci.*, 18, pp. 18-25, 1983.
- [143] S. Langlois and F. Courert, *J. Appl. Elecchem.*, 26, pp. 733, 1993.
- [144] P.S. Lui and K.M. Liang, *Mater. Sci. Technol.*, 16, pp.341, 2000.
- [145] I.W. Hall, M. Guden and C.J. Yu, "Crushing of aluminum closed cell foams: Density and strain rate effects", *Scripta Mater.*, 43, pp. 515-521, 2000.
- [146] A. Paul and U. Ramamurty, "Strain rate sensitivity of a closed-cell aluminum foam", *Mater. Sci. Eng.*, A281, pp 1-7, 2000.
- [147] D. Ruan, G. Lu, F.L. Chen and E. Siores, "Compressive behaviour of aluminium foams at low and medium strain rates", *Composite Structures*, 57, pp. 331-336, 2002.
- [148] T.W. Kim, "Determination of densification behaviour of Al-SiC metal matrix composite during consolidation process", *Mater. Sci. Eng.*, A 483-484, pp. 648-651, 2008.
- [149] Z. Song, J. Zhu, L. Ma and D. He, "Evolution of foamed aluminum structure in foaming process", *Mater. Sci. Eng.*, A298, pp. 137-143, 2001.
- [150] C. Motz and R. Pipan, "Deformation behaviour of closed-cell aluminium foams in tension", *Acta Mater.*, 49, pp. 2463-2470, 2001.
- [151] B. Kriszt, Characterization of cellular metals. In: Degischer, H.P., Kristz, B. (Eds), Handbook of cellular metals: Production, Processing, Applications, WILEY-VCH Verlag GmbH, Weinham, 2002, pp. 127-129.
- [152] K.A.. Dannemann, J. Lankford, "High strain rate compression of closed-cell aluminium foams", *Mater. Sci. Eng.*, A293, pp. 157-164, 2000.
- [153] A. Paul and U. Ramamurty, "Strain rate sensitivity of a closed-cell aluminum foam", *Mater. Sci. Eng.*, A281, pp 1-7, 2000.
- [154] A-F. Bastawros, H. Bart-Smith and A.G. Evans, "Experimental analysis of deformation mechanisms in a closed-cell aluminum alloy foam", *J. Mech. Phys. Solids*, 48, pp. 301-322, 2000.
- [155] M.C. Gui, D.B. Wang, J.J. Wu, G.J. Yuan and C.G. Li, "Deformation and damping behaviors of foamed Al-Si-SiCp composite", *Mater. Sci. Eng.*, A286, pp. 282-288, 2000.
- [156] M. Seitzberger, F.G. Rammerstorfer, R. Gradingner, H.P. Degischer, M. Blaimschein and C. Walch, "Experimental studies on the quasi-static axial crushing of steel columns filled with aluminium foam", *Int. J. Solids Structures*, 37, pp. 4125-4147, 2000.

- [157] A.G. Hanssen, M. Langseth and O.S. Hopperstad, "Static and dynamic crushing of circular aluminium extrusions with aluminium foam filler", *Int. J. Impact Eng.*, 24, pp. 475-507, 2000.
- [158] S.P. Santosa, T. Wierzbicki, A.G. Hanssen and M. Langseth, "Experimental and numerical studies of foam-filled sections", *Int. J. Impact Eng.*, 24, pp. 509-534, 2000.
- [159] A. Reyes, O.S. Hopperstad, T. Berstad, A.G. Hanssen and M. Langseth, "Constitutive modeling of aluminum foam including fracture and statistical variation of density", *Euro. J. Mech. Solids*, 22, pp. 815-835, 2003.
- [160] W.M. Huang, "A simple approach to estimate failure surface of polymer and aluminum foams under multiaxial loads", *Int. J. Mech. Sci.*, 45, pp. 1531-1540, 2003.
- [161] M. Doyoyo and T. Wierzbicki, "Experimental studies on the yield behavior of ductile and brittle aluminum foams", *Int. J. Plasticity*, 19, pp. 1195-1214, 2003.
- [162] V. Crupi and R. Montanini, "Aluminium foam sandwiches collapse modes under static and dynamic three-point bending", *Int. J. Impact Eng.*, 34, 509-521, 2007.
- [163] A. Reyes, O.S. Hopperstad and M. Langseth, "Aluminum foam-filled extrusions subjected to oblique loading: experimental and numerical study", *Int. J. Solids Str.*, 41, pp. 1645-1675, 2004.
- [164] C. Chen and N.A. Fleck, "Size effects in the constrained deformation of metallic foams", *Journal of the Mechanics and Physics of Solids*, 50, 2002, pp. 955 - 977.
- [165] F. Yi, Z. Zhu, F. Zu, S. Hu, P. Yi, "Strain rate effects on the compressive property and the energy-absorbing capacity of aluminum alloy foams", *Mater. Characterization*, 47, pp. 417- 422, 2001.
- [166] E.W. Andrews, G. Gioux, P. Onck, L.J. Gibson, "Size effects in ductile cellular solids. Part II: experimental results", *Int. J. Mech. Sci.*, 43, pp. 701-713, 2001.
- [167] C.S. Marchi, A. Mortensen, "Deformation of open-cell aluminum foam", *Acta mater.*, 49, pp. 3959-3969, 2001.
- [168] S.R. Guillow, G. Lu, R.H. Grzebieta, "Quasi-static axial compression of thin-walled circular aluminium tubes", *Int. J. Mech. Sci.*, 43, pp. 2103-2123, 2001.
- [169] A. E. Markaki and T. W. Clyne, "The effect of cell wall microstructure on the deformation and fracture of aluminium-based foams", *Acta mater.*, 49, pp. 1677-1686, 2001.
- [170] C.C. Yanga, H. Nakae, "Foaming characteristics control during production of aluminum alloy foam", *J. Alloys Compds.*, 313, pp. 188-191, 2000.
- [171] O.B. Olurin, N.A. Fleck, M.F. Ashby, "Indentation resistance of an aluminium foam", *Scripta Mater.*, 43, pp. 983-989, 2000.
- [172] O.B. Olurin, N.A. Fleck, M.F. Ashby, "Deformation and fracture of aluminium foams", *Mater. Sci. Eng.*, A291, pp. 136-146, 2000.
- [173] G. Gioux, T.M. McCormac, L.J. Gibson, "Failure of aluminum foams under multiaxial loads", *Int. J. Mech. Sci.*, 42, pp. 1097-1117, 2000.
- [174] T.G. Nieh, K. Higashi, J. Wadsworth, "Effect of cell morphology on the compressive properties of open-cell aluminum foams", *Mater. Sci. Eng.*, A283, pp. 105-110, 2000.

- [175] T. Miyoshi, M. Itoh, T. Mukai, H. Kanahashi, H. Kohzu, S. Tanabe, K. Higashi, "Enhancement of energy absorption in a closed cell aluminum by the modification of cellular structures", *Scripta Mater.*, 41-10, pp. 1055–1060, 1999.
- [176] E. Andrews, W. Sanders, L.J. Gibson, "Compressive and tensile behaviour of aluminum foams", *Mater. Sci. Eng.*, A270, pp. 113–124, 1999.
- [177] M. Liqun, Z. Song, H. Deping, "Cellular structure controllable aluminium foams produced by high pressure, infiltration process", *Scripta Mater.*, Vol. 41, No. 7, pp. 785–789, 1999.
- [178] J.L. Yu, X. Wang, Z.G. Wei, E.H. Wang, "Deformation and failure mechanism of dynamically loaded sandwich beams with aluminum-foam core", *Int. J. Impact Eng.*, 28, pp. 331–347, 2003.
- [179] M. Merklein, M. Geiger, "New materials and production technologies for innovative lightweight constructions", *J. Mater. Process. Technol.*, 125–126, pp. 532–536, 2002.
- [180] O. Kesler, L.J. Gibson, "Size effects in metallic foam core sandwich beams", *Mater. Sci. Eng.*, A326, pp. 228–234, 2002.
- [181] E. Maire, L. Babout, J.-Y. Buffiere, R. Fougères, "Recent results on 3D characterisation of microstructure and damage of metal matrix composites and a metallic foam using X-ray tomography", *Mater. Sci. Eng.*, A319–321, pp. 216–219, 2001.
- [182] X. Zhu, D. Jiang, S. Tan, "Reaction bonding of open cell SiC–Al₂O₃ composites", *Materials Research Bulletin*, 36, 2001, pp. 2003–2015.
- [183] E. Andrews, W. Sanders, L.J. Gibson, *Mater. Sci. Eng.*, A270, pp. 113, 1999.
- [184] P.S. Lui, K.M. Liang, *Mater. Sci. Technol.*, 16, pp.341, 2000.
- [185] P.Y. Huang, Principals of Powder Metallurgy, *Metallurgical Industry Press*, Beijing, 1997.
- [186] T. Benard, J. Burzer, H.W. Bergmann, "Mechanical properties of structures of semifinished products joined to aluminium foam", *J. Mater. Processing Technol.*, 115, pp. 20–24, 2001.
- [187] V.S. Deshpande, N.A. Fleck, "Isotropic constitutive models for metallic foams", *J. Mech. and Phys. Solids*, 48, pp.1253–1283, 2000.
- [188] Y.P. Kathuria, "Laser assisted aluminum foaming", *Surface and Coatings Technology*, 142–144, pp. 56–60, 2001.
- [189] F. Scheffler, R. Herrmann, W. Schwieger, M. Scheffler, "Preparation and properties of an electrically heatable aluminium foam/zeolite composite", *Microporous and Mesoporous Materials*, 67, 2004, pp. 53–59.
- [190] K. Boomsma, D. Poulikakos, F. Zwick, "Metal foams as compact high performance heat exchangers", *Mechanics of Mater.*, 35, pp. 1161–1176, 2003.
- [191] S.A. Meguid, J.C. Stranart, J. Heyerman, "On the layered micromechanical three-dimensional finite element modelling of foam-filled columns", *Finite Elements in Analysis and Design*, 56, 2001, pp. 423–433.
- [192] F.Y.C. Boey, A.I.Y. Tok, "Porous AlN ceramic substrates by reaction sintering", *J. Mater. Processing Technol.*, 140, pp. 413–419, 2003.
- [193] N. Altinkoka, A. Demira, I. Ozsertb, "Processing of Al₂O₃/SiC ceramic cake performs and their liquid Al metal infiltration", *Composites: Part A*, 34, 2003, pp. 577–582.

- [194] D.D. Durda, G.J. Flynn, T.W.V. Veghten, Impacts into porous foam targets: possible implications for the disruption of comet nuclei, *Icarus* 163 (2003) 504–507.
- [195] V.S. Sokolinsky, H. Shen, L. Vaikhanski, S.R. Nutt, “Experimental and analytical study of nonlinear bending response of sandwich beams”, *Composite Structures*, 60, pp. 219–229, 2003.
- [196] M. Zupan, C. Chen, N.A. Fleck, “The plastic collapse and energy absorption capacity of egg-box panels”, *Int. J. Mech. Sci.*, 45, pp.851–871, 2003.
- [197] E.E. Gdoutos, I.M. Daniel, K.A. Wang, “Compression facing wrinkling of composite sandwich structures”, *Mech. Mater.*, 35, pp. 511–522, 2003.
- [198] E.W. Andrews, L.J. Gibson, “On notch-strengthening and crack tip deformation in cellular metals”, *Mater. Lett.*, 57, pp. 532–536, 2002.
- [199] G.A. Kardomateas, G.J. Simitses, L. Shen, R. Li, “Buckling of sandwich wide columns”, *Int. J. Non-Linear Mechanics*, 37, pp. 1239 – 1247, 2002.
- [200] M.S. Phanikumar, R.L. Mahajan, “Non-Darcy natural convection in high porosity metal foams”, *Int. J. Heat and Mass Transfer*, 45, pp. 3781–3793, 2002.
- [201] C. Motz, R. Pippin, “Fracture behaviour and fracture toughness of ductile closedcell metallic foams”, *Acta Mater.*, 50, pp. 2013–2033, 2002.
- [202] O.B. Olurin, M. Arnold, C. Köfner, R.F. Singer, “The investigation of morphometric parameters of aluminium foams using micro-computed tomography”, *Mater. Sci. Eng.*, A328, pp. 334–343, 2002.
- [203] I.W. Hall, M. Guden, T.D. Claar, “Transverse and longitudinal crushing of aluminum-foam filled tubes”, *Scripta Mater.*, 46, pp. 513–518, 2002.
- [204] W.Chen, T. Wierzbicki, O. Breuer, K. Kristiansen, “Torsional crushing of foam- filled thin-walled square columns”, *Int. J. Mech. Sci.*, 43, pp. 2297–2317, 2001.
- [205] B. Zettl, H. Mayer, S.E. Stanzl-Tschegg, “Fatigue properties of Al–1Mg–0.6Si foam at low and ultrasonic frequencies”, *Int. J. Fatigue*, 23, pp. 565–573, 2001.
- [206] V.S. Deshpande, N.A. Fleck, M.F. Ashby, “Effective properties of the octet-truss lattice material”, *J. Mech. Physics of Solids*, 49, pp. 1747 – 1769, 2001.
- [207] H.X. Peng, Z. Fan, J.R.G. Evans, “Bi-continuous metal matrix composites”, *Materials Science and Engineering*, A303, 2001, pp. 37–45.
- [208] E.W. Andrews, L.J. Gibson, “The role of cellular structure in creep of two-dimensional cellular solids”, *Mater. Sci. Eng.*, A303, 2001, pp. 120–126.
- [209] O.B. Olurin, K.Y.G. McCullough, N.A. Fleck, M.F. Ashby, “Fatigue crack propagation in aluminium alloy foams”, *Int. J. Fatigue*, 23, pp. 375–382, 2001.
- [210] E.W. Andrews and L.J Gibson, “The influence of crack-like defects on the tensile strength of an open-cell aluminum foam”, *Scripta Mater.*, 44, pp. 1005–1010, 2001.
- [211] W. Chen, T. Wierzbicki, “Relative merits of single-cell, multi-cell and foam-filled thin-walled structures in energy absorption”, *Thin-Walled Structures*, 39, pp. 287–306, 2001.
- [212] S.Y. Kim, B.H. Kang, J. Kim, “Forced convection from aluminum foam materials in an asymmetrically heated channel”, *Int. J. Heat and Mass Transfer*, 4, pp. 1451–1454, 2001.

- [213] C. Chen, T.J. Lu, N.A. Fleck, "Effect of inclusions and holes on the stiffness and strength of honeycombs", *Int. J. Mech. Sci.*, 43, pp. 487-504, 2001.
- [214] K. Boomsma, D. Poulikakos, "On the effective thermal conductivity of a three-dimensionally structured fluid-saturated metal foam", *Int. J. Heat and Mass Transfer*, 44, pp. 827-836, 2001.
- [215] B. Zettl, H. Mayer, S.E. Stanzl-Tschegg, H.P. Degischer, "Fatigue properties of aluminium foams at high numbers of cycles", *Mater. Sci. Eng.*, A292, pp. 1-7, 2000.

APPENDIX A
RECORD OF PUBLICATIONS

RECORD OF PUBLICATIONS		
CONFERENCE ATTENDED	ORGANIZER	DATE
Conference on Advanced Materials and Nanotechnology (CAMAN 2009).	Institute of Advanced Technology, UPM	3 rd – 5 th November 2009
3 rd Powder Metallurgy Symposium & Exhibition 2009.	Faculty of Engineering & Architecture, UKM	12 th – 13 th August 2009
National Postgraduate Conference on Engineering, Science & Technology (NPC 2009).	Universiti Teknologi PETRONAS (UTP)	25 th – 26 th March 2009
International Conference on Plant Equipment and Reliability (ICPER 2008).	Universiti Teknologi PETRONAS (UTP)	27 th – 28 th March 2008
National Postgraduate Conference on Engineering, Science & Technology (NPC 2008).	Universiti Teknologi PETRONAS (UTP)	31 st March 2008

PUBLICATIONS	JOURNAL/BOOK CHAPTER	DATE ACCEPTANCE/ PUBLISHED/SUBMITTED
Fabrication of Aluminium Foam Through Pressure Assisted High-Frequency Induction Heated Sintering Dissolution Process: An Experimental Observation.	Powder Metallurgy A publication of the Institute of Materials, Minerals and Mining (IOM ³), London, UK.	Accepted on 09/11/2009 DOI:10.1179/003258909X12573447241581
Preliminary Development of the Fabrication of Aluminium Foam Through Pressure Assisted Sintering Dissolution Process.	Journal of Materials Processing and Technology (Elsevier Impact Factor = 1.143)	Accepted on 18/15/2010 DOI:10.1016/j.matprotec/2010.05.007
The Effect of Mechanical Milling and Temperature on The Carbothermal Process of Silica Sand.	American Institute of Physics (AIP)	Published in May 2008 Volume 1017 pp. 310-314

Empirical Relationship Between Relative Electrical Conductivity and Relative Density of The Al Foam Fabricated Through Pressure Assisted Sintering Dissolution Process.	Science Publication Journal Cited in Scopus and Thompson ISI index	First review: Accepted to journal with minor changes on 21/08/09
A Method For The Manufacturing Aluminium Foam Body Using Powder Metallurgy Technique	Malaysian Patent	Draft of the patent is under the review process by UTP
Process of Producing Silicon Carbide Compound	Application No. For Malaysian Patent: PI 20060688 Applicant: SIRIM Berhad	Filing Date: 15 December 2006
Award Received During Period of Study (01/12/2006 – 30/11/2009)		
“Gold” – Participation in Postgraduate Studies in the 24 th edition of Universiti Teknologi Petronas Engineering Design Exhibition.		
“2nd Runner Up” – – Participation in Most Innovative Award in the 24 th edition of Universiti Teknologi Petronas Engineering Design Exhibition		

Acceptance letter for Powder Metallurgy Journal

Date: 09/11/2009
To: "Mazli Mustapha" mazli_mustapha@sirim.my,weu7685@yahoo.com
From: "Powder Metallurgy" pom.ed@maney.co.uk
Subject: Your submission POM1609R1

Ref.: POM1609R1
 Fabrication of Aluminium Foam Through Pressure Assisted High-Frequency Induction Heated Sintering Dissolution Process (PASDP): An Experimental Observation

Dear Mazli

Thank you for submitting a revised version of the above submission and your response to the comments made by the reviewers. I am pleased to confirm that the paper is accepted for publication in Powder Metallurgy. It was accepted on 09/11/2009

The paper will be passed to the Production Department who may contact you if there are problems with the figure or text files supplied. You will receive PDF proofs by email in the near future. If you require further information on the progress of your paper, please contact pom@maney.co.uk.

The final version of your paper will be posted online shortly before being assigned to a journal issue. You can view your paper at <http://www.ingentaconnect.com/content/maney/pm/pre-prints>. Please note that you can cite your paper using the Digital Object Identifier (DOI).

Thank you for submitting your work to Powder Metallurgy.

With kind regards

John W Martin
 Executive Editor, Powder Metallurgy

Powder Metallurgy

ISSN 0032-5899, Online ISSN: 1743-2901



 **Maney Publishing**
Research • Knowledge • Innovation

 **IOM³**
The Journal of Materials, Minerals and Mining

Authors wishing to cite fast track papers should give the journal name and the article DOI. This will enable reference linking via CrossRef and allow forward and backward citation tracking systems to associate the fast track citation with the final journal reference.

Publisher: Maney Publishing on behalf of Institute of Materials, Minerals and Mining

64 fast track articles have been identified for this journal

all issues

- **Fabrication of aluminium foam through pressure assisted high frequency induction heated sintering dissolution process: an experimental observation**
Author: M. Mustapha, F. Mustapha, O. Mamat, P. Hussain
Appeared or available online: May 14, 2010
- **Production of bronze powders by water jet cooled rotating disc atomisation**
Authors: S. Öztürk, G. Usta, B. Öztürk
Appeared or available online: May 14, 2010
- **Stiffness variation of porous titanium developed using space holder method**
Authors: L. Reig, V. Amigó, D. Busquets, J. A. Calero
Appeared or available online: May 14, 2010
- **Mechanical alloying of Cu-SiC materials prepared with utilisation of copper waste chips**
Author: A. S. Prosviryakov, A. A. Aksenov, M. E. Samoshina, M. G. Kovaleva, D. O. Ivanov
Appeared or available online: May 14, 2010
- **Preparation and characterisation of metal powder slurries for use as precursors for metal foams made by gel casting**
Author: A. R. Kennedy, Y. Lin
Appeared or available online: May 14, 2010
- **Simplified PM processing of mechanically alloyed aluminium**
Authors: J. J. Fuentes, J. A. Rodríguez, E. J. Herrera
Appeared or available online: May 10, 2010

Browse

Search

- ☒ Electronic content
 - ☐ Journal or book title
- Advanced search
Search history

Shopping cart

Tools

Print

Bookmarking options

Sign In

Text size: A | A | A

Fabrication of aluminium foam through pressure assisted high frequency induction heated sintering dissolution process: an experimental observation

Authors: M. Mustapha, F. Mustapha, O. Mamat, P. Hussain

Source: Powder Metallurgy

Publisher: Maney Publishing

next > | view fast track articles

Abstract:

A process based on powder metallurgy approach was developed to produce open celled aluminium foam. In the preparation of foam specimens, the Al powder and the NaCl (leaching agent) were dry mixed together in order to prepare a homogeneous mixture. The blended mixture was then subjected to pressure assisted sintering in which a pressure beyond atmospheric level is externally applied to the specimen during high frequency induction heated sintering. The embedded leaching agent was then dissolved in order to leave behind an open celled Al with the same chemical composition as that of the original Al powder. The final material is highly porous and has an interconnected porosity network. The structure of the resulting material has three levels of porosity (i.e. main cells, windows and microporosity). The X-ray diffraction analysis shows that, as the content of NaCl is increased to the volume fraction of 60%, no traces of NaCl presents in the foam.

Document Type:

DOI: 10.1179/003258909X12573447241581

The full text article is not available for purchase.

The publisher only permits individual articles to be downloaded by subscribers.

next > | view fast track articles

Share this item with others: These icons link to social bookmarking sites where readers can share and discover new web pages.



Browse

Search

- ☒ Electronic content
 - ☐ Journal or book title
- Advanced search
Search history

Shopping cart

Tools

Bookmarking options

Sign In

Content Key:

- ☐ Free
- ☒ New
- ☒ Open Access
- ☐ Subscribed
- ☐ Free Trial

Text size: A | A | A

Acceptance letter for Journal of Materials Processing Technology

Date: May 18, 2010
To: mazli_mustapha@sirim.my;weu7685@yahoo.com
cc: c.caceres@uq.edu.au
From: "Journal of Materials Processing Technology" protec@elsevier.com
Subject: Your Submission

Ms. Ref. No.: PROTEC-D-09-01593R2
Title: Preliminary development of the fabrication of aluminium foam through pressure assisted sintering dissolution process
Journal of Materials Processing Technology

Dear Mr Mustapha,

I am pleased to tell you that your paper "Preliminary development of the fabrication of aluminium foam through pressure assisted sintering dissolution process" has been accepted for publication in the Journal of Materials Processing Technology.

Congratulations.

With kind regards,

Carlos Horacio Caceres, Ph.D.
Subject Editor
Journal of Materials Processing Technology

Publication of part of work in American Institute of Physics (AIP)

The screenshot shows a web browser window displaying the AIP conference proceedings page. The title of the paper is "The Effect of Mechanical Milling and Temperature to the Carbothermal Reduction Process of Silica Sand". The authors listed are E. A. Ghapur, M. Mustapha, F. Ismail, S. Sidek, and B. Loh. The abstract describes the investigation into the formation of silicon nitride and silicon carbide compounds from silica sand powders with carbon in a nitrogen atmosphere at temperatures between 1350 °C and 1550 °C. The paper is part of the AIP Conf. Proc. - May 20, 2008 - volume 1017, pp. 310-314. The page also includes a sidebar with links to download the citation, email abstract, and other related resources.

The Effect of Mechanical Milling and Temperature to the Carbothermal Reduction Process of Silica Sand

AIP Conf. Proc. - May 20, 2008 - volume 1017, pp. 310-314
CURRENT ISSUES OF PHYSICS IN MALAYSIA: National Physics Conference 2007 - PERFIK 2007. doi:10.1063/1.2949860
Issue Date: 20 May 2008

ABSTRACT

E. A. Ghapur^a, M. Mustapha^a, F. Ismail^a, S. Sidek^a and B. Loh^a
^aDepartment of Physical Science, Faculty of Science & Technology, Universiti Malaysia Terengganu, 21030 Kuala Terengganu, Terengganu, Malaysia
^bStructural Materials Program, Advanced Materials Research Center, SIRIM Berhad, Lot 34, Jalan Hi-Tech 3/5, Kulim Hi-Tech Park, 09000 Kulim, Kedah, Malaysia

This paper presents the investigation carried out to study the formation of silicon nitride and silicon carbide compound from the reaction of silica sand powders with carbon in nitrogen with 5% hydrogen atmosphere at temperatures between 1350 °C to 1550 °C. The effect of mechanical milled silica sand and different temperature during carbothermal reduction process was determined. The morphology of the synthesis products was characterized using scanning electron microscopy and its composition was determined by elemental and X-ray phase analysis. The formation of silicon nitride compound was facilitated by using silica sand with distorted structure by mechanical milling method. Further increased on temperature will lead to the formation of silicon carbide compound. ©2008 American Institute of Physics

Permalink: <http://link.aip.org/link/JAPPCPS10173101>

BUY THIS ARTICLE (US\$24)

Correlate | CiteLike | CiteUs | CiteSource

DOWNLOAD CITATION | MYCITATION
EMAIL ABSTRACT | PERMISSIONS/REPRINTS
EPUB/HTML ALERT | RESEARCH TOOLKIT
BLOG THIS ARTICLE | PRINTER FRIENDLY

KEYWORDS and PACS

Keywords
machining, scanning electron microscopy, ceramics

PACS